ORNL
MASTER COPY

ORNL-3789
UC-4 – Chemistry
TID-4500 (39th ed.)

REACTOR CHEMISTRY DIVISION

ANNUAL PROGRESS REPORT

FOR PERIOD ENDING JANUARY 31, 1965

OAK RIDGE NATIONAL LABORATORY
operated by
UNION CARBIDE CORPORATION
for the
U.S. ATOMIC ENERGY COMMISSION

Printed in USA. Price $7.00. Available from the Clearinghouse for Federal Scientific and Technical Information, National Bureau of Standards, U.S. Department of Commerce, Springfield, Virginia

LEGAL NOTICE

This report was prepared as an account of Government sponsored work. Neither the United States, nor the Commission, nor any person acting on behalf of the Commission:

A. Makes any warranty or representation, expressed or implied, with respect to the accuracy, completeness, or usefulness of the information contained in this report, or that the use of any information, apparatus, method, or process disclosed in this report may not infringe privately owned rights; or

B. Assumes any liabilities with respect to the use of, or for damages resulting from the use of any information, apparatus, method, or process disclosed in this report.

As used in the above, "person acting on behalf of the Commission" includes any employee or contractor of the Commission, or employee of such contractor, to the extent that such employee or contractor of the Commission, or employee of such contractor prepares, disseminates, or provides access to, any information pursuant to his employment or contract with the Commission, or his employment with such contractor.

ORNL-3789

Contract No. W-7405-eng-26

REACTOR CHEMISTRY DIVISION ANNUAL PROGRESS REPORT

For Period Ending January 31, 1965

Director

W. R. Grimes

Associate Directors

E. G. Bohlmann
H. F. McDuffie
G. M. Watson

Senior Scientific Advisors

F. F. Blankenship
C. H. Secoy

APRIL 1965

OAK RIDGE NATIONAL LABORATORY
Oak Ridge, Tennessee
operated by
UNION CARBIDE CORPORATION
for the
U. S. ATOMIC ENERGY COMMISSION

Summary

PART I. MOLTEN-SALT REACTORS

1. HIGH-TEMPERATURE PHASE EQUILIBRIUM STUDIES

Equilibrium phase behavior was examined in systems of relevance to molten-salt reactor technology. A three-dimensional model of the LiF-BeF_2-ZrF_4 phase diagram was constructed to afford a simple graphic display of the crystallization behavior of the MSRE fuel and coolant salt. Reexamination was made of the LiF-BeF_2 system, using very pure mixtures of LiF and BeF_2. Significant refinement in the liquidus values was achieved. Equilibrium constants for the disproportionation of UF_3 were determined in a study of $UF_3 \rightleftharpoons UF_4$ high-temperature equilibria. The phase diagram of the system was constructed as a part of the study and shows a substantial solid solubility of UF_4 in UF_3. Fractionation experiments were conducted with the MSRE four-component fuel mixture LiF-BeF_2-ZrF_4-UF_4 at cooling rates approximating those in the reactor drain tanks. Little compositional variation was observed. Crystallographic data were obtained for all solid phases in the LiF-LnF_3 and NaF-LnF_3 (Ln = La through Lu) binary systems, and phase diagrams were constructed for the 30 systems. A high-temperature fluorite phase was found in 12 of the NaF-based systems; its compositional variability is extended in proportion to the difference in Na^+/Ln^{3+} cation size. Hexagonal-orthorhombic transitions were determined for SmF_3, GdF_3, TbF_3, TmF_3, and LuF_3, using quenching and high-temperature x-ray methods. Further information relating cationic sizes with fluoride crystal chemistry was obtained in examinations of the systems NaF-ScF_3, NaF-BiF_3, and KF-LaF_3. Systems of potential use in advanced reactor technology, KCl-UCl_3, NaF-KF-ThF_4, and LiF-NaF-ThF_4, were examined with respect to liquid-solid equilibrium transitions and crystal phase properties. The crystal structure of $NaNdF_4$ and related compounds was established from single-crystal data. Accurate values for the atom positions in Li_2BeF_4 were obtained from a structural analysis of single crystals.

2. RADIATION CHEMISTRY OF THE MOLTEN-SALT REACTOR SYSTEM

A series of in-pile tests, at the Materials Testing Reactor (MTR), of the compatibility of Molten-Salt Reactor materials has been completed. Earlier tests in the series had furnished evidence, such as the presence of CF_4 and F_2 in the gas phase, that raised searching questions about the stability of the fuel under irradiation. Favorable answers to these questions were confirmed by the most recent test. The key factor was the use of heaters to maintain a high temperature in the fuel during periods when the MTR was inoperative. Under these circumstances there was no evidence of F_2 release from the fuel, and virtually none of the untoward effects encountered earlier were manifested. Off-gas from the in-pile capsules was analyzed for CF_4, but none could be detected, even at a level of 0.1% of the xenon resulting from fission; the limiting level of detection is lower by a factor of 1000 than that which would be of significance for MSRE operation. The amount of uranium deposited on the graphite specimens proved to be inconsequential, particularly in light of evidence that it arose from traces of adhering fuel. The actual amounts were about 2 orders of magnitude lower than those found in earlier experiments in which F_2 was evolved. Other results of experiment 47-6 showed that the radiolysis of CF_4 was low, the fission product iodine and tellurium were partially removed from

capsules that were swept with helium during irradiation, the molybdenum test specimens may have been embrittled during the exposure, the ruthenium had mainly left the salt, and the graphite and INOR-8 surfaces were apparently unaffected. The MSRE components appear to be quite compatible for use under the planned conditions of temperature and power density.

A prototype in-pile capsule experiment has been designed to obtain further information of the effects of irradiation on fuel salt for a Molten-Salt Reactor. Primary objectives are to obtain high power density in the fuel salt (up to 200 w/cm^3) and high burnup (up to 50% ^{235}U) through operation of the experiment in an existing facility of the ORR. Pertinent features of the experiment are: (1) circulation of the fuel salt (by thermal convective flow), (2) provisions for removing samples of the salt and cover gas while operating in-pile, (3) provisions for salt additions to maintain salt inventory, and (4) ability to maintain the fuel molten at all times. Operation for more than 1200 hr of an out-of-pile mockup of the proposed capsule experiment shows that salt circulation in the range of 2 to 10 cm^3/min (total volume of salt is $\sim$85 cm^3) can be maintained, and that sampling and addition of salt are feasible with procedures suitable for in-pile use. Sufficient heating capacity and cooling capacity are provided in duplicate. The salt can be kept molten at all times, and operating temperature ($\sim$1200°F) can be maintained while removing up to $\sim$8 kw of fission heat.

The gamma irradiation of a solid fluoride salt, simulating MSR fuel, resulting in the generation of substantial quantities of fluorine gas, was reported previously. The examination of salt and graphite recovered from this experiment has revealed results in each material consistent with fluorine generation; no such effects were found in an unirradiated control. No effects on the INOR-8 container were noted in either experiment. A mechanism involving reaction of fluorine and uranium hexafluoride with the graphite is suggested to explain an observed transport of uranium to the graphite.

Fluorine release from solid inorganic fluorides under electron irradiation was studied further to (1) provide more complete and accurate information on the dependence of G_{F_2} on dose and (2) determine the effect of thermal annealing upon this dependence. Three materials of interest to the Molten-Salt Reactor Program were studied: simulated MSRE fuel, Li_2BeF_4, and Li_6BeZrF_{12}. No fluorine was released from the Li_6BeZrF_{12}, but the other two materials produced fluorine on irradiation. The G_{F_2} values for both salts passed through maximum values with increasing irradiation time; values for annealed MSRE fuel salt were about half those of the directly frozen salt; values for the Li_2BeF_4 were still lower. A model is proposed to account for the characteristics of the radiolysis of MSRE fuel salt at temperatures below 110°C.

A beryllium-window x-ray tube, coupled closely to a beryllium-window cell, permitted x-ray doses of 10^{21} ev/hr to a 10-g sample of test salt (simulated MSRE fuel). The yield of fluorine was found to increase with the length of the irradiation period, up to 90 hr, while the yield of oxygen decreased; the total equivalent *G* value was constant at around 0.09 molecule per 100 ev of energy absorbed. The *G* value for equivalent fluorine from the irradiation of ThF_4 was raised from 0.005 to 0.014 following treatment with 100% fluorine at 350°C to remove impurities.

3. CHEMICAL STUDIES OF MOLTEN SALTS

Continued studies of the chemistry and thermodynamics of molten fluorides are being made by the method of equilibrating the melts with gaseous HF and H_2O. The reactions which occur produce both oxide and hydroxide ions in the melts. Equilibrium measurements made on melts saturated with BeO and ZrO_2 gave, respectively, the activity coefficients of BeF_2 and ZrF_4, both of which varied with composition. In addition, the solubilities of these oxides were found to be lower than previous, less direct, estimates. The capacity of an LiF-BeF_2-ZrF_4 melt, approximating the MSRE fuel composition, to contain oxide without ZrO_2 precipitation was found to be generally higher than previous estimates, and to be strongly a function of melt composition and temperature. The efficiency of oxide removal from molten fluorides by HF under equilibrium sparging conditions was calculated and compares well with experience during purification of large batches of salt for the MSRE.

Equilibrium measurements have been made, over the temperature interval of 565 to 970°C, of the reaction

$$UF_4 + \tfrac{1}{2}H_2 \rightleftharpoons UF_3 + HF ,$$

both with solid UF_4 and UF_3 and with these compounds dissolved in molten $LiF\text{-}BeF_2$ mixtures. These measurements suggest that $-\Delta F^f_T(UF_3) = 351.4 - 52.8(T°K/1000)$ is in agreement with previous estimates by Brewer, and that disproportionation of UF_3 should prove no problem under UF_4 and UF_3 concentrations and temperature conditions of the MSRE.

Reduction of SO_4^{2-} in molten fluoride mixtures and subsequent removal of sulfur as H_2S on sparging with H_2-HF mixtures has been studied to improve sulfur removal in the processing of MSRE fuels.

Reference electrodes based on the Be/Be^{2+} and H_2, HF electrode reactions have been found suitable for use in molten Li_2BeF_4. When they were combined to form the cell

$$Be(s) + 2HF(g, 1\ atm) = H_2(g, 1\ atm) + BeF_2(d)\ ,$$

potential values of 1.916, 1.849, and 1.775 v were obtained at 504, 597, and 703°C respectively. These values are in fair agreement with the existing thermochemical data.

A practical method was deduced for interpreting the peak-shaped current-voltage curves obtained by linear voltage scan voltammetry of molten fluoride solutions. The method was verified by studies of the reductions of Fe(II) and Ni(II).

Good reproducibility was achieved by the use of derivative voltammetry in the determination of U(IV) in molten $LiF\text{-}BeF_2$ mixtures by electrochemical reduction at pyrolytic graphite electrodes.

A continuing study of the viscosity of the $LiF\text{-}BeF_2$ system is showing how viscosity changes with composition, how these changes are correlated with structural parameters of the individual components, and how this system compares with the analogous $MgO\text{-}SiO_2$ system. Measurements were obtained with a rotational viscometer on 17 mixtures having compositions varying between pure BeF_2 and 50 mole % LiF–50 mole % BeF_2. Over this composition range the viscosity changed by more than 6 orders of magnitude while the energy of activation for viscous flow decreased from 60 kcal for pure BeF_2 to 14 kcal for 50 mole % LiF–50 mole % BeF_2. The pronounced lowering of viscosity and energy of activation with increasing LiF concentration is believed to be associated with the gradual breakup of the disordered three-dimensional network of Be-F tetrahedra.

A simple experimental method for estimating the density of molten fluoride mixtures in the laboratory was developed for use in an inert-atmosphere glove box enclosure. It is based on measurement, by means of an electrical probe, of the height of a known weight of melted mixture in a cylinder of known diameter.

Studies of the vapor species given off from an $LiF\text{-}BeF_2$ (66-34 mole %) near its liquidus temperature were made by the use of a time-of-flight mass spectrometer. The results suggested that BeF_2 was the dominant species evolved from the molten state. A sudden, small temperature increase after a long period of time below the melting point was followed by a large relative increase in the Li_2F^+ peak, suggesting that dimeric $(LiF)_2$ was the species vaporizing.

Vacuum distillation of simulated MSRE fuel salt afforded essentially complete recovery of the carrier salt and recovery of about 80% of the UF_4 with an overall separation factor in excess of 50 from europium trifluoride used to simulate rare earth fission products. The separation was done in an INOR-8 still, by single-pass distillation, with heat supplied by an ordinary vertical tube furnace. The balance of the UF_4 should be readily recovered free from rare earths by fluorination.

Gas transport properties of an impregnated graphite (CGB grade) chosen for use in the MSRE have been evaluated and compared with those for other reactor and commercial graphites. Permeability of the MSRE graphite to gases (such as krypton and xenon) is considerably higher than that of CEY graphite, which is much inferior with regard to permeation by the MSRE fuel.

Removal of ^{135}Xe from the MSRE by stripping of gas from fluid flowing at a low rate through the pump bowl has been re-estimated. Assumption of a film which controls mass transfer to the core graphite (and a similar film restricting transfer to the gas bubbles in the stripper), with the known characteristics of the MSRE and its graphite, leads to the conclusion that xenon poisoning will be a considerable problem in the reactor.

Prompt removal of protactinium from irradiated thorium would minimize neutron losses to ^{233}Pa and permit production of isotopically pure ^{233}U. Such a prompt removal requires a mobile thorium-bearing blanket as well as an associated protactinium-separation process. Malm and Fried, in an old study (1951) at Argonne National Laboratory, found some volatility of protactinium from a mixture

of $ThCl_4$ and $AlCl_3$. We have made a brief study of this system to assess its usefulness as a special mobile blanket. The solubility of thorium chloride in molten aluminum chloride at temperatures in the range 200–350°C was found to be 1 mole %. In tracer experiments, it was shown that protactinium could be leached from solid $ThCl_4$ by liquid $AlCl_3$ in amounts substantially exceeding the thorium chloride which dissolved, and could be volatilized with the $AlCl_3$. Quartz and other adsorbents were shown to be capable of removing protactinium from $AlCl_3$ in both liquid and vapor phases.

4. FLUORIDE SALT PRODUCTION

A total of 15,300 lb of ^7LiF-BeF_2 (66 mole % ^7LiF) is required as coolant (44 ft^3) and flush (75 ft^3) mixtures for the Molten-Salt Reactor Experiment (MSRE). About 11,250 lb of ^7LiF-BeF_2-ZrF_4-UF_4 (65.0-29.1-5.0-0.9 mole % respectively) is required as reactor fuel. Uranium tetrafluoride (some enriched to 93% in ^{235}U and the rest depleted in this isotope) and ^7LiF were obtained from AEC sources; other fluorides were obtained by competitive bids from commercial sources at the highest purity available at a reasonable price.

The tuel was prepared an an ^7LiF-BeF_2-ZrF_4 fuel solvent mixture, an ^7LiF-$^{235}UF_4$ (27 mole % UF_4) fuel concentrate, and an ^7LiF-UF_4 mixture with 27 mole % of depleted UF_4; these mixtures are to be blended to the proper fuel composition in startup of the MSRE. The ^7LiF-BeF_2 mixtures (coolant and flush salt) were prepared to the final composition in one operation.

All chemicals except ^7LiF were blended into the predetermined mixture composition as received. The ^7LiF was heated to 600°C with occasional agitation under hydrogen fluoride–helium atmospheres to increase the bulk density and to diminish the water content of the material before use. All mixtures except those containing $^{235}UF_4$ were processed in batches of 250 to 300 lb; batches containing enriched uranium were restricted to 6-in.-diam vessels and to $^{235}UF_4$ contents of not more than 15 kg.

All the large batches were mixed, blended, and melted under hydrogen fluoride–helium atmospheres. Metallic beryllium was added to aid in the rapid reduction of SO_4^{2-} and the liquid was decanted into the nickel processing equipment. Oxide, sulfide, and chloride ion were removed, with little attack on the equipment, by treatment with gaseous mixtures of HF and H_2. Final treatment, to reduce FeF_2 and NiF_2, was accomplished by treatment with pure H_2. The small ^{235}U-containing batches were given a similar treatment but without the addition of metallic beryllium. All purified melts were stored under pure helium until needed.

The coolant and flush salts have been transferred into the MSRE tanks. The MSRE fuel is in final stages of preparation.

PART II. AQUEOUS REACTORS

5. CHEMISTRY OF PRESSURIZED-WATER REACTOR SYSTEMS

Studies of the water chemistry of the pressurized-water loop at the ORR were continued until loop operation was shut down in the summer of 1964. With the water temperature in the range 149 to 176°C, average concentrations of corrosion product Fe, Ni, Mn, Cr, and Co were (in 10^{-9} *M*), respectively, 200, 150, 14, 3, and 1 as soluble species, and 40, 3, 0.1, 5, and <0.1 as suspended solids. The corrosion products (and the associated radioactivity) were thus largely in the soluble form. The behavior of this dissolved material, the apparent recrystallization of suspended solids, and the results of further testing of magnetite absorbents, all continued to support the possibility that a bed of high-temperature magnetite could be used to recover radioactive corrosion products from circulating water in PWR systems after the water had passed through the reactor core.

The solubility of Fe_3O_4, the normal corrosion product of PWR steel-water systems, has been studied in pure H_2O saturated at room temperature with 1 atm of H_2. The tests indicate that the solubility is $\sim 0.33 \times 10^{-6}$ *M* (in iron) at 260°C, and 1.5×10^{-6} *M* at 200°C.

6. CORROSION STUDIES FOR AQUEOUS REACTORS AND CHEMICAL PROCESSES

Corrosion testing in support of the High Flux Isotope Reactor has been completed. Both dynamic and static tests were conducted in water adjusted

to a pH of 5.0 at 50 and 100°C. Although aluminum alloys pitted in crevice regions and beryllium pitted randomly on all surfaces, the attack of neither metal was sufficient to preclude its use in the construction of the reactor. Tests with numerous other materials, including plastics, were conducted to determine their suitability in reactor components.

Corrosion tests in various chloride-containing solutions of direct interest to the Transuranium Processing Facility have been completed. Because of the corrosive nature of these solutions, most tests were of the behavior of tantalum and zirconium. Both materials have adequate corrosion resistance to the process solutions, but both absorb corrosion-product hydrogen which, in sufficient quantities, produces embrittlement.

The corrosion resistance of numerous metals and alloys has been examined in both gaseous and aqueous environments of interest to various fuel element reprocessing schemes. In addition, the corrosion resistance of type 304 ELC stainless steel was determined in calcining waste products with and without additions of different glass-forming chemicals.

7. MECHANISMS OF CORROSION OF ZIRCONIUM ALLOYS

The mechanism of radiation corrosion is being investigated by comparing the behavior of fast-neutron-irradiated specimens with unirradiated controls. Specimen pretreatments were varied in order to provide different amounts of oxide film and different amounts of dissolved oxygen near the surface during irradiation. Weight gain and ac film impedances were measured during postirradiation exposure to 300°C steam plus oxygen. Tentative conclusions from previous work were verified: irradiation damage in the metal enhances corrosion, and a small retardation of corrosion results from irradiation of oxide film. It was also concluded that the damage in the metal is probably associated with dissolved oxygen, and it increases with increasing concentrations of oxygen.

The general equation $i = 2A \sinh BE$, which related the anodic film growth current i to the field across the oxide film E has been shown to apply for anodic film growth on zirconium in oxygenated dilute H_2SO_4 at temperatures from 200 to 284°C. The temperature dependence of the field coefficient B was investigated. The results have shown that B increases with temperature, contrary to theory, which predicts $B = qa/kT$, where q is the valency charge on the mobile ion (or vacancy) and a is the activation distance. Others have reported similar observations for zirconium and other metals at temperatures below 100°C. However, the temperature dependence is more marked and the activation distance is much larger than expected. The applicability of local field concepts which relate the dielectric behavior of the oxide through the dielectric constant ϵ was tested. Use of the Lorentz field, $[(\epsilon + 2)/3](V/X)$, led to more reasonable agreement with these than did use of the Maxwell field, V/X. It appears that a field-dependent movement of ions across the oxide film is an important step in the corrosion.

8. PHYSICAL CHEMISTRY OF HIGH-TEMPERATURE AQUEOUS SYSTEMS

The electrical conductances of sulfuric acid solutions were measured at temperatures from 0 to 800°C and at pressures to 4000 bars. From the results, limiting equivalent conductances of H_2SO_4 were obtained as a function of temperature and density. The second ionization constant of H_2SO_4 was calculated at temperatures up to 300°C, and the first constant at temperatures between 400 and 800°C.

By using computer techniques and available experimental values for the dielectric constant of water at temperatures to 350°C, an empirical three-parameter equation was developed to represent the behavior of $\mu^2 g$ (where μ is the dipole moment and g is the Kirkwood correlation function) as a function of temperature and density. Values of $\mu^2 g$ calculated from this equation were introduced into the Kirkwood equation to estimate the dielectric constant of water to 800°C and 1.0 g/cm^3.

The second dissociation constant of H_2SO_4 was calculated at temperatures from 25 to 350°C through the use of values for the solubility of $CaSO_4$ and its hydrates determined both in aqueous sulfuric acid solutions and NaCl solutions at temperatures from 25 to 350°C. The values calculated compared favorably with literature values to 225°C and with those obtained at these and higher temperatures by the conductance method.

By using equivalent conductances from both the present studies and the literature, and some transference numbers for low temperature from the

literature, limiting ionic conductances of the potassium, sodium, hydrogen, chloride, bisulfate, and sulfate ions in water were estimated to 400°C. The limiting conductances of lithium, ammonium, and hydroxide ions were estimated to 300°C.

Isopiestic studies of aqueous salt solutions were extended to 165°C with the results confirming observations previously made at 150°C. Specifically, the ϕ vs m curves of the 1-1 salts possess a curvature opposite to that encountered at 25°C. Evidence is provided which discounts the phenomenon of hydrolysis of the weaker electrolytes, for example, LiCl, as a relevant factor in accounting for the unusual ϕ vs m behavior.

Previously reported measurements of the hydroalysis of Th^{4+} in 1 m $(Na)ClO_4$ solution at 0 and 95°C, along with similar measurements of others at 25°C, have been analyzed by means of a general least-squares computer program to determine the simplest set (scheme) of hydrolysis products $Th_x(OH)_y^{(4x-y)+}$ with which they are consistent. At least four species must be assumed to approximate the data; however, the best such schemes – (I) x,y: 1,1 – 1,2 – 2,2 – 5,12 or (II) x,y: 1,1 – 1,2 – 2,3 – 6,15 – yield systematic deviations from the data which are similar at all three temperatures. Two schemes of five species – (III) x,y: 1,1 – 1,2 – 2,2 – 3,6 – 6,15 and (IV) x,y: 1,1 – 1,2 – 2,2 – 4,8 – 6,15 – fit the data within the expected experimental error; scheme (IV) is the better. Formation quotients were obtained for the species in each scheme at all three temperatures. Those for scheme (IV) indicated that the enthalpy and entropy changes per OH^- bound in the three polymeric species were nearly constant.

The solubilities of $MgSO_4 \cdot H_2O$ (and $MgSO_4 \cdot D_2O$) were determined in H_2SO_4-H_2O (and D_2SO_4-D_2O) solutions at temperatures from 200 to 350°C and at concentrations of H_2SO_4 to 1.8 m. At solution concentrations of SO_3 (total sulfate) between approximately 10^{-4} and 0.1 m, the monohydrate was found to be hydrolytically unstable; it was converted partially to an oxysulfate or $Mg(OH)_2$ (or both) depending upon temperature and solution concentration.

9. INTERACTION OF WATER WITH PARTICULATE SOLIDS

Differential heats of adsorption of water on thoria have been calculated for three characteristic samples of thoria from calorimetrically determined heats of immersion with varying amounts of presorbed water. Data for two of the three indicate a high degree of surface heterogeneity, while the third appears to possess regions of near homogeneity. Evidence is presented that the surface area is a function of the amount of water on the sample. The data also suggest that, if the contribution from chemisorption is properly excluded, excellent agreement of surface areas obtained by water adsorption and by nitrogen adsorption can be realized.

Gravimetric adsorption-desorption studies of water vapor yield type II isotherms with a high-relative-pressure hysteresis loop characteristic of porous solids. However, samples which have been outgassed at temperatures higher than the isotherm temperature show an extremely slow ability to adsorb water which cannot be recovered by normal high-vacuum procedures. This phenomenon manifests itself by the failure of the adsorption and desorption branches to close at low coverage and even at high vacuum. During months of exposure to water vapor, the separation diminishes until eventually the curves coincide.

Exploratory experiments have demonstrated the applicability of infrared spectroscopy to the identification of adsorbed species and their bonding characteristics. Thin thoria disks have been prepared which seem to meet the requirements of high-resolution infrared spectroscopy. The intensities of the absorbance peaks of both water and carbon dioxide shift with temperature.

Waterlogging failure of a leaky fuel element is dependent on stresses imposed on the cladding as water is ejected by heat-up upon increasing reactor power. These stresses are interrelated functions of (1) the permeability of the fuel element, (2) the available void volume, (3) the geometry of the fuel elements, and (4) the rate of temperature rise. Experimental data indicate that an analytic interpretation of waterlogging stresses in terms of these variables and the pressure-volume-temperature properties of water is feasible. This is particularly true for the stresses imposed by flow from water expansion within the element. The effect of defect parameters on the pressure drop across the defect has not yet been considered in depth. Flashing flow both at the defect and within the fuel element appears important. Critical flow controls the flow rate through the defect. Reasonable limitations on reactor startup procedures, even if empirical,

should supply guidelines which will minimize the likelihood of waterlogging failure.

Gas evolution from sol-gel (thoria–3% urania) reactor fuel material was studied by outgassing samples at temperatures up to 1200°C. The amount of gas evolved was found to be a linear function of the surface area of the material. The composition of the gas, a mixture of CO_2, CO, H_2, and probably H_2O, also appeared to be strongly affected by the surface area of the material; nearly pure CO_2 was evolved from materials of low (0.1 m^2/g) surface area. Reversible adsorption of CO_2 was demonstrated; removal of CO_2 by outgassing was rapid and complete at temperatures of 500°C and above.

PART III. GAS-COOLED REACTORS

10. DIFFUSION PROCESSES

The "dusty-gas" model, a mathematical model that describes gas transport in porous media as the migration of gas molecules through a uniformly distributed collection of giant molecules (dust particles) which are fixed in space, has been applied in previous reports to account for the isothermal diffusion of binary gas mixtures through porous septa under uniform total pressure and in the presence of a pressure gradient. The model has recently been extended to include the relative separation of two gas components as the result of a thermal gradient. As required, the model predicts no separation at very low pressures (Knudsen region), and pressure-independent separation in the hydrodynamic region. In the transition region, however, the behavior is predicted to be quite complex; it varies with the temperature, molecular masses, and intermolecular forces of the gas molecules involved.

Isothermal gaseous diffusion measurements were made with the systems He-Ar, Ar-Xe, and He-Xe over the temperature range 0 to 120°C in an effort to resolve a previous discrepancy between directly measured diffusion coefficients for He-Xe mixtures and values determined from the composition dependence of the viscosity coefficients of such mixtures. The present results are in good agreement with those derived from viscosity data. This agreement suggests the feasibility of an indirect determination of diffusion coefficients for cases and conditions where viscosity is the more expedient property to measure.

Investigations of the migration behavior of actinides in pyrocarbons have continued to employ two distinct types of diffusion experiments: (1) thin-layer experiments that yield penetration data and diffusion coefficients related to the concentration profiles, and (2) constant-potential experiments that yield estimates of the actinide solubility in pyrocarbons – as well as additional values of the coefficients.

The thin-layer experiments indicate that no appreciable actinide migration occurs at temperatures below 1460°C. Above this temperature, all actinides studied show comparable behavior. Sets of coefficients obtained at two different thorium concentrations, in identical pyrocarbons, show that the extent of migration increases as the actinide concentration increases.

The extent of actinide migration increases with increase in concentration of defects (as revealed by x-ray and electron-microscope techniques) in pyrocarbons. Autoradiographs well establish the nonuniform diffusion of actinides in highly defective pyrocarbons. Defect concentrations (and diffusion rates) in pyrocarbons can be markedly reduced by ultrahigh-temperature anneals of actinide-free specimens.

Preliminary results from constant-potential experiments verify the effect of concentration on actinide migration. Structural changes resulting from the presence of actinide within the specimens are quite apparent through electron-microscope examinations, since the uranium concentration associated with these experiments is relatively high. The uranium solubility does not depend upon the temperature at which the diffusion experiment is performed; rather, it assumes a constant value within the temperature range wherein defect concentrations remain constant. It is clear that structural changes induced by ultrahigh temperatures depress actinide migration, but structural changes induced by the presence of actinides enhance actinide migration.

11. REACTIONS OF GRAPHITE WITH OXIDIZING GASES

The rates of reaction of a 1-in.-diam sphere of ATJ graphite (the graphite used as the outer shell of AVR fuel spheres) with low concentrations of

H_2O and CO_2 in flowing helium (1 atm) were measured at temperatures of 775 to 975°C. Activation energies of ~50 and ~60 kcal/mole were found for H_2O and CO_2, respectively, at oxidant concentrations in the range of 100 to 500 vpm (parts per million by volume). Apparent orders of ~0.6 were observed for both the H_2O- and CO_2-graphite systems at 875°C and oxidant concentrations ranging from 50 to 750 vpm. Reaction rates increased with increasing burnoff and increasing flow rates. The H_2O- and CO_2-graphite reactions were found to be strongly retarded by both H_2 and CO additions.

Oxidation of 1.5-in.-diam unfueled spheres of ATJ and Speer Mod-2 graphites by steam (partial pressure of ~730 torrs) was studied at 800, 900, and 1000°C. Similar studies of 2.36-in.-diam ATJ graphite spheres, simulated AVR spheres, and fueled mold-injected AVR spheres also were performed. A linear relationship was found between the reaction rates and surface area of the remaining specimen over a wide range of burnoffs for both grades of graphites at 1000°C. Surprisingly, the specific reaction rates (based on BET surface) of the two graphites are essentially equal at 1000°C. Activation energies of ~50 and ~60 kcal/mole were measured for 2.36- and 1.5-in.-diam ATJ spheres respectively. Smaller CO to CO_2 ratios were found in the effluent gases obtained from the larger spheres. Simulated and fueled AVR spheres gave reaction rates and activation energies approximating those found for the 2.36-in.-diam ATJ spheres.

12. IRRADIATION BEHAVIOR OF HIGH-TEMPERATURE FUEL MATERIALS

Effect of uranium burnup on rate of release of five fission-gas isotopes from fuel particles with laminar, duplex, and triplex pyrocarbon coatings has been determined during irradiation of the particles to temperatures as high as 1400°C. Fission-gas retention of both the duplex and triplex coatings was shown to be sufficient (at least to 16% burnup) for present reactor applications. The duplex coatings showed reaction zones and cracks at the interface between the core and inner laminar layer. The triplex coating, with an inner buffer layer of porous carbon, exhibited, on postirradiation examination, little or no reaction with the fuel core. Mechanical breaking of selected layers showed that the outer layer of triplex coatings contained very small quantities of fission products.

Simple gamma scanning of irradiated fuel spheres can show fuel loading patterns and abnormalities in fuel distribution and can give relative uranium burnup values. Irradiation has no detectable effect on compression or impact resistance of 1-½-in.-diam spheres, but compression resistance of 2.36-in.-diam spheres, on the basis of extremely limited data, may be somewhat reduced by irradiation. Metallographic examinations indicate less damage to triplex coatings of the fuel particles than to duplex or laminar coatings.

Three metal-clad fuel elements, of ten that have been examined, had suffered cladding failures during irradiation. One failure was caused by a combination of nitride embrittlement of the cladding and overheating of the fuel, and the other two were caused by fuel element distortion and loss of sufficient cooling at local areas.

13. FISSION-GAS RELEASE DURING FISSIONING OF UO_2

The defect-trap model previously described for release of fission gases from UO_2 has been refined, and an equation has been developed which qualitatively reconciles the experimental observations. The irradiation facility has been modified to allow neutron flux or temperature to be maintained at a constant value while the other is cycled sinusoidally. From fission-gas release behavior under these conditions we hope to determine the parameters in the mathematical model.

An experiment with fine-grain UO_2 has demonstrated that grain boundaries do not act as paths of rapid escape, as once believed, but rather as traps which anchor migrating fission gas. This experiment also verified the effect of fission rate and temperature on fission-gas release as predicted by the defect-trap model.

14. BEHAVIOR OF CERAMIC MATERIALS UNDER IRRADIATION

The annealing of radiation-induced changes was studied by x-ray diffraction for the silicates cordierite, zircon, steatite, and forsterite. Five different irradiation doses were used; annealing was

studied at temperatures to 1250°C. The threshold temperature for stored-energy release is compared with the temperature that initiates restoration of x-ray diffraction lines. Phase transformations are identified.

A fluxmeter method for thermal conductivity measurements has been developed for use in studies of the annealing of radiation effects.

Fast-neutron irradiation to high dosage levels produces effects that may prejudice the use of ceramic materials as fuel matrices, moderators, or other components of nuclear devices. Irradiation of BeO compacts and crystals has been carried to dosages of nearly 10^{22} neutrons (of energy >1 Mev)/cm^2; similar experiments with MgO and other oxides are in progress, and a study of radiation stability of refractory carbides has been initiated.

Gross damage to BeO results primarily from the breaking of grain boundaries by the radiation-induced anisotropic expansion of the crystal lattice; this damage increases with neutron dosage and decreases with increasing irradiation temperature. Magnesium oxide, a cubic crystal, cannot fail by this mechanism. However, it shows considerable damage, spread randomly among samples receiving more than 7×10^{20} neutrons/cm^2, and increasing with increasing temperature. Expansion of MgO compacts saturates at 1% on exposure to 10^{21} neutrons/cm^2 at 150°C, and is very slight at 800°C and above. The gross damage, which increases with temperature at high temperatures, is probably due primarily to thermal stresses.

15. MISCELLANEOUS STUDIES FOR SOLID-FUELED REACTORS

The cubic fluorite-structure solid solution of thoria and urania after equilibration in air at temperatures from 1000 to 1550°C gives, by chemical analysis, values for the mole fraction of UO_3 in the range from 0.3 to nearly 0.4 if the mole fraction of thoria is less than about 0.4. However, a correlation of lattice parameter with composition suggests that the mole fraction of UO_3 never exceeds 0.25. Efforts to improve the quenching, handling, and analytical techniques have yielded UO_3 mole fractions slightly lower than heretofore but have not resolved the discrepancy.

Studies of the UO_2-ZrO_2 system by equilibrating the oxide phases in the presence of molten fluoride mixtures at temperatures of 500 to 1000°C have been supplemented by high-temperature x-ray diffractometric observations of transformations in oxide mixtures of various overall compositions. In agreement with the results of previous studies in the presence of molten fluoride fluxes, the equilibrium oxide phases were found to consist only of the pure components (cubic UO_2 and monoclinic ZrO_2) at temperatures below 800°C. Between 800 and 1100°C there was evidence of a very small solubility of ZrO_2 in UO_2. At temperatures of 1100 to 1450°C, face-centered UO_2 and tetragonal ZrO_2 solid solutions were found as the equilibrium solids in diffractometric studies. A tentative phase diagram for the UO_2-ZrO_2 system, involving a postulated intermediate phase of composition near $UO_2 \cdot 3ZrO_2$, is proposed for use in planning further work.

A preliminary investigation has been made of the stability of gaseous SO_2, a potential coolant for fast reactors, to irradiation at room temperature by alpha particles from radon. Initial mixing of the gases produced evidence of damage (marked Tyndall effect and separation of liquid phase), but examination after nearly complete decay of the radon suggested little damage. It appears that the decomposition products recombined, even at room temperature, as the radiation level diminished.

A compilation of the neutron flux spectra in the various experimental facilities (including the horizontal beam hole, poolside, and capsule irradiation facilities) has been made. The compilation includes both the energy and the spatial variations of the neutron flux whenever data were available. The results are presented in both tabular and graphical form.

PART IV. NUCLEAR SAFETY

16. EXPERIMENTS WITH THE CONTAINMENT MOCKUP FACILITY

The Containment Mockup Facility (CMF) consists primarily of a 6.7-ft^3 stainless steel tank in which fission product aerosols released from irradiated fuel specimens by induction heating can be aged and sampled to study the transport behavior of the fission products. This equipment is located in a hot cell to facilitate experimentation with

high-burnup fuel materials. It has been in operation for approximately two years. During the past year it was modified by the addition of a more elaborate filter pack (May pack) to separate the different forms of iodine and equipment for counting and separating particles into different size groups. It was also changed to permit operation with air or steam-air pressures up to 30 psig.

Two experiments were performed in the CMF with stainless-steel-clad UO_2 fuel specimens irradiated to a trace level. The specimens were melted in a flowing air stream, and the fission product aerosol was transferred to the tank and allowed to age for approximately 3 hr. It was found that ten times as much iodine penetrated a 1.5-in.-thick charcoal bed when part of the air in the tank was unfiltered, as compared with the penetration observed when only filtered air was present in the aging tank. Approximately equal amounts of particulate and molecular iodine were present at the end of the aging period.

The first meltdown experiment with highly irradiated (7000 Mwd/ton) UO_2 was performed with the furnace and aging tank filled with air at atmospheric pressure for comparison with the results obtained with trace-level-irradiated fuel. Release values were about the same with both irradiation levels except for tellurium, which was 55% for the high-burnup fuel and 12% for the trace-level material. Only 0.005% of the plutonium content of the fuel and about the same percent of the UO_2 vaporized. The iodine, cesium, and tellurium concentrations in the tank aerosol dropped rapidly in the first 10 min of the aging period; about 75% of the iodine on the tank wall desorbed during passage of 1.5 tank volumes of argon through the tank after the 3-hr aging period. The number of airborne particles decreased by a factor of 10^3; but the amount of filterable activity did not change significantly, indicating that the particles were too small to deposit rapidly.

Organic iodine compounds have been observed to form in simulated reactor accident experiments and presumably could be formed in real accidents. Iodine combined in this form is frequently called "penetrating" iodine because it is poorly retained by charcoal beds, which are very efficient in trapping molecular iodine. In an effort to determine the mechanism by which molecular iodine is converted to organic compounds, attempts were made to make methyl iodide by the gas-phase reaction of methane and iodine. Only trace amounts of methyl iodide were formed under all the conditions used, including exposure to a high-level gamma source, showing that gas-phase reactions probably do not account for the observed amounts of organic iodine compounds.

Different fractions of "penetrating" iodine were found in experiments in the containment tank. The highest fraction (0.21) was found when the aerosol contained vaporized fuel particles in a steam-air mixture. Low concentrations of iodine seemed to result in a higher penetration of charcoal beds. Wet stainless steel retained less iodine than a dry surface. "Washout" of iodine from the tank atmosphere by condensing steam removed about 50% of the iodine in the tank.

Iodine produced in simulated reactor accidents can be separated into three fractions: particulate iodine (iodides or iodine adsorbed on particles), reactive iodine (principally molecular iodine or HI), and nonreactive iodine (organic compounds are the principal constituents identified to date). It is necessary to know the fraction of iodine that may be present in each form in different accident environments to permit evaluation of the hazard of this important fission product. The effectiveness of some components of the filter pack used for this separation is reduced by steam. Side streams removed between stages of the complex filter pack are passed through diffusion tubes or through additional filter packs to evaluate the efficiency of the different components of the main-stream filter pack. In one experiment, it was found that 13% of the iodine that passed through a series of eight silver screens was in a reactive form.

In nuclear safety experiments, it is desirable to use fuel materials which have been blended with the proper concentrations of various elements simulating a high-burnup fuel, along with millicurie amounts of tracer isotopes of each element. The simulated fuel has the advantage of not being highly radioactive and of having the same amount of fission product elements as high-burnup fuel. However, it has the disadvantage that the distribution and the chemical form of the fission products are different from those in real fuel elements. Accordingly, it is essential to establish the validity of the simulation. In the first simulation test, fuel pellets were fabricated containing the concentration of iodine, tellurium, ruthenium, cesium, strontium, and molybdenum corresponding to a burnup of 10,000 Mwd/ton. The pellets were clad in stainless steel and were melted in the CMF;

and the behavior of the resulting aerosol, after aging for 3.5 hr, was compared with that of one released from an actual fuel element melted under similar (but not identical) conditions. Iodine, cesium, strontium, and ruthenium showed comparable release values, but differences were found in the release values of tellurium. The validity of the simulation will be examined again after results of an experiment with high-burnup fuel under conditions strictly comparable to those employed in the simulation run become available.

A new facility, designed for installation in one of the hot cells in Building 4501, will have the following features:

1. a fission product aerosol generator for heating 100-g quantities of high-burnup fuel to the melting point of UO_2 and at intermediate temperatures,
2. a primary vessel simulator that can be heated to 800°C,
3. a 1000-gal pressurized containment shell that can be supplied with different interior surfaces,
4. a recycle filter test facility,
5. provision for simulation of top or bottom breaks in the primary vessel.

This versatile nuclear safety research facility is currently being designed, and construction will start in the near future.

The possibility exists that movement of overheated UO_2 fuel in a loss-of-coolant reactor accident could occur at lower temperatures than have been generally assumed, due to interaction of oxidized cladding materials with the UO_2 fuel. It becomes of interest, therefore, to determine melting points of such mixtures. A resistance-heating device was used in a preliminary examination of this problem. Iridium ribbons were used for measurements made in air, while tungsten foil was used for vacuum measurements. A significant atmospheric effect on the melting point of oxidized stainless steel–UO_2 mixtures was observed, with much lower values being obtained in air than in vacuum. Melting points increased with increased weight of UO_2 in the mixture. Oxidized stainless steel–UO_2 mixtures melted in the range 1500 to 1650°C (compared to 2850°C, the melting point of pure UO_2). A ZrO_2-Zr-UO_2 mixture prepared by melting a Zircaloy-clad UO_2 fuel specimen in air melted at 2150°C in air as compared with 1435°C for an oxidized stainless steel–UO_2 mixture under the same conditions.

17. BEHAVIOR OF FISSION PRODUCTS RELEASED DURING IN-PILE SIMULATED LOSS-OF-COOLANT ACCIDENTS

In-pile experiments are being continued to study the characteristics and behavior of fission products released by melting or vaporizing miniature stainless-steel-clad UO_2 fuel elements in the ORR in a variety of atmospheres. Atmospheres of dry helium, moist helium, steam-helium-hydrogen, dry air, moist air, and steam-air have been employed. The appearance of the fuel residue was affected markedly by the type of atmospheric environment. The most significant variation in the behavior of fission products as a function of atmosphere is the high release of ruthenium and iodine in moist air from a zone whose minimum temperature is 1000°C. The ruthenium was retained by high-efficiency filters. The iodine penetrated the high-efficiency filters to a greater extent than in other atmospheres, but was retained by charcoal. The nonvolatile fission products do not appear to be greatly affected by the composition of the atmosphere, and in all cases less than 1% of the inventory was released from the 1000°C zone.

In experiments in which steam was a component of the sweep gas, substantial quantities of fission products were trapped by the condensate and collected in the condenser.

In a single experiment which used a long period of heating at high temperature, the fuel appeared to have melted even though the temperature never reached the melting point of UO_2; it is likely that components of oxidized stainless steel (particularly Fe_2O_3) may substantially reduce the melting point of UO_2. Release of iodine and tellurium from this experiment was lower than from others because their precursors at the time of release were nonvolatile. The strontium and barium release was higher because their precursors were volatile.

Interpretation of the iodine data from in-pile UO_2 melting experiments leads to the conclusions that: (1) a major fraction of released iodine stops on metal surfaces, although this deposition is inhibited by moisture in the atmosphere, (2) particulate filters effectively stop iodine released in all atmospheres investigated except moist air, and (3) only 0.0001% of the iodine found in each of these experiments penetrated the filter system, in-pile charcoal trap, and outlet tubing.

A facility designed and built in the ORR to provide high-burnup fuel for the in-pile UO_2 melting experiments is being used to irradiate UO_2 capsules to approximately 21,000 Mwd/ton. Additional equipment required to perform hot-cell assembly of the experimental apparatus has been installed and satisfactorily tested.

18. RELEASE OF FISSION PRODUCTS DURING MELTING OF FUELS UNDER REACTOR TRANSIENT CONDITIONS

Previously irradiated pellets of UO_2 clad in stainless steel have been melted under moist air at 45 psia in the TREAT reactor; in each of two experiments, a reactor transient of 75 msec period melted the cladding and about 75% of the UO_2. Analysis of the gas, distribution of the fission products, and analysis of particle sizes of the gas-borne material were obtained. About one-third of the volatile fission products (I, Te, and Cs) were released from the UO_2, but less than 1% escaped from the fuel autoclave.

The experimental assembly was successfully modified to permit melting of miniature UO_2 fuel elements in steam at about 1000 psia and sampling of the gases, aerosols, and fission products produced. With this assembly, a stainless-clad and a Zircaloy-clad UO_2 specimen have been exposed to 77-msec-period transients in TREAT. Effective operation of the valves to permit sampling was obtained in only one of the attempts. Analysis of the materials is in progress.

19. BEHAVIOR OF RADIOIODINE

Radioiodine, prepared by decomposition of palladium iodide or by action of dichromate upon alkali iodides, can be separated by distillation at −78°C into two fractions. The less-volatile fraction appears to consist almost entirely of molecular iodine. The more-volatile fraction, which is of interest because of its similarity to forms of iodine which occur in reactor accidents, has been examined by partition between water and organic solvent, by Knudsen effusion cell techniques, by gas chromatography, by mass spectrometry, and by use of composite diffusion tubes. All techniques indicate this fraction to consist primarily of methyl iodide with perhaps a trace of higher homologs. The composite diffusion tubes, however, suggest that an additional and perhaps unstable species that is less volatile than I_2 occurs in the less-volatile fraction.

The presence of compounds of radioiodine in air-steam mixtures can be detected in modified composite diffusion tubes at temperatures above 100°C, but alternative and better methods are needed for identification of these compounds.

Filter systems used to retain particulate matter have been shown to sorb appreciable radioiodine from particulate-free air streams. Cellulose filters remove the least, and polyvinyl chloride and cellulose acetate filters remove the most, iodine of the materials tested. The correction necessary to obtain the radioiodine carried on particulates is appreciable.

Reaction of radioiodine and the vapors of complex organic materials (such as lubricating oil, paint, rubber and plastic insulation, and dioctyl phthalate, DOP) likely to be found in reactor environments have been shown to occur at room temperature. As much as 10% of the radioiodine was converted to organic iodide compounds.

Iodine is removed efficiently from He-H_2O and H_2-H_2O atmospheres and somewhat less efficiently from H_2O-air atmospheres by heated mild steel surfaces. Stainless steel surfaces remove iodine less efficiently from neutral or reducing atmospheres and very inefficiently in oxidizing atmospheres above 250 to 300°C.

Sorption of iodine at low pressures by stainless steel follows a logarithmic rate law; the surface reaction becomes slower the more heavily oxidized the steel surface. Sorption of cesium by stainless steel is much slower, but it proceeds to much higher surface coverages than those shown by iodine.

Composite diffusion tubes have been employed in evaluating the performance of the different components of May packs; the latter are iodine samplers designed to discriminate between the various forms of gas-borne radioiodine. The behavior of volatile iodine in two May packs, one operated with fairly dry air and one operated with moderately moist air, was observed to be generally consistent with the designed functions of the May pack components.

The retention of methyl iodine and of I_2 by four American and one British activated charcoals has been studied as functions of temperature and

relative humidity over a wide range. At relatively low humidity and at temperatures ranging up to 150°C, all charcoals tested effectively retain CH_3I and I_2. At room temperature with a relative humidity of approximately 75%, all the charcoals were effective for I_2 but relatively ineffective for CH_3I. With high steam concentrations, methyl iodide is poorly retained at temperatures of 95 to 130°C; efficiency of retention of I_2 under these conditions is reduced to about 98%.

20. BEHAVIOR OF RADIOACTIVE AEROSOLS

A program is under way to improve techniques for the study of radioactive aerosols, and to provide effective and easy-to-handle aerosols that will simulate, in their behavior in filter systems, the radioactive species released in nuclear accidents. Effective testing of iodine removal systems of the NS "Savannah" and of the ORR has been accomplished with elemental iodine. Promising simulated dispersions of particulate materials have been prepared in arcs struck between electrodes of UO_2. These "simulants" have been used in tests of the efficiency of absolute filters. A technique for studying radioactive aeresols, using fibrous filters, has been refined and is being used to test filtration theory. When this program has been carried further, it is anticipated that materials and techniques will be available which will permit a valid in-place demonstration of the reliability of an engineered safeguard.

PART V. OTHER ORNL PROGRAMS

21. CHEMICAL SUPPORT FOR SALINE WATER PROGRAM

Solubilities of $CaSO_4$ in aqueous $NaNO_3$ solutions were determined at temperatures from 125 to 350°C. They correlated rather well with the previously determined solubilities in $NaCl$-H_2O solutions and with an extended Debye-Hückel relationship in which the logarithm of the solubility was plotted against a function of the ionic strength, $\sqrt{I}/(1 + 1.5\sqrt{I})$.

On the basis of newly and previously determined values for the solubilities of $CaSO_4$ in $NaCl$-H_2O and $NaNO_3$-H_2O solutions to 350°C, a general computer program was written that permitted the iterative calculation of concentration limits in saline waters at temperatures between 25 and 350°C within which precipitation either of $CaSO_4$, $CaSO_4 \cdot \frac{1}{2}H_2O$, or $CaSO_4 \cdot 2H_2O$ is avoided.

A small titanium loop has been equipped for carrying out electrochemical corrosion studies in flowing solutions. Exploratory experiments indicate that polarization behavior and corrosion rates can be studied to temperatures of 200°C.

Serious attack of titanium alloys in sodium chloride solutions at elevated (≧100°C) temperatures has been observed. This attack was initially observed in connection with studies of the corrosion of aluminum alloys in such solutions, being carried out in titanium equipment. Titanium specimen holders used in exposing the aluminum alloys were clamped together with bands made of 0.008-in. A55 titanium sheet stock. The holders are inserted in the loop piping with fittings which direct the solution flow through the holders so that the titanium bands are in a semistagnant annulus between the holder and the pipe. Characteristically, but by no means consistently, the corrosion originated in the crevice between the specimen holder and the clamping band. Similar results have been obtained with bolted coupon specimens in autoclaves.

The observations thus far indicate the following:

1. The severity and frequency of attack increase with temperature above 100°C.
2. Attack increases with acidity but has been observed at pH values up to 8.7.
3. The frequency of attack increases with exposure time.
4. Attack occurs with a variety of alloys, although preliminary results indicate that a 0.2% palladium alloy is more resistant.

In an effort to gain some insight into the mechanism of titanium crevice corrosion in sodium chloride solutions, electrochemical polarization studies have been initiated. Polarization studies with titanium electrodes indicate appreciable overvoltage for the reduction of oxygen in 1 *M* NaCl solutions. As expected, the lower the pH or the higher the temperature, the greater the ease of reduction. In the absence of oxygen, titanium polarizes severely, with cathodic current densities being very low until a cathodic potential

sufficient for the reduction of water is achieved. Anodic polarization experiments show no active region in 1 *M* NaCl at pH values of either 3 or 6, with or without oxygen, at temperatures between 100 and 200°C. The tests suggest that for titanium to corrode in the crevice region, the small volume of solution in the crevice must develop a pH of less than 3. Studies to determine the pH at which activation of titanium is possible in the temperature range 100 to 200°C are planned.

22. SOLVENTS FOR THE FLUORIDE VOLATILITY PROCESS

The solvent system $KF-ZrF_4-AlF_3$ seems to possess optimum combination of low cost, high AlF_3 capacity, and low corrosivity for use in fluoride volatility processing of aluminum-uranium alloy fuels. Data have been obtained to establish within 1 mole % the compositions along the 600°C isotherm for this system. Potassium fluoride–zirconium tetrafluoride and $LiF-NaF-ZrF_4$ mixtures offer promise, in dissolving high concentrations of UF_4 at 600°C, as solvents for dissolving zirconium-clad UO_2 fuel elements. It is possible that the LiF-KF eutectic can dissolve sufficient FeF_2, NiF_2, and CrF_3 to serve as a medium for reprocessing stainless-steel-clad UO_2 fuels.

23. SUPPORT FOR SPACE PROGRAMS

The fate of the hydrogen entering the NaK-78 primary coolant of the SNAP-8 reactor from the zirconium-uranium hydride fuel elements will depend on the diffusion rates of the hydrogen from the NaK through the metal walls of the system, and on the solubility behavior of the hydrogen. The permeation rates of hydrogen through the major structural metal, type 316 stainless steel, in the presence of NaK at temperatures of 543, 593, and 704°C were found to differ little from values obtained in the absence of NaK. Slight increases were attributed to removal of oxides from permeation cell surfaces by the NaK.

The solubility of hydrogen in NaK-78 was determined at six temperatures from 300 to 704°C. For unsaturated solutions the solubility depended on the square root of the hydrogen pressures, and varied only slightly with temperature. At temperatures of 300 to 400°C enough hydrogen could be dissolved at pressures below 1 atm to result in precipitation of a metal hydride. Precipitation-decomposition pressures were consistent with the literature.

The addition to NaK-78 of 1 to 4 at. % lithium considerably diminished the hydrogen activity both by association with it in the NaK and by precipitation. The behavior suggests that dissolved hydrogen exists in liquid metal mixtures as largely undissociated metal hydride molecules; fraction of the dissolved hydrogen with a particular alkali metal depends on the concentration of that metal and its affinity for hydrogen.

The Reactor Chemistry Division is participating in a project the objectives of which are to (1) collect available information and data on the thermophysical, electrical, mechanical, and chemical properties of space power source and capsule container materials; (2) critically evaluate and estimate limits of confidence in the data; (3) evaluate the capabilities of ORNL and other organizations to obtain any particular data; and (4) forecast data which may be forthcoming for current or projected programs of other organizations.

24. EFFECT OF RADIATION ON ORGANIC MATERIALS

The earlier findings of a linear energy transfer (LET) effect in the irradiation of polystyrene have been followed by measurements of free-radical yields by electron-spin-resonance techniques. Radical yields from gamma radiation and from fast neutrons were equal within experimental error for a single series of specimens. The absolute yield was 0.12 ± 0.08 radical per 100 ev, with the large experimental error resulting from the uncertainty in the concentration of spins in the standard and from variations in the position of the standard within the electromagnetic field of the spectrometer. The equal radical yields from gamma radiation and fast neutrons contrast with the increased yields of cross links and volatile products at high LET and are difficult to reconcile with a mechanism based on second-order recombination reactions of the observed radicals in spurs.

Apparatus is being assembled for sample handling and product analysis to study the addition of

radiation-generated alkyl radicals to naphthalene. Apparatus has been constructed for the handling of mixtures of ammonia and hydrocarbons for an investigation of the radiolysis of such mixtures. These studies will mark our start in a chemonuclear program.

Flux mapping has been performed on our new 18,900-curie ^{60}Co source to provide calculation of doses to various specimens both inside and outside the source.

25. PREPARATION OF PURE MATERIALS

Several large single crystals of LiF of various isotopic compositions were produced with cationic impurity concentrations not exceeding 30 ppb. Distribution coefficients for Na^+, Mg^{2+}, Ca^{2+}, and Mn^{2+} on zonal melting of LiF show that the relative size of impurity ions markedly affects the rate of removal. A large ($0.6 \times 1.3 \times 3.8$ cm) single crystal of terbium metal was produced for ORNL research programs. By application of vapor-zone sublimation techniques, very pure polycrystalline ZrF_4 was produced; the iron content of the commercial starting materials (550 ppm) was reduced to less than 100 ppm.

26. CHEMICAL SUPPORT FOR THE CONTROLLED THERMONUCLEAR PROGRAM

Surface diffusion, rather than vapor transport, was indicated to be the dominant mechanism by which vacuum systems become contaminated with diffusion pump oil. The combination of electron bombardment of surfaces with mass spectrometric analysis of the emitted gaseous species was demonstrated to be a valuable diagnostic method for showing the presence of oil in very small amounts. The origin of methane in certain high-vacuum systems was indicated to be the reaction of carbon atoms in the surface of titanium metal with ionically pumped hydrogen. The reaction of water vapor with such titanium surfaces was found to produce H_2 and CO. Methane, ethane, and higher hydrocarbons were found to be present in gases produced during operation of the DCX-2 experiment, indicating the presence of a surface contamination.

Consideration of fuel cycle chemistry in tritium-burning controlled-fusion devices must include recognition of possible intolerably large inventory levels. Steady-state inventory levels in the presence of tritium ion or atom fluxes will be flux dependent but will in any event require appropriate design considerations. Processing for tritium recovery and for isotope separation from protium and deuterium will probably be an essential part of a tritium-burning device. Basic chemical considerations and some experimental corroboration have led to the conclusion that inventory control by processes appropriate to the various regions of a controlled-fusion reactor is chemically possible. Initial power cost estimates for these processes were made and appear to be not prohibitive.

Contents

SUMMARY iii

PART I. MOLTEN-SALT REACTORS

1. HIGH-TEMPERATURE PHASE EQUILIBRIUM STUDIES 3
   - Phase Equilibria Among the Fluorides 3
     - Fuel System for the Molten-Salt Reactor Experiment 3
   - Cation Size Effects in Lanthanide and Actinide Fluoride Systems 10
     - The $LiF-LnF_3$ Systems 10
     - The $NaF-LnF_3$ Systems 13
     - Dimorphism of the Rare-Earth Trifluorides 14
     - Properties of the Rare-Earth Halides 16
     - The Systems $NaF-ScF_3$ and $NaF-BiF_3$ 16
   - Salt Systems for Application in Advanced Reactor Technology 23
     - Core and Blanket Fluids for Fast Reactors 23
   - Crystal Structure Determinations 28
     - Crystal Structure of Hexagonal $NaNdF_4$ and Related Compounds 28
     - X-Ray Diffraction Studies on Compounds in the System $NaF-LnF_3$ 28
     - Refinement of the Crystal Structure of Li_2BeF_4 30
     - Crystallographic Data for Some Pure Materials 33
     - Complex Fluorides of U(III), U(IV), and U(V) 33

2. RADIATION CHEMISTRY OF THE MOLTEN-SALT REACTOR SYSTEM 36
   - In-Pile Irradiation Experiment 47-6 36
     - Introduction 36
     - Experimental 37
     - Results and Discussion 39
     - Acknowledgments 45
   - Design and Mockup Tests of a Proposed In-Pile Molten-Salt Irradiation Experiment 45
     - Experimental Objectives and Design Considerations 45
     - Reactor Irradiation Facility 45
     - Experiment Design 45
     - Mockup Tests 48
     - Conclusions 48
   - Radiolysis of Solid Metallic Fluorides 49
     - Effects of Gamma Irradiation of Simulated MSRE Fuel Salt 49
     - Discussion 51

Effects of Beta Irradiation of Solid Fluorides 51
Effects of Irradiation with Soft X Rays 54

3. CHEMICAL STUDIES OF MOLTEN SALTS 56

$HF-H_2O$ Equilibria and Oxide Chemistry in Molten Fluorides 56
Methods of Data Reduction 56
$LiF-BeF_2$ Melts 58
$2LiF-BeF_2-ZrF_4$ Melts 61
Removal of Oxide by HF Sparging 63

The Stability of UF_3 65

Removal of Sulfur from Molten Fluorides 72
Reduction of Sulfur 72
H_2S Reaction with Nickel 75

Electrochemistry of Molten Fluoride Mixtures 76
Reference Half-Cells for Molten $LiF-BeF_2$ Mixtures 76
Reversible Deposition of Metals on Solid Electrodes by Voltammetry with Linearly Varying Potential 79
Electrochemistry of UF_4 in Molten Fluorides 80

Viscosity in the $LiF-BeF_2$ System 81

Densities of Molten-Fluoride Mixtures 83

Mass Spectrometric Studies of Molten Fluoride Vapor Species 83

Recovery of Carrier Salt by Distillation 86
Theoretical Considerations 86
Experimental Studies 87
Conclusions 88

Gas Transport Characteristics of MSRE Graphites 88

The Removal of ^{135}Xe in the MSRE 91

Separation of Protactinium from Irradiated Thorium Salts 93
$AlCl_3-ZrCl_4$ Phase Studies 94
$AlCl_3-ThCl_4$ Phase Studies 96
Protactinium-233 Tracer Experiments 96

4. FLUORIDE SALT PRODUCTION 99

Process Chemistry 99
Oxide Removal 100
Sulfur Removal 100
Removal of Structural-Metal Impurities 100

Production Operations 101
Starting Materials 101
^7LiF Densification 102
Charging and Meltdown Operations 102
Melt Purification 102

Process Control 104
Process Gas Analyses 105
Salt Analyses 106

Production of Component Mixtures for the MSRE Fuel 106
Preparation of Enriched Fuel Concentrate 107
Preparation of Fuel Enriching Capsules 108

Reactor Loading 108
Production Economics 108

PART II. AQUEOUS REACTORS

5. CHEMISTRY OF PRESSURIZED-WATER REACTOR SYSTEMS 113
Behavior in ORR Loop 113
Corrosion-Product Chemistry 113
Fission Product Chemistry 118
Fe_3O_4 as High-Temperature Adsorbent 120
Solubility of Fe_3O_4 120

6. CORROSION STUDIES FOR AQUEOUS REACTORS AND CHEMICAL PROCESSES 122
Corrosion Tests for the High Flux Isotope Reactor 122
Laboratory Studies 122
Dynamic Loop Studies 123
Corrosion Studies for the Transuranium Processing Facility 123
Corrosion Testing Program in Support of Power-Reactor Fuel-Element Reprocessing 124
Acceptance Tests 125

7. MECHANISMS OF CORROSION OF ZIRCONIUM ALLOYS 126
Oxide Growth and Capacitance on Preirradiated Zircaloy-2 126
Experimental 126
Results and Discussion 126
Conclusions 134
Electrochemistry of Zirconium Corrosion in High-Temperature Aqueous Solutions 135

8. PHYSICAL CHEMISTRY OF HIGH-TEMPERATURE AQUEOUS SYSTEMS 139
Electrical Conductances of Aqueous Solutions at Temperatures from 0 to 800°C and Pressures up to 4000 Bars: the Conductances and Ionization Constants of Sulfuric Acid Solutions 139
Introduction and Experimental Procedure 139
Results and Discussion 139
Estimation of the Dielectric Constant of Water to 800°C 143
Second Dissociation Constant of H_2SO_4 from 25 to 350°C Evaluated from Solubilities of $CaSO_4$ in Sulfuric Acid Solutions 145
Experimental Procedures 145
Results 146
Assignment of Limiting Equivalent Conductances to Single Ions to 400°C 148
Osmotic Behavior of Aqueous Solutions at 165°C 149
Introduction 149
Experimental 149
Discussion 150
Thorium Hydrolysis in 1 *M* $(Na)ClO_4$ at 0, 25, and 95°C 151
Data Analysis 151
Tests of Schemes Involving Four Hydrolysis Products 152
Schemes of Five Hydrolysis Products 152

Solubility and Hydrolytic Instability of $MgSO_4$ in H_2SO_4-H_2O and D_2SO_4-D_2O Solutions, 200–350°C 159
Experimental 160
Results 160

9. INTERACTION OF WATER WITH PARTICULATE SOLIDS 164

Surface Chemistry of Thoria 164
Heats of Immersion and Differential Heats of Adsorption 164
Vapor Adsorption and Desorption 169
Infrared Spectra of Adsorbed Species on Thorium Dioxide 172

Permeability of Vibratorily Compacted Fuels 174
Variable Properties of Fuel Elements 174
Theoretical Considerations 174
Experimental Studies 175
Results 176
Conclusions 177

Gas Evolution from Thoria–3% Urania Sol-Gel Material 177
Introduction 177
Effects of Particle Size 177
Effect of Temperature 178
Reversible Gas Adsorption on Sol-Gel Material 178
Discussion 180

PART III. GAS-COOLED REACTORS

10. DIFFUSION PROCESSES 183

Transport Properties of Gases 183
Pressure Dependence of the Thermal Diffusion Factor 183
Thermal Transpiration 185
Gaseous Diffusion 186
Gas Transport Characteristics of Uranium-Fueled Graphites 188

Actinide Diffusion in Pyrocarbons 190
Thin-Layer Experiments at High Concentrations 190
Thin-Layer Experiments at Low Concentrations 191
Constant-Potential Experiments 193

11. REACTIONS OF GRAPHITE WITH OXIDIZING GASES 202

Oxidation of ATJ Graphite by Low Concentrations of Oxidants in Helium 202

Reactivity of Fueled and Unfueled Graphite Spheres with Steam 204

12. IRRADIATION BEHAVIOR OF HIGH-TEMPERATURE FUEL MATERIALS 208

Introduction 208

Radiation Effects in Pyrolytic-Carbon-Coated Fuel Particles 208

Postirradiation Testing of Coated Fuel Particles 212
Fission Product Release on Annealing 212
Fission Product Release Into Outer Coating 213

Postirradiation Examination of Fueled Graphite Spheres 213
Fuel Distribution and Burnup 214
Mechanical Properties 214

Postirradiation Examination of EGCR Fuel Element Prototype Capsules 218
Postirradiation Examination of Metal-Clad Fuel Elements of Advanced Gas-Cooled Reactor Designs 219

13. FISSION-GAS RELEASE DURING FISSIONING OF UO_2 223
Introduction 223
Release from Fine-Grain Specimens 224
Effect of Fission Rate 225
Magnitude of Release Rate 225
Mathematical Model 226
Oscillating Experiments 227

14. BEHAVIOR OF CERAMIC MATERIALS UNDER IRRADIATION 230
Radiation Stability of Silicate Ceramics 230
Cordierite 230
Zircon 231
Steatite 232
Forsterite 232
Irradiation-Induced Thermal Conductivity Changes of Ceramics 232
Behavior of High-Temperature Materials Under Irradiation 233
Effect of Fast Neutrons on Beryllium Oxide 234
Fast-Neutron Damage to Magnesium Oxide 235
Effects of Fast-Neutron Irradiation on Al_2O_3 237
Behavior of Refractory-Metal Carbides and High-Purity Oxides of Yttrium and Aluminum 238

15. MISCELLANEOUS STUDIES FOR SOLID-FUELED REACTORS 239
Equilibrium Studies in the System ThO_2-UO_2-UO_3 239
Phase Equilibrium Studies in the UO_2-ZrO_2 System 243
Equilibration with Molten Fluoride Fluxes 244
X-Ray Diffractometric Observation of Transformations 244
Tentative Phase Diagram 244
Irradiation of Sulfur Dioxide with Alpha Particles 245
Neutron Flux Spectra in the Experimental Facilities of the Oak Ridge Research Reactor 246

PART IV. NUCLEAR SAFETY

16. EXPERIMENTS WITH THE CONTAINMENT MOCKUP FACILITY 251
Fission Product Release from Melting Trace-Level-Irradiated UO_2 251
Fission Product Release from Highly Irradiated UO_2 252
Comparison of Release Behavior from Trace-Level-Irradiated UO_2 with That from High-Burnup-Level Fuel 252
Total Nuclei Count in the Aerosol 253
Fission Products Remaining Airborne as a Function of Time 254
Factors Affecting the Behavior of Iodine in a Containment System 254
Gas-Phase Reactions 254

Iodine History 254
Effect of Atmosphere and Concentration of Iodine 255

Differentiation of Iodine Forms by Use of Complex Filter Packs 257

Simulation of High-Burnup Fuel 258
The Containment Research Installation (CRI) 259

Melting Points of Mixtures of Oxidized Fuel Cladding with UO_2 261

17. BEHAVIOR OF FISSION PRODUCTS RELEASED DURING IN-PILE SIMULATED LOSS-OF-COOLANT ACCIDENTS 263

Effects of Atmosphere on Behavior of Released Fission Products 263
Physical Condition After Melting of Fuels 263
Distribution of Fission Products and Uranium 264

Effects of Sustained Overheating of Reactor Fuels 265

Fission Products Retained by Cool Metal Surfaces, by Filters, and by Steam Condensers 266

Iodine Behavior in In-Pile UO_2 Melting Experiments 267
Iodine Analyses 267
Behavior of Iodine Released from the High-Temperature Zone 268

Major Modifications and Additions to Experimental Equipment 268

18. RELEASE OF FISSION PRODUCTS DURING MELTING OF FUELS UNDER REACTOR TRANSIENT CONDITIONS 271

Behavior on Melting in Moist Air 271

Behavior on Melting in Steam 275

19. BEHAVIOR OF RADIOIODINE 277

Identification and Behavior of Radioiodine Vapors 277
By Solubility Behavior 277
By Knudsen Effusion Cell 277
By Gas Chromatographic Identification 278
By Fractional Sublimation and Mass Spectrometry 278
By Composite Diffusion Tubes 278
Identification and Determination of Radioiodine Species in Steam 279

Chemical Behavior of Radioiodine Vapors 280
Iodine Sorption by Filter Materials in a Particulate-Free Atmosphere 280
Reaction of Radioiodine Vapors with Organic Vapors 282
Deposition of Radioiodine on Heated Steels 282
Sorption of Radioiodine and Radiocesium by Metals 283
Iodine Behavior in May Packs 284

Removal of Iodine and Volatile Iodine Compounds from Air Systems by Activated Charcoal 286
From Dry and Moist Air 286
From Steam-Air Mixtures 286

20. BEHAVIOR OF RADIOACTIVE AEROSOLS 287

Simulation of Dispersions 287
Tests of Iodine Removal Systems 287
Simulation of Particulate Dispersions 287

Filtration of Dispersions of Reactor Materials 288

Measurements of the Characteristics of Radioactive Aerosols by Use of Fibrous Filters 288

PART V. OTHER ORNL PROGRAMS

21. CHEMICAL SUPPORT FOR SALINE WATER PROGRAM 293
Solubility of $CaSO_4$ in Aqueous Solutions of $NaNO_3$ at Temperatures of 125–350°C 293
Calculation of Allowable Concentration Limits of Saline Waters Before Precipitation of $CaSO_4$ 294
Corrosion of Aluminum Alloys in Salt Solutions 296
Titanium Corrosion in Saline Water 297
Observations in Loop Tests 297
Observations in Autoclave Tests 301
Electrochemical Studies 302

22. SOLVENTS FOR THE FLUORIDE VOLATILITY PROCESS 306
The System $KF-ZrF_4-AlF_3$ 306
Zirconium-Matrix Fuels of High Uranium Content 307
Solvents Applicable to Stainless Steel Matrix Fuels 307

23. SUPPORT FOR SPACE PROGRAMS 308
SNAP-8 Chemistry Studies: the Chemistry of Hydrogen in Liquid Alkali Metal Mixtures 308
Hydrogen Permeation Studies 308
Solution Chemistry of Hydrogen in Liquid Alkali Metal Mixtures 312
Space Materials Properties Information Center 316

24. EFFECT OF RADIATION ON ORGANIC MATERIALS 318
Effect of Radiation on Polystyrene 318
Chemonuclear Studies 320
Radiation-Induced Reactions of Hydrocarbons 320
Radiation Flux Measurements in the Gamma-Irradiation Facility 320

25. PREPARATION OF PURE MATERIALS 323
Preparation of Single-Crystal Lithium Fluoride 323
Purification of LiF by Vacuum Sublimation 324
Purification of LiF by Zone Refining 326
Preparation of Pure Terbium Metal Crystals 329
Purification of Zirconium Tetrafluoride 330

26. CHEMICAL SUPPORT FOR THE CONTROLLED THERMONUCLEAR PROGRAM 334
Vacuum Studies 334
Oil Behavior in Vacuum Systems 334
Synthesis and Decomposition of Methane in Vacuum Systems 335
The Chemistry of Tritium in Controlled-Fusion Devices 336
Source Processing 336
Vacuum System Processing 337
Blanket Assembly Processing 338
Coolant Processing 339
Tritium Inventory 340
Startup Processing 340

PUBLICATIONS 341

PAPERS PRESENTED AT SCIENTIFIC AND TECHNICAL MEETINGS 348

Part I

Molten-Salt Reactors

1. High-Temperature Phase Equilibrium Studies

R. E. Thoma
G. D. Brunton
J. H. Burns
H. A. Friedman
G. M. Hebert
H. L. Hemphill
D. R. Sears
B. J. Sturm
H. Insley
T. N. McVay

PHASE EQUILIBRIA AMONG THE FLUORIDES

Fuel System for the Molten-Salt Reactor Experiment

The System $LiF-BeF_2-ZrF_4$. – Liquid-solid phase equilibria in the system $LiF-BeF_2-ZrF_4$ are now well defined except for compositions of less than approximately 20 mole % LiF. Within this composition region, accurate determination of the phase boundaries of the immiscible liquids[1] is incomplete because of the volatility of ZrF_4 at high temperatures and because of the high viscosity of the liquid phases. Until the boundary limits of the immiscible liquids are established, the phase diagram reported previously[1] serves as the most accurate description of phase behavior in this system. A three-dimensional model of the $LiF-BeF_2-ZrF_4$ phase diagram was constructed (Fig. 1.1) as a means of affording a simple graphic display of the crystallization behavior of the MSRE fuel and coolant salts. The model is now on display at the MSRE site. Except for the crystallization reaction in which the uranium phase $7LiF \cdot 6UF_4$ is produced, all equilibrium crystallization reactions of the fuel and coolant salt are evident from the model.

The System $LiF-BeF_2$ (jointly with S. Cantor and W. T. Ward). – Although numerous investigations of the system $LiF-BeF_2$ have been conducted,[2–8] the phase diagram is still uncertain, especially the liquidus curve for compositions greater than 33 mole % BeF_2. The liquidus temperatures have been reexamined for compositions 33 to 70 mole % BeF_2, the concentration range of greatest significance to MSRE performance. Very pure component salts were used for these measurements – crystalline LiF was selected from slowly cooled melts of analytical-grade material, and very pure BeF_2 was obtained by distillation. The total cationic and oxide contaminant concentrations in the salt mixtures used for these determinations did not exceed 0.2%. For the composition range 33.5 to 52 mole % BeF_2, liquidus and solidus temperatures were readily obtained by conventional thermal analysis techniques.[9] These temperatures were measured with NBS-calibrated thermocouples and have a precision of 0.3°C. Such a precision was not achieved for mixtures in which BeF_2 is precipitated as the primary phase, probably because of

[1] R. E. Thoma, *Reactor Chem. Div. Ann. Progr. Rept. Jan. 31, 1964*, ORNL-3591, p. 4.

[2] E. Thilo and H. A. Lehman, *Z. Anorg. Allgem. Chem.* **258**, 332 (1949).

[3] A. V. Novoselova, Yu. P. Simanov, and E. I. Jarembash, *Zh. Fiz. Khim.*, **26**, 1244 (1952).

[4] D. M. Roy, R. Roy, and E. F. Osborn, *J. Am. Ceram. Soc.* **33**, 85 (1950).

[5] D. M. Roy, R. Roy, and E. F. Osborn, *J. Am. Ceram. Soc.* **37**, 300 (1954).

[6] L. J. Wittenberg, *J. Am. Ceram. Soc.* **42**, 209 (1959).

[7] J. L. Spiers, "The Binary and Ternary Systems Formed by Calcium Fluoride, Lithium Fluoride, and Beryllium Fluoride: Phase Diagrams and Electrolytic Studies," thesis, Michigan State University (1952).

[8] T. B. Rhinehammer and C. R. Hudgens, *Phase Equilibria in the System $LiF-BeF_2$*, MLM-1084, to be published.

[9] These measurements were carried out by S. Cantor and W. T. Ward.

PHOTO 67435A

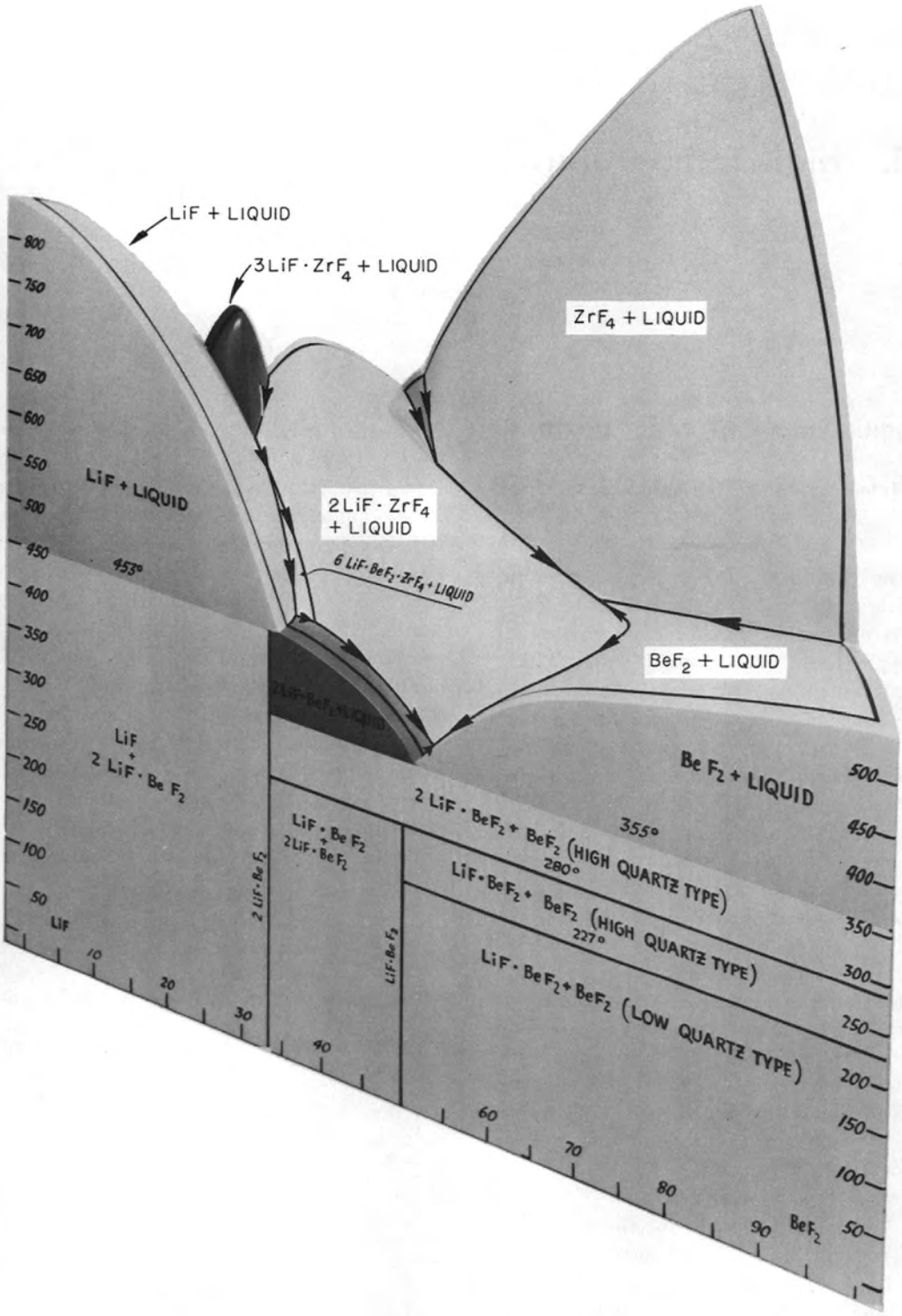

Fig. 1.1. Three-Dimensional Model of the $LiF\text{-}BeF_2\text{-}ZrF_4$ System.

the high viscosities in the liquid phase. Liquidus data for compositions 52 to 70 mole % BeF_2 were obtained by using the thermal gradient quenching method. Rapid cooling of LiF-BeF_2 mixtures in which crystalline BeF_2 is the saturating phase retains the liquid phase as a true glass. This behavior facilitates determination of the liquidus in quenched specimens by x-ray and petrographic methods. Figure 1.2 (parts *a*, *b*, and *c*) shows the typical appearance of BeF_2 that has precipitated out of the LiF-BeF_2 system.

The LiF-BeF_2 phase diagram, constructed from the cooling curve and the quench data (Table 1.1) as well as from data selected from refs. 2 to 5, is shown in Fig. 1.3.

In principle, the liquidus temperatures at which BeF_2 crystallizes can be calculated from thermodynamic activities of BeF_2 in the melt, provided that the requisite BeF_2 thermochemical data (heat of fusion, melting point, and heat capacities of solid and liquid) are available. Trial calculations, using current measurements of activities[10] and the heat capacity and heat of fusion of BeF_2,[11] gave liquidus temperatures, for the 52 to 70 mole % BeF_2 concentration range, much lower than seems reasonable from the available phase equilibrium data.

The System UF_4-UF_3 (G. Long and R. E. Thoma). – Previously, the collection of equilibrium phase data in UF_3 systems has been impeded by the tendency of most experimental procedures to induce a shift toward the right in the reactions

$$UF_3 \rightleftharpoons \tfrac{1}{4}U^0 + \tfrac{3}{4}UF_4 , \qquad (1)$$

$$UF_3 + H_2O \rightleftharpoons \tfrac{1}{2}UF_4 + \tfrac{1}{2}H_2 + HF + \tfrac{1}{2}UO_2 . \qquad (2)$$

These reactions take place at elevated temperatures if the container metals form solid solution alloys or liquid eutectic mixtures with uranium metal at the temperature of the study or if the opportunity is available for water to adsorb on UF_3, as from exposure to laboratory atmosphere. The system UF_4-UF_3 was (tentatively) described some time ago. Its further elucidation, however, appeared to be possible only through dynamic methods, since equilibration periods resulted in a conversion of UF_3 to UF_4. As a part of a study of the stability of UF_3 (see section on "The Stability of UF_3," this report), the reaction

$$UF_3 \rightleftharpoons \tfrac{3}{4}UF_4 + \tfrac{1}{4}U^0 ,$$

for which

$$K_D = \frac{\left(a_{UF_4}\right)^{3/4}\left(a_{U^0}\right)^{1/4}}{a_{UF_3}} ,$$

Table 1.1. Phase Transition Data for the System LiF-BeF_2

Composition (mole %)		Phase Transition Temperature (°C)			
		Thermal Analysis		Thermal Gradient Quenching	
LiF	BeF_2	Liquidus	Solidus	Liquidus	Solidus
67.03	32.97		457.8		
65.5	34.5		457.6		
65.0	35.0	456.5			
64.01	35.99	454.0			
63.0	37.0	451.9			
61.02	38.98	442.8			
59.02	40.98	431.7			
56.0	44.0	411.5			
55.0	45.0	404.5			
51.98	48.02	386.3	360.02		
49.97	50.03	374.6	360.4		
45.0	55.0			422	
42.5	57.5			425	
40.0	60.0	431.3	359.7		
39.0	61.0			392	
37.0	63.0			392	
35.0	65.0			479	
32.5	67.5			479	

[10] A. L. Mathews, C. F. Baes, and B. F. Hitch, "Chemical Studies of Molten Salts," this report.

[11] A. R. Taylor and T. E. Gardner, U.S. Bureau of Mines, Tuscaloosa, Ala. (unpublished data).

PHOTO 68702

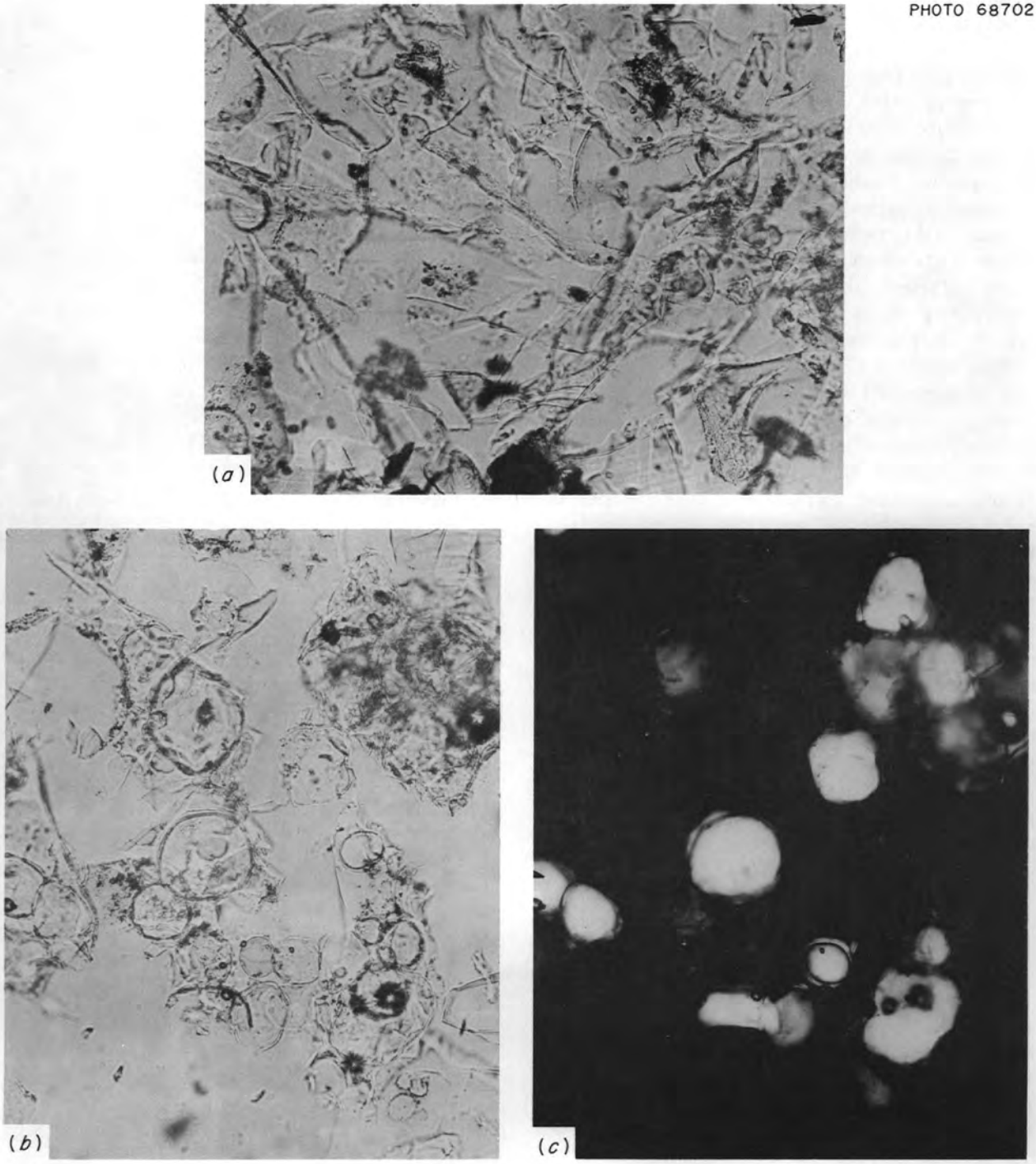

Fig. 1.2. (*a*) **LiF-BeF_2 (37–63 mole %) Quenched from 483°C.** Glass and quench growths. Circular areas are bubbles. Halos typical of crystalline BeF_2 are absent. (160× white light). (*b*) **LiF-BeF_2 (37–63 mole %) Quenched from 475°C.** Halos surrounding crystalline BeF_2 denote occurrence of saturating phase. (160× white light). (*c*) **LiF-BeF_2 (37–63 mole %) Quenched from 475°C.** White areas denote location of birefringent BeF_2 crystals. Glass is isotropic and invisible in polarized light. (160× polarized light).

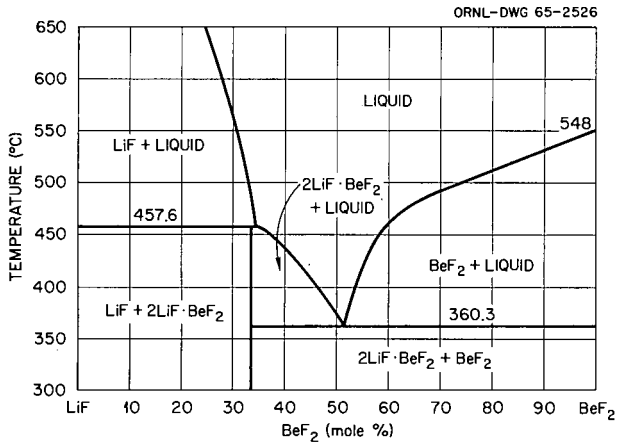

Fig. 1.3. The System LiF-BeF$_2$.

was examined by measuring partial pressures of HF produced when H_2 was passed through a bed containing UF_3 and UF_4 to establish the equilibrium

$$UF_4 + \tfrac{1}{2}H_2 \rightleftharpoons UF_3 + HF .$$

In one series of measurements beginning with pure UF_4, the reduction reaction was allowed to proceed to completion, and, from observations as the temperature was altered at several stages of completion, some deductions could be made about the phase behavior. For example, a change in pressure drop across the reaction vessel as temperature was increased indicated that the eutectic temperature was 895 ± 5°C, while a melting-point determination at 60% conversion to UF_3 gave a thermal arrest at 892°C, which coincided with cessation of bubbling; all the observations were consistent with a eutectic temperature of 892 ± 2°C. The UF_4 solubility in UF_3 appeared to be approximately 38 mole % at the eutectic, in good agreement with the previous report. The value obtained for the disproportionation reaction equilibrium constant, $\log K_D = 0.328 - 3.30(1000/T)$, is sufficiently low to suggest that UF_4-UF_3 liquids should not change composition during short exposures to the conditions that prevail in our thermal analysis experiments. Accordingly, we obtained cooling curve data for UF_4-UF_3 compositions ranging from 10 to 40 mole % UF_3 and discounted all but the highest liquidus temperatures for repeated runs. On the basis of our previous data and from the results of the reduction of UF_4 by H_2, we have constructed the phase diagram of the UF_4-UF_3 binary system shown in Fig. 1.4.

MSRE Fuel Fractionation Experiments (H. A. Friedman and R. E. Thoma). – The homogeneity generally characteristic of multicomponent salt mixtures in the liquid state is progressively destroyed as the mixture undergoes gradual crystallization (see Table 1.2). The possibility that the MSRE fuel mixture LiF-BeF$_2$-ZrF$_4$-UF$_4$ (65-29.1-5.0-0.9 mole %) might, on cooling in the MSRE drain tanks, experience sufficient solid phase fractionation to create potentially hazardous conditions has been examined via laboratory-scale experiments. Some 650 g of the fuel salt was cooled at rates approximating that expected of the entire drain tank assembly and that expected of the fuel alone, 3.46 and 0.387°C/hr respectively. In both cases the radiative cooling geometry was controlled to simulate as nearly as possible that expected in the drain tanks, even though it is realized that the horizontal ΔT profile in the cooling radioactive fuel mixture may be substantially different from that prevailing in the laboratory experiment.

The concentrations of uranium were found to be identical at the top and bottom fractions of each

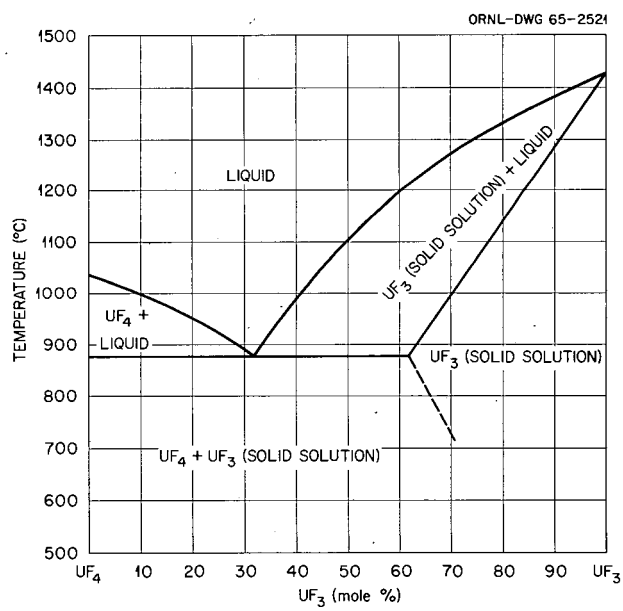

Fig. 1.4. The System UF$_4$-UF$_3$.

Table 1.2. Equilibrium Crystallization Behavior of the MSRE Fuel Mixture $LiF-BeF_2-ZrF_4-UF_4$ (65-29.1-5.0-0.9 mole %)

Temperature (°C)	Solid Phases Crystallizing	Crystal Density (g/cm^3)
434	$2LiF \cdot BeF_2$	2.167
431	$2LiF \cdot BeF_2 + 2LiF \cdot ZrF_4$	2.167, 3.163
416	$2LiF \cdot BeF_2 + 2LiF \cdot ZrF_4 + 7LiF \cdot 6UF_4$	2.167, 3.163, 4.770
350	$2LiF \cdot BeF_2 + 2LiF \cdot ZrF_4 + 7LiF \cdot 6UF_4 + BeF_2$	2.167, 3.163, 4.770, 2.234

Constitution of frozen salt: 77.07 $2LiF \cdot BeF_2$, 14.29 $2LiF \cdot ZrF_4$, 2.57 $7LiF \cdot 6UF_4$, 6.07 BeF_2 (mole %)

of the two ingots, irrespective of cooling rate. A photograph of the ingot resulting from the slower cooling rate experiments is shown in Fig. 1.5. Chemical analyses of the salt specimens from each of the locations designated in Fig. 1.5 were obtained. For areas 1 to 7, the uranium concentrations were found to be 2.94, 3.49, 4.15, 3.32, 4.28, 4.62, and 5.74 wt %. In comparison with the nominal concentration of uranium in the MSRE fuel, 5.13 wt %, these experiments show a maximum increase of 23.4% in uranium concentration on very slow static cooling. A fact which accounts for the small degree of segregation of the uranium phases in these experiments is that, at the onset of crystallization of $7LiF \cdot 6UF_4$, simultaneous crystallization of the three solid phases $2LiF \cdot BeF_4$, $2LiF \cdot ZrF_4$, and $7LiF \cdot 6UF_4$ is proceeding. In addition, the volume of the liquid phase is being reduced steadily, so sharply, in fact, that in this experiment as well as in previous ones, some of the liquid phase is apparently occluded among dendritic-like crystals of the solidified phase, a phenomenon which helps prevent compositional variation in the mixture.

In the freezing of multicomponent mixtures, maximum segregation of crystalline phases takes place under equilibrium cooling conditions. The segregation represented by the results obtained in the fractionation experiments reported here represents in a practical way the nearest approach to equilibrium cooling that the MSRE fuel salt may experience in a single crystallization sequence.

Removal of Lanthanides from MSRE Fuel by Zone Melting (G. D. Brunton, H. L. Hemphill, R. G. Ross, A. J. Singh,[12] R. E. Thoma). – The scheduled tests of the MSRE in early 1965 have increased the interest in all chemical methods for reprocessing the $LiF-BeF_2-ZrF_4-UF_4$ fuel salt. Among the nonvolatile fission products that will form during the operation of the MSRE are the rare earths, which are poisons because of their very large thermal neutron cross sections.

Preliminary phase relationships of the lanthanide trifluorides (LnF_3) and LiF (ref. 13) (see section on "The $LiF-LnF_3$ Systems," this report) suggested that the distribution coefficient, *k* (ref. 14) (the ratio of the concentration of the impurity in the freezing solid to that in the liquid at equilibrium), for the lanthanide trifluorides in LiF would be significantly less than unity. The composition of the MSRE fuel salt $LiF-BeF_2-ZrF_4-UF_4$ (65.0-29.1-5.0-0.9 mole %) was chosen to lie just outside the LiF primary phase field. Consideration of the $LiF-LnF_3$ and $LiF-BeF_2-ZrF_4$ phase diagrams suggests that the solubility of the rare-earth trifluorides in LiF-rich compositions of these mixtures is not highly composition dependent. By inference, the MSRE fuel salt might possibly be amenable to zone melting

[12]Present address: Chemistry Division, Atomic Energy Establishment, Trombay, Bombay, India.

[13]G. D. Brunton *et al.*, unpublished work (1964).

[14]W. F. Pfann, *Zone Melting*, Wiley, New York, 1958.

PHOTO 67747A

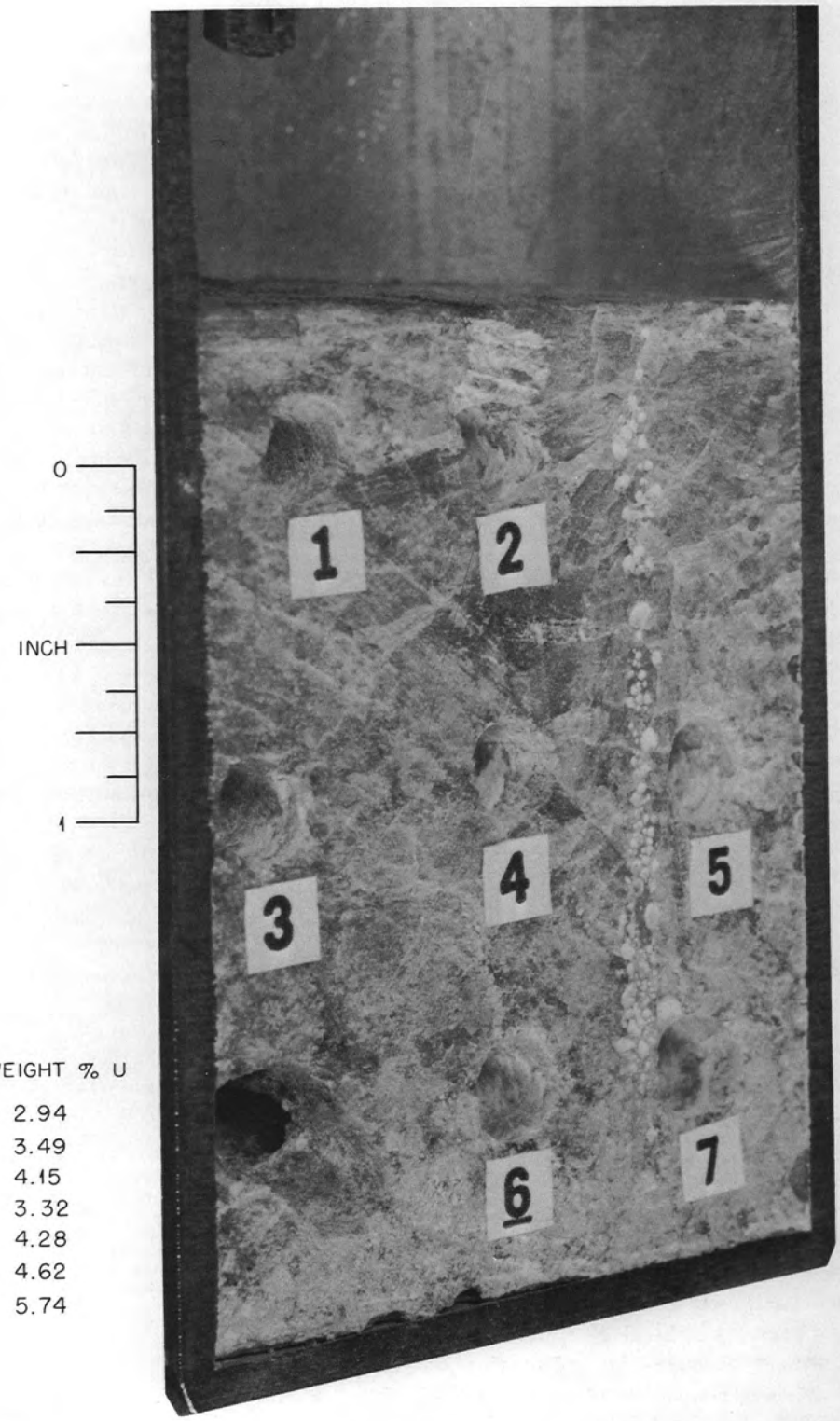

POSITION	WEIGHT % U
1	2.94
2	3.49
3	4.15
4	3.32
5	4.28
6	4.62
7	5.74

Fig. 1.5. Ingot from Slower Cooling Rate Experiments of MSRE Fuel.

purification. In initial evaluations of the potential applicability of this technique, we first investigated the removal of rare-earth trifluorides from LiF with zone melting.[15] Ingots of LiF doped with CeF_3, GdF_3, and LuF_3 were zone refined, using conventional zone melting apparatus. The results of analyses for rare earths showed that half of the rare-earth trifluoride was removed in 1 to 3 passes, and nearly all of it was removed in 12 passes. From graphs given by Pfann,[14] the effective distribution coefficient, k_E, was calculated to be less than 0.2 for these experiments.

A similar experiment was conducted with the MSRE fuel salt $LiF-BeF_2-ZrF_4-UF_4$ (65.0-29.1-5.0-0.9 mole %) instead of LiF. The results of incomplete analyses indicated that at the midsection of the ingot, generally less than half the LnF_3 was removed in ten passes, and therefore that k_E for the MSRE fuel was much larger than k_E for LiF. The molten-zone temperature for the MSRE fuel was chosen as 460°C, just above the liquidus of the fuel at 435°C, because, for practical engineering reasons, the temperature of the molten zone should be as low as possible. The inefficient separation of LnF_3 from the MSRE salt may be attributed partly to the large differences in the temperatures of the molten zone used in the LiF and MSRE fuel experiments. The temperature of the molten zone for LiF was arbitrarily chosen at 1000°C, about 150°C above the melting point of LiF. This ΔT helps assure better mixing, more rapid diffusion, and more vigorous convection circulation. Future experiments will be conducted to see whether more favorable conditions can be found.

CATION SIZE EFFECTS IN LANTHANIDE AND ACTINIDE FLUORIDE SYSTEMS

R. E. Thoma G. M. Hebert
H. Insley J. H. Burns

The chemistry of the rare-earth trifluoride systems has been the subject of increasingly intense investigations because the information obtained is relevant to the problems of chemical reprocessing of reactor fuels as well as to the chemistry of the actinides. In addition, the rare-earth fluorides have become employed in many current fundamental investigations of intraconfigurational electronic transitions. For such purposes, spectroscopists require well-characterized host matrices through which rare-earth ions may be distributed homogeneously over wide concentration ranges. It is also anticipated that the chemical data obtained from the fluoride systems may provide new insight to the general problem of complex compound formation in ionic systems. In connection with attempts to obtain information of potential significance to each of these applications, we have examined the phase behavior in the binary systems of the lanthanide trifluorides (LnF_3) with lithium and sodium fluoride. Phase diagrams of each of the systems are shown in Figs. 1.6 and 1.7. Diagrams of the $LiF-LnF_3$ systems were constructed from relatively few data. The $NaF-LnF_3$ systems are so complex, however, that much more data were required for their elucidation.

The $LiF-LnF_3$ Systems

Tentative phase diagrams were constructed for the systems $LiF-LnF_3$ primarily to determine whether significant differences of the lanthanide distribution coefficient in LiF could be observed even though intermediate compounds are formed only by some of the rare-earth trifluorides with LiF. A prediction based on correlation of ion size to formation of complex fluoride compounds indicated that a single intermediate compound, $LiF{\cdot}LnF_3$, would occur in only the $LiF-LnF_3$ systems TbF_3 through LuF_3.[16] Vorres and Riviello[17] confirmed this prediction that the heavier rare-earth trifluorides would form an $LiF{\cdot}LnF_3$ compound. They reported the existence of isomorphous $LiF{\cdot}LnF_3$ phases (where Ln is Gd to Lu) of the scheelite type but did not present optical or x-ray data or descriptions of melting behavior of the phases. Our results (Fig. 1.6) indicate that among the $LiF-LnF_3$ systems (1)

[15] A. J. Singh, R. G. Ross, and R. E. Thoma, *Zone Melting of Inorganic Fluorides*, ORNL-3658 (in preparation).

[16] R. E. Thoma, *Inorg. Chem.* 1, 220 (1962).

[17] K. S. Vorres and R. Riviello, "Rare Earth Oxyfluorides and Mixed Oxides, Fluorides and Oxyfluorides with Lithium," *Proceedings of the Fourth Rare Earth Research Conference*, Phoenix, Ariz., April 22–25, 1964.

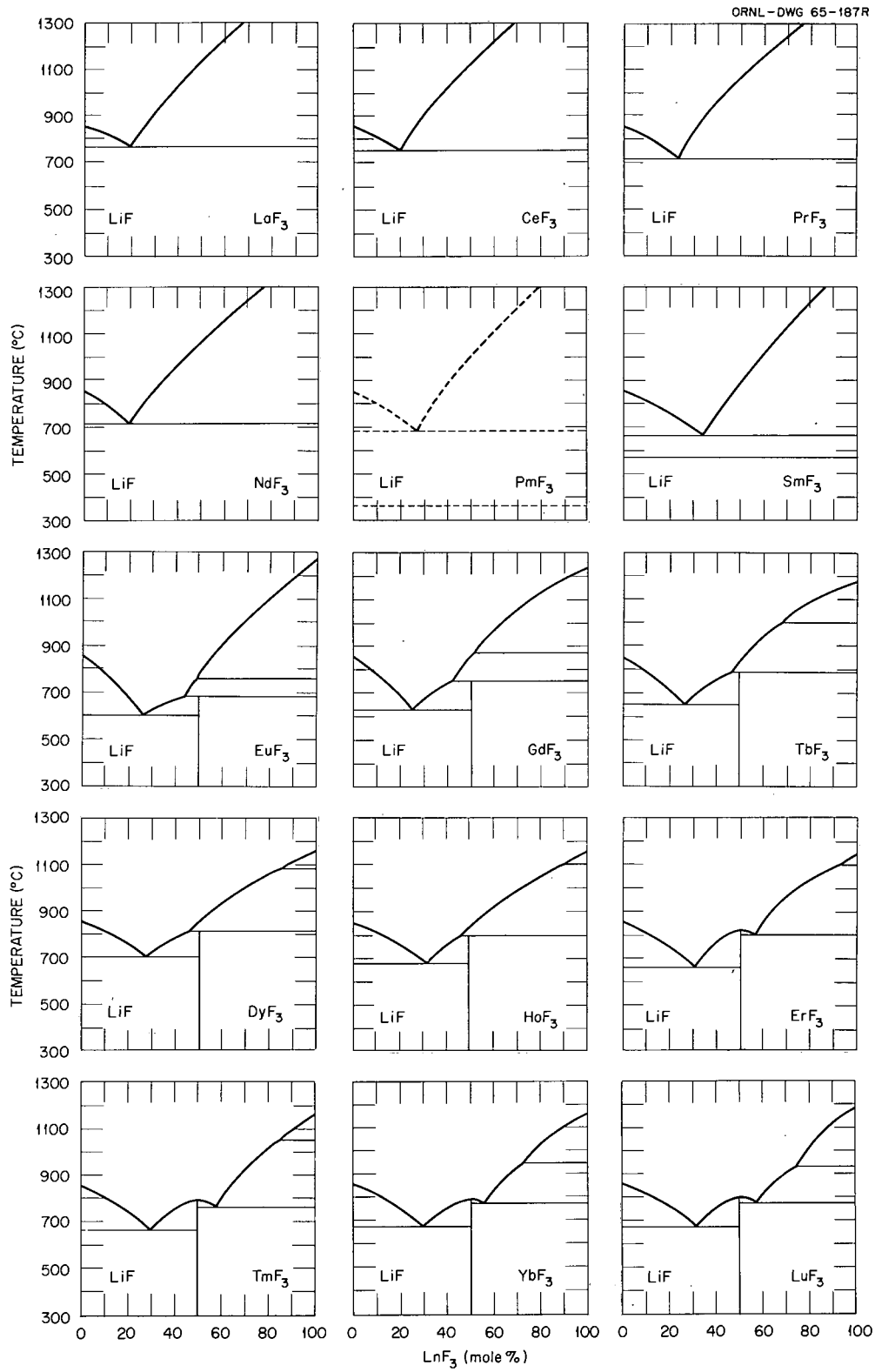

Fig. 1.6. Phase Diagrams of the LiF–Rare Earth Trifluoride Systems.

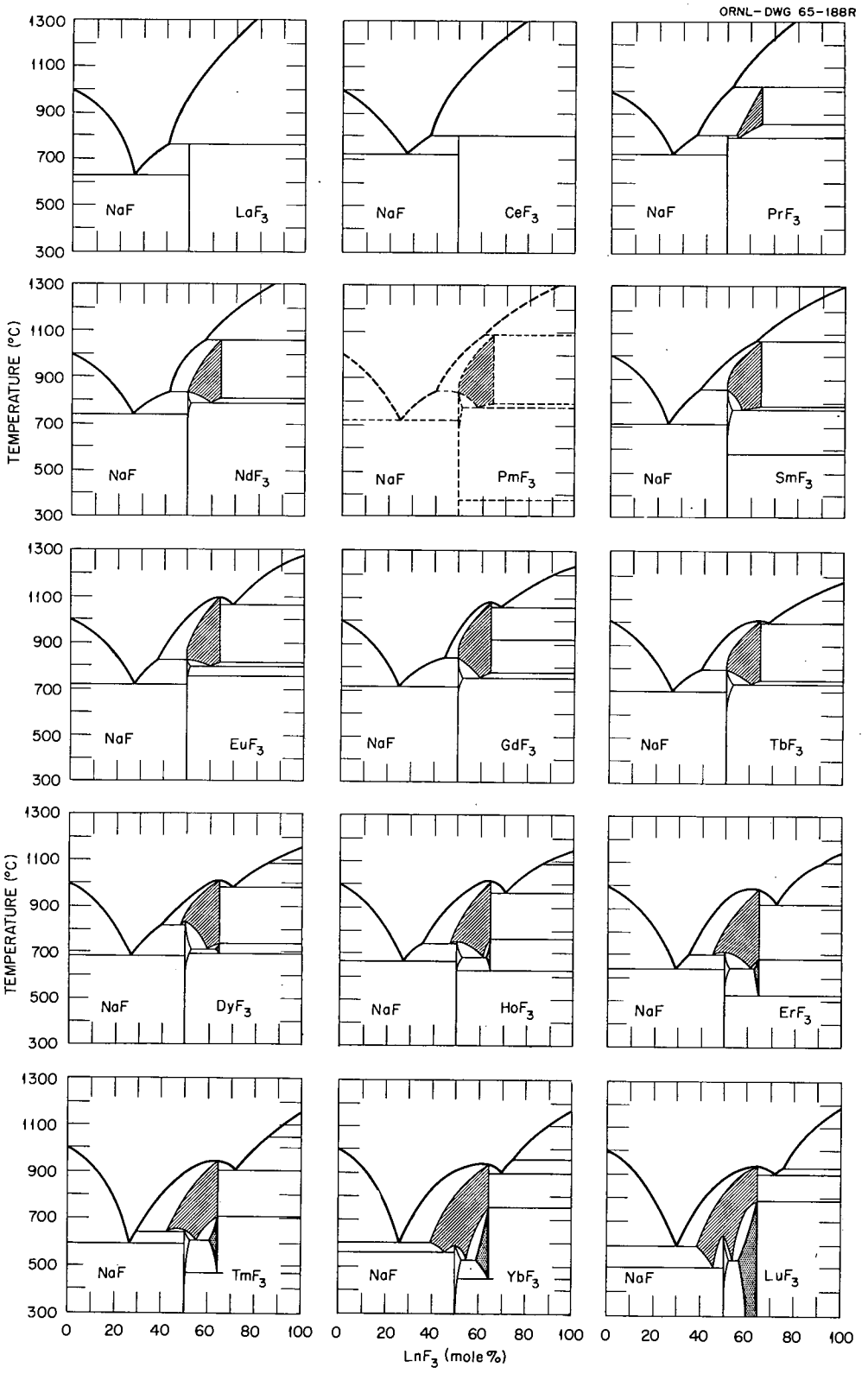

Fig. 1.7. Phase Diagrams of the NaF–Rare Earth Trifluoride Systems.

the first group, $LiF\text{-}LaF_3$ to $LiF\text{-}SmF_3$, is comprised of simple eutectic systems in which no intermediate compound is formed; (2) the component pairs $LiF\text{-}EuF_3$ to $LiF\text{-}DyF_3$ form a single intermediate compound, $LiF{\cdot}LnF_3$, which melts incongruently to LnF_3 and liquid; and (3) the component pairs $LiF\text{-}HoF_3$ to $LiF\text{-}LuF_3$ form a single intermediate compound, $LiF{\cdot}LnF_3$, which melts congruently. Lattice constants and refractive indices of the tetragonal $LiF{\cdot}LnF_3$ compounds are shown in Table 1.3.

The $NaF\text{-}LnF_3$ Systems

As is indicated in the phase diagrams, the $NaF\text{-}LnF_3$ systems (Fig. 1.7) vary considerably in their complexity. They are distinguished by a tendency to produce intermediate phases whose capability for stoichiometric variability differs remarkably as the disparity in cation sizes changes through the series. Within each of the 12 $NaF\text{-}LnF_3$ systems from $NaF\text{-}NdF_3$ through $NaF\text{-}LuF_3$, two equilibrium compounds occur: $NaF{\cdot}LnF_3$ and $5NaF{\cdot}9LnF_3$. In all of the lanthanide systems the 1:1 compound exists in a hexagonal crystalline form (J. H. Burns, "Crystal Structure of Hexagonal $NaNdF_4$ and Related Compounds," this report). At temperatures above approximately 700°C, most of the $NaF{\cdot}LnF_3$ phases become converted to a disordered fluorite phase of variable composition (diagonally hatched regions in Fig. 1.7). The fluorite phase region is particularly interesting because its compositional variability is extended in proportion to the difference in ion size between Na^+ and Ln^{3+} (ref. 18). The compound $5NaF{\cdot}9LnF_3$ is found empirically to be the phase limit of the solid solution as the interstitial sites for anions become filled. At high temperatures this phase displays the disordering typical of the fluorite solid solution; at lower temperatures, however, the $5NaF{\cdot}9LnF_3$ fluorite phase may become ordered (where Ln is Dy to Lu) (cross-hatched section of Fig. 1.7).

Several results of the $Na^+\text{-}Ln^{3+}$ size disparity are noted in the crystal chemistry of the sodium fluoride–rare-earth trifluoride binary systems. First, there is a marked tendency for the number of intermediate crystal phases, produced by the interactions of a given $NaF\text{-}LnF_3$ component pair, to increase with increasing cation radius ratio.[18] Second, a trend prevails toward the formation of increasingly ordered crystalline phases at low temperatures throughout the series as cation size

[18] R. E. Thoma, "Complex Compounds in the Sodium Fluoride–Rare-Earth Trifluoride Systems," *Proceedings of the Fourth Rare Earth Research Conference*, Phoenix, Ariz., April 22–25, 1964.

Table 1.3. X-Ray, Optical, and Melting-Point Data for $LiMF_4$ Compounds

	Lattice Constants (A)		Calcd. Density (g/cm^3)	Refractive Indices		Melting Point (°C)
	a_0	c_0		N_ω	N_ϵ	
$LiEuF_4$	5.21	11.02	5.22	1.477	1.510	681[a]
$LiGdF_4$	5.21	11.00	5.34	1.474	1.502	748[a]
$LiTbF_4$	5.19	10.89	5.48	1.476	1.502	787[a]
$LiDyF_4$	5.19	10.81	5.60	1.476	1.504	811[a]
$LiHoF_4$	5.16	10.75	5.74	1.472	1.498	788[a]
$LiErF_4$	5.16	10.70	5.84	1.474	1.502	815
$LiTmF_4$	5.15	10.64	5.93	1.470	1.498	785
$LiYbF_4$	5.14	10.59	6.09	1.470	1.496	800
$LiLuF_4$	5.13	10.55	6.18	1.468	1.494	800

[a] Incongruent to MF_3 + liquid.

disparity increases. Further, increasing stability of the ordered solid phases is noted as Na^+/Ln^{3+} increases (see Fig. 1.7).

The Na^+/Ln^{3+} radius ratio varies only from 0.93 to 1.21 across the entire lanthanide series and is nearest unity for the pairs $NaF\text{-}NdF_3$ and $NaF\text{-}SmF_3$ (0.99 to 1.02). A priori, the systems in which the Na^+ and Ln^{3+} ion radii are nearly identical should be expected to contain the least ordered phases, and increasingly ordered structures when the discrepancy in ion size is greatest. Indeed, the trends throughout the lanthanide series appear generally to reflect the plausibility of this hypothesis, for the lighter members, LaF_3 and CeF_3, form a single intermediate crystal phase, the hexagonal $NaF{\cdot}LnF_3$ compound, which decomposes on heating to LnF_3 and liquid. The latter group, $\text{-}PrF_3$ to $\text{-}LuF_3$, is described in general by the system $NaF\text{-}YF_3$, in which three types of intermediate phases prevail – the $NaF{\cdot}LnF_3$ fluorite cubic, the $NaF{\cdot}LnF_3$ hexagonal, the $5NaF{\cdot}9LnF_3$ cubic, and the $5NaF{\cdot}9LnF_3$ ordered orthorhombic phases. In each of these phases alkali-metal and rare-earth cations are randomly substituted to varying degrees. Although the number and stability of ordered phases tend to increase throughout the $NaF\text{-}LnF_3$ series, a strange effect appears concurrently in the broadening of the composition range through which the disordered fluorite-like solid solution phase is found at high temperatures. This effect, although not understood, is possibly related to the difficulty of dissociating Na^+ ions from the larger charge density fields of the heavier lanthanide ions.

The trends toward increasing number, order, and stability of the $NaF\text{-}LnF_3$ crystal phases formed as the radius ratio Na^+/Ln^{3+} increases appear to be distinct, not only with respect to crystal chemistry of the binary compounds, but also in their modes of crystallization from molten mixtures. The fluorite-like phase, for example, is unstable below approximately 600 to 700°C with respect to the hexagonal $NaF{\cdot}LnF_3$ and LnF_3 phases, but it may easily be retained metastably in the cooled melts of appropriate compositions in the system group $NaF\text{-}DyF_3$ to $NaF\text{-}LuF_3$. These tendencies are so marked that in the $NaF\text{-}LuF_3$ system the ordered $5NaF{\cdot}9LuF_3$ phase, which in the other systems where it occurs must be prepared by prolonged annealing in the solid state at elevated temperatures, can be easily crystallized from $NaF\text{-}LuF_3$ melts simply by very slow cooling.

Tentative evidence that the lanthanide fluoride phase diagrams are approximate models for the actinides arises from comparisons based on cation sizes, as shown in Fig. 1.8. Although the systems are not exact analogs, they are sufficiently similar to permit qualitative estimates concerning the nature of the transplutonium trifluoride systems. The fact, for example, that all of the NaF–heavy metal trifluoride systems in the Na^+/M^{3+} cation size ratio 0.93 to 1.21, including all of the $NaF\text{-}LnF_3$ systems, $NaF\text{-}BiF_3$, $NaF\text{-}UF_3$, and $NaF\text{-}PuF_3$, form the hexagonal $NaF{\cdot}MF_3$ phase (see section on "Crystal Structure of Hexagonal $NaNdF_4$ and Related Compounds," this report) indicates that this phase may be expected throughout the NaF–actinide trifluoride series.

Dimorphism of the Rare-Earth Trifluorides

R. E. Thoma H. Insley G. D. Brunton

Dimorphism of the rare-earth trifluorides was studied extensively by Zalkin and Templeton,[19] who determined the crystal structures of two forms. They observed only the hexagonal form for the trifluorides LaF_3 to NdF_3, a hexagonal and an orthorhombic form for SmF_3, EuF_3, HoF_3, and TmF_3, and only an orthorhombic form for GdF_3, TbF_3, DyF_3, ErF_3, YbF_3, and LuF_3. The melting points of the trifluorides were determined by Spedding and Daane,[20] who noted that SmF_3, GdF_3, ErF_3, YbF_3, and LuF_3 produced thermal effects at temperatures below the melting points; they inferred these effects to be due to crystalline inversions in the solid state. In recent investigations of the alkali fluoride–LnF_3 systems, we found that in $NaF\text{-}GdF_3$ and $NaF\text{-}TbF_3$ mixtures containing 75 mole % LnF_3 the GdF_3 and TbF_3 inverted from the hexagonal (high temperature) to orthorhombic (low temperature) form at 918 and 950°C respectively. Although these values are somewhat lower than those reported by Spedding and Daane for the transition temperatures, they are in close enough agreement

[19] A. Zalkin and D. H. Templeton, *J. Am. Chem. Soc.* **25**, 2453 (1953).

[20] F. H. Spedding and A. H. Daane (eds.), *The Rare Earths*, p. 78, Wiley, New York, 1961.

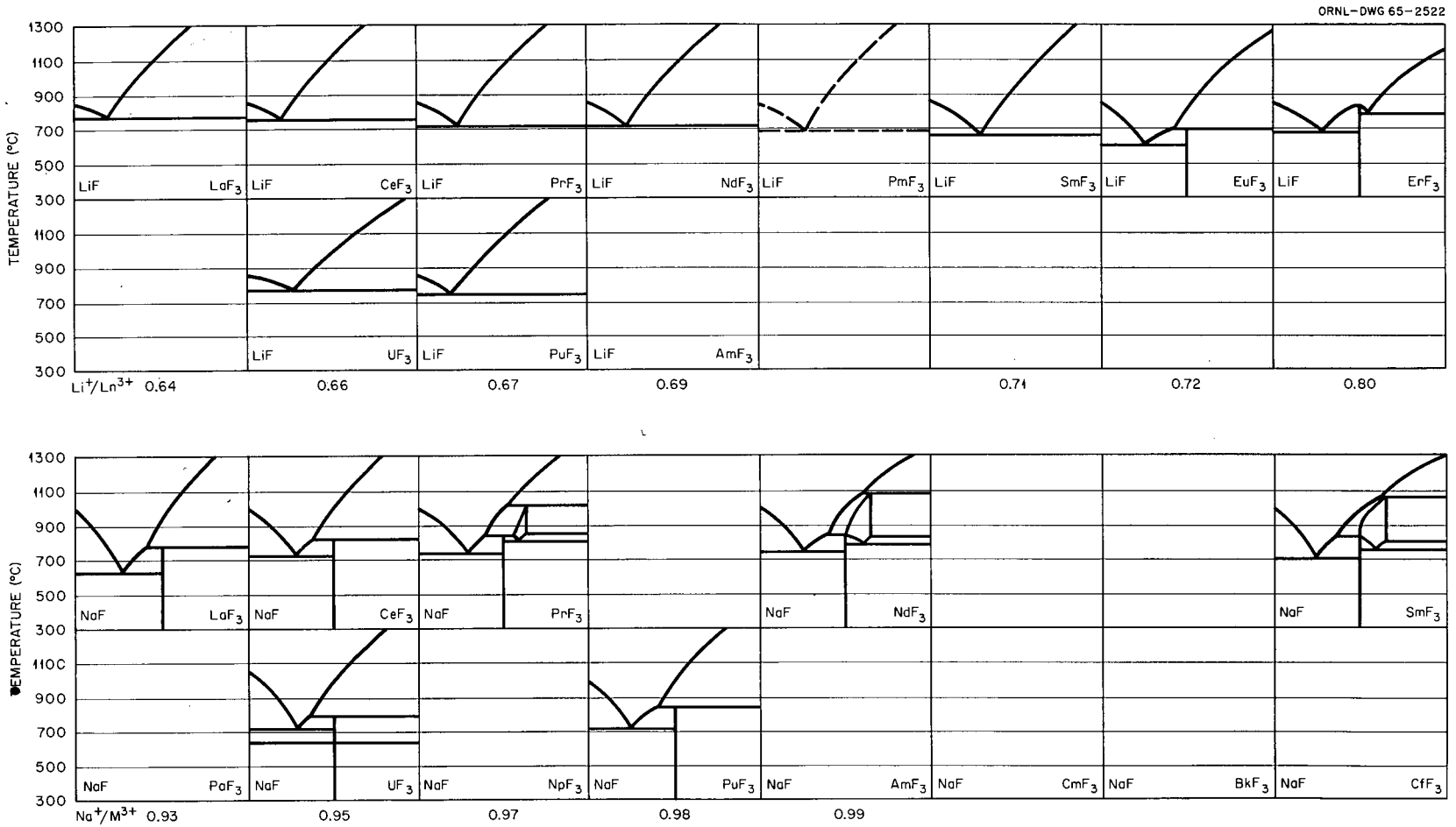

Fig. 1.8. Comparison of the LiF- and NaF-Lanthanide and Actinide Trifluoride Binary Systems on the Basis of Cation Radius Ratios.

to suggest that thermal data are representative of the hexagonal-orthorhombic equilibrium transition temperature. On the basis of these results and from the results of our recent preliminary examinations of these transitions with the high-temperature x-ray diffractometer, we have concluded that the high-temperature dimorphism of the rare-earth trifluorides occurs as shown in Fig. 1.9. The results make possible the following new generalizations concerning the rare-earth trifluorides:

1. The equilibrium allotropes of the rare-earth trifluorides are comprised only of the hexagonal and orthorhombic modifications.
2. All rare-earth trifluorides crystallize from the molten state as hexagonal crystals.
3. Although the orthorhombic form may be a stable modification of LaF_3, CeF_3, NdF_3, and PmF_3, the inversion temperature will occur at such low temperatures that its determination may not be experimentally feasible.

Properties of the Rare-Earth Halides

R. E. Thoma

Current data for the known halides of the rare-earth elements are summarized in Table 1.4, which was prepared as a part of a current survey of the chemistry of the rare-earth halides and complex halides.[21]

The Systems $NaF-ScF_3$ and $NaF-BiF_3$

R. H. Karraker[22] R. E. Thoma D. R. Sears

The chemistry of the trivalent state affords the most useful means of interrelating the chemical similarities of the lanthanides and actinides. For many of these elements, this state is either the most stable or the only oxidation state observed in their chemical compounds. The variation in chemical phase behavior in the binary systems of the alkali fluorides with the trifluorides of the lanthanide, actinide, and other metals affords a broad experimental base from which detailed theories of phase behavior and complex compound formation may be anticipated. For the reasons implicit in these statements, we recently extended the investigation of the lithium and sodium fluoride–lanthanide trifluoride relationships to include the systems $NaF-ScF_3$ and $NaF-BiF_3$.

The System $NaF-ScF_3$. – The alkali fluoride–MF_3 pair in which the M^+/M^{3+} radius ratio is just larger than that for $NaF-LuF_3$ is $NaF-ScF_3$. Since the Na^+/Sc^{3+} ratio more nearly approaches that of Na^+/Lu^{3+} than of Na^+/Al^{3+}, $NaF-ScF_3$ melts would behave, we assumed, more nearly like $NaF-LuF_3$ than like $NaF-AlF_3$. Initial results showed, however, that even though the radius of Sc^{3+} is considerably closer to that of Lu^{3+} than to that of Al^{3+}, the liquidus profile

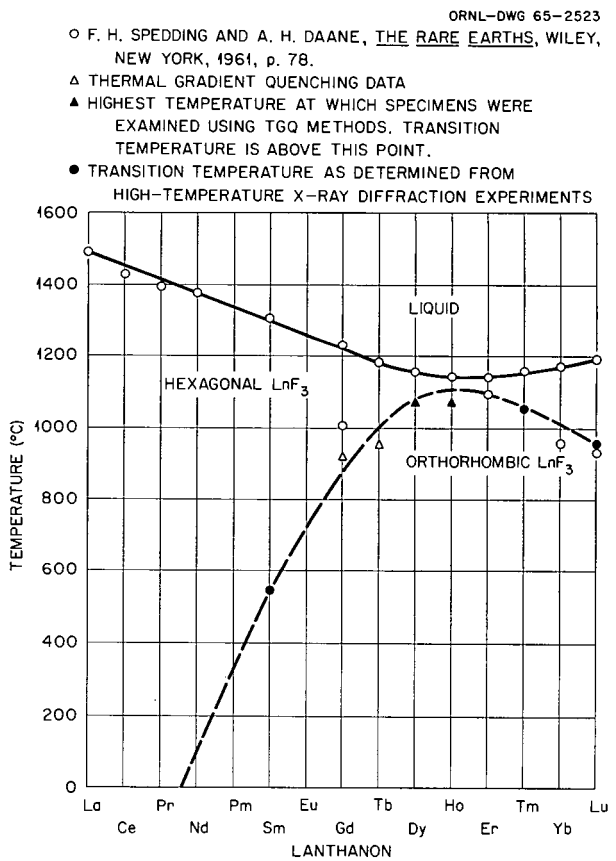

Fig. 1.9. Dimorphism Among the Rare Earth Trifluorides.

[21] To be published as a chapter in vol. II of the forthcoming work, *Progress in the Science and Technology of the Rare Earths*, ed. by LeRoy Eyring.

[22] ORINS research participant, Memphis State University, Memphis, Tenn.

Table 1.4. Physical Properties of the Rare-Earth Halides

Compound	Melting Point (°C)	Boiling Point (°C)	Crystal Structure Data					Density (g/cc)	Thermochemical Data (kcal/mole)		
			Symmetry	Space Group	Lattice Parameters (A)				$\Delta H_{formation}$ (298°K)	ΔH_{fusion}	$\Delta H_{vaporization}$[a]
					a_0	b_0	c_0				
LaF_3	1490		Hexagonal	*P63/mcm*	7.186		7.352	5.936	(−421)[b]		
$LaCl_3$	852	2700	Hexagonal	*P63/m*	7.483		4.364	3.848	−255.9	13.0	
$LaBr_3$	783								(−233)	13.0	
LaI_3	761		Orthorhombic	*Ccmm*	4.37	14.01	10.04	2.246	−189		
LaI_2	830		c								
CeF_4	*d*	c	Monoclinic	*I2/c*	12.6	10.6	8.3		(−442)		
CeF_3	1437, 1430	2327	Hexagonal	*P63/mcm*	7.112		7.279	6.157	(−416)		
$CeCl_3$	802	1925	Hexagonal		7.450		4.315		252.8		
$CeBr_3$	722	1705							(−228)		
CeI_3	761	1397	Orthorhombic	*Ccmm*	4.341	14.00	10.015	2.273	−185	12.4	
CeI_2			c								
PrF_4			Monoclinic	*I2/c*							
PrF_3	1395	2327	Hexagonal	*P63/mcm*	7.075		7.238	6.14	(−413)	8	62
$PrCl_3$	786	1905	Hexagonal		7.422		4.275		−252.1	12.1	52.3
$PrCl_2$									−163		
$PrBr_3$	693	1547							−225	11.3	45
PrI_3	733	1377	Orthorhombic	*Ccmm*	4.309	13.98	9.958	2.309	−152	12.7	41
PrI_2	760		c								
NdF_4			Monoclinic	*I2/c*							
NdF_3	1374		Hexagonal	*P63/mcm*	7.030		7.200		(−410)		62
$NdCl_3$	760								−245.6	12.0	51.8
$NdCl_2$	835								−163.2		
$NdBr_3$	684								(−223)	10.8	46.8
NdI_3	775		Orthorhombic	*Ccmm*	4.284	13.979	9.948	2.342	(−158.9)	9.7	41
NdI_2	565		c								

Table 1.4 (continued)

Compound	Melting Point (°C)	Boiling Point (°C)	Crystal Structure Data: Symmetry	Space Group	Lattice Parameters (A) a_0	b_0	c_0	Density (g/cc)	Thermochemical Data (kcal/mole): $\Delta H_{formation}$ (298°K)	ΔH_{fusion}	$\Delta H_{vaporization}$[a]
SmF_3	1306	(2327)	Hexagonal	$P63/mcm$	6.956		7.120	6.925	(−405)	8	
			Orthorhombic	$Pnma$	6.669	7.059	4.405	6.643			
SmF_2	(1377)	(2427)	Cubic	$Fm3m$	5.79				(−290)	5	
$SmCl_3$	678		Hexagonal		7.378		4.171		−243	8	
$SmCl_2$	859, 740	(2027)	Orthorhombic		8.973	7.532	4.497		−195.6	6	
$SmBr_3$	664	1645							(−216)		
$SmBr_2$	700	(1877)	e						(−182)	6	
SmI_3	820		Hexagonal	$R\bar{3}$	7.490		20.80	3.141	(−174)	9	
SmI_2	(527)	(1577)	f						(−155)	5	
EuF_3	1276	(2277)	Hexagonal	$P63/mcm$	6.916		7.091	7.088	(−391)		
			Orthorhombic	$Pnma$	6.622	7.019	4.396	6.793			
EuF_2	(1377)	(2527)	Cubic	$Fm3m$	5.842				(−300)		
$EuCl_3$	774, 623	d	Hexagonal		7.369		4.133		(−233)		
$EuCl_2$	738	(2027)	Orthorhombic	$Pnmb$	8.914	7.499	4.493		(−210)		
$EuBr_3$	(705)	d							(−203)		
$EuBr_2$	(702)	(1873)	Orthorhombic						(−187)		
EuI_3	(880)	d							(−159)		
EuI_2	(527)	(1573)	f								
GdF_3	1228, 1231	(2277)	Hexagonal	$P63/mcm$	(7.064)		(6.900)				
			Orthorhombic	$Pnma$	6.571	6.985	4.393	7.056	(−404)	8	60
$GdCl_3$	609, 602	(1577)	Hexagonal		7.363		4.105		(−240.1)	9.6	45
$GdBr_3$	785	(1487)							(−214)	8.7	44
GdI_3	931	(1377)	Hexagonal	$R\bar{3}$	7.539		20.83	3.138	−170	10	40
GdI_2	831										
TbF_4			Monoclinic	$I2/c$	12.1	10.3	7.9				

Table 1.4 (continued)

Compound	Melting Point (°C)	Boiling Point (°C)	Crystal Structure Data: Symmetry	Space Group	Lattice Parameters (A) a_0	b_0	c_0	Density (g/cc)	Thermochemical Data (kcal/mole): $\Delta H_{formation}$ (298°K)	ΔH_{fusion}	$\Delta H_{vaporization}$ [a]
TbF_3	1172	(2277)	Hexagonal	$P63/mcm$	(7.035)		(6.875)			8	60
			Orthorhombic	$Pnma$	6.513	6.949	4.384	7.236	(−400)		
$TbCl_3$	588	(1547)							(−241)	7	45
$TbBr_3$	(830)	(1483)							(−211)	9	44
TbI_3	955	(1327)	Hexagonal	$R\bar{3}$	7.526		20.838	3.155	(−169)	10	40
DyF_3	1154	(2227)	Hexagonal	$P63/mcm$	(7.010)		(6.849)		(−398)	8	60
			Orthorhombic	$Pnma$	6.460	6.906	4.376	7.465			
$DyCl_3$	654	(1627)	Monoclinic		6.91	11.97	6.40		(−236)	7	45
$DyBr_3$	881	(1473)							(−209)	9	44
DyI_3	955	(1317)	Hexagonal	$R\bar{3}$	7.488		20.833	3.210	−166	10	41
HoF_3	1143	(2227)	Hexagonal	$P63/mcm$	6.833		6.984	7.829			
			Orthorhombic	$Pnma$	6.404	6.875	4.379	7.644	(−395)	8	60
$HoCl_3$	720	(1507)	Monoclinic		6.85	11.85	6.39		−233	7.0	44
$HoBr_3$	914	(1467)							(−207)	10	43
HoI_3	1010	(1297)						3.240	−164	10	41
ErF_3	1140	(2227)	Hexagonal	$P63/mcm$	(6.952)		(6.797)				
			Orthorhombic	$Pnma$	6.354	6.848	4.380	7.814	(−392)	8	60
$ErCl_3$	776	(1497)	Monoclinic		6.80	11.79	6.39		211.4	7.8	44
$ErCl_2$									−150		
$ErBr_3$	950	(1457)							(−205)	10	43
ErI_3	1020	(1277)	Hexagonal	$R\bar{3}$	7.451		20.78	3.279	−162	10	40
TmF_3	1158	(2223)	Hexagonal	$P63/mcm$	6.763		6.927	8.220	(−391)		
			Orthorhombic	$Pnma$	6.283	6.811	4.408	7.971		8	60
$TmCl_3$	821	(1487)	Monoclinic		6.75	11.73	6.39		−229	9	44
$TmBr_3$	(955)	(1437)							(−203)	10	43
TmI_3	(1015)	(1257)	Hexagonal	$R\bar{3}$	7.415		20.78	3.321	−137.8	10	40

Table 1.4 (continued)

Compound	Melting Point (°C)	Boiling Point (°C)	Crystal Structure Data: Symmetry	Space Group	Lattice Parameters (A) a_0	b_0	c_0	Density (g/cc)	Thermochemical Data (kcal/mole): $\Delta H_{formation}$ (298°K)	ΔH_{fusion}	$\Delta H_{vaporization}$[a]
TmI_2			Hexagonal		4.520		6.967				
YbF_3	1157	(2227)	Hexagonal	*P63/mcm*	(6.897)		(6.745)		(−376)		
			Orthorhombic	*Pnma*	6.216	6.786	4.434	8.168		8	60
YbF_2	1477	(2377)	Cubic		5.571				(−280)	5	75
$YbCl_3$	854	*d*	Monoclinic		6.73	11.65	6.38		−228.7, −223	9	
$YbCl_2$	723	(1927)	Orthorhombic		6.53	6.68	6.91		184.5	6	50
$YbBr_3$	940	*d*							(−185)	10	
$YbBr_2$	677	(1827)							(−157)	6	48
YbI_3	(1030)	*d*	Hexagonal	$R\bar{3}$	7.434		20.72	3.331	(−143)	10	
YbI_2	527	(1327)	Hexagonal[g]	*C6*	4.503		6.972		(−135)	5	37
LuF_3	1182	(1427)	Hexagonal	*P63/mcm*	(6.87)		(6.72)				
			Orthorhombic	*Pnma*	6.181	6.731	4.446	8.44	(−392)	8	60
$LuCl_3$	892	(1477)	Monoclinic		6.72	11.60	6.39		−227.9	9	43
$LuBr_3$	960	(1407)							(−200)	10	42
LuI_3	1045	(1207)	Hexagonal	$R\bar{3}$	7.395		20.71	3.386	−133.2	11	38

[a]Vapor pressure data may be found in reports by J. A. Gibson *et al.*, *The Properties of the Rare Earth Metals and Compounds*, Battelle Memorial Institute, Columbus, Ohio, 1954, and by E. Shimazaki and K. Niwa, *Z. Anorg. Allgem. Chem.* **314**, 21 (1962).

[b]Figures in parentheses are estimates.

[c]LaI_2, CeI_2, and PrI_2 are isostructural but of a different structure than NdI_2, SmI_2, and YbI_2, which comprise a second isomorphous series [G. I. Novikov and O. G. Polyachenok, *Usp. Khim.* **33**, 732 (1964)].

[d]Decomposes.

[e]$SrBr_2$ structure.

[f]SmI_2 and EuI_2 are considered to be isostructural, although neither structure has been determined.

[g]Isostructural with TmI_2.

Table 1.4 (continued)

BIBLIOGRAPHY

L. B. Asprey and B. B. Cunningham, "Unusual Oxidation States of Some Actinide and Lanthanide Elements," p. 267–302 in *Progress in Inorganic Chemistry*, ed. by F. A. Cotton, vol. II, Interscience, New York, 1960.

L. B. Asprey, T. K. Keenan, and F. H. Kruse, *Inorg. Chem.* **3**, 1137 (1964).

H. Bommer and E. Hohmann, *Z. Anorg. Allgem. Chem.* **248**, 357 (1941).

D. T. Cromer, *J. Phys. Chem.* **61**, 753 (1957).

R. B. Cunningham, D. C. Feay, and R. M. Rollier, *J. Am. Chem. Soc.* **76**, 3361 (1954).

W. Doll and W. Klemm, *Z. Anorg. Allgem. Chem.* **241**, 239 (1939).

L. F. Druding and J. D. Corbett, *J. Am. Chem. Soc.* **81**, 5512 (1959).

A. S. Dworkin and M. A. Bredig, *J. Phys. Chem.* **67**, 697 (1963).

A. S. Dworkin and M. A. Bredig, *J. Phys. Chem.* **67**, 2499 (1963).

J. A. Gibson *et al.*, *The Properties of the Rare Earth Metals and Compounds*, Battelle Memorial Institute, Columbus, Ohio, 1954.

G. Jantsch and N. Skalla, *Z. Anorg. Allgem. Chem.* **193**, 391 (1930).

O. Kubachewski and E. L. Evans, *Metallurgical Thermochemistry*, Wiley. New York, 1956.

G. R. Machlan, C. T. Stubblefield, and L. Eyring, *J. Am. Chem. Soc.* **77**, 2975 (1955).

J. E. Mee and J. D. Corbett, *Inorg. Chem.* **4**, 88 (1965).

G. I. Novikov and O. G. Polyachenok, *Usp. Khim.* **33**, 732 (1964).

B. Porter and E. A. Brown, *J. Am. Ceram. Soc.* **45**, 44 (1962).

L. L. Quill, ed., *Chemistry and Metallurgy of Miscellaneous Materials, Thermodynamics*, McGraw-Hill, New York, 1950.

E. Shimazaki and K. Niwa, *Z. Anorg. Allgem. Chem.* **314**, 21 (1962).

F. H. Spedding and J. P. Flynn, *J. Am. Chem. Soc.* **74**, 1474 (1954).

F. H. Spedding and A. H. Daane, eds., *The Rare Earths*, Wiley, New York, 1963.

A. Zalkin and D. H. Templeton, *J. Am. Chem. Soc.* **75**, 2453 (1953).

of the $NaF\text{-}ScF_3$ system more nearly approximates that of the $NaF\text{-}AlF_3$ system than that of the $NaF\text{-}LuF_3$ system. Although the two intermediate phases that form in the $NaF\text{-}ScF_3$ system correspond to formula analogs in the system $NaF\text{-}AlF_3$ (i.e., a 3:1 and a 1:1 compound), crystals of the pairs are not isomorphous. The phase diagram of the system, constructed from preliminary thermal analysis, thermal gradient quenching, and direct visual observation data, is shown in Fig. 1.10. The phase diagram as described here affords an interesting contrast to that reported during the course of this investigation by Fedorov and associates,[23] who believed that the system was described as is also

[23] N. Ya. Federov, S. I. Sklyarenko, and E. S. Petrov, *Akad Nauk. SSSR* 1, 104 (1964).

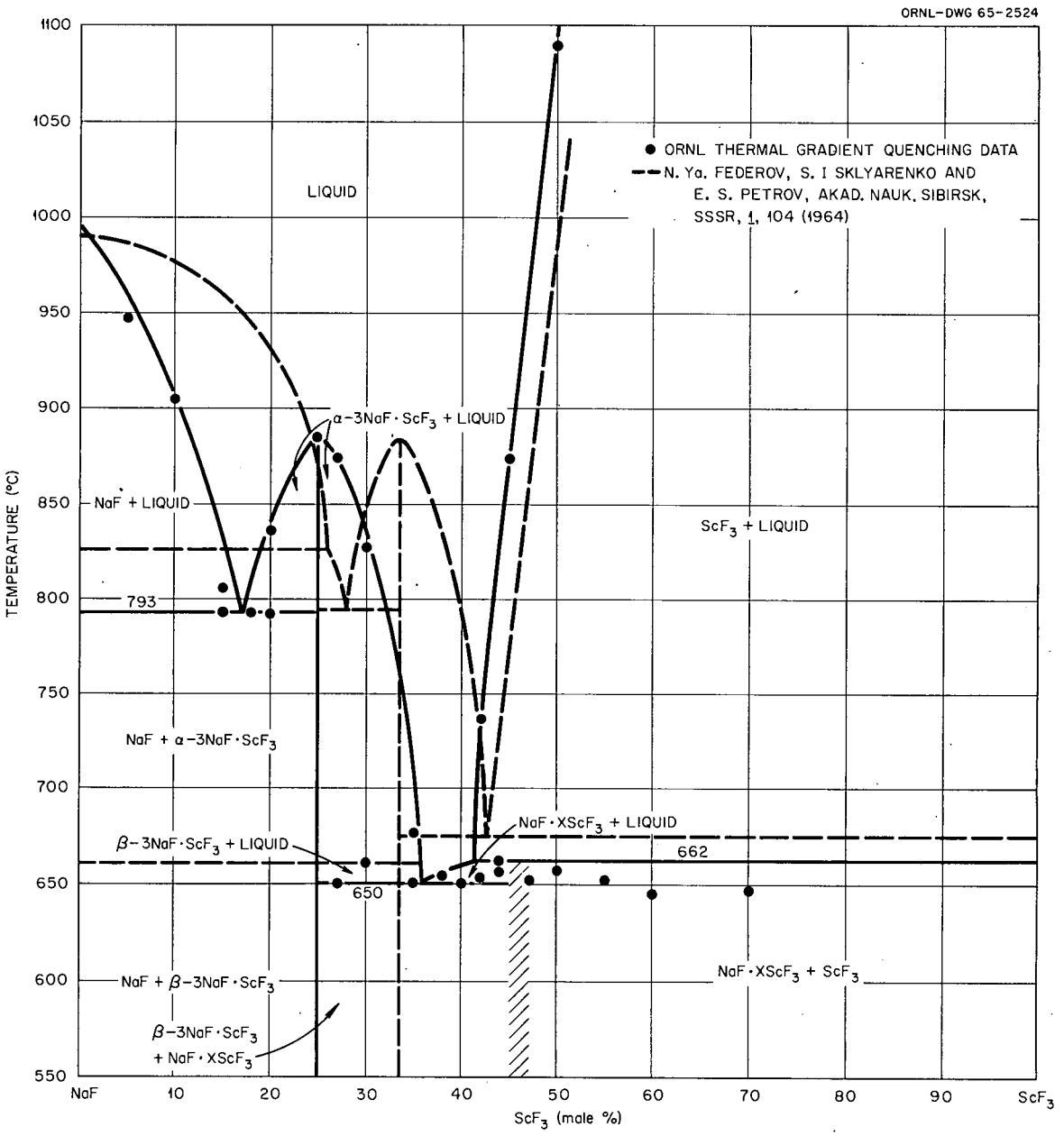

Fig. 1.10. The System $NaF\text{-}ScF_3$.

shown in Fig. 1.10. The reasons for the remarkable difference between the two diagrams are not directly deducible from the literature. Scandium trifluoride, like many of the metal fluorides, is very easily hydrolyzed at high temperatures by traces of moisture in the atmosphere. Hydrolysis, proceeding through reactions of the following sort,

$$2Na_3ScF_6 + 2H_2O \rightleftharpoons 2NaF{\cdot}ScOF + 4NaF + 4HF ,$$

would account for the anomalous activity of NaF at low ScF_3 concentrations and for a 2:1 oxyfluoride phase not encountered in ORNL measurements, a phase which might have been inferred to be Na_2ScF_5.

The System NaF-BiF$_3$. – A preliminary investigation of intermediate compound occurrence in the system NaF-BiF_3 was made because the relative cation sizes of Na^+/Bi^{3+} (1.11) are nearly identical with the Na^+/Ln^{3+} pairs, Na^+/Tb^{3+} (1.09), Na^+/Dy^{3+} (1.11), and Na^+/Y^{3+} (1.11). Results of this investigation showed that a hexagonal intermediate phase was formed from slowly cooled melts of NaF and BiF_3. Optical and x-ray diffraction measurements with the crystals showed that the compound has a 1:1 formula, with the properties listed elsewhere (see section on "Crystal Structure of Hexagonal $NaNdF_4$ and Related Compounds," this report). The x-ray diffraction pattern of the new phase was successfully indexed and refined, using a recently developed least-squares program, and was found to be isomorphous with $NaNdF_4$ (see section on "Crystallographic Data for Some Pure Materials," this report). That the lattice constants so nearly approach those of $NaNdF_4$ rather than those of $NaDyF_4$ suggests that further study of the spatial relationships in $NaBiF_4$ may be worthwhile.

SALT SYSTEMS FOR APPLICATION IN ADVANCED REACTOR TECHNOLOGY

R. E. Thoma
H. Insley
H. A. Friedman
G. D. Brunton
G. M. Hebert
T. N. McVay

Core and Blanket Fluids for Fast Reactors

As a reactor concept, the molten-salt system offers great flexibility with respect to application and design. It may be possible that future reactors, evolutionary daughters of the MSRE, will include fast as well as thermal versions. The neutron energy spectrum that must prevail in the core of a fast reactor imposes rather restrictive limits on the materials which can be considered as suitable core or blanket fluids. Virtually the only class of salts which may be employed as fuel mixtures in such reactors is that of the isotopically pure chlorides ($^{35}Cl^-$). A previous report[24] showed that the expected phase behavior in NaCl-KCl-$PuCl_3$ mixtures would make them attractive as fast-reactor core fluids. Crystallographic and phase data for UCl_3 indicate that it should be completely miscible with NaCl-KCl-$PuCl_3$ mixtures at elevated temperatures. Little or no data were available for the two systems we consider to be of primary relevance to appraisals of core (KCl-UCl_3) and blanket (NaF-KF-ThF_4) fluids. We therefore conducted partial examinations of the equilibrium behavior in these two systems to appraise the possibility that the materials would serve as useful core and blanket fluids; the satisfactory results of this examination have permitted us to defer further investigations of these fluids.

The System KCl-UCl$_3$. – The lability of uranium trichloride with respect to disproportionation (to U^0 and UCl_4) as well as to hydrolysis continues to evoke questions as to the nature of its equilibrium behavior at high temperatures. After testing various methods of obtaining and preserving trivalent uranium in chloride mixtures, we concluded that there are two good procedures for preparation of these materials. One entails removal of water by treatment of the salts with hexachloropropene at 200 to 300°C. This reagent, however, oxidizes uranium to the tetravalent state at these temperatures. If, however, uranium metal is present in the melt throughout the purification procedure, the uranium in the melt is retained in the trivalent state. A more suitable procedure for obtaining KCl-UCl_3 mixtures of accurately ascertained composition consists in purging KCl-$PbCl_2$ melts with dry HCl gas and subsequently reducing Pb^{2+} with uranium metal to produce the KCl-UCl_3 mixtures of desired stoichiometry. In practice, a slight excess of U^0 was generally retained in the melt to minimize contamination by UCl_4. It is recognized that finite solubility of U^0 in KCl-UCl_3 may occur and affect apparent

[24] H. A. Friedman, *Reactor Chem. Div. Ann. Progr. Rept. Jan. 31, 1964*, ORNL-3591, p. 9.

phase transition temperatures on the system; this effect, however, appeared to be negligible on the basis of the assumption that uranium metal dissolved in the salt phases should induce opacity.

The phase diagram of the system $KCl-UCl_3$, inferred from results of thermal analysis and thermal gradient quenching experiments, is shown in Fig. 1.11. This phase diagram differs substantially from the preliminary description given by Kraus.[25] Data contributing to the construction of the diagram reported here were obtained from melts in which the U^{4+} concentration was minimized by the presence of excess uranium metal. Melts prepared without excess uranium metal behaved identically as described by Kraus, and, on cooling, contained some 10 to 30% tetravalent uranium.

The results of the current investigation of the $KCl-UCl_3$ system show the existence of only one intermediate compound, $2KCl{\cdot}UCl_3$. Crystallographic data for this compound are given elsewhere (see section on "Crystallographic Data for Some Pure Materials," this report). Uranium trichloride appears to be capable of forming an extensive solid solution with the $2KCl{\cdot}UCl_3$ phase. Two eutectics occur in the system at 19 and 55 mole % UCl_3 and at 560 and 553°C respectively. The reason for an apparent persistence of the eutectic break in mixtures that contain as much as 85 mole % UCl_3 is not known. Similarly, the cause of large thermal effects at approximately 588°C up to 30 mole % UCl_3 is also not known. Kraus reported two thermal effects on cooling melts containing up to 30 mole % UCl_3 and inferred the existence of the compound $3KCl{\cdot}UCl_3$ on the basis of them. No evidence for the existence of this compound was found, however, in the present investigation.

Small persistent thermal effects were noted on cooling at approximately 650 and 770°C; these appeared to be related to the amount of excess uranium metal present.

The System $NaF-KF-ThF_4$. – Although the salts which may be considered as fuels for fast reactors are apparently restricted essentially to the isotopically pure ^{35}chlorides, blankets for use in molten-salt fast breeder reactors could be composed of fluoride salts. Blanket salt mixtures

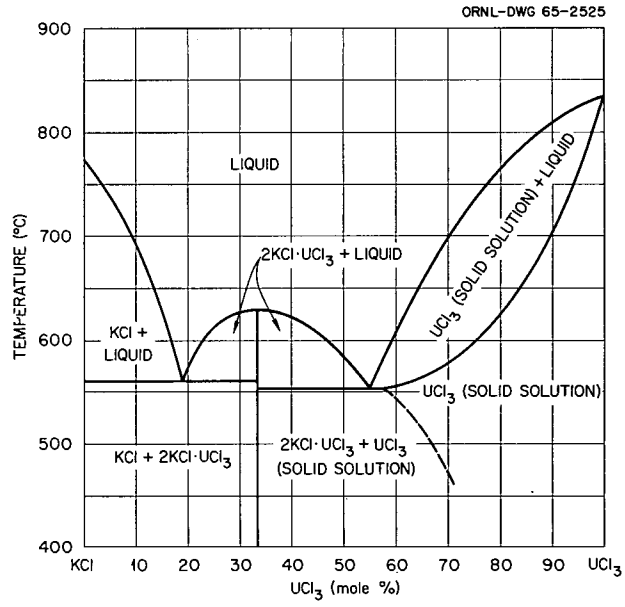

Fig. 1.11. The System $KCl-UCl_3$.

should exist as homogeneous fluids at temperatures of 550 to 600°C. In examination of the system $NaF-KF-ThF_4$, it was discovered that this criterion is met by several ternary mixtures containing 60 to 70 mole % NaF and 20 to 28 mole % ThF_4. The results of the current investigation are shown in Fig. 1.12. The lowest-melting eutectic is located at an $NaF-KF-ThF_4$ composition of about 68-6-26 mole % and melts at about 562°C. A salt mixture of this composition contains about 2400 g of thorium per liter. As in the analogous system $NaF-KF-UF_4$,[26] a 1:1:1 compound markedly influences phase behavior in the low-melting region of the system.

The ternary compound $NaF{\cdot}KF{\cdot}ThF_4$ (see section on "Crystallographic Data for Some Pure Materials," this report) melts incongruently at about 713°C to $7(Na,K)F{\cdot}6ThF_4$ + liquid. The large primary phase field of the ternary compound relative to that of $2NaF{\cdot}ThF_4$ is probably due to the fact that a large fraction of the K^+ ions (radius = 1.33 A) in $NaF{\cdot}KF{\cdot}ThF_4$ can be replaced by the smaller Na^+ ions (radius = 0.98 A), while for $2NaF{\cdot}ThF_4$ the converse is not possible.

[25] C. A. Kraus, Brown Univ. Report M-251, July 1, 1943.

[26] R. E. Thoma, *Phase Diagrams of Nuclear Reactor Materials*, ORNL-2548, p. 103 (Nov. 2, 1959).

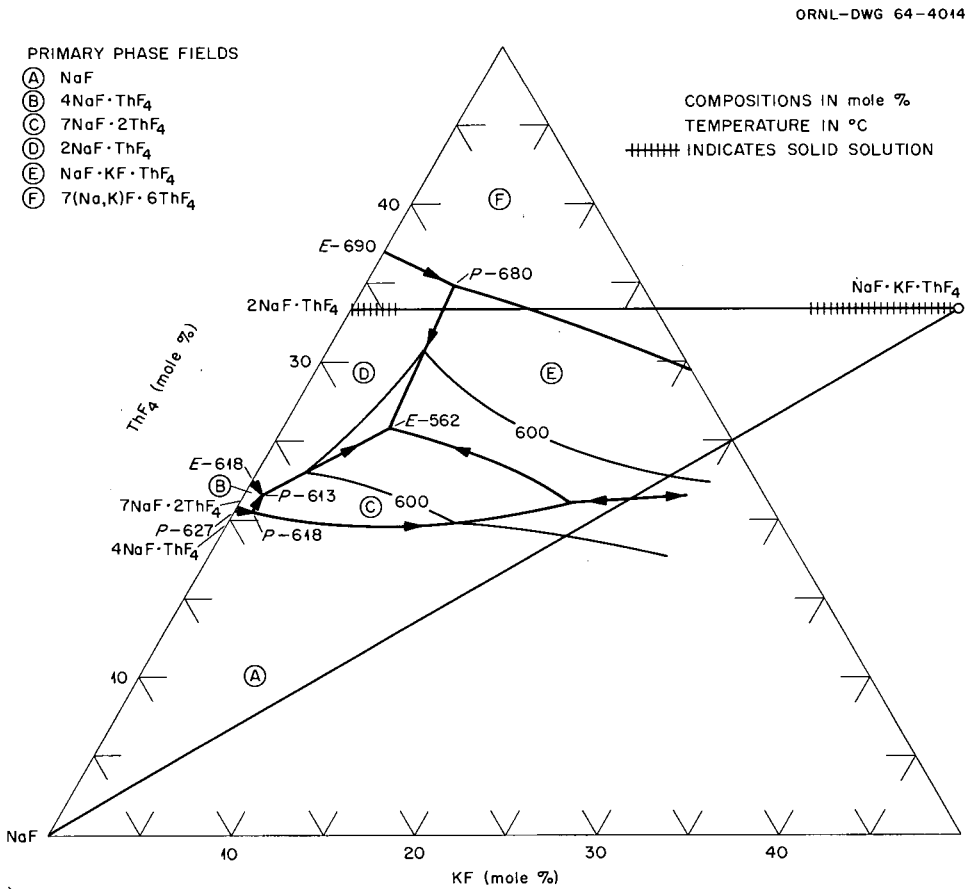

Fig. 1.12. Partial Phase Diagram of the System NaF-KF-ThF_4.

Although $7NaF{\cdot}2ThF_4$ does not appear as a primary phase in the binary system NaF-ThF_4, it has a relatively large primary phase field in the ternary system because it forms a very extensive if not complete solid solution with the compound $7KF{\cdot}2ThF_4$.

The System LiF-NaF-ThF_4. — An investigation of the phase equilibria in the system LiF-NaF-ThF_4 has been conducted over the last several years because of the long-range prospect that these salts may find various applications in nuclear technology. As thorium solvents, LiF-NaF mixtures of compositions near the eutectic afford homogeneous molten solutions of very high thorium density. The phase diagram of the LiF-NaF-ThF_4 system (Fig. 1.13) shows that at 500 to 600°C the saturating compositions of ThF_4 are 28 and 32 mole % ThF_4; liquids of these compositions contain more than 3000 g of thorium (as metal) per liter. At such high thorium concentrations, LiF-NaF-ThF_4 mixtures would appear to be attractive as breeder blankets which may be conveniently and cheaply reprocessed. The prospect of exploiting the high solubility of ThF_4 in this system also makes its application in the fluoride volatility process attractive in connection with chemical reprocessing of breeder fuel elements.

Determinations of the locations of boundary curves separating the 13 primary phase fields in the LiF-NaF-ThF_4 ternary system are nearly complete, as are the determinations of the important liquid-solid transition temperatures. The principal remaining questions concern the limits of solid solubility in the complex solid phase. The compositions and temperatures at which invariant equilibrium reactions occur are shown in Table 1.5.

ORNL-DWG 64-1993

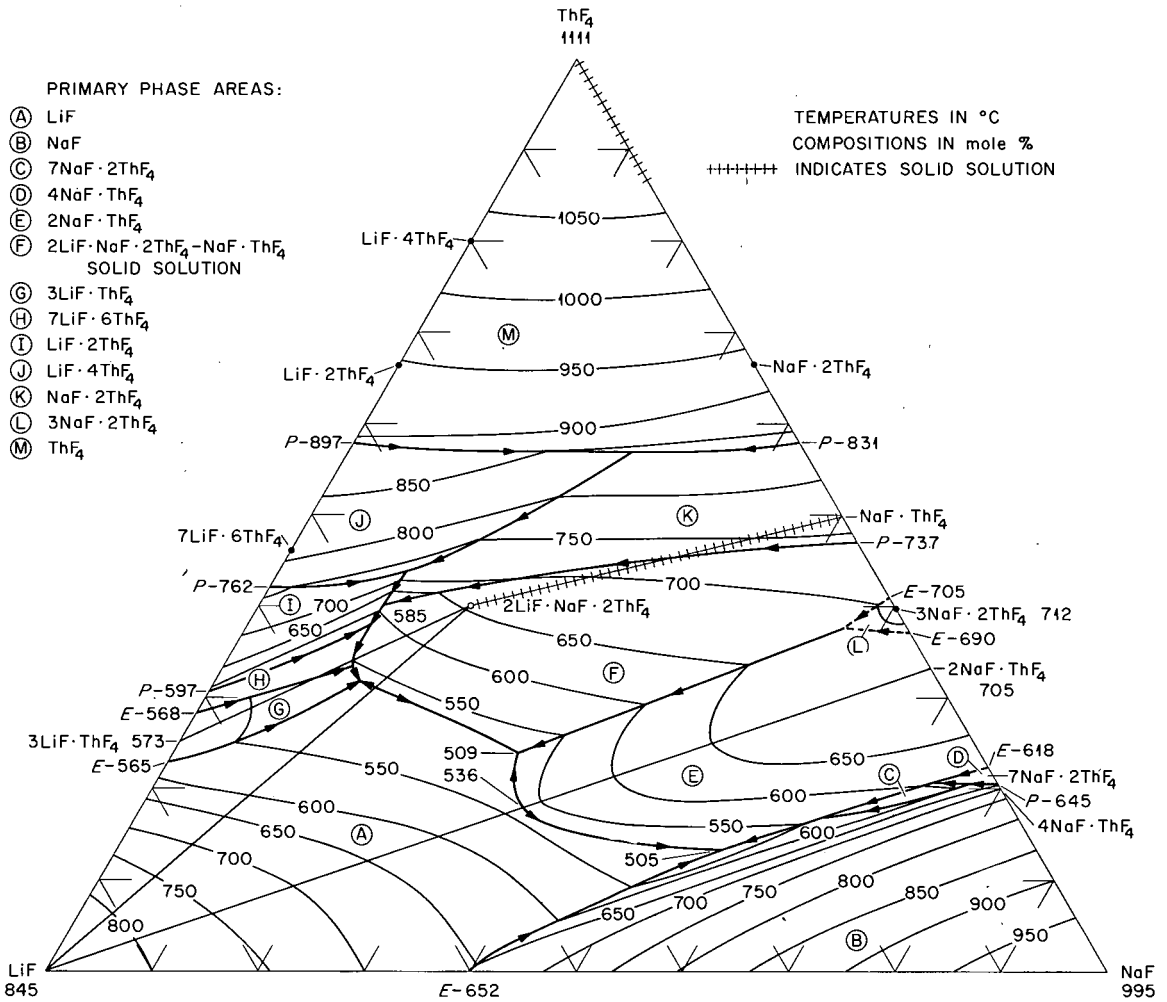

Fig. 1.13. The System LiF-NaF-ThF_4.

The LiF-NaF-ThF_4 system and its counterpart, LiF-NaF-UF_4, are of potentially continuing interest in molten-salt reactor technology because of their similar liquidus surfaces and because of the previously demonstrated[27] ease with which Th^{4+} and U^{4+} ions may be substituted for one another in such systems without grossly affecting liquid-solid reaction temperatures. One major phenomenon which takes place in the LiF-NaF-ThF_4 system has not been examined as yet regarding its implication for the four-component system LiF-NaF-ThF_4-UF_4. A ternary compound, NaF·2LiF·2ThF_4, crystallizes as a hexagonal phase from LiF-NaF-ThF_4 liquids. The phase is isostructural with β-NaF·ThF_4 and forms a continuous solid solution with β-NaF·ThF_4, as shown in the hatched section in Fig. 1.13. The crystallographic data for these solids are given elsewhere (see section on "Crystallographic Data for Some Pure Materials," this report). It is evident from the phase diagram that the solubility relationships involving NaF·ThF_4 and NaF·2LiF·2ThF_4 are the salient features of the system LiF-NaF-ThF_4. The substitutional mechanism effecting solid solution formation between

[27] C. F. Weaver *et al.*, *J. Am. Ceram. Soc.* **43**, 213 (1960).

Table 1.5. Invariant Equilibria and Singular Points in the System $LiF-NaF-ThF_4$

Composition of Liquid (mole %)			Temperature (°C)	Type of Equilibrium	Solid Phases Present at Invariant Point
LiF	NaF	ThF_4			
30	57	13	505	Eutectic	LiF, NaF, $2NaF \cdot 2ThF_4$
18	65	17	(560)[a]	Decomposition	NaF, $7NaF \cdot 2ThF_4$, $2NaF \cdot ThF_4$
46	36	18	536	Boundary curve maximum	LiF, $2NaF \cdot ThF_4$
3	76	21	(620)	Peritectic	NaF, $4NaF \cdot ThF_4$, $7NaF \cdot 2ThF_4$
6	73	21	(605)	Decomposition	$4NaF \cdot ThF_4$, $7NaF \cdot 2ThF_4$, $2NaF \cdot ThF_4$
43.5	32.5	24	509	Eutectic	LiF, $2NaF \cdot ThF_4$, $NaF \cdot ThF_4$-$LiF \cdot 2NaF \cdot 2ThF_4$ ss
53.5	15.5	31	530	Boundary curve maximum	LiF, $NaF \cdot ThF_4$-$LiF \cdot 2NaF \cdot 2ThF_4$ ss
54.5	13.5	32	525	Eutectic	LiF, $3LiF \cdot ThF_4$, $NaF \cdot ThF_4$-$LiF \cdot 2NaF \cdot 2ThF_4$ ss
54.5	12.5	33	540	Peritectic	$3LiF \cdot ThF_4$, $7LiF \cdot 6ThF_4$, $NaF \cdot ThF_4$-$LiF \cdot 2NaF \cdot 2ThF_4$ ss
6	56.5	37.5	(640)	Decomposition	$2NaF \cdot ThF_4$, $3NaF \cdot 2ThF_4$, $NaF \cdot ThF_4$-$LiF \cdot 2NaF \cdot 2ThF_4$ ss
50	12	38	585	Peritectic	$7LiF \cdot 6ThF_4$, $LiF \cdot 2ThF_4$, $NaF \cdot ThF_4$-$LiF \cdot 2NaF \cdot 2ThF_4$ ss
48	12	40	(625)	Peritectic	$LiF \cdot 2ThF_4$, $NaF \cdot ThF_4$-$LiF \cdot 2NaF \cdot 2ThF_4$ ss, $NaF \cdot 2ThF_4$
44	12	44	(725)	Peritectic	$LiF \cdot 2ThF_4$, $LiF \cdot 4ThF_4$, $NaF \cdot 2ThF_4$
16	27	57	(825)	Peritectic	$LiF \cdot 4ThF_4$, $NaF \cdot 2ThF_4$, ThF_4

[a]Figures in parentheses represent estimated values.

the two compounds is therefore of considerable interest. One might speculate, for example, that the ternary compound can be considered to be formed from $NaF \cdot ThF_4$ and the hypothetical compound $2LiF \cdot ThF_4$. Such speculations become fruitless when the following data are considered: The unit-cell volume of the ternary compound $NaF \cdot 2LiF \cdot 2ThF_4$ is 1115.28 A^3 and contains six formula weights of the compound; the unit-cell formula is therefore $Na_6Li_{12}Th_{12}F_{66}$. In the binary compound $NaF \cdot ThF_4$, the unit-cell volume is 1176.78 A^3; the formula weights per cell give the formula $Na_{12}Th_{12}F_{60}$. Although the unit cell of $Na_6Li_{12}Th_{12}F_{66}$ contains approximately 10% more fluoride ions than $Na_{12}Th_{12}F_{60}$ ($NaF \cdot ThF_4$), it is also 61.5 A^3 smaller. The size decrease accompanying the substitutions of Na^+ by Li^+ would be expected to be offset by the significant volume contributed by the additional fluoride ions (61.5 A^3).

The general structure of these crystalline phases may be outlined through x-ray diffraction studies. In these materials the ions of low atomic number, particularly lithium, would contribute so little to the diffraction intensities that their location could not be determined. The interesting questions concerning solution formation between $NaF \cdot ThF_4$ and $NaF \cdot 2LiF \cdot ThF_4$ will, therefore, be necessarily deferred until they can be investigated by neutron diffraction methods.

CRYSTAL STRUCTURE DETERMINATIONS

Crystal Structure of Hexagonal $NaNdF_4$ and Related Compounds

J. H. Burns

The structure of hexagonal $NaNdF_4$ was analyzed in detail because of the wide occurrence of compounds isomorphous with it (see section on "Cation Size Effects in Lanthanide and Actinide Fluoride Systems," this report), with the aim of explaining the order-disorder transformations observed in the NaF-LnF_3 systems. Procedures for the structure determination are presented elsewhere;[28] only the results are given here. Figure 1.14 shows one unit cell of the crystal and some neighboring fluoride ions needed to complete the coordination polyhedra of cations in the cell. All F^- ions are in triangular arrays in the planes $Z = 0$ and $Z = \frac{1}{2}$. Cation sites are of three types: a onefold site occupied by Nd^{3+}, a onefold site occupied randomly by $\frac{1}{2}Na^+$ and $\frac{1}{2}Nd^{3+}$, and a twofold site occupied randomly by Na^+ and vacancies.

The fluoride coordination about the first two sites is ninefold, a trigonal prism with each vertical face bearing a pyramid, and about the third site is irregular octahedral. In the third site the Na^+ ion is displaced from the center of a trigonal prism toward one end or the other to attain sixfold coordination, thereby leaving the other end vacant. This displacement produces one type of disorder in the crystal but has a relatively small effect on the x-ray diffraction intensities. More important is the occupancy of the other two cation sites. Except for the small scattering by $\frac{1}{2}Na^+$ ion, the intensity of $00l$ reflections, with $l = 2n + 1$, depends on the difference in scattering power of cations in sites one and two. In fact, if the cations are randomly dispersed over these two sites, the intensity of these reflections is essentially zero, and the space group becomes $P6_3/m$ instead of $P\bar{6}$. Thus, even without a complete structure analysis, determination of the space group provides information about the cation distribution.

When single crystals of $NaLnF_4$ were x-ray photographed and their diffraction symmetries

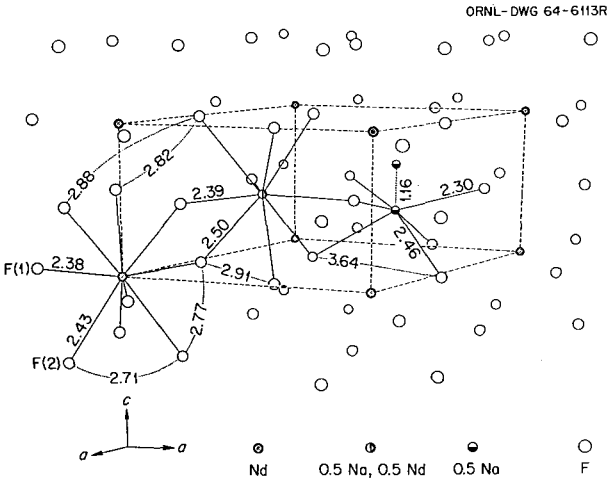

Fig. 1.14. Structure of Hexagonal $NaNdF_4$.

established, the ones with Ln = La, Ce, Pr, Nd, Eu, Gd, Tb, Ho, and Er could be assigned to space group $P\bar{6}$; with Ln = Y, Sm, and Tm, the crystals could be assigned to space group $P6_3/m$; and for $NaDyF_4$, one crystal of each symmetry was found. Some of the samples were obtained from slowly cooled melts, while others were made by quenching; indeed, the symmetry exhibited (hence the degree of randomness) may depend on the mode of cooling. Since most of these compounds have a high-temperature form in which all the cations are randomly distributed over equivalent sites, it is reasonable that some of them segregate, as the substance is cooled, into nonequivalent sites.

X-Ray Diffraction Studies on Compounds in the System NaF-LnF_3

J. H. Burns R. E. Thoma

The crystal structure of the cubic form of $NaF{\cdot}LnF_3$ was established (for the case of $NaYF_4$) by Hund[29] and is illustrated in Fig. 1.15. It is of the CaF_2 (fluorite) type with the Ca^{2+} positions randomly occupied by Na^+ and Ln^{3+} ions. The length of the unit cube, a_0, is related to the cation-anion distance, d_{CA}, by $a_0 = (4/\sqrt{3})d_{CA}$; hence the expected values of

[28] J. H. Burns, submitted to *Inorganic Chemistry*.

[29] F. Hund, *Z. Anorg. Allgem. Chem.* **261**, 106 (1950).

a_0 can be calculated from the radii of the ion involved. Measurement of a_0 by x-ray diffraction was carried out for the series of compounds with Ln = Nd to Lu, and the values obtained are plotted in Fig. 1.16. Calculated values, also shown in Fig. 1.16, were obtained as follows. For cases where the Ln^{3+} ion is larger than the Na^+ ion (0.95 A), the radius of the Ln^{3+} ion[30] was added to that of the F^- ion (1.36 A) and corrected for ligancy to obtain d_{CA}; but for lanthanides smaller than sodium, the average $\frac{1}{2}[r(Ln^{3+}) + r(Na^+)]$ was taken as the cation radius.

The good agreement between the observed a_0's and those calculated in this manner suggests that this is a valid procedure. This mode of calculation implies that the trivalent ion is the more important in determining d_{CA}. Thus, when $r(Ln^{3+}) > r(Na^+)$, the repulsion of the trivalent ions, separated by $a_0/\sqrt{2}$, keeps them at equilibrium distances as if the smaller Na^+ ions were not present; but when $r(Na^+) > r(Ln^{3+})$, the larger Na^+ ion is easily compressed by the Ln-F attractive force, yielding a radius smaller than $r(Na^+)$ but not as small as if the Na^+ ion were not present, that is, approximately an average radius. Consequently, the lanthanide contraction, usually measurable in an isomorphous series of crystals containing Ln^{3+} ions, is masked in this group by structural constraints; that is, the random intermixing of a nonlanthanide of intermediate size, Na^+, inhibits contraction of the lattice for cases where the Ln^{3+} ion is smaller than the Na^+ ion.

In the fluorite structure, each cation such as the one at the origin (Fig. 1.15) is coordinated by a cube of eight F^- ions; but for each cube with a cation at its center, there is another which is empty, such as the one at the center of the unit cell. It was shown by Hund[31] that the dissolution of YF_3 in cubic $NaYF_4$ occurs by substitution of Y^{3+} for Na^+ ions and the filling of some of the holes with F^- ions to produce electroneutrality. The limit of this substitution occurs at the composition $5NaF{\cdot}9LnF_3$ (see section on "The NaF-LnF_3 Systems," this report); the unit-cell constants for these compounds were determined and are shown in Fig. 1.16. The values are all

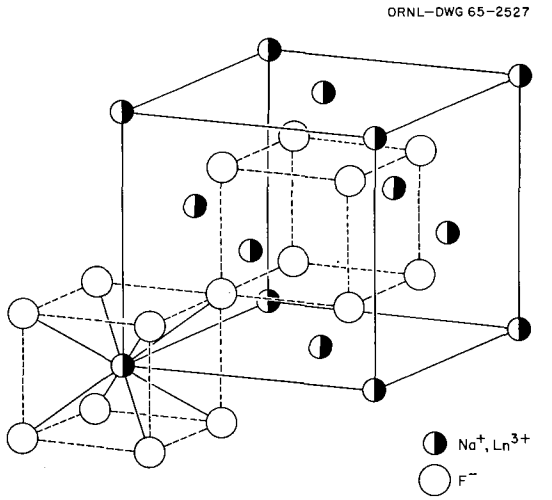

Fig. 1.15. Fluorite Structure of $NaLnF_4$.

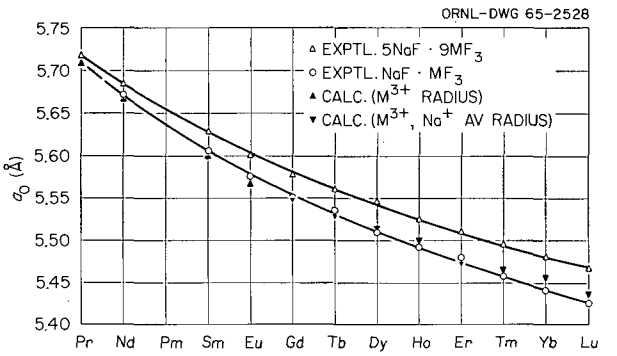

Fig. 1.16. Unit-Cell Constants of $NaF{\cdot}LnF_3$ and $5NaF{\cdot}9LnF_3$.

greater than those of the corresponding 1:1 compounds because of the stuffing of the lattice with fluoride ions, and the trend away from the 1:1 curve shows that the effect of stuffing is more important than the lanthanide contraction.

In addition to a structure analysis of a typical hexagonal $NaLnF_4$ crystal (see section on "Crystal Structure of Hexagonal $NaNdF_4$ and Related Compounds," this report), the unit-cell dimensions were determined for the entire series. The values, given in Table 1.6, were refined by least-squares adjustment to data from an x-ray powder diffractometer. Some of these constants were measured previously by Roy and Roy[32] and

[30] D. H. Templeton and C. H. Dauben, *J. Am. Chem. Soc.* **76**, 5237 (1954).

[31] F. Hund, *Z. Anorg. Allgem. Chem.* **263**, 102 (1950).

[32] D. M. Roy and R. Roy, *J. Electrochem. Soc.* **111**, 421 (1964).

Table 1.6. Unit-Cell Dimensions of Hexagonal $NaLnF_4$

Lanthanide	a_0 (A)	$\sigma(a_0)$	c_0	$\sigma(c_0)$
La	6.157	0.006	3.822	0.008
Ce	6.131	0.006	3.776	0.004
Pr	6.123	0.004	3.743	0.002
Nd	6.100	0.002	3.711	0.002
Sm	6.051	0.010	3.640	0.007
Eu	6.044	0.003	3.613	0.003
Gd	6.020	0.003	3.601	0.008
Tb	6.008	0.004	3.580	0.002
Dy	5.985	0.004	3.554	0.003
Ho	5.991	0.001	3.528	0.002
Er	5.959	0.002	3.514	0.002
Tm	5.953	0.002	3.494	0.002
Yb	5.929	0.002	3.471	0.002
Lu	5.912	0.003	3.458	0.003
(Y)	5.967	0.002	3.523	0.002

are in agreement with the present values. There is no simple relationship between the ionic radii and the cell constants as above, but a general decrease in unit-cell volume is observed with decreasing size of the lanthanide ions. In the hexagonal modification of each compound, the molar volume is about 13% less than in the corresponding cubic form, since the interstitial holes are not present in the former.

The x-ray diffraction studies make it possible to rationalize some of the features of the NaF-LnF_3 phase diagrams from a crystal-chemical viewpoint. At high temperature the fluorite form of $NaLnF_4$ exists (for Nd and heavier Ln) with random distribution of cations. The octahedral vacancies in the fluorite structure readily accommodate extra F^- ions, so substitutional plus interstitial solid solution occurs out to an empirically established limit of $5NaF \cdot 9LnF_3$.

As the temperature is lowered, the two kinds of cations with their different charges tend to find different environments and hence to segregate. This occurs in three ways. At compositions near 1:1 a polymorphic transition to the hexagonal $NaNdF_4$ structure takes place, partially separating the cations as described above (see section on "Crystal Structure of Hexagonal $NaNdF_4$ and Related Compounds," this report). As the composition is enriched in LnF_3 by its dissolution in the fluorite structure, the transformation to the hexagonal form is no longer possible; hence exsolution occurs on cooling. Near the 5:9 composition, however, another low-temperature structure, designated tetragonal but not yet solved in detail, is possible; so transformation to it occurs on cooling. Preliminary results[33] show that some of the cations are segregated in this structure also.

Refinement of the Crystal Structure of Li_2BeF_4

J. H. Burns E. K. Gordon[34]

The predominant compound in solidified MSRE fuel mixture is Li_2BeF_4; consequently, it has been the object of numerous physical chemical measurements. One property, the knowledge of which is often basic to the understanding of solid-state behavior, is the crystal structure. Last year a detailed description of the crystal structure of $Li_6BeF_4ZrF_8$, another primary phase in the LiF-BeF_2-ZrF_4 system, was reported.[35] Examination of the literature on Li_2BeF_4 revealed that it was not described nearly as well – a direct structure determination had not been made – but it had been inferred from x-ray powder data that it is isomorphous with Be_2SiO_4.[36]

We have carried out a structure analysis on a single crystal of Li_2BeF_4. About 620 x-ray intensities were collected from a spherically ground sample by means of a single-crystal orienter and scintillation-counter detector apparatus. The hexagonal unit-cell dimensions, $a = 13.29 \pm 0.01$ and $c = 8.91 \pm 0.01$ A, and the space group, $R\bar{3}$, were found, in agreement with those previously reported. The intensity data were

[33] H. Steinfink, University of Texas, unpublished results (1964).

[34] Summer student trainee, now at California Institute of Technology.

[35] D. R. Sears and J. H. Burns, *Reactor Chem. Div. Ann. Progr. Rept. Jan. 31, 1964*, ORNL-3591, p. 11; *J. Chem. Phys.* 41, 3478 (1964).

[36] W. L. Bragg and W. H. Zachariasen, *Z. Krist.* 72, 518 (1930).

used to refine the atomic positions by least squares. The positional parameters of Be_2SiO_4 (ref. 36) were used as starting values with the additional feature that each atom be described by variable anisotropic thermal parameters. All atoms are in general positions of the space group.

The refined atomic positions, their standard deviations, and the values used initially (in parentheses) are given in Table 1.7. Anisotropic thermal parameters are listed in Table 1.8 and are graphically displayed in Fig. 1.17.

The small positional shifts from their starting values (Table 1.7) indicate that Li_2BeF_4 is indeed isostructural with Be_2SiO_4. In Li_2BeF_4, each Be atom and each Li atom is tetrahedrally coordinated by F atoms; these tetrahedra share all their corners to form a three-dimensional network. Two types of linkages are of interest. Figure 1.17 shows how the tetrahedra are joined in a chain as the sequence of central atoms is repeated along the c direction, and Fig. 1.18 is a view down the c axis showing how six of these chains are "cross linked" in a hexagonal arrangement.

The free volume within each hexagonal array is about 2 A in diameter if conventional radii are assigned to the surrounding atoms. This cylindrical free space is continuous through any perfect domain of the crystal and should provide a path for rapid diffusion. There are some empty spaces in the $Li_6BeF_4ZrF_8$ structure also, but they are smaller (approximately 0.5 A in diameter) and are not continuous. The diffusion of decomposition products out of irradiated fuel should proceed more rapidly from the Li_2BeF_4 phase than from the $Li_6BeF_4ZrF_8$ phase.

Table 1.7. Positional Parameters from Least-Squares Refinement

[Standard deviations ($\times 10^4$) are in parentheses after the values, and the starting parameters from phenacite are in parentheses below.]

Atom	x	y	z
Li(1)	−0.0216 (2) (−0.01)	−0.2156 (2) (−0.21)	0.5816 (2) (0.58)
Li(2)	−0.0162 (2) (−0.01)	−0.2073 (2) (−0.21)	−0.0848 (2) (−0.08)
Be	−0.01550 (8) (−0.011)	−0.21170 (8) (−0.211)	0.2494 (1) (0.250)
F(1)	0.11052 (4) (0.120)	−0.10578 (4) (−0.092)	0.25192 (5) (0.250)
F(2)	−0.00582 (4) (0.000)	−0.32315 (4) (−0.320)	0.24855 (6) (0.250)
F(3)	−0.07502 (4) (−0.074)	−0.20352 (4) (−0.204)	0.10408 (5) (0.083)
F(4)	−0.08185 (4) (−0.074)	−0.20919 (4) (−0.205)	0.39229 (5) (0.417)

ORNL-DWG 64-8472

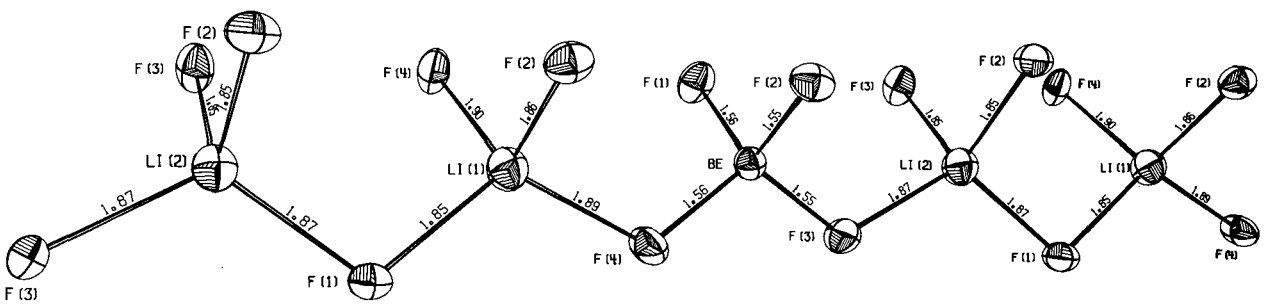

Fig. 1.17. Tetrahedral Symmetry of Li_2BeF_4.

Table 1.8. Thermal Parameters ($\times 10^5$) from the Expression $\exp[-(\beta_{11}h^2 + \beta_{22}k^2 + \beta_{33}l^2 + \beta_{12}hk + \beta_{13}hl + \beta_{23}kl)]$, and Their Standard Deviations ($\times 10^5$)

Atom	β_{11}	β_{22}	β_{33}	β_{12}	β_{13}	β_{23}
Li(1)	230 (9)	263 (9)	338 (4)	117 (8)	10 (9)	4 (9)
Li(2)	233 (9)	268 (9)	332 (14)	126 (8)	−1 (9)	−5 (9)
Be	166 (6)	170 (6)	239 (9)	87 (5)	5 (6)	−1 (6)
F(1)	185 (4)	211 (4)	359 (6)	24 (3)	−13 (3)	13 (3)
F(2)	215 (4)	175 (4)	472 (6)	104 (3)	24 (3)	18 (3)
F(3)	237 (4)	367 (4)	245 (6)	192 (3)	−32 (3)	2 (3)
F(4)	267 (4)	372 (4)	256 (6)	213 (3)	47 (3)	20 (3)

Table 1.9. New Crystallographic Data

Compound	Optical Properties	X-Ray Data
α-$CsF \cdot BeF_2$	Biaxial negative, $N_\alpha = 1.378$, $N_\gamma = 1.382$, $2V \sim 75^\circ$	
$2CsF \cdot 3UF_4$	Biaxial positive, $N_\alpha = 1.560$, $N_\gamma = 1.570$, $2V \sim 70^\circ$	Monoclinic, $a_0 = 8.39$ A, $b_0 = 8.46$ A, $c_0 = 20.88$ A, $\beta = 119.89^\circ$, space group $-P2_1/n$ or $P2_1$
$2LiF \cdot NaF \cdot 2ThF_4$	Uniaxial positive, $N_\omega = 1.520$, $N_\epsilon = 1.525$	Hexagonal, $a_0 = 9.87$ A, $c_0 = 13.22$ A, $z = 6$, $d = 6.342$, space group $-P3c_1$ or $P3c_1$, isomorphous with α-$NaF \cdot ThF_4$
$3LiF \cdot UF_4$	Biaxial negative, $N_\alpha = 1.512$, $N_\gamma = 1.530$, $2V = 20$ to 30°	Tetragonal, $a_0 = 6.132$ A, $c_0 = 6.391$ A, $z = 2$, $d = 5.416$, space group $-P4/nnn$ or $P4/n$, isomorphous with $3LiF \cdot ThF_4$
$2KCl \cdot UCl_3$	Biaxial positive, $N_\alpha = 1.745$, $N_\gamma = 1.800$, $2V$ very small, very deep blood-red color	Orthorhombic, $a_0 = 12.71$ A, $b_0 = 8.82$ A, $c_0 = 8.00$ A, $z = 4$, $d = 3.70$, space group $Pna21$ or $Pnma$
$RbF \cdot 6ThF_4$	Uniaxial negative, $N_\omega = 1.530$, $N_\epsilon = 1.526$	Hexagonal, $a_0 = 8.33$ A, $c_0 = 25.40$ A, space group P_{3121} or P_{3112} or P_{3212} or P_{3221}
$NaF \cdot BiF_3$	Uniaxial positive, $N_\omega = 1.636$, $N_\epsilon = 1.656$	Hexagonal, $a_0 = 6.126$, $c_0 = 3.716$, space group $P\bar{6}$
$NaF \cdot KF \cdot ThF_4$	Uniaxial negative, $N_\omega = 1.454$, $N_\epsilon = 1.448$ $N_\epsilon = 1.448$	Hexagonal, $a_0 = 6.29$ A, $c_0 = 7.88$ A, $z = 2$, $d = 5.02$, space group P_3 or $P\bar{3}$
$NaF \cdot KF \cdot UF_4$	Uniaxial positive, $N_\omega = 1.578$, $N_\epsilon = 1.584$	Hexagonal, $a_0 = 6.24$ A, $c_0 = 7.80$ A, $z = 2$, $d = 5.23$, space group P_3 or $P\bar{3}$
α-$NaF \cdot ThF_4$	Biaxial negative, $N_\alpha = 1.506$, $N_\gamma = 1.540$	Hexagonal, $a_0 = 10.15$ A, $c_0 = 13.19$ A, $z = 12$, $d = 5.928$, space group $P3_{c1}$ or $P\bar{3}_{c1}$
ScF_3	$N = 1.400$	Rhombohedral, $a_0 = 4.0124$ A, $\alpha = 90.05$

ORNL DWG 64-8340

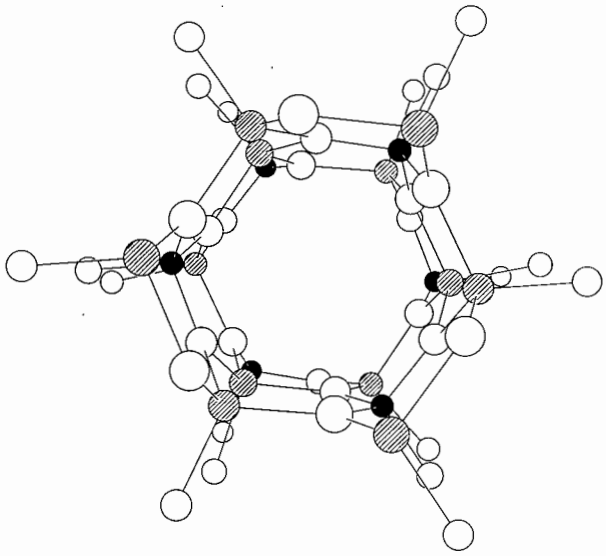

Fig. 1.18. C-Axis Symmetry in Li_2BeF_4.

Crystallographic Data for Some Pure Materials

R. E. Thoma G. D. Brunton
J. H. Burns H. Insley

Heretofore, a section of this report has been devoted to optical and x-ray diffraction data characterizing new compounds that were discovered in the Reactor Chemistry Division's research programs. Within the last year we have prepared new standards for some 20 crystalline compounds, about whose crystal symmetry little or nothing was previously known, from single crystals and pure polycrystalline specimens. Accurate powder patterns for pure crystalline compounds are frequently obtainable only when single-crystal data are used to establish unequivocally the symmetry of a phase. In attempting to obtain correct powder patterns for some compounds of current technological significance, we have obtained single-crystal data for the compounds listed in Table 1.9. These and other crystallographic data, representing our best current measurements of the crystal properties of the fluorides, chlorides, and oxides with which we have been concerned, are included in a recent topical report.[37] Included in the compilation are data for all compounds previously characterized in the course of the Reactor Chemistry Division's researches.

Complex Fluorides of U(III), U(IV), and U(V)

R. E. Thoma R. A. Penneman[38]

Recently, LASL scientists found that several stable complex compounds are formed from the alkali fluorides and UF_5.[39,40] Uranium(IV) analogs of these compounds were discovered previously in investigations of alkali fluoride–UF_4 systems at ORNL.[37] On comparing crystallographic data for U(V)-U(IV) analogs, Penneman[41] noted that $3RbF{\cdot}UF_5$ and $3RbF{\cdot}UF_4$ are apparently isostructural and of nearly identical unit-cell size. In subsequent interlaboratory discussions, we noted corresponding properties for $3RbF{\cdot}UF_4$ and $3RbF{\cdot}UF_3$. We consider the remarkable similarity in properties of the three phases $3RbF{\cdot}UF_5$, $3RbF{\cdot}UF_4$, and $3RbF{\cdot}UF_3$ as evidence of the existence of an isostructural series of complex uranium fluorides for the III, IV, and V oxidation states. If so, we should also expect the crystalline compounds to be hosts for uranium ions of different oxidation states. In attempts to test this hypothesis, personnel at the two laboratories have embarked on a cooperative program to prepare and characterize the various complex fluorides of U(III), U(IV), and U(V). As part of these efforts, we have synthesized the compounds $3KF{\cdot}UF_3$, $3RbF{\cdot}UF_3$, and $3CsF{\cdot}UF_3$ by reaction of uranium metal with the appropriate fluoride mixtures at temperatures of approximately 1000°C. The U(III) compounds formed are extremely sensitive to moisture and were accordingly protected from exposure to moisture-laden atmospheres. Crystals produced by this method were not large enough to be used for single-crystal x-ray examinations. Petrographic and x-ray powder were obtained, however. Crystallographic data for the uranium complex compounds are listed in Table 1.10.

[37] G. D. Brunton *et al.*, *Crystallographic Data for Some Metal Fluorides, Chlorides, and Oxides*, ORNL-3761 (February 1965).

[38] Los Alamos Scientific Laboratory.

[39] R. A. Penneman, G. D. Sturgeon, and L. B. Asprey, *Inorg. Chem.* 3, 126 (1964).

[40] R. A. Penneman, G. D. Sturgeon, and L. B. Asprey, *J. Am. Chem. Soc.* 84, 4608 (1962).

[41] R. A. Penneman, unpublished data.

Table 1.10. Crystallographic Data for Alkali Fluoride–Uranium Fluoride 3:1 Complex Compounds

Compound	Crystallographic Data
$3LiF \cdot UF_5$	Not investigated
$3LiF \cdot UF_4$	Tetragonal $P4/nmm$ $a = 6.132$ A[c] $c = 6.391$ A Biaxial (–) $N_\alpha = 1.512$ $N_\gamma = 1.530$
$3LiF \cdot UF_3$	Not formed[e]
$3NaF \cdot UF_5$	Tetragonal D_{4h}^{17}-$I4/mmm$ $a = 5.470$ A $c = 10.94$ A[a]
$3NaF \cdot UF_4$	Tetragonal D_{4h}^{17}-$I4/mmm$ $a = 5.458$ A $c = 10.917$ A[d] Uniaxial (–) $N_\omega = 1.417$ $N_\epsilon = 1.411$
$3NaF \cdot UF_3$	Not formed[f]
$3KF \cdot UF_5$	Cubic $a_0 = 9.21$ A
$3KF \cdot UF_4$	Cubic[d] $a_0 = 9.21$ A $N = 1.436$
$3KF \cdot UF_3$	Cubic $a_0 \cong 9.2$ A $N \cong 1.44$
$3RbF \cdot UF_5$	Cubic, possibly isomorphous with $3RbF \cdot UF_4$[b]
$3RbF \cdot UF_4$	fcc $a_0 = 9.5667$ A $N = 1.438$
$3RbF \cdot UF_3$	fcc $a_0 = 9.5704$ A $N = 1.440$
$3CsF \cdot UF_5$	Not investigated
$3CsF \cdot UF_4$	fcc $a_0 = 10.62$ A $N = 1.478$
$3CsF \cdot UF_3$	fcc $a_0 \cong 10.6$ A $N \cong 1.48$

[a]W. Ruedorff and H. Lentner, *Ann. Chem.* **632**, 1 (1960).
[b]L. B. Asprey, R. A. Penneman, and G. D. Sturgeon, *Inorg. Chem.* **3**, 126 (1964).
[c]G. D. Brunton (1964), see Table 1.5, this report.
[d]W. H. Zachariasen, *J. Am. Chem. Soc.* **70**, 2147 (1948).
[e]C. J. Barton *et al.*, *Phase Diagrams of Nuclear Reactor Materials*, ORNL-2548 (Nov. 2, 1959).
[f]C. J. Barton *et al.*, *Phase Diagrams of Nuclear Reactor Materials*, ORNL-2548 (Nov. 2, 1959).

No attempts were made to synthesize reduced phases in the LiF- or NaF-based systems, because the phase diagrams[42,43] of these systems do not indicate the occurrence of stable 3:1 compounds. That multiple oxidation states may be exhibited by an element in a particular crystal structure is not at all surprising. It is noted in this report (see section on "The System UF_4-UF_3," this report) for UF_3-UF_4 solid solutions and was observed by Hoppe[44] for the strikingly similar case of $3CsF \cdot DyF_3$. In attempts to oxidize Dy(III) to Dy(IV), Hoppe found from magnetic susceptibility measurements that he could convert approximately half of the Dy^{3+} ions to the tetravalent state.

[42]C. J. Barton *et al.*, "The System LiF-UF_3," p. 83 in *Phase Diagrams of Nuclear Reactor Materials*, ed. by R. E. Thoma, ORNL-2548 (Nov. 20, 1959).

[43]C. J. Barton *et al.*, "The System NaF-UF_3," p. 86 in *Phase Diagrams of Nuclear Reactor Materials*, ed. by R. E. Thoma, ORNL-2548 (Nov. 20, 1959).

[44]L. B. Asprey and B. B. Cunningham, pp. 267–302 in *Progress in Inorganic Chemistry*, vol. II, ed. by F. A. Cotton, Interscience, New York, 1960.

Ruedorff and Leutner found that the x-ray powder diffraction photographs of $3NaF \cdot UF_4$ and $3NaF \cdot UF_5$ were almost identical, indicating a close structural relationship. Zachariasen reported that $3NaF \cdot UF_4$ was tetragonal with dimensions a = 5.458 A, c = 10.917 A.[45] This was confirmed by Ruedorff and Leutner, who then found a slightly larger cell for $3NaF \cdot UF_5$, a = 5.47 A, c = 10.94 A.[46] Since $3NaF \cdot UF_4$ is composed of two fluorite lattices adjacent to each other, with two of the eight cation sites occupied by U^{4+} ions, six by Na^+ ions, and 14 of the 16 anion sites occupied by F^- ions, they suggested that the corresponding $3NaF \cdot UF_5$ structure is formed by filling the two vacant anion sites by F^- ions. They anticipate a continuous transition possible between the two structures. This system cannot be extended to include U(III), since $3NaF \cdot UF_3$ is not formed.[43] With the heavier alkalis it is possible to make the entire series, $3MF \cdot UF_3$, $3MF \cdot UF_4$, and $3MF \cdot UF_5$ (M = K, Rb). Although scarcely examined as yet, it is very likely that a similar situation will be found with multivalent heavy elements, for example, protactinium, uranium as we have shown, neptunium, plutonium, and americium. Curium and berkelium have shown valences III and IV and could well be included.

[45] W. H. Zachariasen, *J. Am. Chem. Soc.* **70**, 2147 (1948).

[46] W. Ruedorff and H. Leutner, *Ann. Chem.* **632**, 1 (1960).

2. Radiation Chemistry of the Molten-Salt Reactor System

IN-PILE IRRADIATION EXPERIMENT 47-6

F. F. Blankenship S. S. Kirslis
H. A. Friedman

Introduction

Review of Previous Results. – The current series of irradiation experiments[1] in the Materials Testing Reactor (MTR), designed to test the compatibility and stability of Molten-Salt Reactor materials in a fissioning environment, has now been completed. The materials under investigation were the fuel salt, a uranium-containing fluoride mixture; INOR-8, an alloy composed mainly of nickel, molybdenum, and chromium; and dense reactor-grade graphite of low gas permeability. In the three previous tests of this series, the INOR-8–fuel–graphite test assemblies generally survived irradiation without gross damage to the test materials, but evidence accumulated that fluorine gas was slowly evolved from the irradiated fuel after it had solidified and cooled to room temperature. As reported last year, test 47-5,[2] in which the INOR-8 capsules were equipped with gas lines so that the cover gas could be sampled during irradiation, showed that fuel radiolysis occurred only during periods of reactor shutdown after the fuel had solidified and cooled to 35°C. This was confirmed by out-of-pile irradiation experiments.[3] Cover gas samples from test 47-5, taken while the salt was molten and fissioning, occasionally showed minute traces of CF_4 which probably originated from F_2 generated during previous shutdowns.

The other indications of material incompatibilities observed in experiments 47-3, 47-4, and 47-5 were thought to be related also to the radiolysis of the fuel during reactor shutdowns. Graphite specimens exposed to the capsule cover gas were sometimes badly corroded. Thin deposits of uranium, up to 4 mg per cm^2 of exposed graphite, were observed on the submerged 47-4 and 47-5 graphite specimens. The 47-3 molybdenum specimens were badly corroded. These undesirable reactions probably occurred during the sudden heating accompanying reactor startup after a shutdown period during which fuel radiolysis had produced fluorine and a chemically reduced fuel salt.

Objectives of Experiment 47-6. – The general objective of this final test was to prove that the undesirable effects listed above could all be avoided by never permitting the fuel salt to cool to room temperature, even during periods of reactor shutdown. The two primary specific objectives were to test for the presence of CF_4 in capsule cover gases (with the use of instruments of high sensitivity) and to examine the graphite specimens thoroughly after the experiment for positive or negative evidence of uranium deposition. Reassuring evidence of the compatibility of molten, fissioning salt with unclad graphite was considered essential to the Molten-Salt Reactor Program.

Objectives less important to the overall program, though perhaps more interesting from the chemical point of view, included measurements of the rate of radiolysis of deliberately added CF_4, studies of the effect of changes in the uranium concentration in the test salt (from 0.5 to 4.0 mole % in the four capsules of this experiment), tests of the

[1] *MSRP Semiann. Progr. Rept. July 31, 1964*, ORNL-3708, p. 252.

[2] *Reactor Chem. Div. Ann. Progr. Rept. Jan. 31, 1964*, ORNL-3591, p. 20.

[3] *Ibid.*, p. 27.

corrosion resistance of molybdenum metal in the absence of fuel radiolysis, and information relating to the volatility of fission products (particularly iodine, tellurium, and ruthenium) under conditions likely to be characteristic of reactor operation.

Experimental

Capsule and Heater Design.[4] – The principal innovation of the 47-6 design was the provision of individual heaters on the four capsules to keep the fuel salt molten during reactor shutdowns. This change required a redesign of the complete nose end of the in-pile assembly to permit fission heat removal by means of individual water jackets around each heater and capsule (Fig. 2.1). Four of these cylindrical capsules were mounted vertically in a horizontal array in the nose end at positions numbered 1 through 4 in order of increasing flux. Whenever the reactor shut down, the heaters operated automatically to maintain the fuel salt molten during the complete 12-week irradiation period. Thermocouples were provided to measure the temperature of the water entering and leaving each cooling jacket; from these temperatures, the total capsule power could be calculated and the fission power estimated. As in previous experiments of this series, the nose end of the in-pile assembly could be mechanically moved 13 in. toward or away from the MTR core during irradiation, permitting controlled variation of the capsule fission power density.

Capsules 1, 2, and 4 each contained a 1.35-in.-long, 0.5-in.-diam graphite core, held in position by a central thermocouple and a bottom pin. The core of capsule 3 was only half as long, to test the effect of variation in the exposed graphite area on CF_4 evolution. Two flat surfaces were milled on opposite sides of each cylindrical core to facilitate postirradiation examinations of surface deposits by x-ray diffraction. Each core was submerged in about 27 g (12 cm^3 at 650°C) of fuel salt, leaving a capsule gas space of about 4 cm^3. Fuel salt in capsule 1 contained 4.0 mole % UF_4, that in capsules 2 and 3 contained 0.9 mole % UF_4 [like MSRE fuel, which is nominally $LiF-BeF_2-ZrF_4-UF_4$ (65-29.1-5-0.9 mole %)], and the fuel in capsule 4 contained 0.5 mole % UF_4, the uranium being highly enriched (93.26% ^{235}U) in each case. The sealed capsules 1 and 4 each contained three molybdenum corrosion specimens, $1 \times \frac{1}{8} \times 0.020$ in., mounted vertically in slots in the capsule side and bottom walls so that contact with the graphite was avoided.

Provisions for Gas Analysis. – Capsules 2 and 3 were equipped with gas lines for purging the capsule gas spaces with purified helium and for sampling the effluents. The first 7 to 9 in. of the capsule inlet and outlet lines were 0.305 in. ID to minimize the possibility of plugging by volatilized fuel; no plugging occurred. The remaining 50 ft of each line to the sample station was $\frac{1}{8}$-in.-OD nickel tubing. Separate purge-gas supplies and sample collection systems were provided for each capsule. The helium was purified before use by passage through a molecular sieve drying column and hot (600°C) titanium sponge.

A simplified schematic drawing of the flow circuit for capsule 3 is shown in Fig. 2.2. The sample station cubicle, shielded by at least 6 in. of lead, enclosed a similar circuit for capsule 2. During purging, the capsule effluent was led directly to the shielded carbon trap and thence to the off-gas line. During sampling, the Dewar flask containing the Linde 13X molecular sieve trap was filled with liquid nitrogen, and the gas leaving the capsule was passed through this trap, which caught and held all gases but helium. After the desired volume of helium had been passed, in a period of 1 to 48 hr, the helium was evacuated from the trap, the trap was warmed to 250°C, and the released gases were swept with helium into an evacuated sample bottle, furnishing a 24.6-cm^3 sample at 600 mm pressure and room temperature. The concentration factor achieved by this collection method was more than 100 for the usual sampling times and purge flows.

Qualitative information on the rate of radiolysis of CF_4 was obtained from the regular concentrated gas samples taken at different purge flow rates, but more definitive measurements of this rate were obtained by passing helium-CF_4 mixtures (0.5 and 5.0% CF_4) through capsule 3 and determining the change in thermal conductivity with a sensitivity corresponding to 0.005% CF_4. Since the helium purification system could not be used with these mixtures, some contamination was

[4]The design, construction, and in-pile operation were performed by the Irradiation Engineering Department of the Reactor Division in cooperation with Reactor Chemistry Division personnel.

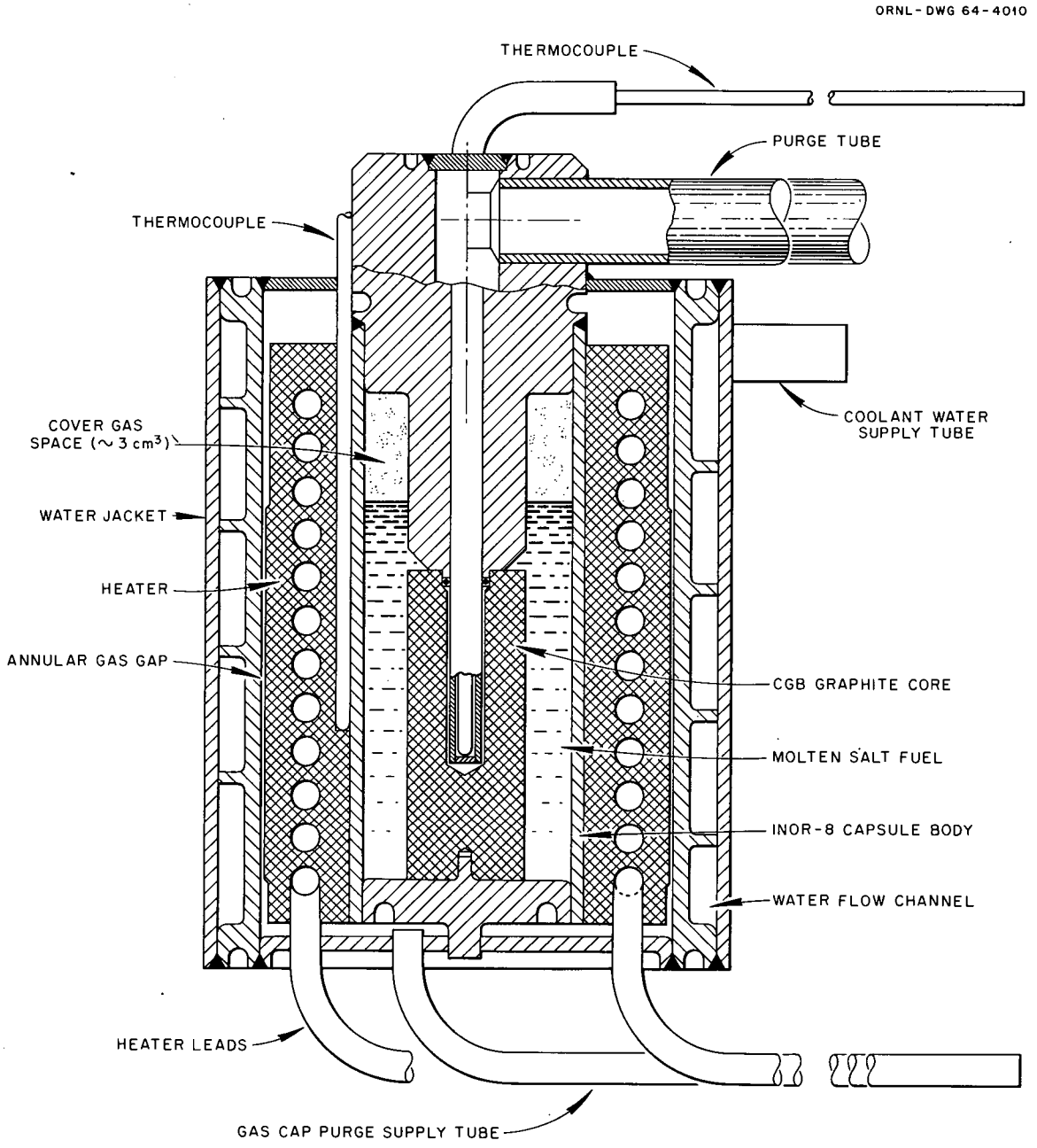

Fig. 2.1. Typical Capsule Assembly Equipped for Purging, Experiment ORNL-MTR-47-6.

ORNL-DWG 65-2530

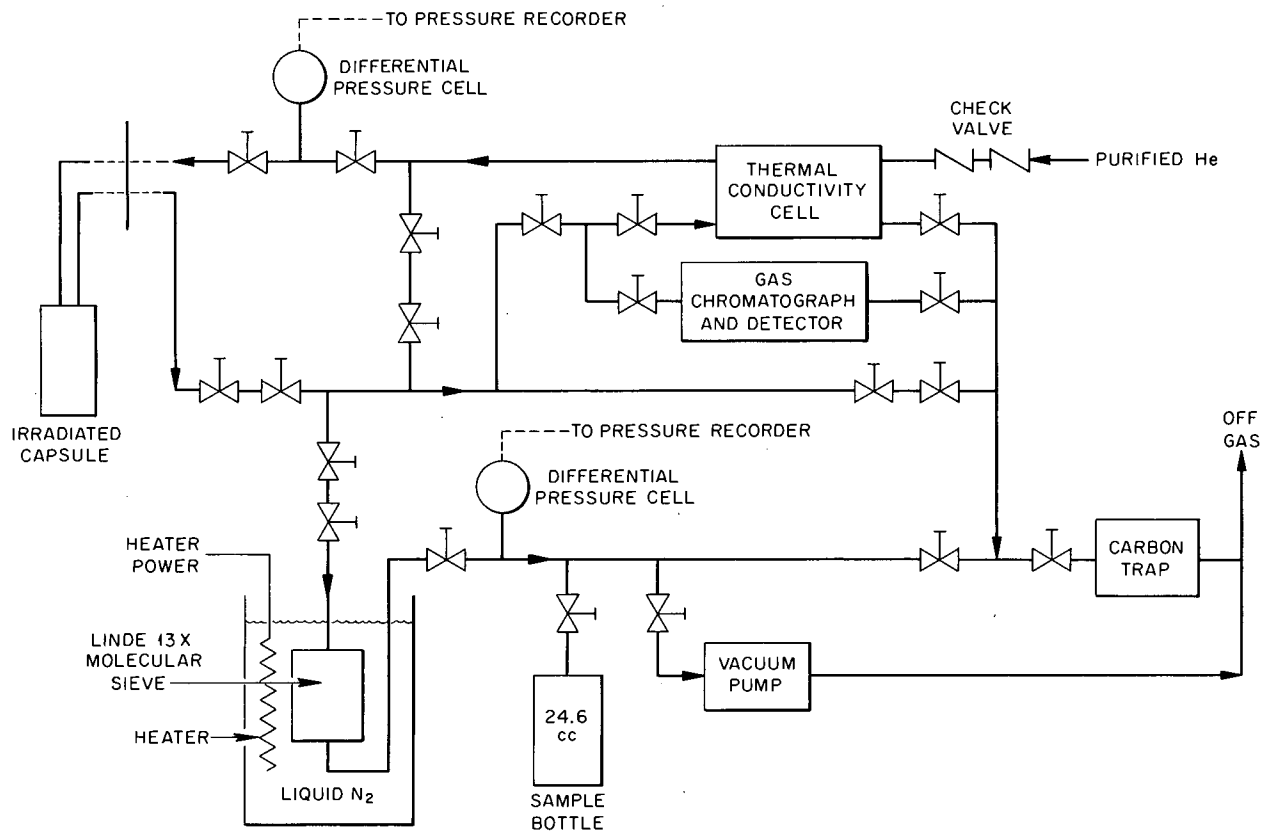

Fig. 2.2. MTR-47-6 Sample Station.

unavoidably introduced into the flow circuit during these tests.

A gas chromatographic method[5] for detecting parts per billion levels of impurities in helium, using a newly developed sensor which measured impurity-caused changes in helium breakdown voltage, was applied to the detection of CF_4 in direct unconcentrated samples of purge gas from capsule 3. A special purge gas mixture, containing 1 ppm CF_4, was passed through the capsule 3 circuit to calibrate the detector and to measure the change when the 1-ppm mixture was passed through capsule 3.

Postirradiation Disassembly. – When four MTR cycles of irradiation, accumulating 1500 hr at full reactor power, had been completed, the fuel was allowed to decay for 32 hr while still molten to help minimize fuel radiolysis during and after dismantling. The dismantling was performed as rapidly as possible in an MTR hot cell; the nose end of the in-pile assembly was sawed off, the individual capsule jackets were sawed apart, and finally the capsules themselves were milled open. The fuel from the last capsule opened was isolated from the other capsule components within 48 hr after the freezing of the salt. The fuel salt, graphite, and metal specimens from the capsules were packed in separate metal containers and shipped to ORNL for postirradiation examinations.

[5]*MSRP Semiann. Progr. Rept. July 31, 1964*, ORNL-3708, p. 328.

Results and Discussion

In-Pile Operation. – The in-pile assembly and the sample station performed according to design in all crucial respects.

Flux and Power Density Determinations. – The most reliable indications of burnup, average flux, and average power density were obtained from $^{236}U/^{235}U$ ratios determined on salt samples from each capsule. The results are given in Table 2.1. The average results correspond to the average insertion position of 4 in.; the power density for capsules 1, 3, and 4 at their maximum insertion of 10.1 in. was estimated to be near 65 w/cm^3 and, for capsule 2, about half this value.

Analysis of Gas Samples for CF_4. – No CF_4 or other volatile fluoride was detected by mass analysis (detection limit 2 to 10 ppm) in any of the regular concentrated gas samples. The gas chromatograph analyses on direct unconcentrated samples of capsule 3 effluent likewise indicated no CF_4 with a detection limit of about 250 ppb. The most sensitive determination involved a 48-hr sample collection from capsule 3 operating at a power density of 68 w/cm^3. The sample analysis showed no detectable CF_4, but over 2000 ppm of fission product xenon. For fuel radiolysis to be of significant practical effect on the operation of the MSRE, the CF_4 generation would have to exceed the xenon production. Since the radiolysis results reported below indicated a negligible degree of CF_4 radiolysis under the sampling conditions used, the negative CF_4 analyses may be taken as definite proof that molten MSRE fuel is stable to radiolysis in a fissioning or highly radioactive environment over the whole range of power densities and temperatures investigated. This demonstration accomplished one of the major objectives of the 47-6 experiment.

Analyses for Uranium in Graphite. – Uranium was found to have deposited in the surface of graphite cores from earlier tests.[6] Since the evolution of fluorine was also encountered in these same tests, there was a strong likelihood that the transport of uranium was associated with the fluorine. However, the mechanism remained obscure, and the possibility that the uranium deposition was inherent in the exposure of graphite to fissioning fuel lingered as a question of considerable concern.

The importance of the question was such that the presence of uranium in the graphite was sought by several methods. Two types of quantitative analysis were employed: fluorimetry and neutron activation. For the first, samples of graphite, cylindrical cross sections weighing approximately 1 g, were taken from the upper and lower portions of the cores. These were dissolved in a mixture of nitric and perchloric acid, and portions of the solutions were analyzed spectrographically for the other fuel constituents. The results for uranium, shown in column 5 of Table 2.2, corresponded roughly to the trace amounts of fuel that adhered to the graphite, as evaluated from the amounts of other fuel constituents found. In the second analytical method, adjacent samples of graphite, cylindrical cross sections about 20 mils thick, were analyzed by counting delayed neutrons after activation in the Oak Ridge Research Reactor (ORR). The results, shown in column 7 of Table 2.2, applied only to ^{235}U and were generally lower than those found by fluorimetric analysis, which measured the total uranium. Samples of the solutions used for fluorimetric analysis were also analyzed by the

[6] *Reactor Chem. Div. Ann. Progr. Rept. Jan. 31, 1964*, ORNL-3591, p. 17.

Table 2.1. Burnup, Average Flux, and Average Power Density for the 47-6 Capsules

Capsule	Burnup[a] (%)	Average Flux (neutrons cm^{-2} sec^{-1})	Average Power Density (w/cm^3)
1	0.835	2.7×10^{12}	54
2	1.45	4.6×10^{12}	23
3	2.86	9.2×10^{12}	47
4	5.53	1.8×10^{13}	53

[a] Burnup by fission; does not include burnup by capture.

Table 2.2. Uranium in Graphite from In-Pile Experiment 47-6

Capsule	Type	Uranium in Fuel (mole %)	Estimated Burnup (%)	Uranium in Graphite Samples (ppm)		
				Dissolved		Solid
				Fluorimetric	Delayed Neutron	Delayed Neutron
1	Sealed	4	0.8	40	30	10
				96	89	40
2	Purged	0.9	1.5	7	4.8	3
				8	5.2	9
3	Purged	0.9	2.9	60	19.4	6
						12
4	Sealed	0.5	5.5	51	12.2	6
				175	8.5	130
Blank				20	0.1	0.11
					(16)[a]	(16)[a]

[a]The delayed-neutron analyses applied only to ^{235}U; the figures in parentheses are corrected to give the total uranium in the blank, which had the normal isotopic distribution.

delayed-neutron method, and the results are shown in column 6 of the table. These results were considered the most reliable of the three sets. The differences between the results of the two types of analysis of the solutions, representing the larger graphite samples, were too great to permit any conclusion as to whether the adjacent graphite samples differed significantly in their uranium contents.

In spite of the scatter in the results, the amount of uranium found was inconsequential, particularly in light of the evidence that it arose from traces of adhering fuel. A search for uranium by means of x radiography of thin sections of graphite gave negative results, in contrast with the results from earlier exposures. Also, x-ray diffraction from flat surfaces of the graphite gave negative results.

The amounts of uranium were *lower by about 2 orders of magnitude* than those found in earlier experiments where F_2 was involved. Although questions about detailed mechanisms that produced the earlier deposits were unresolved, the prospects now seem excellent that operation of the MSRE will not be impaired by the deposition of uranium in the graphite. Thus, the second primary objective of the experiment is also considered to have been satisfactorily achieved.

Other Gas Analyses. – The voluminous gas analysis results are described in detail in a forthcoming report[7] and will be only briefly summarized here. The levels of impurities such as N_2, O_2, H_2, H_2O, and CH_4 were generally gratifyingly low, indicating satisfactory leak-tight operation of the sampling system. Water was detected only in the first few concentrated samples.

Xenon isotopic analyses revealed low ^{131}Xe and ^{132}Xe percentages compared with fission yields. These particular isotopes had relatively long-lived precursors, 8-day ^{131}I and 77-hr ^{132}Te. It is believed that the volatilized precursors were swept out of the system during purging, resulting in low quotas of ^{131}Xe and ^{132}Xe in subsequent gas samples. It was also noted that the $^{136}Xe/^{134}Xe$ ratios were intermediate between those calculated from fission yields for no conversion of ^{135}Xe to ^{136}Xe by neutron capture and those calculated for conversion corresponding to the exposure of ^{135}Xe to the neutron flux for its complete 13.3-hr mean life. From these data it was calculated that the average residence time of ^{135}Xe in the high-flux region was about 7 hr. The gamma spectrometer

[7]Topical report (in preparation).

results on the more radioactive gas samples showed ^{133}Xe as the only detectable activity. The detection limit for ^{131}I and ^{129}Te activities was 0.05% of the ^{133}Xe activity.

CF_4 Radiolysis. – Since no CF_4 was detected in capsule 3 effluent at any purge flow rates, the regular concentrated gas samples yielded no quantitative information on the rate of radiolysis of CF_4. During the third MTR cycle of irradiation, special radiolysis tests were performed in which helium containing 5% CF_4 was passed through capsule 3. The mixture was admitted through one side of a thermal conductivity bridge, passed through the capsule, and exited through the other side of the conductivity cell. The reading was compared to that when the same gas was passed through both sides of the cell without passing through the capsule containing fissioning molten salt. With the instrument set at highest sensitivity, a 1-mv output change (read on a 10-mv recorder) corresponded to 0.05% CF_4 concentration change. The data of Table 2.3 indicate a CF_4 radiolysis rate of less than 4%/hr above fuel fissioning at the design power density and temperature for the MSRE (14 w/cm^3 and 1200°F). The strong inverse temperature dependence of the radiolysis rate could mean that back reaction of the radiolysis products is accelerated by increasing temperature. A second, more sensitive but less accurate, method involved isolating the capsule containing a known CF_4 concentration for several hours, then flushing this gas through the thermal conductivity cell with the original mixture. Radiolysis rates obtained by this static method, reading the minimum of the effluent concentration, were uniformly lower than rates determined by the flowing method, since some mixing of 5% CF_4 flush gas with capsule gas was inevitable. A static test, isolating 0.1% CF_4 in the capsule for 10 hr, indicated a radiolysis rate of 4.2%/hr, with the capsule temperature at 1077°F, minimum insertion (power density of approximately 29 w/cm^3), and a flushing rate of 192 cm^3/hr.

The dynamic radiolysis results, taken as a whole, indicate that the negative CF_4 analyses from the 47-6 gas samples may not be ascribed to rapid CF_4 radiolysis.

Table 2.3. Radiolysis of 5% CF_4 Mixture

Type of Run	Flow (cm^3/hr)	Temperature (°F)	Insertion (in.)	Power Density (w/cm^3)	Rate (%/hr)	Uncertainty (%/hr)
Dynamic	1000	1075	0	29	5.0	±3
Static	1000[a]	1075	0	29	3.1	+2, −0
Dynamic	100	1075	0	29	4.1	±0.4
Static	100[a]	1075	0	29	3.6	+1, −0
Dynamic	100	1275	10	68	8.8	±0.5
Dynamic	100	1290	2	35	4.1	±0.4
Dynamic	100	1042	2	35	6.5	±0.5
Dynamic	100	831	2	35	8.6	±0.5
Dynamic	100	1047	2	0[b]	2.0	±0.5
Static	100[a]	1049	2	0[b]	1.6	±0.3
Dynamic	100	1049	2	0[b]	1.6	±0.4

[a]Flush rate.

[b]Testing during reactor shutdown.

Some puzzling observations related to radiolysis of CF_4 were made while the 1-ppm CF_4 mixture was passing through capsule 3. With the reactor operating, both the gas chromatograph and mass spectrometric analysis of the gas samples indicated the destruction of 1 ppm of CF_4 on passage through the capsule. With the reactor down, mass spectrometry indicated the survival of CF_4, while the chromatograph indicated its conversion to an unidentified product. Since mass analysis of CF_4 actually measures a peak for CF_3^+, a fragment produced also from other fluorocarbons, these observations may not be contradictory.

Fission Product Volatilization. – In previous postexposure examinations, little emphasis was placed on determining the location of iodine, tellurium, and ruthenium because the liberation of F_2 had disturbed the chemical picture in the capsules. Since fluorine evolution was suppressed in the 47-6 experiment, more could be learned about the fate of these elements. The possibilities of releasing iodine and tellurium from the fuel as volatile compounds and of plating of ruthenium on the graphite and metal walls were of particular practical concern.

Salt samples from each of the four capsules were analyzed radiochemically for ^{131}I; samples from capsules 2 and 3 were also analyzed for ^{103}Ru and ^{129}Te. In addition, three sections of inlet and exit gas lines from capsules 2 and 3 were analyzed quantitatively for ^{131}I and ^{129}Te and qualitatively for ^{103}Ru. The four 7- to 9-in.-long, $\frac{3}{8}$-in.-OD tubes attached to the capsules, four 3-ft sections of $\frac{1}{8}$-in.-OD tubing 30 ft from the capsules, and four 1-ft sections of $\frac{1}{8}$-in. tubing at the sample station were taken as representative samples of the gas lines.

The analytical results for the salt and for the gas lines are given in Tables 2.4 and 2.5, respectively, expressed as percentage of total fission product calculated from the known uranium contents, fission yields, and neutron fluxes. The iodine evidently remained in the salt in the sealed capsules, but volatilized to an appreciable extent from capsules 2 and 3. Correspondingly, sizable percentages of the total iodine were found by leaching the gas lines. About 70% of the ^{129}Te had left the fuel salt in capsules 2 and 3, but only traces were found in the gas lines. Presumably the volatile tellurium compound did not react with

Table 2.4. Fission Products in 47-6 Fuel Salt

Sample[a]	Percent of Total ^{131}I	Percent of Total ^{129}Te	Percent of Total ^{103}Ru
1FS	6.4		
1FS	109.0		
1F18	44.0		
1F3 (black)	85.0		
1F3 (green)	96.5		
2FS	19.0	34.0	36.0
2F18	8.6		
3FS	9.0	26.0	0.34
3FS	33.0		
3F18	53.0		
4FS	120.0		
4F18	74.0		

[a]The first numeral is the capsule number; FS represents a composited bulk fuel sample; F18 represents a sample of fuel from the bottom of the capsule; F3 refers to special colored fuels from capsule 1.

Table 2.5. Fission Products in 47-6 Gas Line Samples

Capsule	Location	Percent of Total ^{131}I	Percent of Total ^{129}Te	^{103}Ru
2	Near capsule	8.0	0.004	Some
2	30 ft from capsule	0.2	0	
2	50 ft from capsule	1.0	0	
3	Near capsule	6.0	0.07	Some
3	30 ft from capsule	5.0	0.006	
3	50 ft from capsule	1.0	0	

the metal walls but passed through to the carbon trap. The ^{103}Ru also mainly left the salt phase; its activity was detected in the gas lines by qualitative gamma scans of the leach solutions, but much of it may have plated on the capsule walls. Examinations of the latter for ^{103}Ru are planned.

As mentioned above, the low ^{131}Xe and ^{132}Xe percentages found in the isotopic analyses of the gas samples are consistent with volatilization of tellurium and iodine from the fuel salt. Qualitative gamma scans of the graphite specimens (and their solutions) indicated higher ^{103}Ru than ^{95}Zr-^{95}Nb activities, a reversal of the situation in gamma scans of bulk salt samples. Thus plating of ruthenium on graphite is suggested. Similar observations were made on some salt samples taken from the top meniscus of the fuel or from the material deposited on the capsule walls above the fuel level.

Examination of Irradiated Salt. – The salt specimens from the 47-6 test were generally gray-green in color, rather than black as in previous tests. The salt from capsule 1 had segregated into two clearly separated regions, one pale green and the other black. Chemical analyses of the green and black portions revealed a lower uranium concentration in the green fraction. The paler color of the 47-6 salt specimens may be related to the heating for 32 hr after the final shutdown. Petrographic examination of selected salt specimens yielded limited results since most samples were microcrystalline due to rapid cooling. The Li_2BeF_4 phase was identified in all samples and the $3LiF{\cdot}UF_4$ phase in a few (notably in a black sample of capsule 1 salt).

The gamma scans of samples selected from various parts of the capsules indicated principally a tendency for ^{103}Ru to concentrate at interfaces.

Chemical analyses of the salt samples for bulk constituents have been nearly completed and so far show better agreement with original salt compositions than previous analyses of used fuel.

Examination of Molybdenum Specimens. – The molybdenum specimens, on visual and low-magnification examination, showed no damage except for scratches probably made during disassembly of the capsules. A crude hot-cell bend test indicated marked embrittlement of the molybdenum by the exposure. The specimens broke cleanly after bending only 5°. No oxidation nor surface films could be detected visually to which the embrittlement could be attributed. The survival of the specimens with no visual evidence of corrosion was in marked contrast to the gross attack observed on the 47-3 molybdenum specimens. The difference was ascribed to the suppression of fluorine evolution during the 47-6 exposure.

Examination of Graphite. – The graphite was in good condition, and its x-ray diffraction pattern was normal. Observations on pertinent features of its behavior are discussed under other headings in this report.

Examination of INOR-8. – Examination of the inner capsule surfaces visually and with low-power magnification revealed no evidence of damage or corrosion. The metal surfaces were shiny, and the

original machining marks were visible. Metallographic and x-ray examinations are under way, and a search for ^{103}Ru deposition by leaching is planned.

Acknowledgments

Acknowledgment is made to personnel of the Analytical Chemistry Division and the Hot-Cells Operations group, to R. E. Thoma and D. R. Sears of the Reactor Chemistry Division for assistance in x-ray diffraction examinations, and to T. N. McVay (ORNL consultant) for petrographic examinations.

DESIGN AND MOCKUP TESTS OF A PROPOSED IN-PILE MOLTEN-SALT IRRADIATION EXPERIMENT

H. C. Savage J. M. Baker
G. H. Jenks E. G. Bohlmann

The radiation chemistry of the Molten-Salt Reactor (MSR) system has been investigated in a number of in-pile capsule[8,9] and pump loop[10] experiments which have been operated in the Materials Testing Reactor (MTR). These experiments were designed to determine the effects of irradiation on the fuel salt and on its compatibility with the proposed materials of construction (INOR-8 and graphite). These tests have shown that operation of the MSRE should not be adversely affected by irradiation effects on fuel and materials, but a continuing irradiation program is needed to provide supporting information for an understanding of both short-term and long-term effects of irradiation on fuels and materials – especially for reactors that will follow the MSRE.

Whereas most past experiments demanded very little attention during operation, the future experiments projected will require daily attention to the operation and data by both scientists and technicians, rapid analysis of gas and fuel samples, and concessions in reactor operating schedules. These requirements and the availability of hot-cell and analytical facilities especially equipped to handle radioactive fuel from the MSRE dictate that the experiments be carried out in the Oak Ridge Research Reactor (ORR).

Experimental Objectives and Design Considerations

Some objectives for an irradiation (in-pile) program with an MSR fuel salt are tabulated below. Experiment requirements and reasons are listed in Table 2.6.

Irradiation objectives:	200 w/cm^3 fuel fission power
	50% ^{235}U burnup
	One year of in-pile operation
Information objectives:	Graphite-salt compatibility
	INOR-8–salt compatibility
	Salt (fuel) stability
	Fission product chemistry

Reactor Irradiation Facility

It is proposed to make use of horizontal beam hole HN-1 in the ORR, since this will result in appreciable economies through use of equipment left by the homogeneous reactor irradiation program. Neutron flux mapping of beam hole HN-1 indicates that a thermal flux of $\sim 5 \times 10^{13}$ would be available. It is estimated that a thermal flux of 5×10^{13} will produce a fission power density of 190 w/cm^3 in a fuel salt containing 0.6 mole % ^{235}U and 320 w/cm^3 in a 1 mole % ^{235}U salt.

Experiment Design

Consideration of the experimental objectives and requirements previously described indicate that salt circulation and mixing are necessary. In order to avoid costly, complex pump loop experiments requiring substantial research and development effort, an autoclave (capsule type) experiment with thermally induced flow has been investigated and designed. A schematic diagram of the proposed autoclave is shown in Fig. 2.3, and a photograph of the partially assembled autoclave is shown in Fig. 2.4. The overall dimensions are such that the autoclave assembly will fit in beam hole HN-1 of the ORR.

---

[8] *Reactor Chem. Div. Ann. Progr. Rept. Jan. 31, 1963*, ORNL-3417, pp. 17–30.

[9] *Reactor Chem. Div. Ann. Progr. Rept. Jan. 31, 1964*, ORNL-3591, pp. 16–27.

[10] D. B. Trauger and J. A. Conlin, Jr., *Nucl. Sci. Eng.* **9**, 346 (1961).

Table 2.6. Experiment Requirements and Reasons

Requirement	Reasons
Fuel circulation through cold and hot regions	Move fuel past graphite and gas interface to favor transfer of gaseous products (F_2, CF_4, Xe) to gas phase for sampling
	Study transport and deposition of fission products and corrosion products
	Homogenize fuel for sampling and enrichment for long-term operation (one year)
Fuel salt sampling	Fuel stability assessment
	Fission product chemistry
	Corrosion product accumulation and chemistry
	Power density estimation
	Fuel enrichment possibility
Cover-gas sampling	CF_4 generation
	Xenon generation and removal
	Volatile fission product fluorides behavior
	Power density estimation
Drain fuel salt	Facilitate examination of salt and container for deposits and precipitates
Maintain fuel molten at all times	Avoid fluorine generation and loss at low temperature (frozen)

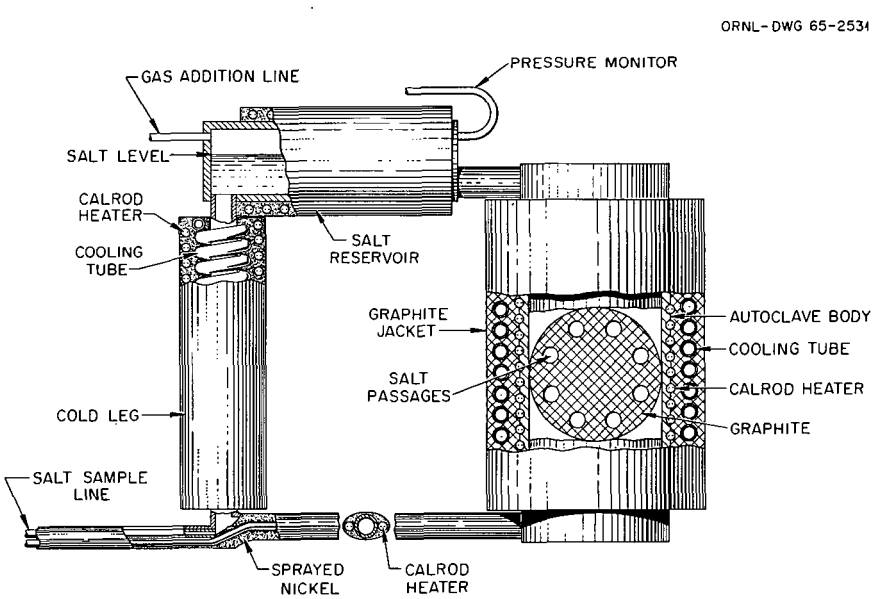

Fig. 2.3. In-Pile Molten-Salt Autoclave Mockup.

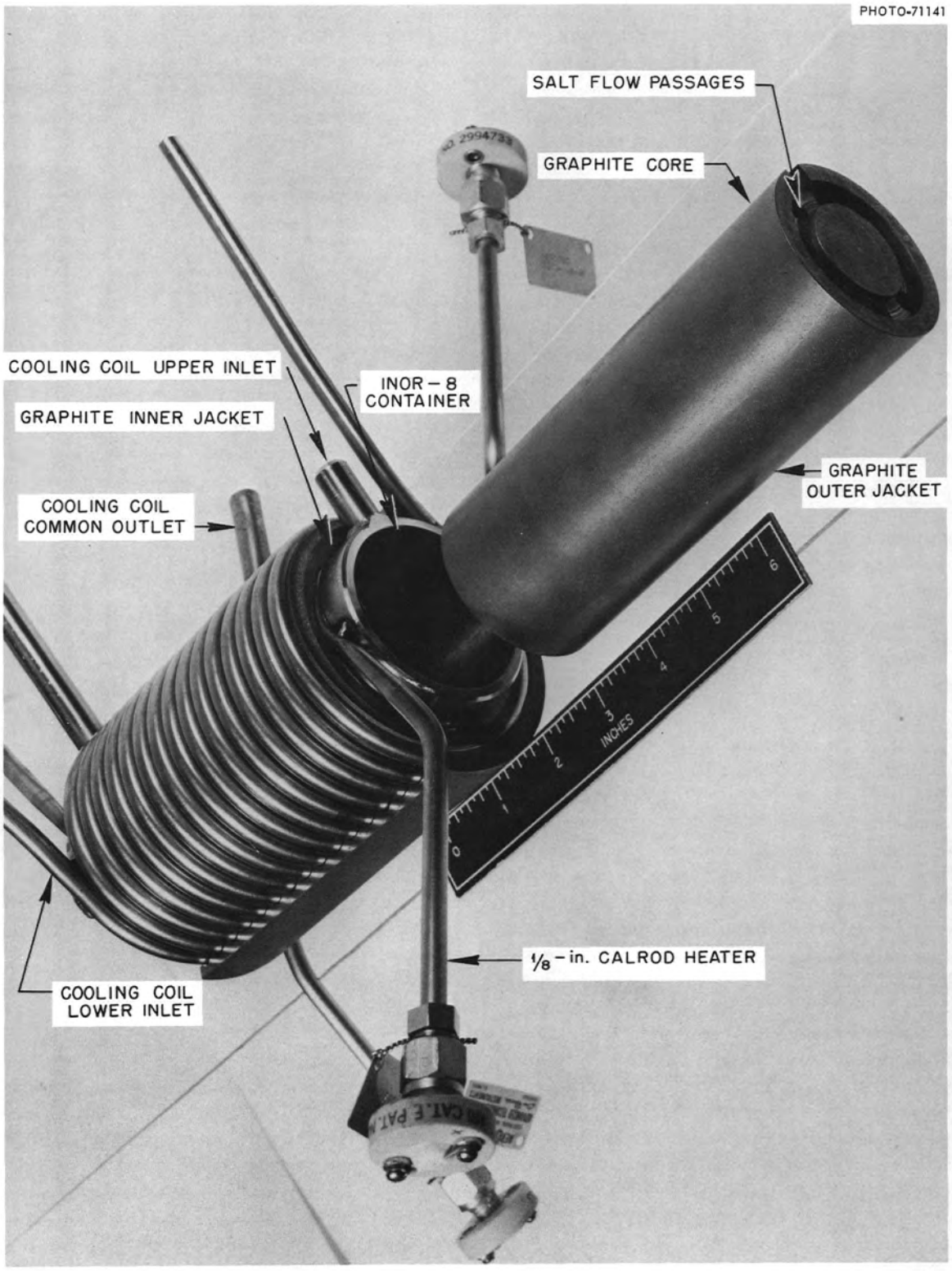

Fig. 2.4. In-Pile Molten-Salt Autoclave.

The main autoclave body is fabricated of 2-in. sched-40 INOR-8 pipe with a graphite core. The graphite core contains eight longitudinal $\frac{1}{4}$-in. holes, which serve as fuel passages and provide a fuel volume of ~ 42 cm^3 in the core. A reservoir tank serves as a salt reservoir and provides for a liquid-vapor interface. A cold leg and return line complete the circuit for salt flow. The total circulating salt volume is ~ 85 cm^3. Calrod electric heaters and cooling coils are used to provide temperature control and to maintain the thermal gradients necessary to induce thermal convective flow. Tubes of capillary dimensions interconnect the vapor space of the reservoir tank with remotely located pressure monitoring and gas sampling equipment. The salt sample line ($\frac{1}{8}$ in. OD $\times$ 0.075 in. ID) is ~ 12 ft long and is traced with Calrod heaters. The sample line is routed to the sample station at the reactor shield face, where samples of molten salt can be routed either to a dump tank for storage or a sample capsule for subsequent chemical analysis. The sample station also contains necessary tanks, valves, and lines so that salt additions to the autoclave can be made during in-pile operation.

Mockup Tests

Flow rates of 2 to 10 cm^3/min were obtained with a temperature gradient of 30 to 90°C between the main autoclave and the cooled leg in preliminary tests with a model of the assembly. A mockup assembly was constructed and was operated for more than 1200 hr at temperatures of ~ 1200°F with a salt mixture whose composition was LiF-BeF_2-ZrF_4-UF_4 (65-29-5-1 mole %, liquidus temperature ~ 842°F). Evidence of salt circulation was sought by three different methods: (1) heat balance around the cold leg, (2) heat addition to one segment of the flow circuit and measurement of the temperature response time in a downstream segment, and (3) by spiking of the melt with additional UF_4 and subsequent chemical analysis of a sample. These tests indicated a flow rate in the range of 2 to 10 cm^3/min. There was, however, disagreement in the results from each of these methods, and further tests are required. Heat balance measurements around the circuit should provide a reliable means of monitoring the salt flow rate during in-pile operation.

The adequacy of the salt sampling and addition system was demonstrated by removing 12 samples (10 cm^3 each) of the salt while operating at elevated temperature. After each sample removal, an equivalent amount of salt was added in order to maintain the original salt inventory of 192 g (85 cm^3 at 1200°F). The salt inventory was checked periodically by observing the salt level in the reservoir tank by gamma graphs.

After termination of the mockup test, the salt was drained from the autoclave into the dump tank without difficulty. Portions of the autoclave assembly exposed to molten salt were sectioned and examined. Little or no visual evidence of corrosion of these surfaces (INOR-8 and nickel) was found. The graphite core was in good condition, with no evidence of salt penetration when examined microscopically.

A test was made of the ability of the autoclave heater-cooler unit to remove the predicted 12 kw of fission and gamma heat (8 kw fission heat) during in-pile operation. Some 9 kw of heat, the maximum that could be generated in existing test equipment, was removed with the autoclave at 1000°F; the cooler capacity is accordingly considered adequate for an autoclave operating in-pile taking into account the higher design temperature of ~ 1200°F. Also the equipment is designed for a larger throughput of the air-water coolant than was used in the above test.

Conclusions

Results of the mockup tests indicate that the proposed in-pile autoclave is suitable for use in a fuel salt irradiation program with the objectives previously outlined. Experimental requirements of (1) fuel circulation through cold and hot regions, (2) sampling of fuel salt and cover gas, (3) ability to drain the salt, and (4) maintaining the salt molten at all times were demonstrated. Additional design and development work is continuing on a prototype autoclave designed for easy dismantling after in-pile operation.

RADIOLYSIS OF SOLID METALLIC FLUORIDES

Effects of Gamma Irradiation of Simulated MSRE Fuel Salt

E. L. Compere H. C. Savage
J. M. Baker

Introduction. – The generation of substantial quantities of fluorine gas by the gamma irradiation of a solid fluoride salt simulating the MSRE fuel was reported earlier.[11,12] The operation of an unirradiated control experiment has also been reported.[13] Since these reports, the irradiated and control experiment capsules have been opened and the contents recovered and examined.

Résumé of Experiment. – In each experiment 35 g of a fluoride salt simulating MSRE fuel was placed in a prefluorinated INOR-8 capsule covering spheres of several selected graphite types. Tables 2.7 and 2.8 give the salt composition and identify the graphites. The salts were melted in place and then allowed to freeze around the

[11]H. C. Savage, E. L. Compere, and J. M. Baker, *Reactor Chem. Div. Ann. Progr. Rept. Jan. 31, 1964*, ORNL-3591, pp. 27–31.

[12]E. L. Compere, H. C. Savage, and J. M. Baker, *MSRP Semiann. Progr. Rept. Jan. 31, 1964*, ORNL-3626, pp. 101–5.

[13]H. C. Savage and J. M. Baker, internal memorandum, July 6, 1964.

Table 2.7. Results of Chemical Analysis of Simulated MSRE Fuel Salt Without and After Gamma Irradiation

Major Elements	Original Salt					Autoclave Salt			
	Original Analysis			Control Analysis		Nonirradiated		Gamma-Irradiated	
	mole %	Wt %	F meq/g[a]	Wt %	F meq/g	Wt %	F meq/g	Wt %	F meq/g
Fluorine		61.1	32.16	59.9	31.53	62.0	32.63	61.2	32.21
Lithium	69.0	10.6	15.27	10.4	14.99	10.9	15.71	10.6	15.27
Beryllium	23.0	4.59	10.18	4.52	10.02	4.65	10.31	4.63	10.27
Zirconium	5.2	10.5	4.60	8.26	3.62	10.8	4.74	10.9	4.78
Thorium	1.7	8.88	1.53	12.0	2.07	5.52	0.95	6.13	1.06
Uranium	1.1	5.59	0.94	5.10	0.86	5.33	0.90	5.25	0.88
Total	100.0	101.26		100.18		99.20		98.71	
Metals total			32.52		31.56		32.61		32.26
Reducing power					<0.005		<0.005		0.288
Impurities		ppm		ppm		ppm		ppm	
Oxygen		305		675		542		1121	
Water		<250							
Iron		130		330		192		157	
Chromium		8		960		11		81	
Nickel		861		62		70		90	
Copper				15		65		80	
Weight percent of sample of above impurities		0.0504		0.2042		0.0880		0.1529	

[a]F meq/g is the number of milliequivalents of fluorine which would react with the amount of the indicated material in 1 g of sample to form stable fluoride compounds, e.g., UF_4.

Table 2.8. Weight Changes in Graphite from Non- and Gamma-Irradiated Autoclaves

Graphite	Average Original Weight (mg)	Individual Sphere Weight Change (mg)			Total Weight Change (mg)
		High	Low	Average	
		Unirradiated			
CEQ	200	+7	−5	−1	−9
TSX	229	−1	−6	−2	−19
ATU	240	+8	−10	−2	−15
		Irradiated			
AGOT	223	+42	+5	+30	+241
R0025	247	+22	+3	+13	+105
PYRO	292	+1	−1	0	0

graphite spheres prior to the irradiation or control exposure; the salt in the irradiated autoclave was again melted during calibration prior to irradiation. The salts of the two experiments were never subsequently remelted. Helium was used as a cover gas. The irradiation experiment[11,12] subjected the autoclave to a ^{60}Co gamma dose rate of 0.45×10^{20} ev hr^{-1} g^{-1} for a total of 7391 hr at controlled temperatures between 38 and 150°C. The control autoclave was operated for 3119 hr at temperatures of 25 to 150°C.

Several additions of fluorine gas, 149.5 cm^3 (STP) total, were made during the course of the control exposure to simulate the conditions found in the irradiated autoclave. Only 10.1 cm^3 of this fluorine was recovered; the loss was not explainable by leaks, equipment malfunctions, or, as discussed later, uptake by the graphite.

Gas Analyses. – Four samples of gas removed from the irradiated autoclave at various times during the experiment yielded a total 30 cm^3 (STP) fluorine, 0.89 cm^3 CF_4, 0.52 cm^3 CO_2, 2.5 cm^3 excess O_2, and lower amounts of COF_2 and SiF_4. The amount of fluorine recovered was 8 to 10% of that corresponding to the UF_4 originally present. Uranium hexafluoride, though sought, was not detected.

Examination of the Salt. – When both autoclaves were opened, there was no evidence that the salt had wet the wall or the graphite and no evidence of corrosion; the salt broke cleanly away from the graphite spheres. During the test, both salts had remained a single solid mass with interspersed voids formed during initial solidification; the control salt was light green (as expected), and the irradiated salt was dull, sooty black throughout.

Spectrophotometric examination of some melted, irradiated salt showed that it was red, with the spectrum indicating that essentially all the uranium was in the trivalent form; on solidification under helium atmosphere the sample was a "dirty light-green" color.

Table 2.7 presents results of chemical analyses of the various salt samples; the unexpected variability in the thorium and zirconium results may indicate nonhomogeneity of the samples. The reducing power of the irradiated sample is a clear indication of a radiation effect; three times as much fluorine was indicated, by this result, to have been lost from the samples as that accounted for by the fluorine recovered in the gas samples.

Optical (petrographic) and x-ray diffractometric examination of samples revealed small amounts of deeply colored brown cubic crystals which appeared

to be lithium fluoride; other results were consistent with the known variations in phase occurrence and crystallinity ascribable to the relatively rapid solidification following the original loading and melting.

Examination of the Graphite. – Table 2.8 presents the observed weight changes for the total of forty-eight $\frac{1}{4}$-in.-diam graphite spheres (eight of each type) used in the experiments. The graphites of the unirradiated control test were equally or more porous (had lower average original weights) but did not show any significant weight changes over the course of the exposure. The pyrolytic-graphite samples in the irradiated test also appeared to be unaffected, but the other two irradiated graphite types showed substantial weight gains. Spectrographic analysis showed that these graphites, after irradiation, contained 10^3 to 10^5 ppm uranium but negligible quantities of lithium, beryllium, or zirconium. The presence of uranium in these graphites in such quantities, and its substantial absence from others, was confirmed by the use of activation analysis.

Fluorine analysis of irradiated, control, and unexposed material by chemical methods and in some cases by activation analysis indicated that unexposed spheres (weighing 200 to 300 mg) contained ~0.2 mg of fluorine. Spheres exposed to fluorine in the unirradiated control contained 0.7 to 1.3 mg of fluorine, far above the stoichiometric equivalent of the uranium found in these spheres. A pyrolytic-graphite sphere exposed to the irradiated salt contained 0.7 mg of fluorine (about 50 atoms of fluorine per uranium atom). Substantial quantities of fluorine as well as uranium were found in the two more porous graphites exposed to irradiated salt. The R0025 sphere which was analyzed contained 4 mg of fluorine (3 fluorine atoms per uranium), and the AGOT sphere contained 7 mg of fluorine (5 fluorine atoms per uranium).

Discussion

The most significant postirradiation finding was that under the associated influences of irradiation and fluorine gas, both uranium and fluorine, and no other materials from the salt, combined in substantial quantities with the more porous graphites. Although UF_6 was not detected in any of the gas samples, it might well have been the volatile intermediate through which the uranium was transferred to the graphite; the fluorine/uranium ratio observed in the irradiated spheres and the available material balance information for gas recovery, reducing power, and total weight gain by the graphite lend support to this hypothesis.

The results of examination of the unirradiated control samples indicate, in agreement with the literature, that fluorine can be taken up by the graphite under these conditions and that small amounts of uranium can be transferred from the salt.

The much larger transfer of uranium to the graphite in the presence of radiation was not consistent with a hypothesis of monolayer adsorption on the low-surface-area graphites under test nor with the idea of capillary condensation of the volatile species which might have been present. The direct reaction of UF_6, in the presence of fluorine, with graphite seems more consistent with the results, but information is not available to demonstrate whether carbon monofluoride or tetracarbon monofluoride (known to be produced by the action of fluorine on graphite) is involved.

These findings were, it should be noted, incidental to the primary goal of the experiment, which was to show the evolution of fluorine from gamma irradiation of solid MSRE-type fuel. No concern for the success of the MSRE is raised by the observed transport of uranium to graphite, since the results of other experiments have shown that no fluorine is generated from the irradiation of molten salt in contact with graphite. However, these experiments indicate that any continued proximity of reactor graphite to solidified fuel salt material containing fission products or otherwise subject to substantial ionizing radiation should be minimized.

Effects of Beta Irradiation of Solid Fluorides

J. E. Baker G. H. Jenks

Introduction. – The study of fluorine evolution from inorganic fluorides exposed to Van de Graaff electrons[14] has been continued in efforts to develop an understanding of the mechanisms controlling the process. Such understanding should be useful in connection with the design and operation

[14] J. E. Baker and G. H. Jenks, *Reactor Chem. Div. Ann. Progr. Rept. Jan. 31, 1964*, ORNL-3591, pp. 31–34.

of molten-salt reactors and would contribute to the general study of radiation damage to solid ionic crystals. The use of gamma radiation, soft x rays, and self-radiation from fission products is being explored in other studies.[9,11,15]

In the previous work,[14] the values of G_{F_2} were found to change with increasing dose. The results suggested that information regarding the mechanism might be deduced from more complete and accurate data. Additional electron-irradiation experiments have now been completed for this purpose. In other electron-irradiation experiments the release of fluorine from the compounds Li_2BeF_4 and Li_6BeZrF_{12} has been studied because these complex compounds are among those which are formed during cooling of the MSRE fuel salt.

Experimental Procedures and Results. – The experimental procedures were similar to those previously described,[14,16] except as noted specifically. Dose rates were estimated by exposing a 1:9 mixture of KNO_3 and LiF to a cobalt source of known intensity and comparing the NO_2^- formation with that obtained from electron irradiation. The irradiation of nitrates has been discussed elsewhere.[17,18] The result for the MSRE-type salt was 4.2×10^{16} Mev g^{-1} μa-hr^{-1}, in near agreement with that calculated previously. The uncertainty is estimated to be ~20%. Electron currents of 1 μa were employed in almost all tests.

Calculations of the temperature gradient in the test salt during irradiation at a current of 1 μa gave a value of 20°C (from about 19°C at the wall to about 39°C at the center of the sample).

Irradiation of MSRE-Type Salt. – For the two final experiments (14 and 15), four changes in conditions were made over those used in previous work:

1. The cell was modified so that all the test salt was exposed to radiation.
2. Gas samples were swept from the cell without disturbing its position.
3. The total dose was accumulated in a continuous series of 3-hr exposures, with minimum time between exposures for gas sampling and gas recharging.
4. Prior to one experiment, the test salt was annealed at 400°C for 1 hr.

The results of experiments 14 and 15 are shown in Fig. 2.5. They do not show the second maximum found in an earlier experiment,[14] but the shapes of the curves during the initial exposure periods are similar. The reduction in G values in experiment 15 is attributed to the prior annealing of the test salt. The total fluorine removed in these experiments was 2.0 and 1.1% of that in the original samples.

In experiment 12, the same procedures were used except that the exposure periods were only 2 hr each, separated by periods of varying duration (from 30 min to 1 day). Control determinations of fluorine absorption were made during many of these interim periods, and the test salt was not annealed.

The observed fluorine evolution in this experiment reached a maximum G value of 8.6×10^{-3} at 1.8×10^4 sec, after which it dropped markedly and became negligible after about 5.7×10^5 sec. These results differed from those of all other electron irradiation experiments with MSRE-type salt.

Irradiation of Li_2BeF_4. – The procedure used for the first half of experiment 13 was the same as that described above for experiment 12; that for the last half was the same as that used in experiments 14 and 15. The salt was examined petrographically and reported to be typical Li_2BeF_4 plus some LiF.[19] Fluorine evolution at relatively low rates was found as illustrated in Fig. 2.6.

Irradiation of Li_6BeZrF_{12}. – The procedures of experiments 10 and 11 with this salt were the same as those used in experiment 12. Petrographic examination of the salt indicated that it was mostly the desired phase but with some cryptocrystalline growth.[19] No significant fluorine evolution was found during exposures in two different experiments in which the total dose was about the same as that in the Li_2BeF_4 experiment. The measured G value was slightly negative but, at the 95% confidence level, not significantly different from zero.

---

[15] W. T. Rainey, Jr., *et al.*, *Reactor Chem. Div. Ann. Progr. Rept. Jan. 31, 1964*, ORNL-3591, pp. 34–37.

[16] *MSRP Semiann. Progr. Rept. July 31, 1963*, ORNL-3529, pp. 98–103.

[17] E. R. Johnson, *J. Phys. Chem.* **66**, 755 (1962).

[18] Tung-Ho Chen and E. R. Johnson, *J. Phys. Chem.* **66**, 2249 (1962).

[19] G. D. Brunton, private communication.

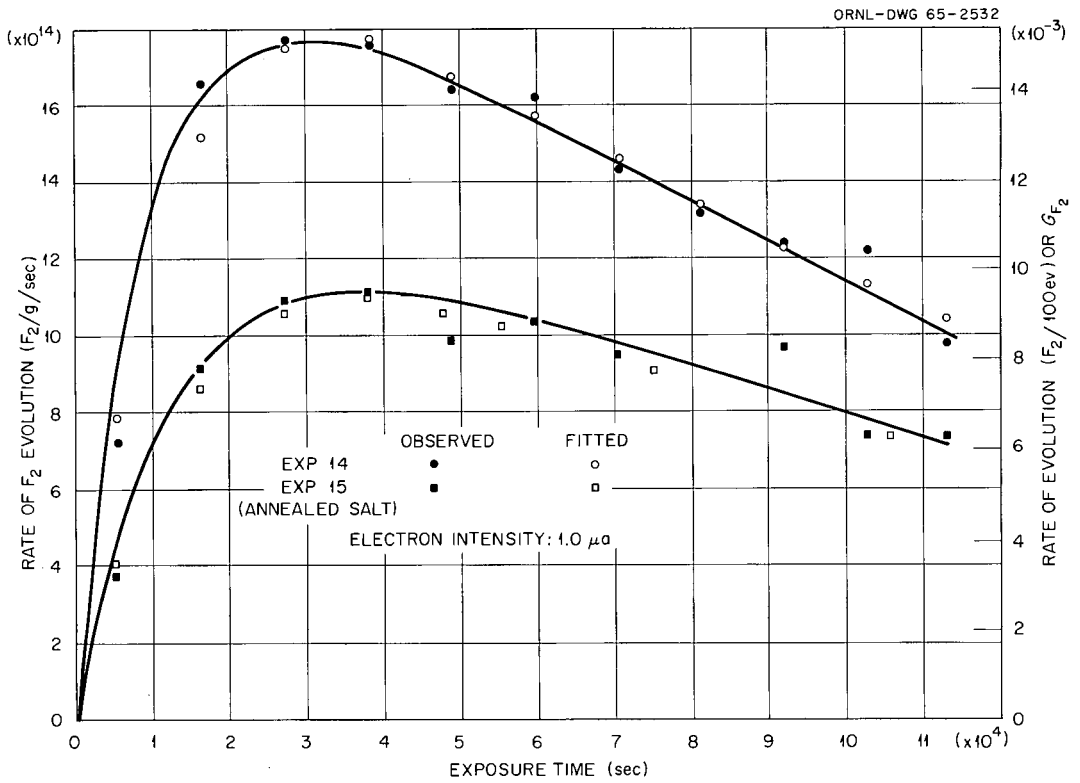

Fig. 2.5. Fluorine Evolution Rates from MSRE-Type Salt.

Discussion of Results. – The occurrence of a second maximum in the previous work with MSRE-type salt is now believed to have been due to mechanical exchange of unirradiated and irradiated salt due to movement of the cell after the first maximum had been passed; the unirradiated salt then exposed to the electron beam probably led to the observation of the second maximum. The procedures of experiments 14 and 15 avoid this possibility.

No explanation for the anomalous results of experiment 12 is known; it is possible that the interim periods of exposure to fluorine permitted radiolytic fluorine to diffuse out of the salt, thus invalidating both the radiation and the control results.

A similar possibility could be used to explain the results of experiments with the Li_6BeZrF_{12}, but the lack of any detected fluorine evolution supports the conclusion that no fluorine is evolved upon electron irradiation at the intensities used. Previous workers[15] have reported the evolution of fluorine after exposure to soft x rays; no explanation of the difference is apparent.

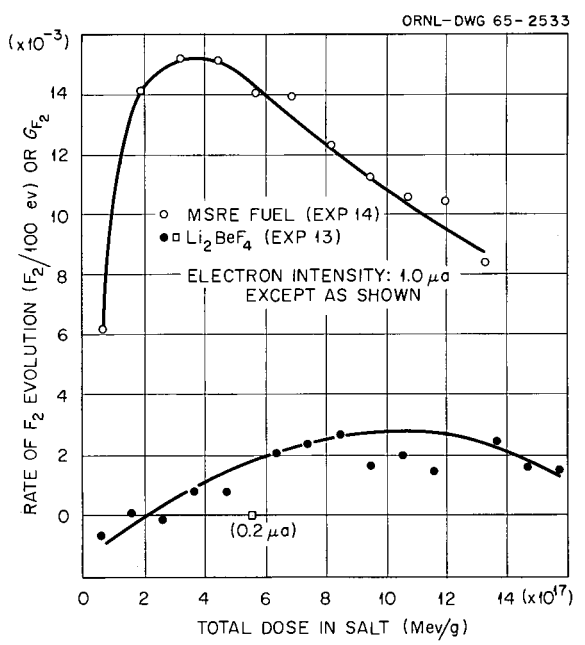

Fig. 2.6. Fluorine Evolution Rates from MSRE-Type Salt and from Li_2BeF_4.

The results of the irradiation of Li_2BeF_4 seem to show that fluorine is evolved from this phase, but at rates which are low relative to those for MSRE fuel salt.

Model for the Release of Fluorine from MSRE-Type Salt During Irradiation. – A model has been postulated to explain the relationships between the rate of fluorine evolution and exposure time in experiments 14 and 15 as well as the other characteristics of the fluorine release from MSRE-type salt. It assumes the presence within the solid mixture of an unspecified material of some particular composition and degree of crystalline imperfection. Fluorine release occurs at a rate proportional to the concentration of this material; this concentration depends upon the thermal and mechanical history of the solid, and it can be reduced by thermal annealing. It is also reduced in proportion to the amount of fluorine which has been released during irradiation. The evolution of fluorine from the solid is proportional to the concentration of radiation-released fluorine within the solid. Back reaction of fluorine and the sites from which it was generated is assumed to be negligible.

The model appears to offer plausible explanations for most of the reported[9,11,14,15] experimental observations for temperatures below 110°C. Modification may be necessary to accommodate the possibility of back reaction, which would account for the reported uptake of fluorine by irradiated salt at higher temperatures.[11]

Effects of Irradiation with Soft X Rays[20]

W. T. Rainey[21] D. N. Hess
H. F. McDuffie

The use of soft x rays for the liberation of fluorine from solid inorganic fluorides[22] was continued during part of 1964 with a Muller 150 MG (constant dc) beryllium-window tube, operated at 150 kv and 12 ma to give an output through the window of 2×10^{21} ev/hr. Figure 2.7 shows the

[20]W. T. Rainey, Jr., *et al.*, "Chemical Effects of X-Rays on Inorganic Fluorides. I. Apparatus, Techniques, and Preliminary Results," presented at 1964 Annual Meeting of the American Nuclear Society, San Francisco, Calif., 1964.

[21]Formerly Reactor Chemistry Division, now Analytical Chemistry Division.

[22]*Reactor Chem. Div. Ann. Progr. Rept. Jan. 31, 1964*, ORNL-3591, p. 34.

ORNL–DWG 64–10235

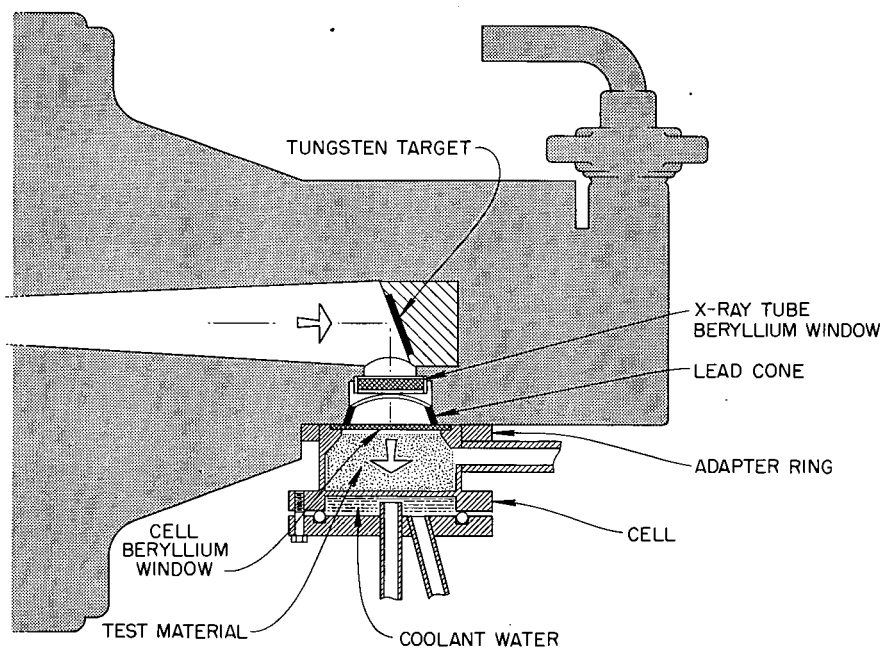

Fig. 2.7. Apparatus for X Irradiation of Inorganic Fluorides.

arrangement of the tube and the beryllium-window test cell. The absorbed radiation dose to a 10-g sample of salt was measured to be 10^{21} ev/hr by conventional dosimetry.

Continuation of the irradiation of MSRE-type fuel salt with the beryllium-window tube gave results consistent with those previously observed at lower dose rates; during a 69-hr irradiation, a concentration of 3.6% fluorine was produced in the helium cover gas – an order of magnitude higher than previously achieved concentrations.

The importance of impurities was shown by studies of the effect of changes in the irradiation period. A single sample of fine-particle fuel salt was used throughout the series of tests. The sample had been prefluorinated at 95°C with 100% fluorine (the conditions were not so severe as to cause any detectable release of UF_6). Figure 2.8 shows the observed increase of fluorine yield and decrease of oxygen yield as the irradiation period was lengthened; the figure also shows a total yield of irradiated products, calculated on the assumption that one molecule of oxygen was equivalent to two molecules of fluorine. The apparent constancy of this sum suggests that the initial yield of radiolytic products is around 0.09, some six times as high as the maximum values reported for irradiation with Van de Graaff electrons[23] but within a factor of 2 of the value of 0.05 reported for irradiation with gamma rays[24] and the value of less than 0.05 reported for postfission decomposition of MSRE fuel salt samples which had been irradiated in the MTR.[25]

A low G value (0.003 to 0.008 equivalent molecule of F_2 per 100 ev energy absorbed) had been reported for ThF_4[22] after prefluorination at 160°C to remove impurities. A more drastic fluorination of this ThF_4 – with 100% fluorine at 350°C for several weeks – produced a material which, upon subsequent irradiation, gave a yield of 0.014, with only F_2 and CF_4 as products; none of the previously observed fluorine compounds and equivalent species were present.

Future studies in this program will be directed toward the effects of composition, crystal structure, crystallinity, and the presence of controlled amounts of impurities on the yields of radiolytic products.

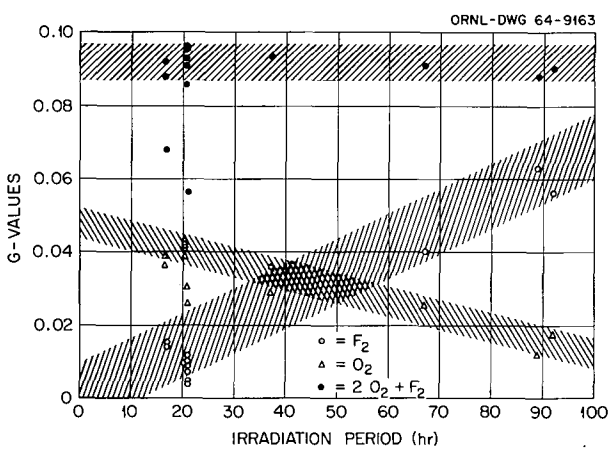

Fig. 2.8. Dependence of G Value on Length of Irradiation Period.

[23]This report, chap. 2, p. 51.

[24]*Reactor Chem. Div. Ann. Progr. Rept. Jan. 31, 1964*, ORNL-3591, p. 31.

[25]*Reactor Chem. Div. Ann. Progr. Rept. Jan. 31, 1963*, ORNL-3417, p. 30.

3. Chemical Studies of Molten Salts

HF-H_2O EQUILIBRIA AND OXIDE CHEMISTRY IN MOLTEN FLUORIDES

A. L. Mathews[1] C. F. Baes, Jr.
B. F. Hitch

Investigation of the oxide chemistry and the thermodynamics of LiF-BeF_2 melts by the method of equilibration with gaseous HF and H_2O has continued during the past year. As indicated previously,[2] these measurements can yield several kinds of information. Knowledge of the equilibrium

$$H_2O(g) + 2F^-(soln) \rightleftharpoons O^{2-}(soln) + 2HF(g) \quad (1)$$

can be used to predict the extent of oxide contamination of melts exposed to water vapor, as well as the efficiency of the reverse process, the removal of oxide by HF sparging. When the melt is saturated with an oxide, $MO_{x/2}$, such measurements can yield information about the thermodynamic activity of the corresponding metal fluoride in the melt, since reaction (1) may then be written in the form

$$H_2O(g) + \frac{2}{x} MF_x(soln) \rightleftharpoons \frac{2}{x} MO_{x/2}(c) + 2HF(g) \quad (2)$$

(where c denotes the crystalline solid). Finally, these measurements can yield estimates of the low solubilities of metal oxides in these melts.

The experimental procedure was that described previously.[2] Melts (0.2 to 1 kg), at 500–700°C in nickel vessels, were sparged with a stream of H_2 gas (up to ~0.2 liter/min) containing known partial pressures of HF and H_2O (up to 0.02 atm). The effluent gas was analyzed alternately for HF (by alkalimetric titration) and for H_2O (by Karl Fischer titration). Under the conditions used, good equilibration of the melt with the flowing gas stream was obtained in nearly all of a large number of runs.

Methods of Data Reduction

From the results of these measurements it became evident that hydroxide ion was formed in addition to oxide ion in melts exposed to HF and H_2O:

$$H_2O(g) + F^-(soln) \rightleftharpoons OH^-(soln) + HF(g) . \quad (3)$$

This additional equilibrium complicated the treatment of the data, but the treatment was facilitated by computer calculations. The effluent partial pressures P_{HF} and P_{H_2O} were assumed to be related to $[O^{2-}]$ and $[OH^-]$ by equilibrium quotients to be determined:

$$Q_O = (P^2_{HF}/P_{H_2O})[O^{2-}] \text{ atm mole kg}^{-1} , \quad (4)$$

$$Q_M = P^2_{HF}/P_{H_2O} \text{ atm (for } MO_{x/2} \text{ saturation)} , \quad (5)$$

$$Q_A = (P_{HF}/P_{H_2O})[OH^-] \text{ mole/kg} . \quad (6)$$

These quotients, derived from reactions (1), (2), and (3), were assumed constant for a given LiF-BeF_2 composition and temperature. In addition, two material balance differential equations could be written.

$$d[OH^-] = [(P^0_{HF} - P_{HF}) + 2(P^0_{H_2O} - P_{H_2O})]\, dW \quad (7)$$

[1]ORINS Graduate Research Fellow from the University of Mississippi.

[2]*Reactor Chem. Div. Ann. Progr. Rept. Jan. 31, 1964*, ORNL-3591, p. 46.

and

$$d[O^{2-}] + d[OH^-] = (P^0_{H_2O} - P_{H_2O})\, dW \text{ (for unsaturated melts)}, \quad (8)$$

wherein P^0_{HF} and $P^0_{H_2O}$ are influent pressures, in atmospheres, and

$$W = V/(RT \times \text{melt wt.}) \text{ mole kg}^{-1} \text{ atm}^{-1} .$$

The quantity W is the number of standard volumes (~24 liters) of gas passed per kilogram of melt; T is the absolute temperature at which the gas volume was measured (~300°K).

For saturated melts, Eqs. (5), (6), and (7) were combined to yield a differential equation which could be integrated to give a linear expression of the form[3]

$$f(Q_M, P_{HF}) = \frac{Q_M}{Q_A} W + \text{const} . \quad (9)$$

When melts saturated with BeO were sparged with HF and H_2O, the initial effluent partial pressures rose with time (with W) and then leveled off at constant values (Fig. 3.1). The low initial values of P_{HF} and P_{H_2O} reflect the consumption of HF and H_2O to form OH^- ion. The quotient Q_M (Eq. 5) was usually estimated after P_{HF} and P_{H_2O} became constant. Then the above expression (Eq. 9) was fitted to the data in the region where P_{HF} and P_{H_2O} were changing, giving Q_A.[4]

For melts not saturated with oxide, Eqs. (4), (6), (7), and (8) all were to be satisfied. Except for a crude graphical calculation, no method could be found by which Q_O and Q_A could be determined directly from the observed values of P_{HF} and P_{H_2O} as a function of W. Instead, two simul-

[3]In Eq. 9, $f(Q, P_{HF}) \equiv (1/D) \ln [(Y+D)/(Y-D)]$, where $D = 1 + 8(P^0_{HF} + 2P^0_{H_2O})/Q$, $Y = (4/Q)P_{HF} + 1$.

[4]The program which performed these calculations was written by R. J. McNamee, Operations Analysis Division, ORGDP.

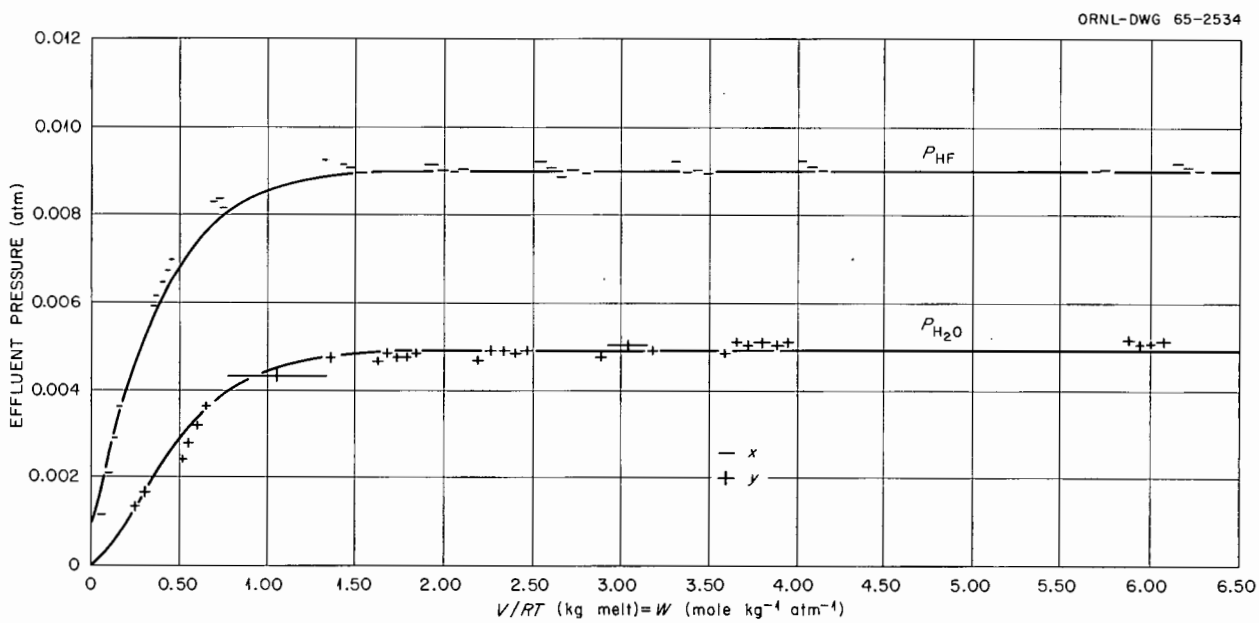

Fig. 3.1. Effluent Partial Pressures of HF and H_2O From BeO-Saturated Melt vs Standard Volumes of Sparging Gas. 30 mole % BeF_2–70 mole % LiF at 700°C. P_{HF} = 0.00567 atm, P_{H_2O} = 0.00653 atm. The curves were calculated with Q = 0.0165 atm and Q_A = 0.0161 mole/kg.

taneous differential equations[5] were derived which expressed the changes in $[O^{2-}]$ and $[OH^-]$ with W as a function of Q_O, Q_A, P^0_{HF}, and $P^0_{H_2O}$. These equations were solved numerically, with Q_O, Q_A, and the initial values of $[O^{2-}]$ and $[OH^-]$ as adjustable parameters, to produce calculated curves of P_{HF} and P_{H_2O} vs W. By a least-squares procedure, the four parameters were then varied to give the best fit to the data (Fig. 3.2).[6] This rather involved calculation was further complicated by the fact that the least-squares refinement of the parameters usually did not succeed unless the initial guessed values of Q_O, Q_A, $[O^{2-}]$, and $[OH^-]$ were fairly good ones. The fits finally obtained were usually satisfactory, however, and there seems little doubt that the assumed equilibria, Eqs. (1) and (3), account for the measurements.

[5]These equations are:

$$d[OH^-]/dW = (P^0_{HF} + 2P^0_{H_2O}) - (Q_O[OH^-]/Q_A[O^{2-}])(1 + 2[OH^-]/Q_A)\,,$$

$$d[O^{2-}]/dW = -(P^0_{HF} + P^0_{H_2O}) + (Q_O[OH^-]/Q_A[O^{2-}])(1 + [OH^-]/Q_A)\,.$$

[6]These calculations were performed by a computer program, "FIASCO," written by M. T. Harkrider, Mathematics Division, ORNL.

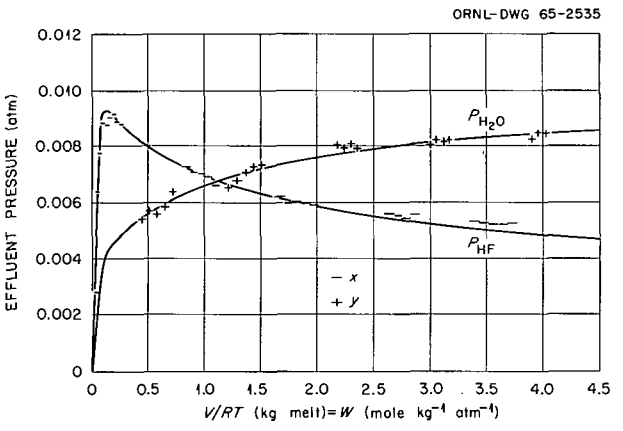

Fig. 3.2. Effluent Partial Pressures of HF and H_2O From Melt Not Saturated with Oxide vs Standard Volumes of Sparging Gas. $(2LiF\text{-}BeF_2)$ + 0.062 mole of ZrF_4 per kg at 515°C. P_{HF} = 0.0029 atm, P_{H_2O} = 0.0099 atm. The curves were calculated with Q_O = 7.76×10^{-6} atm mole kg^{-1}, and Q_A = 6.11×10^{-3} mole/kg.

$LiF\text{-}BeF_2$ Melts

The observed dependence of Q_B (the quotient P^2_{HF}/P_{H_2O} for BeO-saturated melts) upon the $LiF\text{-}BeF_2$ composition and upon temperature is shown in Fig. 3.3. The smooth curves were calculated from the empirical expression

$$\log(Q_B/X_{BeF_2}) = A + BX^2_{LiF} - CX^4_{LiF}\,, \quad (10)$$

where X denotes mole fraction and each of the coefficients A, B, and C varies linearly with $1/T$. The agreement between the observed values of Q_B and those calculated from this expression

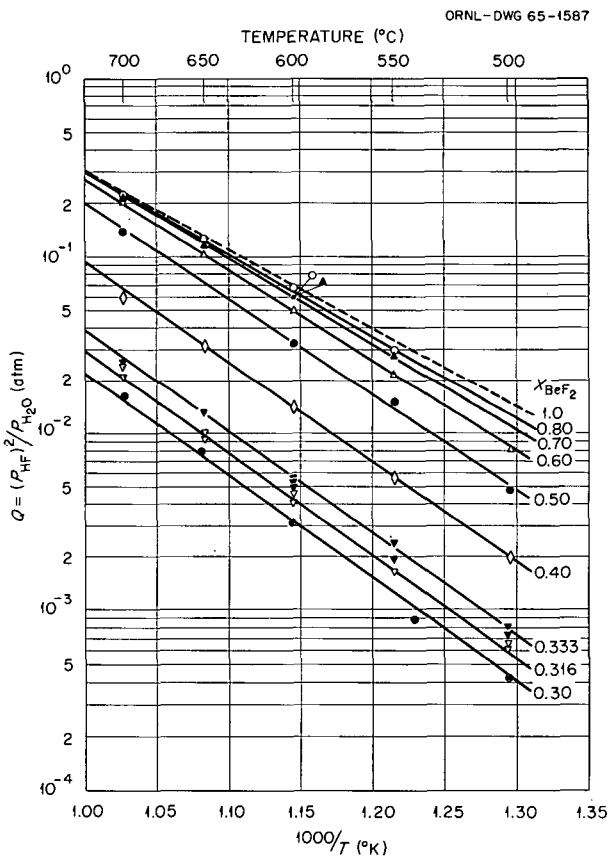

Fig. 3.3. Variation of Q_B for BeO-Saturated $LiF\text{-}BeF_2$ Melts with Temperature and with Mole Fraction of BeF_2. The lines were calculated from Eq. (6).

compares favorably with the estimated experimental errors in Q_B (these averaged approximately ±5%). Some of the thermodynamic quantities which can be derived from Eq. (10) are summarized in Table 3.1 and Fig. 3.4.

If the discrepancy (1.4 kcal) between the value of ΔF for reaction (2) derived from the present measurements and that derived from the JANAF Tables[7] is caused by an error in free energy of BeF_2 formation, the corrected value would be $\Delta F^f_{1000°K} \equiv -208.5$ kcal (vs 207.1 kcal). However, emf measurements now in progress (see the subsection "Reference Half-Cells for Molten LiF-BeF_2 Mixtures," this chapter) suggest also that an error may be present in the JANAF Table value for ΔF^f of BeO. The greater discrepancy between the ΔH values in Table 3.1 (4.7 kcal) may largely be caused by an error in the heat of fusion of BeF_2, which the JANAF Tables take to be 2 kcal. Combination of the present estimates of γ_{BeF_2} (Fig. 3.4) with the BeF_2 liquidus temperatures in the LiF-BeF_2 phase diagram suggests that the heat of fusion of BeF_2 is 11 ± 4 kcal.

Table 3.1. Thermodynamic Quantities Derived for the Reaction $H_2O(g) + BeF_2(l) \rightleftharpoons BeO(c) + 2HF(g)$

$\text{Log } K = 3.90 - 4.420/T$	
$\Delta F_{1000°K} = 2.4$ kcal	(1.03 kcal)[a]
$\Delta H_{1000°K} = 20.2$ kcal	(24.88 kcal)[a]

[a]Calculated from JANAF Tables.[7]

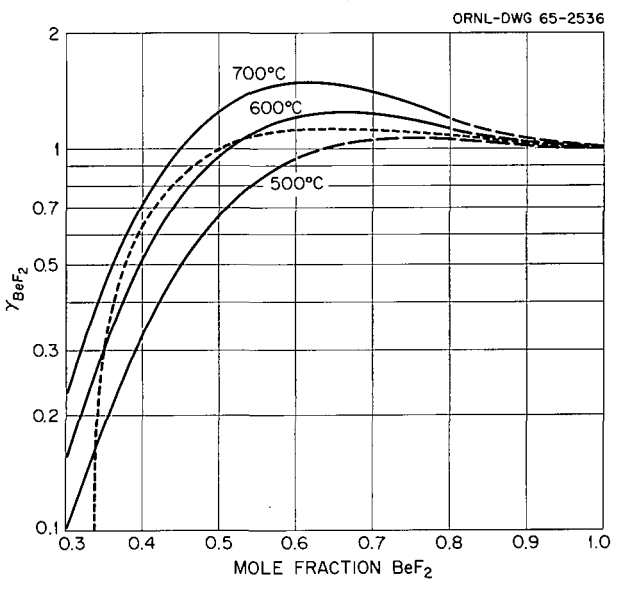

Fig. 3.4. Variation of BeF_2 Activity Coefficient in LiF-BeF_2 Melts with Mole Fraction of BeF_2 and with Temperature. Curves, based on Eq. (6), are dashed in the regions where the data were extrapolated. The dotted curve shows the expected variation of γ_{BeF_2} if melts were ideal mixtures of BeF_2 and Li_2BeF_4.

It is seen (Fig. 3.4) that LiF-BeF_2 mixtures are quite non-ideal; they exhibit both positive and negative deviations from ideal behavior. If, for X_{BeF_2} (BeF_2 mole fraction) > 0.33, the components are chosen to be $Li_2BeF_4 + BeF_2$ rather than LiF + BeF_2, and if it is assumed that the mole fraction of BeF_2 calculated on this basis is equal to the activity of BeF_2, then it is possible to calculate[8] a curve (Fig. 3.4) representing the variation to be expected in γ_{BeF_2} with composition. This curve is seen to have a shape similar to those based on the measurements, and showing both positive and negative deviations of LiF-BeF_2 mixtures from ideal behavior. This might be taken as evidence for the formation of BeF_4^{2-} in this system; however, the rapidly increasing viscosity as X_{BeF_2} approaches 1 (which limited the present measurements to $X_{BeF_2} < 0.80$) indicates these melts are increasingly polymeric, and the reality of the simple species BeF_4^{2-} cannot be established by this

[7]*JANAF* (Joint Army–Navy–Air Force) *Interim Thermochemical Tables*, Thermal Research Laboratory, Dow Chemical Company, Midland, Mich. (in loose-leaf binders; revised quarterly).

[8]The mole fraction of BeF_2 in $BeF_2 + Li_2BeF_4$ mixtures, X'_{BeF_2}, is related to the mole fraction in BeF_2 + LiF mixtures, X_{BeF_2}, by $X'_{BeF_2} = (3/2) - (1/2X_{BeF_2})$. Taking $a_{BeF_2} \equiv X'_{BeF_2}$, the activity coefficient of BeF_2 in BeF_2-LiF mixtures is given by

$$\gamma_{BeF_2} = (3X_{BeF_2} - 1)/2X^2_{BeF_2}.$$

correlation alone. An analogous test in the composition range below $X_{BeF_2} = 0.33$, in which the components would be chosen as LiF + Li_2BeF_4, would perhaps be more informative on this point, but the composition range here is greatly restricted by the LiF liquidus.

The quotients Q_O (Eq. 4) and Q_A (Eq. 6) could be estimated over a limited range in X_{BeF_2} from measurements on melts not saturated with BeO. The scatter in the results (Figs. 3.5 and 3.6) reflects the poorer accuracy of these quotients. Since Q_O and Q_A are related to the equilibrium constants of reactions (1) and (3) by

$$Q_O = K_1 a^2_{F^-}/\gamma_{O^{2-}}$$

and

$$Q_A = K_3 a_{F^-}/\gamma_{OH^-} ,$$

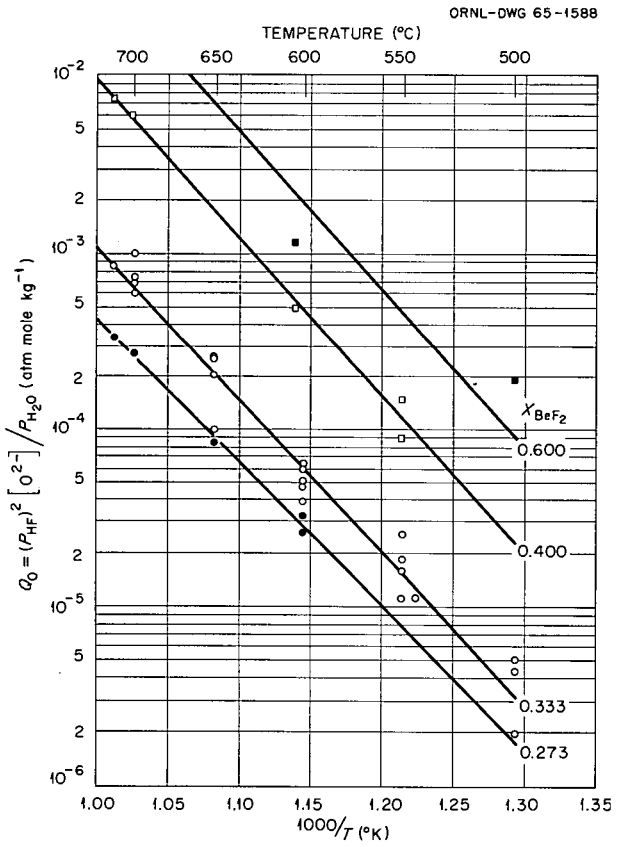

Fig. 3.5. Variation of the Oxide Ion Formation Quotient with Temperature and LiF-BeF_2 Melt Composition.

the variations of Q_O and Q_A with the LiF-BeF_2 composition reflect the variation in the activity of fluoride ion and/or in the activity coefficients of oxide and hydroxide ion. The ratio of Q_O to Q_B (the P^2_{HF}/P_{H_2O} quotient at BeO saturation) gives the concentration of oxide ion at BeO saturation (Fig. 3.7). The indicated solubility of BeO in 2LiF-BeF_2 at 600°C, 0.01 mole/kg, is

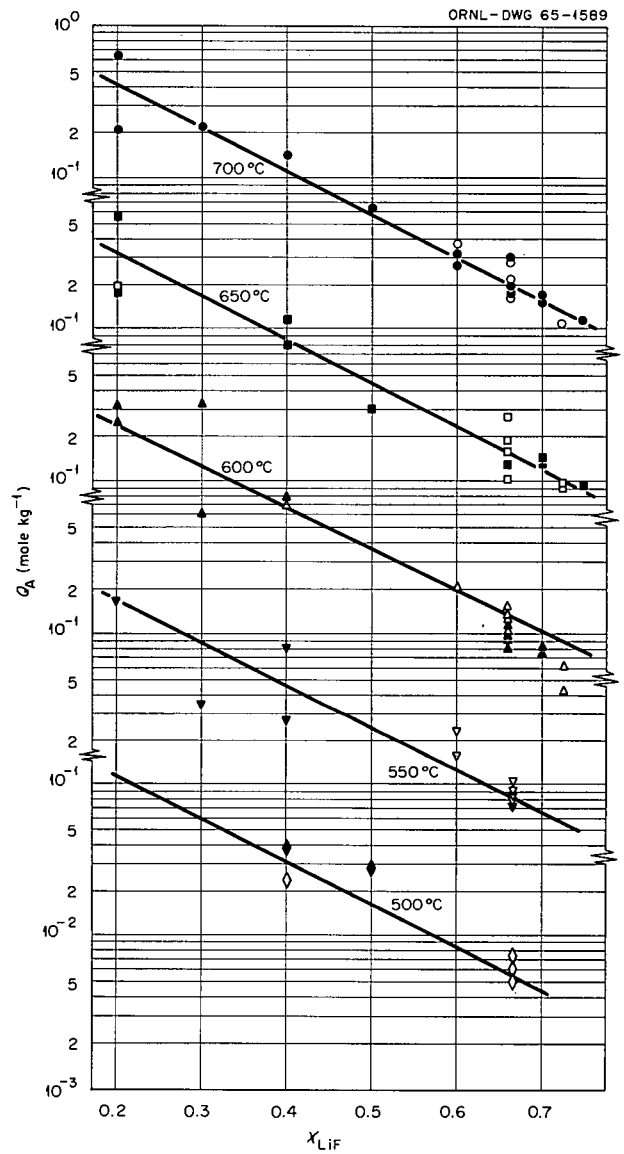

Fig. 3.6. Variation of the Hydroxide Ion Formation Quotient with LiF-BeF_2 Melt Composition and Temperature. Closed symbols denote measurements on BeO-saturated melts.

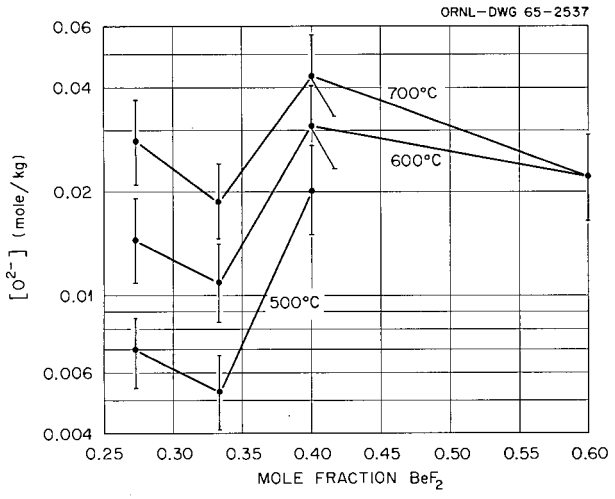

Fig. 3.7. Estimated Variation with Composition and Temperature of the Oxide Ion Concentration for LiF-BeF_2 Melts Saturated with BeO. The points with estimated uncertainties were derived by interpolation of the data in Figs. 3.3 and 3.5.

lower by a factor of about 6 than a previous estimate by a less direct method.[9]

2LiF-BeF_2-ZrF_4 Melts

It has been found in previous measurements of oxide solubilities in 2LiF-BeF_2 that with ZrF_4 present (greater than ~0.01 mole/kg) the stable oxide precipitated is ZrO_2.[9,10] Continuing measurements of Q_Z (the quotient P^2_{HF}/P_{H_2O} for ZrO_2-saturated melts) are summarized in Fig. 3.8. As expected, Q_Z rises with ZrF_4 concentration, in accordance with the equilibrium constant expression (cf. Eq. 2)

$$K_Z = Q_Z/(a_{ZrF_4})^{1/2} .$$

The activity coefficient of ZrF_4 (with the crystalline solid as the standard state) is given by

$$\gamma_{ZrF_4} = Q_Z^2/(K_Z^2 X_{ZrF_4}) .$$

[9]*Reactor Chem. Div. Ann. Progr. Rept. Jan. 31, 1963*, ORNL-3417, p. 38.

[10]*Reactor Chem. Div. Ann. Progr. Rept. Jan. 31, 1964*, ORNL-3591, p. 46.

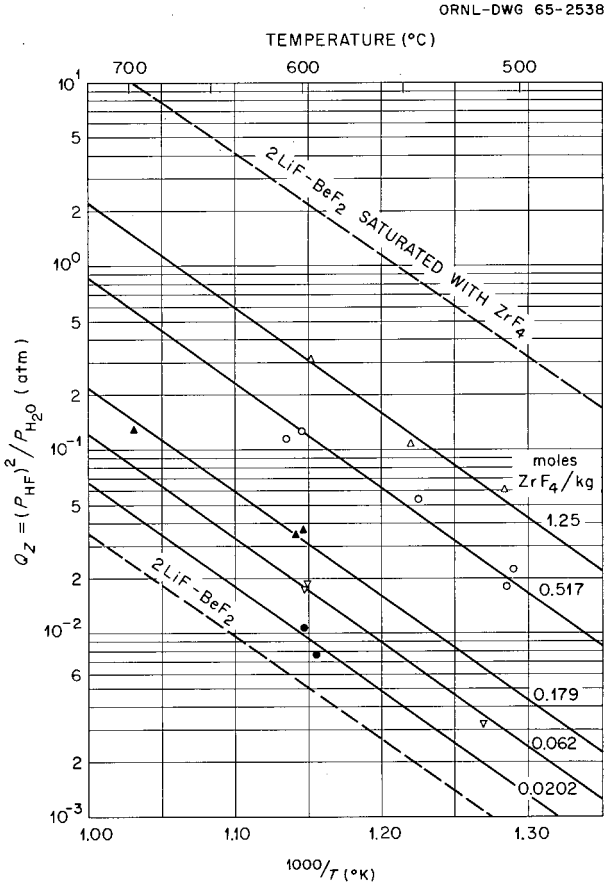

Fig. 3.8. Variation of Q_Z for ZrO_2-Saturated (2LiF-BeF_2) + ZrF_4 Melts with Temperature and ZrF_4 Concentration. The dashed curve, representing equilibrium P^2_{HF}/P_{H_2O} values for 2LiF-BeF_2 melts saturated with both ZrO_2 and ZrF_4, is based on free-energy data in the *JANAF* (Joint Army–Navy–Air Force) *Interim Thermochemical Tables*, Thermal Research Laboratory, Dow Chemical Company, Midland, Mich. (in loose-leaf binders; revised quarterly).

The value of K_Z ($\equiv Q_Z$ for melts saturated with both ZrO_2 and ZrF_4) has not been determined experimentally, but it may be estimated (Fig. 3.8) from data in the JANAF Tables.[7] In addition to the indicated uncertainties in γ_{ZrF_4}, which are based on estimated uncertainties in Q_Z (Fig. 3.9), all values are subject to a larger systematic uncertainty caused by any errors in the free energy values used. The approximate effect of a 1-kcal error in the standard free energy of the reaction in Eq. (2) is indicated in Fig. 3.9.

The quotients Q_O and Q_A (Eqs. 4 and 6) similarly are being determined in these ZrO_2-saturated melts. Both increase with addition of ZrF_4 (Figs. 3.10 and 3.11). The expression $Q_O^2[Zr^{4+}]/Q_Z^2$ is equal to the apparent solubility product of ZrO_2:

$$Q_{sp} = [Zr^{4+}][O^{2-}]^2 \ . \qquad (11)$$

This quantity has been estimated from the present, as yet incomplete, measurements. While quite approximate, these estimates indicate that the solubility product of ZrO_2 increases markedly with ZrF_4 concentration. This could be caused by the formation of ZrO^{2+} ion,

$$Zr^{4+} + O^{2-} \rightleftharpoons ZrO^{2+} \ , \qquad (12)$$

since in that case the concentration of oxide $[O^{2-}]$ determined in the present measurements would be the sum of the concentrations of O^{2-} and ZrO^{2+}; the apparent solubility product would be larger than that calculated from the uncomplexed oxide ion concentration and would increase with the zirconium concentration. The formation of ZrO^{2+} cannot be definitely established by these measurements alone, however, since γ_{ZrF_4} clearly changes – and other activity coefficients probably change as well – with melt compositions.

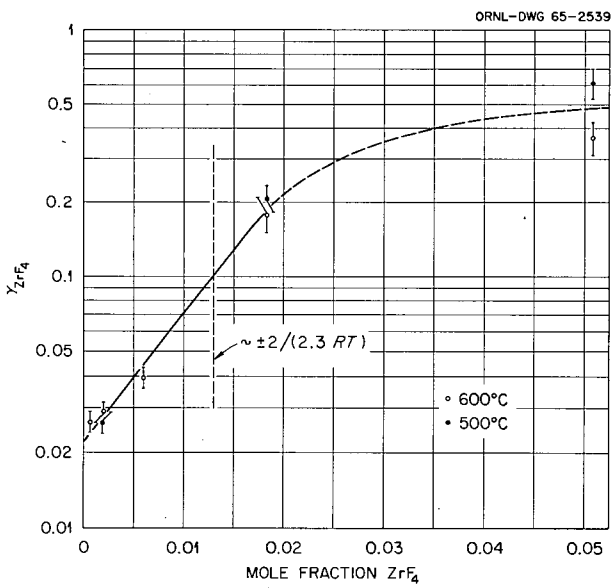

Fig. 3.9. Estimated Variation of γ_{ZrF_4} in $(2LiF\text{-}BeF_2) + ZrF_4$ Melts with ZrF_4 Concentration.

The resulting "oxide tolerance" of $(2LiF\text{-}BeF_2) + ZrF_4$ mixtures – corresponding approximately to MSRE flush salt and fuel salt mixtures – is indicated in Fig. 3.12. The amount of oxide

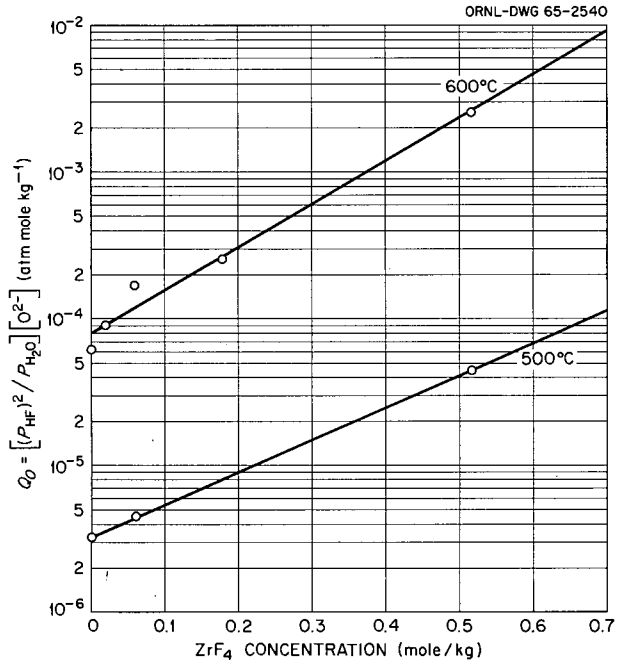

Fig. 3.10. Variation of the Oxide Ion Formation Quotient with ZrF_4 Concentration and Temperature in $(2LiF\text{-}BeF_2) + ZrF_4$ Melts.

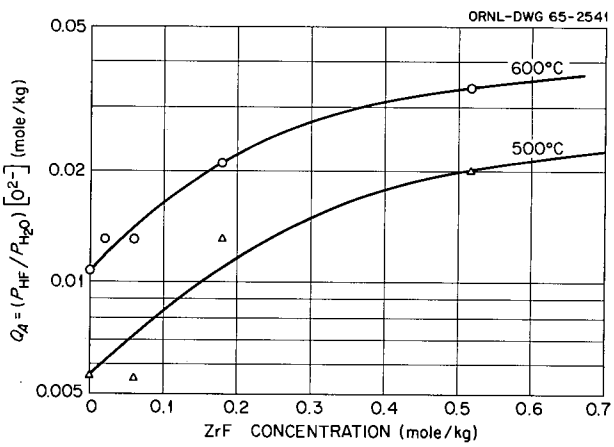

Fig. 3.11. Variation of the Hydroxide Ion Formation Quotient with ZrF_4 Concentration and Temperature in $(2LiF\text{-}BeF_2) + ZrF_4$ Melts.

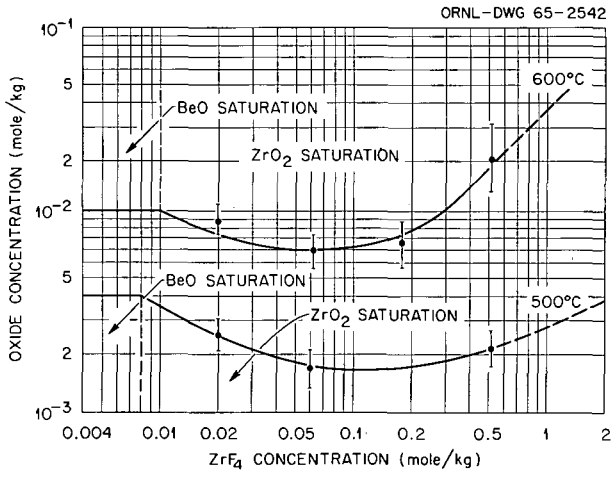

Fig. 3.12. Estimated Variation of Oxide Concentration with ZrF_4 Concentration in $(2LiF\text{-}BeF_2) + ZrF_4$ Melts Saturated with ZrO_2.

which these melts can contain without precipitation is not only a function of composition but also strongly a function of temperature.

This temperature dependence is consistent with observations that ZrO_2 tended to precipitate from fuel salt onto cooler surfaces of the engineering test loop.[11] This could provide a means for the collection of any excess oxide which might be present in the MSRE fuel as ZrO_2 in a cold trap in the MSRE system. The cold trapping of sparingly soluble solids in an MSR system has been discussed previously.[12]

Removal of Oxide by HF Sparging

From the present measurements of Q_B, Q_O, and Q_A in $LiF\text{-}BeF_2$ melts, it is possible to predict the course of removal of oxide from such mixtures by $HF\text{-}H_2$ sparging under equilibrium conditions. Calculations were made by means of the relationships previously cited for saturated melts[13] (Eq. 9) and for unsaturated melts.[14,15] The course of oxide removal, as water, by sparging of $2LiF\text{-}BeF_2$ at 500°C with 0.1 atm HF is shown in Fig. 3.13. Initially the effluent pressure of water should be low, but increasing, as the formation of OH^-

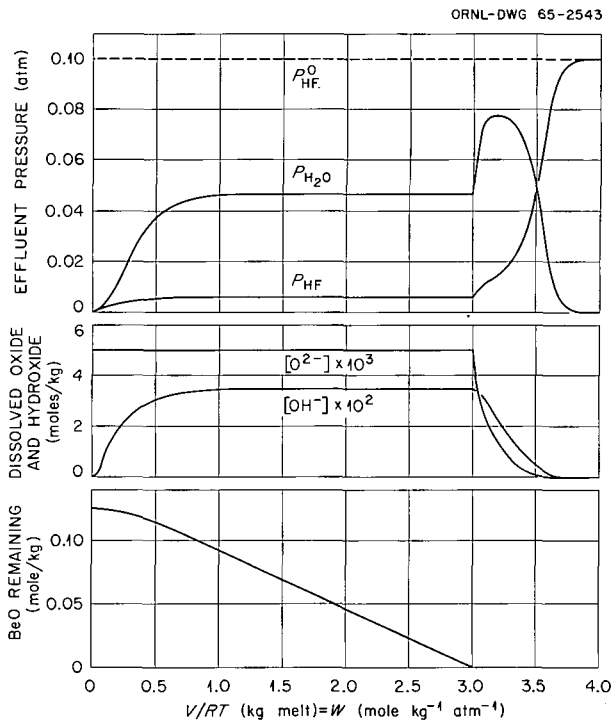

Fig. 3.13. Removal of Oxide from $2LiF\text{-}BeF_2$ by HF Sparging with 0.1 atm HF at 500°C, Assuming Equilibrium Between Melt and Gas Stream. Q_B, Q_O, and Q_A values are 7.91×10^{-4} atm; 3.9×10^{-6} atm mole kg^{-1}; and 4.5×10^{-3} mole/kg respectively.

[11] Dunlap Scott, Jr., and J. L. Crowley, Reactor Division, private communication; R. E. Thoma, *Identification of Crystalline Phases from Engineering Test Loop No. 3 Graphite Loading Port Annulus*, MSR-64-21 (May 11, 1964) (internal use only).

[12] R. B. Evans *et al.*, *Reactor Chem. Div. Ann. Progr. Rept. Jan. 31, 1960*, ORNL-2931, p. 90.

[13] In Eq. 9, $f(Q, P_{HF}) \equiv (1/D) \ln [(Y + D)/(Y - D)]$, where $D = 1 + 8(P^0_{HF} + 2P^0_{H_2O})/Q$, $Y = (4/Q)P_{HF} + 1$.

[14] These equations are:

$$d[OH^-]/dW = (P^0_{HF} + 2P^0_{H_2O}) - (Q_O[OH^-]/Q_A[O^{2-}])(1 + 2[OH^-]/Q_A),$$

$$d[O^{2-}]/dW = -(P^0_{HF} + P^0_{H_2O}) + (Q_O[OH^-]/Q_A[O^{2-}])(1 + [OH^-]/Q_A).$$

[15] These calculations were performed by the computer programs SATPLOT for oxide-saturated melts and RUNG for melts not saturated with oxide. Both yield plots of P_{HF} and P_{H_2O} as a function of W for specified equilibrium quotients. These programs were written by E. E. Branstetter and M. T. Harkrider of the ORNL Mathematics Division.

occurs (Eq. 3) in the presence of solid BeO. This should be followed by a steady-state period during which the effluent H_2O and HF partial pressures and the dissolved oxide and hydroxide concentrations all remain constant as long as BeO is present. Finally, after all the solid oxide has been consumed, a peak in the effluent P_{H_2O} is expected, followed by a sharp drop as the last of the dissolved oxide and hydroxide is removed.

The rapidity with which P_{H_2O} initially rises to a steady state is inversely related to Q_A. The efficiency of HF utilization thereafter is determined by, and varies inversely with, the value of Q_B. Finally, the rapidity of the removal of the dissolved oxide after the solid has been consumed is inversely related to both Q_O and Q_A.

Provided agitation is sufficient to maintain equilibrium between the sparging gas and the melt, the removal of oxide from $2LiF\text{-}BeF_2$ should be readily accomplished. This is indicated by plots (Fig. 3.14) of the initial amount of oxide present, dissolved and suspended as BeO, vs W, the number of standard volumes of sparging gas per kilogram of melt required to reduce the oxide level to 0.001 mole/kg (16 ppm). With an influent HF partial pressure of 0.1 atm and with more than 0.1 mole of oxide per kilogram initially present, 85% utilization of the gas is predicted at 500°C. With reduced inlet P_{HF}, with reduced initial oxide, or with increased temperature, the utilization of HF is decreased, but there is a wide range of conditions over which greater than 50% HF utilization is predicted.

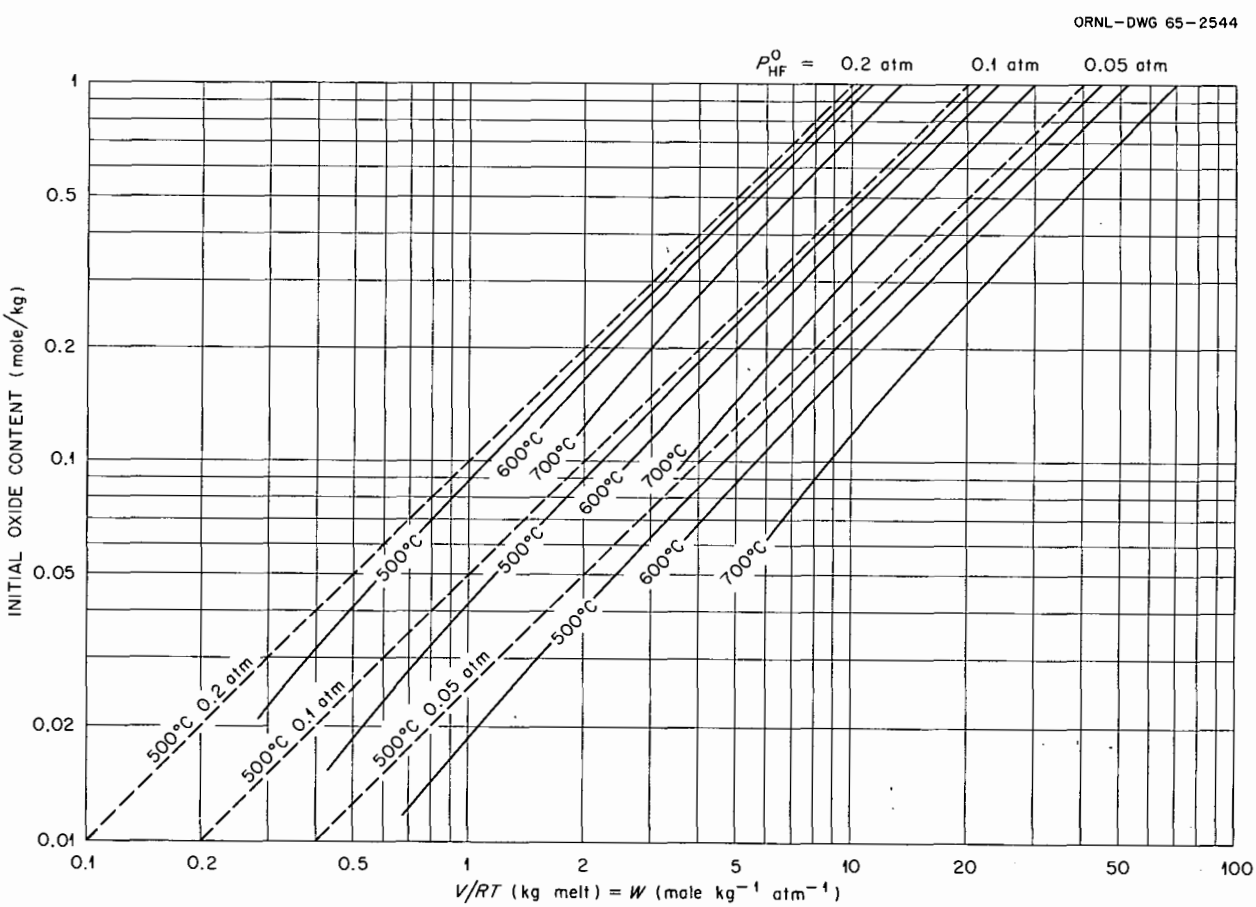

Fig. 3.14. Calculated Number of Standard Volumes of Sparging Gas per Kilogram of Melt Required to Reduce the Oxide Content of $2LiF\text{-}BeF_2$ to 0.001 mole/kg. The dashed lines represent 100% utilization of HF.

Table 3.2. Conversion of HF to H_2O at Steady State with ZrO_2 Present

T (°C)	Q_Z	HF Converted (%) at Specified P^0_{HF}		
		0.05 atm	0.1 atm	0.2 atm
500	~0.06	47	58	68
600	~0.3	20	30	42
700	~1.6	6	10	13

During the purification of numerous batches of $2LiF\text{-}BeF_2$ as flush salt for the MSRE, the experience with removal of oxide was reasonably consistent with these calculations. In the treatment of a typical 120-kg batch of salt at 600°C, ~8 moles of oxide (equivalent to 1000 ppm) was removed by sparging at 10 liters/min for 16 hr with an H_2–0.09 atm HF mixture. The estimated HF utilization was ~46%, which may be compared with a value of 70% expected for equilibrium sparging under these conditions. While the observed value is lower, its closeness to the calculated value indicates that equilibrium sparging was rather well approached in the simple equipment used and that great improvements in efficiency will not be realized by improvements in the equipment alone. Considerably shorter treatment times should result, however, if the sparging temperature is lowered and if provisions are made for higher sparging rates.

The removal of oxide from melts containing ZrF_4 may be expected to become more difficult with increasing ZrF_4 concentration, since Q_Z, Q_O, and Q_A all increase. The utilization of HF to be expected during the steady-state period when ZrO_2 is present may be calculated (Table 3.2) from present estimates of Q_Z. Limited experience at the molten-salt production facility is consistent with these estimates; for example, with $2LiF\text{-}BeF_2$–5 mole % ZrF_4 (~1.25 moles/kg) the HF utilization with $P^0_{HF} \approx 0.09$ atm at 600°C was 13–25%. This low oxide removal efficiency could be circumvented, however, by transfer of the melt away from the ZrO_2 in the meltdown vessel, followed by a short sparging treatment of the salt to remove the small amount of dissolved oxide.

At the MSRE, treatment of the fuel to remove oxide in the chemical reprocessing facility is not expected to be difficult, since the amount of oxide to be removed should be small.

THE STABILITY OF UF_3[16]

G. Long[17]

Equilibrium measurements on the reduction of UF_4 to UF_3 by hydrogen have been made with a view toward improving the thermochemical information on UF_3. The difference in the free energies of formation of UF_3 and UF_4 is involved in corrosion equilibria arising from the presence of UF_4 in molten fluoride reactor fuels and is also manifested in the stability of UF_3 toward disproportionation to give UF_4 and U^0. Both these behaviors are of prime interest in connection with the Molten-Salt Reactor Program.

A schematic diagram of the apparatus is shown in Fig. 3.15. Experimental details will appear elsewhere.[16]

When solid crystalline UF_4 was reduced by hydrogen, the products were HF and a saturated solid solution of UF_4 in UF_3. The concentrations of HF and H_2 at equilibrium with pure UF_4 and the solid solution were measured at 17 temperatures between 565 and 970°C; overall compositions in the binary condensed phases ranged from 1% to more than 50% UF_3 (mole basis). The results, in terms of the equilibrium pressures P_{HF} and P_{H_2} combined as the ratio $Q_R = P_{HF}/(P^{1/2}_{H_2})$

[16]G. Long, "Stability of UF_3," paper in preparation; this version prepared by F. F. Blankenship.

[17]Visiting Scientist from AERE, Harwell, Berks, U.K.

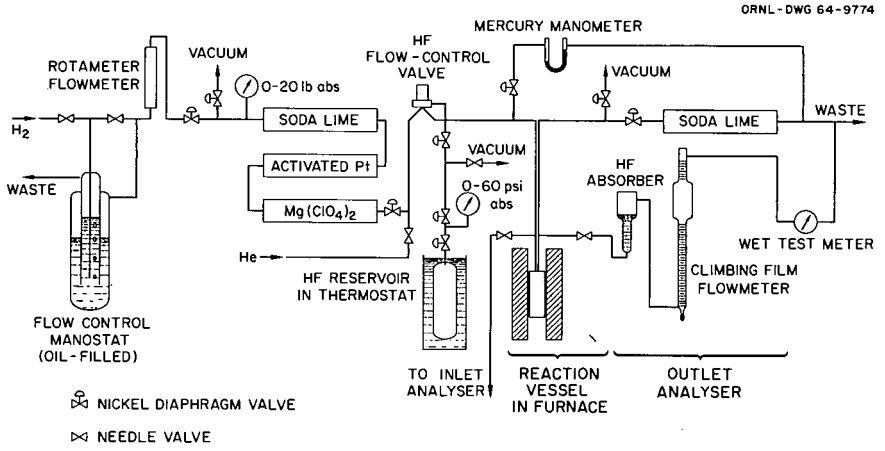

Fig. 3.15. Schematic Diagram of the Experimental Equipment.

pertaining to the reaction

$$\tfrac{1}{2}H_2 + UF_4(c) \rightleftharpoons UF_3(ss) + HF\ , \qquad (13)$$

could be correlated by means of the expression

$$\log_{10} Q_R = 3.95 \pm 0.057 - \frac{7000 \pm 58}{T°K}\ , \qquad (14)$$

as depicted graphically in Fig. 3.16. Hence, between 840 and 1160°K, the free energy change,

$$\Delta F^R_{T(ss)} = -RT \ln Q_R = (32.03 \pm 0.27) - (18.08 \pm 0.26)\frac{T}{1000}\ \text{kcal/mole}\ , \qquad (15)$$

where the subscript (*ss*) refers to the fact that the reference state for UF_3 is the saturated solid solution. (*R* denotes reduction as distinguished from *D* for disproportionation that is used later.)

In order to extrapolate beyond the experimental range, an estimated heat capacity difference, $\Delta C_{P(ss)} = -0.9 \pm 0.7$ cal deg^{-1} mole^{-1}, for the reaction was employed. Since the mean temperature of the experiments was 1000°K, this gave

$$\Delta H^R_{298(ss)} = 32.03 - (-0.9)(1000 - 298) = 32.67 \pm 0.58\ \text{kcal/mole}\ , \qquad (16)$$

$$\Delta S^R_{298(ss)} = 18.08 - (-0.9)(\ln 1000/298) = 19.17 \pm 0.89\ \text{cal deg}^{-1}\ \text{mole}^{-1}\ . \qquad (17)$$

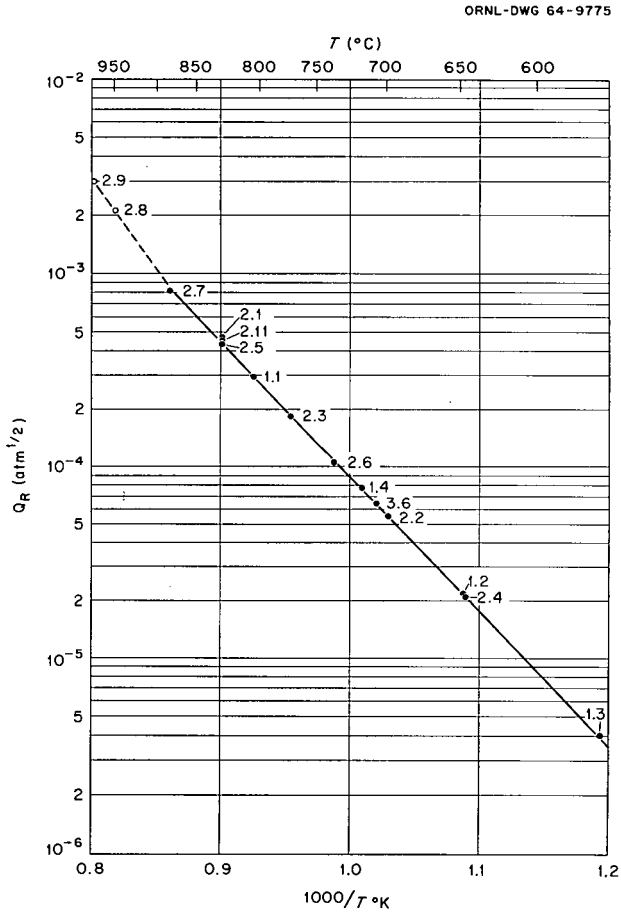

Fig. 3.16. Plot of $\log_{10} Q_R$ vs the Reciprocal of the Absolute Temperature for the Reaction $UF_{4(c)} + \tfrac{1}{2}H_{2(g)} \rightleftharpoons UF_{3(ss)} + HF_{(g)}$.

For a single temperature, 980°K, additional experimental measurements, involving an extrapolation to zero time, gave the pressures of HF and H_2 at equilibrium with UF_4 and UF_3, both as pure solid crystals. This provided a value for $\Delta F^R_{980(c)}$ of 15.43 ± 0.3 kcal/mole and afforded a basis for estimating ΔF^R_T for the reaction producing UF_3 in its customary standard state.

By assuming that at 298°K the solid solution is ideal and contains 80 ± 10 mole % UF_3 at saturation, the standard $\Delta S_{298(c)}$ could be estimated:

$$\Delta S^R_{298(c)} = \Delta S^R_{298(ss)} - R \ln (0.8 \pm 0.1)$$
$$= 18.73 \pm 0.95 \text{ cal deg}^{-1} \text{ mole}^{-1} . \quad (18)$$

If, in addition, ΔC_p was estimated as −2.0 ± 0.3 cal deg^{-1} mole^{-1}, the resulting change in heat content at 298°K, $\Delta H^R_{298(c)}$ was 32.8 ± 1.0 kcal/mole. This value is nearly the same as for the reaction to yield solid solution, indicating a heat of solution at 298°K of only 0.13 ± 0.4 kcal/mole. The effect of temperature on the reaction involving pure solids was given by

$$\log K_R = 3.57 - 6.87(1000/T) . \quad (19)$$

With standard entropies (S^0_{298}) for HF,[18] H_2,[19] and UF_4[20] of 41.51, 31.21, and 36.3 ± 0.1 cal deg^{-1} mole^{-1} and standard heats of formation (ΔH^f_{298}) for HF[7] and UF_4[21] of −64.8 ± 0.3 and −450 ± 5 kcal/mole, we find

$$\Delta H^f_{298}(UF_3) - \Delta H^f_{298}(UF_4)$$
$$= 97.6 \pm 3.3 \text{ kcal/mole} ,$$
$$\Delta H^f_{298}(UF_3) = -352 \pm 6 \text{ kcal/mole} , \quad (20)$$

$$S^0_{298}(UF_3) - S^0_{298}(UF_4)$$
$$= -7.2 \pm 0.9 \text{ cal deg}^{-1} \text{ mole}^{-1} ,$$
$$S^0_{298}(UF_3) = 29.1 \pm 1.0 \text{ cal deg}^{-1} \text{ mole}^{-1} . \quad (21)$$

The difference in the free energies of formation of UF_3 and UF_4 [$\Delta F^f_T(UF_3) - \Delta F^f_T(UF_4)$] and the free energy of formation of UF_3 [$\Delta F^f_T(UF_3)$] have been calculated from the free energy change for the reduction reaction,

$$\Delta F^R_T = \Delta F^f_T(UF_3) - \Delta F^f_T(UF_4) + \Delta F^f_T(HF) , \quad (22)$$

over the temperature range 298 to 1400°K. The values of ΔF^R_T were calculated from the heat and entropy changes for the reduction reaction at 298°K with a ΔC^R_p of −2.0 ± 0.3 cal deg^{-1} mole^{-1}, while the values of $\Delta F^f_T(HF)$ and $\Delta F^f_T(UF_4)$ were taken from the recent compilations of Cantor.[22] The results of the calculations are presented in Table 3.3.

Over this temperature range the calculated free energies can be represented to within 0.1 kcal/mole by the empirical expressions

$$\Delta F^f_T(UF_3) - \Delta F^f_T(UF_4) = 97.0 - 15.6(T/1000) ,$$
$$\Delta F^f_T(UF_3) = -351.4 + 52.8(T/1000) . \quad (23)$$

The value for UF_3 agrees with that estimated by Brewer[23] rather than those by more recent authors.[24,25] The extent of disproportionation at 1000°K according to these figures is quite low. Comparisons are given in Table 3.4.

Series of measurements on five liquid compositions containing UF_4 dissolved in LiF-BeF_2 melts were made. These melts were chosen because of their relation to the MSRE fuel. In terms

[18] *JANAF* (Joint Army–Navy–Air Force) *Interim Thermochemical Tables*, Thermal Research Laboratory, Dow Chemical Company, Midland, Mich. (in loose-leaf binders; revised quarterly).

[19] O. Kubaschewski and E. L. Evans, *Metallurgical Thermochemistry*, 3d ed., p. 248, Wiley, New York, 1956.

[20] J. H. Burns, D. W. Osborne, and E. F. Westram, Jr., *J. Chem. Phys.* 33, 387 (1960).

[21] M. H. Rand and O. Kubaschewski, *The Thermochemical Properties of Uranium Compounds*, p. 14, Interscience, New York, 1963.

[22] S. Cantor, personal communication.

[23] Leo Brewer *et al.*, *The Thermodynamic Properties and Equilibria at High Temperatures of Uranium Halides, Oxides, Nitrides, and Carbides*, MDDC-1543 (Sept. 20, 1945).

[24] A. Glassner, *The Thermodynamical Properties of the Oxides, Fluorides, and Chlorides to 2500°K*, ANL-5750 (1957).

[25] M. H. Rand and O. Kubaschewski, *The Thermochemical Properties of Uranium Compounds*, Interscience, New York, 1963.

of the quantities measured, the equilibrium quotient, $Q_{R(d)}$, for the reduction of dissolved UF_4, yielding dissolved UF_3, was

$$Q_{R(d)} = \frac{M_{UF_3}}{M^0_{UF_4} - M_{UF_3}} \left(\frac{P_{HF}}{P_{H_2}} \right) P^{1/2}_{H_2} , \qquad (24)$$

where

P_{H_2} = pressure of hydrogen, atm = 1.05,

$M^0_{UF_4}$ = total amount of UF_4 initially present, millimoles,

M_{UF_3} = total amount of UF_3 present, millimoles,

P_{HF}/P_{H_2} = ratio of partial pressures of HF and H_2 at equilibrium,

and the subscript (d) refers to the dissolved state.

In three of the compositions, the solvent was held constant at 66 mole % LiF, 34 mole % BeF_2,

Table 3.3. Calculated Values of $\Delta F^f_T(UF_3) - \Delta F^f_T(UF_4)$ and $\Delta F^f_T(UF_3)$ Over the Temperature Range 298 to 1400°K

Temperature (°K)	$\Delta F^f_T(UF_3) - \Delta F^f_T(UF_4)$ (kcal/mole)	$-\Delta F^f_T(UF_3)^a$ (kcal/mole)
298	92.5 ±0.8	335.8
400	90.8	320.2
500	89.2 ±0.6	324.8
600	87.6	319.5
700	86.0	314.3
800	84.4	309.1
900	32.9	303.8
1000	81.3 ±0.3	299.0
1100	79.8	293.4
1200	78.3	288.2
1300	76.8	282.9
1400	75.2 ±0.6	278.8

[a] ±~6 kcal/mole.

Table 3.4. Calculated Activity of Uranium in Equilibrium with Pure UF_4 and UF_3 at 1000°K

	This Work	Brewer[23]	Glassner[24]	Rand and Kubaschewski[25]
$-\Delta F^f_{1000}(UF_3)$, kcal/mole	299	299	281	290
$-\Delta F^f_{1000}(UF_4)$, kcal/mole	380.3	375	373	381
$\Delta F^f_{1000}(UF_3) - \Delta F^f_{1000}(UF_4)$, kcal/mole	81.3	76	92	91
Calculated uranium activity	5×10^{-11}	3×10^{-16}	8×10^{-2}	2×10^{-4}

Table 3.5. Values of the Equilibrium Quotient, $Q_{R(d)}$, the Parameters of the Expression $\log_{10} Q(\text{atm}^{1/2}) = A + B/T$, and the Derived Values of ΔH and ΔS for Each Solvent Studied (σ is Standard Deviation)

Experiment Number	Initial Composition of Solution (mole %)		Temperature (°C)	$10^5 Q_{R(d)}$ ($\text{atm}^{1/2}$)	$10^5\,\sigma$ ($\text{atm}^{1/2}$)	A (σ_A)	$-B$ (σ_B) (°K)	ΔS ($\sigma_{\Delta S}$) (cal deg^{-1} mole^{-1})	ΔH ($\sigma_{\Delta H}$) (kcal/mole)
1	LiF	62.7	724	0.78	0.08	4.255	9.357	19.5	42.9
	BeF_2	32.3	772	1.99	0.08	±0.090	±0.10	±0.4	±0.5
	UF_4	5.0	831	5.93	0.37				
			881	14.5	0.4				
			948.5	39.3	0.7				
2	LiF	65.0	774	1.61	0.07	4.350	9.581	19.9	43.4
	BeF_2	33.4	824	3.93	0.15	±0.12	±0.14	±0.6	±0.6
	UF_4	1.6	879	11.2	0.4				
			949.5	32.4	0.5				
3	LiF	63.8	824	4.89	0.10	3.895	9.000	17.8	41.2
	BeF_2	32.8	879	12.3	0.3	±0.081	±0.10	±0.4	±0.5
	UF_4	3.4	949.5	34.1	0.7				
4	LiF	69.0	774	1.54	0.03	4.244	9.490	19.4	43.4
	BeF_2	26.0	824	3.77	0.22	±0.118	±0.13	±0.5	±0.6
	UF_4	5.0	879	10.6	0.2				
			949.5	29.9	0.6				
5	LiF	52.6	724	3.85	0.20	3.998	8.403	18.29	38.5
	BeF_2	42.4	774	9.25	0.60	±0.207	±0.24	±1.0	±1.1
	UF_4	5.0	824	21.8	1.5				
			879	52.2	1.2				
			949.5	133	4.0				
Hypothetical standard solution (see text)	LiF	70.0				4.233	9.329	19.4	42.7
	BeF_2	30.0				±0.063	±0.081	±0.3	±0.4
	UF_4	0.0							

and the initial concentration of UF_4 was 1.60, 3.34, and 5.06 mole %. For the other two compositions, the UF_4 content was held constant at 5.0 mole %, while the LiF content of the solvent was 72.6 and 55.3 mole %.

In general, the values of $Q_{R(d)}$ were independent of the extent of conversion to UF_3 over the range studied. The mean values of $Q_{R(d)}$ at each temperature, with standard deviations, are presented in Table 3.5. For each solution composition the individual values for $Q_{R(d)}$ were fitted by the method of least squares to an expression of the form

$$\log_{10} Q_{R(d)} = A + B/T \,. \tag{25}$$

Values of A and B with the derived enthalpy and entropy changes for the reaction are also summarized in Table 3.5. The values of $Q_{R(d)}$ on a logarithmic scale are plotted against the reciprocal of the absolute temperature in Fig. 3.17.

The effects of changing the UF_4 and BeF_2 concentrations are shown in Figs. 3.18 and 3.19. The

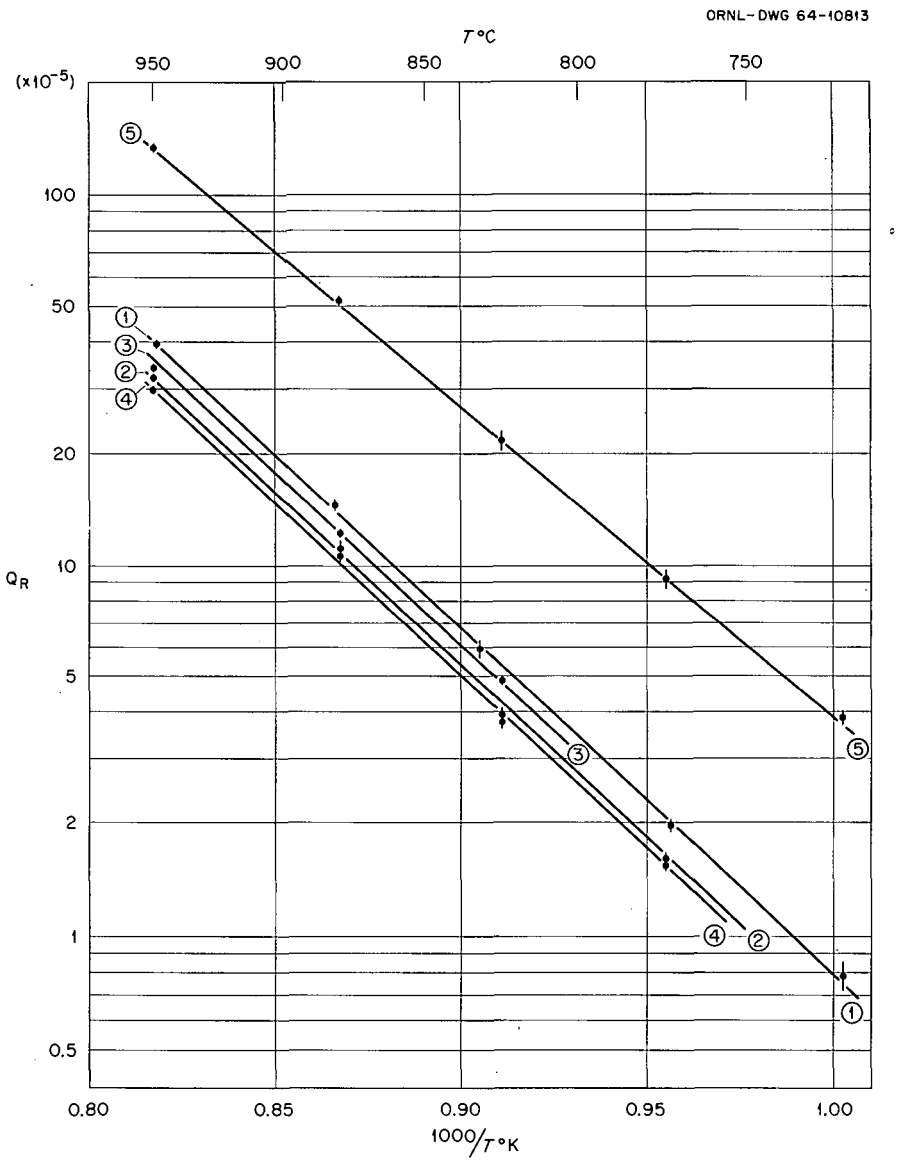

Fig. 3.17. Plot of $\log_{10} Q_{R(d)}$ vs $10^3/T°K$ for the Hydrogen Reduction of UF_4 in Various Solutions. (Plots numbered according to Table 3.5.)

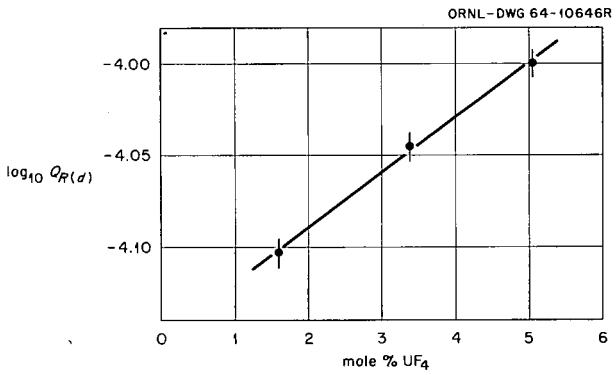

Fig. 3.18. Effect on $Q_{R(d)}$ at 860°C of Varying the Initial UF_4 Concentration with Constant Solvent Composition (66 mole % LiF, 34 mole % BeF_2).

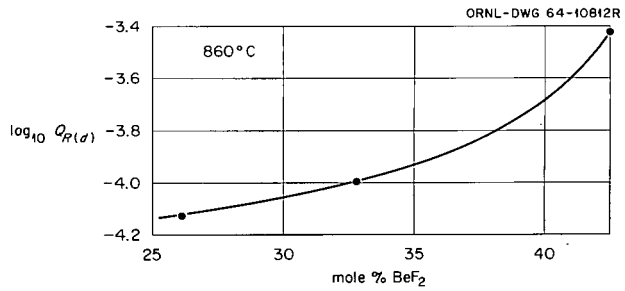

Fig. 3.19. Effect on $Q_{R(d)}$ at 860°C of Varying the BeF_2 Content of the Solution with Constant UF_4 Concentration (5.0 mole %).

Table 3.6. Estimated Activity Coefficients of UF_4 in LiF-BeF_2-ZrF_4-UF_4 (65.0-29.2-5.0-0.8 mole %)

Temperature (°C)	This Work (5% UF_4)	Phase Diagram (25% UF_4)	UF_4-UO_2 Equilibria[a] (<1% UF_4)
500	5	9	1.0
700	2	2.5	0.6

[a]C. F. Baes *et al.*, *Reactor Chem. Div. Ann. Progr. Rept. Jan. 31, 1964*, ORNL-3591, p. 46.

experimental data may be summarized by the expression

$$\log_{10} Q_{R(d)} = 3.995 - 9.329(10^3/T) + 3.77(10^{-2})x_{UF_4} + 2.09(10^{-2})(x_{BeF_2} - 30.0) \ . \quad (26)$$

The expression strictly applies only for UF_4 concentrations up to 5 mole % in a solvent containing 66 mole % LiF and for variations in solvent composition at a constant 5.0 mole % UF_4. Nevertheless the changes are so small that it can probably be applied to any solution containing up to 10 mole % UF_4 and between 25 and 35 mole % BeF_2 without introducing errors of greater than 10% in $Q_{R(d)}$. The relatively low value found for Q_R implies that a relatively low concentration of corrosion products corresponds to equilibrium in the MSRE, where alloyed chromium, rather than H_2, is the reducing agent.

Since $K_R = Q_{R(d)}\gamma_{UF_3}/\gamma_{UF_4}$, where γ is the activity coefficient with saturated solution as the reference state, the activity coefficient ratio, $\gamma_{UF_3}/\gamma_{UF_4}$, is readily obtainable. From the solubility of UF_3[26] in the MSRE fuel, LiF-BeF_2-ZrF_4-UF_4 (65.0-29.2-5-0.8 mole %), the activity coefficient of UF_3 is found to be

$$\log \gamma_{UF_3} = -1.62 + 3.77(1000/T) \ . \quad (27)$$

In the same solution, the interpolated value of $Q_{R(d)}$ is

$$\log Q_{R(d)} = 4.20 - 9.33(1000/T) \ . \quad (28)$$

In accord with the ΔF_R^T for pure solids from above,

$$\log K_R = 3.57 - 6.87(1000/T) \ . \quad (29)$$

Solving for γ_{UF_4}, the resulting expression is

$$\log \gamma_{UF_4} = -0.99 + 1.31(1000/T) \ . \quad (30)$$

Values of γ_{UF_4} as calculated from this relation are compared with other estimates in Table 3.6.

[26]J. H. Shaffer *et al.*, *Reactor Chem. Div. Ann. Progr. Rept. Jan. 31, 1964*, ORNL-3591, p. 50.

If, for the disproportion reaction in the same molten fluoride solution,

$$UF_3(d) \rightleftharpoons \tfrac{3}{4}UF_4(d) + \tfrac{1}{4}U^0 , \qquad (31)$$

the equilibrium quotient is written as

$$Q_D = \frac{x_{UF_4}}{x_{UF_3}} \left(\frac{a_{U^0}}{x_{UF_4}} \right)^{1/4} , \qquad (32)$$

where x is mole fraction, the relations for γ_{UF_4} and for $Q_{R(d)}$ can be combined with the free energies of formation $\Delta F^f(HF)$ and $\Delta F^f(UF_4)$ to give

$$\log Q_D = -0.57 - 0.56(1000/T) . \qquad (33)$$

For comparison,

$$\log K_D = -0.328 - 3.30(1000/T) . \qquad (34)$$

For example, a melt containing 0.5 mole % each of UF_3 and UF_4 at 1000°K is in equilibrium, according to Q_D, with uranium metal at an activity of 1.5×10^{-7}. The expression for the dissolved state, Q_D, also has a smaller temperature coefficient than could have readily been anticipated.

REMOVAL OF SULFUR FROM MOLTEN FLUORIDES

H. H. Stone C. F. Baes, Jr.

Sulfate impurities in MSRE raw materials have, in the past, resulted in instances of severe sulfide corrosion of nickel containers and piping during salt purification by the H_2-HF treatment. Accordingly laboratory studies were undertaken[27,28] to learn more of the behavior of sulfur in molten fluorides and to search for an improved method of its removal.

In these experiments, 1½-in. or 2-in. × 15-in. cylindrical nickel vessels were used. They were fitted with a dip leg extending to within ⅛ in. of the bottom of the vessel, a thermocouple well, an off-gas line, and a sampling port through which filtered samples of the melt could be removed by means of a copper filter stick. The H_2S evolved in H_2-HF sparging runs was trapped in ammoniacal $CdCl_2$ solution, which in turn was acidified and titrated against standard iodine solution. The amount of H_2S released was determined as a function of the measured flow rates of H_2, HF, and He.

Reduction of Sulfur

While thermodynamically favored, the reduction of sulfate by massive nickel was found to be inappreciable at 600°C (Table 3.7, subheading A). However, an excess of finely divided nickel powder reduced sulfate in 2LiF-BeF_2, presumably to sulfide, in a few hours at this temperature (Table 3.7, subheading B). An excess of iron filings and only a slight excess of beryllium metal behaved similarly (Table 3.7, subheadings C and D). The reactions occurring were probably of the type

$$4M^0 + SO_4^{2-} \rightleftharpoons 4M^{2+} + 4O^{2-} + S^{2-} . \qquad (35)$$

The Ni^{2+} and Be^{2+} evidently were precipitated mainly as NiO and BeO; Fe^{2+} remained in solution as FeF_2. The sulfide produced was also precipitated, though the composition of this precipitate was not determined.

Reduction of sulfate by beryllium metal alone would be an attractive means of sulfur removal, provided the resulting precipitate could be removed by filtration.

H_2-HF Sparging. – The removal of sulfur, by H_2-HF sparging after its reduction to sulfide with beryllium metal, was expected to occur by the reaction

$$MS(s) + 2HF(g) \rightleftharpoons H_2S(g) + M^{2+} + 2F^- . \qquad (36)$$

However, the removal rate was found to be controlled primarily by the hydrogen flow rate. This is illustrated in Fig. 3.20. The accumulated amount of H_2S released in one run is plotted in the upper half of the figure as a function of time. There are breaks in the curve at points where the H_2 flow rate was changed. When these same data are plotted vs the moles of H_2 passed (lower part of Fig. 3.20) a smooth curve is obtained. Moreover, when the results of other runs at the same

[27] *MSRP Semiann. Progr. Rept. July 31, 1963*, ORNL-3529, p. 117.

[28] *MSRP Semiann. Progr. Rept. Jan. 31, 1964*, ORNL-3626, p. 141.

Table 3.7. Reduction of Sulfate in $2LiF\text{-}BeF_2$ by Various Metals
(600°C with Helium Sparging)

Time (hr)	Analyses of Filtered Samples[a]		
	Sulfate (ppm)	Total Sulfur (ppm)	M(II)[b] (ppm)
	A. New Ni Vessel		
0	2000 (added)	2000 (added)	
$1\frac{3}{4}$	508	2225	53
3	2358	2310	38
4	1241	2195	43
6	1588	2155	51
7	2501	2330	69
31	1826	2240	102
	B. Ni Powder (3–100 μ), 25 g in 296 g of Melt		
0		1970 (added)	
2		350	243
3		175	292
$3\frac{3}{4}$		<5	241
	C. Fe Filings (30–50 Mesh), 25 g in 320 g of Melt		
0	800 (added)	800 (added)	
$\frac{1}{2}$	567	682	926
$2\frac{1}{4}$	464	486	1298
$3\frac{1}{4}$	445	497	1479
$4\frac{1}{4}$	435	495	1716
$5\frac{1}{4}$	229	266	2144
$6\frac{1}{4}$	212	245	2551
24		<5	3441
	D. Be Turnings, 0.86 g in 354 g of Melt		
0	2000 (added)	2000 (added)	
$\frac{1}{6}$	348	1034	
$\frac{1}{2}$	262	796	
1	301	419	
$1\frac{1}{2}$	176	388	
$3\frac{1}{4}$	121	240	
$4\frac{1}{4}$	108	135	
$5\frac{1}{4}$	61	171	

[a]Analyses performed by Analytical Chemistry Division.
[b]Concentration of oxidized metal (i.e., ppm Ni^{2+} in A and B; ppm Fe^{2+} in C).

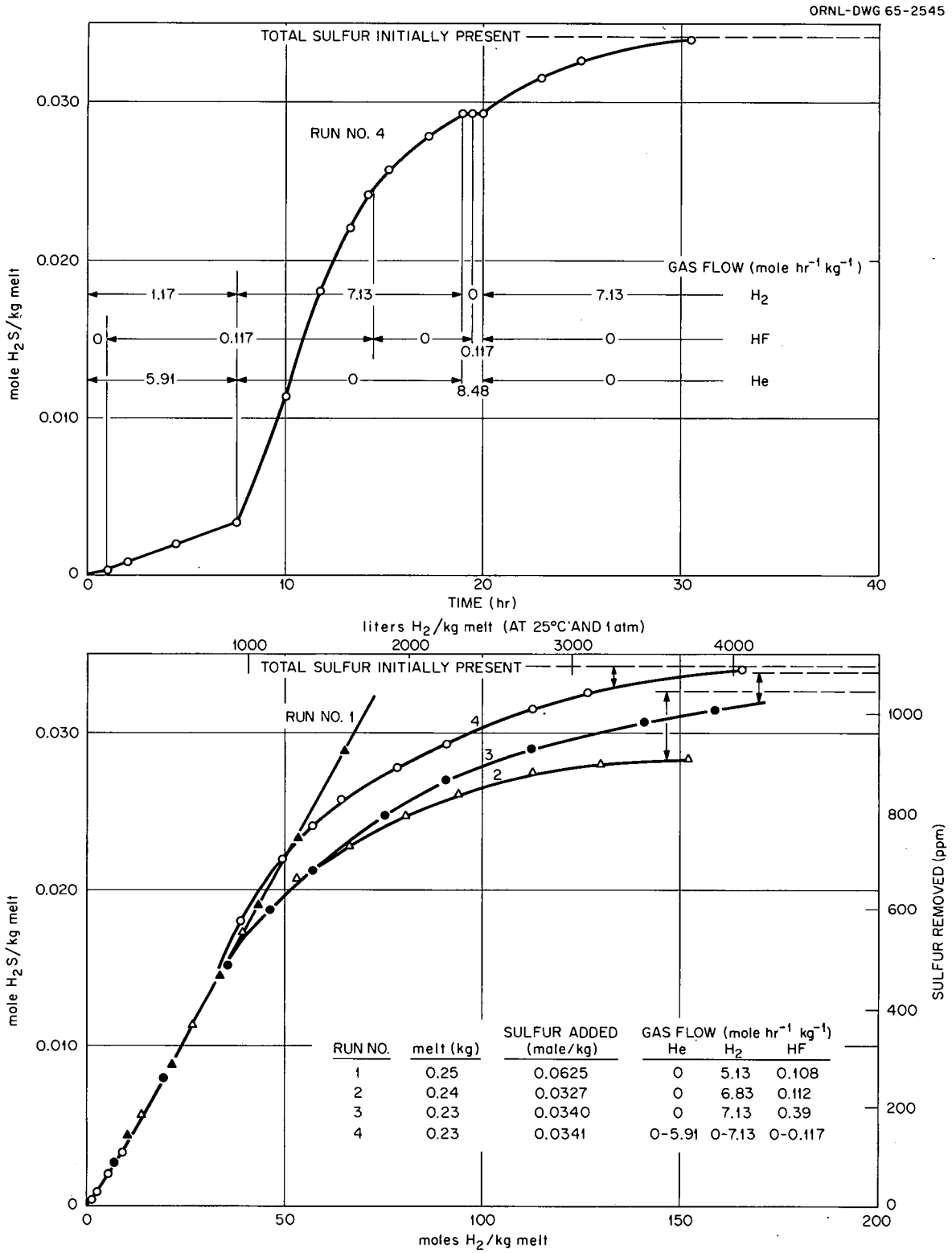

Fig. 3.20. Removal of Sulfur as H_2S by Sparging $2LiF\text{-}BeF_2$ Melts Containing Sulfur With $He\text{-}H_2\text{-}HF$ Mixtures at 600°C After Reduction with Beryllium Metal.

temperature – but otherwise differing in conditions – are plotted in the same way, the data are seen to coincide in the initial period of relatively rapid H_2S evolution. The H_2S/H_2 mole ratio of the effluent gas here was roughly constant at ~0.00044 for the various runs. When the amount of sulfur remaining to be removed had fallen to ~0.02 mole/kg (~600 ppm), the H_2S evolution rates began to decrease at a rate roughly proportional to the amount of sulfur remaining and the corresponding half times for the decay in the rate appeared to be proportional to the hydrogen flow rate.

In the experiments at 600°C, it was possible to remove >95% of the sulfur in 20–40 hr of sparging. This was with 1000–2000 ppm sulfur initially present in 0.25 kg of melt and with H_2 gas flow rates of ~40 liters/hr. To remove similar amounts of sulfur in similar time periods from 100-kg batches, such as those treated in the production facility at Y-12, evidently ~400 times this flow rate (16,000 liters of H_2 per hour) would be required. Because of the expected decrease in the H_2S/H_2 ratio below ~900 ppm sulfur, the gas flow rates required for melts containing <600 ppm sulfur, while they should be less, unfortunately would not decrease proportionately.

In the tests at 800°C, although initially the effluent H_2S/H_2 ratios were higher (~0.001 vs ~0.0004), it was possible to remove only about 70% of the sulfur as H_2S. It is thought that the remainder was lost by irreversible reaction with the nickel vessel.

H_2S Reaction with Nickel

The constancy of the effluent H_2S/H_2 mole ratio during the initial sparging of sulfide-containing melts with HF-H_2 mixtures suggests that an equilibrium of the type

$$MS + H_2 \rightleftharpoons H_2S + M^0$$

is involved. Of the three metallic elements which were present in major amounts, lithium, beryllium, and nickel, the first two may reasonably be ruled out since reduction of Li(I) or Be(II) to the metals could not occur in the presence of HF. In the case of nickel, however, already present as the metal in the container walls, reaction with H_2S to form a nickel sulfide is quite possibly the equilibrium which controls the effluent H_2S/H_2 mole ratio. The observed initial values of this ratio at 600 and 800°C, when compared with the results of Rosenquist[29] for the reaction of Ni with H_2S, are seen to be comparable but lower:

	Observed	Rosenquist
600°C	0.00044	0.0011
800°C	0.0010	0.0023

This could be because the nickel sulfide was formed in the cooler region of the system (e.g., in the upper part of the reaction vessel or in the off-gas line). This was supported by results of an experiment in which the off-gas line was packed with fine nickel wire. At the end of an H_2-HF sparging run, nickel sulfide was observed to be present only at the upper, cooler extremity of the wire packing. The decrease in the effluent H_2S/H_2 ratio with continued sparging can be explained in terms of a decreasing reactivity of nickel sulfide as the amount decreases or as it formed on cooler surfaces.

The evident formation of nickel sulfides (probably Ni_2S_3) nonetheless appeared largely reversible, since nearly all of the sulfur initially added could be removed in runs at 600°C and the nickel vessels when examined after use were found to be free of severe corrosive attack. The failure to remove all the sulfur at 800°C was to be expected, since this is above the temperature (645°C) at which an Ni–33 at. % S eutectic is formed. It is this eutectic which is thought to be responsible for the penetrating, and probably irreversible, attack of nickel by sulfur which can occur.

Sulfur Removal Methods. – On the basis of these tests, the treatment of sulfate-containing batches of flush salt (2LiF-BeF_2) at the Molten-Salt Production Facility involved addition of a small excess of beryllium metal to reduce the sulfate to sulfide, followed by H_2-HF sparging which was continued until the H_2S evolution rate decreased to a low value. The temperature was usually 600°C, below the eutectic temperature at 645°C. This treatment, while effective, was prolonged as expected at the gas flow rates used

[29] Terkel Rosenqvist, *J. Iron Steel Inst. (London)* **176**, 37 (1954).

(~10 liters/min); H_2-HF sparging was often continued for more than 100 hr per 100-kg batch. A much improved treatment would be to filter the salt after the beryllium reduction, thus removing most of the sulfur, the oxide, and the reducible metallic impurities in one step. However, such filtrations have proven to be difficult with existing techniques, the nickel filters being easily clogged by finely divided solids.

Alternatively, since the present results indicate that the sulfur is removed relatively rapidly from the melt during H_2-HF sparging, and then reacts with the container walls and piping, a cooled reactive bed of nickel metal or other getter could be located in the gas phase of the treatment vessel to quickly and safely remove the H_2S evolved from the melt. If it should become necessary in the future to again treat molten fluoride salts containing sulfur impurities, laboratory studies of such a method would be desirable.

ELECTROCHEMISTRY OF MOLTEN FLUORIDE MIXTURES

Reference Half-Cells for Molten LiF-BeF_2 Mixtures

G. Dirian[30] K. A. Romberger
C. F. Baes, Jr.

The development of reference electrode half-cells that are compatible with molten fluorides in general and with the MSRE fuel salt in particular has been in progress during the past year. Such half-cells would permit the determination of the redox potentials of some of the major fuel constituents, fission products, and possible impurities such as corrosion products. This information could form a basis for the development of remote-controlled, on-stream analytical methods that would be extremely valuable indicators of the chemical condition of the reactor fuel system. In addition, the reversible potentials obtained could be used to derive important thermodynamic quantities which either are not otherwise available or can be compared with values from other experimental sources.

A reference electrode half-cell must have a potential that is stable, reproducible, and reversible. Also, it should be nonpolarizable, rugged, simple to use, and inert to the system under investigation. Two electrodes which have been found to meet most of these requirements are those based on the beryllium metal–beryllium ion and the hydrogen–hydrogen fluoride couples, i.e.,

$$Be = Be^{2+} + 2e \,, \tag{37}$$

$$2F^- + H_2 = 2HF + 2e \,. \tag{38}$$

The construction of the beryllium electrode that was used is shown in Fig. 3.21. It consisted of

ORNL-DWG 65-2546

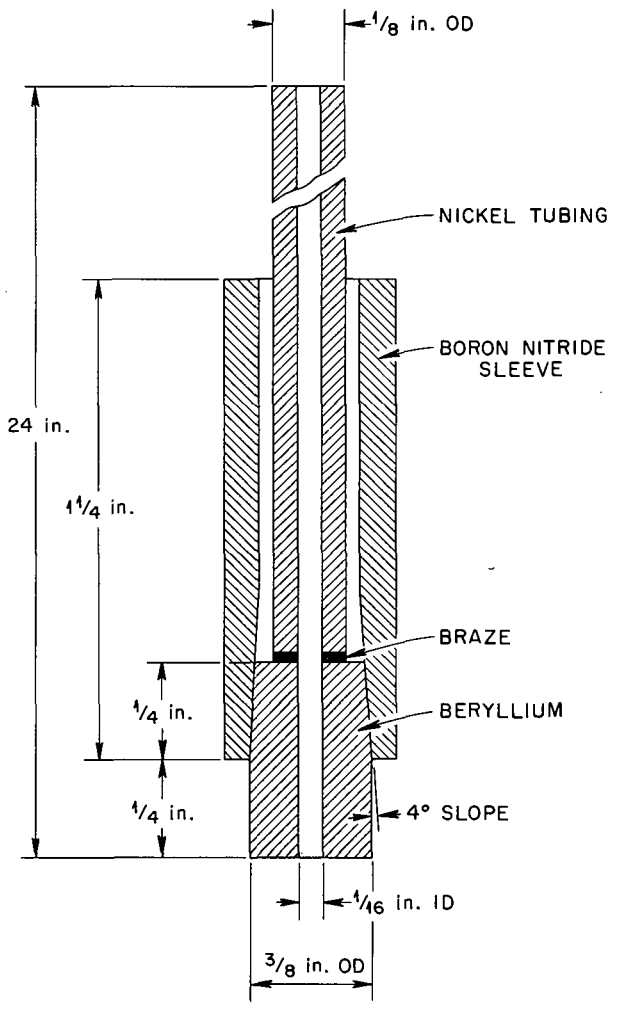

Fig. 3.21. Beryllium Electrode.

[30]Euratom Exchange Scientist, C.E.N., Saclay, France.

a tubular piece of beryllium metal brazed onto a nickel support tube. A boron nitride sleeve prevented contact between the nickel and the melt, while helium gas bubbling through the centered hole protected the beryllium from attack by any residual HF.

The H_2, HF/Pd electrode is illustrated in Fig. 3.22. Thin-walled palladium tubing dipped into the melt to act as an inert substrate for the H_2-HF reaction. The nickel tube transmitted the premixed H_2-HF gas mixture and provided electrical contact to the outside.

Both electrodes were isolated from the bulk of the melt (and thus from each other) by compartments of the type shown in Fig. 3.23. The small $^3/_{32}$-in. hole provided a passage for melt flow into and out of the compartments during insertion or removal of the electrode assemblies.

Tests involving two beryllium electrodes vs each other in molten Li_2BeF_4 showed them to be perfectly stable and reversible for current densities up to 2 ma/cm^2. Reversibility was obtained initially even at current densities of 100 ma/cm^2, but rapid potential decay occurred, apparently because of beryllium ion depletion from the melt near the electrode surface. Reproducibility was ±0.1 mv. Other beryllium electrodes, formed by electroplating the metal onto a nickel rod, were also found to be reproducible and reversible, but the metal deposit was spongy and porous, and beryllium ion depletion was more quickly observed.

When two H_2, HF/Pd electrodes, supplied with the same H_2-HF mixture, were used together, the potential was also found to be reversible up to 2 ma/cm^2. These electrodes were stable to ±1 mv. These small potential fluctuations were caused by slight pressure changes as bubbling occurred, but no bias was observed.

ORNL-DWG 65-2547

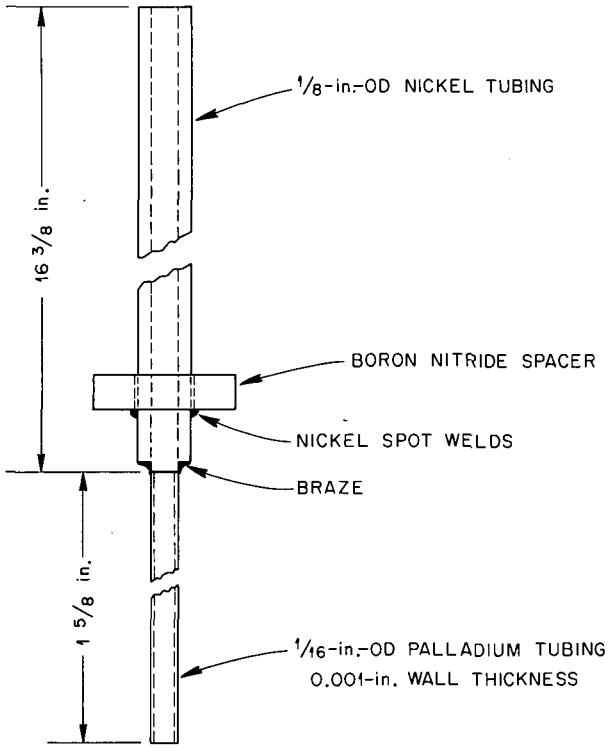

Fig. 3.22. H_2, HF/Pd Electrode.

ORNL-DWG 65-2548

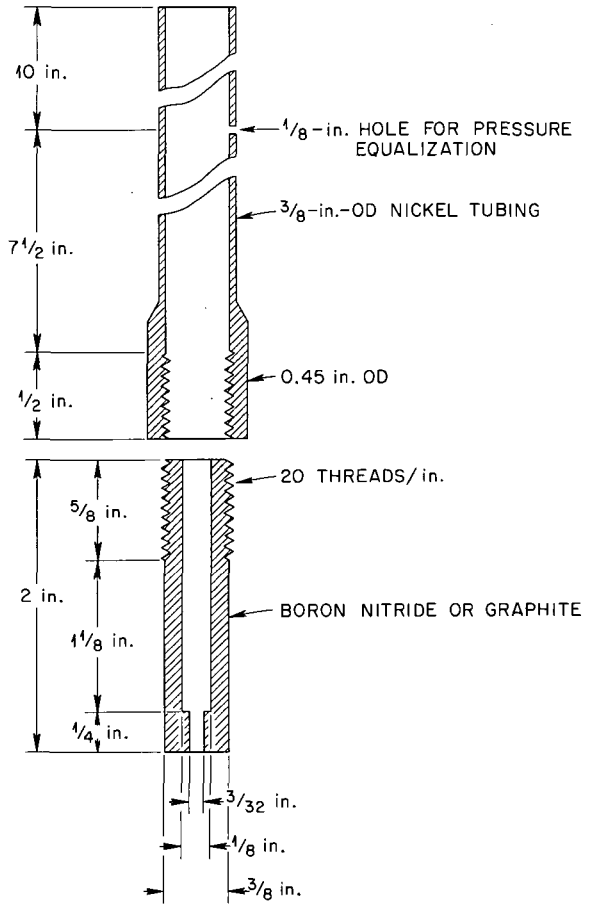

Fig. 3.23. Separation Compartments for Electrodes.

Since both the Be/Be^{2+} and the H_2, HF/Pd electrodes responded reversibly, the cell reaction

$$Be(s) + 2HF(g) = H_2(g) + BeF_2(d) \quad (39)$$

could be studied. At any one beryllium ion composition, the potential should depend only on the partial pressures of H_2 and HF. Figure 3.24 shows a plot of the potential values observed for HF partial pressures from 0.04 to 0.78 atm. The reversible slope of 0.0775 v at 508°C was closely approximated.

The potential value when $\log (P_{HF})^2/P_{H_2}$ equals zero is a measure of the free energy, $\Delta F_{(40)}$, of the cell reaction

$$Be(s) + 2HF(g, 1\ atm) = H_2(g, 1\ atm) + BeF_2(d)\ ; \quad (40)$$

$\Delta F_{(40)}$ can be compared with the free energy, $\Delta F_{(41)}$, associated with the reaction

$$BeO(s) + 2HF(g, 1\ atm) = H_2O(g, 1\ atm) + BeF_2(d)\ , \quad (41)$$

which has been determined independently in an Li_2BeF_4 solvent (see the subsection "LiF-BeF_2 Melts," this chapter). These free energies should differ by an amount equal to the difference in the standard free energies of formation of BeO and H_2O; that is, $\Delta F_{(40)}$ should equal $\Delta F_{(41)} + \Delta F^0_{BeO} - \Delta F^0_{H_2O}$. The latter sum of terms, labeled $\Delta F_{(S)}$, is calculated in Table 3.8 and compared with $\Delta F_{(40)}$. This comparison shows that the free energies obtained by the present emf measurements, $\Delta F_{(40)}$, are more negative than the corresponding calculated quantities, $\Delta F_{(S)}$, by 1.5 to 1.1 kcal for the temperature range 504 to 703°C. This difference may be due in part to an

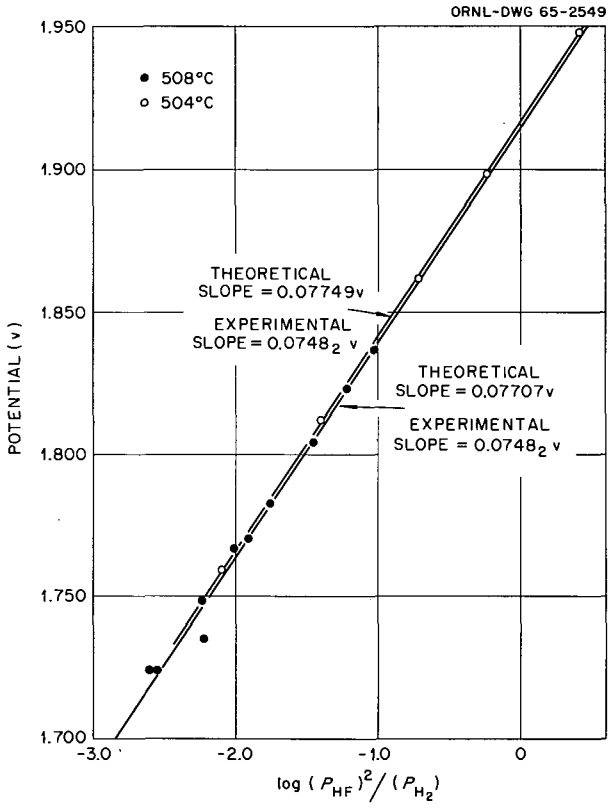

Fig. 3.24. Plot of Potential vs $\log (P_{HF})^2/P_{H_2}$ for the Cell $Be(s) + 2HF(g) = H_2(g) + BeF_2(d)$ in Li_2BeF_4.

Table 3.8. Comparison Between Measured Free Energies, $\Delta F_{(40)}$, and Calculated Free Energies, $\Delta F_{(S)}$, for the Reaction $Be(s) + 2HF(g, 1\ atm) = H_2(g, 1\ atm) + BeF_2(d)$

Temperature (°C)	E_{cell} $[(P_{HF})^2/P_{HF} = 1]$ (v)	$\Delta F_{(40)}$ (cell) (kcal)	$\Delta F_{(41)}$ (reaction) (kcal)	ΔF^o_{BeO} (kcal)	$\Delta F^o_{H_2O}$ (kcal)	$\Delta F_{(S)}$ (kcal)	$\Delta F_{(40)} - \Delta F_{(S)}$ (kcal)
504	$+1.915_5$	−88.35	−10.90	−124.85	−48.94	−86.81	−1.54
508	$+1.913_0$	−88.23	−10.82	−124.76	−48.89	−86.69	−1.54
597	$+1.848_5$	−85.26	− 9.06	−122.69	−47.74	−84.01	−1.25
703	$+1.774_9$	−81.86	− 6.90	−120.24	−46.36	−80.78	−1.08

error in the value of ΔF^0_{BeO}. The values of ΔF^0_{BeO} and $\Delta F^0_{H_2O}$ were interpolated from those given in the JANAF Tables.[31]

Both electrodes performed acceptably for use as reference electrode half-cells. In the future, metal–metal ion couples other than Be/Be^{2+} will be investigated to determine their reversibility. In particular, if either of the couples

$$Ni^0 \longrightarrow Ni^{2+} + 2e$$
$$Fe^0 \longrightarrow Fe^{2+} + 2e$$

is reversible, then the concentration of the corresponding structural metal ion could, in principle, be monitored continuously in a molten fluoride reactor system such as the MSRE by use of a cell of the type

$$M \mid M^{2+}(\text{in MSRE fuel}) \mid\mid 2LiF\text{-}BeF_2 \mid R.E.$$

wherein either the Be/Be^{2+} or the H_2, HF/Pd electrode could be used as the reference electrode.

Reversible Deposition of Metals on Solid Electrodes by Voltammetry with Linearly Varying Potential

Gleb Mamantov[32] D. L. Manning[33]
J. M. Dale[33]

In the studies of the electrochemical reduction of metallic ions in molten salt solvents, it became necessary to extend the available theoretical treatment for the reversible deposition of metals on solid electrodes during voltammetry with linearly varying potential (stationary electrode polarography).

Equation (42), proposed by Kolthoff and Lingane,[34]

$$E = E^0_M - \frac{2.3RT}{nF}\log(k_s/f_s) + 2.3\frac{RT}{nF}\log(i_l - i)\ , \quad (42)$$

where

E^0_M = the standard potential for the couple $M^{n+} + ne \rightleftharpoons M$,

k_s = a constant,

f_s = the activity coefficient of the metal ion,

i_l = limiting current,

i = current at any potential E,

has been used for reversibility tests and for the determination of n values in the case of the deposition of metals at solid microelectrodes (applications to molten salt systems are discussed by Liu, Johnson, and Laitinen[35]). It is assumed for stationary electrodes that mass transfer is *convection* controlled, that the metal is deposited on the electrode surface at constant activity without alloy formation, and that the reaction proceeds reversibly. It is evident that the slope of E vs $\log(i_l - i)$ is given by $2.3(RT/nF)$.

If the mass transfer is *diffusion* controlled, usually encountered with rapid scan rates, no steady limiting currents are obtained; instead, the current-voltage curves are peak-shaped. Berzins and Delahay[36] have shown that for the reversible deposition of metals at solid microelectrodes, the current is given by

$$i = \frac{2}{\pi^{1/2}}\frac{n^{3/2}F^{3/2}}{R^{1/2}T^{1/2}} \times AC^0D^{1/2}v^{1/2}\,\Phi\left[\left(\frac{nF}{RT}vt\right)^{1/2}\right]\ , \quad (43)$$

where

v = rate of voltage scan,

A = electrode area,

C^0 = concentration,

D = diffusion coefficient,

t = scan time,

---

[31] *JANAF* (Joint Army–Navy–Air Force) *Interim Thermochemical Tables*, Thermal Research Laboratory, Dow Chemical Company, Midland, Mich. (in loose-leaf binders; revised quarterly).

[32] Consultant, University of Tennessee Chemistry Department.

[33] Analytical Chemistry Division.

[34] I. M. Kolthoff and J. J. Lingane, *Polarography*, vol. 1, 2d ed., pp. 203–205, Interscience, New York, 1952.

[35] C. H. Liu, K. E. Johnson, and H. A. Laintinen, "Electroanalytical Chemistry of Molten Salts," pp. 695–99 in *Molten Salt Chemistry*, ed. by M. Blander, Interscience, New York, 1964.

[36] T. Berzins and Paul Delahay, *J. Am. Chem. Soc.* **75**, 555 (1953).

and the term

$$\Phi\left[\left(\frac{nF}{RT}\,vt\right)^{1/2}\right],$$

denoted as $\Phi(\alpha)$, represents the function

$$\Phi(\alpha) = e^{-\alpha^2}\int_0^{\alpha} e^{z^2}\,dz\,.$$

The values of $\Phi(\alpha)$ for different values of α have been tabulated.[37]

It was of interest to obtain a relationship from Eq. (43) between the applied electrode potential E and log $(i_p - i)$, where i_p is the peak current, in similarity to the Kolthoff-Lingane equation.

The detailed analysis is given elsewhere.[38] It can be summarized by stating that the plot of log $(i_p - i)$ vs E approaches linearity over the approximate current range $0.5i_p$ to $0.9i_p$, the slope being $2.2(nF/RT)$. The experimental verification included the study of the current-voltage curves for the reductions of Fe(II) in molten $LiF\text{-}BeF_2$ (66-34 mole %) and LiF-NaF-KF (46.5-11.5-42 mole %) at 500° and Ni(II) in LiF-NaF-KF (46.5-11.5-42 mole %) at pyrolytic graphite electrodes.

Electrochemistry of UF_4 in Molten Fluorides

Gleb Mamantov[32]

Electrochemical studies in molten fluorides have been continued; the equipment has been described previously.[39] Electrochemical reduction of U(IV) by voltammetry with linearly varying potential in molten $LiF\text{-}BeF_2\text{-}ZrF_4$ (65-33-2 mole %) at 500°C has been observed at approximately −1.2 v vs the platinum quasi-reference electrode (Fig. 3.25*A*); the reduction of the solvent, presumably involving the Zr(IV) species, takes place at approximately −1.7 v. The limiting current increases with the concentration of U(IV) in the range 0.09–0.33 mole %), although it has not yet been possible to establish direct proportionality. This is likely to be caused by the poor definition of the area of the unsheathed platinum working electrode. The definition of the U(IV) voltammogram at a pyrolytic graphite electrode is poor after several runs.

Good reproducibility has been achieved, however, with derivative voltammetry (Fig. 3.25*B*); for example, the relative standard deviation for 10 consecutive runs made at 10-min intervals was 1.8%.

The mechanism of U(IV) reduction and other aspects of the electrochemistry of uranium in this solvent are presently being investigated.

This method appears to be potentially useful for the development of an in-line monitoring device for molten-salt reactor systems.

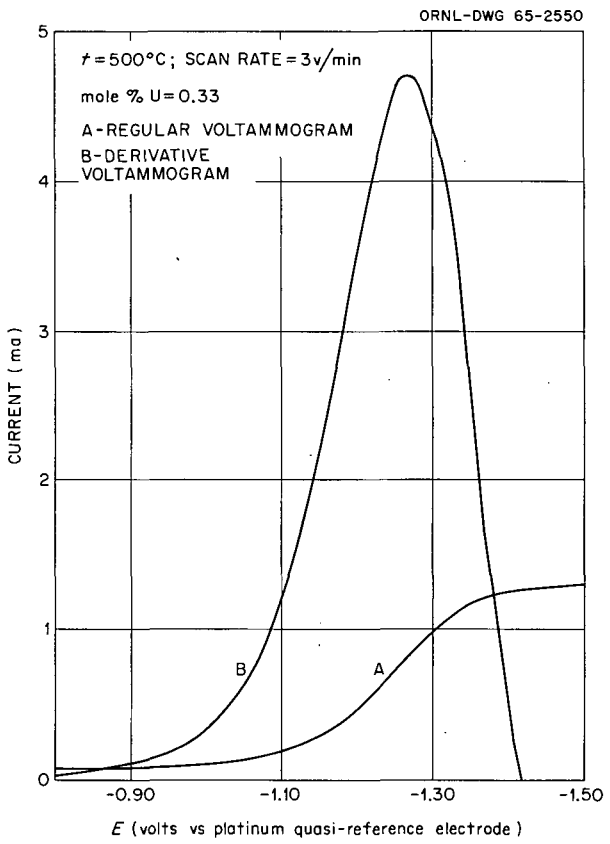

Fig. 3.25. Reduction of U(IV) at a Platinum Microelectrode (Area = 0.06 cm^2) in $LiF\text{-}BeF_2\text{-}ZrF_4$ (65-33-2 mole %).

[37] W. L. Miller and A. R. Gordon, *J. Phys. Chem.* **35**, 2875 (1931).

[38] Gleb Mamantov, D. L. Manning, and J. M. Dale, *J. Electroanal. Chem.* (in press).

[39] Gleb Mamantov, *Reactor Chem. Div. Ann. Progr. Rept. Jan. 31, 1964*, ORNL-3591, pp. 53–55.

VISCOSITY IN THE $LiF\text{-}BeF_2$ SYSTEM

S. Cantor W. T. Ward

Viscosities of the $LiF\text{-}BeF_2$ system are being measured to provide significant physical data in support of molten-salt reactor technology and to systematically explore a series of fluoride melts which vary from the very viscous (pure BeF_2) to the very fluid (pure LiF).

These viscosities have been measured by determining the torque required to maintain constant angular velocity of a cylindrical spindle immersed in the test liquid. The reliability of the instrument (Brookfield LVT), which both measures the torque and maintains constant rotation rates, has been thoroughly checked with oils of known viscosity purchased from the National Bureau of Standards.

Seventeen compositions, having BeF_2 concentrations ranging from 50 to 100 mole %, have been investigated, and the data for these are summarized in Table 3.9. All compositions, with the possible exception of pure BeF_2, appeared to fit the equation

$$\eta = K \exp (E_\eta / RT) , \tag{44}$$

where

η = the viscosity in centipoises,

K = a constant (also in centipoise units),

E_η = the energy of activation for viscous flow,

R = the gas constant,

T = the temperature in degrees Kelvin.

Table 3.9. Summary of Data and Constants for the Viscosity-Temperature Equation, $\log \eta = A/T - B$ (η in centipoises; T in °K), for the System $LiF\text{-}BeF_2$

Composition (mole % BeF_2)	Temperature Range Measured (°C)	A	B	Viscosity at 600°C (centipoises)
100	712–829	13,100	7.05	90,000,000[a]
99.01	692–967	11,390	5.955	12,300,000[a]
98.01	632–917	10,300	5.135	4,710,000[a]
97.00	601–897	9,540	4.595	2,160,000[a]
96.01	601–844	8,995	4.29	1,020,000[a]
94.91	557–837	8,620	4.13	550,000
93.01	572–842	8,185	3.96	258,000
91.02	545–832	7,690	3.77	110,000
90.02	594–882	7,405	3.65	68,000
85.00	539–747	6,580	3.37	14,500
79.99	558–745	5,950	3.185	4,250
75.00	490–705	5,405	3.085	1,275
70.00	480–704	4,695	2.695	480
65.00	451–724	4,150	2.45	200
60.00	437–584	3,775	2.35	92[a]
55.01	389–584	3,390	2.22	46[a]
50.00	376–577	3,065	2.08	27[a]

[a]Extrapolated.

For more convenience in calculations, Eq. (44) was recast in the form

$$\log \eta = A/T - B \ , \qquad (45)$$

where

$A \equiv E_\eta/2.303R,$

$B \equiv -\log K.$

Of the data listed in Table 3.9, that for pure BeF_2 is the least reliable, because of difficulties in measuring very high viscosities with the apparatus at hand. For the other compositions, the viscosities are probably accurate to within 10%. The temperature dependence of the viscosity (reflected in the constant, A), however, is accurate to within 3%.

As illustrated in the last column of Table 3.9, the viscosity decreases rapidly with increasing LiF concentration. Also declining rapidly with LiF concentration is the energy of activation for viscous flow (see Fig. 3.26). If we first assume that liquid BeF_2 is a disordered three-dimensional network of tetrahedra[40] held together by beryllium-fluorine bonds, the changes in η and E_η with the addition of LiF become explainable. When LiF is introduced, bond rupture occurs, causing the network to break down into clusters. The bond rupture may be pictured as

$$-\overset{|}{\underset{|}{Be}}-F-\overset{|}{\underset{|}{Be}}- + LiF \longrightarrow -\overset{|}{\underset{|}{Be}}-F \quad Li^+ \quad F^- - \overset{|}{\underset{|}{Be}} \ .$$

As more LiF is put into the system, still more bonds break, and the average cluster size decreases. If we assume (1) that the flow unit is proportional to cluster size and (2) that the number of flow units increases as the number of clusters increases, then it follows that viscosity decreases with increasing LiF concentration. Furthermore, as the size of the flow unit decreases, the energy required to surmount the potential energy barrier to flow also decreases; hence E_η (which is a measure of this required energy) decreases with increasing LiF concentration. If we imagine, alternatively, that the unit of flow tunnels through the potential energy barrier, then the smaller unit should get through easier; hence, a tunneling mechanism leads to the same conclusion: E_η decreases with increasing LiF concentration.

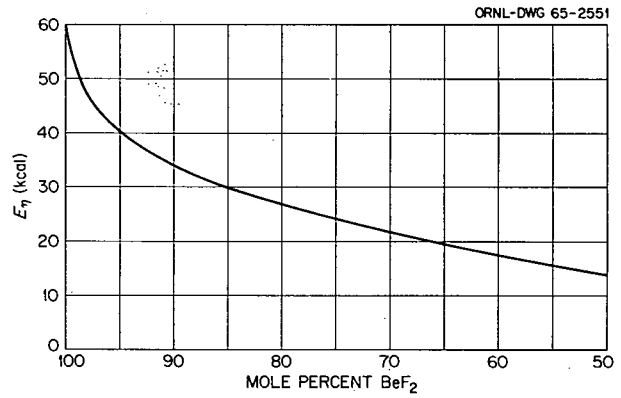

Fig. 3.26. Energy of Activation for Viscous Flow vs Composition in the LiF-BeF_2 System.

A binary system analogous in many properties to LiF-BeF_2 is MgO-SiO_2. The bases of the analogy are the approximate equalities in ionic sizes ($Li^+ \cong Mg^{2+}$, $Be^{2+} \cong Si^{4+}$, $F^- \cong O^{2-}$). Bockris, Mackenzie, and Kitchener[41] have measured the viscosities of the MgO-SiO_2 system over the composition range 44.3 to 51.4 mole % MgO. For the corresponding compositions and temperatures, these authors found that the viscosities of three other (CaO, SrO, BaO) alkaline earth oxide–silica binary systems were roughly equal to the viscosities measured in the MgO-SiO_2 system. Furthermore, for any composition up to 55 mole % alkaline earth oxide, E_η was the same, regardless of the alkaline earth oxide. The curve of E_η vs composition in these silica binaries is nearly proportional to the same plot in the LiF-BeF_2 system. In other words,

$$\frac{E_\eta \text{ (pure } BeF_2)}{E_\eta \text{ (}x\text{ mole \% } BeF_2,\ y\text{ mole \% LiF)}} \cong \frac{E_\eta \text{ (pure } SiO_2 \text{ at } 1700°C)}{E_\eta \text{ (}x\text{ mole \% } SiO_2,\ y\text{ mole \% MO)}} \ ,$$

where M is Mg, Ca, Sr, or Ba.

Further viscosity studies in the LiF-BeF_2 system are in progress or planned. Liquids being or to be measured are: (*a*) pure BeF_2, using

[40] W. H. Zachariasen, *J. Am. Chem. Soc.* **54**, 3841 (1932).

[41] J. O'M. Bockris, J. D. Mackenzie, and J. A. Kitchener, *Trans. Faraday Soc.* **51**, 1734 (1955).

special spindles for high viscosity determination, (*b*) liquids having higher concentrations of LiF, and (c) solutions of UF_4, ThF_4, or ZrF_4 in the $LiF\text{-}BeF_2$ system.

DENSITIES OF MOLTEN-FLUORIDE MIXTURES

B. J. Sturm R. E. Thoma

Values for the densities of molten-fluoride mixtures have generally been obtained from estimates such as the relatively imprecise method of mixtures employed by Cohen *et al.*,[42,43] in which experimental values for the densities of the components at room temperature were used, or the more satisfactory method employed by Cantor,[44] which assumes additivity of molar volumes. In order to obtain more precise densities, we assembled a simple experimental device to measure the height of a known weight of fluoride contained in a cylindrical vessel; the apparatus is contained in an inert-atmosphere glove box to permit safe handling of beryllium compounds and to prevent contamination of the test salt mixtures. The liquid heights are obtained by perpendicularly probing the liquid surface and the vessel bottom with a rod attached to calipers. When the rod just touches the surface of the liquid, a simple electrical circuit is completed and a light bulb goes on. From the height of the liquid, the diameter of the nickel vessel and the weight of fluoride, the density is then calculated. Experimental values of densities obtained for four salt mixtures of current use in MSRE or Fluoride Volatility Process technology are shown in Table 3.10 and Fig. 3.27. Some of the experimental values obtained in this work are somewhat higher than those obtained in previous estimations. Reasons for the differences in experimental and calculated values are not yet ascribable.

[42]S. I. Cohen and T. N. Jones, *A Summary of Density Measurements on Molten Fluoride Mixtures and a Correlation Useful for Predicting Densities of Fluoride Mixtures*, ORNL-1702 (July 19, 1954).

[43]S. I. Cohen, W. D. Powers, and N. D. Greene, *A Physical Property Summary for ANP Fluoride Mixtures*, ORNL-2150 (Aug. 23, 1956).

[44]S. Cantor, p. 38 in *Reactor Chem. Div. Ann. Progr. Rept. Jan. 31, 1962*, ORNL-3262.

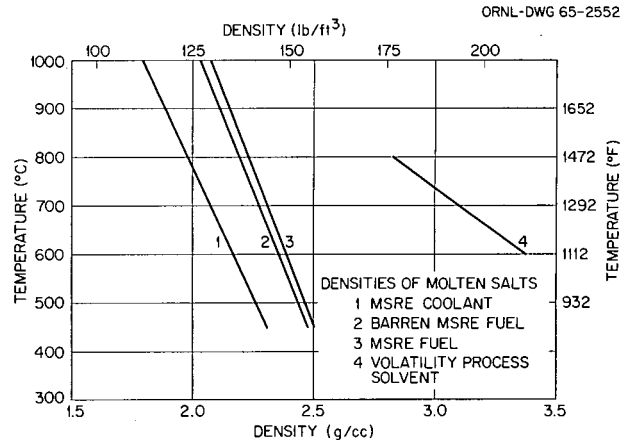

Fig. 3.27. Densities of Molten Salts.

MASS SPECTROMETRIC STUDIES OF MOLTEN FLUORIDE VAPOR SPECIES

R. A. Strehlow J. D. Redman

During the past year studies were begun of the vapor species given off from solid or molten fluoride mixtures. It was expected that the results would contribute to our general knowledge of the behavior of inorganic fluorides, would assist the present evaluation of vacuum distillation as a possible purification method for reactor fuels (see the next section, "Recovery of Carrier Salt by Distillation," this chapter), and would bear on the question of whether solid plugs might be deposited in reactor off-gas lines via true vapor transport (vs mechanical transport as mist). The first experiments were made with a lithium fluoride–beryllium fluoride salt composition (66 mole % LiF) corresponding nearly to that of the compound Li_2BeF_4.

Measurements were made near the melting point (452°C) of the salt. The vapor source was a tiny quartz crucible, 0.045-in.-diam, heated by an external tungsten filament. The top of the crucible was about half an inch below the ionizing electron beam of a Bendix time-of-flight mass spectrometer used for detecting the vapor species. The vacuum system of the spectrometer was modified in order to obtain lower source pressures; the normal operating pressure was reduced from 10^{-5} to $3\text{–}5 \times 10^{-7}$ torr. Since the quartz-crucible vapor

Table 3.10. Densities of Molten Salts

	Composition (mole %)	Expression (Metric) (d in g/cm^3; t in °C)	Expression (English Units) (d in lb/ft^3; t in °F)	Temperature	Density	
					This Work	Previous Estimate
MSRE fuel	LiF 65.0 BeF_2 29.1 ZrF_4 5.0 UF_4 0.9	$d = 2.857 - 0.00087t$	$d = 179 - 0.0271t$	1200°F	146 lb/ft^3	146 lb/ft^3 [a] 141 lb/ft^3 [b]
MSRE barren fuel	LiF 65.6 BeF_2 29.4 ZrF_4 5.0	$d = 2.842 - 0.000808t$ [c]	$d = 178 - 0.028t$	1200°F	145.5 lb/ft^3	132.7 lb/ft^3 [d]
MSRE coolant	LiF 66.0 BeF_2 34.0	$d = 2.742 - 0.00095t$ [c]	$d = 171.5 - 0.0329t$	1200°F	132 lb/ft^3	122 lb/ft^3 [e] 124 lb/ft^3 [e] 118 lb/ft^3 [a,f]
Volatility solvent	KF 63.8 ZrF_4 21.3 AlF_3 14.9	$d = 5.025 - 0.00275t$		650°C ~600–650°C	3.237 g/cm^3	2.5 g/cm^3 [g]

[a]W. R. Grimes, "Molten Salts as Reactor Materials," *Nuclear News* (May 1964).

[b]E. S. Bettis and W. B. McDonald, "Molten-Salt Reactor Experiment," *Nucleonics* (Jan. 1964).

[c]Based on addition of a second portion of salt; therefore, in effect, these values are corrected for the curvature of the meniscus.

[d]Estimated from empirical molar volumes (see ref. 44).

[e]J. R. Engel, private communication, February 1965.

[f]Corrected for temperature.

[g]S. Mann, private communication, February 1965, calculation based on difference in pressure of two probes in Pilot Plant reaction vessel.

source used for these studies was not really suitable for melted fluorides, it was not possible to obtain quantitative results at high temperatures; nevertheless, various peaks were assignable to expected species, and some interesting transient phenomena were found.

Table 3.11 lists the observed mass peaks with assigned formulas. No peaks corresponding to $Li_2BeF_4^+$, $Li_2BeF_3^+$, or $Li_2BeF_2^+$ ions were found. The presence of $LiBeF_2$ ions indicated that, for the 66 mole % LiF composition, $LiBeF_3$ was the dominant and possibly the sole species containing both lithium and beryllium.

The effects of small uncontrolled temperature perturbations on the peak intensities of Li_2F^+ and BeF_2^+ relative to the intensity of $LiBeF_2^+$ near two temperatures (416 and 460°C) are shown in Figs. 3.28 and 3.29. It will be noted that below the melting point the Li_2F^+ intensity increased relative to that of the beryllium-containing ions for a short time following a small temperature increase, while above the melting point the BeF_2^+ ion intensity increased temporarily relative to those of both of the lithium-containing species. Such behavior was observed at several temperatures from 375 to 570°C and indicates that, under nonequilibrium vaporization conditions, BeF_2 rather than a lithium-containing species vaporized from liquid Li_2BeF_4. The species which vaporized from the solid salt appeared to be dimeric lithium fluoride.

Although the peak height ratios cannot give a direct quantitative measure of the amounts of BeF_2 relative to the amounts of all the other species, an ion intensity for BeF_2 of more than 60% of the total peak heights has been occasionally observed from the liquid. From the solid, as much as 90% of the vapor has appeared to be dimeric lithium fluoride. It was assumed that the small temperature perturbations did not grossly affect the ionizing efficiency, spectral patterns, or detection efficiency of the mass spectrometer.

Table 3.11. Mass Numbers Observed During Vaporization of Li_2BeF_4

Mass Number	Assigned Formula
7	Li^+
26	LiF^+
33	Li_2F^+
47	BeF_2^+
54	$LiBeF_2^+$
59	$Li_3F_2^+$

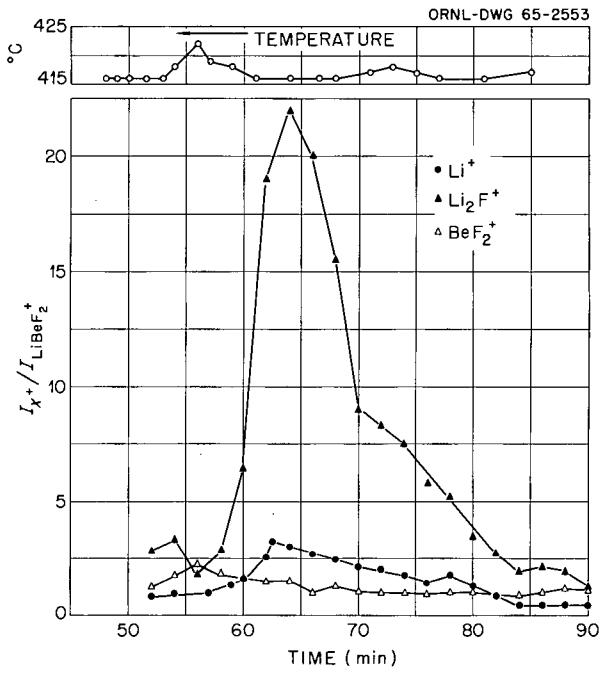

Fig. 3.28. Ion Intensity Ratios Near 416°C from Li_2BeF_4 (Solid).

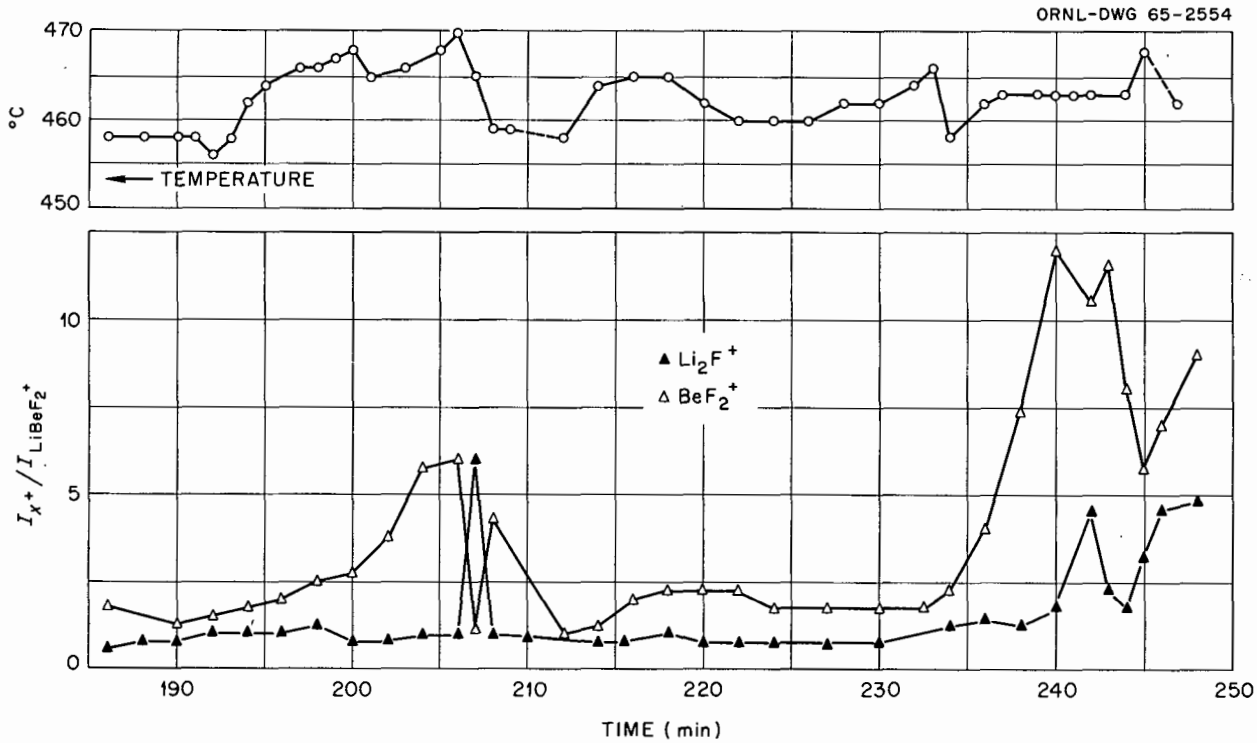

Fig. 3.29. Ion Intensity Ratios Near 460°C from Li_2BeF_4 (Liquid).

RECOVERY OF CARRIER SALT BY DISTILLATION

M. J. Kelly

Uranium fluoride dissolved in a carrier salt of beryllium, lithium, and zirconium fluoride in the molten state is the fuel for the Molten Salt Reactor Experiment. A similar fuel (probably without the zirconium) is proposed for a thermal breeder. To achieve a significant breeding gain, the average thermal cross section of the fuel must remain low. As fission products (particularly the rare earths) accumulate, neutron losses by capture increase. If a process for removal of fission products which will keep their concentration at an arbitrary low value is economically practical, the potential attractiveness of the fluid fuel becomes a reality. Such a removal process would also allow long-term usage of the carrier salt, which otherwise must be discarded, because of fission product accumulation, at a cost of ~$1100/ft^3.

Theoretical Considerations

Purification of metals and compounds by diffusion of their vapor from hot to cold surfaces has been successfully practiced for decades. Vacuum distillation is also commonly used in the metal industry and in biochemical processes. For the fluoride salts Brewer[45] estimated vapor pressures, shown on Fig. 3.30, which indicate that a good separation of the MSRE fuel components from the rare earth fluorides could be achieved by the above techniques. For volume production purposes, vacuum distillation appears much more attractive than a diffusion process. The vapor pressure required for practical distillation is estimated in the metal industry as about 2 mm Hg. This value can be achieved for each fuel component at temperatures compatible with the use

[45] Leo Brewer, "The Thermodynamic and Physical Properties of the Elements," *Report for the Manhattan Project*, 1946.

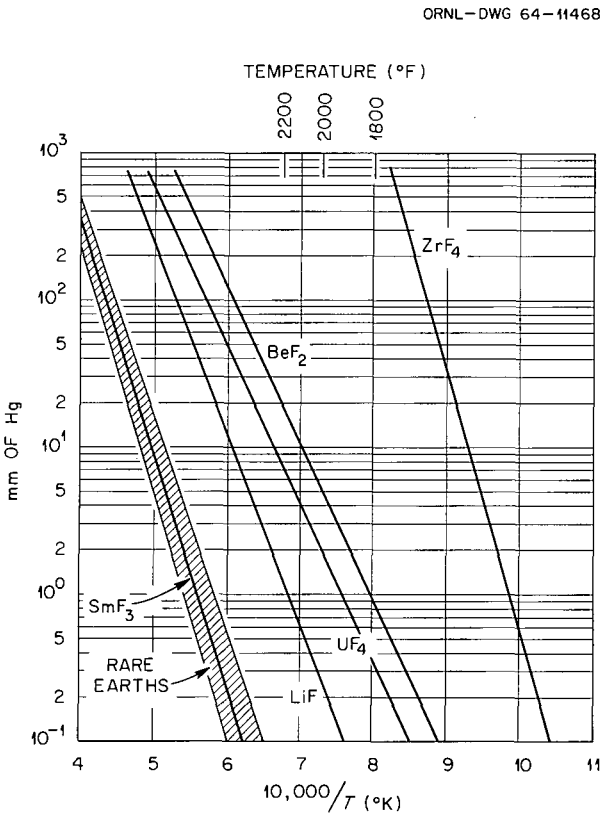

Fig. 3.30. Estimated Vapor Pressures for MSRE Fuel Components and Rare Earths (Brewer, 1946).

of oxidation resistant alloys necessary for containment. The unknown quantities are the activity coefficients of the various components in the molten mixture.

Experimental Studies

Since determination of these activity coefficients presented a difficult problem, it appeared simpler to examine the actual problem of distillation and acquire some knowledge of the relative volatility of the fuel components by experiment. Initial experiments demonstrated the feasibility of distilling pure lithium fluoride and a lithium-beryllium fluoride mixture. Then samples of MSRE fuel salt, with europium trifluoride added as the simulator for the rare earth fission products, were distilled. Successive aliquots of the distillate were analyzed. In one experiment, the separation factor for europium was over 1000 after 80% of the initial charge was distilled. All experiments were single-pass distillations with or without some thermal reflux. The equipment involved was a simple tubular still heated with an ordinary vertical tube furnace.

Table 3.12 shows the summarized results for an experiment with 98% of the original charge

Table 3.12. Recovery of Simulated MSRE Fuel by Vacuum Distillation

	Charged		Recovered in Distillation		Recovered in Still Bottoms	
	(mole %)	(wt %)	(g)	(%)	(g)	(%)
LiF	62.0	37.8	35.18	100	0.0014	0
BeF_2	32.0	35.2	32.26	100	0.0008	0
ZrF_4	5.0	19.5	18.89	100	0.003	0
UF_4	1.0	7.3	5.18	80	1.33	20
EuF_3		0.2	0.003	2	0.15	98
Unknown			5.38		0.49	
Total	99.7 g		96.89	98.1	1.89	1.9
			SF[a] = 50			

[a]Separation factor.

distilled; the separation factor of 50 obtained with total recovery of the carrier salt is adequate. The remaining uranium can be recovered by fluoride volatility processing.

Experimental data from completed experiments enable us to construct a very preliminary diagram of the vapor-liquid relationship at various stages of distillation. This is shown in Fig. 3.31. As more data are acquired, alterations will occur, but it is felt that these changes will be minor in nature.

Conclusions

It appears evident that separation of the MSRE fuel components from the rare earth fission products by distillation is practical. In addition, it seems likely that the process will provide reasonable separations from other (and less important) fission product species such as SrF_2, BaF_2, and that fraction of the Nb, Mo, Ru, Rh, and Pd which is suspended in the metallic state in the salt. Separation from fission product ZrF_4 will clearly not occur, and no separation from RbF, CsF is expected. Many technical details are unresolved, and some difficulties are probably even unrecognized. It is expected that a continued research effort will find and resolve these problems, as well as provide valuable fundamental information on the interactions between the various molten complexes.

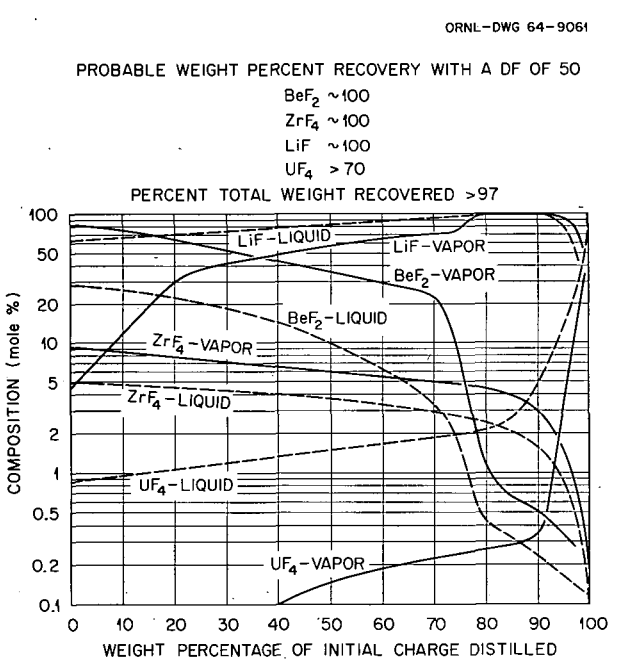

Fig. 3.31. Estimated Composition of Liquid and Vapor During Distillation of MSRE Fuel.

GAS TRANSPORT CHARACTERISTICS OF MSRE GRAPHITES

R. B. Evans III J. Truitt

Direct contact of the unclad graphite moderator and the fuel in the MSRE offers an opportunity for the fission gases to permeate the graphite; this permeation may lead to variable reactivity resulting from variations of the ^{135}Xe concentration within the moderator, and, perhaps, to a high xenon poison fraction retained in the core. Accordingly, studies have been made of the gaseous interdiffusion and flow properties of the MSRE graphite (CGB grade).

In an earlier investigation[46] of the removal of xenon from the MSRE, two grades of graphite, denoted as AGOT and CEY, were considered. Comparison of the CGB grade with these shows striking differences in the resistance to penetration by the molten fluoride fuel (see Fig. 3.32). AGOT grade graphite (basically the type used in the EGCR) is given little or no additional treatment to lessen its permeability; total invasion by the molten salt is not surprising. An impregnation treatment, given to the base stock, drastically lowers the permeability of the CEY grade. The impregnation is not uniform, however, and the end product takes the appearance of a coated pipe. This can be clearly seen in Fig. 3.32*b*, where the molten salt appears to have penetrated the coating, possibly through a crack, and has moved with relatively little restriction within the central portion of the specimen. The CGB material, also produced by impregnation of a base stock, clearly yields a more uniformly impermeable graphite; it is invaded by the molten salt to a very minor extent.

[46] G. M. Watson and R. B. Evans III, ORNL-CF-61-2-59 (Feb. 15, 1961).

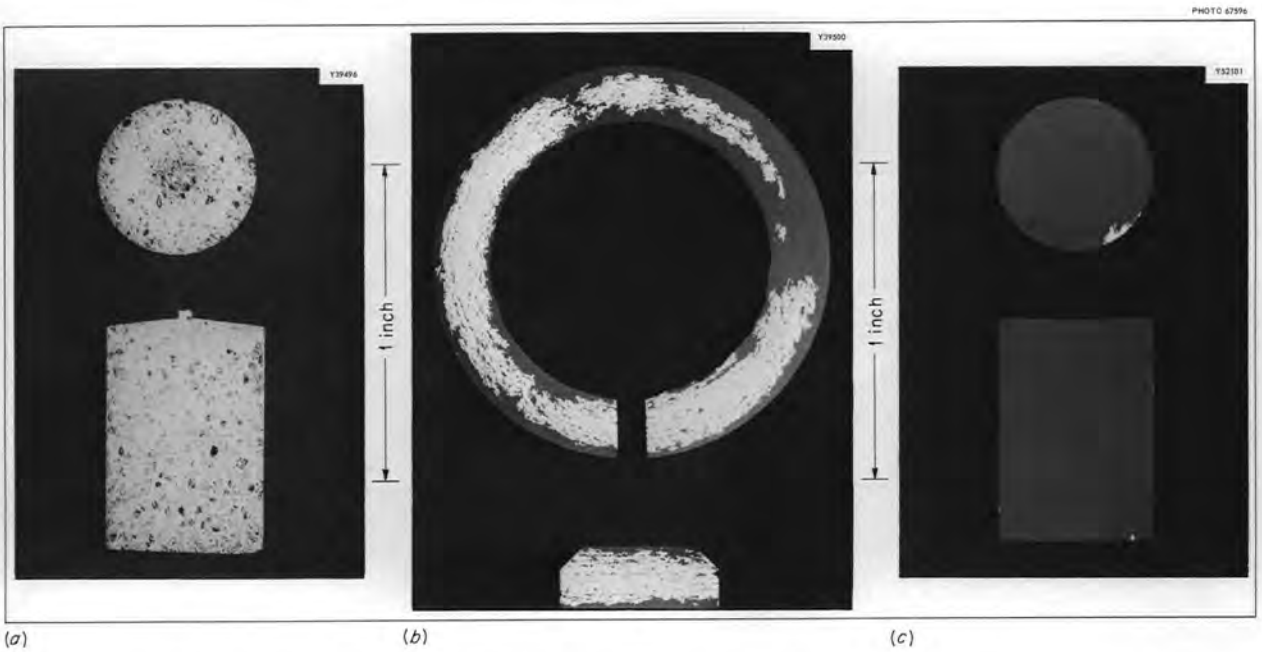

Fig. 3.32. Salt Distribution in Graphite Grades (*a*) AGOT, (*b*) CEY, and (*c*) CGB Following 100-hr Exposure to Molten Salt at 1300°F (704°C) Under 150 psig, as Shown by Radiographs of Thin Sections.

Pore-size spectra of representative samples of the three graphite grades are illustrated in Fig. 3.33. The significant difference is that CGB appears to have a single distribution of pore sizes, whereas the other two might be more correctly described by the superposition of two distribution functions, one for small pore sizes, and another for somewhat higher values of the pore entrance diameter. The effect of such bidisperse systems on the gas transport characteristic of porous media has already been considered by deBethune and Rowell.[47]

From the pore-size spectra, it would appear that the relative magnitudes of the permeabilities of the three samples should be given by: $K_{AGOT} > K_{CEY} > K_{CGB}$. That this is not the case is clearly shown in Fig. 3.34. In a previous observation of a similar effect, it was suggested that the reversal is due to the relative effective lengths of the pores.[48] The results, shown below, of our diffusion studies support this view.

Interdiffusion experiments with He-Ar gas mixtures were conducted with the CGB sample under both uniform and nonuniform pressure conditions. The data obtained in these studies indicate that the effective diffusion coefficient for the system He-Ar at 23°C and 1 atm is given by:

$$D_{12}(\text{eff}) = 7.68 \times 10^{-4}\ \text{cm}^2/\text{sec}\ . \qquad (46)$$

The coefficient $D_{12}(\text{eff})$ is related to the diffusion coefficient in free space through a porosity-tortuosity factor (ϵ/q), which is characteristic only of the porous septum. If D_{12} and the porosity (fractional void volume) of the medium are known, it is possible to calculate the tortuosity (q). This tortuosity is, in turn, taken to be a measure of the average effective length $L(\text{eff})$ of the pores comprising the septum relative to the actual length L. Specifically,

$$q = \left[\frac{L(\text{eff})}{L}\right]^{1/2} \qquad (47)$$

Similar He-Ar diffusion experiments have been made by Malinauskas[49] with the CEY graphite, from which it was found that

[47] A. J. de Bethune and R. L. Rowell, *J. Phys. Chem.* **67**, 2065 (1963).

[48] Paper presented by A. P. Malinauskas and F. L. Carlson at the 66th Annual Meeting of The American Ceramic Society, Chicago, April 18–23, 1964, and to be published in the *Bulletin of the American Ceramic Society*.

[49] A. P. Malinauskas, private communication.

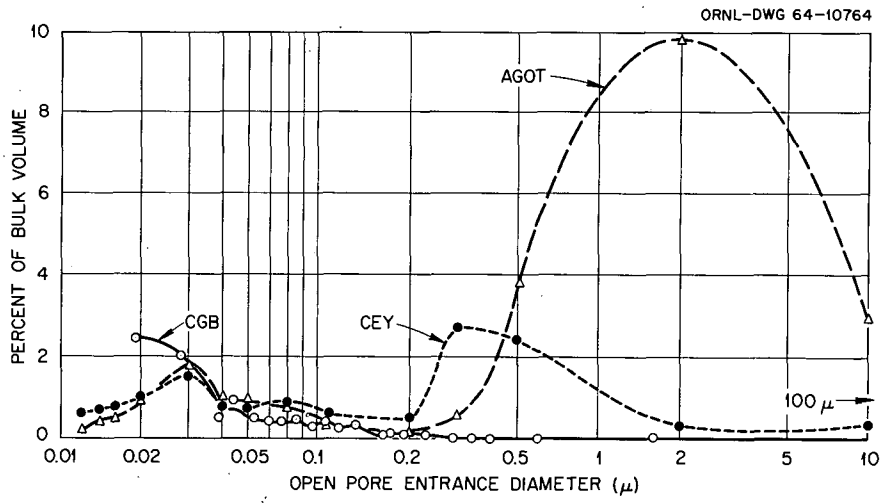

Fig. 3.33. Representative Pore-Size Spectra of AGOT, CEY, and CGB Graphite Grades.

$$D_{12}(\text{eff}) = 1.71 \times 10^{-5}\ \text{cm}^2/\text{sec} \qquad (48)$$

at 24°C and 1 atm. The porosities of the CGB and the CEY grades of graphite have been determined by a gas expansion method and were found to be 9.0 and 11.1% respectively. By combining these values for the porosities with the effective diffusion coefficients of Eqs. (46) and (48), the tortuosities of the two graphites are in the ratio

$$\frac{q(\text{CGB})}{q(\text{CEY})} = 0.018\ . \qquad (49)$$

If the interpretation of q as given by Eq. (47) is correct, Eq. (49) indicates that the average effective length of the pores within the CEY specimen is 7–8 times as great as that for the CGB sample.

Another basis for comparison is the relative contribution of Knudsen (free molecular) diffusion to the overall transport. Of the number of ways in which this comparison can be made, we have chosen to use the pressure dependence of the apparent effective diffusion coefficient reduced to unit molecular concentration.[50] This apparent diffusion coefficient $(nD_{12})_{\text{app}}$ is calculated from the diffusion data by assuming a negligible Knudsen contribution. If the assumption is valid,

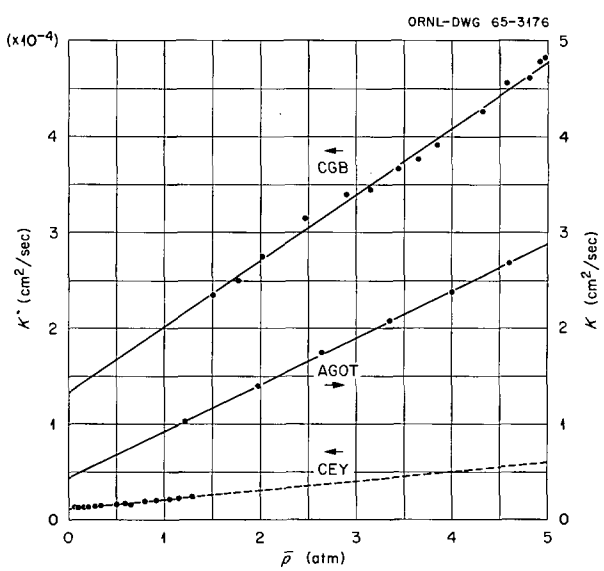

Fig. 3.34. Permeabilities to Argon of AGOT, CEY, and CGB Graphites.

then $(nD_{12})_{\text{app}}$ is equal to the actual effective diffusion coefficient reduced to unit molecular concentration and is independent of pressure. On the other hand, if the assumption is not valid, a plot of $(nD_{12})^{-1}_{\text{app}}$ vs the reciprocal of the mean pressure, $\langle p \rangle^{-1}$, will show a linear relationship having a positive, nonzero slope. The intercept, however, is equal to $(nD_{12})^{-1}$, and the magnitude of the slope is a measure of the relative contribution due to free molecule diffusion. A normalized

[50] R. B. Evans III, G. M. Watson, and J. Truitt, *J. Appl. Phys.* 33, 2682 (1962).

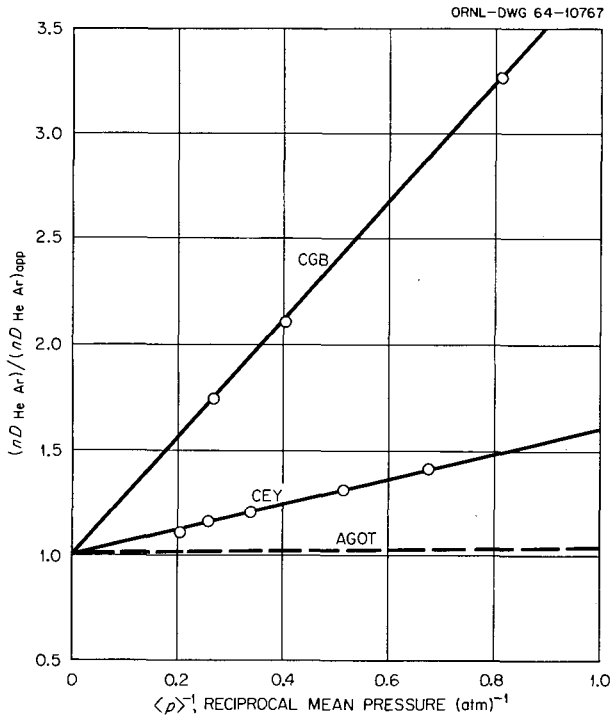

Fig. 3.35. Normalized Plot of the Pressure Dependence of the Apparent Effective Diffusion Coefficient for the System He-Ar for AGOT, CEY, and CGB Graphites.

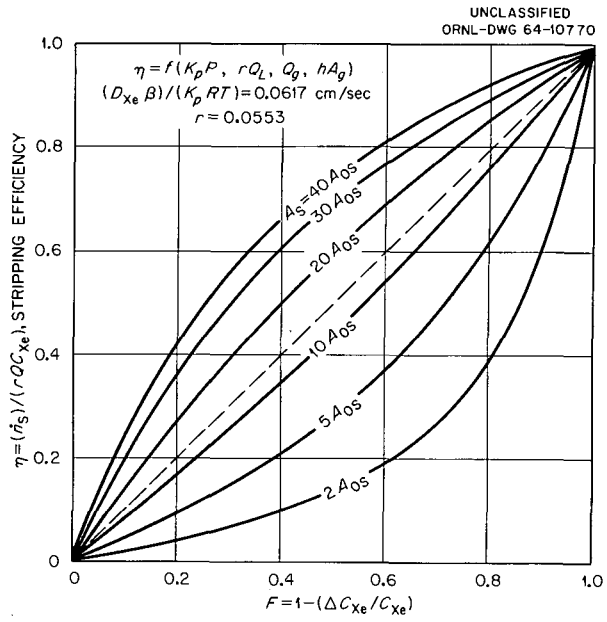

Fig. 3.36. Effect of a Molten Salt–Gas Film on the Stripping Efficiency of the MSRE for Various Areas of Salt Exposed in the Pump Bowl. Graphite and salt-flow parameters are fixed at MSRE conditions.

plot of $(nD_{12})^{-1}_{app}$ is shown in Fig. 3.35 for the three grades of graphite. It is seen from the slopes of the lines in the figure that the relative effects of Knudsen transport increase in the sequence: AGOT, CEY, and CGB.

THE REMOVAL OF ^{135}Xe IN THE MSRE

R. B. Evans III

An analysis of temperature profile measurements on molten salts flowing through tubes suggests the existence of a film at the liquid-solid interface which provides an effective barrier to heat and mass transfer.[51] In a previous analysis[52] of the removal of ^{135}Xe in graphite-moderated, molten-salt reactors, the effect of such a film was considered negligible; we have therefore re-examined the problem with the assumption that this film exists and that a similar film also exists at the salt-gas boundary in the stripper. The parameters used in the previous report[52] have been altered somewhat to conform to the present operational specifications of the MSRE and the gas transport characteristics of the graphite as determined in the work presented above.

The penetrability of the film is conveniently expressed in terms of a film factor, F, defined by

$$F \equiv 1 - (\Delta C_{Xe}/C_{Xe}) , \qquad (50)$$

where ΔC_{Xe} represents the concentration drop across the film and C_{Xe} is the concentration of ^{135}Xe in the bulk molten salt. It is easily seen from Eq. (50) that a completely impermeable film ($\Delta C_{Xe} = C_{Xe}$) corresponds to $F = 0$, whereas the absence of such a film ($\Delta C_{Xe} = 0$) is denoted by $F = 1$. The effect of the film factor on the amount of xenon which is removed in the pump bowl (stripper) is shown in Fig. 3.36 for various assumed values of the effective area of the salt,

[51] H. W. Hoffman and J. Lones, *Fused Salt Heat Transfer. Part II. Forced Convection Heat Transfer in Circular Tubes Containing NaF-KF-LiF Eutectic*, ORNL-1777 (Feb. 16, 1955).

[52] G. M. Watson and R. B. Evans III, ORNL-CF-61-2-59 (Feb. 15, 1961).

A_s, measured relative to the area of bulk salt exposed to the helium sweep gas in the pump bowl, A_{os}. The stripping efficiency, η, is defined as the ratio of the actual strip rate of xenon to the strip rate in the absence of a film. It is apparent from this figure that the stripping efficiency can be significantly increased, for a given film factor, by increasing the effective area of the salt-gas interface (e.g., by bubbling the helium sweep gas through the molten salt).

Diffusion into the graphite moderator, burnout and decay, and removal at the stripper, all compete in the depletion of the total amount of ^{135}Xe produced. Absorption by the graphite is overwhelmingly favored by present MSRE design parameters, in that the $(D_{Xe}A)_{eff}$ of the graphite is comparatively large – even when films are present – because the fraction of total salt flow permitted to discharge ^{135}Xe via the stripper has been fixed at a small value (6% recycle). The presence of a film under these conditions does not enhance xenon removal at the stripper; rather, the major film effect is to force ^{135}Xe into solution, as shown in Fig. 3.37. Furthermore, the steady-state ^{135}Xe concentration in the bulk salt is virtually independent of the stripping efficiency (as it is related to A_s for a given value of F). This situation is perhaps more clearly presented in Fig. 3.38, where fractions of ^{135}Xe removed by stripping have been plotted as a function of the salt flow rate within the pump well, assuming fixed areas and graphite parameters. One objective here was to explore for future applications the possibility of increasing ^{135}Xe removal by in-

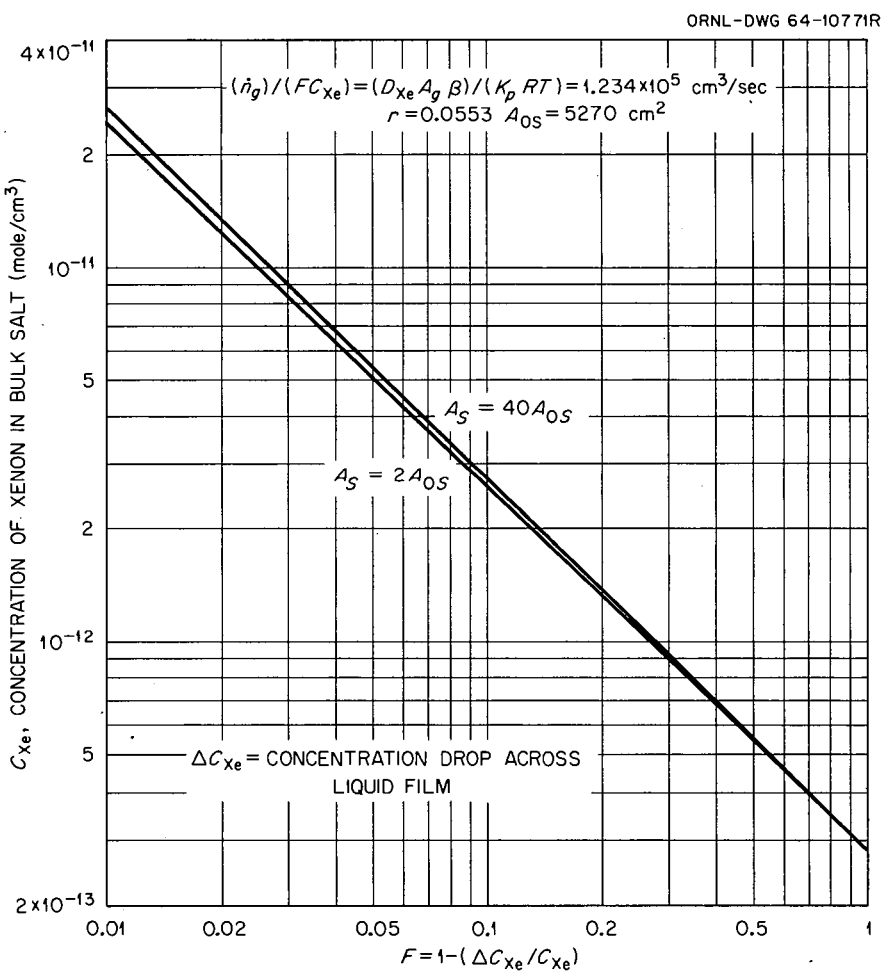

Fig. 3.37. Steady-State Concentration of ^{135}Xe in the Bulk Salt as a Function of the Film Factor at Two Values of the Area of Salt Exposed in the Pump Bowl. Graphite and salt-flow parameters are fixed at MSRE conditions.

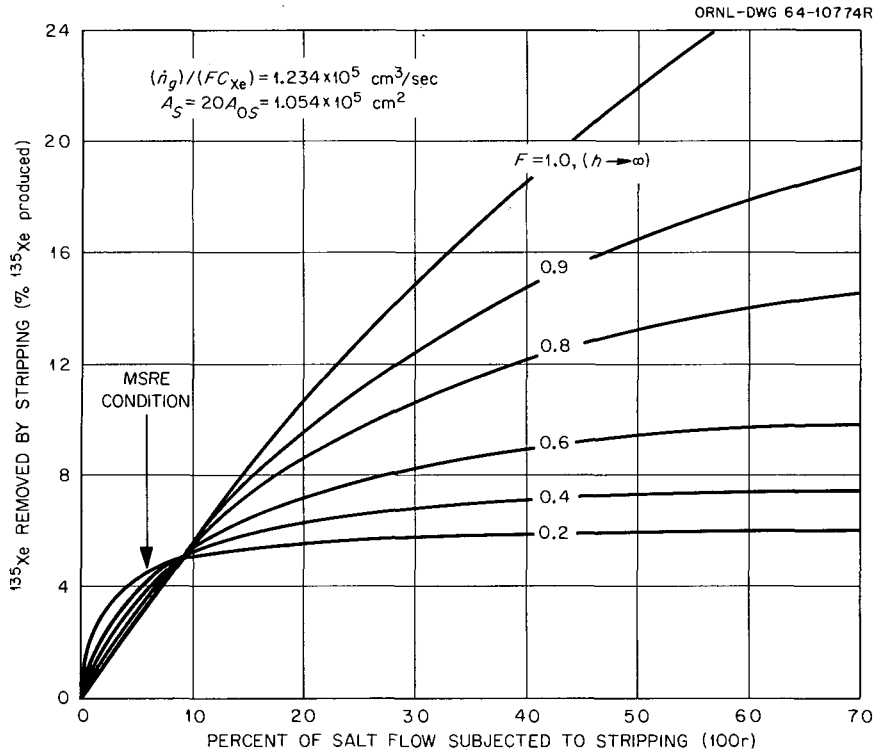

Fig. 3.38. Steady-State Fraction of ^{135}Xe Removed in the MSRE as a Function of the Film Factor and the Salt Circulation Rate in the Pump Bowl.

creasing the recycle rate. In line with the present discussion, note that the MSRE salt flow rate within the stripper is in the range of flow rates at which the fraction of xenon removal by stripping varies inversely with the film factor. Thus the stripping efficiency varies in a similar fashion. The point emphasized here is that our preliminary analysis clearly demonstrates the complex manner in which ^{135}Xe removal rates vary within the range of variables near MSRE conditions. A detailed presentation of this analysis, and, hopefully, a comparison with actual MSRE behavior, will be presented at a later date.

SEPARATION OF PROTACTINIUM FROM IRRADIATED THORIUM SALTS

A. J. Shor E. L. Compere

A number of significant benefits may be derived from the prompt removal of ^{233}Pa from thorium irradiated in a nuclear reactor or blanket. If ^{233}Pa is permitted to reach appreciable concentrations, neutron capture with the production of nonfissionable ^{234}U can result in a reduction of the conversion factor and reactivity of the reactor system. Isotopic purity of the ^{233}U and its ultimate value are markedly reduced. Appreciable production of ^{232}U occurs by $n,2n$ reactions on ^{233}Pa or ^{233}U, and high radiation levels from unstable high-energy α-emitting daughters of ^{232}U lead to increased shielding requirements and to higher costs in the design of ^{233}U recovery facilities. Thus a process for prompt withdrawal of ^{233}Pa at reasonable levels from a reactor blanket could have important consequences in the economics of the thorium fuel cycle; a low steady state protactinium level could be maintained in the reactor, and high-purity ^{233}U could be produced.

In a series of experiments Malm and Fried[53,54] succeeded in demonstrating that a process based

[53] J. G. Malm and S. Fried, Sec. C-1, *Chemistry Division Summary Report July–September, 1950*, ANL-4545, p. 12.

[54] J. G. Malm and S. Fried, "Separation of Protactinium from Contaminants," U.S. Patent 2,893,825, July 7, 1959; USAEC Application April 11, 1951.

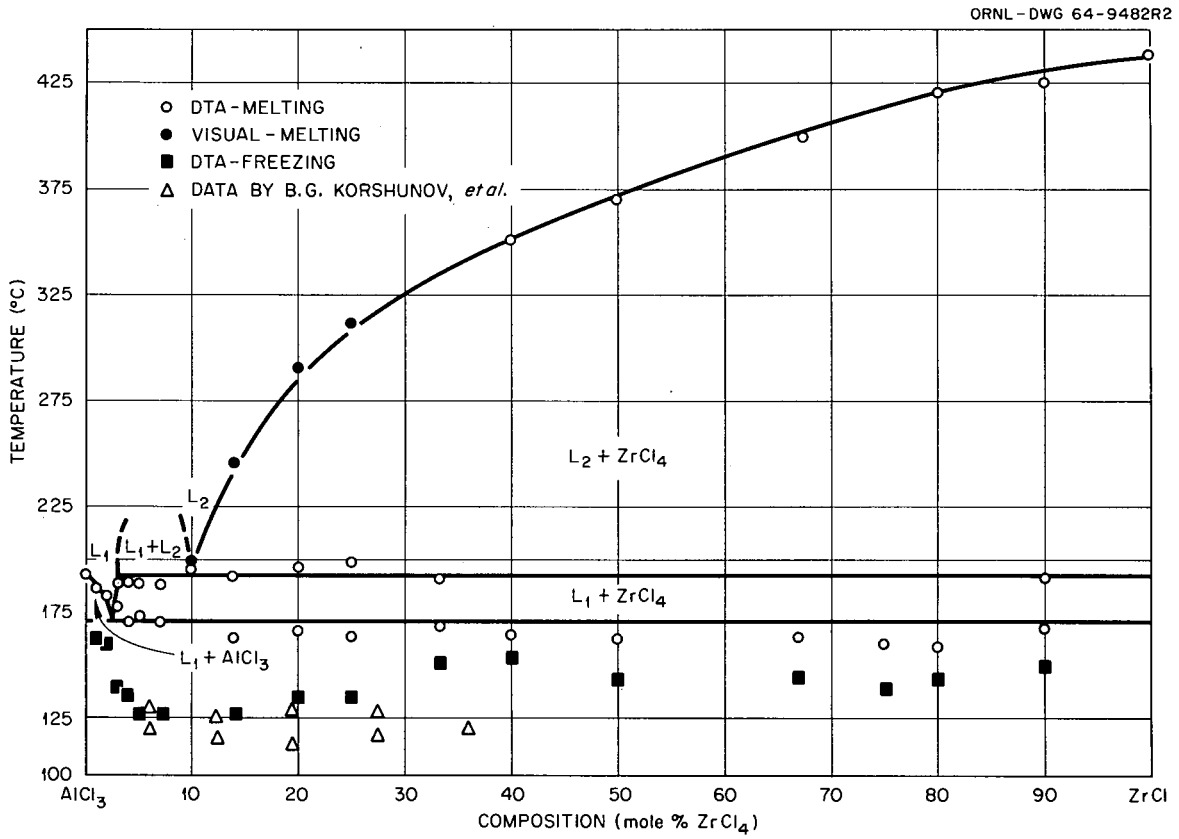

Fig. 3.39. Tentative Phase Diagram, $AlCl_3$-$ZrCl_4$ System.

on the apparent volatility of protactinium chloride might be useful in the prompt removal of Pa from irradiated thorium. It was claimed that upon chlorination of thorium metal or oxide with $AlCl_3$ or with $AlCl_3$ and Cl_2 or upon direct reaction of irradiated $ThCl_4$ with $AlCl_3$, protactinium chloride might be distilled from the mixture at temperatures as low as 100°C. The latter process, which promised the highest yield of Pa, was selected for further investigation.

Previously reported data[55] indicated the solubility of $ThCl_4$ in $AlCl_3$ to be low. Inference from the examination of the phase diagrams of analogs of thorium chloride with aluminum chloride suggested that the presence of a third component such as $ZrCl_4$ might enhance thorium solubility, and work on the relevant binary systems was initiated. Previous studies[55] had indicated little mutual solubility in the $ZrCl_4$-$ThCl_4$ system. Work on the $AlCl_3$-$ZrCl_4$ binary system is reported below.

[55]A. J. Shor and E. L. Compere, *Reactor Chem. Div. Ann. Progr. Rept. Jan. 31, 1964*, ORNL-3591, pp. 56–58.

$AlCl_3$-$ZrCl_4$ Phase Studies

The aluminum chloride–zirconium chloride system was studied throughout the range of composition using differential, thermal, and visual analysis. Figure 3.39 shows a preliminary binary phase diagram; concentrations shown assume monomeric $AlCl_3$. The open circles on the diagram represent information derived from differential thermal analysis (DTA) experiments; the solid circles are data obtained by the direct viewing of melting in quartz capsules. Visual observations were necessary for the 10 to 25 mole % $ZrCl_4$ region of the diagram, due to the steepness of the liquidus curve in this range. Direct visual observations of eutectic and monotectic temperatures on heating were obscure and difficult to reproduce. Differential thermal analysis data are shown for those transitions. Data obtained on cooling are shown as solid squares. Supercooling effects on the freezing point of the eutectic mixture are readily apparent. At $ZrCl_4$ concentrations greater than ~33 mole %, supercooling of the liquidus transitions was relatively small. Throughout the

Table 3.13. Melting- and Freezing-Point Temperatures of the $ZrCl_4$-$AlCl_3$ Binary Phase System

Mole % $ZrCl_4$	Transition Temperatures on Heatup (°C)			Transition Temperatures on Cooldown (°C)	
	I	II	Liquidus	I and II	Liquidus
100			437		435
90	167	191	425	150[a]	420
80	159		419	144	417
75	160			139	396
67	163		399	144	396
50	162		369	143	366
40	166		350	154[a]	
33	168	191[c]	320[a]	150	317
25	164	198	312[b]	135	262
20	167	193	291[b]	130	234
14	163	192	245[b]	125	
10	170	192	194[b]	120	
7	170	187[c]		125	
5	172	188[c]		127	
4	171	190[c]		132	
3	178	188[c]		135	
2	183			160	
1	185			162	
100% $AlCl_3$	193			183	

[a]Vague transition. [b]By direct visual observation. [c]Poor resolution of second peak.

entire range of concentrations, supercooling of the monotectic and eutectic compositions ranged from 10 to 50°C.

Sparse data reported by B. G. Korshunov *et al.*[56] for the $AlCl_3$-$ZrCl_4$ system are also shown in Fig. 3.39, as triangles. These data parallel cooling data obtained in our studies by thermal analysis and represent supercooled freezing temperatures in the binary liquid mixtures.

In the region of ~10 to 100 mole % $ZrCl_4$ complete miscibility of the liquid mixture is postulated, while in the region of ~3 to 10 mole % $ZrCl_4$ a narrow two-phase section may exist with a monotectic composition of 10% $ZrCl_4$ at 192°C. An $AlCl_3$-$ZrCl_4$ eutectic is evident at ~2.5% $ZrCl_4$ and 170°C. Table 3.13 lists the data from which the curves are derived, together with notes on the observations. The phase diagram appears to be consistent with the trend of data reported in other investigations of binary systems containing $AlCl_3$. For example, the presence of a eutectic of high percentage $AlCl_3$, the sharp initial rise of the liquidus curve, and the presence of two liquid phases appear to be characteristic of a number of such systems.[57] However, the sharp drop in the melting point of mixtures in the $AlCl_3$-rich side of the eutectic composition and the possibility that the existence of the monotectic may be an artifact have led to several alternative interpretations of the data. These are still under consideration.

[56]B. G. Korshunov, A. M. Reznik, and I. S. Morozov, *Tr. Mosk. Inst. Tonkoi Khim. Teckhnol.* **7**, 127 (1958).

[57]I. N. Belyaev, *Russ. Chem. Rev. (English Transl.)* **29**, 428 (1960).

Thermodynamic activities of $ZrCl_4$ as a function of temperature were calculated for the $ZrCl_4$-rich part of the phase diagram. Assumptions of constancy of heat capacity and partial molar heat of solution were made in these calculations. Activities were compared with the corresponding concentrations in mole fraction units in two ways: First, as a mixture with dimeric $(AlCl_3)_2$, which is the usual state of the pure liquid; and, second, as a mixture with monomeric $AlCl_3$. It was found that from about 33 to 100 mole % $ZrCl_4$, the $ZrCl_4$ liquidus curve showed apparent ideal behavior, based on a model of a solution of monomeric $AlCl_3$ and $ZrCl_4$. A manuscript containing a more complete discussion of this system will be submitted for publication.

$AlCl_3$-$ThCl_4$ Phase Studies

Investigation[55] of the $AlCl_3$-$ThCl_4$ system by thermal methods and by direct observation of melting and freezing for concentrations of 100, 90, 75, 50, 25, and 10 mole % $ThCl_4$ in $AlCl_3$ showed no indication of mutual solubility. Some recent Russian work[58] has also suggested that the solubility of $ThCl_4$ in $AlCl_3$ should be much less than 10 mole %.

Direct measurement of the solubility of $ThCl_4$ in liquid $AlCl_3$ was obtained by equilibrating 10 mole % mixtures of $ThCl_4$ in $AlCl_3$ at constant temperature. The $ThCl_4$ was separated by settling at temperature, and the system was rapidly frozen. The $AlCl_3$-rich phase was analyzed for thorium content. Measurements were conducted at five temperatures with the following results:

Temperature (°C)	Solubility (mole % $ThCl_4$)
210	0.98
215	0.96
250	1.01
300	0.85
350	0.88

The solubility over this range is regarded as constant at 1 mole % $ThCl_4$ in $AlCl_3$.

[58] B. G. Korshunov *et al.*, *Izv. Vysshikh Uchebn. Zavedenii, Tsvetn. Met.* **6**, 114–18 (1960).

Protactinium-233 Tracer Experiments

Tracer quantities (2–30 μc) of ^{233}Pa were generated in selected mixtures of $ThCl_4$ and $AlCl_3$ by thermal-neutron irradiation in the Oak Ridge Research Reactor pool. The salts were contained in an evacuated 9-mm-ID quartz tube, divided into two sections joined by a short 4-mm-ID neck. The tube was sealed under vacuum while the body of the tube was immersed in liquid nitrogen to prevent escape of volatile salts. During attempts to distill the protactinium, the shorter, 75-mm, section of the tube was used as the salt container while the longer, 125-mm, section served generally as the receiver. In some cases a loose quartz wool plug was placed in the neck section to prevent physical carryover of material.

The relative distribution of protactinium after distillation was measured by moving the quartz tube in 1-cm steps past a slit (~1 cm) between two sections of lead shielding, and determining with a G-M tube the collimated radiation.

Salts with starting compositions of 100, 50, 10, and 0.5 mole % $ThCl_4$ in $AlCl_3$ were distilled at salt temperatures ranging from 160 to 275°C. Results are summarized in Table 3.14.

No transfer of protactinium activity to an air-cooled receiver was observed when heating pure $ThCl_4$ or a salt mixture containing 50 mole % $ThCl_4$ in $AlCl_3$ to temperatures as high as 275°C for periods up to 46 hr. With the mixtures containing substantially more $AlCl_3$, an appreciable fraction of the protactinium activity was transferred when the $AlCl_3$ was distilled under these conditions. The retention of the protactinium when 50 mole % $AlCl_3$ or less was used may have been due to retention of protactinium in the interior of the $ThCl_4$ grains or to strong adsorption of protactinium from $AlCl_3$ solution on the relatively abundant surface of the solid $ThCl_4$. Evidence below supports the latter view.

At 10 mole % $ThCl_4$ in $AlCl_3$, from 10 to 90% of the protactinium was transferred when one end of each of the tubes containing salt mixtures was heated in the range 160 to 260°C for 2 to 7 hr and the $AlCl_3$ was distilled to the receiver end. The volatilization of such proportions of protactinium, when only 1 mole % $ThCl_4$ is soluble in $AlCl_3$, implies that protactinium was leached to a substantial degree from $ThCl_4$ grains, and then volatilized with $AlCl_3$.

Table 3.14. ^{233}Pa Volatilization Experiments with Tubes Containing Irradiated $ThCl_4$-$AlCl_3$ Mixtures

Tube No.	$ThCl_4$ in $ThCl_4$-$AlCl_3$ Mixture (mole %)	Quartz Fiber Filter Present	Time Heated (hr)	Temperature (°C)		^{233}Pa Found in "Original Receiver" Region[a] (%)	$AlCl_3$ Found in Receiver Region (%)	Comments
				Original Mixture Region	Original Receiver Region			
3	100	Yes	46	250	60	None	–	
7	50	Yes	7	275	95	None	All	
9	10	Yes	7	160	55	10	All	
10	10	No	4	212	37	30	All	
11	10	Yes	4	208	32	50	All	
8	10	Yes	4	220	350[d]	90	All	Mostly on quartz fiber
13	0.5	No	4	267	35	40	All	
17	0.5	*b*	4	200	203[d]	45	All	Mostly on quartz fiber in receiver
17	0.5	*b*	4	60	205	45	All	Attempt to transfer back was ineffective
16	0.5	c	4	202	60	0	All	Quartz fiber in original mixture
15	0.5	No	1/3	215	60	9.5	56	Quartz container
T 29	0.5	No	1/2	256	118	33	All	Teflon capsule
T 29	0.5	No	2 1/2	267	95	28	All	Teflon capsule

[a]Based on integrated count of entire tube. This includes the material found on "receiver" side of filter at constriction between regions.

[b]Quartz wool in receiver only.

[c]Quartz wool in original mixture only.

[d]Maximum temperature of receiver region. Distillation of $AlCl_3$ doubtless occurred during cooldown, apparently more rapid in receiver.

The fraction transferred seems substantially affected by adsorption phenomena, including an affinity of protactinium for quartz fiber, for $ThCl_4$, and possibly for the quartz tube.

This phenomenon might be the basis of a protactinium separation process; some pertinent observations follow.

In distillation experiments involving 10 mole % $ThCl_4$, the use of quartz fiber in the neck region appeared to result in greater protactinium transfer (Table 3.14). Without the quartz wool 30% of the protactinium was transferred; with quartz wool present 50% was transferred, and a large part of the activity was found in the region of the quartz. With the quartz at high temperature for a time, an even greater quantity was transferred; this material remained fixed to the quartz.

In experiments with 0.5 mole % $ThCl_4$ in $AlCl_3$ in which quartz wool was placed entirely in the receiver region, distillation at 200°C transferred 45% of the protactinium irreversibly to this region. In another experiment, quartz wool in the original mixture region prevented the distillation of protactinium under similar conditions. Though confirmatory experiments (such as percolation) were not included in the present program, it is implied that quartz wool might serve as an effective adsorbent for protactinium from aluminum chloride in either liquid or vapor phase.

Nickel distillation tubes retained protactinium more strongly than did quartz. Most of the retained protactinium was recovered by leaching the nickel with dilute nitric acid or with HF solution. Some reaction of the salt mixture with nickel seems to have occurred; the salt was found to contain about 200 ppm Ni after the experiment.

In order to study the protactinium volatility phenomena with as little interference as possible from adsorption, two distillations were conducted in mechanically sealed Teflon tubes. A thorium chloride concentration of 0.5 mole % was used in order to have, initially, the materials entirely in solution. Distillation of 0.5 mole % $ThCl_4$–$AlCl_3$ mixtures contained in the Teflon tubes in the presence of helium atmosphere (dry glove box ambient) resulted in the transfer of 33% of the protactinium. A reverse distillation of the $AlCl_3$ (not shown in Table 3.14) transferred all of the activity back to the original region. Subsequent redistillation transferred 28% of the protactinium activity to the receiver. Complete transfer in the back distillation implies that there was no interaction between Teflon and protactinium. If this is accepted, then the lack of complete forward transfer must be interpreted as being due to the presence of $ThCl_4$. This, in turn, probably indicates adsorption of protactinium on precipitated $ThCl_4$, though complexing with $ThCl_4$ dissolved in the liquid $AlCl_3$ is also possible.

4. Fluoride Salt Production

J. H. Shaffer
W. K. R. Finnell
Wiley Jennings
F. A. Doss
W. P. Teichert
C. E. Roberts[1]

Prenuclear test operation of the Molten Salt Reactor Experiment (MSRE) is currently in progress with fused fluoride mixtures prepared by the Reactor Chemistry Division. When fully operational, the MSRE will have an inventory of approximately 26,500 lb of these fluoride mixtures. In addition to the fuel and the secondary coolant, the salt mixture now used in place of the reactor fuel will be retained for subsequent use to flush and clean the fuel circuit when maintenance on that system becomes necessary.

The coolant and flush salts currently in use in the MSRE are mixtures of ^{7}LiF and BeF_2 containing 66 mole % ^{7}LiF. All ^{7}LiF used in the production of MSRE fluoride mixtures was at least 99.99% pure ^{7}Li. However, that material having the highest ^{6}Li content was used for the reactor coolant mixture. Approximately 15,300 lb of the binary salt mixture was required for a coolant salt volume of about 44 ft^3 and a flush salt volume of about 75 ft^3.

Approximately 11,260 lb of the mixture ^{7}LiF-BeF_2-ZrF_4-UF_4 (65.0-29.1-5.0-0.9 mole % respectively) is required for the initial fuel loading of approximately 75 ft^3 in the reactor assembly. The MSRE fuel salt is being prepared as a fuel concentrate mixture and as a barren fuel solvent mixture. The fuel concentrate mixture will consist of the binary eutectic mixture ^{7}LiF-UF_4 (73-27 mole %) and will include all UF_4 required for the reactor fuel. Since fissionable ^{235}U will comprise only a third of the uranium inventory, this mixture will be produced as an enriched fuel concentrate mixture (with UF_4 that is highly enriched in ^{235}U) and as a depleted fuel concentrate mixture. The barren fuel solvent will consist of the balance of materials required to achieve the desired overall composition of the reactor fuel mixture. Since these mixtures will be combined in the MSRE fuel drain tank, the final fuel composition will, in fact, depend upon the amount of ^{235}U required to bring the system to the critical, and then to the operating conditions.

The production of fluoride mixtures for the MSRE was begun in March 1964. The coolant and flush salt mixtures were made available to the MSRE in September 1964. The various mixtures required for the reactor fuel will be completed by March 1965. The production process is based on techniques previously used for preparing fluoride mixtures for the Aircraft Reactor Experiment[2] together with refinements realized from process development programs during the intervening years.

PROCESS CHEMISTRY

MSRE fluoride mixtures are prepared from starting materials of very high purity, but further purification is needed before they are acceptable for reactor use. The removal of a limited number of impurity species during production operations is achieved by treatment of the fluoride melts with anhydrous HF, hydrogen, and, in some instances, a strong metallic reducing agent. Impurities that can be volatilized are removed in the process gas effluent stream; those that can be converted into insoluble particles are removed by filtration.

[1]The assistance of R. W. Ray, R. G. Ross, and B. F. Hitch is gratefully acknowledged.

[2]G. J. Nessle and W. R. Grimes, *Chem. Eng. Progr., Symp. Ser.* **56**(28), 51 (1960).

Oxide Removal

The raw materials, as received, undoubtedly contain some oxide or hydroxide. In addition, oxides or hydroxides are formed through reaction of the fluoride salts with their adsorbed water on heating. Oxides, which are sparingly soluble in the molten mixtures,[3] are removed during the initial gas sparging of the fluoride melt at 600°C with an anhydrous mixture of hydrogen fluoride in hydrogen. They react directly with hydrogen fluoride by the reaction

$$O^{2-} + 2HF \rightleftharpoons 2F^- + H_2O ,$$

and are conveniently removed from the process as water vapor. Recent measurements of equilibrium quotients for this reaction show that the efficiency of oxide removal by this process is high,[4] and, in the process equipment, the reaction with HF proceeds rapidly to near completion. Thus, the MSRE fluoride mixtures, as delivered, should have some "oxide capacity" to accommodate inadvertent contamination during reactor operations without formation of precipitates.

Sulfur Removal

Sulfur impurities need to be absent from MSRE fluoride mixtures to avoid corrosive attack on nickel-base alloys at elevated temperatures. Sulfur is found in the starting materials primarily as sulfate; this requires multiple treatment for removal from the fluoride mixture. During a preliminary treatment, sulfates are reduced to sulfides by the addition of beryllium metal turnings to the molten raw material.[5] Hydrogen sulfide is produced by the reaction

$$S^{2-} + 2HF \rightarrow 2F^- + H_2S ,$$

and is removed from the system (with the H_2O) in the gas effluent. However, the rate at which H_2S can be removed is low and is proportional to the hydrogen flow rate.[6] This condition may result from an intermediate reaction of H_2S with the nickel salt container; sulfur removal would be controlled by the reaction

$$H_2 + NiS \rightleftharpoons Ni^0 + H_2S .$$

Hydrogen flow rates of about 10 liters/min are used in the production process; the maximum sulfur removal rate has been approximately 0.7 g/hr.

Since removal of sulfur from molten fluoride mixtures is difficult, efforts were made to obtain raw materials that are free from sulfur. Of these raw materials, only beryllium fluoride was found to contain sulfur impurities, and through cooperative efforts with the vendors, sulfur impurities in this material were substantially reduced. Approximately two-thirds of the BeF_2 required by the MSRE was sulfur-free; the balance contained sulfur concentrations of 10 to 1000 ppm.

Removal of Structural-Metal Impurities

The INOR-8 alloy (Hastelloy N) used as the structural-metal container in the MSRE contains 6–8% chromium as a constituent. It is expected[7] that the chromium activity in the surface layer of metal in contact with MSRE fuel will be depleted until the following equilibrium is established:

$$Cr^0 + 2UF_4 \rightleftharpoons 2UF_3 + CrF_2 .$$

Nonequilibrium concentrations of structural-metal fluoride impurities that are more easily reduced than UF_4 (e.g., NiF_2 or FeF_2) would result in further depletion of chromium activity in the INOR-8 container. Structural-metal fluorides are present as impurities in the fluoride raw materials and may also be introduced by corrosion of the process equipment during production operations. Thus, the control of structural-metal fluoride concentrations in the purified fluoride mixtures is an important process consideration.

Hydrogen fluoride will readily attack structural metals and alloys that are suitable as salt containers at the operating temperatures of the produc-

[3] A. L. Mathews, C. F. Baes, Jr., and B. F. Hitch, p. 56, this report.

[4] *MSR Program Semiann. Progr. Rept. Jan. 31, 1964*, ORNL-3626, p. 137.

[5] *MSR Program Semiann. Progr. Rept. July 31, 1963*, ORNL-3529, p. 117.

[6] H. H. Stone and C. F. Baes, Jr., p. 72, this report.

[7] J. A. Lane, H. G. MacPherson, and F. Maslan (eds.), *Fluid Fuel Reactors*, p. 599, Addison-Wesley, Reading, Mass., 1958.

tion processes (600 to 800°C) by reactions of the type

$$M^0 + 2HF \rightleftharpoons MF_2 + H_2 .$$

However, metal surfaces that are in contact with the fluoride mixture cannot be protected by a fluoride corrosion film since the generated fluoride dissolves in the fluoride melt.

Process development studies have shown that the corrosion of nickel could be controlled by using mixtures of HF with hydrogen and that non-corrosive mixtures of these gases would also be effective for oxide and sulfur removal.[8] Thermodynamic values for corrosion processes in molten fluorides,[9] which also substantiate this process refinement, show that similar control of corrosion of iron and chromium would be impractical. Accordingly, nickel metal is used as the primary salt containment material in the process equipment. A gas mixture containing approximately $\frac{1}{10}$ mole fraction of HF in H_2 has been used effectively in the fluoride purification process.

Gas sparging of the melt at 700°C with hydrogen alone is used as a final phase of the purification process to reduce FeF_2 (initially present) and any remaining NiF_2 (formed during the process). The reduction of CrF_2 by hydrogen is too slow to be effective at process temperatures, but chromium concentrations of 25–50 ppm that are present in the starting materials are not prohibitive for reactor applications. When structural-metal fluoride concentrations are exceedingly high, beryllium metal, a strong reducing agent, is added to the melt. This treatment is followed by a mild hydrofluorination to convert the unreacted excess of beryllium metal to its fluoride salt. Insoluble metallic impurities are separated from the purified fluoride mixture by decantation and by filtration through sintered nickel during transfer of the molten mixture to its storage container.

PRODUCTION OPERATIONS

The MSRE fluoride mixtures are prepared in two batch processing units which are charged alternately with molten raw materials from a single meltdown furnace assembly. All operations are coordinated so that the batch processing units will operate on a semicontinuous schedule. Figure 4.1 shows the floor plan of the main operating level of the production facility and indicates the flow of materials through the processing units.

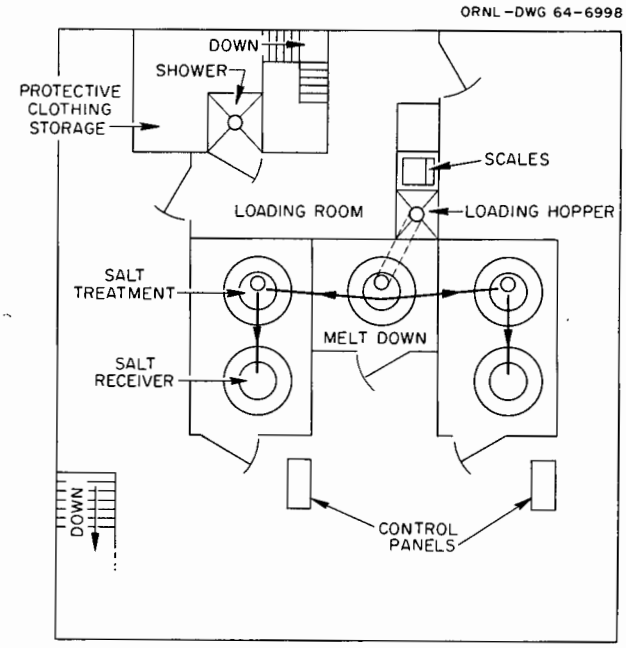

Fig. 4.1. Fluoride Production Facility – Layout of Operating Level.

Starting Materials

When possible, fluoride salts that are used as starting materials for the production of fused fluoride mixtures for the MSRE were purchased from commercial sources on a competitive bid arrangement; the chemical specifications are shown in Table 4.1. While materials obtained for use in preparing MSRE fluoride mixtures were generally within these specified limits, iron concentrations of 250 and 500 ppm were allowed in BeF_2 and LiF respectively. Some carbonaceous impurities were also allowed since they are converted to finely divided carbon at high temperature and are swept out by gas sparging. Approximately 12,000 lb of beryllium fluoride was purchased for preparing the first reactor loading of fluoride mixtures. Zirconium tetrafluoride, relatively free of hafnium (<100 ppm) and otherwise of high purity, was also found to be readily available from commercial

[8] J. H. Shaffer *et al.*, *Reactor Chem. Div. Ann. Progr. Rept. Jan. 31, 1962*, ORNL-3262, p. 27.

[9] C. M. Blood, *Solubility and Stability of Structural Metal Difluorides in Molten Fluoride Mixtures*, ORNL-CF-61-5-4 (Sept. 21, 1961).

Table 4.1. Fluoride Production for MSRE – General Chemical Specifications for Starting Materials

Impurity	Allowable Concentration (wt %) (1 ppm = 0.0001 wt %)
Water	0.1
Cu	0.005
Fe	0.01
Ni	0.0025
S	0.025
Cr	0.0025
Al	0.015
Si	0.01
B	0.0005
Na	0.05
Ca	0.01
Mg	0.01
K	0.01
Li (natural)	0.005
Zr (natural)	0.025
Cd	0.001
Rare earths (total)	0.001

sources. Approximately 2300 lb of this material was purchased for use in the MSRE fuel mixture.

To minimize the neutron-absorption cross section of the MSRE fuel, all lithium fluoride used in salt mixtures for the MSRE must be essentially free of the ^{6}Li isotope. Sufficient ^{7}LiF (22,000 lb) was obtained from the USAEC for one complete reactor loading and for the planned replacement of the flush and fuel salt mixtures.

Although the ^{235}U enrichment in the MSRE fuel mixture during power operation will be only approximately 30%, all ^{235}U was obtained for processing as highly enriched (93% in ^{235}U) uranium tetrafluoride. About 90 kg of ^{235}U will be required for reactor tests currently scheduled. The balance of uranium inventory in the reactor fuel system will be made up of UF_4 that is depleted of ^{235}U. These materials were obtained from USAEC sources.

^{7}LiF Densification

The lithium fluoride, as received, was found to have a very low bulk density and to contain substantial amounts of water. Since the direct use of this material would result in loss of production capacity and excessive oxide contamination, all ^{7}LiF was pretreated to improve these properties.

Heating the LiF, with periodic agitation, to 400°C under a flowing mixture of helium and anhydrous HF and then to 650°C under helium produced a free-flowing granular product with a minimum of LiOH.[10] All 22,000 lb of ^{7}LiF on hand was processed in this fashion in batches of 200 to 300 lb each. The production-scale equipment consisted of a horizontal Monel reaction vessel (17 in. in diameter by 8 ft long) equipped with a full-length agitator and a heating jacket. The average bulk density of the ^{7}LiF was increased from about 0.6 to 1.1 g/cm^{3} by this operation.

Charging and Meltdown Operations

Because of the toxicity of beryllium fluoride, the handling of raw materials is done in a loading room that is isolated by air locks from other areas of the production plant. Personnel working within the loading room wear fully protective plastic fresh-air suits to avoid exposure to these hazardous chemicals. Raw materials are assembled in this area, weighed into appropriate batch sizes in a well-ventilated hood enclosure, and transferred to the meltdown furnace by a vibratory conveyor.

The meltdown furnace assembly shown in Fig. 4.2 adjoins the raw materials loading room; it provides a molten charge to each of the two adjacent batch processing units. After meltdown, the molten fluoride mixture is sparged with hydrogen and helium at relatively high flow rates to remove insoluble carbon by entrainment. Beryllium metal turnings are also added to the molten charge to reduce sulfate impurities to sulfides and to reduce structural-metal impurities to their insoluble metallic states. During subsequent transfer of material to a batch processing unit, some separation of these insoluble impurities by decantation is achieved.

Melt Purification

Each of the two processing units has a capacity of 2 ft^{3} of salt per batch; 94 batches are required

[10] J. H. Shaffer *et al.*, *Reactor Chem. Div. Ann. Progr. Rept. Jan. 31, 1964*, ORNL-3591, p. 62.

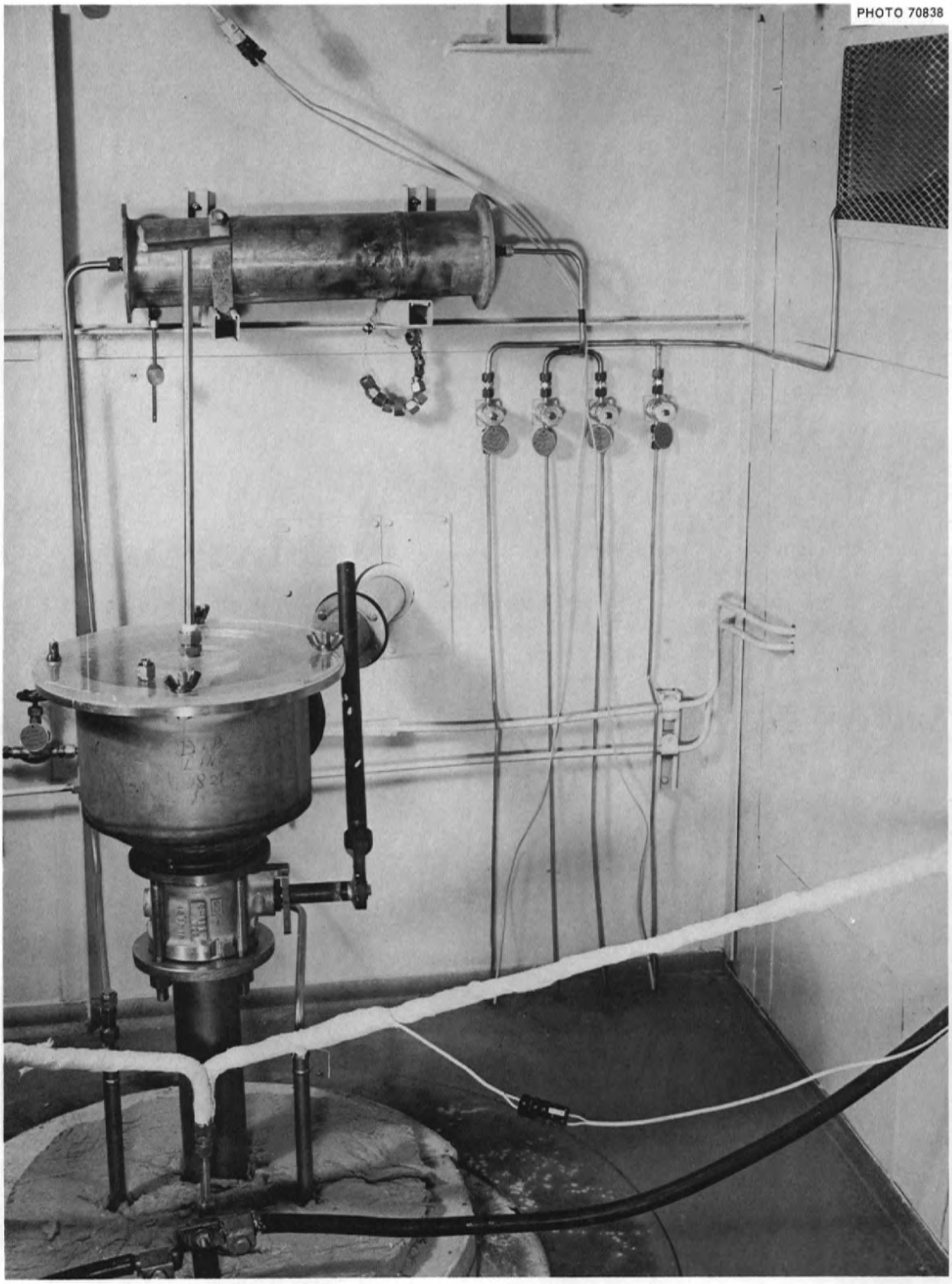

Fig. 4.2. Fluoride Production Facility – Premelting Furnace Assembly.

for the MSRE, and a 10% excess is planned to allow for usual contingencies. Although production rates vary with the quality of the starting materials, the average batch cycle encountered for MSRE production, including maintenance shutdown periods, has been about 164 hr.

Salt treatment vessels used in the process and the meltdown units are constructed of 12-in. IPS 304L stainless steel pipe and are approximately 6 ft in length. An inner liner fabricated from $\frac{1}{8}$-in. grade A nickel sheet provides primary salt containment. Except for conventional loading ports and gas line connections, the vessel is of welded construction. Nickel containers, of the same approximate diameter but 3 ft in length, are used to store and dispense purified salt mixtures. The treatment vessels and salt storage vessels are heated by commercial resistance furnaces of 50 and 25 kw respectively.

A simplified schematic flow diagram of the unit process is shown in Fig. 4.3. The salt treatment vessel connects directly to the receiver vessel (salt storage container) through a small diameter tube, which functions as the process gas entry line during purification of the fluoride mixture and as the salt transfer line at the completion of the process. These vessels are also connected through the gas manifold system to provide centralized control over process conditions during salt purification and regulation of the differential gas pressure on the system during transfer of the molten charge to its storage container.

The gas effluent from the process is passed through a bed of sodium fluoride pellets to reduce HF concentrations to low values before discharge to the atmosphere. Since large quantities of hydrogen are used, exhaust gases are bubbled through an inert liquid trap to isolate the process equipment from the atmosphere.

At the completion of the production cycle, the purified fluoride mixture is transferred to the salt storage container and allowed to cool. Interim storage under a static helium cover gas is provided within the production facility.

PROCESS CONTROL

To ensure delivery of acceptable fluoride mixtures to the MSRE, control of material balances and process conditions is maintained for each phase of the production operation. In addition to accounts that show the source, quality, and amounts of raw materials used in each production batch, various measures are exercised during the processing cycle to provide quality control of the finished product. Primary process control is

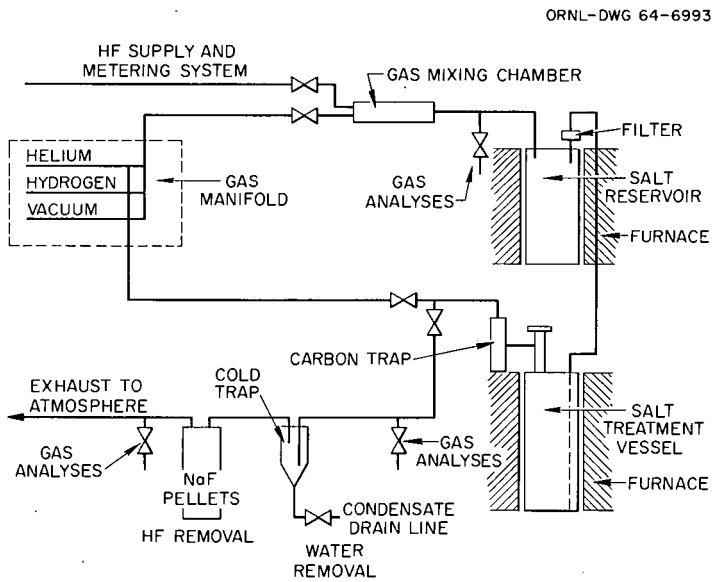

Fig. 4.3. Fluoride Production Facility – Simplified Schematic Process Diagram.

achieved by frequent analyses of the process gas streams. These analyses serve as guides for alteration or termination of process conditions and are, therefore, directly related to production efficiency and quality control. Secondary control of product quality is derived from chemical analyses of salt samples that are withdrawn from melts during processing operations.

Process Gas Analyses

The HF-H_2 concentration ratio in the gas influent to the salt treatment vessel is monitored by direct titration of a side stream with a standard KOH solution. A similar titration of the gas effluent stream is used to determine HF utilization. Typical results obtained during preparation of the MSRE coolant salt mixture, illustrated in Fig. 4.4, show the high HF utilization that is characteristic during initial treatment of the molten raw materials.

Hydrogen sulfide, collected in an ammoniacal cadmium chloride solution from the gas effluent stream, is determined by titration with a standard iodine solution. Material balances on sulfur evolved as H_2S from the treatment vessel as compared with the quantity of sulfur believed to be present in the raw materials charge are often in disagreement and probably result from the precipitation of sulfur compounds in the meltdown furnace. However, experience obtained during the production operations shows that, when all sulfate is reduced to sulfide, the rate of H_2S evolution indicates the concentration of sulfur remaining in the melt. Removal of sulfur from the melt, therefore, is not considered complete until a subsequent addition of beryllium metal fails to result in an increase in the H_2S evolution rate.

Water vapor, which results from the reaction of HF with oxide ion in the melt, is nearly completely recovered from the gas effluent stream, with some HF, in a cold trap maintained at about −12°C. The contents of the cold trap are drained periodically and analyzed for water content. The reproducibility of results obtained by this process control method on a number of salt preparations is shown in Fig. 4.5. Oxide removal is considered complete when the water removal rate becomes negligible. During the final gas sparging treatment, the reduction of structural metals by hydrogen results in the evolution of HF. The rate of HF evolution indicates the reduction rate and, as shown by Fig. 4.6, is also a function of the structural-metal ion concentration of the melt. Therefore, the HF content of the gas effluent is monitored periodically by direct titration with a standard KOH solution. Values obtained by this procedure are used to determine the practical completion of the H_2 stripping process.

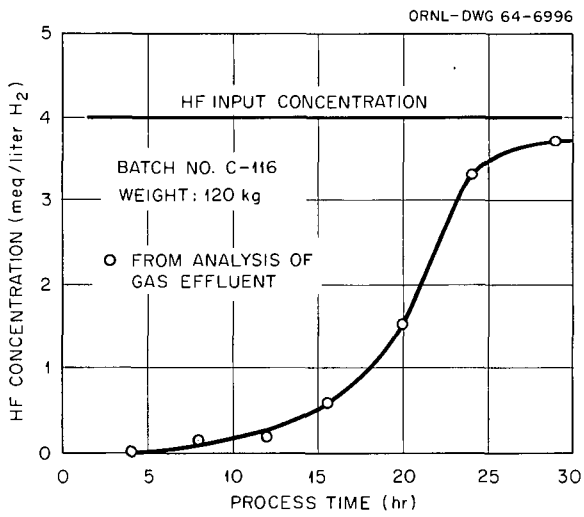

Fig. 4.4. Fluoride Production for MSRE – Utilization of HF During Purification of ^7LiF-BeF_2 (66-34 mole %) at 600°C.

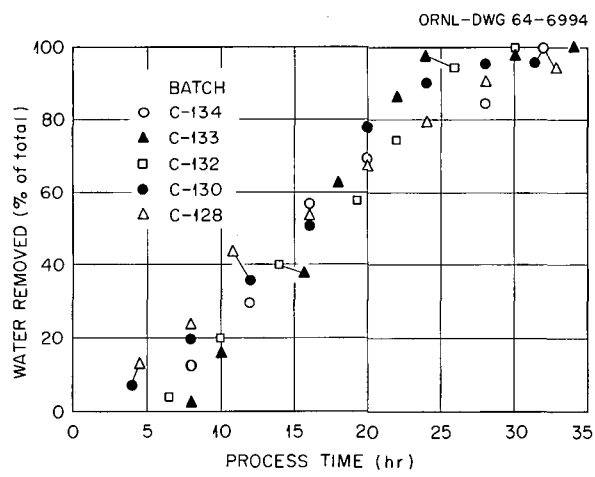

Fig. 4.5. Fluoride Production for MSRE – Removal of Oxides from ^7LiF-BeF_2 (66-34 mole %) During HF-H_2 Treatment at 600°C.

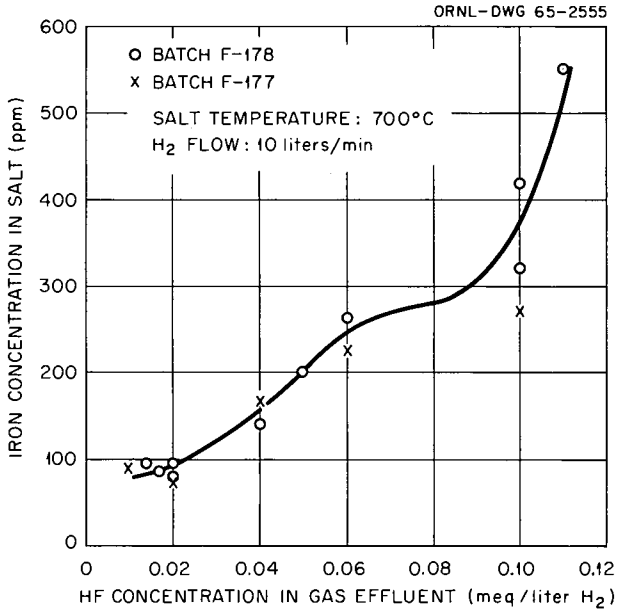

Fig. 4.6. Reduction of Iron Fluoride from MSRE Barren Fuel Solvent at 700°C by Hydrogen Sparging.

Salt Analyses

Samples of molten salt in process are withdrawn for analysis into copper filter tubes that have been previously fired in an atmosphere of flowing hydrogen. The sampling assembly, when fitted onto a valved port of the treatment vessel, permits sampling under existing process conditions without extraneous contamination to the batch or the sample.

Chemical analyses of filtered salt samples taken just prior to salt transfer into its storage container are considered to be representative of the production batch. Averages of concentrations of various impurities found in fluoride mixtures provided thus far for the MSRE are shown in Table 4.2. Values for "oxide removed" were determined from quantities of water collected in the effluent gas cold trap during the hydrofluorination treatment; they do not include water removed during the meltdown step.

PRODUCTION OF COMPONENT MIXTURES FOR THE MSRE FUEL

The fueling of the MSRE will be accomplished by the addition of component fluoride mixtures to the reactor fuel drain tank until the required salt volume (~75 ft^3) having the approximate composition ^7LiF-BeF_2-ZrF_4-UF_4 (65.0-29.1-5.0-0.9 mole % respectively) is achieved. These component mixtures are commonly referred to as the enriched fuel concentrate, which contains all ^{235}U required by the MSRE as the mixture ^7LiF-$^{235}UF_4$ (73-27 mole %), the depleted fuel concentrate, which contains the balance of nonfissionable uranium (also as the binary eutectic of UF_4 with ^7LiF), and the barren fuel solvent, which consists of the remaining components as the mixture ^7LiF-BeF_2-ZrF_4 (64.7-30.1-5.2 mole %). Two batches (~600 lb) of the ^7LiF-UF_4 mixture with depleted uranium

Table 4.2. Fluoride Production for MSRE – Average of Chemical Analyses of Salt Batches

Salt Mixture	Chemical Composition	Average Concentration of Impurities (ppm)				
		Cr	Ni	Fe	S	"Oxide Removed"
Coolant	^7LiF-BeF_2 (66-34 mole %)	19	26	166	<5	1460
Flush	^7LiF-BeF_2 (66-34 mole %)	16	39	123	<5	1650
Fuel solvent	^7LiF-BeF_2-ZrF_4 (64.7-30.1-5.2 mole %)	21	15	77	<5	728
Fuel concentrate	^7LiF-UF_4 (73-27 mole %)	24	35	49	10	1700

will be prepared in the large-scale production apparatus. Production of the enriched fuel concentrate required special apparatus and procedures to provide for nuclear safety and for planned reactor operations.

Preparation of Enriched Fuel Concentrate

MSRE operations, as currently scheduled, will require approximately 90 kg of ^{235}U. The preparation of this quantity of fissionable uranium, in six equal batches containing 15 kg of ^{235}U each, satisfactorily met requirements for nuclear safety and reactor fueling operations and permitted the economical use of existing process equipment.

The reaction vessel was constructed from a 36-in. length of 6-in. IPS, sched 40 pipe (stainless steel 304L). The vessel was provided with an inner liner fabricated from $\frac{1}{8}$-in. nickel sheet. Storage containers for the finished batches of enriched fuel concentrate mixture were constructed from 36-in. lengths of 4-in. IPS, sched 40 grade A nickel pipe. All vessels were of welded construction except for loading ports and gas line connections. The overall design of these vessels provided for a liquid depth of about 29 in. in the salt storage container and a dry mix depth of about 26 in. in the reaction vessel.

Batches of raw material were blended and loaded into the salt treatment vessels by the Special Processing Group of the Y-12 Plant. Each batch contained about 4.9 kg of ^{7}LiF and about 21.6 kg of $^{235}UF_4$. The loaded vessels were then transferred to the fluoride production facility, where

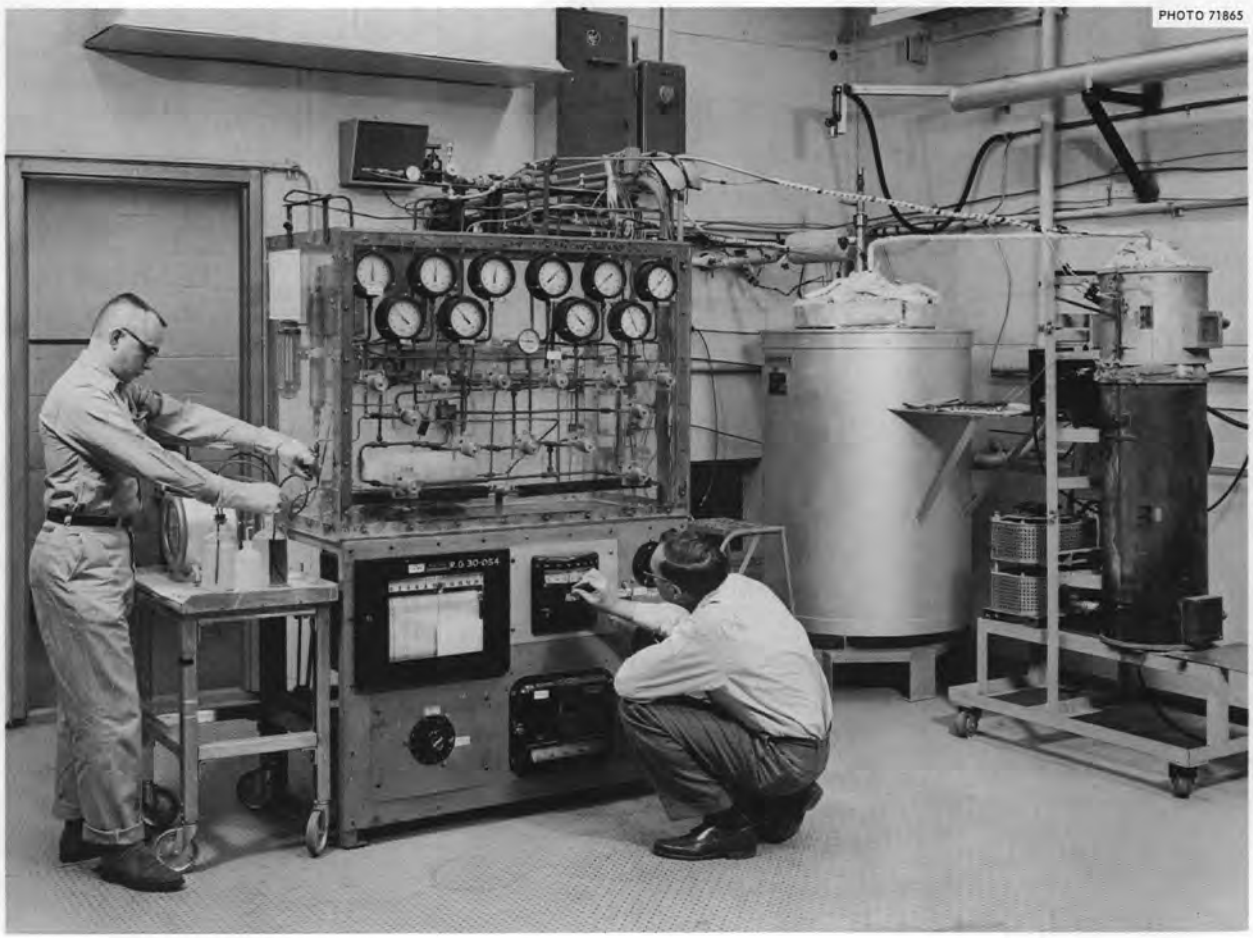

Fig. 4.7. Fluoride Production for MSRE – Process Equipment for Enriched Fuel Concentrate Mixture.

the salt mixture was melted, further purified, and transferred to salt storage containers by procedures previously described for the production of other MSRE mixtures. A photograph of the process equipment is shown in Fig. 4.7. The processed batches of enriched fuel concentrate are in storage in the Y-12 Plant.

Preparation of Fuel Enriching Capsules

Incremental additions of ^{235}U will be made to the circulating reactor fuel by dissolving a fused eutectic mixture of ^{7}LiF-$^{235}UF_4$ (73-27 mole %) from a small capsule that will be lowered into the bowl of the fuel pump. The fuel enriching capsules are constructed from 6-in. lengths of $\frac{3}{4}$-in.-OD × 0.035-in.-wall nickel tubing with hemispherical bottoms. The top plug of each capsule is penetrated by two $\frac{1}{8}$-in.-OD × 0.025-in.-wall nickel fill tubes. For filling purposes, seven capsules will be connected in series by their fill tubes and clustered within a 4-in.-diam heating chamber. Some 154 capsules will be filled from a prepared batch of the enriched fuel concentrate mixture. Each fill operation will be monitored by radiography using a Norelco 160-kv, 6-ma portable x-ray unit and a TVX camera to control the salt liquid level in the last capsule. The filled capsule clusters will be sealed individually in watertight cans and placed in storage until needed at the reactor site.

REACTOR LOADING

In addition to the preparation of all fluoride mixtures for the MSRE, the Fluoride Production Group has been responsible for loading these materials into the drain tanks of the reactor facility. During the latter part of October 1964, approximately 5755 lb of the mixture ^{7}LiF-BeF_2 (66-34 mole %) was transferred from 22 salt storage containers to the coolant drain tank in the MSRE. An additional 9200 lb of this mixture was transferred from 36 containers into a fuel drain tank during November 1964. This material is currently in use in place of the fuel mixture for prenuclear test operation of the reactor. These operations were accomplished routinely and without detectable beryllium contamination to the reactor facility.

The fuel salt is scheduled for addition to the MSRE in April 1965. Although the filling operations will be similar to those encountered for the coolant and flush salt additions, the loading procedure will accommodate the calibration of drain tank weigh cells, a check-out of uranium inventory procedures and salt-mixing characteristics, and an orderly approach to critical operation of the reactor. After the bulk of the fuel solvent mixture has been added (and the weigh cell calibrations compared with those previously obtained during the flush salt addition), the depleted fuel concentrate will be added in controlled increments. The salt mixture will be homogenized by gas sparging and by salt transfers within the fuel circuit. Chemical analyses of salt samples withdrawn from the mixture will be the basis for evaluating salt mixing characteristics and the uranium inventory.

The approach to critical operation will be made by incremental additions of the enriched fuel concentrate to the fuel drain tank. Although the quantity of ^{235}U that will be added in this manner will be regulated by the nuclear characteristics of the fuel mixture, it is anticipated that approximately 90% of the ^{235}U required for initial reactor operation will be added via the fuel drain tank. The balance of ^{235}U required will be added from enriching capsules in the fuel pump bowl.

PRODUCTION ECONOMICS

During the course of fused fluoride production at ORNL, modifications and revisions have been made on the facility to meet specific safety requirements and to incorporate procedural changes that have resulted from process development programs. The replacement value of the production facility is probably in the range of $300,000 to $500,000.

The operation of the production facility for the preparation of MSRE materials has been conducted on a seven-day, three-shift schedule. Each of the four shifts has required a technician for operational control and a research mechanic for routine maintenance. Other supporting crafts were employed for nonroutine maintenance as required. Operation, maintenance, and equipment costs were budgeted at an average of $20,000 per month.

Fluoride starting materials that have been acquired for the production of MSRE materials have values as shown in Table 4.3. The raw materials cost for the coolant and flush salt mixture, ^{7}LiF-BeF_2 (66-34 mole %), is $11.29 per pound and that of the fuel salt, excluding ^{235}U costs, is $10.13 per pound. As calculated from operating and raw materials costs (but not plant amortization), the coolant and flush salt mixture has an estimated value of $19.71 per pound. A similar cost for the fuel salt mixture, excluding ^{235}U, is estimated at $17.33 per pound. Thus, the initial charge of coolant, flush, and fuel salt mixtures for the MSRE will have an estimated value of $496,400, exclusive of plant amortization and uranium costs.

Table 4.3. Fluoride Production for MSRE – Raw Materials Costs

Material	Quantity	Unit Cost	Total Cost
^{7}LiF	22,000 lb	$16.50[a]	$363,000
BeF_2	12,000 lb	5.70	68,400
ZrF_4	2,300 lb	8.00	18,400
UF_4	90 kg (^{235}U Basis)	12,000	1,080,000
		Total	$1,529,800

[a]Includes $1.82 per pound for preparation as fluoride salt.

Part II

Aqueous Reactors

5. Chemistry of Pressurized-Water Reactor Systems

F. H. Sweeton C. F. Baes R. W. Ray

Behavior of ionic species in the very pure coolant water circulating in PWR systems has been studied[1] to provide, if possible, improved design and operation of such reactors and their auxiliary water purification systems. The primary tool for this study has been the pressurized-water loop[2] that was operated in the ORR from 1959 to the summer of 1964. Data discussed below were obtained during the last ten months of this period, when the loop temperature was relatively low (300–350°F or 149–176°C) in order to avoid overheating the cores of fuel experiments that were simultaneously being tested for the Army. This study was terminated when operation of the loop was discontinued in the summer of 1964.

BEHAVIOR IN ORR LOOP

Corrosion-Product Chemistry

Corrosion products were sampled, as previously reported, from cooled loop water flowing in a special side stream containing a flowmeter, a Millipore filter (normally with 0.10-μ pores), and a cation exchanger column. Samples of solids and of soluble cations were each analyzed[3] spectrographically and radiochemically. The results of the analyses are shown in Table 5.1; the radiochemical data are presented in the form of activation times calculated under the assumptions given at the foot of the table. Data given in the previous report[1] are included for completeness.

These data show that the different corrosion products were transported to different degrees and by different mechanisms. Table 5.2 shows that dissolved iron, dissolved nickel, and suspended iron were the major corrosion products in the loop water. Dissolved manganese and suspended chromium were of intermediate importance; dissolved chromium and cobalt and suspended nickel, cobalt, and manganese were of minor importance. Table 5.3 shows the abundance of various corrosion products in loop water, relative to iron.

The relative radioactivity of the various nuclides in the loop water is shown by the averages in Table 5.4. These nuclides, when arranged in decreasing order of importance as sources of penetrating radiation, are ^{60}Co, ^{59}Fe, ^{54}Mn, ^{58}Co, ^{51}Cr, and ^{55}Fe. The table shows that the soluble constituents were the chief source of radioactivity. The most important of these was ^{60}Co. The normal source of ^{60}Co in pressurized-water systems is the cobalt impurity normally found in the stainless steel used in construction. However, in the present case the average ^{60}Co concentration was perhaps doubled by the inadvertent release of soluble cobalt from an irradiated flux suppressor in one of the fuel assemblies being tested in the loop. The nuclides next in importance, soluble ^{59}Fe, ^{54}Mn, and ^{58}Co, were at least an order of magnitude below the ^{60}Co in importance as sources of radiation.

The series of chemical analyses was helpful in following the release of soluble cobalt from the defective flux suppressor. The fuel assembly bearing this suppressor was inserted into the loop during the fourth month of this series of tests. During the first three weeks of its irradiation the concentration of cobalt increased enough to be

[1] F. H. Sweeton *et al.*, *Reactor Chem. Div. Ann. Progr. Rept. Jan. 31, 1964*, ORNL-3591, pp. 67–69.

[2] I. T. Dudley, D. E. Tidwell, and D. B. Trauger, *Design Report for NSMR Pressurized-Water Loop at ORR*, ORNL-3188 (Dec. 19, 1962).

[3] The analyses were made by the Analytical Chemistry Division under the supervision of W. R. Musick and E. I. Wyatt.

Table 5.1. Characterization of Soluble and Insoluble Corrosion Products in Water of ORR Pressurized-Water Loop

Sampling Time		Filter Pore Diameter	Loop Temperature	Concentration (moles/liter)					Calculation Activation Times[a] (days)					
Start	End	(μ)	(°C)	Fe	Co	Cr	Mn	Ni	^{55}Fe	^{59}Fe	^{58}Co	^{60}Co	^{54}Mn	^{51}Cr
				Insoluble Components										
				$\times 10^{-9}$	$\times 10^{-9}$	$\times 10^{-9}$	$\times 10^{-9}$	$\times 10^{-9}$						
8-30-63	8-31-63	0.45	149	444	<25	551	2.2	40.7	110	42	13.3	>0.3	107	0.23
8-31-63	9-03-63	0.45	149	16.3	<2	5.6	<0.05	1.2	49	12.5	10.2	>0.5	22	0.33
9-03-63	9-13-63	0.45	149	6.4	<0.3	0.6	< 0.03	0.4	29	4.9	3.4	>0.7	19	0.64
9-19-63	10-11-63	0.45	149	20.3	<1.6	2.0	<0.09	0.8	8.4	3.1	4.4	>0.3	8.7	0.32
10-17-63	10-24-63	0.10	149	79.5	<0.3	0.6	<0.09	1.9	4.5	0.76	1.38	>0.9	0.6	0.30
10-29-63	10-30-63	0.10	149											
11-01-63	11-13-63	0.10	149–177	206	<1.1	19	<0.11	3.7	12.6	2.3	4.6	>2.5	1.0	0.16
11-22-63	12-03-63	0.10	177	50	<0.5	1.9	<0.06	0.93						
12-06-63	12-13-63	0.10	38	22	<0.8	1.2	<0.09	0.87	5.1	0.96	1.02	>0.16	0.35	0.28
12-20-63	12-23-63	0.10	177	136	<5.1	6.2	<0.5	4.3	3.1	0.45	0.88	>0.11	0.51	0.18
12-23-63	1-07-64	0.10	177	21	<1.9	2.1	0.0	1.2	3.5	0.70	0.67	>0.07	2.3	0.12
1-16-64	2-03-64	0.10	177	15	<0.3	0.3	<0.7	1.5	7.8	1.05	1.9	>1.3	1.4	0.07
2-18-64	2-22-64	0.10	135	16	<0.8	<0.7	<0.2	3.1	13.5	3.7	12.3	>1.7	19	>0.09
2-27-64	3-05-64	0.10	149	8.7	<0.5	<0.4	<0.12	1.1	10.0	1.17	1.6	>0.74	2.4	>0.04
3-11-64	3-30-64	0.10	149	6.3	<0.3	0.23	<0.10	0.9	6.3	1.36	0.68	>0.46	1.4	0.38
3-31-64	4-05-64	0.10	177	10	<0.5	0.4	<0.17	1.5	10.7	1.63	1.1	>0.78	9.8	0.23
4-16-64	5-04-64	0.10	149–177	109	<0.4	0.9	0.0	16	4.9	0.36	0.16	>3.0	1.02	1.02
5-08-64	5-31-64	0.10	149–177	15	<0.5	<0.9	<0.17	1.8	13.4	2.12	1.28	>0.9	6.4	>0.16
6-18-64	7-14-64	0.10	149	6.8	<0.6	0.78	0.28	1.6	10.7	0.99	1.22	>0.49	3.4	0.28

Table 5.1 (continued)

Sampling Time Start	Sampling Time End	Filter Pore Diameter (μ)	Loop Temperature (°C)	Concentration (moles/liter) Fe	Co	Cr	Mn	Ni	Calculation Activation Times[a] (days) ^{55}Fe	^{59}Fe	^{58}Co	^{60}Co	^{54}Mn	^{51}Cr
				Soluble Cations										
				$\times 10^{-9}$	$\times 10^{-9}$	$\times 10^{-9}$	$\times 10^{-9}$	$\times 10^{-9}$						
8-30-63	8-31-63	0.45	149	60	<31	0.0	9	507	<8	<0.5	0.04	>0.13	29.5	
8-31-63	9-03-63	0.45	149	70	<2.6	0.0	8	44	6.4	1.2	0.75	>1.5	94	
9-03-63	9-13-63	0.45	149	119	0.0	0.3	4.5	16.2	4.2	0.72	2.77		35	<0.3
9-19-63	10-11-63	0.45	149	646	<1.6	0.7	29	277	0.22	0.06	0.17	>3.5	4.6	<0.03
10-17-63	10-24-63	0.10	149	491	<1.0	4.2	18	152	1.2	0.34	0.35	>6.5	10.5	<0.13
10-29-63	10-30-63	0.10	149	2300	<4.8	21	93	752	0.3	0.09	0.09	>1.75	2.2	<0.03
11-01-63	11-13-63	0.10	149–177	11.3	<0.5	0.4	2.1	6.6	56.5	11.5	5.6	>9.3	576	<0.2
11-22-63	12-03-63	0.10	177	157	<8.3	2.2	3.8	10.5		0.85	4.4	>0.7	46	<0.03
12-06-63	12-13-63	0.10	38	13.9		<0.2	1.3	23	2.9	0.65	1.2		61	<0.03
12-20-63	12-23-63	0.10	177	98		1.0	10.9	90	6.5	1.05	0.88		70	<0.04
12-23-63	1-07-64	0.10	177	131	1.2	1.3	14	74	4.0	0.99	1.06	9.3	34	<0.11
1-16-64	2-03-64	0.10	177	442	1.8	7.2	47	252	1.0	0.39	0.39	25	26	<0.09
2-18-64	2-22-64	0.10	135	130	3.2	0	8.6	407	3.1	2.4	0.75	20	42	
2-27-64	3-05-64	0.10	149	111	1.55	0	6.0	146	5.9	0.91	0.85	22	22	
3-11-64	3-30-64	0.10	149	122	1.8	<0.24	5.5	146	10.1	1.7	1.05	16	24	
3-31-64	4-05-64	0.10	177	123	1.3	<0.4	7.0	63	9.7	1.7	2.17	21	36	
4-16-64	5-04-64	0.10	149–177	145	0.9	0.2	11.7	164	4.8	0.67	0.72	25	43	<45
5-08-64	5-31-64	0.10	149–177	95	0.85	<1.1	7.5	188	4.4	1.0	1.01	34	17	>10
6-18-64	7-14-64	0.10	149	150	<0.4	13	8.5	102	3.0	0.45	2.9	>45	190	1.0

[a]For this calculation it has been assumed that the thermal and fast fluxes were 5.0 and 4.0×10^{13} neutrons cm^{-2} sec^{-1}, respectively, that the irradiation was continuous until sampling time, and that the radionuclide remained with its parent. The last assumption should be valid for ^{55}Fe, ^{59}Fe, ^{60}Co, and ^{51}Cr, whose parents are nuclides of the same elements, but may well be in error for ^{58}Co and ^{54}Mn, whose parents are ^{58}Ni and ^{54}Fe. The cross sections (10^{-24} cm^2) and abundances (%) of the parents of these six nuclides have been taken to be: 2.3, 5.84; 0.98, 0.31; 0.091, 67.8; 36.0, 100; 0.050, 5.84; 15.0, 4.31.

Table 5.2. Average[a] Concentrations of Corrosion Products Found

Element	Average Concentration (10^{-9} M)	
	Dissolved	Suspended
Fe	219	40
Ni	145	2.9
Cr	2.9	4.7
Co	0.7–1.7[b]	<0.9
Mn	14	0.04–0.12[b]

[a]Each analysis weighted according to the length of sampling period.

[b]Ranges in value arise from averaging results which include "less than" values.

readable by spectrographic analysis, and the ^{60}Co activity rose significantly.

A considerable amount of information about the transport of iron and the other corrosion products can be deduced from the analytical data. Iron was the primary constituent of both soluble and the insoluble fractions of corrosion products. The iron was present largely in the soluble form; we believe this was due to both the higher solubility of Fe_3O_4 at the relatively low operating temperature of the loop, and a low rate of solids generation by the thick protective film formed during four years of prior operation. Using the Fe and ^{59}Fe analytical data for samples 13 and 19 of Table 5.1 (samples taken when the fuel experiments had been in the reactor for two months or more), and knowing that the ratio of in-flux to out-of-flux surface was 0.04, we can calculate that the in-flux surface

Table 5.3. Corrosion-Product Ratios

	Moles Ni / Moles Fe	Moles Cr / Moles Fe	Moles Mn / Moles Fe	Moles Co / Moles Fe
Type 300 stainless steel	0.12–0.18	0.24–0.29	≦0.02	
Found in solution	0.66	0.013	0.064	0.003–0.008[a]
Found in suspension	0.07	0.12	0.001–0.003[a]	<0.02

[a]Ranges in value arise from averaging results which include "less than" values.

Table 5.4. Nuclide Concentrations Found and Calculated Activation Times

Nuclide	Parent	Half-Life	Average[a] Concentration (dis sec^{-1} $liter^{-1}$)		Average[a] Calculated Activation Time (days)	
			Dissolved	Suspended	Dissolved	Suspended
^{55}Fe	^{54}Fe	2.94 years	1400	1500	7.2	10.6
^{59}Fe	^{58}Fe	45.1 days	160	175	1.4	2.3
^{58}Co	^{58}Ni	72 days	1800	90	1.5	2.2
^{60}Co	^{59}Co	5.27 years	7600	230	>20	>1.2
^{54}Mn	^{54}Fe	300 days	1100	48	80	5.3
^{51}Cr	^{50}Cr	27.8 days	1300–1560	545	~5	>3.1

[a]Each analysis weighted according to the length of sampling period.

released insoluble iron at about the same rate per unit area as the out-of-flux surface. In the case of soluble iron we can calculate that the in-flux surface was probably somewhat less effective than the out-of-flux.

Electron micrographs furnish further qualitative information about the transport of iron in the loop water. We expect that the fine irregular crystallites shown in the left side of Fig. 5.1 were formed in some region of supersaturation. The large sharply defined crystals in the right side of Fig. 5.1 indicate, as has been noted previously,[4] that considerable regrowth occurred. The long rods in this same micrograph are, we think, crystals grown by the mechanism of screw dislocation and substantiate that appreciable crystal growth was from solution. The dendrite formation of Fig. 5.2 was found in one crud sample and is a special case of the same growth mechanism.

The presence of cobalt was seen mainly in terms of the ^{60}Co formed from it. An appreciable part of the cobalt released by the defective fuel assembly was not directly removed by the purification system, but was adsorbed by the loop walls. This was shown by the fact that, although the ^{60}Co concentration quickly dropped to one-half on removal of the assembly, it decreased slowly thereafter. The purification rate (3% of the loop volume per minute) had apparently been unable to remove cobalt as rapidly as it was released to solution.

Nickel, present in the water almost entirely in soluble form, was of interest primarily as the parent of ^{58}Co, one of the important radioactive corrosion species. The ratio of nickel to iron in the loop water averaged about three times that in the original stainless steel, showing that nickel

[4] C. F. Baes and T. H. Handley, "PWR Chemistry Studies of the ORR In-Pile Loop," pp. 367–89 in *The Third Conference on Nuclear Reactor Chemistry*, TID-7641, Office of Technical Services, Department of Commerce, Washington, D.C., 1962.

PHOTO 68703

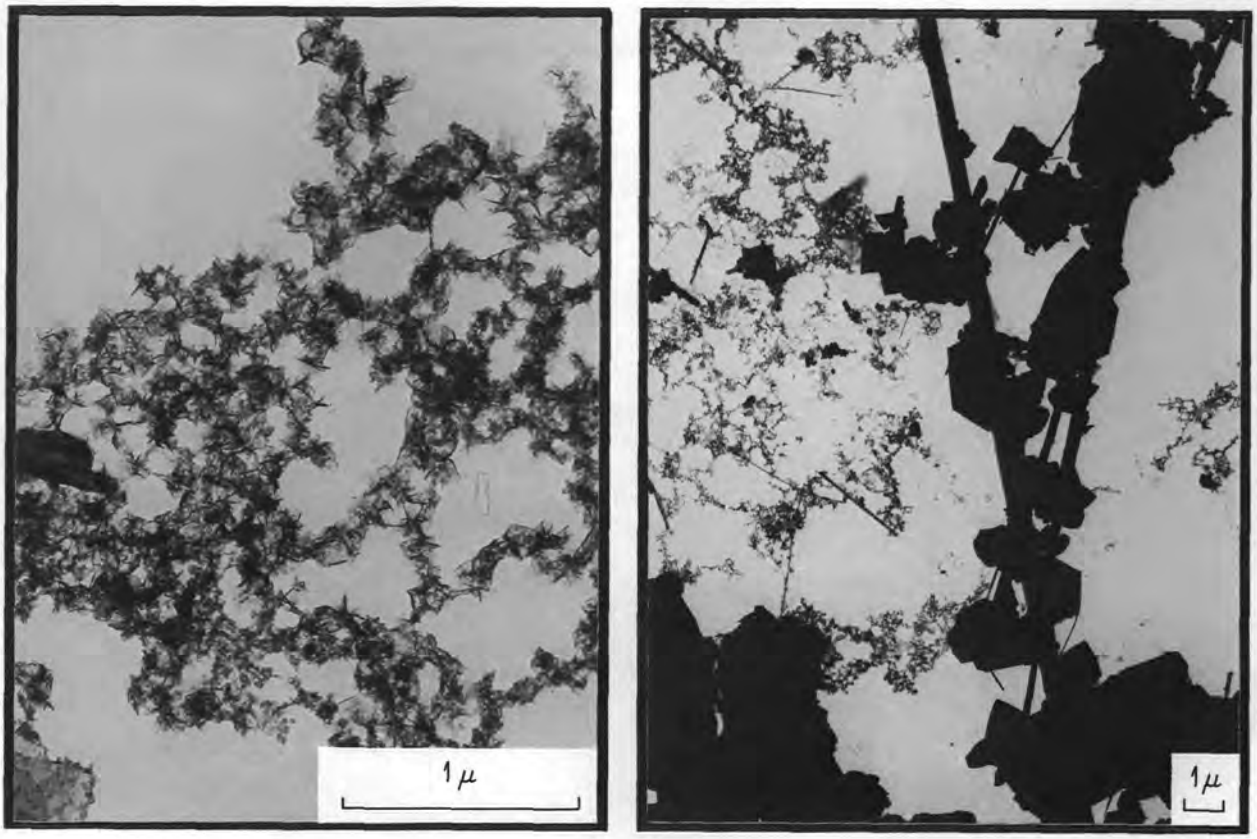

Fig. 5.1. Chemistry of Pressurized-Water Reactor Systems (Crud from ORR Pressurized-Water Loop).

was either being leached from the corrosion film faster than the iron, was being removed from the solution less effectively than was iron, or both. The ^{58}Co occurred in the water largely in the soluble form.

Manganese was also found to be almost completely in the soluble form; the Mn/Fe ratio in solution was three times that in the stainless steel. We presume that much of the manganese separated from the iron during regrowth of the Fe_3O_4 crystals and that additional manganese may have diffused out of the corrosion film.

Very little chromium appeared in the loop water under normal conditions. The Cr/Fe ratio, both in solution and in suspension (see Table 5.3), averaged definitely less than that of the original stainless steel. The surface of the oxide layer on the stainless steel must have been growing rich in chromium, as is commonly observed in corrosion of stainless steel. The fact that the suspended solids did not normally show such an enrichment lends support to the conclusion that a considerable portion of the suspended crud had been reformed from soluble constituents.

Some of these observations of corrosion-product behavior suggest methods for reducing the transport of corrosion-product activity from in-flux to out-of-flux regions of pressurized-water reactors. The appearance of the solids indicates that they were formed in regions where the solution was supersaturated in iron. The qualitative indication of a low in-flux release rate suggests that the supersaturation occurs in this region. Our solubility studies (see below) give independent evidence that the iron solubility should decrease as the solution is heated on passing through the in-flux region. Such supersaturation in a circulating solution leaving a reactor core should be removed easily by a bed of Fe_3O_4.

Fission Product Chemistry

The fission product activity level in the loop water was studied by occasional analyses of spot

PEM-3890-3

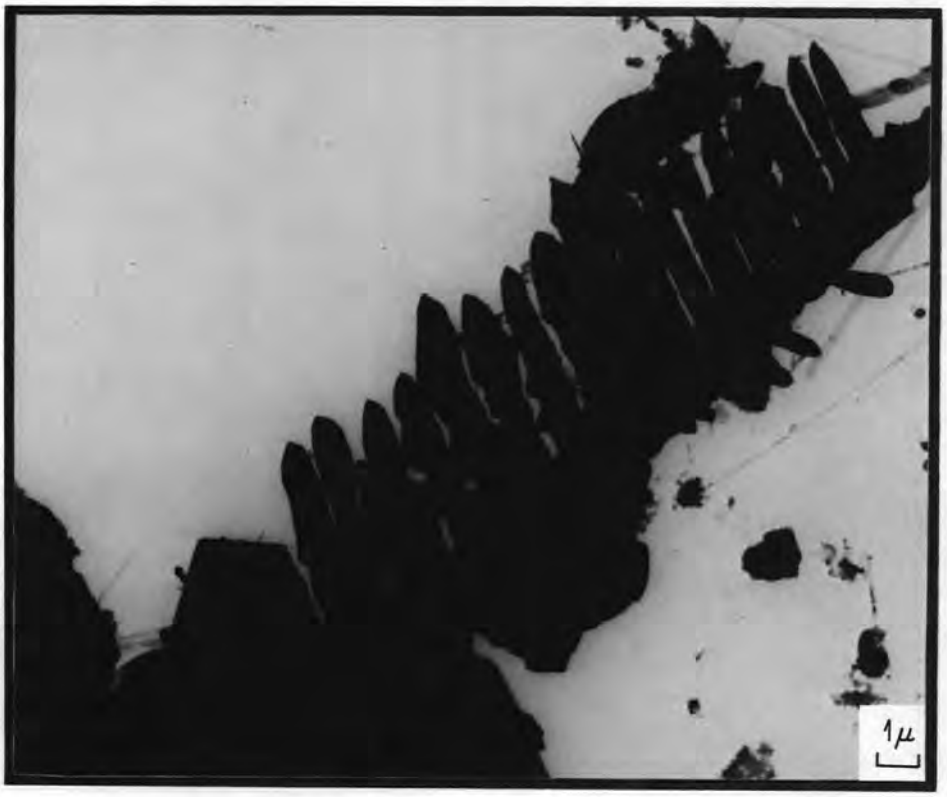

Fig. 5.2. Chemistry of Pressurized-Water Reactor Systems (Crud from ORR Pressurized-Water Loop).

samples of the water. One-liter samples were passed through a 0.30-μ Millipore filter before analysis, although early checks showed that less than 5% of the fission product activity could be stopped by the filter. The results of these analyses are given in Table 5.5; some data from the previous year are included for completeness.

The results appear to be routine up to May 1964. The first four samples, and that taken on February 26, 1964, represent loop operation without any fuel-test assemblies in the loop. The significant, yet limited, increase in fission product levels with the insertion of the fuel-test assemblies is undoubtedly due to small ^{235}U impurities on the

Table 5.5. Fission Product Analyses of Water from Pressurized-Water Loop

Date of Sample	Disintegrations per Second per Liter at Sampling Time[a]				
	^{91}Sr (9.67 hr)	^{92}Sr (2.6 hr)	^{132}I (2.33 hr)	^{133}I (20.8 hr)	^{134}I (52.5 min)
6-21-63	112[b]		586[b]	81[b]	
7-10-63	194[b]	311[b]	418[b]	87[b]	
7-31-63	99[b]	311[b]	434[b]	83[b]	
8-21-63	61[b]	272[b]	472[b]	87[b]	
9-18-63	209	505	1,852	292	
10-18-63	120	412	995	160	
11-14-63	255	536	1,087	172	
12-24-63	318	1466	222	377	3,495
1-09-64	245	956	948	317	3,384
2-04-64	640	932	893	300	
2-26-64	177[b]	275[b]	144[b]	89[b]	1,074[b,c]
4-02-64	301	426	735	168	1,896[c]
4-21-64	485	678	1,061	369	3,161[c]
5-26-64	630	786	5,605	7,655	9,290[c]
5-28-64	602	754	3,693	6,515	7,135[c]
5-31-64	384	561	2,680	2,222	5,259[c]
6-15-64	506	484	2,542	8,932	11,350
6-23-64	527	587	2,227[c]	2,332	6,026
6-30-64	742	633	15,350	21,715	44,000
7-02-64	280	590	8,823	9,070	4,307
7-10-64	719	1110	8,568	8,433	
7-15-64	426	599	11,200	14,000	12,470[d]
7-28-64				6,660[c,e]	

[a]Expected accuracy is 10% or better unless otherwise indicated.
[b]With no fuel-test assemblies in the loop.
[c]Expected accuracy is 20%.
[d]Expected accuracy is 40%.
[e]Corrected back to reactor shutdown.

surface of the assemblies. The sharp increase in the iodine fission products in May was due to a leak in a specimen in the fuel assemblies.

Fe_3O_4 as High-Temperature Adsorbent

We repeated a test of Fe_3O_4 as a high-temperature adsorbent, using the experimental method previously reported.[1] This time the Fe_3O_4 sample had been sintered at 1200°C instead of 1400°C, the loop operating temperature was 350°F (177°C) instead of 300°F (149°C), and the test was not periodically interrupted as before to take gamma-spectrometer readings on the various units of the test system. The high concentration of ^{60}Co in the loop water at the time of this test interfered with our obtaining a good material balance for ^{59}Fe. We accounted for about half of the ^{59}Fe entering the system; about 90% of this was found on the Fe_3O_4, and the remainder on the cation exchanger placed downstream to scavenge any cations that could get through the Fe_3O_4 column. In addition, the Fe_3O_4 stopped about half of the cobalt activity and about two-thirds of the manganese. These data confirm the earlier conclusion that, under certain conditions at least, Fe_3O_4 can adsorb corrosion-product activity effectively from solution at elevated temperatures.

Our observation that the surface area of the Fe_3O_4 doubled during this test appears to be real, but we have no explanation. Our plans for further tests of Fe_3O_4 with water taken isothermally from the loop had to be canceled when the operation of the loop was discontinued.

SOLUBILITY OF Fe_3O_4

Magnetite (Fe_3O_4), the stable oxide resulting from high-temperature reaction of steel with water in the presence of hydrogen, is a recognized constituent of the corrosion film on steel in PWR systems. To dissolve in water, Fe_3O_4 must undergo an oxidation-reduction reaction of the type

$$Fe_3O_4 + 6H^+ + H_2 = 3Fe^{2+} + 4H_2O \ .$$

The extent of reaction, and the solubility, depends on hydrogen activity as well as on acidity and temperature. We are studying the solubility of Fe_3O_4 in neutral and slightly acid solutions at hydrogen pressures near 1 atm and at temperatures as high as 260°C to better understand transport of iron in reactor systems of the PWR type. The low solubility ($\sim 10^{-7}$ *M*) of Fe_3O_4 under these conditions makes use of radiotracer ^{59}Fe virtually essential.

The flowing system shown as Fig. 5.3 consists of a glass reservoir holding 12 liters of solution protected from air by a continuous flow of pure H_2 at 1 atm. Other integral components (not shown in Fig. 5.3) are connections through which water can circulate through thallium, and a mixed ion exchanger for removal of O_2 and ionic impurities. The water normally contained 10 to 30 ppb of O_2 and had a conductivity of less than 0.5 micromho/cm at 25°C. The Pulsafeeder pump which circulated the solution developed a pressure of about 1200 psi. The preheater, which brought the solution to the furnace temperature, contained platinum black to catalyze reaction of residual traces of O_2 with the dissolved H_2. The solution passed through the heated column containing 2.7 g of 30- to 50-mesh particles of Fe_3O_4 formed by sintering submicron particles at 1400°C, through a cooler, a Millipore filter (0.10-μ pores), a fine platinum capillary that limited the flow rate, and a cation exchanger, before returning to the reservoir. The solution in the system was in contact with glass, plastic, Teflon, stainless steel,

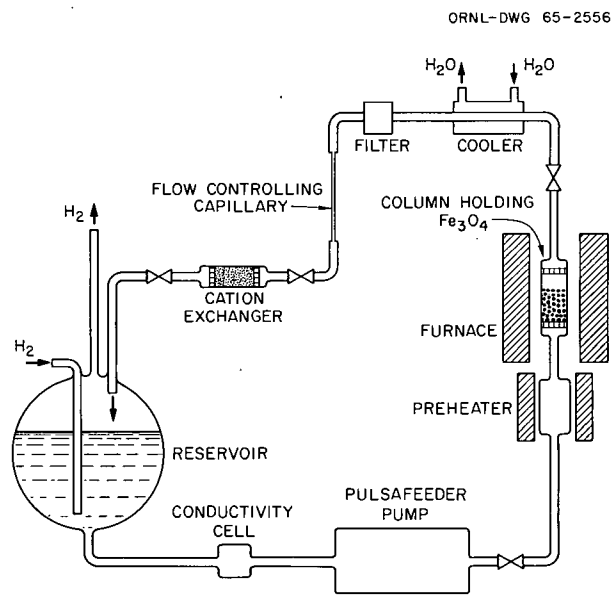

Fig. 5.3. Schematic Diagram of Flowing System for Determination of Solubility of Fe_3O_4.

platinum, nickel, and Monel alloy. Only the last three were used in the high-temperature regions. No stopcock grease was used in the system.

Dissolved iron was assayed through the radioactive ^{59}Fe induced in the Fe_3O_4 sample by prior irradiation in the ORR. During the tests, contamination of the sample with ^{60}Co, generated during the irradiation from cobalt impurity in the Fe_3O_4, became a problem. Cobalt-60 gamma radiation is difficult to separate from that of ^{59}Fe because the energies are almost the same. The ^{59}Fe activity, which was appreciably greater than the ^{60}Co at first, decayed with its 45-day half-life, and eventually became smaller than the ^{60}Co. Although cobalt in the sample on the ion exchanger could be easily separated by chemical methods, that on the filter and the metal parts of the solution-handling system could not. These parts were analyzed on a gamma spectrometer, and the ^{59}Fe and ^{60}Co peaks were resolved by comparison of the observed peaks with those of the pure ^{59}Fe and ^{60}Co.

The gamma spectra of the filters after these tests normally showed an $^{59}Fe/^{60}Co$ ratio 1.6 to 8 times that in the original Fe_3O_4. This indicated that essentially no solid Fe_3O_4 was being carried out of our column. As a result we have considered all of the activity found on the filter and the system both before and after the filter as actually representing soluble iron. Three tests showed the same $^{59}Fe/^{60}Co$ ratio in the material on the filter as in the original Fe_3O_4; we concluded that some of the solid had passed the retaining nickel frit of the column during a surge in flow. We therefore rejected the data from these tests.

In the initial experiments we determined only the activity on just the ion exchanger and filter. After a number of experiments we found that appreciable activity was held on the metal system. The first entry of Table 5.6 is a composite of these tests; it includes this latter activity. In each subsequent test we redetermined the activity on the metal system.

The flow rate was varied from test to test to check our expectation that the apparent solubility would decrease at higher flow rates due to lack of saturation. With the relatively high solubility at 200°C we may have observed such an effect. No such effect was observed at 260°C; in fact, the apparent solubility may have increased with flow rate.

We think the best values for the solubilities at 260 and 200°C are the averages of the tests, each weighted according to the volume of solution sampled. These averages are 330 and 1500 × 10^{-9} *M*, respectively, with uncertainties of perhaps 50%. The uncertainty cannot be estimated for the single result at 164°C, but, in view of the high flow rate used, this result is likely to be low.

Some solubility tests have been made in a rocking titanium autoclave with a capacity of 147 ml. Special samples of Fe_3O_4, prepared with a high specific activity of ^{59}Fe, were used. When pure H_2O served as the solvent, excessive amounts of activity were held up on the metal parts through which the solution was sampled. As a result we conclude that this static method was unsuitable for studies of such low solubilities.

We plan to use the flowing system for future tests, to minimize the amount of absorption of dissolved iron on the solution-carrying parts of the test system, to hold the solid Fe_3O_4 in its column more reliably, and to improve the accuracy of the assay procedures. Tests have been started to extend the measurements to acidic solutions.

Table 5.6. Solubility Tests by Flowing Method

Date	Flow Rate (ml/min)	Total Flow (liters)	Concentration of Total Iron (*M*)
		260°C	
			$\times 10^{-9}$
7-24-64 to 9-22-64[a]	2.0–8.6	22	312
9-23-64	3.9	3.9	66
9-24-64	4.7	4.6	357
10-05-64	1.7	9.1	128
10-09-64	0.93	8.0	92
10-21-64	2.5	42.5	309
11-13-64	3.0	47.9	457
		200°C	
9-25-64	3.7	14.6	726
9-29-64	2.6	10.0	884
10-02-64	0.97	3.8	1415
12-09-64	1.8	33.1	2100
		164°C	
11-25-64	2.0	33.0	1348

[a]This is a composite of 13 early tests.

6. Corrosion Studies for Aqueous Reactors and Chemical Processes

J. C. Griess
J. L. English L. L. Fairchild P. D. Neumann

CORROSION TESTS FOR THE HIGH FLUX ISOTOPE REACTOR

Corrosion studies with a large variety of materials having more or less permanent usage in the High Flux Isotope Reactor (HFIR) were completed. Preliminary data have been reported,[1,2] and final reports are in preparation on the results of laboratory[3] and dynamic loop tests.[4] Both types of tests were carried out in pH 5.0 water at 100°C and below. The laboratory tests employed water in equilibrium with air. Water in the loop tests contained approximately 5 ppm of dissolved oxygen. The laboratory tests were concerned with quiescent solutions, whereas water velocities in the loop tests varied from around 0.5 fpm to 81 fps. Specimens in the latter tests were electrically insulated from the loop system. In the preparation of dissimilar-metal couples, two or more flat coupons were bolted together with a bolt and nut made of one of the materials present in the couple. Upon completion of the tests, aluminum and beryllium specimens were cleaned cathodically in chromic-phosphoric acid solution. Stainless steels and other high-alloy materials were cathodically cleaned in inhibited sulfuric acid. The following sections summarize the results obtained.

[1] J. C. Griess *et al.*, *Reactor Chem. Div. Ann. Progr. Rept. Jan. 31, 1963*, ORNL-3417, pp. 66–68.

[2] J. C. Griess *et al.*, *Reactor Chem. Div. Ann. Progr. Rept. Jan. 31, 1964*, ORNL-3591, pp. 71–73.

[3] J. L. English and J. C. Griess, *Laboratory Corrosion Studies for the High Flux Isotope Reactor*, ORNL-TM-1029 (to be published).

[4] J. L. English and J. C. Griess, *Dynamic Corrosion Studies for the High Flux Isotope Reactor*, ORNL-TM-1030 (to be published).

Laboratory Studies

The addition of 0.8 ppm copper as cupric nitrate was found to cause a fourfold increase in the pitting frequency on 6061-T6 aluminum. When coupled with stainless steels and other high-alloy materials, 6061 aluminum in both annealed and T6 conditions was subject to substantial pitting on contact surfaces. The deepest penetration was 42 mils after 14,000 hr of contact with annealed type 410 stainless steel. With other materials, penetrations between 20 and 30 mils were not uncommon. Type 1100 aluminum was also subject to pitting when contacted by either Teflon or Celcon plastics.

Types 302, 303, 304, 316, and 17-4 PH stainless steel exhibited excellent resistance during extended exposure periods with corrosion rates less than 0.1 mil/year. These materials were immune to pitting attack. Sensitized specimens of an off-specification heat of type 304L stainless steel (0.4% carbon) showed no evidence of intergranular attack after 13,500 hr of exposure. The observed corrosion rate was less than 0.1 mil/year. Nitrided types 304 and 17-4 PH stainless steel were unsatisfactory, with signs of blistering. Two brazing alloys, designated GE-81 and AMS-4775, appeared the most corrosion resistant of five different alloys that were tested. Alnico V, a magnet alloy, behaved poorly at 50 and 100°C, with considerable scaling and pitting. Defected aluminum-clad rare-earth–aluminum compacts suffered severe swelling, blistering, and exfoliation at 100°C. The behavior of defected aluminum-clad tantalum-aluminum dispersions was excellent.

Plastics such as Chemloy 70719, Fluorogreen, Rulon A, and carbon-filled Teflon were completely

resistant at 50 and 100°C. Celcon and Delrin plastics showed acceptable behavior at 50°, but underwent degradation at 100°C.

Dynamic Loop Studies

Quadruplicate specimens of reactor-grade hot-pressed QMV beryllium were exposed for 17,600 hr at 100°C to two water velocities, 12.5 and 23 fps. Corrosion rates were constant and averaged 1.9 mils/year in each case; agreement in rates among the eight specimens did not deviate from the average rate by more than 0.1 mil/year. Only very thin films formed on all specimens during the exposure; the difference between final as-removed and defilmed weights varied between 0.1 and 0.2 mg/cm^2. All specimens were subject to pitting attack, which gradually increased to a maximum depth between 7 and 9 mils.

Also included in the tests at the two different velocities were specimens of the QMV beryllium coupled with 6061-T6 aluminum and with type 304 stainless steel. The beryllium-aluminum couples were exposed for the entire 17,600 hr. Corrosion rates for the beryllium were 1.7 and 2.0 mils/year, respectively, at flow rates of 12.5 and 23 fps. The aluminum specimens exhibited a rate of 0.2 mil/year at each velocity. As with the uncoupled beryllium specimens, the coupled beryllium specimens were prone to pitting attack on the water-exposed surface as well as on the contact surface. However, the intensity and frequency of the attack, even on contact surfaces, was about the same as was observed on the uncoupled specimens. The aluminum specimens exhibited random pitting to a maximum depth of 3 mils on the contact surfaces only.

The coupling of beryllium to stainless steel had no significant effect on the generalized corrosion rate of either material during an 11,980-hr exposure. However, the beryllium surface in direct contact with the stainless steel had pits up to 13 mils deep, which was about twice that experienced on the rest of the surface or on uncoupled specimens.

In other tests, specimens of 6061-T6 aluminum, X8001-F aluminum, and QMV beryllium were exposed at 100°C to four different flow velocity ranges: 22–23, 33–51, 51–72, and 72–81 fps. Final defilmed corrosion rates are given in Table 6.1. As shown, there was no effect of flow velocity on corrosion rates for the three materials tested.

Table 6.1. Effect of Velocity on the Corrosion of Aluminum Alloys and Beryllium in pH 5.0 Water at 100°C

Material	Exposure Time (hr)	Velocity Range (fps)	Corrosion Rate (mils/year)
6061-T6 Al	12,775	22–33	0.2
		33–51	0.2
		51–72	0.2
		72–81	0.2
X8001-F Al	11,775	22–33	0.3
		33–51	0.3
QMV Be	5,590	22–33	2.1[a]
		33–51	1.9[a]
	17,360	51–72	2.1[a]
		72–81	2.0[a]

[a]Pitting attack.

CORROSION STUDIES FOR THE TRANSURANIUM PROCESSING FACILITY

During the past year the testing program conducted to evaluate the corrosion behavior of materials of interest to the Transuranium Processing Facility (TRU) has been essentially completed. The results obtained have been included in reports issued by the Chemical Technology Division,[5–7] and a topical report covering the entire investigation has been prepared.[8]

Most recent tests have been concerned with hydrogen pickup in Zircaloy-2 and in commercially pure zirconium on exposure to hydrochloric acid solutions. The amount of hydrogen found in the metal after exposure has been roughly proportional to the amount of corrosion for both materials but otherwise independent of the test conditions. About 10 to 40% of the hydrogen formed by the

[5]W. D. Burch, *Transuranium Quart. Progr. Rept. Feb. 29, 1964*, ORNL-3651, pp. 68–69.

[6]W. D. Burch, *Transuranium Quart. Progr. Rept. Aug. 31, 1964*, ORNL-3739 (to be published).

[7]W. D. Burch, *Transuranium Quart. Progr. Rept. Nov. 30, 1964* (to be published).

[8]J. L. English and J. C. Griess, *Corrosion Studies for the Transuranium Processing Facility*, ORNL-TM-1031 (to be published).

corrosion reaction appeared in the metal. In comparable tests, the commercially pure material corroded two to four times faster than Zircaloy-2, although in both cases, corrosion rates were low. An attempt to reduce the amount of hydrogen entering the metal by alloying zirconium with 1% platinum was unsuccessful. A higher corrosion rate and greater hydrogen pickup were experienced by the platinum alloy than by zirconium itself.

In addition to the work with zirconium, tests to determine the resistance of numerous plastic materials to various process solutions, including organic solvents containing extractants, were also conducted.

CORROSION TESTING PROGRAM IN SUPPORT OF POWER-REACTOR FUEL-ELEMENT REPROCESSING

This corrosion testing program assists the Chemical Technology Division in the development of power-reactor fuel reprocessing methods and disposal of associated wastes. Each new dissolution and separation process proposed must be evaluated in terms of corrosion problems resulting from the process. Candidate materials for construction of containers, piping, reaction vessels, and other process equipment are screened under simulated process conditions. Those with potentially useful corrosion resistance are subjected to long-term tests, depending on their required service life. Because of the wide scope of the chemical processing development, a large variety of materials is tested under many different conditions.

Waste disposal tests were carried out to determine the suitability of type 304L stainless steel as a container material for calcination of waste products from the Darex process, either alone or in combination with various glass-forming substances. Straight Darex waste was calcined in type 304L containers at 900°C for 24 hr, with a metal loss of less than 0.003 in. No further metal loss occurred when heating was continued for 168 hr. The addition of various phosphates, borates, and aluminum nitrate improved the physical properties of the final product, but all additions resulted in increased corrosion rates.

For the chemical processing development program, studies were made for the purpose of selecting materials of construction for chemical equipment for processing various uranium-thorium-graphite fuels by both aqueous- and gas-phase processes. Duriron and tantalum were found to resist the 90% H_2SO_4–10% HNO_3 solution used to oxidize graphite in a wet process. Nickel 200, Hastelloy N, and Corronel 230 were found to be satisfactory for oxidizing graphite fuels in pure O_2 at temperatures up to 800°C. Type 309 SCb was slightly less resistant. Nickel 200 and Hastelloy N were also resistant to 60% O_2–40% HF mixtures at temperaatures up to 650°C.

Since midyear the emphasis has been entirely on the Gas Phase Head End Process, and a small-scale gas-circulating loop with a fluidized-bed chemical reactor was constructed to be used in these studies.

Pure nickel (ASTM SB-161, 162) was used for the fluidized-bed vessel, all piping, and orifice plates. Dalton-type fittings of Monel with Teflon gaskets were used in the cold sections of the loop. An ORGDP type B-4 pump having a nickel head, Monel piston, and phosphor-bronze bellows is used to circulate gases through the loop.

A fluidized bed of Al_2O_3 (–60 +120 mesh) serves as a heat transfer medium and support bed. Corrosion specimens are inserted in the fluidized bed and in the gas space above the bed.

A simulated decladding process using a 60-40 mixture of O_2-HF resulted in low corrosion rates for nickel and Hastelloy N in the fluidized bed, but substantial corrosion occurred in the cooler portions of the vessel.

The results of all testing are an integral part of the process development program and as such are included in reports issued by the Chemical Technology Division.[9–11]

---

[9]T. A. Gens, *Laboratory Development of a Process for Chlorinating the Combustion Ash from Graphite Fuels Containing ThC_2 and UC_2 and Recovering the Uranium by Solvent Extraction from a Solution of the Chlorinated Products*, ORNL-TM-789 (May 1964).

[10]F. G. Kitts, *Evaluation of an Engineering Demonstration of the Modified Zirflex and Neuflex Processes for the Preparation of Solvent Extraction Feeds from Unirradiated Zirconium-Base Reactor Fuels*, ORNL-3465 (March 1964).

[11]*Chem. Technol. Div. Ann. Progr. Rept. May 31, 1964*, ORNL-3627, pp. 20–21.

ACCEPTANCE TESTS

Approximately 100 boiling 65% HNO_3 tests and electrolytic oxalic acid etch tests (ASTM:A262-55T) were completed on austenitic stainless steels for use in various ORNL and Y-12 programs. The Y-12 programs accounted for nearly 90% of the tests. The remaining tests dealt with materials for the High Flux Isotope Reactor.

7. Mechanisms of Corrosion of Zirconium Alloys

G. H. Jenks

OXIDE GROWTH AND CAPACITANCE ON PREIRRADIATED ZIRCALOY-2

R. J. Davis

The mechanism of radiation corrosion of Zircaloy-2 is being studied by comparing the behavior of fast-neutron-irradiated specimens with unirradiated controls. Periodic measurements of weight gain and ac film impedance during postirradiation exposure to 300°C steam plus oxygen are employed in evaluating radiation effects.

Previous results[1] have included data on: (1) a specimen irradiated after pretreating at 500°C in helium for 16 hr to provide an oxygen-rich but film-free surface, and (2) a specimen irradiated after exposure to 300°C steam plus oxygen for four days to provide a substantial corrosion film. It was tentatively concluded that an acceleration of corrosion resulted from radiation damage in the metal (rather than in the oxide) and that irradiation of the oxide film did not increase the corrosion rate but did indeed retard it temporarily. Additional experiments, reported below, were carried out with the objective of verifying that the irradiation effect is in the metal and not in the oxide, and determining whether the irradiation effect in the metal is related to dissolved oxygen.

Experimental

Each specimen was first pickled in a mixture of HF and HNO_3 and then subjected to a pretreatment and, in some cases, to neutron irradiation as listed in Table 7.1. After pretreatment and irradiation the specimens were exposed to 300°C steam plus oxygen. Periodically, the specimens were removed from the oxidizing environment, and weight gain and ac film impedances were measured.

Details of the specimens, of the type III irradiation capsules which encase the specimens, and of the experimental procedures and assemblies employed are given in previous reports.[2,3]

Results and Discussion

Postirradiated Corrosion of Irradiated Specimens and Controls. – *Specimens 24 and 23 (Table 7.1).* – This experiment was a repeat of a previous one (specimens 15 and 14, Table 7.1) in which an irradiated, film-free specimen exhibited a greater corrosion than the control. The irradiated specimen in the present experiment also corroded more rapidly than the control, as shown in Fig. 7.1. The enhancement of corrosion due to irradiation was less in the present experiment than in the previous one. This difference in the two results is considered in more detail below.

The result of this experiment qualitatively verifies the previous result and confirms the conclusion that with this particular pretreatment, which leaves considerable dissolved oxygen near the surface, irradiation causes an enhancement of corrosion. Since no film was present during irradiation, the pertinent irradiation damage must have been in the metal.

Specimens 43 and 40 (Table 7.1). – This experiment was similar to a previous one (specimens 17 and 16, Table 7.1) in which a specimen irradiated

[1] R. J. Davis, *Reactor Chem. Div. Ann. Progr. Rept. Jan. 31, 1964*, ORNL-3591, pp. 80–83.

[2] R. J. Davis, *Reactor Chem. Div. Ann. Progr. Rept. Jan. 31, 1963*, ORNL-3417, pp. 70–72.

[3] R. J. Davis and G. H. Jenks, *Reactor Chem. Div. Ann. Progr. Rept. Jan. 31, 1962*, ORNL-3262, p. 84.

Table 7.1. Specimen Pretreatments – Procedures and Purposes

Irradiated[a] Specimen No.	Control Specimen No.	Pretreatment	Purpose of Pretreatment Was To Provide a Surface:
24[b]	23[b]	500°C in He for 16 hr, then 100°C in He for ten days	Free of oxide film, but with some dissolved oxygen near surface
43	40	300°C in steam + O_2 for 1 hr, then 100°C in He for ten days	Covered with a thin oxide film
34	32	800°C in He for 16 hr, then 100°C in He for ten days	Free of both oxide film and dissolved oxygen near surface
36	39	300°C in steam + O_2 for 64 hr, then 500°C in He for ten days	Nearly free of oxide film but very high in dissolved oxygen near surface
	26[b]	600°C in He for 16 hr	
	30[b]	500°C in He for 16 hr	To test effect of 100°C for ten days
	35	500°C in He for 2 hr	To provide extra oxygen near surface
	31	800°C in He for 16 hr	To test effect of 100°C for ten days
15[c]	14[c]	500°C in He for 16 hr, then 100°C in He for ten days	Free of oxide film, but with some dissolved oxygen near surface
17[c]	16[c]	300°C steam + O_2 for four days, then 100°C in He for ten days	Covered with heavy film

[a]Specimens were irradiated to fast neutrons during the ten days at 100°C periods.
[b]Pretreatment in pickled autoclaves.
[c]Data from these specimens were previously reported.[3]

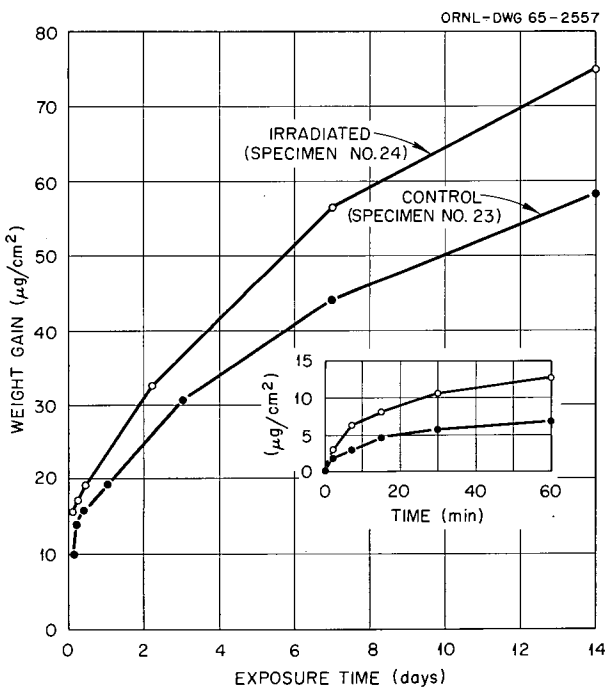

Fig. 7.1. Specimens Pretreated in Helium 16 hr at 500°C–Weight Gains.

with about 2700 A of preformed film was found to corrode less rapidly than the control for several days and then somewhat more rapidly. In the present experiment a specimen was irradiated with about 300 A of preformed film. The corrosion results (Fig. 7.2) were qualitatively the same as in the previous test; the irradiated specimen corroded more slowly than the control for 13 days. At about 13 days and at a weight gain of about 60 $\mu g/cm^2$, a discontinuity in the corrosion-time curve occurred. After 13 days the specimens appeared to corrode at approximately equal rates. Actually, as will be pointed out in a later paragraph, the rate constants for the two specimens were in approximate agreement after the discontinuity. These effects are qualitatively the same as those found in the previous experiment, and the weight gains at transition for the two experiments were approximately the same.

The results of this test confirm the conclusion that under the conditions of these experiments, irradiation of corrosion film results in a temporary retardation of corrosion.

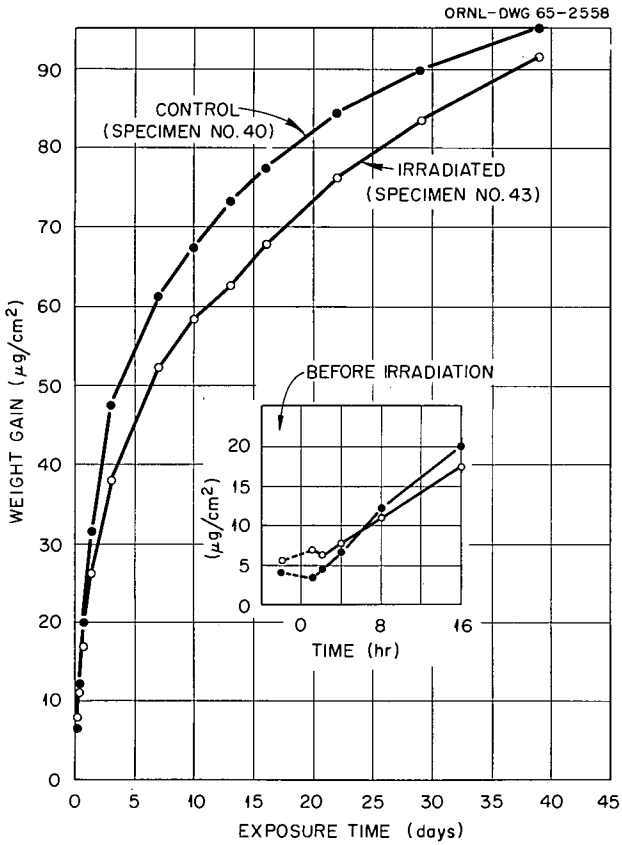

Fig. 7.2. Specimens Pretreated in Steam-Oxygen 1 hr at 300°C–Weight Gains.

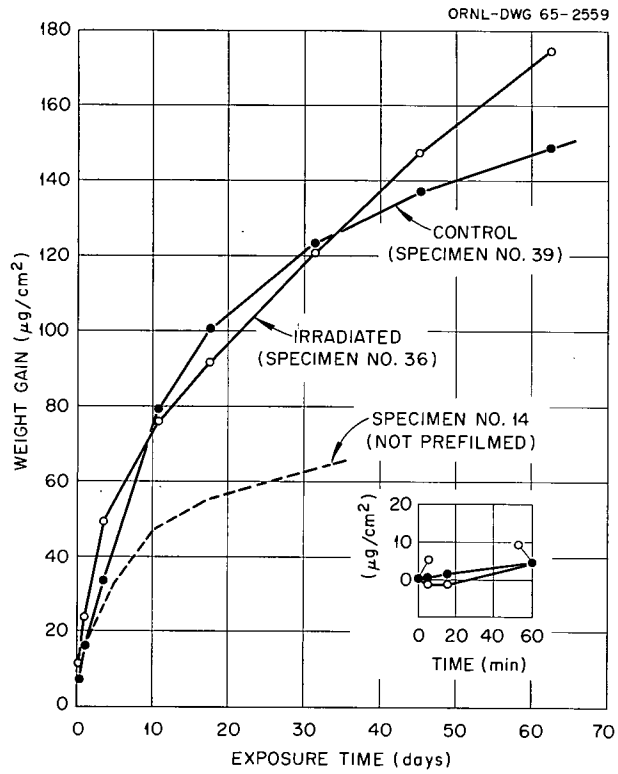

Fig. 7.3. Specimens Prefilmed in Steam-Oxygen 64 hr at 300°C, Then Heated in Helium 16 hr at 500°C–Weight Gains.

Specimens 34 and 32 (Table 7.1). – It had been hypothesized that the enhancement of corrosion which resulted from irradiation of film-free specimens (i.e., specimens prepared by pickling and then heating in helium at 500°C for 16 hr) was associated with the existence of an appreciable concentration of dissolved oxygen near the surface of the metal. As one test of this hypothesis, an experiment was conducted employing specimens which were prepared by pickling and then heating in helium at 800°C for 16 hr. This treatment dissolves any oxide on the surface and distributes the oxygen throughout the specimen, so that the oxygen concentration near the surface was very low in comparison to other treatments used in this work. The results (Fig. 7.4) clearly showed that the irradiated and control specimens corroded at the same rates.

Specimens 36 and 39 (Table 7.1). – To further test the dissolved-oxygen hypothesis, a test was done to see if the irradiation effect could be magnified by increasing the oxygen concentration near the surface. Specimens were prepared by prefilming to 30 to 40 $\mu g/cm^2$ weight gain, then heating in helium at 500°C for 16 hr. It has been reported[4] that this treatment results in dissolution of more than half of the oxide. Both specimens exhibited a dull coloring after the respective treatments, indicating that some film was present during irradiation. The postirradiation corrosion results are shown in Fig. 7.3 along with the curve for a previous control specimen (14) which was pretreated by pickling and heating at 500°C for 16 hr.

Three features of the results are noteworthy: (1) For the first several days (17 to 30 days), control 39 and irradiated specimen 36 corroded about the same amount; (2) after 17 days, irradiated

[4] J. P. Pemsler, *The Diffusion of Oxygen in Zirconium and Its Relation to Oxidation and Corrosion*, NMI-1177 (May 31, 1957).

specimen 36 corroded faster than control 39; and (3) control 36 corroded about twice as fast as a previous control specimen that had only a modest concentration of oxygen near the surface.

These results show that a very high concentration of oxygen enhances corrosion even without irradiation. The corrosion is further enhanced by irradiation, at least after an initial period. The corrosion during the initial period may have been affected by the temporary retardation phenomenon which occurs when specimens are irradiated with films. As will be pointed out in later paragraphs, the difference between the corrosion kinetics of the control and irradiated specimen after the initial period can be correlated with that found in experiments which employed specimens with lower concentrations of oxygen in the metal; this correlation shows that the radiation effect was greatest when the concentration of oxygen was greatest. The results thus support the hypothesis that the irradiation effect requires an appreciable concentration of dissolved oxygen in the metal and also indicate that the amount of effect increases with increasing concentrations of dissolved oxygen.

Film Impedance, Out-of-Radiation Experiments, and Additional Analyses of Kinetic Data. – All kinetic and capacitance data obtained to date are shown for reference in Figs. 7.4 and 7.5. A few of the tan δ data are plotted in Fig. 7.6.

Calculation of Kinetic and Film Impedance Parameters. – Calculated parameters are listed in Table 7.2. The weight gain data were digested on the basis of the logarithmic kinetic equation $dx/dt = Ae^{-Bx}$, where x and t are weight gain and exposure time. The integrated form of the equation is $x = 1/B \ln (ABt + a)$ (ref. 5). Values of A, B, and a determined from experimental data are listed in Table 7.2. The logarithmic equation was chosen as a basis for describing the weight gain data because most of the data fit the equation; and corrosion through pores in the oxide can give rise to these kinetics, and some of the data, as described below, suggest that the films are porous. The significances of the parameters in terms of the Evans[6] pore mechanism are (1) A is a measure of the reactivity of the metal, (2) B is the most powerful parameter in the equation and is related to the rate at which pores are closed off as the film grows, and (3) a is unity if the logarithmic relation is obeyed from time zero; any deviation from unity may result from different kinetics being obeyed in the thin film region. The value of B, but not that of A, can be determined unequivocally from weight gain–time data. The apparent value of A is affected by the presence of an unknown amount of oxide of unknown degree of protective quality at the start of weight gain measurements.

Values of apparent dielectric constant of the films, ϵ, listed in Table 7.2, were calculated from the slopes of the reciprocal capacitance vs weight-gain plots according to the relation

$$\epsilon = \frac{7.77 \times \text{weight gain}}{A/C} . \qquad (1)$$

This relation was derived from the more fundamental relation

$$C = C_1 + C_2 + \ldots + C_i = K \sum_i \frac{\epsilon_i A_i}{S_i} , \qquad (2)$$

where C_1, C_2, etc., are the capacitances of parallel increments, and ϵ_i, A_i, and S_i are the dielectric constant, the area, and the thickness of the ith parallel increment respectively. If the dielectric constant of every increment is the same, then

$$C = K\epsilon \sum_i \frac{A_i}{S_i} . \qquad (3)$$

If the film is also uniform in thickness, S is constant; then

$$C = K\epsilon A_{tot}/S_{av} , \qquad (4)$$

and the value of S_{av} can be estimated from the weight gain, and ϵ can be calculated as in Eq. (1). It will be argued in the discussion that the assumption of uniform film thickness is not valid and that high apparent ϵ values resulted from this assumption. For instance, if, on a particular specimen, 1% of the film area is 1% as thick as the average, then from Eq. (3),

$$C_x = K\epsilon \left(\frac{0.01 A_{tot}}{0.01 S_{av}} + \frac{0.99 A_{tot}}{1.01 S_{av}} \right) = 2 \left(K\epsilon \frac{A_{tot}}{S_{av}} \right) ,$$

[5] A. L. Bacarella, *Reactor Chem. Div. Ann. Progr. Rept. Jan. 31, 1963*, ORNL-3417, pp. 72–74.

[6] U. R. Evans, *The Corrosion and Oxidation of Metals*, p. 836, Edward Arnold, London, 1960.

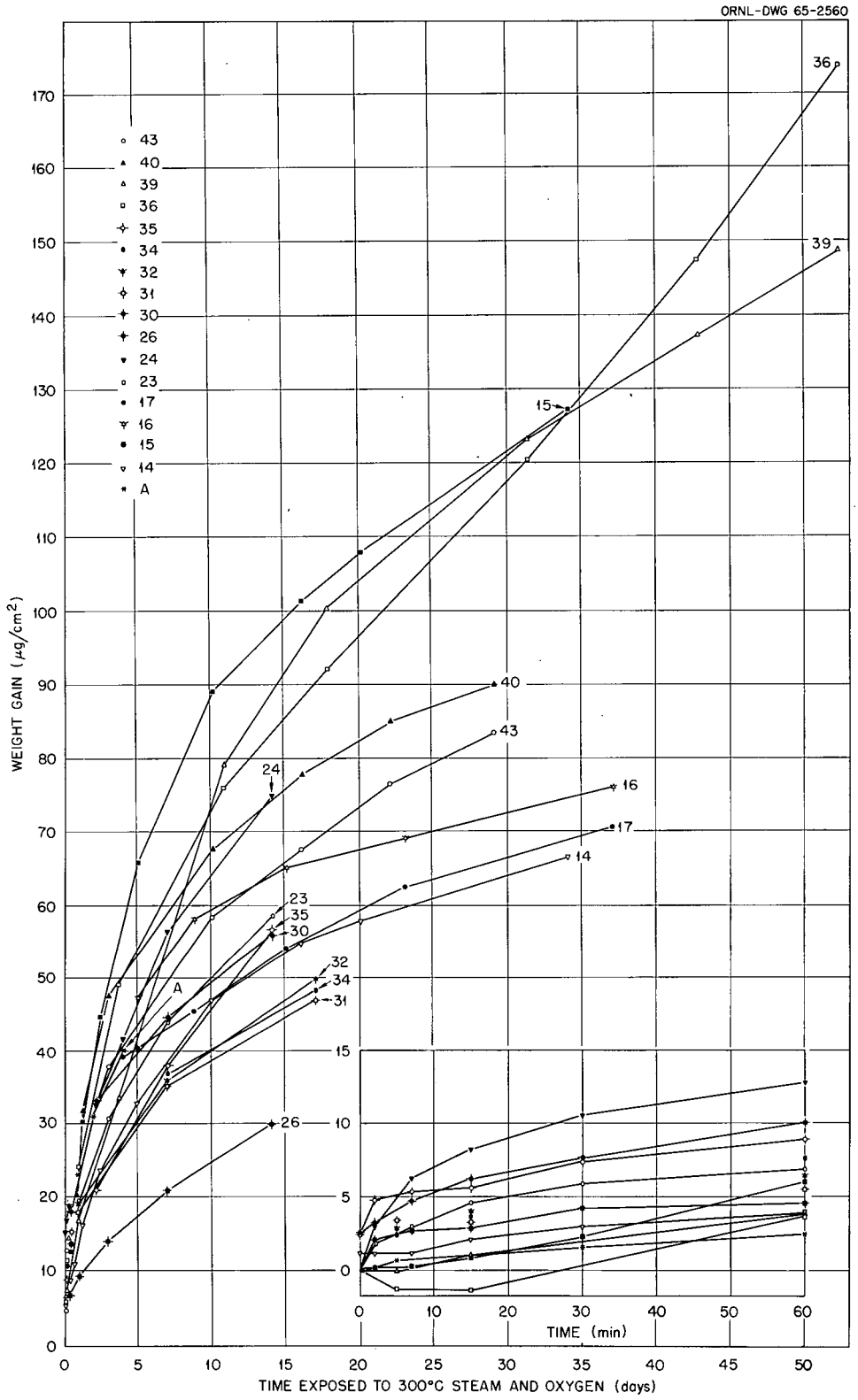

Fig. 7.4. Weight Gains vs Exposure Time.

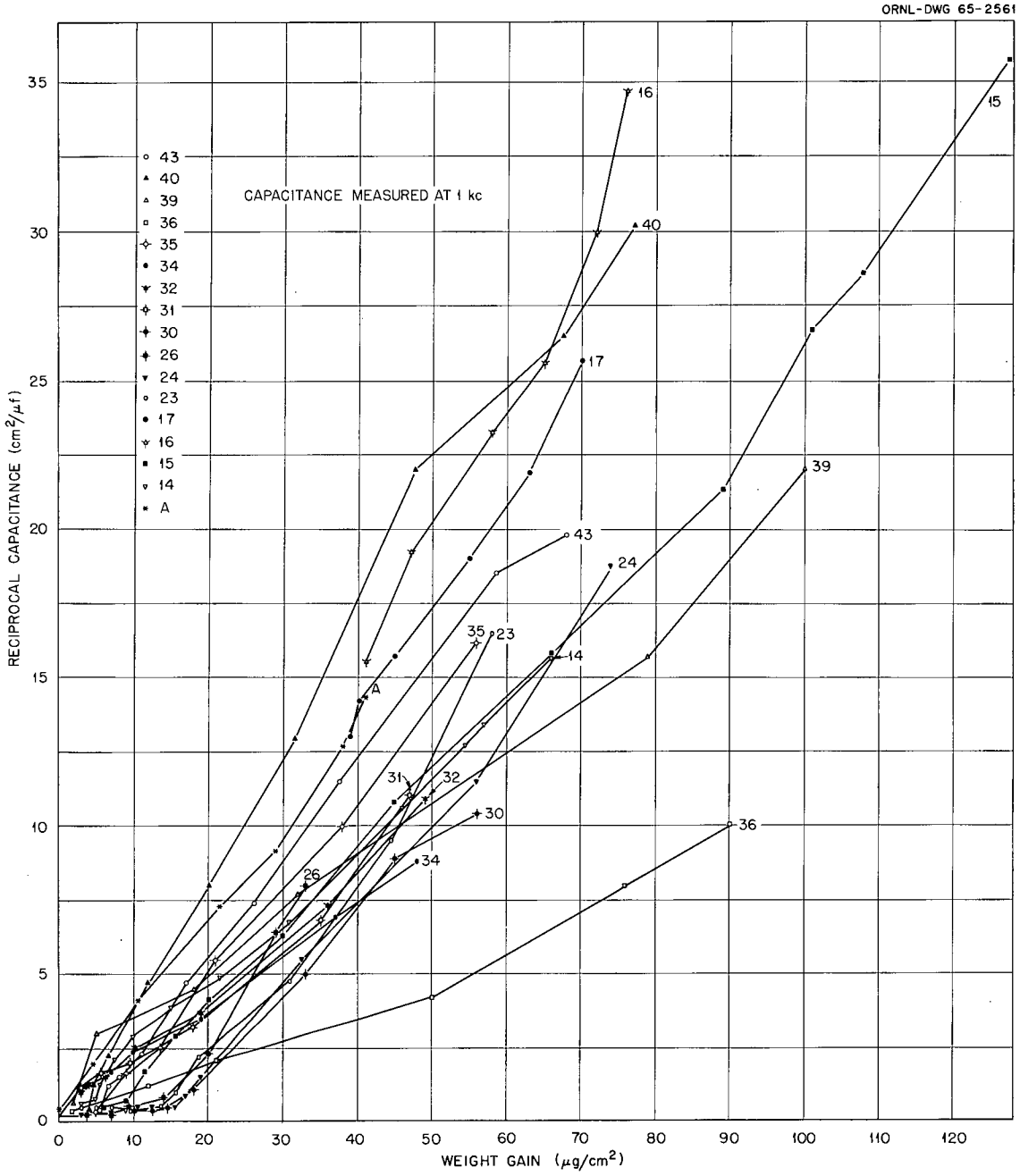

Fig. 7.5. Reciprocal Capacitance vs Weight Gain.

or twice the capacitance expected for a uniform film (Eq. 4), and the apparent ϵ from Eq. (1) would be twice the true value. There are, therefore, two possible interpretations of the values of apparent ϵ in Table 7.2: (1) the apparent ϵ's are the true dielectric constants, and the dielectric constants vary as shown; or (2) the true dielectric constant is 19 (the smallest observed) or less, and the discrepancy between 19 and the apparent ϵ's results from film porosity.

Tan δ is a directly observed parameter; observed values taken from Fig. 7.6 are listed in Table 7.2.

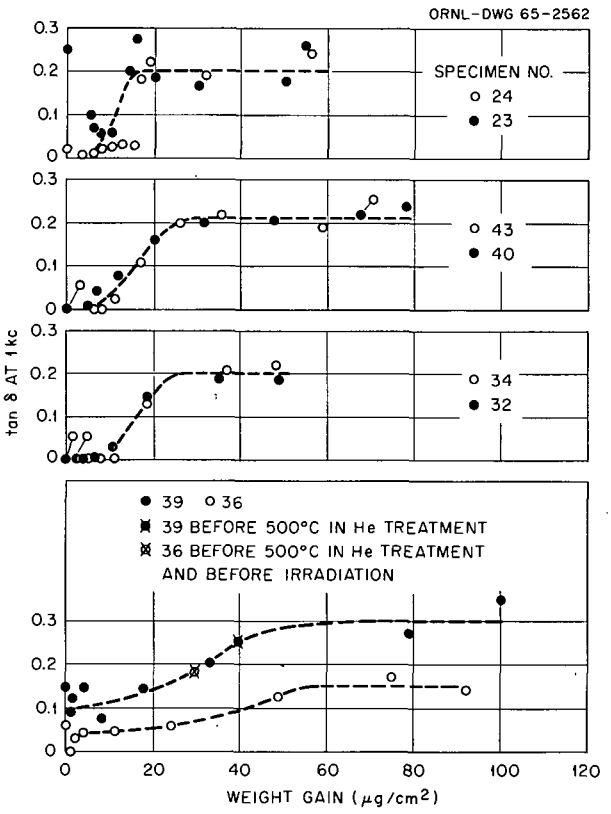

Fig. 7.6. Tan δ vs Weight Gain.

In order to interpret tan δ, some workers[7] have attempted to write equivalent electrical circuits for the film. In some cases, films are described as leaky capacitors (i.e., a capacitance in parallel with a resistance), in which case

$$\tan \delta = 1/2\pi f R_p C_p \,. \tag{5}$$

In other cases the film has been considered equivalent to a capacitance in series with a resistance, in which case

$$\tan \delta = 2\pi f R_s C_s \,. \tag{6}$$

A third definition can be derived in which tan δ is related to the dielectric losses.[7,8] The dielectric constant is conveniently expressed as a complex number:

$$\epsilon = \epsilon_1 + i\epsilon_2 \,, \tag{7}$$

where ϵ_1 is the normal dielectric constant as described above, and ϵ_2 is related to tan δ:

$$\tan \delta = \epsilon_2/\epsilon_1 \,. \tag{8}$$

It is observed in this work that tan δ is nearly constant in the frequency range 20 cps to 10 kc, and thus neither Eq. (5) nor Eq. (6) is applicable. The significance of tan δ is therefore presumed, in this work, to be that indicated in Eq. (8). For the purposes of the following discussion, it is sufficient to note that tan δ is, therefore, assumed to be a property which is characteristic of the material, and, unlike the apparent ϵ values, tan δ does not depend on the geometry of the film.

Capacitance Anomaly. – For all specimens which were heated in helium in pickled autoclaves (23, 24, 26, 30), an anomaly in the reciprocal capacitance vs weight-gain behavior occurred. Virtually no decrease in film capacitance occurred during the first 15 $\mu g/cm^2$ weight gain. An ϵ value calculated from the slopes in the thin film region would be unreasonably high; it is therefore indicated that the apparent high ϵ's were due to film porosity.

Tan δ vs Weight Gain. – There was a definite weight-gain dependence; tan δ increased markedly at about 10 $\mu g/cm^2$ weight gain and reached a constant value beyond about 15 $\mu g/cm^2$. Since tan δ is a property of the material not dependent on geometry, it is indicated that a change in nature of the film material occurred at this characteristic weight gain.

Tan δ vs weight gain was remarkably similar for all cases where good data are available (except for specimen 36) regardless of pretreatment or irradiation. This is evidence that the pretreatment and irradiation did not alter the dielectric properties of the film material. Accordingly, the variation in apparent ϵ values is ascribed to varying amounts of porosity.

Effect of 100°C Treatment. – The ten days at 100°C did not affect the film-free specimens; this is shown by the good agreement between the *A*, *B*, and ϵ values for specimens 23 and 30 and for 31 and 32.

Effect of Other Thermal Treatments. – Heating specimens in helium inside pickled autoclaves resulted in a reduction in *A*; heating in machined autoclaves increased ϵ. With specimens 35

[7] L. Young, *Anodic Oxide Films*, Academic Press, New York, 1961.

[8] H. Frohlich, *Theory of Dielectrics*, 2d ed., pp. 4–9, Oxford Press, London, 1958.

Table 7.2. Calculated Results

Specimens	a	A ($\mu g\ cm^{-2}\ min^{-1}$)	B ($cm^2\ \mu g^{-1}$)	ϵ	tan δ[a]
14[b]	1.2	0.011	0.048	35	
15[b,c]	1.2	0.021	0.024	35	
16[b]	1.0	0.0060	0.094	19	
17[b,c] $<50\ \mu g/cm^2$		0.0009	0[d]	26	
$>50\ \mu g/cm^2$	2.5	0.021	0.059	26	
23	1.5	0.012	0.043	19[e]	0.19
24[c]	1.5	0.010	0.025	19[e]	0.19
40	2.2	0.029	0.044	19	0.21
43[c] $<60\ \mu g/cm^2$	2.2	0.011	0.044	26	0.21
$>60\ \mu g/cm^2$	−7.0	0.02	0.044	26	
32	2.1	0.0095	0.055	35	0.20
34[c]	2.1	0.0095	0.055	35	0.20
36[c]	1.4	0.0038	0.0082	75	0.15
39	1.7	0.0043	0.024	35	0.30
30	2.2	0.015	0.052	19[e]	
35	1.2	0.0036	0.013	27	
26	1.3	0.0016	0.048	19[e]	
31	2.1	0.0095	0.055	35	
As pickled	0.8	0.041	0.067	19	

[a]Tan δ at high weight gain and 1 kc.
[b]Data from these specimens were previously reported.[3]
[c]Specimens were irradiated.
[d]Indicates linear corrosion.
[e]E_1 calculated from slope of A/C vs weight gain after initial 15 $\mu g/cm^2$ weight gain.

Table 7.3. Effects of Thermal Treatments

Main Feature of Treatment	Corrosion Parameters		Dielectric Constant, ϵ
	A	B	
As pickled	0.04	0.067	19
Heated in pickled autoclaves	0.01	0.05	19
Heated in machined autoclaves	0.01	0.05	35
High oxygen concentration in metal (35 and 39)	0.004	0.01–0.02	27–35
600°C, 16 hr, pickled autoclave (26)	0.002	0.05	19

(pickled, then 500°C, 2 hr) and 39 (prefilmed, then 500°C, 16 hr), the pretreatments led to especially high oxygen concentration at the surfaces. In these cases, A and B decreased a great deal. Specimen 26 (600°C, 16 hr in pickled autoclaves) obviously does not fall into the correlation. The results with these specimens are summarized in Table 7.3.

Effects of Irradiation. – The observed effects can be correlated quite well on the basis that (1) there was a strong effect of irradiation to decrease B only if dissolved oxygen was available near the surface, (2) there was probably a temporary (it lasted several days) reduction in A when prefilmed surfaces were irradiated, and (3) irradiation of prefilmed surfaces also increased the subsequent film porosity (apparent ϵ). These results are summarized in Table 7.4.

Summary of Results. – The following points, derived from the calculated parameters in Tables 7.3 and 7.4 and from other results, were used in arriving at the principal conclusions and are also of importance in suggesting further study.

1. Various pretreatments can substantially affect the subsequent corrosion. It is therefore necessary to use control specimens in order to separate irradiation effects from others.
2. A change in the nature of the film material occurring at 600 to 1000 A film thickness is indicated by a sharp rise in tan δ. This finding may be of importance to the understanding of film growth kinetics.
3. Effects on subsequent corrosion due to prior thermal treatments are as follows:
   a. The parameter A in the kinetic equation $dx/dt = Ae^{-Bx}$ is reduced by heating as-pickled surfaces in helium.
   b. Pretreatments which would leave a considerable oxygen concentration in the metal near the surface cause both A and B to be reduced by a factor of 2 to 5.
4. The effects ascribed to irradiation are:
   a. The parameter B is reduced in cases where surfaces rich in oxygen are irradiated. Irradiation appears to magnify the out-of-radiation effect. Factors of 2 and 5 reduction occurred at concentrations at which a negligible change and a factor of 2 change occurred.
   b. Surfaces irradiated with preformed film temporarily corroded more slowly than controls, probably due to a decrease in the A parameter. Irradiation also causes the film to be more porous in these cases.
   c. Surfaces irradiated with neither film nor appreciable dissolved oxygen near the surface show no detectable effects due to irradiation.

Conclusions

The principal conclusions are: (1) There is fast-neutron irradiation enhancement of corrosion which results from damage in the metal. (2) There is a small retardation of corrosion which results from irradiation of oxide film. (3) The damage in the metal is probably associated with dissolved oxygen and increases with increasing concentrations of the oxygen.

Table 7.4. Effects of Irradiation

Main Feature of Pretreatment	A	B	ϵ	tan δ
Heavy film, little dissolved oxygen	Corrosion retarded[a]		1.4[b]	
Thin film, little dissolved oxygen	0.4[a,b]	None	1.4[b]	None
No film, no dissolved oxygen	None	None	None	None
No film, some dissolved oxygen, heated in machined autoclaves	2[b]	0.5[b]	None	
No film, some dissolved oxygen, heated in pickled autoclaves	None	0.5[b]	None	None
Traces of film, much dissolved oxygen	None	0.3[b]	2[b]	0.5[b]

[a]Temporary effect.

[b]Signifies change in parameter by this factor.

ELECTROCHEMISTRY OF ZIRCONIUM CORROSION IN HIGH-TEMPERATURE AQUEOUS SOLUTIONS

A. L. Bacarella A. L. Sutton

In previous reported work,[5,9–12] equipment and techniques were developed for investigations of the electrochemistry of corrosion in high-temperature aqueous environments; these have been used in studies of the electrochemistry of zirconium and Zircaloy-2 corrosion in oxygenated 0.05 *m* H_2SO_4 solutions in the temperature range 200 to 300°C. Much of the effort in these studies has been concerned with the particular rate law governing the corrosion of zirconium. We have found that over a limited period of time (first 500 to 1000 min at about 300°C), both the logarithmic and cubic rate laws can satisfactorily express the data. However, deviations from the initial rate equations occur at longer times. At lower temperatures the logarithmic law is obeyed for longer times. The cubic law is fitted less satisfactorily. Additional investigations of the kinetics of zirconium corrosion have now been carried out. These had the objective of establishing whether sufficiently accurate and extensive data obey one rate expression over extended periods of exposure, and thereby help establish the mechanism.

A method in which measurements are made of the film growth at a constant anodic potential below the oxygen evolution potential was employed in these investigations. This method has been employed in several previously reported investigations of zirconium and zirconium-alloy corrosion.[13,14] However, these were carried out at lower temperatures, and film growth was insufficient to enable satisfactory correlations between film thickness and rate. In our higher-temperature studies, satisfactory correlations could be made. Studies of anodic film growth at high field strengths are numerous, and an excellent monograph by Young[7] has been published. In these it has been found that field strengths of the order of 10^6 to 10^7 v/cm are necessary to produce ionic current densities in the normal experimental range 10^{-8} to 10^{-1} amp/cm^2. At such high field strengths, Ohm's law is not obeyed by the ionic current. Instead, it was shown[15] as early as 1934 that the relation $i = A \exp BE$ represents the dependence of the ionic current i on the field strength E. As the field strength is reduced, this equation should fail, but measurements have not been made at sufficiently small ionic currents for failure to be observed. The general equation covering both high and low field strengths is expected to be $i = 2A \sinh BE$.[16–19] This reduces to $i = 2A\,BE$ at low fields (Ohm's law) and to the above exponential form at high fields. On the basis of the hyperbolic sine relation for the ionic current, Charlesby[16–19] has argued that the apparent rate law relating film thickness to time t will depend on the portion of the range (t) studied. If

$$i = 2A \sinh \frac{BV}{X}$$

$$= A\left[\exp\left(\frac{BV}{X}\right) - \exp\left(-\frac{BV}{X}\right)\right], \quad (1)$$

where $V/X = E$, and V is the voltage drop across the oxide of thickness X, then for small X and values of $BV/X > 3$, a logarithmic law is approximated; as X increases and $BV/X \sim 1$, the film growth approximates a cubic function of time. It is therefore of interest to consider whether the results obtained for zirconium corrosion at temperatures from 200 to 300°C can be interpreted according to the hyperbolic sine relation. Since the constants A and B in Eq. (1) have some basis in theory, a further test on the validity of this interpretation can be made.

[9] A. L. Bacarella, *J. Electrochem. Soc.* **108**, 331 (1961).

[10] A. L. Bacarella, *HRP Quart. Progr. Rept. Oct. 31, 1959*, ORNL-2879, p. 149.

[11] A. L. Bacarella, *HRP Quart. Progr. Rept. July 31, 1960*, ORNL-3004, p. 75.

[12] A. L. Bacarella, *Reactor Chem. Div. Ann. Progr. Rept. Jan. 31, 1964*, ORNL-3591, pp. 77–80.

[13] G. B. Adams, P. van Rysselberghe, and M. Maraghini, *J. Electrochem. Soc.* **102**, 502 (1955).

[14] G. B. Adams *et al.*, *J. Electrochem. Soc.* **105**, 660 (1958).

[15] A. Gunterschulze and H. Betz, *Z. Physik* **92**, 367 (1934).

[16] A. Charlesby, *Acta Met.* **1**, 340 (1953).

[17] A. Charlesby, *Proc. Phys. Soc. (London)* **B66**, 317 (1953).

[18] A. Charlesby and J. J. Polling, *Acta Met.* **2**, 667 (1954).

[19] J. J. Polling and A. Charlesby, *Proc. Phys. Soc. (London)* **B67**, 201 (1954).

The solution was the same as that employed previously, and the temperature range was 200 to 284°C. The zirconium electrode was maintained at a constant potential, about 1 v anodic to the corrosion potential, using an electronic potentiostat, and the anodic current was recorded as a function of film growth. The reference potential was a platinum electrode at 50°C located in one arm of the reaction cell,[12] or a calomel electrode at 25°C and 1 atm bridged into the cell, using a design we developed.[12] Film thicknesses were obtained by integration of the electronic current supplied by the potentiostat. The current efficiency can be taken as 100% based on earlier observations[12] of the current-voltage behavior for zirconium in this environment at these temperatures. It is observed that the rates of O_2 evolution and of O_2 reduction are negligible at the potentials employed, −0.0 v vs Pt/O_2. The values of the film thicknesses calculated by integration of the anodic current are in excellent agreement (±5%) with values estimated from a visual color comparison of the electrode with a standard color chart.[19] The calculation of film thickness was based on an estimate of 60 A per μg of O_2 per cm^2.

The applicability of Eq. (1) to the data obtained in the present investigations was tested as shown in Fig. 7.7. Here the ionic current is plotted as a function of sinh BV/X. A satisfactory fit of the data is obtained for measurements extending over two orders of magnitude of time, 100 to 12,000 min, and over an order of magnitude in rate. Values of BV used in Fig. 7.7 were obtained from plots of log i vs $1/X$, where for small X, Eq. (1) approaches the exponential relation $i = A \exp (BV/X)$. Values of BV as a function of temperature are shown in Fig. 7.8. Values of A obtained from the slopes of lines as in Fig. 7.7 are shown in an Arrhenius plot in Fig. 7.9; they show an activation energy of 26 ± 2 kcal/mole.

It is of interest to consider in further detail the significance of the kinetic constants obtained from the application of Eq. (1) to the data. In its use at temperatures below 100°C the applicability of Eq. (1) has not been tested, since measurements at sufficiently small currents have not been made. However, the high-field approximation to Eq. (1), $i = A \exp B(V/X)$, has been tested, and values for the field coefficient B and its temperature dependence have been obtained. Theory[20] predicts B =

[20]N. F. Mott, *Trans. Faraday Soc.* **43**, 429 (1947).

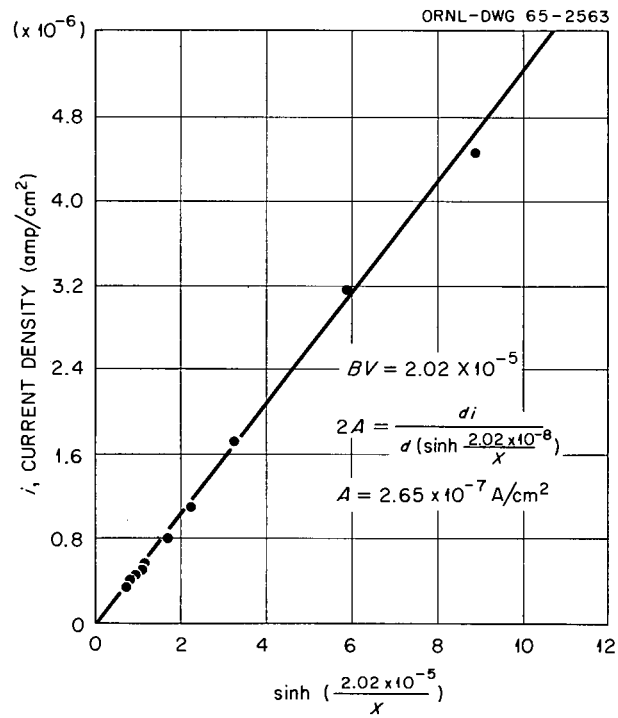

Fig. 7.7. Plot of i vs sinh (BV/X) for Zirconium in 0.05 m H_2SO_4 at + 0.800 v vs Calomel (25°C) at 253°C.

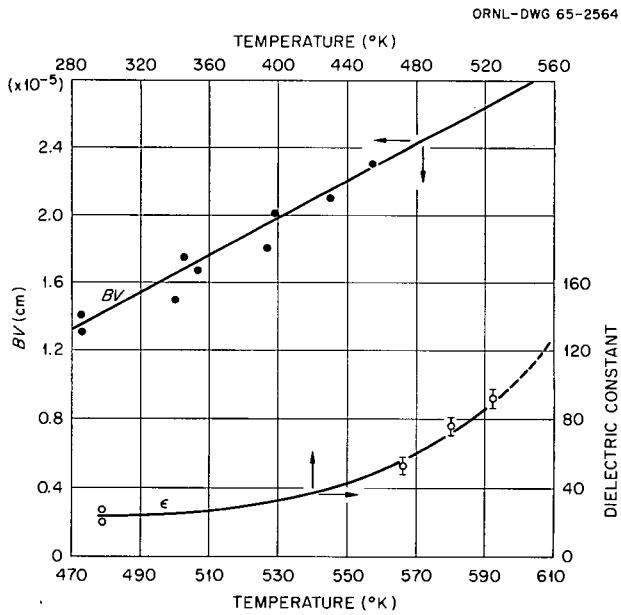

Fig. 7.8. Plot of BV and Dielectric Constant, ϵ, as Function of Temperature for ZrO_2 Films in 0.05 m H_2SO_4.

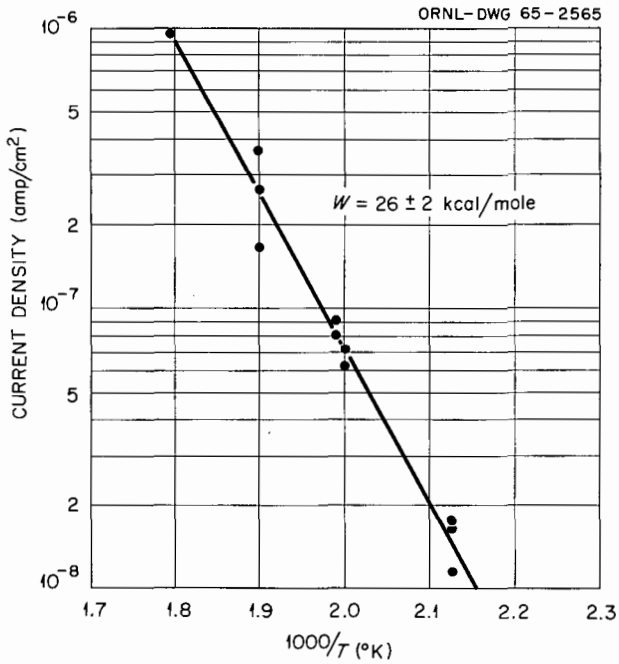

Fig. 7.9. Arrhenius Plot for $A = A_0 \exp(-w/kT)$ for Zirconium in 0.05 m H_2SO_4.

qa/kT, where q is the ionic charge and a is the activation distance (one-half the jump distance). Measurements reported by others have shown an anomalous temperature dependence, with B increasing slightly with temperature.[7] Similar observations have also been obtained for tantalum.[21,22] In the work reported here, the product of the field coefficient, B, with the voltage drop across the oxide, V, is obtained experimentally. Assuming that the voltage drop across the oxide is constant at constant potential, the temperature dependence of values of BV shown in Fig. 7.8 is proportional to that of the field coefficient B. Therefore the anomalous temperature dependence is also obtained for the measurements reported here. The temperature dependence is, however, much larger than has been observed for measurements below 100°C. In addition to this, we find that the apparent activation distances are larger than expected. These values are calculated from theory according to $qaV = BV \times kT$.

Although these unusually large values are not found in studies of anodic film growth, they are observed in related studies of ionic conductivity in soda-lime glass,[23] where the theoretical equation $i = A \sinh BE$ was obeyed over a range of about two decades of current, and the high-field approximation was evident at the higher fields. The apparent activation distance was much larger than expected and increased with temperature. It was 9.5 A at 0°C and 30 A at 110°C. Using the Lorentz field $[(\epsilon + 2)/3]E$ as the effective field acting on an ion in the film, the estimate of the jump distance was more reasonable in magnitude and, because of the rather large estimated temperature dependence of the dielectric constant ϵ, became independent of temperature.

In order to test the applicability of the Lorentz field to ionic processes in ZrO_2, the capacitance of the ZrO_2 films were measured as a function of film thickness, using a galvanostatic pulse technique. A typical plot of capacitance measurements

[21] L. Young, *Trans. Faraday Soc.* 50, 153 (1954).

[22] D. A. Vermilyea, *Acta Met.* 1, 282 (1953).

[23] R. J. Maurer, *J. Chem. Phys.* 9, 379 (1941).

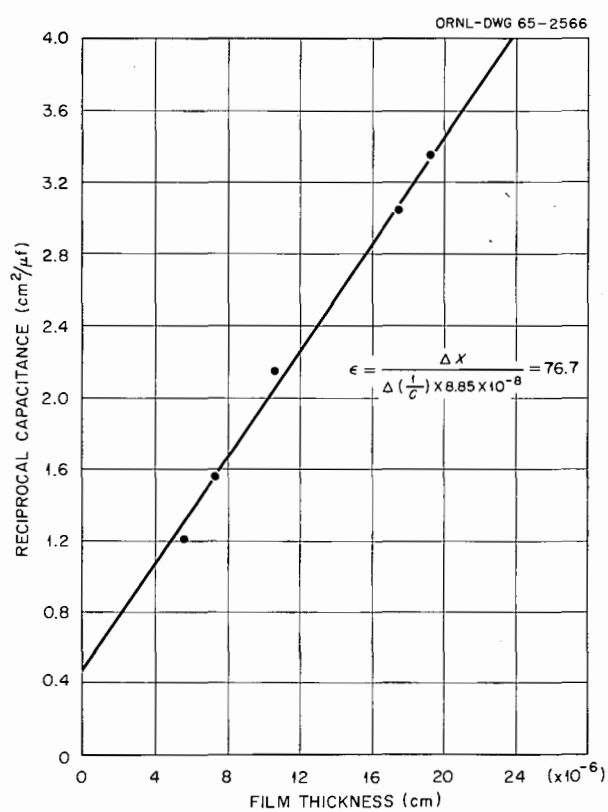

Fig. 7.10. Reciprocal Capacitance as a Function of Film Thickness for Zirconium in 0.05 m H_2SO_4 at 233°C and Constant Potential, −0.00 v vs Pt/O_2 (50°C).

at 233°C, from which the dielectric constant is calculated, is shown in Fig. 7.10. Values of the dielectric constant estimated at other temperatures and also the values reported at 20 to 25°C are shown in Fig. 7.8. With these estimates of the dielectric constant and the values for BV in Fig. 7.8, estimates of qaV, which are proportional to the activation distance, were made, using the Lorentz field in one case and the average field in another. The values are listed in Table 7.5.

It is seen that when the Lorentz field is used, the values are more "reasonable" in magnitude and are independent of temperature. If a value of 2 v can be assumed for the voltage across the oxide, as was done by Charlesby and Polling,[18] then values of $qa = 1.36$ to 1.5×10^{-8} cm are calculated for the measurements reported here, and are in very satisfactory agreement with the results at 25°C reported by others, $qa = 1.3 \times 10^{-8}$ cm.

In summary, the experimental kinetic data are well fitted by the sinh relationship of Eq. (1), and the values of the constant B are in near agreement with those expected from theory when the Lorentz rather than the probably less valid Maxwell field is employed. Accordingly, it is indicated that an important step in the corrosion is a field-dependent movement of ions across an oxide film.

Table 7.5. List of Measured Values of BV and Capacitance at Several Temperatures and Calculated Values of qaV

Temperature (°K)	BV (cm)	qaV (Average Field) (volt-cm)	ϵ	qaV (Lorentz Field) (volt-cm)
473	1.35×10^{-5}	55×10^{-8}	52	3.0×10^{-8}
500	1.65×10^{-5}	71×10^{-8}	76	2.72×10^{-8}
525	1.90×10^{-5}	85×10^{-8}	92	2.75×10^{-8}
298[a]	$B = 4.60 \times 10^{-6}$ cm/volt	$BkT = qa = 11.75 \times 10^{-8}$ cm	27	$BkT \frac{3}{\epsilon + 2} = qa = 1.30 \times 10^{-8}$ cm

[a]These estimates are made from values reported in refs. 11 and 14.

8. Physical Chemistry of High-Temperature Aqueous Systems

ELECTRICAL CONDUCTANCES OF AQUEOUS SOLUTIONS AT TEMPERATURES FROM 0 TO 800°C AND PRESSURES UP TO 4000 BARS: THE CONDUCTANCES AND IONIZATION CONSTANTS OF SULFURIC ACID SOLUTIONS[1]

A. S. Quist H. R. Jolley[2] W. L. Marshall

Introduction and Experimental Procedure

The electrical conductances of dilute sulfuric acid solutions have been measured at temperatures from 0 to 800°C and at pressures from 1 to 4000 bars. Earlier papers have presented a description of the conductance cell and the experimental methods.[3–6] Three concentrations of sulfuric acid (0.002424, 0.004893, and 0.009855 *m*) were studied. Because of the highly corrosive nature of these solutions, the equipment was modified slightly by having high-pressure connections at both ends of the conductance cell; this "flow-through" arrangement permitted more effective flushing of the cell. However, even with these improvements, the estimated uncertainty in the measurements is 4–5%. Reproducible measurements were most difficult to obtain in the temperature range 100–300°C, where the highest conductances were observed.

[1]Summary of paper submitted for publication, *J. Phys. Chem.* (1965).

[2]Summer participant, 1961–63, Loyola University, New Orleans.

[3]A. S. Quist *et al.*, *J. Phys. Chem.* **67**, 2453 (1963).

[4]A. S. Quist *et al.*, *Reactor Chem. Div. Ann. Progr. Rept. Jan. 31, 1964*, ORNL-3591, pp. 84–87.

[5]A. S. Quist *et al.*, *Reactor Chem. Div. Ann. Progr. Rept. Jan. 31, 1963*, ORNL-3417, pp. 77–82.

[6]E. U. Franck *et al.*, *Rev. Sci. Instr.* **33**, 114 (1962).

Results and Discussion

Examples of the types of curves obtained when the specific conductances of H_2SO_4 are plotted vs temperature at constant pressure are shown in Fig. 8.1 for 0.004893 *m* H_2SO_4 at several pressures. The curves at temperatures below 400°C are similar to those observed previously with $KHSO_4$,[4] where isothermal increases of pressure increase the dissociation of the bisulfate ion, and isobaric increases of temperature decrease its dissociation. (A detailed explanation is given in ref. 4.) Above 400°C the behavior of H_2SO_4 solutions differs from that observed for $KHSO_4$ because there appears to be increasing association between H^+ and HSO_4^- ions, while there was very little association between K^+ and HSO_4^- ions.

The molar conductances of 0.004893 *m* H_2SO_4 solutions as a function of density are shown in Fig. 8.2. (The isotherms without individual points

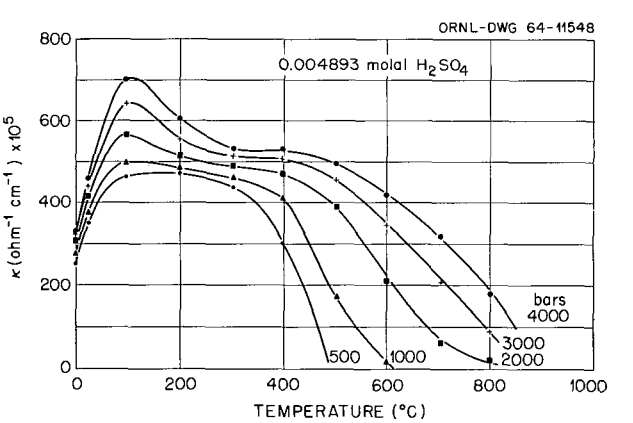

Fig. 8.1. Specific Conductances of 0.004893 *m* H_2SO_4 Solutions as a Function of Temperature at Several Pressures.

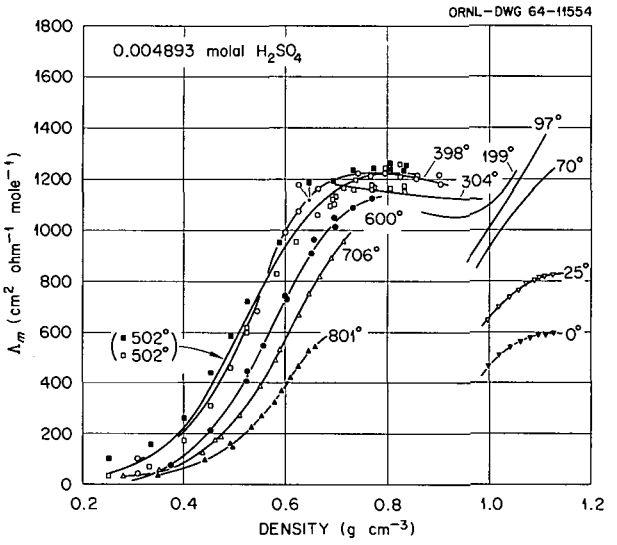

Fig. 8.2. Molar Conductances of 0.004893 m H_2SO_4 Solutions as a Function of the Density of the Solution at Several Temperatures.

represent averages of two or more runs.) At temperatures of 200°C and below, the effect of increasing density on increasing the dissociation of the bisulfate ion is readily apparent. At constant density at temperatures above 400°C, the decrease in the first ionization constant of H_2SO_4 with increasing temperature can be noted by comparing the graphs with those for K_2SO_4.[3,5]

The determination of limiting equivalent conductances of an electrolyte from measured equivalent conductances depends upon the extrapolation to zero concentration of conductance (or some function of conductance) when plotted against concentration (or some function of concentration). Below 300°C, none of several methods tried worked satisfactorily for H_2SO_4, probably because incomplete ionization of HSO_4^- gave extrapolated limiting conductances too low assuming complete ionization to H^+ and SO_4^{2-} ions, but too high for ionization only to H^+ and HSO_4^-. At 300 and 400°C at respective densities of 0.75 and 0.80 (or below) g/cm^3, and at higher temperatures, when the dissociation of HSO_4^- is negligible, sulfuric acid can be considered a uni-univalent electrolyte. Under these conditions, several extrapolation procedures were used with varying degrees of success. When H_2SO_4 behaved as a *strong* uni-univalent electrolyte, extrapolations based on the Onsager limiting law,[7] the Owen method,[8] and the Fuoss-Onsager method[9] could be used. Where H_2SO_4 behaved as a *weak* uni-univalent electrolyte, the best method for obtaining Λ_0 (the limiting equivalent conductance) was presumably that of Shedlovsky,[10,11] in which Λ_0 and the ionization constant are determined simultaneously. At solution densities below 0.6 g/cm^3 and at temperatures above 550°C, H_2SO_4 behaved as a *very weak* electrolyte, and thus conductances were not available at sufficiently low concentrations for reliable use of the previous methods. Estimates of Λ_0 in these regions of uncertainty were obtained by extrapolating the linear relationship of Walden product ($\Lambda_0\eta_0$) vs density to densities below 0.6 g/cm^3. Since there was only a slight variation in this relationship (above d = 0.5 g/cm^3) with temperature from 400 to 550°C, the Walden product was assumed to be independent of temperature (at constant density above 400°C). The following empirical equation, fitting the data at 400 to 550°C at high densities, therefore was used to calculate limiting conductances for H_2SO_4 at the higher temperatures and lower densities,

$$\Lambda_0(H_2SO_4) = (0.60 + 0.78d)/\eta_0 \ , \qquad (1)$$

where d = density (g/cm^3), and η_0 = viscosity (poises). Viscosities used were those estimated by Franck to 800°C and 1.0 g/cm^3.[12] Values of Λ_0 for H_2SO_4 at temperatures of 400°C and higher, calculated by the methods described above, are given in Table 8.1. The upper right portion of the table, separated by a heavy line, contains the values based on the direct extrapolation of the experimental data. The other values in the table are those calculated from the empirical equation given above.

Equilibrium constants for the dissociation of the bisulfate ion,

$$HSO_4^- \rightleftharpoons H^+ + SO_4^{2-} \ , \quad K_2^0 = \frac{a_{H^+}\, a_{SO_4^{2-}}}{a_{HSO_4^-}} , \qquad (2)$$

[7] Lars Onsager, *Physik. Z.* **28**, 277 (1927).

[8] B. B. Owen, *J. Am. Chem. Soc.* **61**, 1393 (1939).

[9] R. M. Fuoss and Filippo Accascina, *Electrolytic Conductance*, Interscience, New York, 1959.

[10] T. Shedlovsky, *J. Franklin Inst.* **225**, 739 (1938).

[11] R. M. Fuoss and T. Shedlovsky, *J. Am. Chem. Soc.* **71**, 1496 (1949).

[12] E. U. Franck, *Z. Physik. Chem. (Frankfurt)* **8**, 107 (1956).

Table 8.1. Limiting Equivalent Conductances of H_2SO_4, Calculated as Described in the Text

Where H_2SO_4 is treated as a 1-1 electrolyte

Temp (°C)	Density (g/cm³) 0.40	0.45	0.50	0.55	0.60	0.65	0.70	0.75	0.80	0.85
400	1720	1640	1595	1560	1505	1460	1380	1370	1360	1325
450	1720	1670	1625	1560	1505	1475	1400	1390	1380	1350
500	1720	1670	1625	1580	1525	1495	1470	1445	1400	1365
550	1690	1670	1625	1580	1525	1515	1490	1465	1425	1400
600	1660	1640	1595	1560	1525	1515	1490	1465	1440	
650	1630	1610	1595	1560	1525	1515	1490	1480		
700	1600	1585	1570	1560	1525	1515	1490	1480		
750	1570	1560	1570	1535	1504	1495				
800	1545	1560	1545	1515	1504	1495				

were calculated at temperatures to 300°C from the conductance data by using the Davies method.[13,4] The results, based on molar concentrations, are given in Table 8.2, and are in good agreement to 200°C with those obtained earlier from the $KHSO_4$ data.[4] At 300°C the values obtained from the $KHSO_4$ data are probably the more reliable.

By using the Shedlovsky method in combination with the limiting equivalent conductances of H_2SO_4 given in Table 8.1, equilibrium constants for the reaction

$$H_2SO_4 \rightleftharpoons H^+ + HSO_4^- , \quad K_1^0 = \frac{a_{H^+} a_{HSO_4^-}}{a_{H_2SO_4}} , \quad (3)$$

were calculated from 400 to 800°C, and are given in Table 8.3.

By following Franck's procedure, used in his treatment of the ionization constants of KCl in supercritical aqueous fluids,[12] Eq. (3) may be rewritten to include water of hydration:

$$H_2SO_4\,(H_2O)_j + kH_2O \rightleftharpoons H(H_2O)_m^+ + HSO_4\,(H_2O)_n^- , \quad (3a)$$

$$K_1' = \frac{a_{H(H_2O)_m^+} a_{HSO_4(H_2O)_n^-}}{a_{H_2SO_4\,(H_2O)_j}\, a_{H_2O}^k} = \frac{K_1^0}{a_{H_2O}^k} , \quad (3b)$$

$$\log K_1' = \log K_1^0 - k \log a_{H_2O} . \quad (3c)$$

Since the activity of a molecular or ionic species is proportional to its concentration, and since the concentration of water is proportional to its

Table 8.2. Negative Logarithm (Base 10) of the Second Ionization Constant of H_2SO_4, $-\log K_2^{0a}$

Temp (°C)	Density (g/cm³) b	0.75	0.80	0.85	0.90	0.95	1.0
100	~3.10[c]						2.60
150							2.83
200	4.09[c]				3.85	3.56	3.13
250					3.85	3.65	3.35
300			4.09	4.03	3.91	3.73	3.58

[a]Standard state is the hypothetical 1 *M* solution.
[b]Density of liquid in contact with saturated vapor.
[c]Values at saturation vapor pressure.

[13]E. C. Righellato and C. W. Davies, *Trans. Faraday Soc.* **26**, 592 (1930).

Table 8.3. Negative Logarithm (Base 10) of the First Ionization Constant of H_2SO_4, $-\log K_1^{0a}$

Temp (°C)	Density (g/cm³) 0.40	0.45	0.50	0.55	0.60	0.65	0.70	0.75	0.80	0.85
400	3.90	3.40	3.00	2.65	2.24	1.61	1.32	0.66	0.37	
450	4.18	3.67	3.19	2.79	2.39	1.99	1.58	1.28	1.04	0.64
500	4.52	3.99	3.43	3.01	2.58	2.20	1.89	1.66	1.46	1.24
550	4.90	4.25	3.67	3.23	2.76	2.42	2.12	1.90	1.75	1.56
600	5.24	4.53	3.91	3.42	2.94	2.62	2.30	2.08	1.99	
650	5.39	4.67	4.10	3.60	3.10	2.76	2.43	2.26		
700	5.53	4.80	4.29	3.79	3.27	2.92	2.52	2.40		
750	5.58	4.90	4.43	3.99	3.46	3.05				
800	5.62	5.05	4.61	4.10	3.66	3.22				

[a]Standard state is the hypothetical 1 *M* solution.

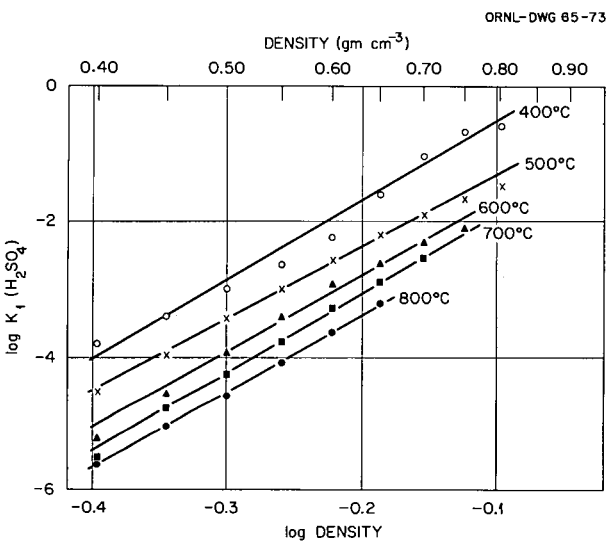

Fig. 8.3. Log K_1 (H_2SO_4) vs log Density at Temperatures from 400 to 800°C.

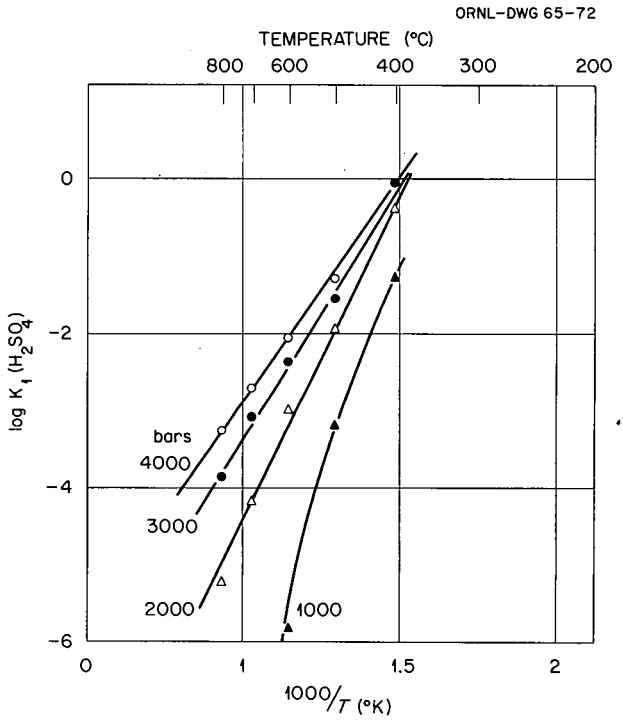

Fig. 8.4. Log K_1 (H_2SO_4) vs 1/T at Several Pressures.

density (C_{H_2O} = 55.55 × d), Eq. (3c) may be rewritten

$$\log K^0 = \log K' + k \log 55.5 + k \log d \,. \quad (3d)$$

According to Eq. (3*d*), if log *K* is plotted against density, a straight line would be obtained, with intercept log K' + *k* log 55.5 and slope *k*. This plot would give only the net change in water of hydration, *k*, with *j*, *m*, and *n* remaining undetermined. Figure 8.3 contains plots of this type for temperatures of 400–800°C over the density range 0.4–0.8 g/cm³. The average slope of the lines in Fig. 8.3 is 11.3 ± 0.2. If the lines in Fig. 8.2

are extrapolated to density = 1.0 g/cm^3, and if these values for log K_1^0 at d = 1.0 g/cm^3 are plotted against $1/T$ (for 400–800°C), and an extrapolation is made to 25°, the extrapolated value for K_1^0 at 25°, 1.0 g/cm^3 is 10^5.

Log K_1^0 (H_2SO_4) was plotted vs pressure at temperatures from 400 to 800°C. Interpolations were made to pressures of 1000, 2000, 3000, and 4000 bars. The values for log K_1^0 at these pressures were then plotted against $1/T$ as shown in Fig. 8.4. The value of ΔH^0 for the ionization process was calculated from the average slopes of the lines and was found to be −63, −39, −30, and −27 kcal/mole at pressures of 1000, 2000, 3000, and 4000 bars respectively.

ESTIMATION OF THE DIELECTRIC CONSTANT OF WATER TO 800°C[14]

A. S. Quist W. L. Marshall

The electrical conductances of dilute aqueous solutions of electrolytes have been measured at temperatures to 800°C and pressures to 4000 bars.[3,4] For the interpretation of these data it is helpful to use equations such as the Onsager limiting law to calculate the theoretical change in equivalent conductances as a function of concentration. In order to use these equations it is necessary to know the dielectric constant of the solvent. Although this constant for water has not been measured at temperatures above 393°C, estimated values to 800°C and to densities of 1.0 g/cm^3 have been published by Franck.[12] These estimates were based on a graphical fit of the Kirkwood equation

$$\frac{(2\epsilon + 1)(\epsilon - 1)}{9\epsilon} = \frac{4\pi N d}{3M}\alpha + \frac{\mu^2 g}{3kT} \qquad (4)$$

(where ϵ = dielectric constant, N = Avogadro's number, k = Boltzmann constant, M = molecular weight, g/mole, α = polarizability = 1.58×10^{-24} cm^3/mole,[15] μ = dipole moment of the water molecule, T = degrees Kelvin, d = density in g/cm^3, and g = Kirkwood correlation factor that accounts for orientation between neighboring molecules) for the dielectric constant of polar liquids[16,17] to several sets of experimental data. Since 1956, additional data on water have been published. Therefore we have reviewed previous and more recent data and have applied computer techniques in an attempt to obtain better estimates of the dielectric constant of water at high temperatures and pressures.

Figure 8.5 contains values of $\mu^2 g$ calculated by the Kirkwood equation from data of those investigations considered to cover the widest ranges of temperature and density. At low densities (and of necessity at high temperatures for water, which has a critical temperature of 374°C and critical density of 0.32 g/cm^3), short-range interactions between molecules (e.g., hydrogen bonding) should become small, and, as density approaches zero,

[14]Summary of paper submitted for publication (1965).

[15]R. M. Waxler and C. E. Weir, *J. Res. Natl. Bur. Std. A* **67**, 163 (1963).

[16]J. G. Kirkwood, *J. Chem. Phys.* **7**, 911 (1939).

[17]G. Oster and J. G. Kirkwood, *J. Chem. Phys.* **11**, 175 (1943).

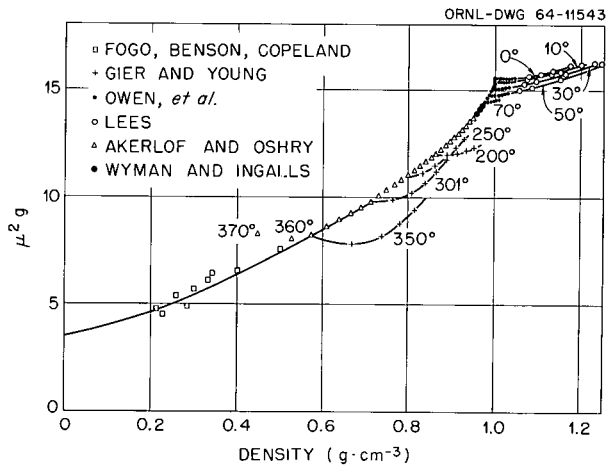

Fig. 8.5. Calculated Values of $\mu^2 g$ (from the Kirkwood Equation) for Water. Experimental values of the dielectric constant from: J. K. Fogo, S. W. Benson, and C. S. Copeland, *J. Chem. Phys.* 22, 209 (1954); T. E. Gier and H. S. Young as reported by A. W. Lawson and A. J. Hughes, chap. 4.iv in *High Pressure Physics and Chemistry*, vol I, ed. by R. S. Bradley, Academic, New York, 1963; B. B. Owen, R. C. Miller, C. E. Milner, and H. L. Cogan, *J. Phys. Chem.* 65, 2065 (1961); W. L. Lees, Dissertation, June 1949, Department of Physics, Harvard University; G. C. Akerlöf and H. I. Oshry, *J. Am. Chem. Soc.* 72, 2844 (1950); J. Wyman, Jr., and E. N. Ingalls, *J. Am. Chem. Soc.* 60, 1182 (1938).

the Kirkwood correlation factor should approach a value of unity. Accordingly, the dipole moment of the water molecule would approach 1.87, the value reported for an isolated water molecule.[18] If the Kirkwood equation is correct, the term $\mu^2 g$ should then approach 3.50 (1.87^2) at low densities and high temperatures. This behavior is observed in Fig. 8.5 where it is seen that $\mu^2 g$ extrapolates to approximately 3.50 at zero density. This observation based on experimental measurements substantiates the use of the Kirkwood equation.

The main object of this investigation was to obtain an equation that would estimate the behavior of $\mu^2 g$ as a function of temperature and density over the range of the experimental dielectric constants and that could be used for extrapolation to higher temperatures. Several types of equations estimating $\mu^2 g$ as a function of temperature and density were fitted to the data in Fig. 8.5 (excepting those of Gier and Young, in which the isothermal variation of $\mu^2 g$ with density is larger than expected at 250, 301, and 350°) by the use of a generalized least-squares program.[19]

[18]R. A. Robinson and R. H. Stokes, *Electrolyte Solutions*, 2d ed., Butterworths, London, 1959.

The equation that best fitted the data (all data given equal weight) is given as follows,

$$\mu^2 g = 3.50 + d(175 + 136d - 111d^2)T^{-1/2} . \quad (5)$$

Dielectric constants calculated from the combination of this equation with the Kirkwood equation are given in Table 8.4. These values are generally somewhat lower than those reported by Franck.[12]

When only the data along the liquid-vapor equilibrium curve were used, the following equation best fitted this set of data:

$$\mu^2 g = 3.50 + d(43.0 + 43.3d - 14.7d^2)T^{-0.32} . \quad (6)$$

Dielectric constants calculated using this equation are compared with the experimental values in Table 8.5. The measured values at 360 and 370° were not used to evaluate the parameters, but they are given in Table 8.5 to show the large differences from calculated values at these two temperatures.

[19]M. H. Lietzke, *A Generalized Least Squares Program for the IBM-7090 Computer*, ORNL-3259 (1962).

Table 8.4. Dielectric Constant of Water Calculated from Eq. (5)

Temp (°C)	Density (g/cm³) 0.0001	0.1	0.2	0.3	0.4	0.5	0.6	0.7	0.8	0.9	1.0
0										(88.4)[a]	88.4
25										(78.1)[a]	78.5
100										(54.6)[a]	58.0
200									(34.3)[a]	36.4	42.3
300								(20.0)[a]	23.8	28.4	33.0
400	1.001	1.83	3.13	4.9	7.1	9.7	12.7	16.0	19.5	23.2	26.8
500	1.001	1.71	2.81	4.3	6.1	8.3	10.8	13.5	16.5	19.5	22.6
600	1.000	1.63	2.58	3.9	5.4	7.3	9.4	11.7	14.2	16.8	19.4
700	1.000	1.56	2.40	3.5	4.9	6.5	8.3	10.4	12.5	14.8	17.0
800	1.000	1.51	2.26	3.2	4.5	5.9	7.5	9.3	11.2	13.2	15.1

[a]For liquid in equilibrium with vapor at the temperatures shown in the heading.

Table 8.5. Experimental and Calculated Values for the Dielectric Constant of Water in Equilibrium With Vapor, 0–350°C

Calculated values using Eq. (6)

Temp (°C)	∈ (exptl)	∈ (calcd)	Temp (°C)	∈ (exptl)	∈ (calcd)	Temp (°C)	∈ (exptl)	∈ (calcd)
0	87.90	87.59	120	50.48	50.44	250	26.75	26.65
10	83.95	83.79	130	48.19	48.15	260	25.29	25.21
20	80.18	80.08	140	46.00	45.96	270	23.86	23.79
25	78.36	78.28	150	43.89	43.85	280	22.45	22.39
30	76.58	76.50	160	41.87	41.84	290	21.05	21.02
40	73.15	73.05	170	39.96	39.89	300	19.66	19.65
50	69.88	69.76	180	38.10	38.03	310	18.27	18.30
60	66.76	66.59	190	36.32	36.24	320	16.88	16.91
70	63.78	63.59	200	34.59	34.51	330	15.51	15.50
80	60.95	60.71	210	32.93	32.84	340	14.10	14.06
90	58.25	57.96	220	31.32	31.22	350	12.61	12.54
100	55.50	55.35	230	29.75	29.66	360	(11.22)	10.84
110	52.89	52.84	240	28.24	28.13	370	(9.74)	8.40

SECOND DISSOCIATION CONSTANT OF H_2SO_4 FROM 25 TO 350°C EVALUATED FROM SOLUBILITIES OF $CaSO_4$ IN SULFURIC ACID SOLUTIONS

W. L. Marshall E. V. Jones

The solubilities of $NiSO_4$,[20] Li_2SO_4,[21] $MgSO_4$,[22] and $CaSO_4$[23] have been determined in aqueous sulfuric acid solutions at temperatures up to 350°C. Of particular interest is the solubility behavior of $CaSO_4$ in high-temperature electrolyte solutions, since this salt produces scale on heat-exchanger surfaces upon distilling sea water. In addition, the solubilities of $CaSO_4$ in acidic solution at high temperature are of interest to geochemistry because they might aid in understanding deposition mechanisms. In this report are given the solubilities of $CaSO_4 \cdot 2H_2O$ at 25, 30, 40, and 60°C, of $CaSO_4 \cdot \frac{1}{2}H_2O$ at 125°C, and of anhydrous $CaSO_4$ (including previous values[23]) from 125 to 350°C in H_2SO_4 solutions varying from 0 to 1 *m*. From these results, combined with previous[24] and new solubilities to 350° of $CaSO_4$ in NaCl solutions, the second dissociation constant of sulfuric acid was calculated from 25 to 350°C.

Experimental Procedures

Reagent-grade $CaSO_4 \cdot 2H_2O$ and sulfuric acid (diluted to the required concentrations) were used in the previous and present experiments. All analytical and experimental procedures have been described elsewhere.[20–22] The times for attainment of equilibrium were approximately the

[20] W. L. Marshall, J. S. Gill, and Ruth Slusher, *J. Inorg. Nucl. Chem.* **24**, 889 (1962).

[21] W. L. Marshall, Ruth Slusher, and F. J. Smith, *J. Inorg. Nucl. Chem.* **25**, 559 (1963).

[22] W. L. Marshall and Ruth Slusher, elsewhere in this report.

[23] W. L. Marshall and E. V. Jones, *Reactor Chem. Div. Ann. Progr. Rept. Jan. 31, 1963*, ORNL-3417, p. 277.

[24] W. L. Marshall, Ruth Slusher, and E. V. Jones, *J. Chem. Eng. Data* **9**, 187 (1964).

same as those found in the study of the solubility of $CaSO_4$ in $NaCl$-H_2O solutions.

Results

In Figs. 8.6 and 8.7, molal solubilities of $CaSO_4$ and its hydrates, experimentally determined in this program, are plotted against the molal concentration of H_2SO_4. Thus, at 25°C the addition of H_2SO_4 moderately increases the solubility of $CaSO_4 \cdot 2H_2O$ but at very high concentrations decreases its solubility. However, at higher temperatures the solubility increases strongly with increasing H_2SO_4 concentration. This behavior is almost certainly due to the sharply decreasing second dissociation constant of H_2SO_4 with rising temperature, which upon addition of H_2SO_4 to saturated $CaSO_4$-H_2O solutions reduces the concentration of SO_4^{2-} and allows increased solubility of $CaSO_4$ to satisfy the solubility product. This increase is due also to the increase in ionic strength by addition of acid. Nevertheless, at a constant H_2SO_4 concentration the solubility of $CaSO_4$ decreases with temperature because of a decreasing solubility product in conformance with the solubility behavior of most sulfate salts at high temperatures.

The Second Dissociation Constant of H_2SO_4. – The second dissociation constant of H_2SO_4 (K_2^0) from 25 to 350°C was calculated using the experimental solubilities both in H_2SO_4 and NaCl solutions. An extended Debye-Hückel equation was used, and assumptions were made that (1) the calcium ion was unassociated, (2) the first dissociation constant of H_2SO_4 was infinite, that is, there were no H_2SO_4 neutral species, and (3) the solubility product (K_{sp}) and second dissociation constant of H_2SO_4 (K_2) were the only equilibrium constants in effect. Thus the following two equations were derived:

$$K_2 = \frac{K_{sp}}{s}\left(\frac{m - s + K_{sp}/s}{m + s - K_{sp}/s}\right), \qquad (7)$$

$$I = 2s + m + \frac{2K_{sp}}{s}, \qquad (8)$$

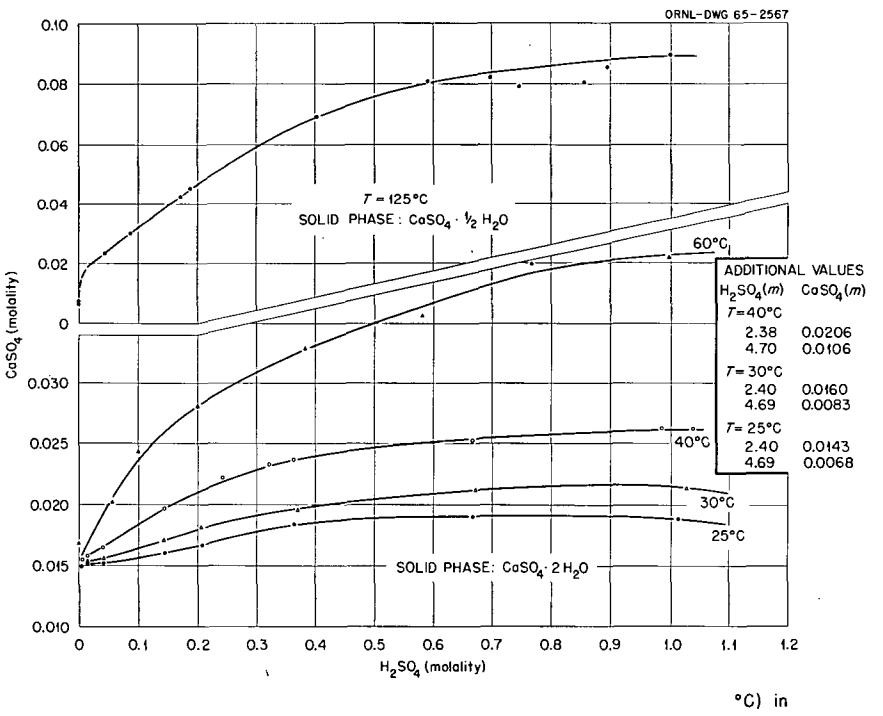

°C) in

Fig. 8.6. The Solubility of $CaSO_4 \cdot 2H_2O$ (at 25, 30, 40, and 60°C) and $CaSO_4 \cdot \frac{1}{2}H_2O$ (at 125°C) in H_2SO_4-H_2O.

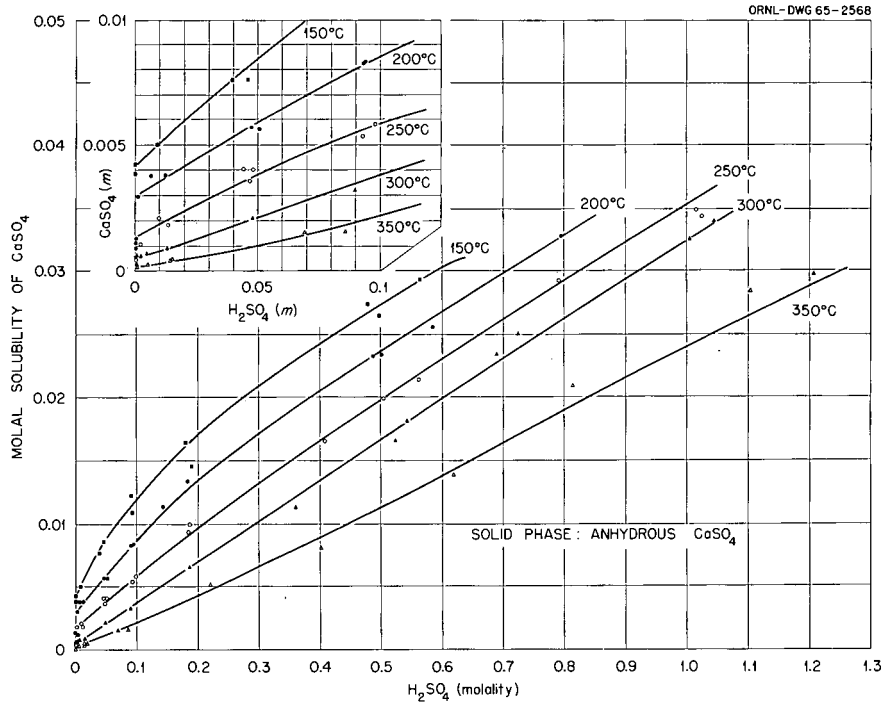

Fig. 8.7. Solubility of $CaSO_4$ in H_2SO_4-H_2O Solutions, 150–350°C.

where s is the molal solubility of $CaSO_4$, m is the formal molality of H_2SO_4, and K_2 and K_{sp} are the constants at ionic strength I. Values of K^0_{sp} and the A parameter in the extended Debye-Hückel equation,

$$\log K_{sp} = \log K^0_{sp} + 8\,\mathcal{D}\frac{\sqrt{I}}{1 + A\sqrt{I}}, \qquad (9)$$

where K^0_{sp} is the (thermodynamic) solubility product at $I = 0$, and $\mathcal{D}$ is the limiting Debye-Hückel slope for a 1-1 electrolyte at each temperature corrected for the use of molal units, were obtained from the solubilities of $CaSO_4$ in NaCl-H_2O solutions at temperatures up to 200°C[24] and estimated from our own (unpublished) solubilities at higher temperatures. A value of A of 1.5 provided the best fit at all temperatures.

A computer program was written that evaluated, by an iterative process, K_{sp}, I, and K_2 from the solubilities of $CaSO_4$ in H_2SO_4-H_2O. However, as $m \to 0$ the calculation failed due to the inability to obtain sufficient accuracy of measurement. Therefore, those values of K_2 at very low m, plotted vs $\sqrt{I}/(1 + 1.5\sqrt{I})$ and showing scatter greater than about ±5%, were ignored. Also, those values at 25, 30, 40, and 60° calculated from solubilities in H_2SO_4 solutions greater than about 0.8 m were not used. The remaining values of K_2 were evaluated by a generalized least-squares computer program[25] to obtain the best values of K^0_2 and A according to the equation

$$\log K_2 = \log K^0_2 + 4S\frac{\sqrt{I}}{1 + A\sqrt{I}}. \qquad (10)$$

These present values of K^0_2, plotted in Fig. 8.8, are in reasonably good agreement both with those determined previously[26] to 225°C by a solubility method (included in Fig. 8.8), those estimated at 100 and 200°C by the conductance method,[27] and with an accepted value of 0.0103 at 25°C.[28]

[25] M. H. Lietzke, *A Generalized Least Squares Program for the IBM-7090 Computer*, ORNL-3259 (1962).

[26] M. H. Lietzke, R. W. Stoughton, and T. F. Young, *J. Phys. Chem.* **65**, 2247 (1961).

[27] A. S. Quist, W. L. Marshall, and H. J. Jolley, elsewhere in this report.

[28] H. S. Dunsmore and G. H. Nancollos, *J. Phys. Chem.* **68**, 1579 (1964).

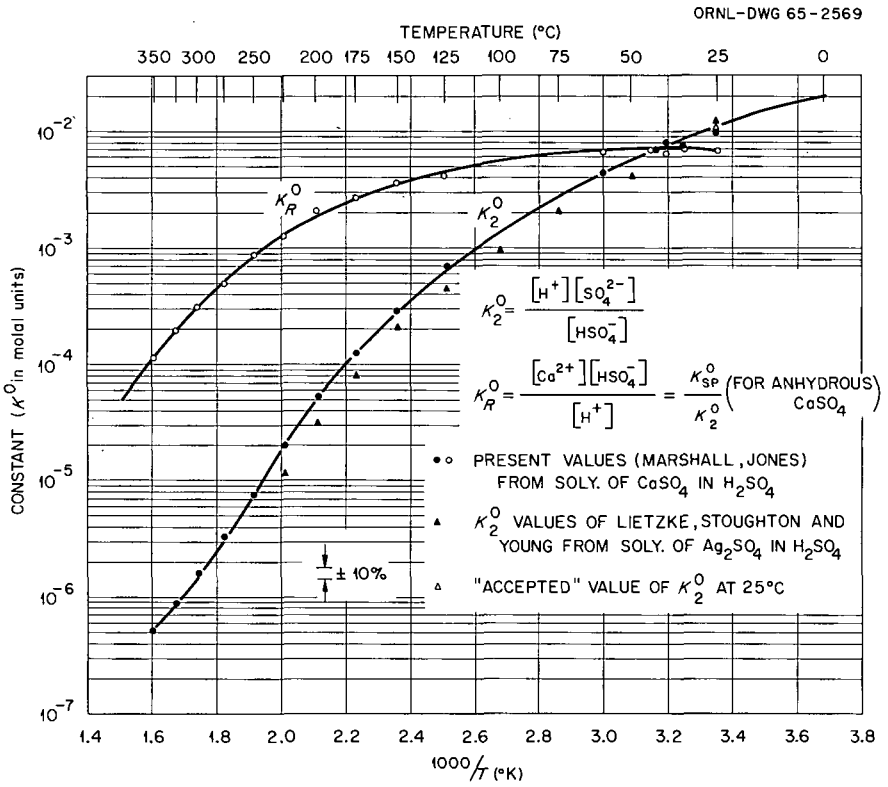

Fig. 8.8. Equilibrium Constants Derived from Solubilities of Anhydrous $CaSO_4$ in H_2SO_4-H_2O and NaCl-H_2O, 25–350°C.

From Eq. (10) the A parameter for the equilibrium expressed by K_2 increases from about 1.0 at 25° and appears to reach a constant value near 1.6 at about 300°C, in contrast to the behavior of A for the solubility product equilibrium, which remains nearly constant at 1.5 from 25°C to the high temperatures.

Values for another related constant,

$$K_R = \frac{[Ca^{2+}]\,[HSO_4^-]}{[H^+]} = s\,\frac{m + s - K_{sp}/s}{m - s + K_{sp}/s}, \quad (11)$$

were obtained and the calculated K_R^0's (solution saturated with anhydrous salt) are included also in Fig. 8.8.

ASSIGNMENT OF LIMITING EQUIVALENT CONDUCTANCES TO SINGLE IONS TO 400°C[29]

A. S. Quist W. L. Marshall

In evaluating electrical conductances of aqueous electrolyte solutions at high temperatures and pressures, the limiting equivalent conductances of single ions to 400°C were needed. Estimates were obtained by using measured transference numbers (t) to 125°C,[30] limiting ionic conductances for several electrolytes to 100°C,[18] reported equivalent conductances to 400°C,[1,3,12,31–35] and the equivalent conductance of K_2SO_4 at 100°, 1 atm, evaluated from data of Noyes *et al.*[31] combined with those of Quist *et al.*[3]

[29] Summary of paper submitted for publication (1965).

[30] J. E. Smith, Jr., and E. B. Dismukes, *J. Phys. Chem.* **67**, 1160 (1963); **68**, 1603 (1964).

[31] A. A. Noyes *et al.*, *The Electrical Conductivity of Aqueous Solutions*, Publication No. 63, Carnegie Institution of Washington, Washington, D. C., 1907.

[32] S. B. Brummer and G. J. Hills, *Trans. Faraday Soc.* **57**, 1817, 1823 (1961).

[33] J. M. Wright, W. T. Lindsay, Jr., and T. R. Druga, *The Behavior of Electrolytic Solutions at Elevated Temperatures as Derived from Conductance Measurements*, WAPD-TM-204 (June 1961).

[34] A. J. Ellis, *J. Chem. Soc.* 545 (1963).

[35] D. Pearson, C. S. Copeland, and S. W. Benson, *J. Am. Chem. Soc.* **85**, 1044, 1047 (1963).

Table 8.6. Estimated Limiting Ionic Conductances ($cm^2\ ohm^{-1}\ equiv^{-1}$) for Several Ions at Temperatures to 400°C

	H^+	Li^+	Na^+	K^+	NH_4^+	OH^-	Cl^-	HSO_4^-	SO_4^{2-}
100°, 1 atm	634	156	151	195	206	447	211	125	246
200°, 0.865 g/cm^3	824	329	304	364	394	701	391	260	521
300°, 0.7125 g/cm^3	894	562	459	504	579	821	561	400	800
400°, 0.8 g/cm^3	945		440	455			520	415	

Smith and Dismukes[30] observed a linear relationship when log t_{Cl^-}/t_{Na^+} was plotted against $1/T$ (°K) from 15 to 125°C for 0.1 N KCl and NaCl solutions. By extrapolating this relationship to temperatures of 400°C, values of t_{Cl^-} in 0.1 N NaCl were obtained. Transference numbers of the chloride ion at infinite dilution from these values with the use of the procedure of Smith and Dismukes[30] were 0.581,[30] 0.563, 0.550, and 0.541 at 100, 200, 300, and 400°C, respectively, from which limiting ionic conductances (at saturation pressure) for Na^+, H^+, K^+, NH_4^+, Li^+, Cl^-, and OH^- at 100, 200, and 300° were calculated (Table 8.6).

The above method was not applicable for estimating $\lambda_0(HSO_4^-)$ since at low temperatures bisulfate ion partially dissociates to hydrogen and sulfate ions. However, $\lambda^0(HSO_4^-)$ at 300°C was obtained indirectly by extrapolating linear plots of log Λ_0 for $KHSO_4$ (at constant solution density) against $1/T$ (°K) from higher temperatures (400–700°C).[32] From $\Lambda_0(KHSO_4)$'s at densities of 0.7 and 0.8 g/cm^3, a $\Lambda_0(KHSO_4)$ of 906 at saturation vapor pressure was obtained by interpolation. The same method was used for obtaining $\Lambda_0(H_2SO_4)$ treated as a 1-1 electrolyte (H^+-HSO_4^- ions only), giving a value of 1335 at 300°C. Calculated $\lambda_0(HSO_4^-)$'s were 400 and 440 from the $KHSO_4$ and H_2SO_4 data respectively. Since the $KHSO_4$ data were considered more reliable, the limiting conductance of the bisulfate ion was taken as 400. At 400°, from $\Lambda_0(KCl)$ values of Franck,[12] our own values of Λ_0 for $KHSO_4$, H_2SO_4, and NaCl, and from the transference number of the chloride ion estimated herein, limiting ionic conductances for Na^+, K^+, H^+, Cl^-, and HSO_4^- ions at 400°C were calculated (Table 8.6).

OSMOTIC BEHAVIOR OF AQUEOUS SOLUTIONS AT 165°C

P. B. Bien B. A. Soldano

Introduction

During the past year the osmotic behavior of aqueous salt solutions[36–39] has been studied at 165°C. Contrary to the customary behavior encountered at temperatures below 100°C, the osmotic coefficients of 1-1 electrolytes decrease with increasing concentration after reaching a maximum. The maximum varies with the individual salt species.

Experimental

The experimental isopiestic ratios at 165°C at fixed water activity,

$$R = \frac{(\nu\, m)_{\text{standard}}}{(\nu\, m)_{\text{salt}}}, \qquad (12)$$

where ν = number of ions formed per formula weight of salt and m = molality of the solute, are reported (Table 8.7) at rounded molalities obtained

[36] B. A. Soldano, R. Fox, R. Stoughton, and G. Scatchard, pp. 224–35 in *The Structure of Electrolytic Solutions*, ed. by W. J. Hamer, Wiley, New York, 1959.

[37] C. S. Patterson, L. O. Gilpatrick, and B. A. Soldano, *J. Chem. Soc.* 273 (1960).

[38] B. A. Soldano and C. S. Patterson, *J. Chem. Soc.* 937 (1962).

[39] B. A. Soldano and M. Meek, *J. Chem. Soc.* 4424 (1963).

Table 8.7. Isopiestic Ratios at 165 ± 0.1°C with NaCl as Standard

m	ϕ_{NaCl}	R_{LiCl}	R_{KCl}	R_{CsCl}	R_{BaCl_2}	$R_{Na_2SO_4}$	R_{MgSO_4}
0.50	0.9109	1.0436	0.9754	0.9733	0.8668	0.7914	
0.75	0.8925	1.0506	0.9642	0.9613	0.8192	0.7083	0.7598
1.00	0.8874	1.0500	0.9536	0.9503	0.7849	0.6392	0.6906
1.25	0.8929	1.0432	0.9438	0.9402	0.7634	0.5842	0.6268
1.50	0.9058	1.0317	0.9346	0.9311	0.7544	0.5483	0.5684
1.75	0.9233	1.0171	0.9262	0.9229	0.7585	0.5165	0.5154
2.00	0.9422	1.0010	0.9184	0.9157	0.7754	0.5038	0.4678
2.25	0.9597	0.9849	0.9114	0.9094	0.8051	0.5012	0.4256
2.50	0.9727	0.9703	0.9050	0.9040	0.8078	0.5206	0.3889
2.75	0.9783	0.9588	0.8994	0.8996		0.5502	0.3575
3.00	0.9734	0.9520	0.8944	0.8961			0.3316
3.25	0.9552[a]	0.9550	0.8902	0.8936			0.3111
3.50	0.9206	0.9580	0.8866	0.8920			0.2960
3.75	0.8667	0.9610	0.8838	0.8913			0.2863
4.00	0.7904	0.9640	0.8816	0.8916			0.2820
4.25	0.6888	0.9670					0.2831
4.50	0.5589	0.9700	0.8794	0.8950			
4.75	0.3977	0.9730					
5.00	0.2022	0.9760	0.8800	0.9022			
5.5		0.9820	0.8834	0.9131			
6.0		0.9880	0.8896	0.9278			
6.5			0.8986	0.9462			
7.0			0.9104	0.9685			
7.5			0.9250	0.9945			
8.0			0.9424	1.00			

[a]This value and values at higher concentrations are extrapolated.

from a least-squares fit of R vs m. Osmotic coefficients (Fig. 8.9) were calculated by Eq. (13),

$$\phi_i = \phi_{NaCl}\left(\frac{\nu_{NaCl}\, m_{NaCl}}{\nu_{salt}\, m_{salt}}\right). \qquad (13)$$

All osmotic coefficients are referred to the data published recently by Gardner, Jones, and deNordwall[40] on NaCl-water solutions.

Discussion

The curves of osmotic coefficients vs molality at 165°C are shown in Fig. 8.9. Generally, they resemble those previously reported for 150°C.[41] The osmotic coefficient curves of the alkali chlorides, after the initial rise (no longer as steep as at lower temperatures), inflect and bend toward the molality axis – the inflexion points vary with different salts. This performance differs from that found at lower temperatures, where the osmotic coefficients rise continuously away from the molality axis.

It was hypothesized[41] that the observed inflexions indicate the existence of an effect in concentrated solutions hitherto unnoticed at lower

[40]E. R. Gardner, P. J. Jones, and H. J. deNordwall, *Trans. Faraday Soc.* **59**, 1994 (1963).

[41]B. A. Soldano, P. B. Bien, and C. H. Secoy, *Reactor Chem. Div. Ann. Progr. Rept. Jan. 31, 1964*, ORNL-3591, pp. 99–101.

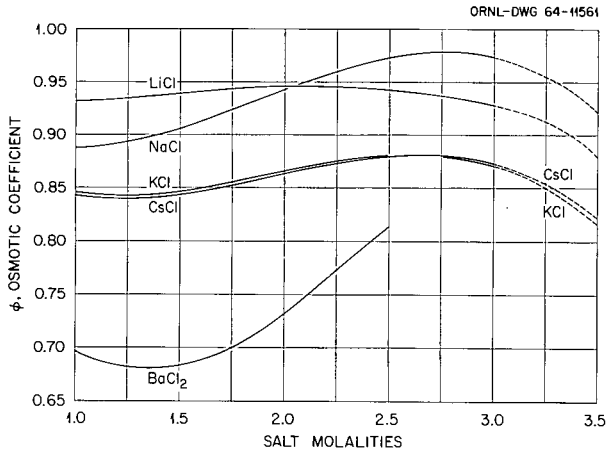

Fig. 8.9. Comparative Osmotic Coefficients at Rounded Molalities at 165 ± 0.1°C.

temperatures. The curve for LiCl was taken not only as a confirmation of the existence of this effect but also as an estimate of the strength of its influence. We note at 165°C that the same behavior for LiCl, previously noted for the first time at 150°C, continues to persist.

A question had been raised whether the observed behavior of LiCl might be due to hydrolysis effects in solution. A test was made to determine whether the hydrolysis of LiCl (creating HCl, which could escape into the vapor phase and change the nature of the salt in the sample dish) might account for the observed low osmotic coefficient values. Isopiestic conditions were simulated in an all-glass apparatus, strong enough to withstand over 5 atm of pressure and provided with a cold leg into which steam could condense together with any free HCl. The condensate was tested by adding to it 3 volumes of 1 *N* $AgNO_3$; turbidity resulting from the precipitation of AgCl was tested by using a Beckman model B spectrophotometer as a nephelometer (sensitivity to a Cl^- concentration of 7×10^{-10} equivalent/liter). A control experiment starting with 0.005 *m* HCl demonstrated HCl transport to the condensate. Experiments with NaCl and LiCl (starting with 1 *m* solution) failed to give any evidence of HCl transport to the condensate. Lithium chloride, therefore, is believed to be too strong an electrolyte to hydrolyze to the extent suggested by the query.

It may be further observed that the ϕ vs *m* curve for KCl at 165°C, which starts above that of CsCl, crosses over at about 2.6 *m* and proceeds below the CsCl curve as concentration increases.

THORIUM HYDROLYSIS IN 1 *M* (Na)ClO_4 AT 0, 25, AND 95°C[42]

C. F. Baes, Jr. N. J. Meyer[43] C. E. Roberts

The measurement of thorium hydrolysis in 1 *M* $NaClO_4$ solutions at 0 and 95°C has been described previously.[44,45] The results, along with the results of Kraus and Holmberg[46] for the same system at 25°C, have been analyzed extensively during the past year to determine the simplest set (scheme) of Th^{4+} hydrolysis products, $Th_x(OH)_y^{(4x-y)+}$, with which these data are consistent.

Data Analysis

In this analysis a computer program[47] was used to compare various possible hydrolysis schemes with the data, which consisted of pairs of values of the hydroxyl number $\bar{n}$ (the average number of OH^- ions bound per Th^{4+} ion in solution) and the pH. A chosen set of hydrolysis products $Th_xOH_y^{(4x-y)+}$ was tested by specifying for each species in the set the values of *x* and *y* and a guessed value of the formation quotient, $Q_{x,y}$:

$$Q_{x,y} = [Th_x(OH)_y^{(4x-y)+}]\,[H^+]^y/[Th^{4+}]^x \,. \quad (14)$$

In the computation, $\bar{n}$ values were calculated at each measured pH, and the stardard deviation $\sigma(\bar{n})$ of these calculated $\bar{n}$ values from the observed values was determined for all the data at a given temperature. In a series of iterative refinements, the initial guessed values of the formation quotients $Q_{x,y}$ were adjusted by means of a general least-squares procedure to yield those

[42]To be published in *Inorganic Chemistry* (April 1965).

[43]Professor of Chemistry, Bowling Green State University, Bowling Green, Ohio.

[44]C. F. Baes, Jr., N. J. Meyer, and C. E. Roberts, *Reactor Chem. Div. Ann. Progr. Rept. Jan. 31, 1963*, ORNL-3417, p. 96

[45]C. F. Baes, Jr., *et al.*, *Reactor Chem. Div. Ann. Progr. Rept. Jan. 31, 1964*, ORNL-3591, p. 94.

[46]K. A. Kraus and R. W. Holmberg, *J. Phys. Chem.* **58**, 325 (1954).

[47]*Hydrolysis Constant Program*, consisting of a subroutine, *Calculation of Hydroxyl Number*, written by R. M. Rush (described by R. M. Rush, J. S. Johnson, and K. A. Kraus, ORNL-3278, pp. 4–7) and a general least-squares program written by W. R. Busing and H. A. Levy.

values which gave the minimum values of $\sigma(\bar{n})$. Usually only two or three refinements were required for this computation to converge to the lowest value of $\sigma(\bar{n})$ and the "best values" of the $Q_{x,y}$'s. Occasionally a computation did not converge, either because at least one of the trial values of $Q_{x,y}$ was a poor guess or because the assumed scheme contained a species which, in the presence of the others, had little effect on the calculated value of $\bar{n}$. These difficulties often could be overcome by improving the trial $Q_{x,y}$ values and/or by increasing the specified increments over which these quotients were varied in the least-squaring calculation.

Tests of Schemes Involving Four Hydrolysis Products

The hydrolysis results at low $\bar{n}$ values at 95 and at 25° gave evidence that the initial hydrolysis products were $ThOH^{3+}$, $Th(OH)_2^{2+}$, and $Th_2(OH)_2^{6+}$. In all schemes tested, these monomeric species (x,y = 1,1 and 1,2) and either this dimeric species (x,y = 2,2) or another dimeric species were assumed to be present. To account for all the data, at least one more species obviously was necessary. The numerous tests which were made to determine the best scheme of four hydrolysis products are summarized in Table 8.8 A along with the standard deviation $\sigma(\bar{n})$ for each scheme. Two schemes of four species were found to be the most consistent with the data:

[I] 1,1 – 1,2 – 2,2 – 5,12; $\sigma(\bar{n})$ = 0.024, 0.021, 0.019;

[II] 1,1 – 1,2 – 2,3 – 6,15; $\sigma(\bar{n})$ = 0.021, 0.020, 0.021.

(The three values of $\sigma(\bar{n})$ for each set of x,y values refer respectively to the 0, 25, and 95° data.) Deviation plots of $\bar{n} - \bar{n}$ (calcd) vs pH for these schemes are presented in Fig. 8.10. All other four-number schemes tested gave $\sigma(\bar{n})$ values >0.03 at least at one temperature, and it seems likely that schemes [I] and [II] are the best possible choices of four species. These "best" choices, however, are not especially good fits (Fig. 8.10) in that the deviations – while they are not much greater than the expected error in the data – are largely systematic rather than random and are similar in appearance at all three temperatures. While there could be such systematic errors present in one set of data, it seems very unlikely that systematic errors at all three temperatures would produce similar appearing deviations from a correct hydrolysis scheme. Hence it may reasonably be concluded that at least five products must be formed in the hydrolysis of Th^{4+}.

Schemes of Five Hydrolysis Products

The search for more consistent schemes of five hydrolysis products was undertaken with the realization that probably no clearly unique scheme could be identified, since systematic errors present in the data or insensitivity of the data to various combinations of so many species would produce good fits to more than one scheme. Yet, $\bar{n}$ vs pH data are probably the best kind of data with which to investigate so complicated a hydrolysis process, and the progress made in identifying consistent schemes, as well as in eliminating others, should be useful when additional evidence becomes available.

In all schemes of five species tested (Table 8.8, B and C) the first three species were assumed to be $ThOH^{3+}$, $Th(OH)_2^{2+}$, and $Th_2(OH)_2^{6+}$. As the fourth species, principally trimers and tetramers were tested. These tests were largely limited to the 0° results, since these seemed to be the most sensitive.

The arrays of $\sigma(\bar{n})$ values listed for the 0° data in Table 8.8 B indicate the best schemes to be:

[III] 1,1 – 1,2 – 2,2 – 3,6 – 6,15;
$\sigma(\bar{n})$ = 0.0126, 0.0128, 0.0175;

[IV] 1,1 – 1,2 – 2,2 – 4,8 – 6,15;
$\sigma(\bar{n})$ = 0.0117, 0.0145, 0.0154.

While the $\sigma(\bar{n})$ values at 25° do not favor scheme [IV], those for scheme [IV] at 0 and 95° were among the lowest ones obtained with any scheme at these temperatures. In other tests at 0°, listed in Table 8.8 C, the degree of polymerization of the fourth and fifth species was varied while holding their y/x ratios at 2 and 2.5, respectively, with the result that scheme [IV] remained the "best" choice. The deviation plots obtained with schemes [III] and [IV], as expected, showed more nearly random scatter of the data (Fig. 8.10).

While the numerous tests listed in Table 8.8 do not reveal a clearly unique hydrolysis scheme,

Table 8.8. Standard Deviation of Calculated from Observed $\bar{n}$ Values for Various Thorium Hydrolysis Schemes

Values listed are $\sigma(\bar{n}) \times 10^3$

A. Four Species: 1,1; 1,2; 2,y; x,y

Fourth Species[a]	Third Species										
	0°		25°[b]				95°				
	2,2	2,3	2,1	2,2	2,3	2,4	None	2,1	2,2	2,3	2,4
5,11	74	94		38	45				35	54	
4,9	67	79		36	41		44	33	33	44	44
7,16	43	72		25					26	47	
6,14	32	55		20	47		45	37	22	38	43
5,12	24	32	49	21	19	42	32	30	19	25	31
7,17	32	34		33	24				30	30	
4,10	43	33	54	37	29	47	22	22	22	15	18
6,15	45	21		39	20		39	39	31	21	28
7,18	70	45			30				44	28	
5,13	70	46		52	28				36	23	
6,16		68			36					34	

Table 8.8 (continued)

B. Five Species: 1,1; 1,2; 2,2; *x,y*; *x,y*												
Fifth Species[a]	Fourth Species											
	None	2,3	3,4	3,5	3,6	3,7	4,7	4,8	4,9	4,10	5,10	5,12
						0°						
5,12	24	20	21	21	23		21	22	24			
7,17	32	21		16	17		15	14	19			
6,15	45	20		18	13	28	20	12	15	39	15	22
7,18	70	45			25	37		25	14	42		21
8,21									19			
						25°[b]						
7,17	33	19					17	14				
6,15	39	19			16			15	16			
7,18		29							15			
						95°						
7,17	30						19	19				
6,15	31	20			18			15	18			
7,18	44								18			

Table 8.8 (continued)

C. Five Species: 1,1; 1,2; 2,2; x,2x; x,2.5x							
Fifth Species[a]	Fourth Species						
	0°			25°[b]		95°	
	3,6	4,8	5,10	3,6	4,8	3,6	4,8
4,10		32					
6,15	13	12	15	13	15	18	15
8,20	20	16					
10,25	28	23					

[a]Species are listed in order of increasing OH/Th ratio.
[b]Values at 25° are based on data of Kraus and Holmberg (ref. 46).

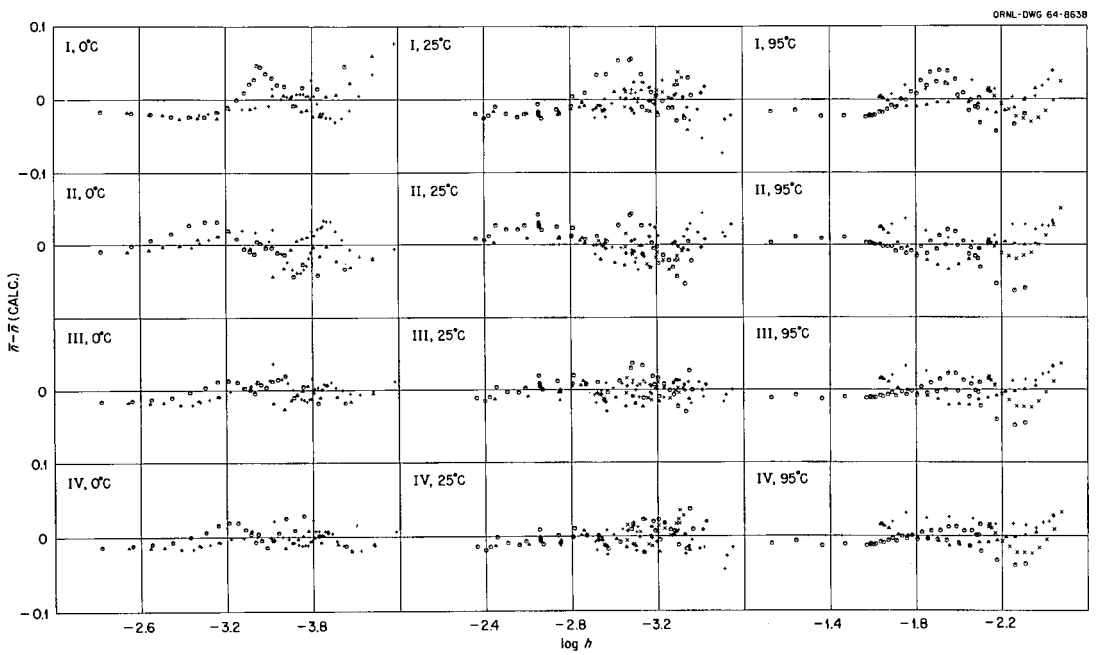

Fig. 8.10. Deviation Plots Obtained with Schemes I–IV. The $\sigma(\bar{n})$ values are listed in Table 8.8.

they do reveal what, to some, may seem a surprising sensitivity of the data to as many as five assumed equilibria. This is illustrated by the variation of $\sigma(\bar{n})$ with the y/x ratios of those species which were varied. Of course, in the relatively few cases at 0° wherein the maximum y/x ratio assumed is lower than the maximum observed $\bar{n}$ values, a relatively poor fit is expected, but in the other cases a correlation was also found. The sensitivity of $\sigma(\bar{n})$ to the assumed degree of polymerization (Table 8.8 C) is also noteworthy in view of the rather high polymers assumed.

Of the various species which appear in schemes [I–IV], all of which have been proposed by one or more previous investigators,[48] the monomers $ThOH^{3+}$ and $Th(OH)_2^{2+}$ and the dimer $Th_2(OH)_2^{6+}$ seem to be well established by the appearance of the data at low $\bar{n}$ values. The hexamer $Th_6(OH)_{15}^{9+}$, which appears in three of the four best schemes, seems most probably to be the correct final product. Of the two schemes, [III] and [IV], which contain these species, the latter seems the better choice. The fact that schemes [I] and [II] both

[48]The species $ThOH^{3+}$, $Th(OH)_2^{2+}$, and $Th_2(OH)_2^{6+}$ were proposed by Kraus and Holmberg (ref. 46) from an analysis of their results at low $\bar{n}$ values. Species of the general formula $Th_n(OH)_{3(n-1)}^{(n+3)+}$ – e.g., $Th_2(OH)_3^{5+}$, $Th_3(OH)_6^{6+}$, $Th_5(OH)_{12}^{8+}$, and $Th_6(OH)_{15}^{9+}$ – were proposed by S. Hietanen [*Acta Chem. Scand.* **8**, 1626 (1954)]. The species $Th_4(OH)_8^{8+}$ was proposed by R. Schaal and J. Faucherre [*Bull. Soc. Chim. France* **15**, 143 (1948)].

Table 8.9. Formation Quotients for Thorium Hydrolysis Products in 1 *m* (Na)ClO_4

Temperature (°C)	$-\log Q_{x,y}$					$\sigma(\bar{n})$
Scheme I	1,1	1,2	2,2	5,12		
0	4.24 ± 0.04	8.83 ± 0.16	5.45 ± 0.03	34.84 ± 0.03		0.024
25[a]	4.16 ± 0.05	7.72 ± 0.04	4.52 ± 0.02	29.26 ± 0.02		0.021
95	2.25 ± 0.02	4.51 ± 0.01	2.51 ± 0.04	16.36 ± 0.02		0.019
Scheme II	1,1	1,2	2,3		6,15	
0	4.38 ± 0.05		8.86 ± 0.02		43.77 ± 0.03	0.021
25	4.13 ± 0.04	8.63 ± 0.27	7.60 ± 0.01		36.81 ± 0.02	0.020
95	2.30 ± 0.02	4.56 ± 0.01	4.40 ± 0.03		20.60 ± 0.03	0.021
Scheme III	1,1	1,2	2,2	3,6		
0	4.23 ± 0.02	9.73 ± 0.65	5.62 ± 0.02	17.80 ± 0.02	43.78 ± 0.02	0.0126
25[a,b]	4.07 ± 0.03	7.95 ± 0.05	4.67 ± 0.03	15.01 ± 0.03		0.0094
25[a]	4.00 ± 0.02	8.05 ± 0.07	4.72 ± 0.03	14.99 ± 0.02	36.81 ± 0.02	0.0128
95	2.26 ± 0.02	4.54 ± 0.01	2.60 ± 0.04	8.59 ± 0.04	20.61 ± 0.03	0.0175
Scheme IV	1,1	1,2	2,2	4,8		
0	4.32 ± 0.02	8.48 ± 0.03	5.60 ± 0.02	22.79 ± 0.02	43.84 ± 0.02	0.0117
25[a,b]	4.12 ± 0.03[c]	7.81 ± 0.03[c]	4.64 ± 0.02	18.64 ± 0.03		0.0096
25[a]	4.15 ± 0.04	7.70 ± 0.03	4.61 ± 0.02[c]	19.01 ± 0.02[c]	36.76 ± 0.02	0.0145
95	2.29 ± 0.02	4.50 ± 0.01	2.55 ± 0.03	10.49 ± 0.03	20.63 ± 0.02	0.0154

[a]These log $Q_{x,y}$ values, based on the data of Kraus and Holmberg in 1 *M* $NaClO_4$ (ref. 46), have been corrected from the molarity to the molality scale. The values on the molarity scale are more negative by a small amount: $\Delta \log Q_{x,y} = 0.020(y - x + 1)$.

[b]These values are based on the data of Kraus and Holmberg at low $\bar{n}$ values wherein m_t was specified for each data point.

[c]Values used in the calculations of ΔH, ΔF, and ΔS (Table 8.10).

give fair agreement with the data may be rationalized as follows: In scheme [I], the 5,12 species approximates the behavior of the two species 4,8 and 6,15; in scheme [II], the 2,3 species approximates the behavior of the two species 2,2 and 4,8.

Of course this reasoning can be extended by supposing that the more polymeric species in scheme [IV] are in reality "standing in" for pairs of other species. Certainly this cannot be disproved. Indeed there is no doubt that replacing one or more in scheme [IV] by pairs of species would yield slightly better fits. However, such a procedure is justified only if the errors in the data are completely random, since the general least-squares procedure then will distinguish between significant and insignificant species. In the present case, however, some systematic errors undoubtedly were present. The decision to examine five-member schemes was made only after it was found that the best four-member schemes gave deviations of calculated from observed $\bar{n}$ values which were somewhat larger than the expected systematic errors and were similar at all three temperatures. The deviations found with the best five-member schemes, however, were not clearly sufficient to justify the assumption of six-member schemes.

The formation quotients $Q_{x,y}$ [Eq. (14)] obtained with schemes [I–IV] are listed in Table 8.9. The ranges shown for log $Q_{x,y}$ represent approximately the computed standard deviations (±) of $Q_{x,y}$. In schemes [I] and [II], both the 1,1 and 1,2 species are relatively unimportant at 0 and 25°; for example, with scheme [I], the formation quotient of the 1,2 species was computed to be negligible at 0°. With a few exceptions, values of the formation quotients are not grossly affected by the choice of scheme.

The predicted distribution of thorium among the various hydrolysis products assumed in scheme [IV] is shown at 0 and 95° and at 0.001 and 0.1 *m* thorium in Fig. 8.11. It is seen that temperature should have the greater effect on the relative abundance of monomeric vs polymeric species

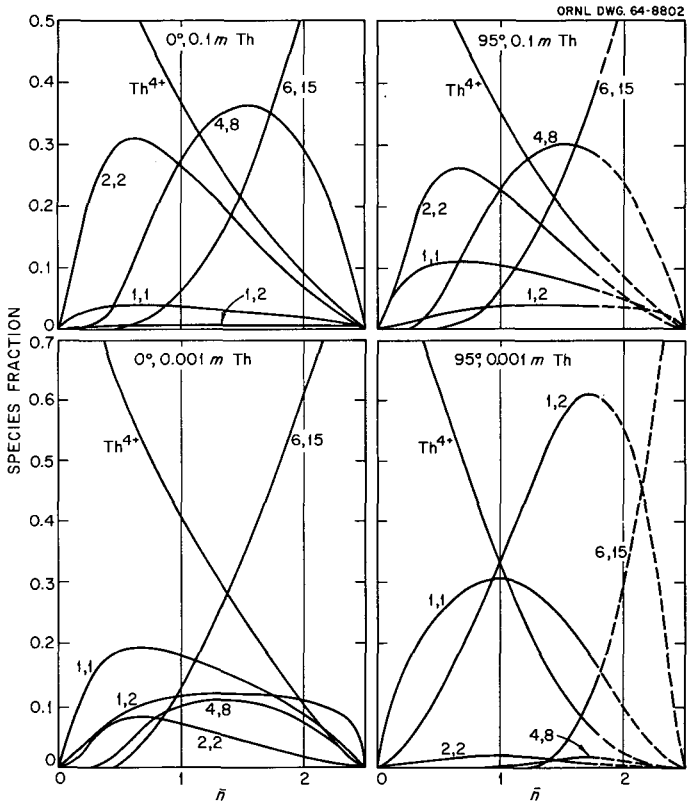

Fig. 8.11. Predicted Distribution of Thorium Among the Various Hydrolysis Products of Scheme IV.

at lower thorium concentrations. There should be a maximum in the concentration of $Th_4(OH)_8^{8+}$ at $\bar{n} \sim 1.5$; however, its presence is predicted to have but little effect on the average degree of polymerization which would be measured by the ultracentrifuge or by light scattering (Fig. 8.12). This, in addition to the uncertainty regarding the charge on the various hydrolysis products, makes these methods of confirming the present interpretation unpromising. While we have arbitrarily written the charge as $(4x - y)+$, it seems probable that at least the higher polymers incorporate or closely associate with ClO_4^- ions. Since the concentration of ClO_4^- was constant in the present measurements, its possible involvement in the equilibria does not affect the other conclusions drawn regarding the species formed, however.

Plots of log $Q_{x,y}$ vs $1/T$ are shown in Fig. 8.13 for the five species in scheme [IV]. The vertical bars indicate the range of values found for the corresponding species in the various schemes. The plots for $Q_{2,2}$, $Q_{4,8}$, and $Q_{6,15}$ all are nearly linear; those for $Q_{1,1}$ and $Q_{1,2}$, however, show a surprisingly small difference between the values at 25 and 0°. Based on these results, values of

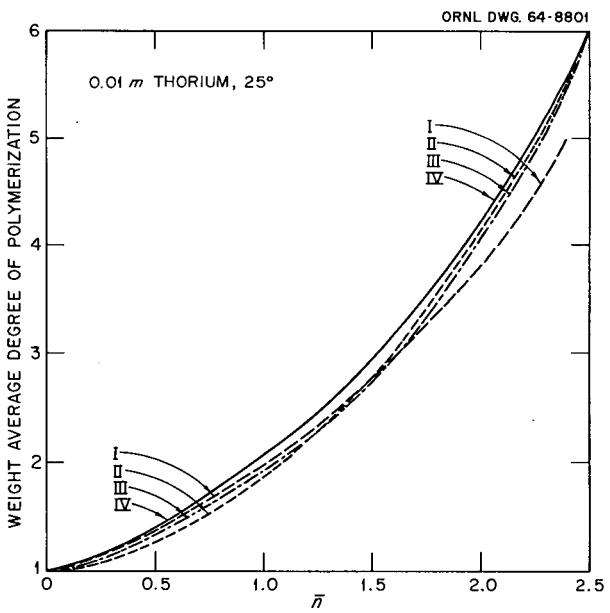

Fig. 8.12. Weight Average Degree of Polymerization Predicted from Schemes I–IV.

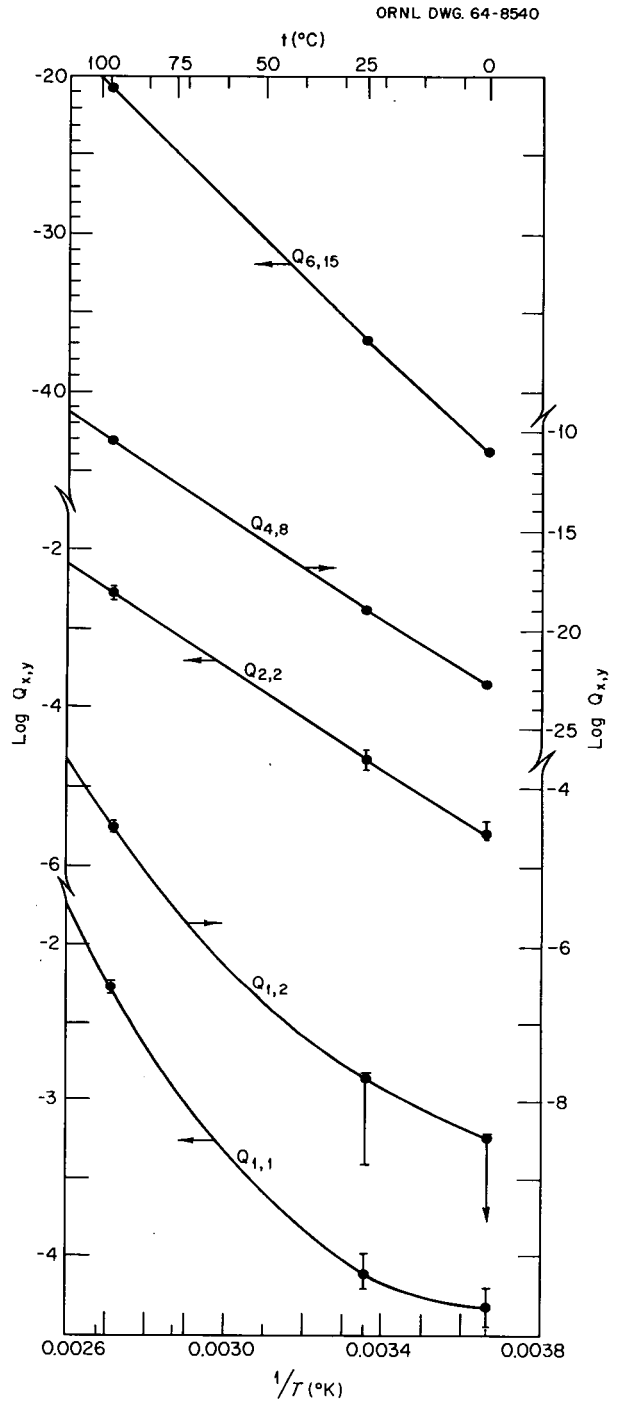

Fig. 8.13. Temperature Dependence of $Th_x(OH)_y^{(4x-y)+}$ Formation Quotients in 1 m $(Na)ClO_4$ According to Scheme IV. Vertical bars indicate range of values from schemes I–IV; curves are based on ΔH and ΔC_p values in Table 8.10.

ΔH, ΔF, and ΔS of reaction at 25° have been calculated[49] assuming ΔC_p to be independent of temperature (Table 8.10). These, of course, are not the usual thermodynamic quantities, the standard states being hypothetical 1 *m* solutions of the solute species in 1 *m* $NaClO_4$ as the solvent. The accuracy of these numbers is difficult to assess without certain knowledge that scheme [IV] is correct – though, from the fair constancy of $Q_{x,y}$ values found for many individual species in the numerous schemes tested, it can be said that the numbers in Table 8.10 are usefully accurate if the species to which they correspond do indeed exist. If scheme [IV] is correct, the ΔF and ΔH values may be good to a few tenths of a kilocalorie; the ΔC_p values are probably no better than ±20 cal/°C.

These approximate thermochemical values suggest a constancy of $\Delta H/y$ and $\Delta S/y$ for the polymeric species.

	$\Delta H/y$	$\Delta S/y$
$ThOH^{3+}$	5.9	0.9
$Th(OH)_2^{2+}$	7.0	5.5
$Th_2(OH)_2^{6+}$	7.4	14.2
$Th_4(OH)_8^{8+}$	7.22	13.3
$Th_6(OH)_{15}^{9+}$	7.23	13.0

These are the average enthalpies and entropies for the reaction shown in Table 8.10 per OH^- ion bound or, alternatively, per H^+ ion produced. From the previous study of uranium(VI) hydrolysis,[50] the corresponding values,

	$\Delta H/y$	$\Delta S/y$
UO_2OH^+	11	11
$(UO_2)_2(OH)_2^{2+}$	5.0	3
$(UO_2)_3(OH)_5^+$	5.0	2

[49]The expression

$$\ln Q_{x,y} = -\frac{A}{RT} - \frac{B}{R}\ln T + D$$

was fitted to the values of $Q_{x,y}$ at the three temperatures; $\Delta H = A - BT$ and $\Delta C_p = -B$.

[50]C. F. Baes, Jr., and N. J. Meyer, *Inorg. Chem.* 1, 780 (1962).

Table 8.10. Estimated Enthalpies, Free Energies, and Entropies of Reaction[a]

25°C, 1 *m* $NaClO_4$

$$xTh^{4+} + yH_2O \rightleftharpoons Th_x(OH)_y^{(4x-y)+} + yH^+$$

Species	ΔH (kcal)	ΔF (kcal)	ΔS (cal/°K)	ΔC_p (cal/°C)
$ThOH^{3+}$	5.9	5.6	0.9	224
$Th(OH)_2^{2+}$	13.9	10.7	11.0	304
$Th_2(OH)_2^{6+}$	14.8	6.3	28.4	1
$Th_4(OH)_8^{8+}$	57.7	25.9	106.6	108
$Th_6(OH)_{15}^{9+}$	108.5	50.1	195.7	239

[a]Calculated (cf. footnote 49) using values of log $Q_{x,y}$ in Table 8.9, scheme [IV].

show roughly the same correlation. The entropy increases associated with thorium hydrolysis are seen to be much greater, owing presumably to the higher charge on the unhydrolyzed ion. The following polymerization reactions

$$4Th(OH)_2^{2+} \rightleftharpoons Th_4(OH)_8^{8+},\ \Delta H = 2.0,\ \Delta S = 63\ ,$$

$$6Th(OH)_2^{2+} + 3H_2O \rightleftharpoons Th_6(OH)_{15}^{9+} + 3H^+,$$

$$\Delta H = 25,\ \Delta S = 130\ ,$$

evidently are favored far more by the accompanying entropy increase than they are hindered by the enthalpy increase. In the latter case, ~22 and ~40, respectively, should be subtracted from ΔH and ΔS to correct for the three protons liberated.

SOLUBILITY AND HYDROLYTIC INSTABILITY OF $MgSO_4$ IN H_2SO_4-H_2O AND D_2SO_4-D_2O SOLUTIONS, 200–350°C

W. L. Marshall Ruth Slusher

In a previous determination of $NiSO_4$ monohydrate solubilities in H_2SO_4-H_2O and D_2SO_4-D_2O solutions between 200 and 350°C, it was shown that $NiSO_4 \cdot H_2O$ solid, in dilute acidic solutions, converted hydrolytically to one or more nickel

oxysulfates, or to $Ni(OH)_2$.[20] Since Benrath[51] showed that near 200°C the apparent solubility of an $MgSO_4$ solid decreased to very low values (but that an "*Aufscheidungskurve*" existed above the true solubility curve), it was of interest to determine the phase relationships of $MgSO_4$ in H_2SO_4-H_2O solutions between 200 and 350°C (in the presence of vapor), and to determine whether $MgSO_4$ was similar to $NiSO_4$ in its solubility and hydrolytic characteristics. The results of this study are also of particular interest to distillation processes for desalination of sea or brackish water, since $Mg(OH)_2$ is one of the constituents of scale that can form on heat exchanger surfaces at high temperature.

Experimental

The experimental methods and procedures have been described previously.[20,21] The rates of attainment of equilibrium were found to be essentially identical with those for the solubility of $NiSO_4 \cdot H_2O$ and Li_2SO_4 in H_2SO_4-H_2O.[20,21]

Results

In Figs. 8.14 and 8.15 the experimental solubilities in the systems MgO-SO_3-H_2O and MgO-SO_3-D_2O at temperatures from 200 to 350°C and at concentrations of SO_3 from 10^{-2} to 3 *m* are plotted as log molality SO_3 vs the saturation molal ratio, $m_{MgO}:m_{SO_3} = R_{Mg}$. At low concentrations of

[51] A. Benrath, *Z. Anorg. Allgem. Chem.* **247**, 147 (1941).

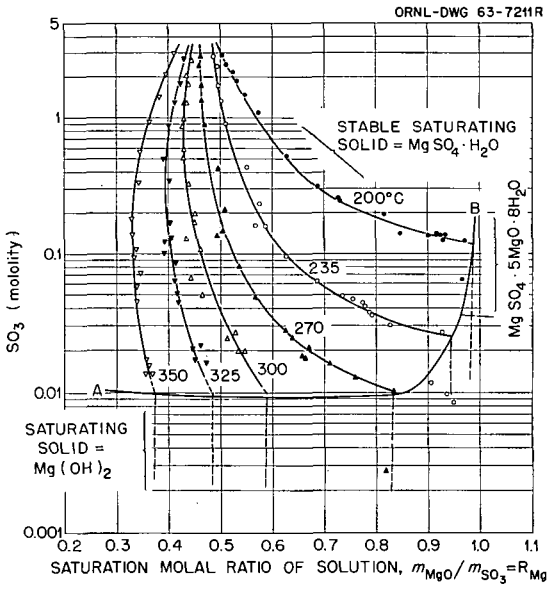

Fig. 8.14. The System MgO-SO_3-H_2O, 200–350°C.

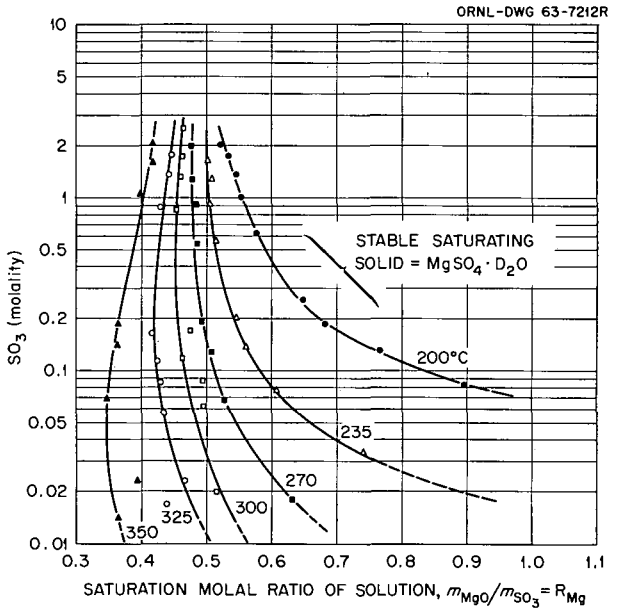

Fig. 8.15. The System MgO-SO_3-D_2O, 200–350°C.

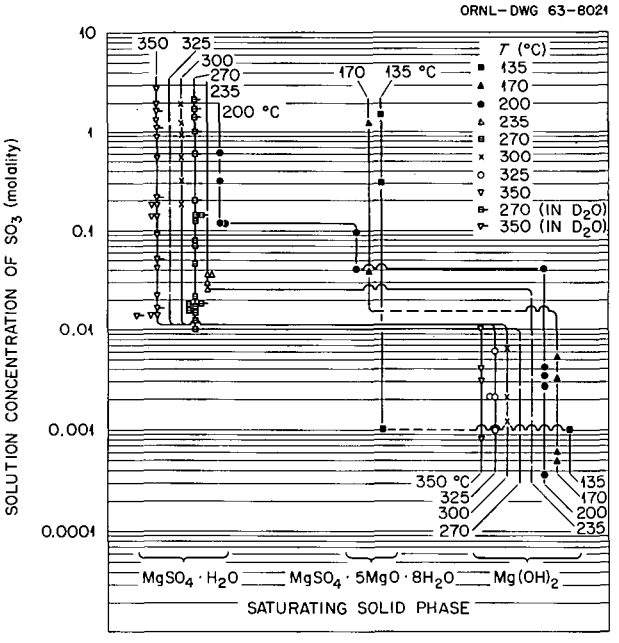

Fig. 8.16. Solid Phases in the System MgO-SO_3-H_2O and Its D_2O Analog, 135–350°C.

SO_3, x-ray diffraction patterns for the saturating solid phases showed lines corresponding to a magnesium oxysulfate ($MgSO_4 \cdot 5MgO \cdot 8H_2O$) and to $Mg(OH)_2$ at the lowest concentrations.

At SO_3 molalities above curve *AB* (Fig. 8.14) $MgSO_4 \cdot H_2O$ (or $MgSO_4 \cdot D_2O$) was identified as the saturating solid phase. At concentrations below curve *AB*, the solid phase was $Mg(OH)_2$ or the oxysulfate (or both) depending upon temperature and concentration. Experimental values for R_{Mg} below curve *AB* (Fig. 8.14) were not sufficiently precise to be displayed; the dashed lines represent the values from ~±5% above 0.01 *m* SO_3 to ±15% near 0.003 *m* SO_3. However, in Fig. 8.16 all identifications of solid phases in equilibrium with solution are given. These solid phases are shown as a function of solution concentration of SO_3. The positions of the crossover lines con-

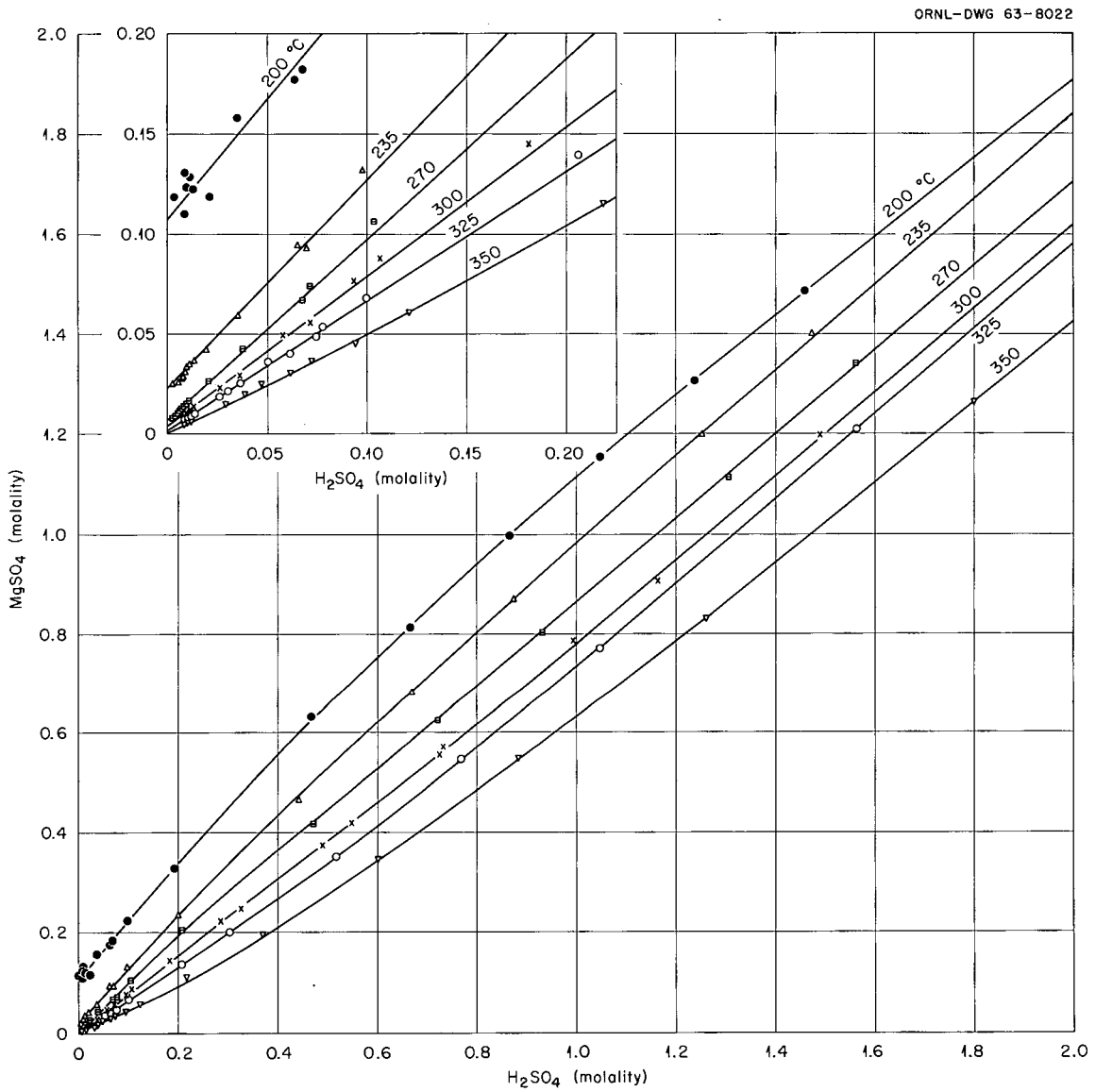

Fig. 8.17. The Solubility of $MgSO_4 \cdot H_2O$ in H_2SO_4–H_2O Solutions, 200–350°C.

necting $MgSO_4 \cdot H_2O$ solid to $MgSO_4 \cdot 5MgO \cdot 8H_2O$ and $Mg(OH)_2$ were estimated both from the identifications of solids and from the overall description of the system shown in Fig. 8.14.

Thus the large decrease in solubility at 200°C reported by Benrath is attributed to hydrolytic instability of stoichiometric $MgSO_4$ solutions, similar to the behavior of $NiSO_4$ solutions.

Solubility of $MgSO_4 \cdot H_2O$ in H_2SO_4-H_2O. – The data expressed as saturation molality $MgSO_4$ vs molality H_2SO_4 are shown graphically in Fig. 8.17. Like $NiSO_4 \cdot H_2O$, the solubility of $MgSO_4 \cdot H_2O$ increases with increasing acidity but decreases with increasing temperature. These results were evaluated by the method of least squares, and are expressed by an empirical equation, together with its coefficients, in Table 8.11.

Solubilities of $MgSO_4 \cdot D_2O$ in D_2SO_4-D_2O. – Solubilities in D_2O, expressed as molalities of $MgSO_4$ and D_2SO_4, are plotted graphically in Fig. 8.18. Coefficients for the empirical quadratic equation expressing the data are given in Table

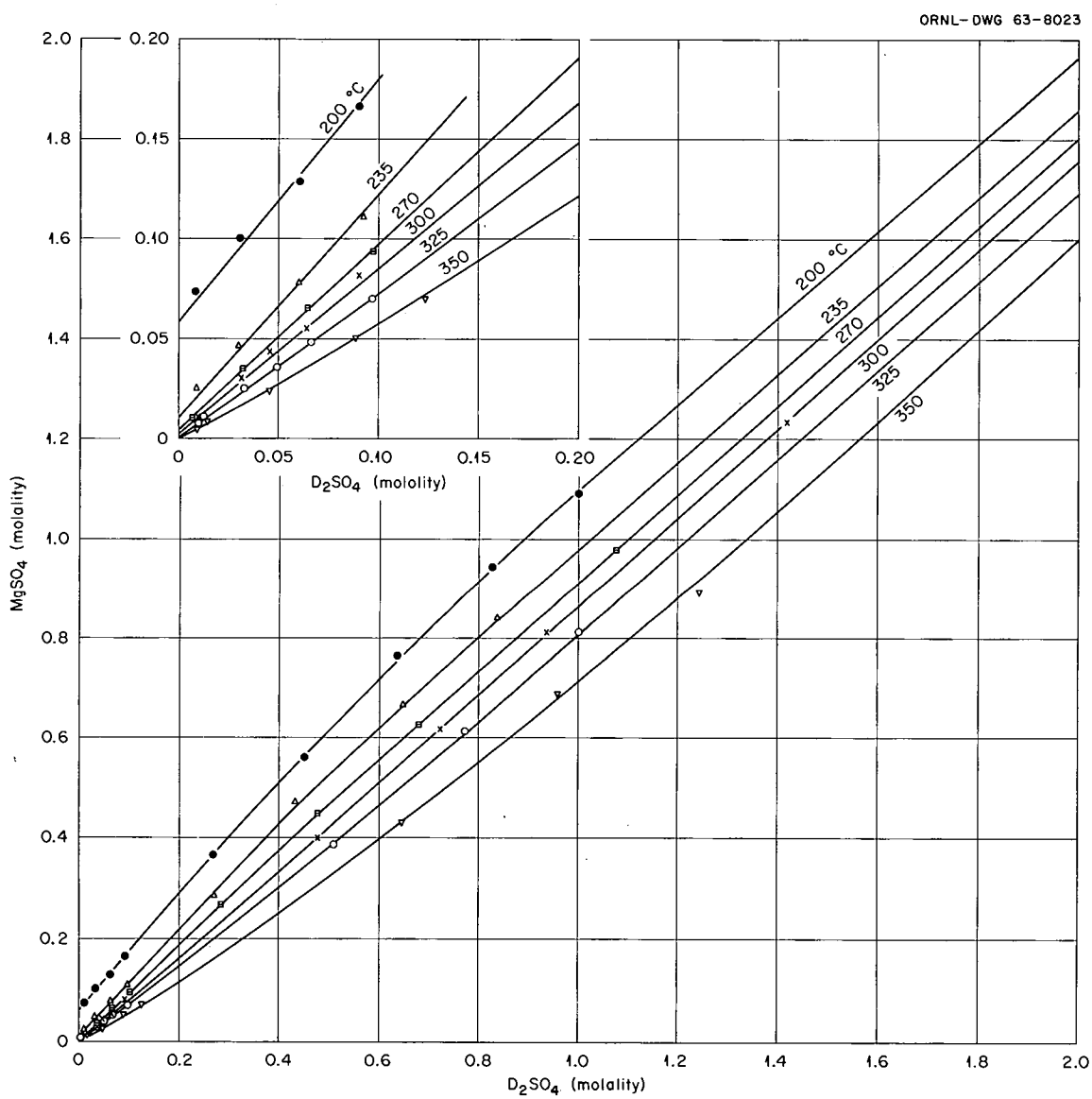

Fig. 8.18. The Solubility of $MgSO_4 \cdot D_2O$ in D_2SO_4–D_2O Solutions, 200–350°C.

8.12. Behavior of $MgSO_4$ hydrates is similar to that of $NiSO_4 \cdot H_2O$ and $NiSO_4 \cdot D_2O$; the hypothetical stoichiometric solubility in H_2O (represented approximately by the coefficient a_0 in Table 8.11) is greater than in D_2O (Table 8.12). In moderately acidic solution there is a crossover and the solubility becomes comparatively greater in D_2SO_4. At 350°C the a_0's are insufficiently precise for comparison.

Table 8.11. Equation and Coefficients for the Solubility of $MgSO_4 \cdot H_2O$ in H_2SO_4-H_2O Solution, 200–350°C

Applicable for ranges of curves shown in Fig. 8.17

$$m_{MgSO_4} = a_0 + a_1 (m_{H_2SO_4}) + a_2 (m_{H_2SO_4})^2 + a_3 (m_{H_2SO_4})^3$$

Temperature (°C)	a_0	a_1	a_2	a_3
200	+0.1078	+1.206	−0.2433	+0.04344
235	+0.02318	+1.052	−0.1075	+0.01651
270	+0.00825	+0.9024	−0.07148	+0.02356
300	+0.00528	+0.7264	+0.06556	−0.01277
325	+0.00348	+0.6033	+0.1589	−0.03344
350	+0.00113	+0.4689	+0.2036	−0.04091

Table 8.12. Equation and Coefficients for the Solubility of $MgSO_4 \cdot D_2O$ in D_2SO_4-D_2O Solution, 200–350°C

Applicable for ranges of curves shown in Fig. 8.18

$$m_{MgSO_4} = a_0 + a_1 (m_{D_2SO_4}) + a_2 (m_{D_2SO_4})^2 + a_3 (m_{D_2SO_4})^3$$

Temperature (°C)	a_0	a_1	a_2	a_3
200	+0.05847	+1.226	−0.2468	+0.05624
235	+0.01033	+1.125	−0.2055	+0.05223
270	+0.00470	+0.9354	−0.04035	+0.01087
300	+0.00473	+0.8190	+0.04903	−0.01012
325	+0.00079	+0.7131	+0.1127	−0.02302
350	−0.00162	+0.5874	+0.1441	−0.01893

9. Interaction of Water with Particulate Solids

SURFACE CHEMISTRY OF THORIA

C. H. Secoy

Heats of Immersion and Differential Heats of Adsorption

H. F. Holmes E. L. Fuller, Jr.

Calorimetric measurements of the heat of immersion of ThO_2 in water have been concerned primarily with samples of ThO_2 containing known amounts of presorbed water. Principal efforts in this area have been directed toward extending the previous study[1] to other samples and to smaller quantities of presorbed water. The utility and advantages of this type of study have been discussed.[2,3] Most pertinent to the present system is the fact that these experiments provide an unambiguous measurement of the heat of adsorption of water on ThO_2 at 25°C for small quantities of adsorbed water. For the present system this quantity (the heat of adsorption) is experimentally unattainable by the conventional technique of measuring adsorption isotherms at several temperatures near 25°C (see subsequent section, Vapor Adsorption and Desorption). A series of samples can be prepared by adsorbing known quantities of water, sealing off, and, if necessary, waiting indefinitely for equilibrium to be attained. Furthermore, a knowledge of the equilibrium water vapor pressures is not necessary. By this technique one can circumvent such difficulties as slow equilibrium, irreversible adsorption, and hysteresis, all of which are usually associated with the measurement of adsorption isotherms.

Heats of Immersion with Presorbed Water. – The previous study[1] was accomplished with samples prepared by equilibration with known water vapor pressures controlled by saturated salt solutions. The main disadvantage of this method of sample preparation is that it cannot be used to prepare samples with very small amounts of presorbed water. There are two reasons for this. The first is that the very low water vapor pressures required cannot be achieved with saturated salt solutions. Second, the amount of adsorbed water is determined by the difference in sample weight before and after equilibration and is therefore relatively inaccurate for small amounts of adsorbed water. Accordingly a new technique for sample preparation was devised. In this method a known volume of water vapor is condensed on a sample of ThO_2 held at 77°K in a liquid-nitrogen bath. After condensation of the required amount of water, the sample bulb is sealed off while still at 77°K. The amount of adsorbed water is readily calculated from the pressure, volume, and temperature of the vapor reservoir. The desired water vapor pressures were established by a liquid water reservoir whose temperature was controlled at a set point below the temperature of the vapor reservoir. The amount of water in the void space of the sample bulb was negligible because of the very low equilibrium pressures and small void volume ($\sim$3 cm^3) in the sample bulb.

Calorimetric equipment and techniques have been described previously.[2,4] Samples used in the studies reported in this and the subsequent section are listed in Table 9.1, along with their calcining temperature and nitrogen surface area

[1] C. H. Secoy, E. L. Fuller, Jr., and H. F. Holmes, *Reactor Chem. Div. Ann. Progr. Rept. Jan. 31, 1964*, ORNL-3591, pp. 102–8.

[2] C. H. Secoy and H. F. Holmes, *Reactor Chem. Div. Ann. Progr. Rept. Jan. 31, 1963*, ORNL-3417, pp. 124–29.

[3] J. J. Chessick and A. C. Zettlemoyer, *Advan. Catalysis* 11, 263 (1959).

[4] H. F. Holmes and C. H. Secoy, *J. Phys. Chem.* **69**, 151 (1965).

as determined by the Analytical Chemistry Division. Other pertinent physical properties of these samples have been discussed.[1,2,4]

The heat of immersion of sample A is shown in Fig. 9.1 as a function of the amount of presorbed water. At this point it is appropriate to explain that the amount of presorbed water for all the calorimetric studies is relative to the vacuum outgassed sample weight at 500°C, that is, zero on the presorbed water axis represents the sample weight in high vacuum at 500°C. These outgassing conditions are not sufficient to obtain a water-free surface (see subsequent section). As will be explained later, this fact introduces some difficulty in the interpretation of the data. The solid points in Fig. 9.1 are reproduced from previous data[1] and demonstrate the good agreement between the two methods of sample preparation.

With the exception of the initial linear part, the general shape of the curve shown in Fig. 9.1 has been classified[3] as being indicative of a heterogeneous surface. Indeed the initial steep slope of this curve indicates a large heat of adsorption which subsequently decreases with increasing amounts of adsorbed water.

The horizontal line labeled h_L in Fig. 9.1 corresponds to the surface energy (118.5 ergs/cm^2) of water at this temperature. At this point it is pertinent to emphasize that the heat of immersion data in Figs. 9.1 to 9.3 have been reduced to unit area basis by means of the measured nitrogen surface area. The significance of heat of immersion values less than 118.5 ergs/cm^2 and their relationship to the Harkins-Jura absolute

Table 9.1. ThO_2 Samples

Code	ORNL Code	Calcining Temperature (°C)	N_2 Surface Area (m^2/g)
A	DT-37-100	650	14.7
B	DT-37-100	800	11.5
C	DT-37-100	1000	5.64
D	DT-37-100	1200	2.20
E	DT-9	1600	1.24

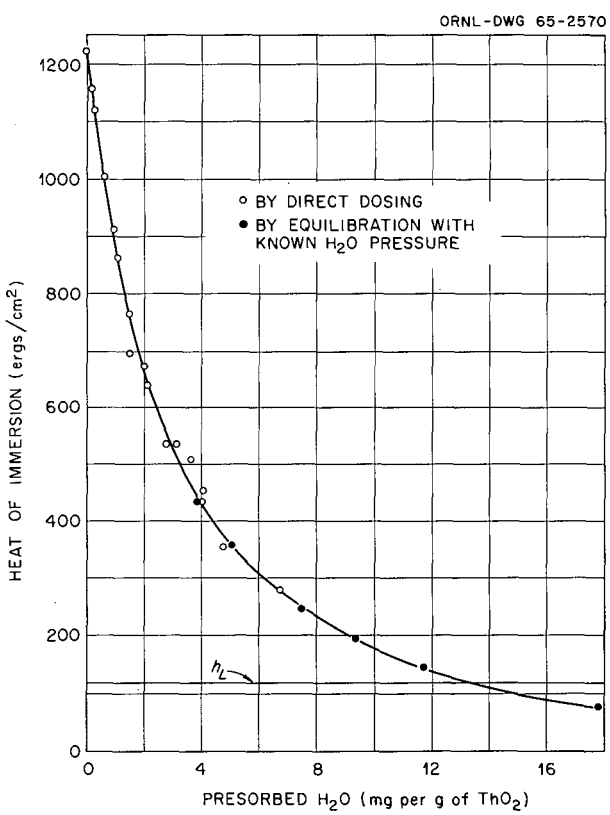

Fig. 9.1. Heat of Immersion of Sample A at 25°C.

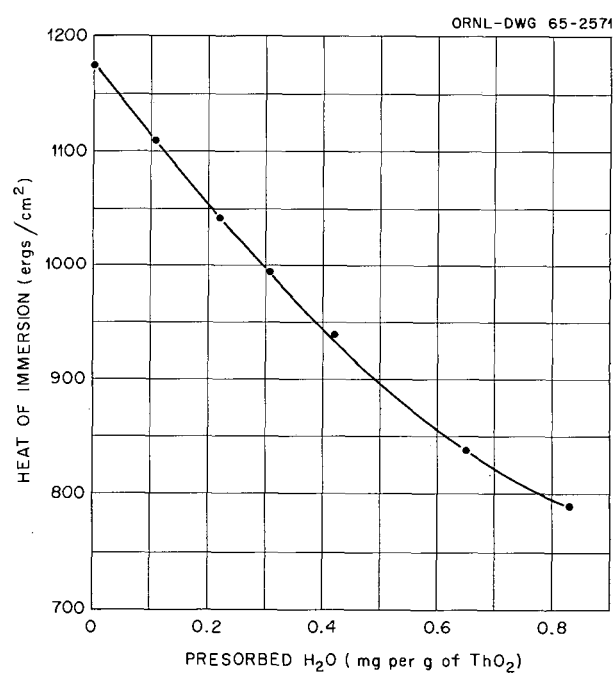

Fig. 9.2. Heat of Immersion of Sample B at 25°C.

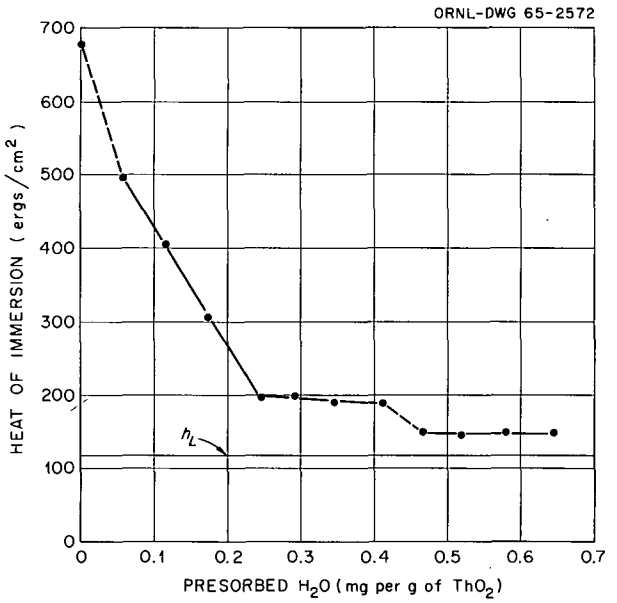

Fig. 9.3. Heat of Immersion of Sample E at 25°C.

method of determining surface areas[5] was discussed in a previous report.[1] Briefly, it was postulated that the effective surface area of the sample decreased with increasing amounts of adsorbed water. A recent article[6] offers experimental evidence that this phenomenon may be much more general than was previously recognized. The discrepancy between the Harkins-Jura absolute surface areas and the BET nitrogen surface areas was found to persist even for nonporous particulate samples. Later measurements from the same laboratory[7] showed that Harkins-Jura and BET surface areas could be reconciled if the BET areas were determined on samples containing known amounts of presorbed water. BET nitrogen surface area measurements by us have demonstrated that the effective surface area of sample A does indeed decrease with increasing amounts of adsorbed water (see subsequent section).

Figure 9.2 illustrates how the heat of immersion of sample B varies with the amount of presorbed water. The general shape of the curve in Fig. 9.2 is similar to that in Fig. 9.1 and is again indicative of a heterogeneous surface. However, as will be shown later, the slopes of the two curves are different. Lack of a sufficient quantity of material prevented us from extending the measurements to larger amounts of presorbed water than those shown in Fig. 9.2. Because of this we cannot definitely say that the effective surface area of sample B decreases with increasing amounts of adsorbed water, although we suspect that it does.

The heat of immersion of sample E is shown in Fig. 9.3. Linear portions of a heat of immersion curve such as that of Fig. 9.3 have been cited[3] as evidence for a homogeneous surface. The sharp discontinuities in Fig. 9.3 are very unusual and indicate abrupt changes in the net heat of adsorption. Due to a lack of data points the exact shape of the curve between 0 and 0.06 mg of H_2O per gram of ThO_2 is uncertain. The horizontal portion of Fig. 9.3 indicates zero net heat of adsorption even though the heat of immersion has not decreased to the surface energy of water (h_L). On an area basis the range of surface coverages included in Fig. 9.3 is not as large as the range in Fig. 9.1 (see Table 9.2). For this reason we are still uncertain as to whether the heat of immersion of sample E (with larger amounts of presorbed water) will decrease to, or below, the surface energy of water. This interesting question will be experimentally resolved in the near future.

The phenomenon of a slow heat of immersion with ThO_2 and water has been reported and discussed.[1,2,4] Briefly, samples A, B, and C had a slow heat of immersion, while samples D and E did not. It was pointed out in a previous report[1]

Table 9.2. Calculated Monolayer Capacities

Sample	Chemical (mg of H_2O per gram of ThO_2)	Physical (mg of H_2O per gram of ThO_2)
A	2.818	4.148
B	2.205	3.245
C	1.081	1.592
D	0.422	0.621
E	0.238	0.350

[5] W. D. Harkins and G. Jura, *J. Am. Chem. Soc.* **66**, 1362 (1944).

[6] W. H. Wade, *J. Phys. Chem.* **68**, 1029 (1964).

[7] N. Hackerman and W. H. Wade, *J. Phys. Chem.* **68**, 1592 (1964).

that samples of A which were equilibrated at relative water vapor pressures less than 0.6 had a slow heat of immersion, while those equilibrated at relative pressures greater than 0.6 did not. The slow-heat phenomena were postulated[1,4] as being due to a slow diffusion of liquid water into the small pores of the ThO_2 particles. The water adsorption isotherms reported in the subsequent section lend additional support to this postulate. The isotherm for sample A, which exhibits a slow heat, has a capillary condensation hysteresis loop which closes at relative pressures well below 0.6 (small pores). The corresponding loop for sample D, which did not have a slow heat, closed at relative pressures greater than 0.6 (large pores).

Net Differential Heats of Adsorption. – From the standpoint of adsorption thermodynamics the most important quantities derivable from Figs. 9.1 to 9.3 are the net differential heats of adsorption. From the preceding discussion on surface areas one might, at first glance, question the validity of results derived from data in which the surface area of the sample is decreasing in an unknown manner. Indeed, many workers in the past have calculated thermodynamic functions for the adsorption process on a unit area basis merely by subtracting the surface enthalpy of water from the heat of immersion for a vacuum-outgassed sample. As is obvious from the present discussion and as pointed out by others,[7,8] such calculations may be drastically erroneous and are certainly not valid for the samples used in the present study. However, it is valid, and probably less ambiguous, to report heat of immersion measurements on other than a unit area basis, for example, calories per gram. This is especially true for results obtained with samples having presorbed water and in which it is not known how the surface area varies with the quantity of adsorbed material. Thus, the derivative of the heat of immersion (in units of calories per gram) as a function of the amount of adsorbed material gives an unambiguous value for the net differential heat of adsorption.

Figures 9.4 to 9.6 are the resulting net differential heats of adsorption for water on samples A, B, and E, respectively, as a function of the amount of adsorbed water. Each of these graphs is a chord-area plot of the heat of immersion

[8] J. J. Chessick, *J. Phys. Chem.* **66**, 762 (1962).

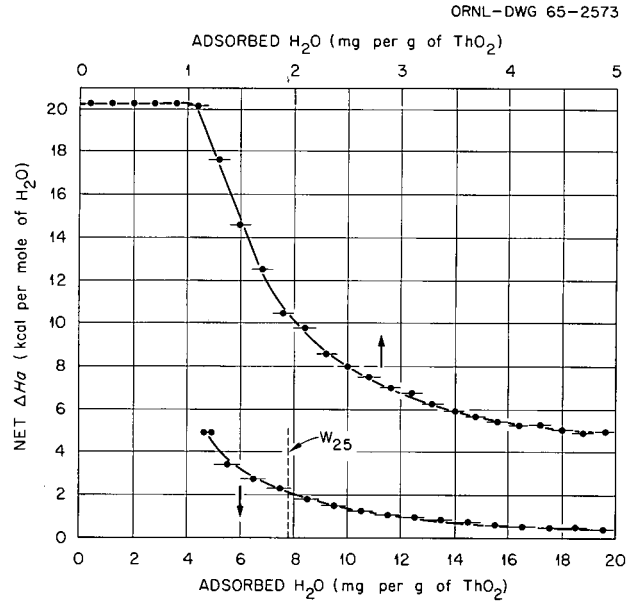

Fig. 9.4. Net Differential Heat of Adsorption of H_2O on Sample A at 25°C.

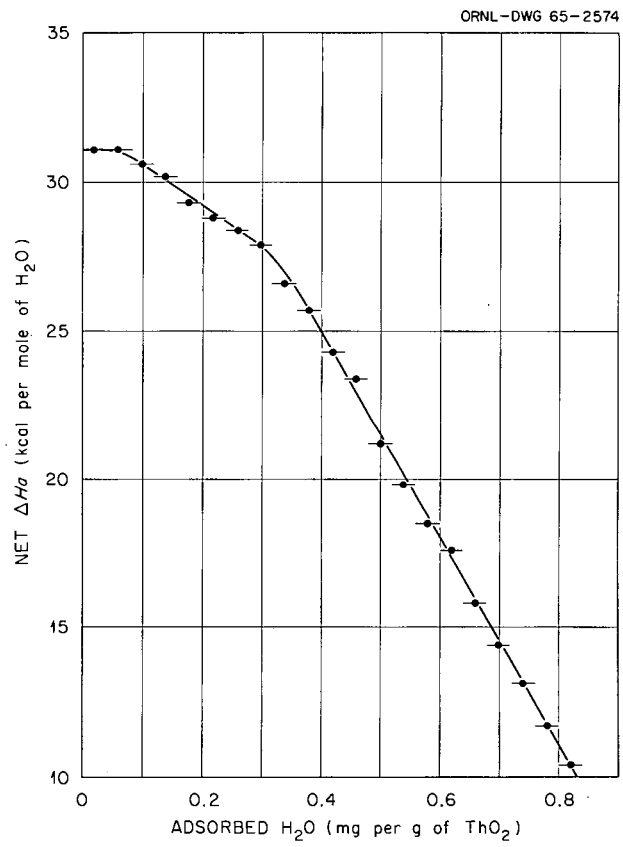

Fig. 9.5. Net Differential Heat of Adsorption of H_2O on Sample B at 25°C.

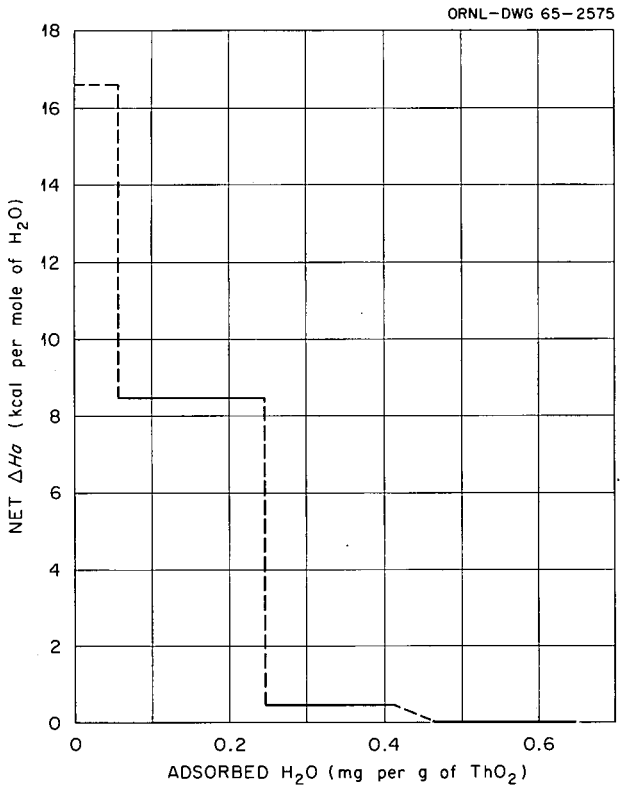

Fig. 9.6. Net Differential Heat of Adsorption of H_2O on Sample E at 25°C.

data shown in Figs. 9.1 to 9.3 except that the data were first converted to units of calories per gram of ThO_2. Lack of a sufficient quantity of material prevented this type of study with samples C and D. The heat of immersion for one sample of C containing 0.3128 mg of H_2O per gram of ThO_2 resulted in an average net heat of adsorption of 21.6 kcal/mole in this range of surface coverage.

Among the most prominent features of these data are the magnitudes of the heats of adsorption. These large net heats are most certainly associated with a chemisorption process. A chemisorption process has previously been proposed[1,2,4] for this particular absorbate-adsorbent system. From the heat of immersion of these samples as a function of outgassing temperature, it was estimated that the net heat of adsorption should range from about 7 to 22 kcal/mole.[4] With the weight loss data for sample A, it was estimated[4] that the average net heat of adsorption was 18 kcal/mole in the range of 0 to 1.8 mg of H_2O per gram of ThO_2 (relative to the 500°C sample weight). This compares quite favorably with the data in Fig. 9.4. Published estimates for the heat of adsorption of water on ThO_2 obtained from adsorption isotherms are 15 to 47 (ref. 9), 20 (ref. 10), and 24 (ref. 11) kcal/mole. Considering the variation between samples A, B, and E, there is no disagreement, but chemisorption is suggested in all cases.

Data such as shown in these figures are usually plotted as a function of the fraction of the surface covered. This is a valuable procedure in that it enables one to correlate the heat data with completion of various monolayers, of which the first monolayer is the most important. There are two very good reasons why we are presently unable to present our data in this manner. Perhaps the most fundamental of these two is the experimental fact that we have been unable to obtain a "dry" ThO_2 surface for use as a reference zero. We do hope to achieve this state in the near future. The second and perhaps more difficult of these two problems is the variation of surface area with the amount of adsorbed water. One would have to know this variation before he could discuss "completion" of a monolayer in a definitive manner.

Nevertheless one can calculate, from the measured nitrogen surface area, the amount of water necessary to form a monolayer on these samples of ThO_2. These monolayer capacities are given in Table 9.2 as chemical and physical capacities. The chemical monolayer capacity was calculated on the basis of the number of sites for surface hydroxyl groups on a crystalline ThO_2 surface (one water molecule occupies 15.6 A^2). The physical monolayer capacity assumes that the adsorbed layer has the density of liquid water and is independent of surface structure (one water molecule occupies 10.6 A^2). Admittedly these monolayer capacities are rough estimates, but perhaps they can be taken as the upper limit for the amount of water in a monolayer on these surfaces.

---

[9] A. G. Oblad, S. W. Weller, and G. A. Mills, *Proceedings of the Second World Congress on Surface Activity*, vol. II, p. 309, Academic, New York, 1957.

[10] A. L. Draper and W. O. Milligan, *Structure and Surface Chemistry of Thorium Oxide*, The Rice University, Houston, Tex., 1959.

[11] M. E. Winfield, *Australian J. Sci. Res.* **3A**, 290 (1950).

The shape of the differential heat curve shown in Fig. 9.4 is somewhat typical of a heterogeneous surface except for the constant initial value. The constant net differential heat up to 1 mg of H_2O per gram of ThO_2 indicates that in this stage of the adsorption process the surface acts as if it were a homogeneous array of adsorption sites having a uniform energy with no interaction between the adsorbed species. Such a system is possible with highly localized chemisorption but is rather unusual in a polar system such as the present one. The vertical line in Fig. 9.4 which is labeled w_{25} represents the weight of water adsorbed by sample A in high vacuum at 25°C after repeated adsorption-desorption measurements with water vapor. The monolayer capacities listed in Table 9.2 coupled with the fact that there is still water on the surface at 500°C (zero on this scale) indicate that there may be three layers of water on this sample which cannot be removed by high vacuum at room temperature. Heats of adsorption at 25°C for surface coverages less than that indicated by w_{25} are clearly inaccessible by the conventional measurement of adsorption isotherms. However, heats of adsorption in this region of surface coverage can be readily obtained by the heat of immersion technique.

Net differential heats of adsorption for sample B are shown in Fig. 9.5. One of the most significant features of this figure is the fact that the initial heats of adsorption are some 50% greater than those observed with sample A. The decline of the net differential heats with increasing coverage indicates a heterogeneous surface, but there is little evidence for a region of surface homogeneity. Perhaps such a region would be found if the measurements were extended to lower surface coverages (by outgassing at temperatures greater than 500°C). Although the data in Fig. 9.5 extend over only about 40% of a chemisorbed monolayer compared to a much larger range of coverage for sample A (Fig. 9.4), the energetics of water adsorption on the two samples are markedly different. This is not unexpected since the heats of immersion for samples A and B as a function of outgassing temperature are also different.[1,4] Both the present and previous data[1,4] serve to emphasize the complexities involved in any attempt to prepare "identical" surfaces.

The most surprising results for the net differential heats of adsorption are those shown in Fig. 9.6 for sample E. For reasons mentioned previously, the net heat of adsorption between 0 and 0.06 mg of H_2O per gram of ThO_2 can only be taken as an average value and is not a true differential heat. Above 0.25 mg of H_2O per gram of ThO_2 the slopes of the integral heat of immersion curve are approaching limitations imposed by the ultimate calorimetric sensitivity. However, the accuracy and reproducibility of the results in this range of surface coverages certainly limit the net heat of adsorption to a very small value (less than 0.5 kcal/mole). The results between 0.06 and 0.25 mg of H_2O per gram of ThO_2 are not limited by the calorimetric sensitivity. Thus, it is almost certain that the net differential heat of adsorption is a constant 8.44 kcal/mole in this region of surface coverage. This is most unusual for a polar adsorbate-adsorbent system and indicates that the adsorption is occurring on an energetically uniform surface with no interaction between adsorbed species, or that these two factors (site energy and lateral interaction) are combined in such a manner that the observed (true) net differential heat of adsorption is constant. This interesting and unusual sample will be subjected to further experimental investigations (both calorimetric and gravimetric adsorption).

Vapor Adsorption and Desorption

E. L. Fuller, Jr., H. F. Holmes

Gravimetric adsorption studies were continued for samples A and D (see Tables 9.1 and 9.2). The apparatus and technique have been described previously.[1,12]

Weight Loss on Outgassing. – Increasing the sample temperature stepwise under vacuum (10^{-5} torr) resulted in a weight loss which relates quite favorably to the surface area of the sample. Figure 9.7 presents the data as the amount of volatile material lost per square meter of sample at each temperature, over and above vacuum weight at room temperature (25°C). The loss in weight following each temperature increment required 16 to 24 hr to reach a steady value. It is

[12] E. L. Fuller, H. F. Holmes, and C. H. Secoy, "Gravimetric Adsorption Studies of Thorium Dioxide Surfaces with a Vacuum Microbalance," in *Vacuum Microbalance Techniques*, ed. by P. M. Waters, vol. 4, p. 109, Plenum, New York, 1965.

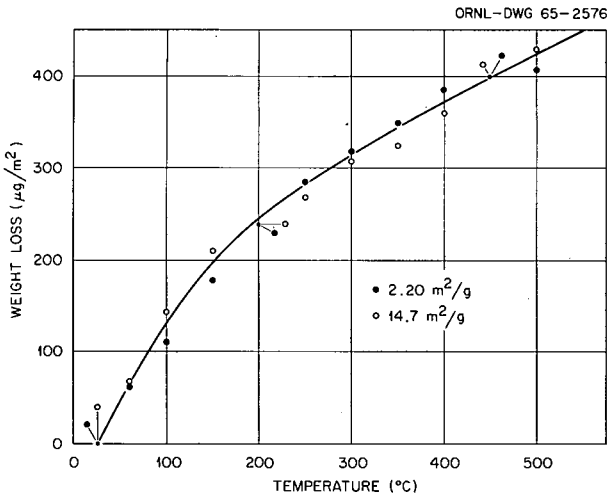

Fig. 9.7. Weight Loss on Outgassing Thoria.

quite apparent that the 500°C temperature limit imposed by the Pyrex system is not adequate to remove all the volatile material from the thoria surface, as noted by others.[13] However, the correlation on the basis of the widely different surface areas of these two samples (14.7 and 2.20 m^2/g) verifies that this desorption is surface related and not a property of the bulk thoria.

The studies performed to date have been limited to 500°C outgassing in an attempt to bolster the heat of immersion work, which has been correlated to this temperature. The sample pan and sample tube have been replaced by fused silica to enable studies up to 1000°C. These investigations will probably have to be performed after characterizing the surfaces, since thoria is known to sinter appreciably above 750°C,[14] thus altering the surface of interest.

Nitrogen Adsorption. – After the 500°C outgassing, the temperature was lowered to 25°C and the samples began to gain weight slowly even though the vacuum pumps continued to operate. Nitrogen BET surface areas were determined, at −195°C, to be 13.78 and 1.39 m^2/g for samples A and D, respectively, compared to the 14.7 and 2.20 m^2/g determined volumetrically by the Analytical Chemistry Division. This discrepancy may be inherent in the different analytical procedures, or possibly our samples underwent some sintering during the 80 to 90 hr they were held at 500°C.

Water Adsorption. – The adsorption of water on thoria reveals complex interactions not observed with nitrogen. The isotherms presented in Fig. 9.8 (sample A) and Fig. 9.9 (sample D) reveal two concurrent processes. There are well-defined type II isotherms (multilayer adsorption accompanied by condensation in pores) superimposed on a slower adsorption process in which some water is held by the surface so firmly that it cannot be removed by reevacuation to 10^{-5} torr at the isotherm temperature. In this discussion this is referred to as "bound" water, in contrast to the less tightly bound water that can be removed by evacuation of the sample chamber. This "bound" water associates itself with the surface in a rather complex kinetically controlled manner, as indicated by the fact that each successive isotherm fails to close upon the previous one by a decreasing amount. Exposure of the sample to high relative pressures of water vapor does not appear to accelerate the reaction appreciably. Repeated adsorptions and desorptions over several months were required to bring the vacuum weight of sample D to a constant value at 18.18°C. Figure 9.10 shows that the desorption branch of this final isotherm closes upon the adsorption branch and that the amount of "bound" water has reached a constant value, indicating that an equilibrium situation has been achieved. In accordance with the data presented in Table 9.2 of the preceding section, this vacuum weight corresponded to 1.8 physically adsorbed layers or 2.6 chemisorbed layers of "bound" water over and above the 500°C vacuum weight. The relative rates of the slow process can be seen by the breaks in the isotherms, corresponding to overnight stops in their construction. These are quite pronounced in the first adsorption branches and become much less predominant in the subsequent isotherms, indicating that the rate of the slow process diminishes as the constant reproducible vacuum weight is approached.

The specific surface area of sample A, computed from each of the water isotherms (each based upon its own vacuum weight), gives values successively decreasing from 28.8 m^2/g to 9.8 m^2/g. It is apparent that each of these calculations involves some "bound" water, for which

[13] M. E. Wadsworth *et al.*, University of Utah Progress Report Jan. 31, 1964.

[14] A. U. Daniels and M. E. Wadsworth, University of Utah, Technical Reports No. XIX (1963) and No. XXIII (1964).

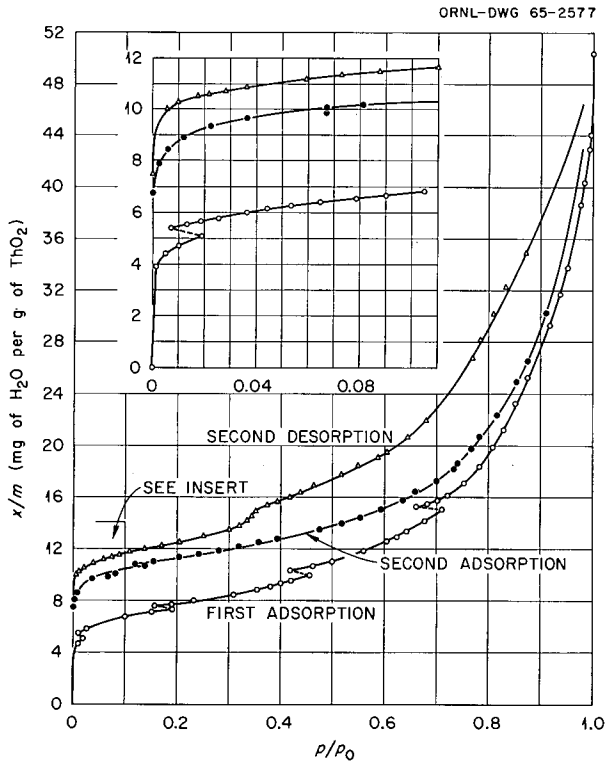

Fig. 9.8. 25°C Isotherm for Sample A.

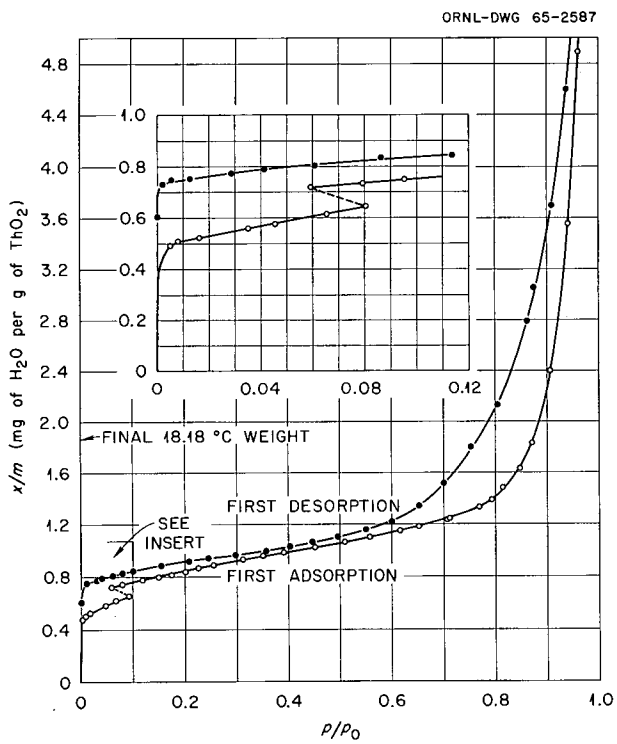

Fig. 9.9. 25°C Isotherm for Sample D.

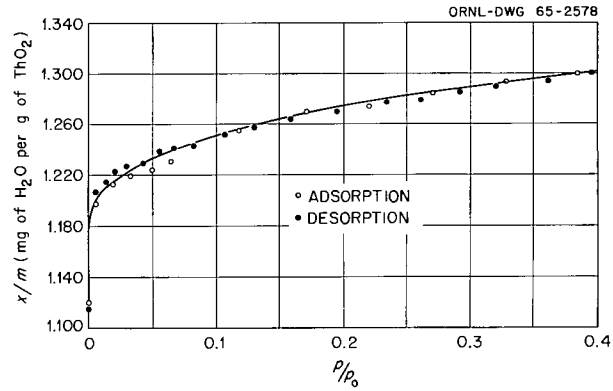

Fig. 9.10. Final 18.18°C Isotherm for Sample D.

the BET theory is not valid, since its derivation considers only "physically" adsorbed water. The final calculations, with little or no "bound" water involved, are undoubtedly the more valid representation of the surface area of the sample. A nitrogen surface area determination, following the last water desorption, gave 9.4 m^2/g. This agreement of these two values is quite good and bears out the validity of using 16.2 and 10.6 A^2 for the cross-sectional area occupied by physically adsorbed nitrogen and water molecules respectively. A similar diminution of the nitrogen-evaluated surface area as water is adsorbed on alumina has been observed.[7]

These isotherms show a high-pressure hysteresis associated with porous structure of the adsorbate. The hysteresis loop appears to close at a partial pressure of 0.35 for sample A, indicating the presence of quite a number of pores of very small radius. In contrast, the hysteresis loop closes at about 0.65 partial pressure for sample D, indicating a minimum pore radius much larger than for sample A.

Thus it appears that the 1200°C calcining temperature is great enough to effectively eliminate the very fine pores found in the 650°C calcination. This elimination of fine pores is also evident by the decrease in specific surface in the 1200°C calcination; apparently the thoria sinters appreciably, closing the small pores. Furthermore the "bound" water in these pores contributes a finite surface thickness which diminishes the area available to other adsorbate molecules, hence the decrease in surface area

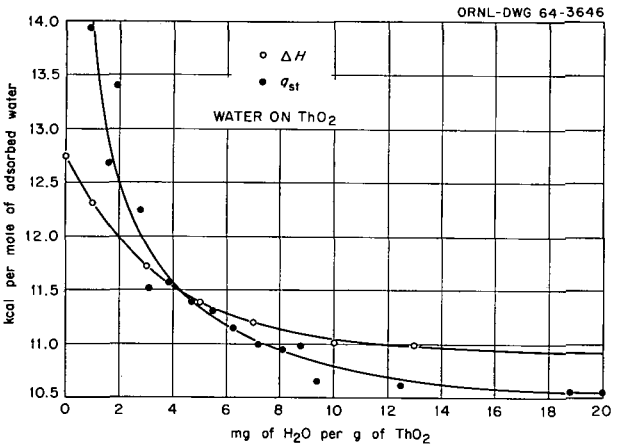

Fig. 9.11. Heat of Adsorption of Water on Thoria A.

determined with nitrogen accompanying the adsorption of "bound" water.

Figure 9.11 compares the isosteric heat of adsorption (q_{st}) and the differential heat of adsorption (ΔH) of water on sample A. The former was calculated from 17.35, 25.00, and 32.18°C isotherms, and the latter was determined calorimetrically and is identical with the curve of Fig. 9.4. The heat of liquefaction of water has been added to the net differential heats of Fig. 9.4, and the scale for the amount of water adsorbed has been shifted from the 500° vacuum weight to the vacuum weight at 17.35°. The isosteric heats were calculated from the adsorption branch of isotherms which, in addition to showing the high-coverage hysteresis loop, had not closed with the desorption branch. The application of the Clausius-Clapeyron equation is, therefore, of questionable validity. Nevertheless, the comparison shows good correlation between these values and also the higher degree of precision inherent in the calorimetric values. The deviation of q_{st} from ΔH at the low coverages may well be a manifestation of the last remnants of the "bound" water becoming associated with the surface.

Infrared Spectra of Adsorbed Species on Thorium Dioxide

C. S. Shoup, Jr.

Calorimetric heats of immersion and gravimetric adsorption experiments have revealed that the thorium dioxide–water interface is a very complex system. Although excellent data have been obtained in terms of weight changes and energies involved as a function of environmental conditions, these measurements reveal little information as to the structure or bonding characteristics of the adsorbed species, information which is necessary for a thorough interpretation of the experimental data, particularly in the low-pressure region.

Techniques such as low-energy electron diffraction,[15] nuclear magnetic resonance,[16] and infrared spectroscopy[17] have been shown to be applicable to surface studies. For example, infrared spectroscopy has been used to detect the presence of three types of OH groups remaining on the surface of γ-alumina after outgassing at temperatures as high as 700°C.[18] Preliminary experiments were therefore undertaken to determine the feasibility of using infrared spectroscopy for a direct investigation of the nature of the species adsorbed on the thoria surface as a function of environmental conditions.

One of the major problems in an investigation of this type is to prepare a sample that simultaneously meets the following conditions:

1. the sample must be reasonably transparent to infrared radiation in the wavelength region of interest;
2. the number of adsorbed species in the radiation beam must be large enough to be detected spectroscopically;
3. if a supporting medium is used, it must not distort the spectra of the species of interest;
4. the sample must be reasonably permeable to gases *if* an *in situ* examination is desired;
5. the sample must maintain its structural integrity during the experimental measurements.

Infrared spectra of the surface of thoria were obtained earlier by dispersing small quantities of the thoria powder in a pressed disk of potassium bromide.[19] The serious disadvantages of the

[15] A. U. MacRae, *Science* **139**, 379 (1963).

[16] W. S. Brey, Jr., and K. D. Lawson, *J. Phys. Chem.* **68**, 1474 (1964).

[17] R. P. Eischens, *Science* **146**, 486 (1964).

[18] J. B. Peri and R. B. Hannan, *J. Phys. Chem.* **64**, 1526 (1960).

[19] M. E. Wadsworth *et al.*, "The Surface Chemistry of Thoria," Progress Report, University of Utah, Jan. 31, 1959.

pressed-salt technique are now well known,[20] and the anomalous effects on the spectra due to the presence of the halide are such as to render most spectra produced by this technique suspect.

Several methods were attempted in an effort to produce thoria samples meeting the above requirements. Success was achieved by pressing thin self-supporting disks of pure thoria powder. These disks were observed to be permeable to water and reasonably transparent to infrared radiation from 4000 cm^{-1} to at least 400 cm^{-1} (2.5 μ to at least 25 μ). Several disks 20 mm in diameter were subsequently prepared from sample A (see Table 9.1) and from thoria designated as DT-102W by pressing the powder at 20,400 psi.[21] The latter sample had been calcined at 650°C and had a nitrogen BET surface area of 33 m^2/g. The disk weights varied from 100 to 300 mg, yielding "optical densities" of 32 to 95 mg/cm^2.

Infrared spectra of these disks were obtained with the disks exposed to the ambient environments within the spectrophotometers. Typical spectra are illustrated in Fig. 9.12 for a disk made from DT-102W thoria in a spectrophotometer which had been purged with dry air to reduce the water vapor and carbon dioxide concentrations to very low levels. Although the environmental conditions represented in Fig. 9.12 were not well known, there is a significant difference in the temperatures of the thoria as represented by spectra *a* and *b*. Spectrum *a* was recorded by placing the thoria disk very close to the entrance to the photometer section of the instrument and was thus close to a focus point of the incident radiation. Spectrum *b* was recorded with the disk in a KBr beam condenser which produced a reduced image of the source on the disk. As a result of the increased intensity of the incident radiation on the thoria, the temperature of the thoria surface was significantly higher in the latter case.

Although it would be premature to attempt any detailed interpretation of the observed spectra, it is obvious that a large amount of chemisorbed carbon dioxide and hydrogen-bonded water is present on the surface of the thoria under the above conditions. An increase in temperature has many effects, one of which is to reduce the surface concentration of hydrogen-bonded water and to increase the concentration of OH groups which are not involved in hydrogen bonding. The infrared spectra of disks of sample A thoria were very similar to the above; however, there were some significant differences, which are being further investigated under more controlled conditions.

[20] W. A. Pliskin and R. P. Eischens, *J. Phys. Chem.* 59, 1156 (1955).

[21] The 20-mm disks were prepared by A. J. Taylor of the Metals and Ceramics Division. The infrared spectrophotometers were used through the courtesy of the Chemistry and Analytical Chemistry Divisions.

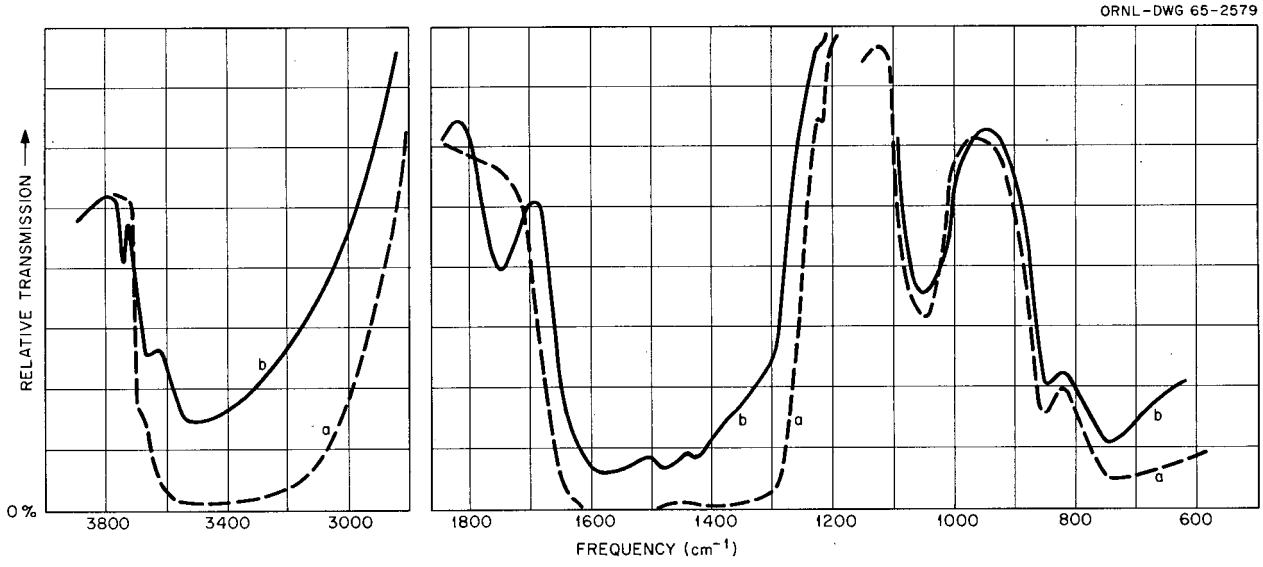

Fig. 9.12. Typical Infrared Spectra of DT-102W Thoria.

PERMEABILITY OF VIBRATORILY COMPACTED FUELS

M. J. Kelly J. C. Griess

Previous studies[22] of the mechanism of waterlogging failures in fuel elements were concerned primarily with permeability measurements of sol-gel oxide fuel elements. Extension of this work has resulted in a broadening of the experimental program, with the permeability of the fuel being only one of several variables considered.

Waterlogging is the entrance of water through a cladding flaw into the available void space within a fuel element. The subsequent possibility of catastrophic failure of a fuel element depends on the stresses imposed on the cladding as the water is ejected upon increasing reactor power. These stresses are interrelated functions of (1) the permeability of the fuel element, (2) the available void volume, (3) the geometry of the fuel element, and (4) the rate of temperature rise. All unbonded fuel elements are subject to waterlogging, and it seems probable that any fully waterlogged element will fail upon a large power excursion from low power. Except for this condition, limitations on reactor startup procedures (based on the interrelations of the above variables) should greatly minimize the possibility of waterlogging failure.

During the past year experimental work to determine the interaction of these variables has been in progress.

Variable Properties of Fuel Elements

Permeability. – The permeability of pellet-loaded fuel rods is much greater than that of powder-packed rods because of the annular clearance between the fuel and the cladding. In powder-packed rods no annular clearance exists, and the permeability of the compact determines the overall permeability of the fuel element.

The permeability of the compacted fuel decreases inversely with the square of the surface area per unit volume and increases directly as the cube of the void percentage[23] although the associated constants are not established for dense packings. Practical considerations dictate as small a void space as possible (8 to 12%); and, while the surface area could be controlled by elimination of very fine material, this is not economically attractive.

The range of permeability for compacts prepared for the Kilorod program is from 10^{-3} to 5×10^{-3} darcy. Other compacts studied have permeabilities ranging from 10^{-4} to 1. Since extremely fine powders pack poorly due to surface effects, it is expected that practical fuel rods will have permeabilities above 10^{-3} as fabricated, and after attaining nuclear power will increase that permeability by condensation of the fine fraction as a result of sintering.

Available Void Volume. – Sintered pellets normally have most of their porosity unavailable (i.e., closed pores). The available void space in a pellet-loaded rod is the annular space plus any fission gas gap. The available porosity within a powder-packed rod corresponds to the void volume, since all of the void space is interconnected by finite passages. In either type of fuel, all the free volume must be considered as available when considering waterlogging failure.

Geometry of the Fuel Element. – In general, fuel elements are long compared to their cross section. Tubular elements are most common, but other shapes are used. For waterlogging failure, flow the full length of an element must be considered at the effective cross section of the fuel.

Rate of Temperature Rise. – This is the most independent of the variables and may be controlled over a wide range during reactor startup. It is not measured directly but can be calculated with reasonable accuracy from the physical characteristics of the reactor assemblies and the rate of reactor power rise.

Theoretical Considerations

The pressure-volume-temperature properties of water are well known. These, together with the description of the properties of fuel elements, make it possible to construct a simplified descriptive relationship as a model from which to work.

Maximum internal pressure is the sum of the pressure drop down the length of the element and the pressure drop across the defect. This

[22] M. J. Kelly and J. C. Griess, *Reactor Chem. Div. Ann. Progr. Rept. Jan. 31, 1964*, ORNL-3591, pp. 109–12.

[23] F. C. Carman, *Flow of Gases Through Porous Media*, pp. 8–20, Butterworths, London, 1956.

total pressure is created by flow from expansion upon increasing temperature plus the vapor pressure. Little work has been done on the defect pressure drop, and, other than noting that critical flow controls, it will not be considered in this report.

The pressure drop down the length of the element depends on the flow caused by the expansion of liquid within the tube and may be described by:

$$\Delta P_{\text{flow}} = \left[\left(\frac{LV}{Ak} \right) \left(\frac{dT}{dt} \right) \left(n \frac{dV}{dT} \right) \right] \times \text{a constant} ,$$

where

V = free volume in fuel element, ml,

dV/dT = rate of volume change with temperature, ml/°K,

n = viscosity at T, centipoises,

L = length of fuel pack, cm,

A = cross-sectional area of fuel pack, cm^2,

k = permeability of fuel pack, darcys,

dT/dt = rate of temperature change with time, °K/sec,

noting that (LV/Ak) is a property of the mechanical system and $(n\ dV/dT)$ is a property of the fluid, with dT/dt associated with both.

Figure 9.13 shows a plot of $n\ dV/dT$ vs T at various conditions prepared using the expansion properties of water and the viscosity of liquid or vapor as required. If dT/dt were constant, the model equation would be simple to use. Assuming, however, that the assembly has a specific heat of about 1 cal per centimeter of length and that when waterlogged 10% of this is due to water, the pressure rise is unduly weighted by the heat of vaporization as the water flashes to steam. This results in a change in dT/dt which depresses the total pressure. The temperature at which this occurs is directly dependent on the pressure drop across the defect.

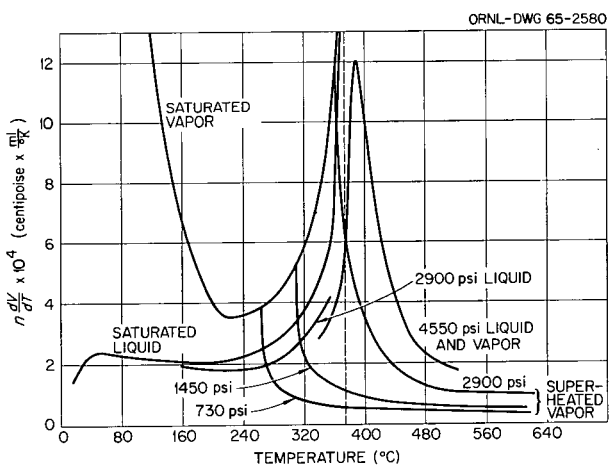

Fig. 9.13. Plot of the Rate of Thermal Expansion Times Viscosity vs Temperature for Water both Liquid and Vapor at Various Pressures.

Experimental Studies

The most practical method to simulate the stresses on a waterlogged fuel element during

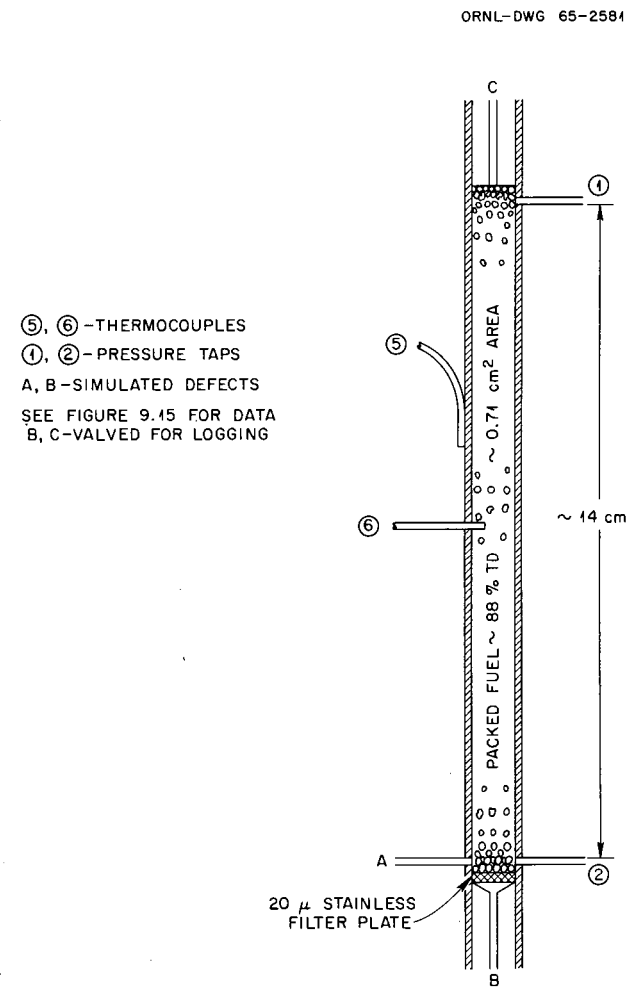

Fig. 9.14. Schematic of Test Element.

reactor startup is to completely fill the void space of a test element with water and then supply energy as if generated by fission. Electrical current passing through the cladding is used for this purpose. It is felt that the rate of expansion of the cladding being greater than that of the fuel does not compromise the results, since flow down the element caused by fluid expansion provides the compressive force necessary to retain firm fuel packing. The current source has been described elsewhere.[24]

The original test elements were rods formed from $\frac{1}{4}$-in. stainless steel pipe, schematically shown in Fig. 9.14. After filling, by the Metals and Ceramics Division, with fuel of nominal "Kilorod" size distribution and density, numerous tests from fully waterlogged conditions were made on two experimental assemblies. Test results showed that a much longer assembly was necessary to obtain data adequate for analytic extrapolation. A prototype "Kilorod" element was therefore obtained and installed in place of the shorter test pieces. Present experiments are obtaining data from this assembly, which has a packed fuel length of ~105 cm and a cross-sectional area of 0.94 cm^2.

Results

A plot of data from a short test element is shown in Fig. 9.15. The time period associated with these experiments was such that the heating current was merely turned on at a previously chosen setting. Neither constant power nor a particular dT/dt program could be obtained. Data from these experiments have been fitted to an empirical equation for the pressure drop down the element:

$$\Delta P = \left(3.1 - 2.3 \times 10^{-3}\, T \frac{dT}{dt}\right)\frac{LV}{Ak} \times 10^{-4}\ , \quad (1)$$

with the units as previously noted.

The experimental data can be fitted to our theoretical equation with gratifying precision up to the temperature at which flashing flow appears within the element if dT/dt is obtained from wall temperature data (5 on Figs. 9.14 and 9.15). Flashing flow can only occur when the internal vapor pressure exceeds the pressure drop across the defect. Once this occurs, rapid loss of internal liquid occurs, and a superheated vapor system is reached before the critical temperature. The extreme volume increase at the critical temperature is avoided, and the maximum pressure occurs shortly after flashing starts.

In order to explain the observed experimental results after flashing occurs, the liquid water must be entrained by the saturated steam and travel at steam velocity and viscosity. After expulsion of the entrained liquid, the superheated steam system can again be related to our theoretical equation with fair agreement with no empirical justifications.

The previously reported change[22] in effective permeability when changing from liquid water to gas as a test fluid was not observed when changing from liquid water to steam. Permeability measurements using steam (250–300°C) gave values identical with liquid water within the precision of the measurement for the test elements. Permeability measurements using nitrogen gas yielded values several times that of water as observed with previous samples. The

ORNL-DWG 65-2582

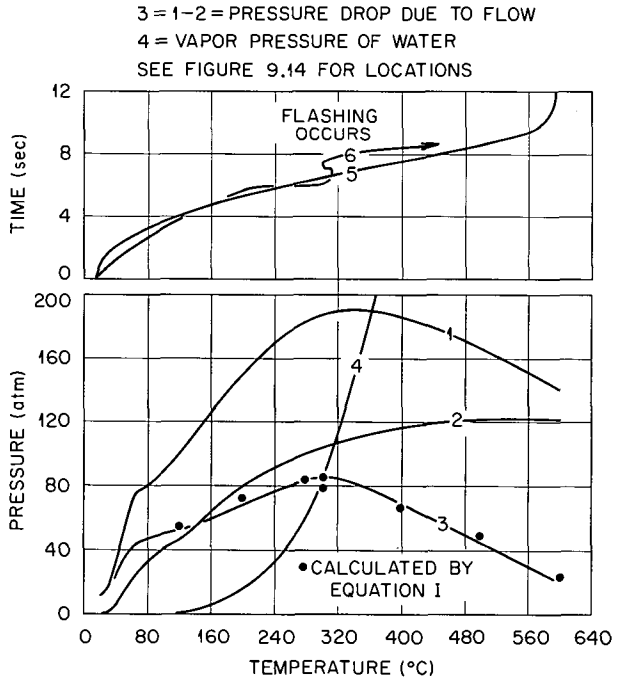

Fig. 9.15. Typical Test Data.

[24] J. C. Griess *et al.*, *Effect of Heat Flux on the Corrosion of Aluminum by Water*, ORNL-2939 (1960), pp. 8–9.

postulated surface interaction with water apparently is equally effective in the vapor phase.

A few preliminary experiments with the "Kilorod" element at a constant power input appear to confirm our assumptions from short-element data.

Conclusions

Present data indicate that an analytic interpretation of waterlogging stresses is feasible. The extension of such results to a general case, even if empirical, should supply guidelines for reactor operations and fuel element designers which will minimize the opportunity for waterlogging failure. The pressure effects at a defect assume greater importance now that a quantitative explanation involves internal steam formation and flashing flow. An effort will be made to determine the effect of various defect parameters.

GAS EVOLUTION FROM THORIA–3% URANIA SOL-GEL MATERIAL

D. N. Hess W. T. Rainey
B. A. Soldano

Introduction

Thoria–3% UO_2 sol-gel material proposed for use as a reactor fuel evolves gases when heated. Development of excessive pressure of such gases in a sealed fuel element could result in rupture of the element; this possibility might be increased if reaction between gas and metal were possible (e.g., zirconium alloy with hydrogen). Studies have been initiated to determine the factors that affect both the nature and the amount of gas evolved from sol-gel material.

Sol-gel material prepared from ^{233}U is of primary interest. Uranium-233 is quite radioactive and requires remote handling. The first experiments have, therefore, been done with sol-gel preparations (designated H-II and SC) of ordinary uranium supplied by the Chemical Technology Division as representative of materials prepared in laboratory-scale equipment. Experimental factors which have been controlled in the experiments to date include the nature of the sol-gel material under observation, the temperature of outgassing, the particle size of the material, and (to some extent) the atmosphere to which the material was exposed prior to the outgassing operation. Previous work by the Chemical Technology Division had shown that the quantity of gas evolved during heating was dependent on the temperature; this factor was held constant at 1000°C in most experiments in order to permit exploration of the effect of other variables. The related factors of surface area and particle size were considered to be of probable primary importance in controlling gas evolution, and considerable attention was paid to the use of various sized fractions of ground and screened material. An attempt was made to prevent the inadvertent adsorption of atmospheric CO_2 or H_2O on the freshly ground and sized material by performing these operations inside a plastic bag in an inert atmosphere; brief exposure to air was, however, permitted in most experiments during the weighing and loading of samples, and no controlled study has yet been made of the effect of this exposure.

The experimentally observed quantities in the study have been the total gas evolved, the composition of the evolved gas, the rates of gas evolution, and the ability of the material to absorb and desorb added gases.

Effects of Particle Size

A strong effect of particle size on the total gas evolved at 1000°C from SC material is indicated by Fig. 9.16; the results are plotted on a scale of relative surface area, derived from the arithmetic average particle diameters with an assumed value of 1.0 for surface area of spherical particles of 1.0 mil diameter. The linearity of the relationship and the extrapolation to zero gas evolution at zero surface area suggest that the evolved gas (essentially all CO_2) was being released only from the surface exposed by grinding and not from the interior of the particles. Such behavior is typical of chemisorbed material.

A strong effect of particle size was also found when the H-II material was tested at 1000°C. Eight times as much gas was released from –270 mesh material as from –20 +40 mesh material. The maximum volumes of gas obtained were as high as 1.0 std cm^3/g; this was six times as much as was released from the SC material. The

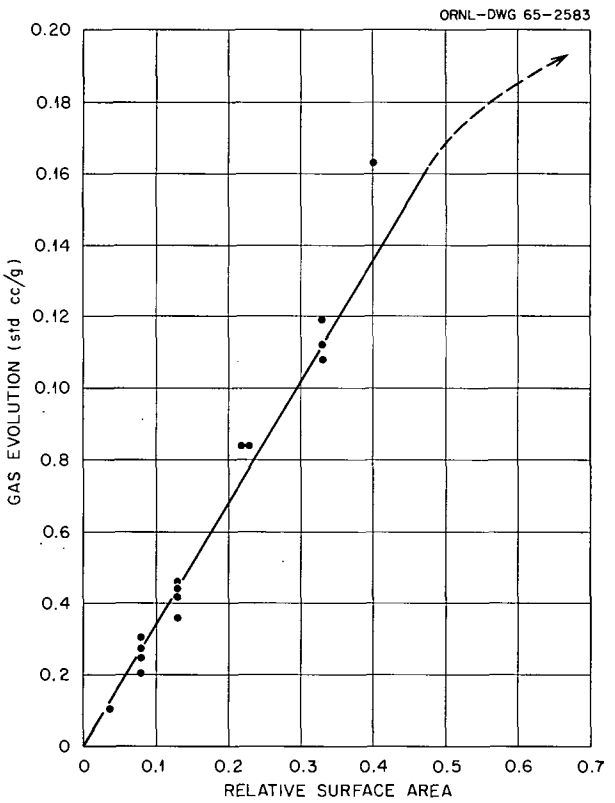

Fig. 9.16. Effect of Particle Size (Relative Surface Area) on Total Gas Evolution from SC Sol-Gel Material at 1000°C.

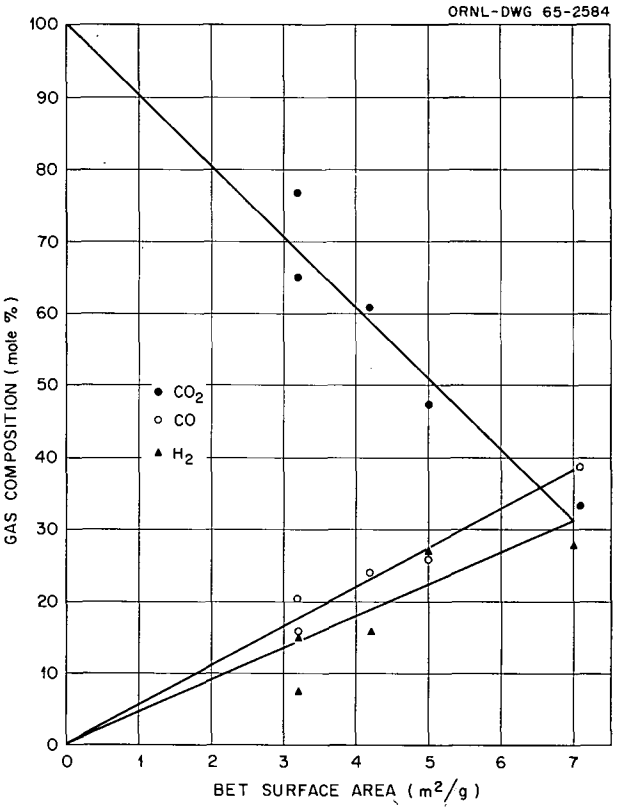

Fig. 9.17. Effect of BET Surface Area on Composition of Gas Evolved from H-II Sol-Gel Material at 1000°C.

composition of the gas was substantially different; CO and H_2 were present as important constituents. Particle size was found to have an important effect on the gas composition as well as the total gas. Figure 9.17 shows the relationship between surface area (measured by the BET method) and the gas composition. Extrapolation of the relationship of Fig. 9.17 to the very low BET surface area of 0.1 m^2/g suggests that the gas evolved would be about 99% CO_2 – just what was observed in tests of the SC material, which had such a low surface area.

Effect of Temperature

Measurements of the total gas evolved and the rate of the evolution were made on –270 mesh samples of the H-II material at temperatures of 1000 and 1200°C. More gas was consistently evolved from the samples at 1000 than at 1200°C, and there was some evidence that, at 1200°C, an initially higher gas release was being followed by a slow removal or consumption process. It is possible that the surface of the sol-gel material at 1200°C was catalyzing the water-gas reaction,

$$H_2 + CO_2 \longrightarrow CO + H_2O ,$$

for which the value of the equilibrium constant is around 2.7 at 1200°C. The gas analytical technique which was used in the experiments did not provide values for H_2O. As a consequence, the reaction of H_2 and CO_2 to form CO and H_2O could have resulted in an apparent decrease in the total gas evolved.

Reversible Gas Adsorption on Sol-Gel Material

In studies of particle size effects, the SC material had released a gas which was essentially

pure CO_2. After these tests, some of the samples were exposed to air to determine whether CO_2 would be adsorbed and, if so, to what extent. Reevacuation at 1000°C was used to remove any adsorbed gas, and it was found that less than 10% of the original amount was evolved. This suggested that, for the SC material, the originally evolved CO_2 had been present in the original material as it was exposed by grinding and had not come from adventitious adsorption from the air during a brief exposure during weighing. The small amount of gas involved made it inadvisable to perform further studies of reversible adsorption with this material.

A sample of –270 mesh H-II material was used for a series of studies of the reversible adsorption and desorption of CO_2; the desorption was followed as a function of time at various temperatures, while the adsorption was always achieved by exposing the sample to 1 atm of dry CO_2 and permitting it to cool to room temperature in this environment. The samples were then evacuated at room temperature before the test boat was inserted into the preestablished temperature region of the furnace. Figure 9.18 shows the results of successive tests at 250, 500, 750, and 1000°C; the desorption was quite rapid, and temperatures of 500°C or higher were apparently adequate to remove all the adsorbed gas in these tests. The reversibility of the CO_2 sorption-desorption is illustrated by Fig. 9.19, showing how the pressure in the apparatus (originally evacuated at room temperature after exposing the sample to 1 atm of CO_2) changed as the H-II sample was heated to 1000°C and then allowed to cool down. A similar reversibility was found for SC material, but the amounts of gas and pressures were negligible.

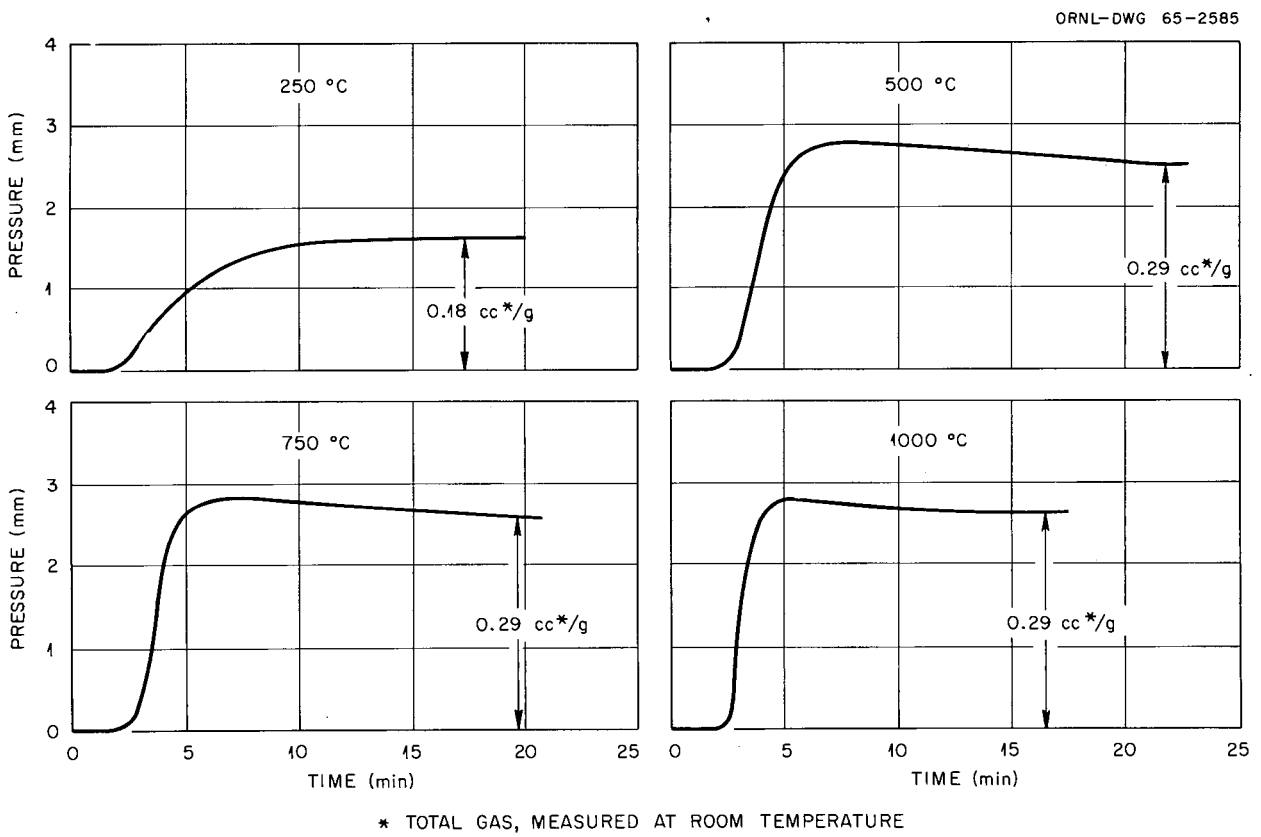

Fig. 9.18. Desorption of CO_2 from H-II Sol-Gel Material at Various Temperatures.

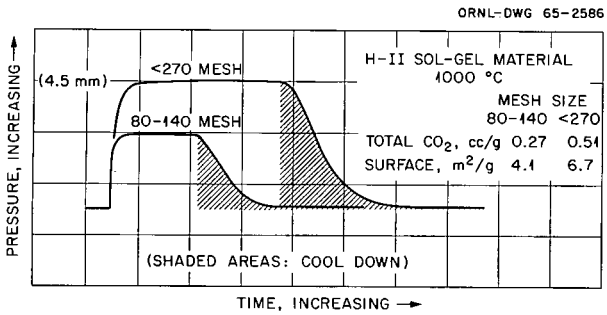

Fig. 9.19. Reversibility of CO_2 Desorption from H-II Sol-Gel Material at 1000°C.

Discussion

The study of gas evolution was undertaken because of the possibility that gas evolution from reactor fuel elements in service might lead to distortion of the fuel element or failure of the fuel element cladding. The following points summarize what has been learned so far by studies on two different samples of nonradioactive laboratory-prepared material:

1. There is a large difference in the behavior of different materials, suggesting that ostensibly similar preparatory methods may ultimately be refined to provide material with more desirable properties.
2. The amount of gas evolved depends strongly on the exposed surface area of the material. It appears to be evolved from the material itself and not to be a consequence of adsorption after grinding and sizing. The question has been raised, but not answered, whether use in a reactor will cause a great increase in surface area and, presumably, release of potentially available gas.
3. The composition of the gas evolved depends significantly on the particle size (surface area exposed) of the material. It is possible that the surface of the material can catalyze the water-gas reaction.
4. Carbon dioxide is reversibly adsorbed on the material but may be removed by treatment at temperatures as low as 500°C.

The study will be continued in order to apply the results to plant material.

Part III

Gas-Cooled Reactors

10. Diffusion Processes

TRANSPORT PROPERTIES OF GASES

Studies of transport phenomena exhibited by gases are motivated in this laboratory by a desire to characterize completely fission-gas migration in high-temperature gas-cooled nuclear reactors. Initial investigations led to the formulation of the "dusty-gas" model, a mathematical model that describes gas transport through porous media as the migration of gas molecules through a localized, uniformly distributed collection of giant molecules or dust particles.[1] The gas-dust interactions are regarded as intermolecular collisions in which one of the molecules is preponderantly greater than the other in both size and mass. Because of this formal view, it is possible to employ the elaborate analytical apparatus of rigorous kinetic theory with little change. Moreover, by suitable substitution for certain geometric parameters, it has also been demonstrated that the model can be applied to describe gas transport through capillaries as well.[2]

In addition to providing a unified and consistent theoretical treatment of concentration-induced migration,[1] extension of the model to include thermal gradients has revealed unsuspected relationships among several gas properties.[2] One of these is the possible use of the thermal transpiration phenomenon (or "thermomolecular pressure effect") in studies of inelastic collisions.[2,3] More recently, a consideration of the simultaneous existence of concentration and thermal gradients has yielded the first mathematical formulation of the effect of surface collisions on thermal diffusion.[4] It is unfortunate in this lattermost case that there are insufficient experimental data with which to test some of the interesting effects predicted.

The theoretical investigation of the effect of pressure (surface collisions) on thermal diffusion and the current experimental studies of thermal transpiration represent a logical continuation of previous work regarding the dusty-gas model; these programs, together with continuing experimentation of gaseous diffusion phenomena, comprise the more fundamental aspects of our gas transport research. Several other problems had also been investigated during the past year that are more directly oriented toward reactor application. Among these is the characterization of gas transport through unclad fuel-admixed graphite and graphites containing pyrolytic-carbon-coated fuel.

Pressure Dependence of the Thermal Diffusion Factor[4]

A. P. Malinauskas E. A. Mason[5]

The simplest apparatus that can be used to study thermal diffusion consists of two bulbs which are maintained at two different uniform temperatures and which are interconnected by a small tube in such a manner that a temperature gradient exists along the entire length of the tube. If a binary gas mixture (e.g., of components 1 and 2) is introduced into the apparatus, a relative drift motion of the two components will occur between the interconnected volumes which usually (but not always) tends to concentrate the heavier component in the colder region. The

[1] R. B. Evans III, G. M. Watson, and E. A. Mason, *J. Chem. Phys.* 35, 2076 (1961); 36, 1894 (1962).

[2] E. A. Mason, R. B. Evans III, and G. M. Watson, *J. Chem. Phys.* 38, 1808 (1963).

[3] E. A. Mason, *J. Chem. Phys.* 39, 522 (1963).

[4] E. A. Mason and A. P. Malinauskas, *J. Chem. Phys.* 41, 3815 (1964).

[5] Consultant, University of Maryland, Institute for Molecular Physics.

concentration gradient so generated causes a relative drift motion opposite to the thermal diffusion. Eventually, transport due to the concentration-induced diffusion just equals the thermally induced transport, and a steady state is attained. Under this condition, the separation of one of the components can be obtained from the equation

$$\nabla x_1 = -x_1(1 - x_1)\alpha_{12}\nabla \ln T , \qquad (1)$$

where x_1 represents the mole fraction of component 1, T is the temperature in °K, and α_{12} is the thermal diffusion factor of the gas pair 1-2. The quantity α_{12} is invariant to an interchange of the subscripts, but may be positive or negative, depending upon the assignment of the subscripts. For this reason the convention has been adopted to assign the subscript 1 to the heavier component, and to write α_{12} positive if the heavier component does indeed concentrate in the colder region. It has been experimentally observed that at certain temperatures or gas compositions the thermal diffusion behavior is reversed; that is, α_{12} changes sign; these are called "inversion points."

In the normal or hydrodynamic region, α_{12} is independent of pressure as long as only binary molecular collisions are important. In the Knudsen region (very low pressures), however, the effective value of α_{12} is zero, since each component of the gas mixture behaves independently, and there is no relative separation of the components even though thermal transpiration occurs. Presumably, then, the effective thermal diffusion factor, α_{12}(eff), would decrease through the intermediate-pressure (transition) region, and would approach zero as the pressure approached zero.

The dusty-gas model is well suited to describe the pressure dependence of α_{12}, since a variation of the mole fraction of the dust component is formally equivalent to a variation in the actual pressure of the gas mixture. Application of the model, in accordance with a theory of thermal diffusion in ternary mixtures that has been recently formulated,[6] leads to an expression for α_{12}(eff) which is the ratio of two polynomials in $1/p$, where p is the actual gas pressure. The numerator is linear in $1/p$, whereas the denominator is quadratic in $1/p$, so that α_{12}(eff) is zero at very low pressures and approaches a constant value at high pressures as required. However, the transition from the low-pressure limit to pressure-independent separation in the hydrodynamic region can be quite complicated and varied, depending upon the temperature, molecular masses, and intermolecular forces of the particular gas molecules. (See ref. 4 for a detailed discussion.)

Results for the effective thermal diffusion factor of He-Ar mixtures in circular capillaries are illustrated in Figs. 10.1 and 10.2. In Fig. 10.1, α_{12}(eff) is plotted as a function of d/l_{He} at 356°K, where d is the diameter of the capillary, and l_{He} represents the mean free path of the helium atoms when only He-He collisions are considered. Three curves are shown: one for $x_{Ar} = 0$; one for $x_{He} = 0$; and a third for an equimolar mixture. The variation of α_{12}(eff) in the three cases is the behavior to be expected when the corresponding pressure-independent α_{12} [the high-pressure limits of α_{12}(eff), shown by dashed lines in the figure] are fairly large and "normal." The experimental points shown in the figure represent experimental data taken by Kotousov[7] for a 50-50 mixture at about 315°K. Because of a lack of experimental details, it was necessary to adjust Kotousov's data by arbitrary scale factors in order to reduce them to the same scale as the calculated curves; we thus claim only qualitative agreement with experiment.

[6]F. van der Valk, *Physica* **29**, 417 (1963).

[7]L. S. Kotousov, *Soviet Phys.—Tech. Phys. (English Transl.)* **7**, 159 (1962).

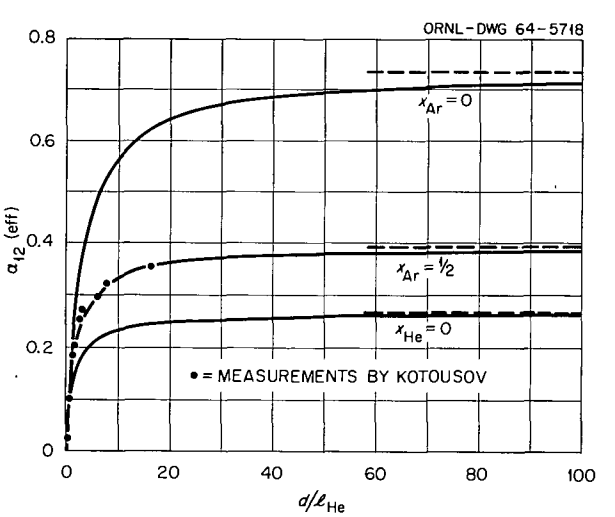

Fig. 10.1. Thermal Diffusion of the System He-Ar at 356°K as a Function of Pressure and Composition.

For a Lennard-Jones (12-6) interaction potential, the system He-Ar is predicted to have an inversion point at a temperature slightly above 32.0°K; thus the high-pressure limits of α_{12}(eff) shown in Fig. 10.2 are both small in magnitude and negative. The pressure dependence of α_{12}(eff) at this temperature, however, is predicted to possess three interesting features:

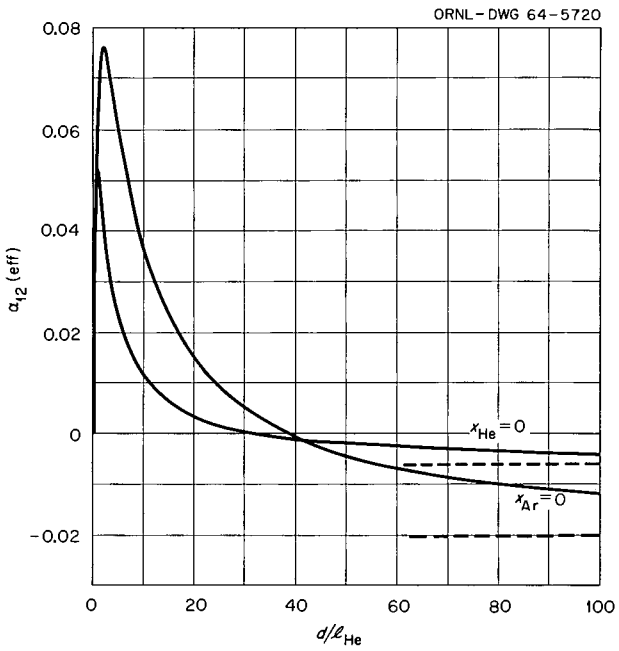

Fig. 10.2. Thermal Diffusion of the System He-Ar at 32.0°K (Slightly Below the Inversion Temperature) as a Function of Pressure and Composition.

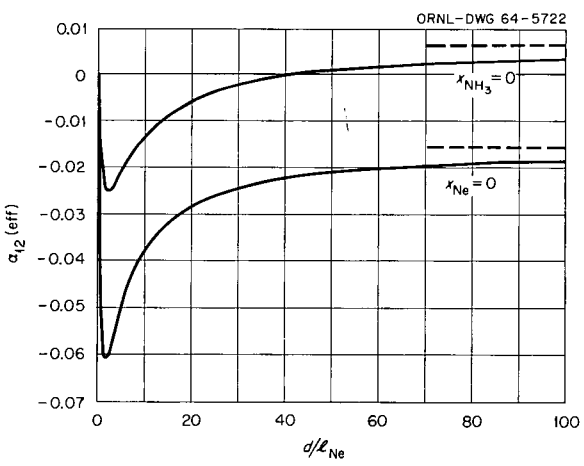

Fig. 10.3. Thermal Diffusion of the System ^{20}Ne-NH$_3$ at 358°K as a Function of Pressure and Composition.

(1) the effective thermal diffusion factor goes through a maximum; (2) if the pressure corresponds to $d/l_{He} \sim 37$, an inversion with respect to composition should be observed; (3) the inversion due to temperature depends upon the pressure at which the experiments are performed. Figure 10.2 clearly illustrates, then, the abnormalities that can occur in the behavior of α_{12}(eff) in the region of a temperature inversion. We have also been led to conclude that a similar behavior is possible in the region of an inversion due to composition; this is illustrated in Fig. 10.3, where we have plotted α_{12}(eff) as a function of d/l_{Ne} for ^{20}Ne-NH$_3$ mixtures.

Until now, the abnormal behavior of α_{12}(eff) with pressure in the region of inversion points was largely unsuspected; hence the experimental studies of thermal diffusion at low pressures are scanty. Admittedly, it is difficult to obtain accurate experimental data at such pressures as are required, but it should be possible to check some of the predictions at least qualitatively.

Thermal Transpiration

A. P. Malinauskas

The apparatus for investigations of the thermal transpiration phenomenon is similar in most respects to the thermal diffusion apparatus described above, except that in this case a pure gas is employed, smaller connecting tubes are used, and pressure, rather than composition, is monitored. The thermal gradient causes a flux of gas molecules in the direction from the colder region to the warmer region; at the steady state, this flux is counterbalanced by a molecular flux whose driving force is the resultant pressure gradient. If the steady-state values of the pressure drop Δp across the connecting tube are plotted as a function of some characteristic pressure (the pressure in the warmer region is commonly chosen), it is observed that Δp initially increases rapidly with pressure until it attains a maximum, and then it gradually decreases to zero.

An application of the dusty-gas model to this phenomenon has postulated that the magnitude of Δp at the maximum is functionally related to the ease with which the gas molecules can transfer

translational energy to internal degrees of freedom via collisions.[2,3] Thus, for example, it is possible to determine the rotational collision number Z_{rot} characteristic of a particular gas molecule from thermal transpiration experiments. The actual procedure has been appropriately discussed elsewhere;[2,3,8] hence we attempt only a brief treatment here. The basic equation used in the calculations is

$$F = F_0\left(\frac{\eta_0}{\eta}\right)\left(\frac{M}{M_0}\right)^{1/2}\left(\frac{\Delta p^*}{\Delta p_0^*}\right), \qquad (2)$$

where η is the gas viscosity, M is the molecular weight of the gas, Δp^* is the value of Δp at the maximum, and F is a quantity that is related to Z_{rot} in a somewhat complex manner. The subscripts zero refer to a gas possessing no internal degrees of freedom, for which $F_0 = 0.8743$ according to rigorous kinetic theory, and is virtually temperature independent.

In order to obtain a measurable Δp, it is necessary in most cases to impose a rather large temperature gradient; thus the choice of a characteristic temperature for the evaluation of the viscosity coefficient ratio becomes a determining factor in the calculation of F. For this reason, our current investigations are directed toward a suitable choice of the characteristic temperature as well as toward a demonstration of the validity and feasibility of the proposed method. The present studies are being conducted with the gases Ne, Ar, Kr, Xe, CO_2, N_2, O_2, CO, and CH_4, but are not sufficiently complete to justify unambiguous conclusions at this time.

Gaseous Diffusion

A. P. Malinauskas

In virtually every treatment of the migration of a species through a porous medium by a gaseous diffusion mechanism, the rate of transport is said to be related to an effective gaseous diffusion coefficient and is taken as

$$D_{12}(\text{eff}) = (\epsilon/q)D_{12}\,, \qquad (3)$$

where D_{12} is the corresponding diffusion coefficient in free space, and (ϵ/q) is a quantity determined only by the internal structure of the porous barrier. [Equation (3) seems never to have been tested experimentally, however.] If Eq. (3) is valid, and if it can be further assumed that the structure of the medium, insofar as (ϵ/q) is concerned, is nearly temperature independent, then it is possible to predict the diffusion of any gas pair *i-j* through the septum from a series of effective diffusion coefficient measurements at a single temperature with some other gas pair, *k-l*, provided that the necessary diffusion coefficient values in free space are known. Unfortunately, for many systems of interest to reactor technology, for example, the gas pair He-Xe, the appropriate diffusion coefficients are either unknown, or are reported only for much lower temperatures, so that the extrapolation to the required temperature range is risky.

From a more fundamental viewpoint, the free-space diffusion coefficients provide a useful means of obtaining information regarding intermolecular forces, but in this case too, unambiguous conclusions can be drawn only if the values have been determined with an accuracy not currently attainable, or if the measurements span a wide range of temperature. It is thus desirable to measure gaseous diffusion coefficients at elevated temperatures, to fill theoretical as well as applied needs.

The direct measurement of D_{12} at temperatures of the order of 1000°K is difficult, and this difficulty is probably the primary reason for the present dearth of data. However, an indirect method has recently been proposed to circumvent much of the apparatus problems. Since viscosity coefficients can be determined with a higher degree of accuracy than the corresponding diffusion coefficients, and can be more conveniently obtained at elevated temperatures, Weissman and Mason[9,10] have suggested that the composition dependence of the viscosities of gas mixtures be used for the indirect determination of D_{12}. In support of this method, they have presented comparisons between values derived from viscosity

[8] A. P. Malinauskas, *Results of Preliminary Experiments on Thermal Transpiration*, ORNL-TM-801 (April 1964).

[9] S. Weissman and E. A. Mason, *J. Chem. Phys.* **37**, 1289 (1962).

[10] S. Weissman, *J. Chem. Phys.* **40**, 3397 (1964).

data and directly measured coefficients; with few exceptions, the agreement is satisfactory.

One of the systems for which discrepancies are evident is the gas pair He-Xe. This is surprising, since the Weissman-Mason procedure follows in a straightforward manner from kinetic theory as formulated by Chapman and Enskog,[11] and it should therefore be particularly applicable to noble-gas systems. For this reason and for the obvious interest in the system He-Xe as applied to high-temperature gas-cooled nuclear reactors, we decided to reinvestigate the diffusion characteristics of the gas pair He-Xe.

The diffusion measurements were made with a two-bulb apparatus described elsewhere.[12,13] To achieve greater accuracy, a relative method was used; the diffusion coefficient values were referred to results obtained for the system He-Ar, for which the coefficients are reasonably well known. As a check on this method, the system Ar-Xe was also included in the investigation.

[11]A thorough discussion of the Chapman-Engskog kinetic theory of gases is contained in the classical text by J. O. Hirschfelder, C. F. Curtiss, and R. B. Bird, *Molecular Theory of Gases and Liquids*, Wiley, New York, 1954.

[12]A. P. Malinauskas, *Reactor Chem. Div. Ann. Progr. Rept. Jan. 31, 1964*, ORNL-3591, pp. 117–18.

[13]A. P. Malinauskas, *J. Chem. Phys.* **42**, 156 (1965).

Some of the experimental data are shown in Figs. 10.4 and 10.5, where D_{12}, reduced to 1 atm pressure in the usual manner, is displayed as a function of temperature. The solid lines in the figures were calculated from the Chapman-Enskog expression for D_{12} and the following Lennard-Jones (12-6) potential-energy parameters: Ar-Xe, ϵ/k = 257°K, σ = 3.367 A; He-Xe, ϵ/k = 67.3°K. σ = 3.273 A.

It is apparent from Fig. 10.4 that both the results of the present work with Ar-Xe and the lone viscosity-derived value are in satisfactory agreement with previous measurements by Amdur and Schatzki[14] and by Srivastava.[15] The largest deviations are about 4%; they are indicative of the difficulty in measuring D_{12} accurately. On the other hand, Fig. 10.5 clearly depicts the almost constant, 9% variance between Srivastava's[15] values and the present results for the system He-Xe. The more recent data are in excellent agreement with the diffusion coefficients calculated from viscosity measurements, however; they thus support the Weissman-Mason procedure.

[14]I. Amdur and T. F. Schatzki, *J. Chem. Phys.* **27**, 1049 (1957).

[15]K. P. Srivastava, *Physica* **25**, 571 (1959).

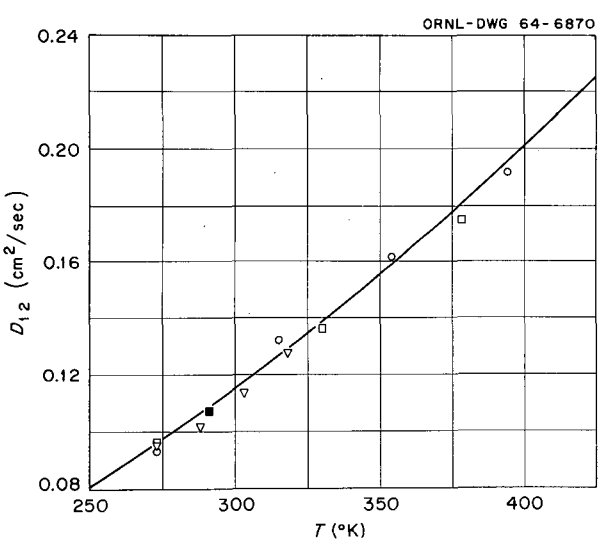

Fig. 10.4. Experimental Values of the Diffusion Coefficient of the System Ar-Xe at One Atmosphere Pressure. Solid Line, Lennard-Jones (12-6) potential; ■ Weissman and Mason; ◻ Amdur and Schatzki; ▽ Srivastava; ○ present work.

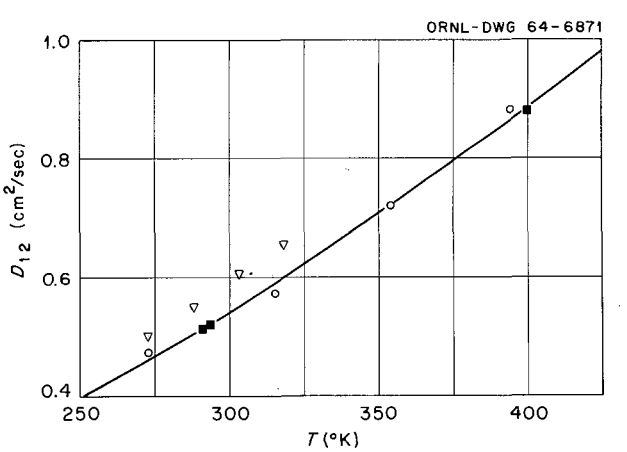

Fig. 10.5. Experimental Values of the Diffusion Coefficient of the System He-Xe at One Atmosphere Pressure. Solid Line, Lennard-Jones (12-6) potential; ■ Weissman and Mason; ▽ Srivastava; ○ present work.

Gas Transport Characteristics of Uranium-Fueled Graphites[16]

A. P. Malinauskas F. L. Carlsen[17]

Two types of fueled graphite prepared by an admixture technique have been under consideration for use in high-temperature gas-cooled nuclear reactors. In one, the graphite is fabricated by molding an admixture of high-fired UO_2 shot and a carbonaceous mix and then baking the compact at temperatures favorable for formation of uranium carbide; in the second, the fuel is admixed in the form of pyrolytic-carbon-coated UC_2 spheroids.[18] In the latter type, fission-gas retention is relegated to the impermeable pyrolytic carbon coating, but in elements containing the uncoated carbon, fission-gas transport is largely a characteristic of the graphite matrix. Furthermore, conversion of the UO_2 to uranium carbide yields a septum with large voids which, due to the consequent migration of the carbide, are partially enveloped by regions of relatively low permeability. Thus, in comparison with extensively studied reactor-grade graphites, graphites containing the uranium fuel show differences due to the necessary modifications in fabrication techniques (smaller batches, lower baking temperatures, etc.) along with, particularly in the case of the uncoated fuel elements, differences due to a direct alteration of the matrix by the fuel. Gas flow properties of both the coated and the uncoated types of fueled graphite were therefore investigated. The limitations of space do not permit a detailed presentation of the aspects of this work, which can be found elsewhere;[16] several highlights are given here.

The first series of investigations, begun in the latter part of 1962, consisted of a set of diffusion and permeability experiments designed to test the sensitivity of the gas transport theories to the gross inhomogeneity of uncoated fuel-admixed graphites.[19] No discrepancies were anticipated and none were detected. In another aspect of the work, a graphite of the same type was machined into six cylinders in such a way that flow measurements could be made parallel to the direction of the molding force applied in forming the compact, as well as in two mutually perpendicular directions to it. These permeability results are displayed in Fig. 10.6, where the pressure dependence of the permeability coefficient K is shown. The two specimens (1P and 2P) in which gas flow was made to occur in the direction parallel to the applied molding force clearly demonstrate an enhancement of gas transport relative to flow in the perpendicular directions (1A and 2A, 1C and 2C). Unfortunately, the same samples also gave higher porosity values when determined by both a gas expansion method and a mercury penetration method. Since the porosity determinations were omnidirectional, the flow enhancement observed appears to be fortuitous; it may be due to the higher porosities of these samples as well. Figure 10.6 also

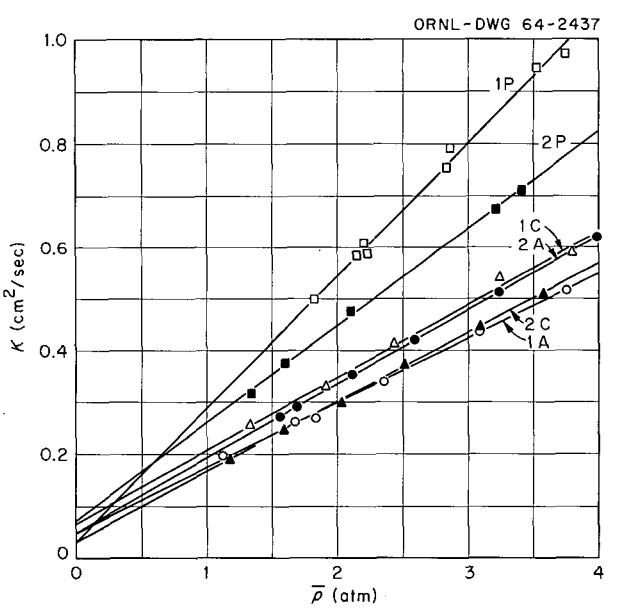

Fig. 10.6. Permeabilities to Argon of an Uncoated Fuel–Admixed Graphite as a Function of Pressure and Alignment Relative to the Direction of the Applied Molding Force. Samples 1P and 2P, flow parallel to molding force; samples 1A and 2A and 1C and 2C, flow in one of two mutually perpendicular directions to molding force.

[16] A. P. Malinauskas and F. L. Carlsen, *Bull. Am. Ceram. Soc.* 44(3), 251 (1965).

[17] Metals and Ceramics Division.

[18] R. A. Reuther and D. D. Johnson, *Proc. Conf. Carbon, Fifth, University Park, Pennsylvania 1961*, 1, 377–83 (1962).

[19] A. P. Malinauskas, *Reactor Chem. Div. Ann. Progr. Rept. Jan. 31, 1963*, ORNL-3417, p. 145. (At that time the material was incorrectly denoted as a "uranium-impregnated graphite.")

graphically illustrates the divergence in the permeability data for "duplicate" samples (from position to position within an otherwise identical specimen). This is readily seen when one compares the data for samples 1P and 2P, 1A and 2A, and 1C and 2C.

In the next series of experiments, the effect of fuel content on the permeability of uncoated uranium-admixed graphites was investigated. The four molded samples used were prepared under identical conditions but with differing uranium content (5.06, 7.26, 10.28, and 14.61% uranium by weight respectively). A comparison of the argon permeabilities of these samples (Fig. 10.7) with the corresponding pore-size spectra (Fig. 10.8) shows good agreement. In particular, the anomalous behavior of sample 916 (14.61% uranium) is obvious in both figures. This anomaly, as well as the lack of reproducibility of flow properties from position to position within the same material, discussed earlier, demonstrates the uniqueness imparted to graphite septa as the result of fabrication, and has led us to conclude that the relative concentration of the voids formed during the formation of uranium carbide in uncoated fuel-admixed graphites does not materially affect the fission-gas retention properties of such septa in the fuel concentration range studied.

Figures 10.9 and 10.10 illustrate flow properties and pore-size distributions of three fuel elements that contain pyrolytic-carbon-coated UC_2 spheroids. As in the previous case, the two sets of data correlate well, but the pore-size spectrum for the sample designated GA-S1, when compared with the spectra of the specimens containing the uncoated fuel, suggests a lower permeability coefficient than that observed. This discrepancy is believed to be due to the relative "effective lengths" of the pores in the

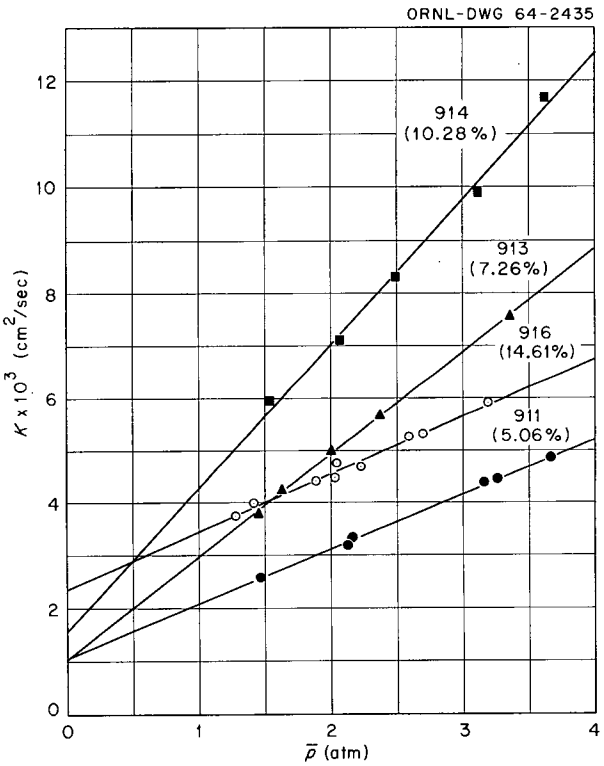

Fig. 10.7. Permeabilities to Argon of Uncoated Fuel–Admixed Graphites as a Function of Pressure and Fuel Content.

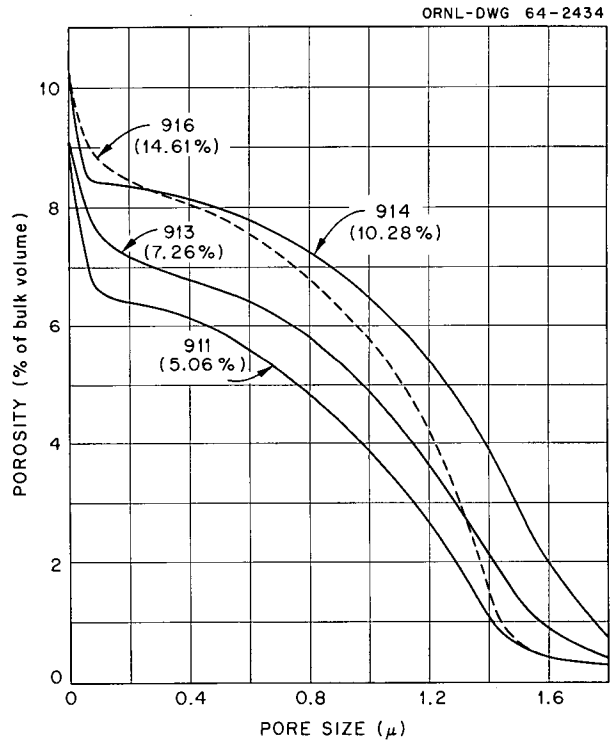

Fig. 10.8. Pore-Size Spectra of Uncoated Fuel–Admixed Graphites of Differing Fuel Content.

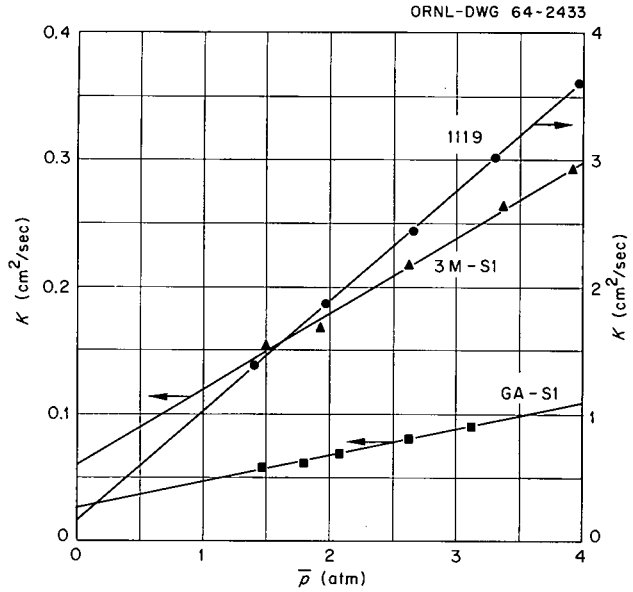

Fig. 10.9. Permeabilities to Argon of Graphites Containing Coated Particles.

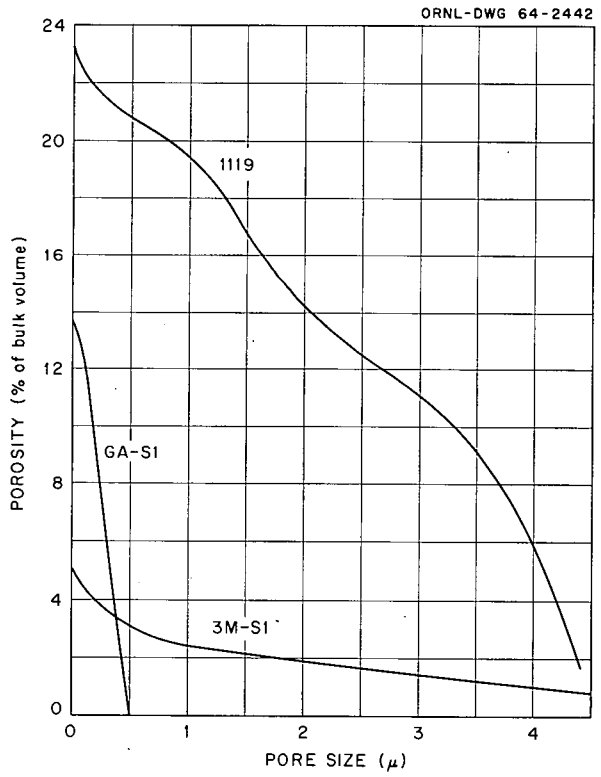

Fig. 10.10. Pore-Size Spectra of Graphites Fueled with Coated Particles.

two types of graphite, and aptly demonstrates that since pore-size spectra do not distinguish between pore length and pore number, whereas the effects of these two parameters on gas transport are in opposition, a simple comparison between the two properties cannot ordinarily be made.

ACTINIDE DIFFUSION IN PYROCARBONS

R. B. Evans III
J. L. Rutherford
J. O. Stiegler[20]
J. Truitt

Experimental determinations of diffusion coefficients for the migration of thorium, protactinium, and uranium as a function of temperature in massive pyrocarbons have continued. Our researches have revealed that variations in matrix structure and actinide concentration greatly influence the mode and extent of the observed migration. Three series of experiments have formed the basis for these findings.

The first series was designed to show comparisons of the migration behavior of various actinides in both as-deposited and improved pyrocarbons when the migration was initiated from thin-layer sources containing 10 to 30 μg of actinide per cm^2 on a unit area of specimen surface. Both $D_\perp$ and $D_{||}$ values were obtained, where D (cm^2/sec) represents the diffusion coefficient. The second series of experiments was restricted to $D_\perp$-thorium measurements in as-deposited pyrocarbons. In this series, the layers contained 2 μg of thorium per cm^2. The third series of experiments involved a constant-potential uranium source in order to produce diffusion results at the highest possible concentrations – as dictated by the limits of actinide solubility in pyrocarbons.

Thin-Layer Experiments at High Concentrations

Adequate descriptions of experimental procedures,[21] details of pyrocarbon structures,[22] peculiarities of the data,[23] and interpretations

[20] Metals and Ceramics Division.

[21] J. Truitt, G. D. Alton, and C. M. Blood, *Appl. Phys. Letters* 3(9), 150 (1963).

[22] R. B. Evans III, J. O. Stiegler, and J. Truitt, *GCR Program Semiann. Progr. Rept. Sept. 31, 1964*, ORNL-3619, p. 111.

[23] R. B. Evans III and J. Truitt, *Reactor Chem. Div. Ann. Progr. Rept. Jan. 31, 1964*, ORNL-3591, p. 118.

of the results[24,25] have been reported previously for the thin-layer experiments with 10 to 30 μg of actinide per cm^2 of pyrocarbon surface. It is important, however, to summarize these earlier results in order to form an introduction for discussions of our more recent findings. The high-concentration thin-layer experiments provided data over the temperature range 1000 to 2400°C; three distinct migration regimes were detected for the case of as-deposited pyrocarbon.

Below a threshold temperature of 1460°C, migration was found to be negligible. Above the threshold temperature but below 2000°C, the migration could be described by applicable diffusion equations. Within this regime, the diffusion behaviors of the actinides studied were similar. The ratio of coefficients $D_{\parallel}/D_{\perp}$ was 280; the associated activation energy applicable to both directions was 60.8 kcal per gram atomic weight; values of the coefficients ranged from 10^{-7} to 10^{-12} cm^2/sec. Supplementary results obtained with porous graphite specimens fell between the two sets of coefficients obtained with pyrocarbon, with approximately the same activation energy.

At temperatures above 2000°C, effects of structural changes within the carbon matrix intruded into the diffusion process, and the apparent coefficients decreased with increased diffusion-anneal times. For example, experiments at 2400°C revealed an arrested migration with respect to the $D_{\perp}$ direction after a sudden initial penetration. This finding, supported by structural characterizations, demonstrated that drastic anneals and dramatic structural changes were not required to suppress actinide migration in the perpendicular direction. These results gave the first suggestion that structural alterations arising from the presence of the actinides might influence migration behavior.

Several pyrocarbon specimens were annealed (without actinide) for 3 hr at temperatures approaching 3000°C. A comparative examination of specimens before and after this annealing treatment indicated definite changes in specimen dimensions, crystallite sizes and orientation, and crystallographic parameters. All changes represented improvements in the carbon structure accompanied by decreases in defect concentrations.

Actinides were found to be immobile (at all times, with respect to perpendicular-direction diffusion) in the improved material produced via high-temperature anneals. Accordingly, actinide mobility in as-deposited pyrocarbon was attributed, in part, to the defective structure of the material.

Attempts to obtain data pertinent to parallel-direction diffusion in improved pyrocarbons met with only partial success, because most of the material possessed cracks along basal surfaces, as shown in Fig. 10.11. From a limited amount of data, we have concluded that the effects of heat treatment on diffusion in the perpendicular direction are much more dramatic than upon diffusion in the parallel direction.

Thin-Layer Experiments at Low Concentrations

The pyrocarbon specimens used in these experiments contained only 2 μg of thorium per cm^2 of carbon surface. They were examined after the diffusion anneal by autoradiography and by sectioning and analyses to establish the nature and extent of migration.

Autoradiographic Results. – Autoradiographic results revealed that the tracer distributions on surfaces normal to the diffusion path in the $\langle +c \rangle$ direction (the direction in which the pyrocarbon "grows" during deposition) are quite different from those in the $\langle -c \rangle$ direction. The orientation of these directions, with respect to the macrostructure of the as-deposited carbon, is illustrated in Fig. 10.11. From an applied point of view, diffusion in the $\langle +c \rangle$ direction is of major interest, since diffusion in particle coatings proceeds in this direction. Most of our experiments, therefore, have involved the $\langle +c \rangle$ direction.

Comparisons of the diffusion patterns associated with the two directions are shown in Fig. 10.12. Several features may be noted from the results shown in this figure: the surface concentration of actinide is uniform before the diffusion anneal, marked segregation occurs during the experiment, the migration patterns for the $\langle +c \rangle$ and $\langle -c \rangle$ directions are inverted, in all cases the patterns correlate with macrostructure,

[24] R. B. Evans III and J. Truitt, *Nucl. Sci. Eng.* 20, 197 (1964).

[25] R. B. Evans III, J. O. Stiegler, and J. Truitt, *Actinide Diffusion in Pyrocarbons and Graphite*, ORNL-3711 (December 1964).

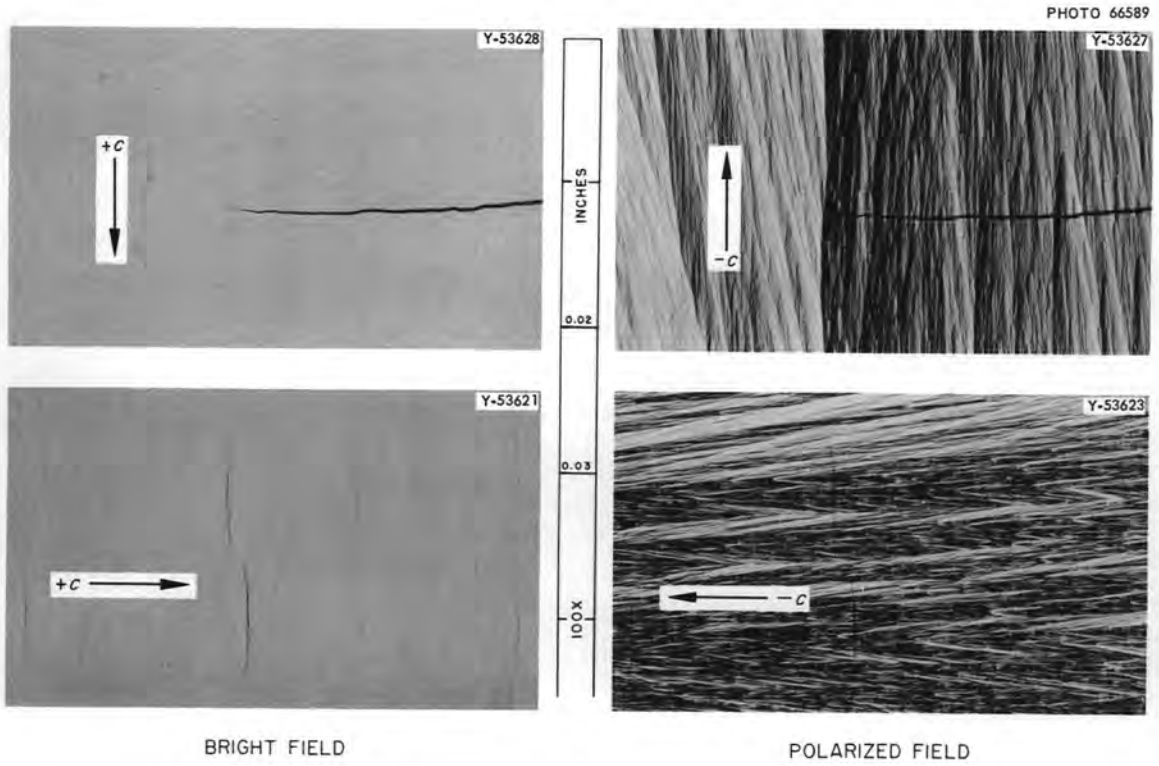

Fig. 10.11. Micrographs Indicating Orientation of Two Diffusion Paths for <c> Direction Migration in Columnar Pyrocarbons. The two figures at the top correspond to one specimen; those at the bottom correspond to another specimen. For each specimen two views of the same areas under different lighting are shown. In micrographs produced at the magnifications indicated above, one actually sees macrostructure. The presence of cracks along basal surfaces is most readily detected under a bright field; such cracks negate most of our attempts to study migration parallel to the basal planes.

and the patterns are the same at various penetration depths.

Segregation probably occurs quite rapidly at low temperatures during the very initial stages of the experiment. Migration rates associated with segregation must be quite high, in view of the short times and relatively large distances involved. In any event, this phenomenon seems to represent the antithesis of a diffusion process. The latter requires net movement toward low-concentration regions in order to yield uniform systems. Our experimental results seem to contradict these requirements.

Although the macrostructure has a marked influence upon the initial segregation effects over areas normal to the diffusion paths, we suspect that the microscopic defects within the surfaces, through which the $\langle c \rangle$ direction diffusion occurs, are distributed uniformly over these surfaces. It is important to note that patterns, such as those shown in Fig. 10.12, are not peculiar to low-concentration experiments; they characterize all our perpendicular experiments – regardless of the actinide concentration.

Penetration Data. – In the low-concentration experiments,[26] major attention was given to migration as it would occur in the $\langle -c \rangle$ direction, since all other perpendicular experiments have

[26]This investigation has been carried out, with the authors assistance, by F. L. Carlsen, Jr., of the Metals and Ceramics Division. Mr. Carlsen has also conducted similar experiments involving pyrocarbons which are intermediate with respect to our improved and as-deposited materials. A complete summary of this work will appear as a thesis to be prepared under joint auspices of the University of Tennessee Graduate School and ORNL.

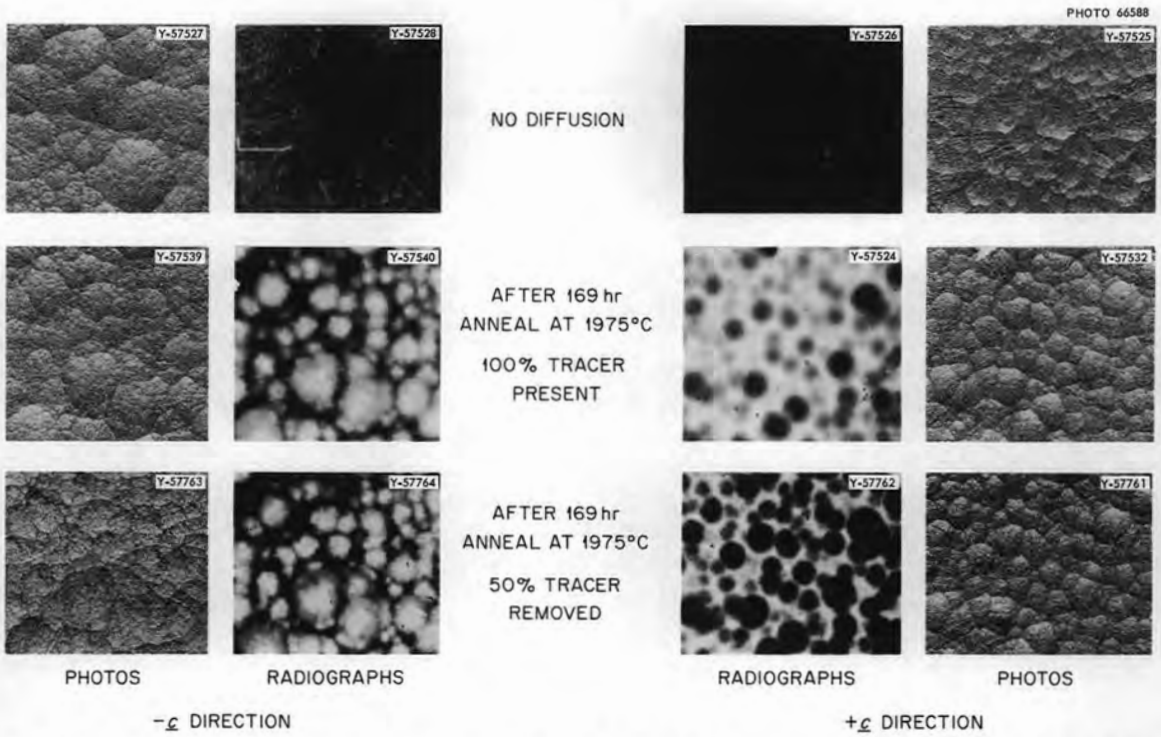

Fig. 10.12. Autoradiographs of Tracer Patterns Arising from <c> Direction Diffusion of Thorium in a Columnar Pyrocarbon. Dark regions on autoradiographs indicate location of ^{239}Pa activity. Film exposure times were not equal. Dimensions of these specimens are approximately 0.68 × 0.78 cm. In all cases the reader is viewing basal surfaces; the migration of interest has proceeded in a direction perpendicular to these surfaces and to the plane of the figure.

been limited to the ⟨+c⟩ direction. Two series of the ⟨−c⟩ direction experiments were carried out at 1850 and 1975°C. In addition, one series of the ⟨+c⟩ direction experiments was conducted at 1850°C. These results – coupled with results of four earlier experiments (conducted at higher concentrations) – suggest equivalent diffusion rates for both directions.

One of the most significant features of the results concerns the relatively low values of penetrations and diffusion coefficients as compared with those obtained at higher concentrations under comparable conditions. Specifically, the penetrations and coefficients for the high-concentration thorium experiments were, respectively, three and ten times greater than those for the low-concentration thorium experiments.

This concentration effect clarifies the apparent time dependence of the coefficients observed in earlier experiments. Similar effects appear in the present experiments. For example, at 1850°C, coefficients at low concentrations corresponding to 2, 64, 144, and 256 hr, respectively, were 77, 3.0, 1.9, and 1.6×10^{-12} cm^2/sec for diffusion in the ⟨+c⟩ direction. We note here that the coefficient should remain constant – if the migration processes were independent of concentration – but the migration rates and coefficients are high when the concentrations are high in our experiments. One might recall that the concentrations should have their maximum values during the early stages of all types of depletion experiments – regardless of complications. Thus the apparent time dependence may be directly related to the observed concentration effects.

Constant-Potential Experiments

Scope and Objectives. – These experiments were designed to study uranium diffusion in both the ⟨+c⟩ and ⟨*a*⟩ directions (frequently

denoted ⊥ and ||) as it occurs in as-deposited pyrocarbon at high levels of uranium concentrations. For this investigation, diffusion-anneal time and temperature were selected as the controllable independent variables. The determination of the so-called saturation concentration, C_0 (g/cm^3), of uranium in a columnar pyrocarbon constituted a major objective of the work. From the standpoint of transport relationships, C_0 represents a time-constant driving force at a boundary.

Since the results of earlier experiments taught the concentration dependence of the actinide-diffusion coefficients, it was realized that coefficients obtained at low concentration would not apply here. Thus, present experiments were broken down into two parts: (1) measurement of the total uranium, ΔM, accepted by pyrocarbon specimens after various anneal times, t, as given by

$$\Delta M/A = 2C_0\sqrt{(Dt)/(\pi)},\ \text{g/cm}^2\ , \qquad (1)$$

where A is the area normal to the diffusion path, and (2) evaluation of coefficients, D (cm^2/sec), to allow computation of C_0 from $\Delta M/A$ values, using the relationship above. The coefficients were evaluated by comparing applicable penetration data, determined by counting and grinding, with the approximate relationship

$$\text{F.R.} = \sqrt{\pi}\, i\text{erfc}\,(u)\ . \qquad (2)$$

The abbreviation F.R. denotes fraction of total ^{238}U-related ^{239}Np activity that remains after grinding (and discarding) specimen volumes over a distance x. The argument u is $x/\sqrt{4Dt}$.

Procedures. – Each experimental series included single diffusion anneals at 1500, 1640, 1820, and 2260°C with some additional 2020°C experiments at different diffusion-anneal times. Specimens prepared to study diffusion in the perpendicular $\langle +c \rangle$ direction were "spiked" with a thin layer of ^{238}U (10 μg/cm^2) prior to the diffusion anneal. This step was omitted in the case of the parallel $\langle a \rangle$ direction specimens. All specimens were loaded into individual graphite holders (see Fig. 10.13) such that the surfaces of interest would contact a constant-potential source. Each experiment involved four specimens.

The source material was composed of a porous graphite containing 26 wt % uranium in the form of dispersed UC_2 granules. Each loading was subjected to a short preanneal at 2020° for 15 min. Preliminary annealing and spiking were included in our procedures to enhance initial equilibration and to ensure a positive zero-time correction. After the diffusion anneals, the specimens were unloaded and drastically trimmed to minimize errors associated with contamination of the coupons at the edges.

Duplicate determinations of the total ^{238}U were performed (using appropriate standards) by counting the ^{239}Np produced by two individual short-term neutron activations. The agreement between the two sets of data was quite good. Averages of the duplicate determinations appear in Table 10.1; these were applied (some time later) in Eq. (1) to compute C_0.

Variations in the values tabulated for different specimens of a given experiment probably result from differences in macrostructure as it occurs in different specimens, rather than variable deviations introduced via assay techniques.

On the basis of the $\Delta M/A$ values given in Table 10.1 (and other considerations), one specimen from each loading was selected as being most representative of a particular experiment, and was put aside for subsequent penetration determinations. This group of specimens was designated series I. Another group (series II) was collected and subjected to grinding to remove a wedge of the specimen surface at the uranium-invaded zone. Angles of the wedges are shown in Fig. 10.13.

At this point, series I and II, for both parallel- and perpendicular-direction experiments, were reactivated to advance the activity to the levels required for autoradiographic techniques and a determination of the coefficients through direct grinding procedures.

Autoradiographic Results. – Results relative to parallel-diffusion specimens are shown in Figs. 10.14*a* and *b*. At the $x = 0$ surfaces, regions of high concentrations of uranium, in the form of pockets or worm holes, appear at delaminations or cracks that proceed along the basal surfaces. Manifestations of delaminated sections, as they affect the actinide-invasion front, are reflected

also in autoradiographs of wedged specimens, shown in Fig. 10.14*b*. Within the invasion zone, the uranium concentration is essentially uniform as suggested by the absence of an intensity gradient in exposures of Fig. 10.14*b*. Definite verification of this has been gained through grinding experiments. A major portion of the penetration data for all $D_{\parallel}$ experiments reveals a uniform concentration profile – irrespective of the actinide concentration involved.

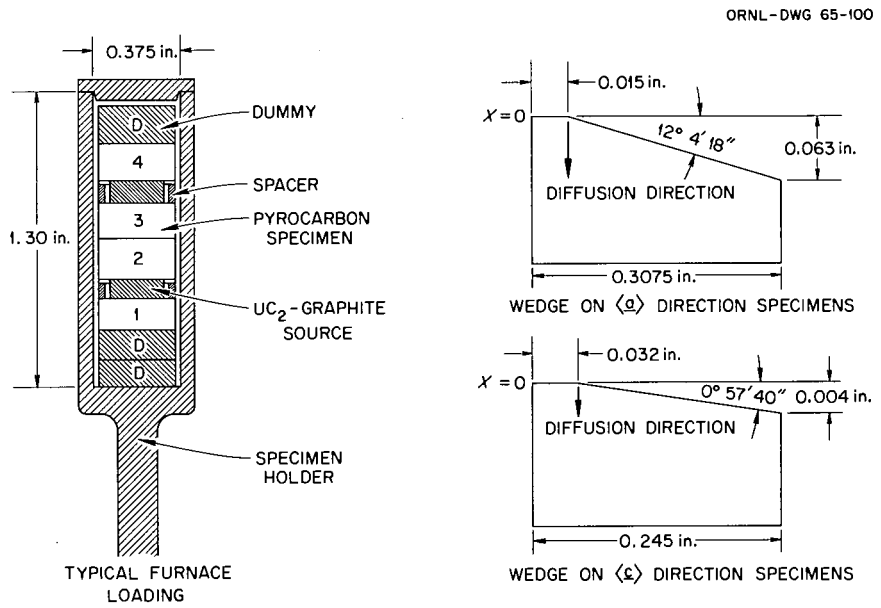

Fig. 10.13. Furnace Loading Diagram and Wedge Angles Pertaining to Constant-Potential Diffusion Specimens. All components at left are composed of various forms of graphite. The angles of the wedges cut on annealed specimens (shown at right) differ because the extent of diffusion in the <a> direction is much greater than that in the <c> direction.

Table 10.1. Total Uranium Content of ⟨+c⟩ Direction Specimens After Diffusion at Various Temperatures

Temperature (°C)	Diffusion Time (hr)	Uranium Content[a] ($\Delta M/A$, μg of uranium per cm^2)				
		Average	I[b]	II[c]	III	IV
2260	12	63.1	60.5	52.9	68.8	70.3
2020	17	25.7	22.9	18.0	30.8	31.1
2020	100	63.5	61.2	65.8	206.5[d]	196.0[d]
1820	192	24.4	17.5	15.3	22.9	42.0
1640	530	14.8	14.1	16.5	14.5	14.3
1500	1,200	11.8	12.5	9.4	16.3	8.8

[a]Uranium contents are referred to a unit area of source-specimen interface.

[b]Specimens used to obtain diffusion coefficients.

[c]Specimens used for wedge autoradiographs.

[d]Values rejected.

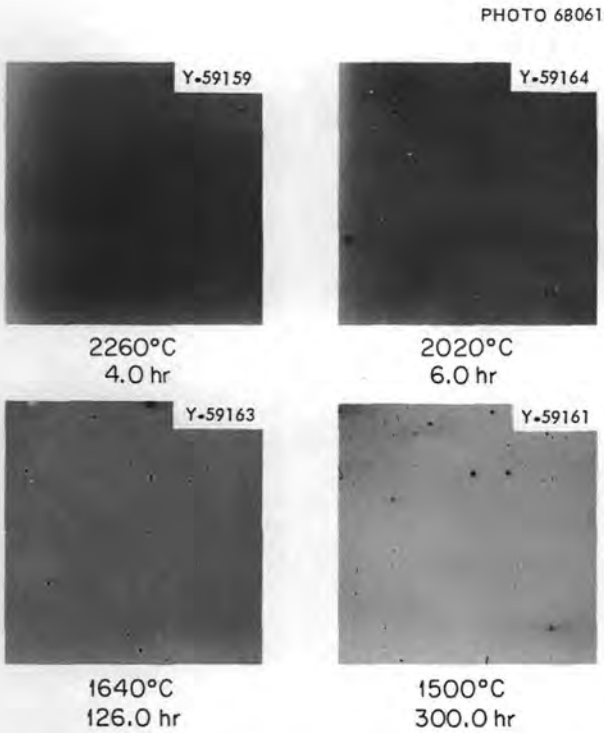

Fig. 10.14*a*. Surface Autoradiographs, at $x = 0$, of Series I <a> Specimens Prior to Grinding. The dark regions indicate the presence of radioactive material arising from neutron activation of ^{238}U which has migrated into the specimen under constant-potential conditions.

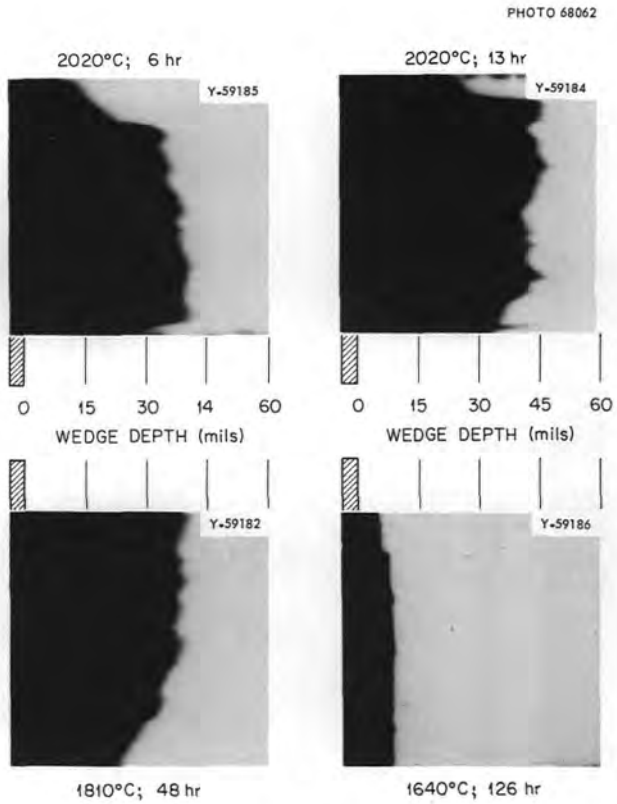

Fig. 10.14*b*. Autoradiographs of Wedge Surfaces on Series II <a> Specimens. Since the wedge angle relates distances across the wedge surface with penetration distances, these figures give an indication of the constant-potential concentration profile within the specimen, particularly at deep penetrations.

Autoradiographs of perpendicular-direction diffusion specimens are shown in Figs. 10.15*a* and *b*. Relatively uniform concentrations at the $x = 0$ surfaces were anticipated; we had expected a continual actinide replenishment in areas that tended to be depleted in the thin-layer experiments. In other words, we had expected a relatively uniform concentration on the specimen surfaces. Although our expectations seem to be verified by the autoradiographs of wedged surfaces in Fig. 10.15*b*, the results of Fig. 10.15*a* clearly indicate the existence of an actinide segregation quite similar to that obtained in the thin-layer experiments. Apparent disagreement arises because films on wedges were somewhat overexposed in order to bring out detail at deep penetrations.

Diffusion Data. – To date, penetration data are available only for the $\langle +c \rangle$ direction experiments. A rather unusual feature of the data is illustrated in Fig. 10.16, namely, the presence of a supersaturated region near the interface at $x < 15\ \mu$. It is clear that the concentrations within this region were quite high in comparison to concentrations in the bulk of the specimens. The reader might recall that the concentrations are proportional to the negative slopes of our experimental F.R. vs x (and/or u) curves. In an effort to correlate the major portion of the penetration data with Eq. (2), it seemed reasonable to us to recompute the F.R. with new bases given by the extrapolations to $x = 0$ as indicated in Fig. 10.16. We should mention that our decision to spike and preanneal specimens prior to the

PHOTO 68063

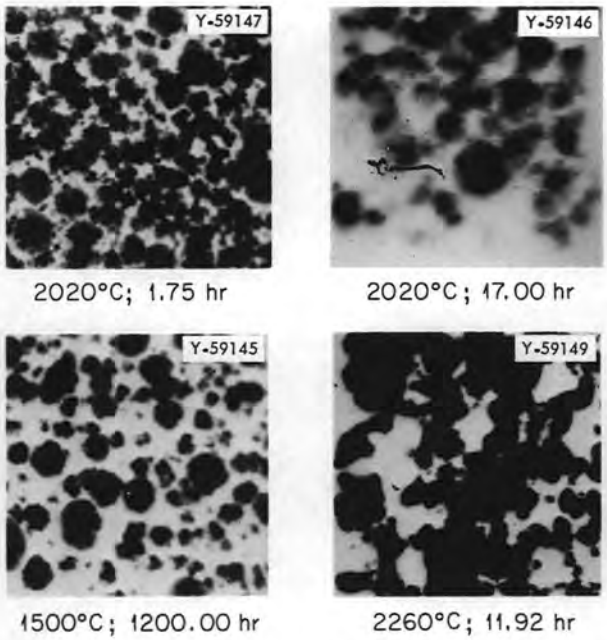

Fig. 10.15*a*. Surface Autoradiographs, at $x = 0$, of Series I <+c> Specimens Prior to Grinding. The dark regions indicate the presence of radioactive material arising from neutron activation of ^{238}U. Actinide segregation, seen also in analogous results from thin-layer experiments, is quite evident in the results above obtained via constant-potential experiments.

PHOTO 68064

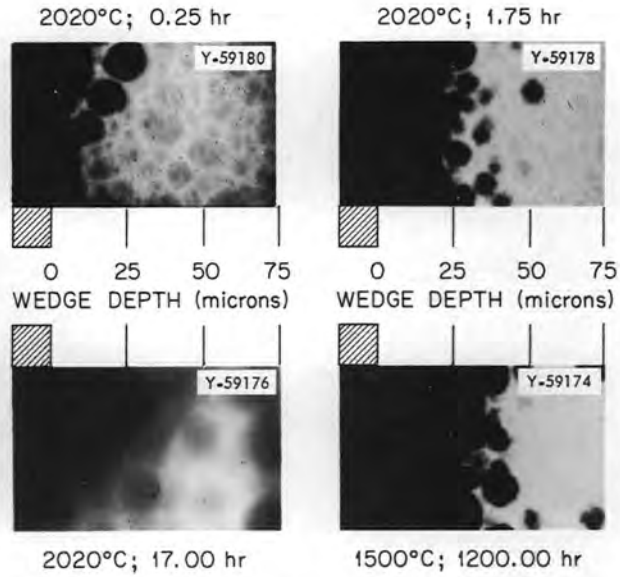

Fig. 10.15*b*. Autoradiographs of Wedge Surfaces on Series II <+c> Specimens. These figures indicate a nonuniform actinide distribution well beyond the specimen surface.

experiments led us to expect supersaturated regions – particularly in the case of low-temperature experiments. The necessity of carrying out these adjustments or corrections was anticipated prior to aquisition of the results.

A family of penetration curves is shown in Fig. 10.17. Here, the data have been recomputed as described above. Apparent diffusion coefficients, $D_{\perp}$ (cm^2/sec), were extracted from these data by comparing or fitting the experimental curves with the generalized curve described by Eq. (2). The fit was only approximate, since the fractional activities at large values of x (low concentrations) were less than those predicted by the generalized curve. It is quite probable that this is a consequence of the marked tendency of the effective value of $D_{\perp}$ to decrease as the concentration decreases. A dramatic indication of the concentration effect is given by the Arrhenius plots in Fig. 10.18, which present coefficients pertinent to perpendicular-direction diffusion. The uranium coefficients obtained through the constant-potential experiments, as extracted from Fig. 10.17, are included on this plot.

Results of Structural Studies. – Several changes are immediately apparent upon electron-microscope examinations of cleavage flakes obtained in the supersaturated regions of a specimen annealed for 12 hr at 2260°C. Microvoids present in the as-deposited material (subjected to the same anneal but without actinide) have been completely eliminated, as well as the severe fine-scale roughness. Continuous trails of

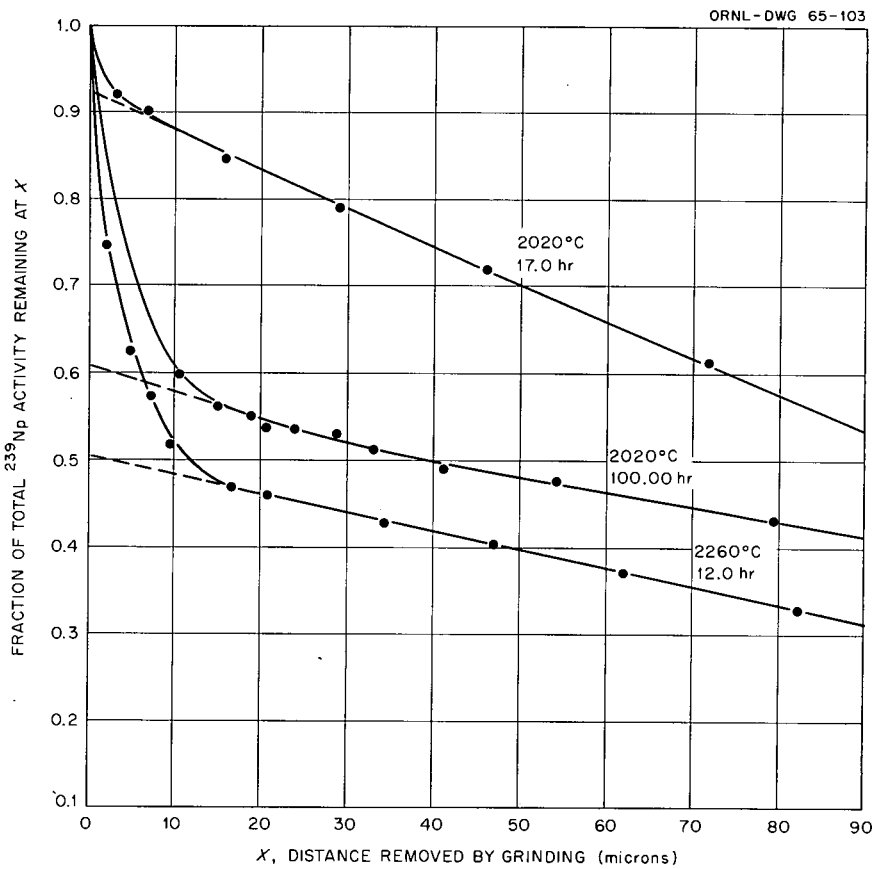

Fig. 10.16. Typical Appearance of Penetration Data for <+c> Direction Constant-Potential Diffusion Experiments in Raw Form. The $x = 0$ intercepts of the broken curves indicate the approximate uranium content of the specimen when contributions of very high concentration actinide layers (7–15 μ thick near the surface of the specimen) are excluded.

material of different texture weave their way throughout the flake. These are quite evident in Fig. 10.19. In addition, isolated patches of scaly material appear. The electron diffraction patterns from such regions reveal the presence of transformed (or reformed) material with the basal planes rotated with respect to the original deposition surface. We cannot, however, identify the transformed material as having either a pyrolytic carbon or a graphite structure.

The structure of the cleavage flakes taken at positions deep in the interior of the specimen is the same as the structure of the as-deposited material. This suggests that the presence of the actinide – not the temperature of the experiment – brought about the structural transformation. In opposition to this idea, the concentration of uranium in the region within the growth cones seems to be too low to promote the change in structure of the type observed near the boundaries. There has, however, apparently been some diffusion (and perhaps some structural changes) within the growth cones as is evidenced by the closed microvoids in this region.

There is no diffraction evidence for the existence of classical forms of uranium carbide in these layers. A few small dark spots are scattered throughout the material, mainly near or in the regions having a pebbled structure. This indicates that the actual uranium concentration of this material is still extremely small after diffusion. Continuous paths of transformed material have not been observed in uranium-invaded zones of specimens subjected to annealing temperatures lower than 2260°C. Additional structural investigations along these lines are in progress.

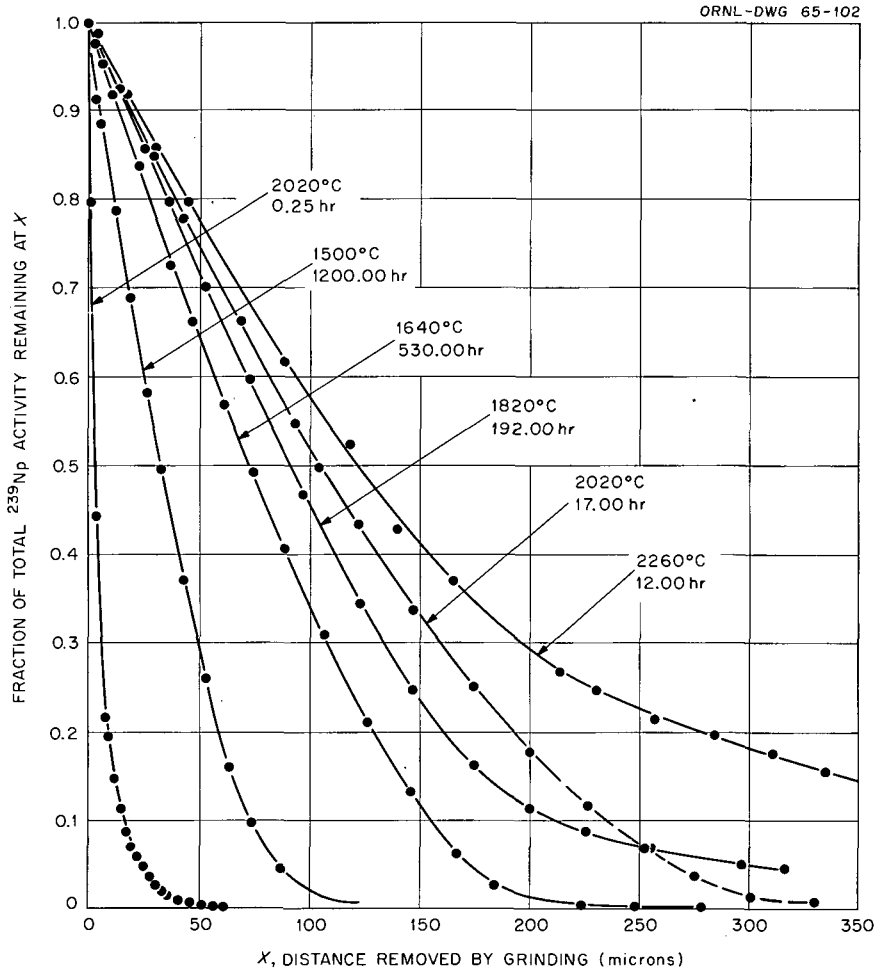

Fig. 10.17. Penetration Curves for the Diffusion of Uranium in the <+c> Direction at Various Anneal Times and Temperatures. These curves are based on the total contents obtained by extrapolations of the original Fraction Remaining (F. R.) vs. x data as indicated on Fig. 10.6.

Summary of Results. – A convenient means for summarizing all the semiquantitative data accumulated in regard to our constant-potential experiments presents itself when one combines the uranium-content values and related diffusion coefficients to compute the apparent uranium solubility, C_0. The data and results associated with such computations are presented in Table 10.2. We should mention that out uranium-content values and diffusion coefficients incorporate depth and area measurements performed at room temperature; accordingly, we have applied a small correction (~6 vol %) to the C_0 values to account for the volume expansion of the pyrocarbons as the temperature was increased from room temperature to the relatively high experimental temperatures.

Inspection of the C_0 values appearing in Table 10.2 suggests that the apparent solubility is independent of the temperature. The average of all C_0 values is 1.32 mg/cm^3. This value is in good agreement with the average of the C_0 values reported by Lonsdale[27] for a comparable system. We note, however, that Lonsdale's results demonstrate a temperature dependence (C_0 increases with T), in opposition to the present results.

[27] H. Lonsdale and J. Graves, *Coated Particle-Fuel Research at G. A., November 31, 1962 – May 31, 1963*, GA-4260, pp. 53–57.

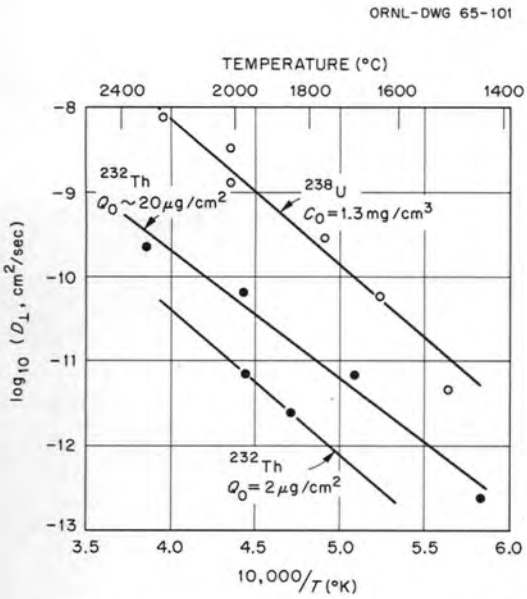

Fig. 10.18. Comparison of Three Sets of Diffusion Coefficients for <c> Direction Actinide Migration Within Identical Columnar Pyrocarbon Specimens. The coefficients are plotted as a function of temperature for three actinide concentration ranges.

One may speculate that the actinide solubility, as well as the coefficient, depends heavily on structural defects in the pyrocarbons, and that the nature of these defects (insofar as actinide solubility is concerned) is relatively insensitive to temperature variations within the temperature range 1500 to 2260°C. Considerations as to the structure of nearly perfect graphite – combined with our results showing a complete lack of the $\langle +c \rangle$ actinide migration (and/or solubility) in improved pyrocarbons – lead one to expect a negligible solubility in the absence of defects. Thus we are not at all surprised by the temperature invariance of the C_0 value in our highly defective material.

We are, on the other hand, amazed by the fact that the coefficients and C_0 values are amenable to correlation of any kind when we consider the obvious variations in the diffusion patterns as indicated by comparisons of the autoradiographs in Figs. 10.15*a* and *b*. In this regard, our volume correction seems to be superfluous. We recognize that the reported C_0 values represent an overall

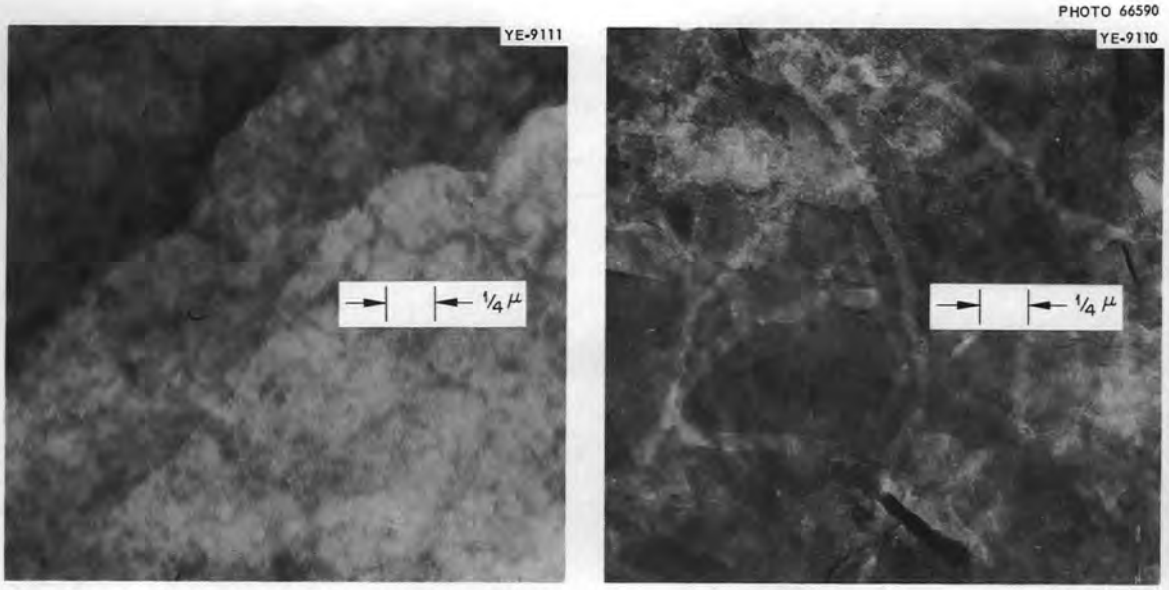

UNCONTAMINATED ZONE

URANIUM INVADED ZONE

Fig. 10.19. Transmission Electron Micrographs Showing Structrual Changes Resulting from Actinide Migration in Pyrocarbons at 2260°C. The locations of re-formed material, which is probably produced by actinide-catalyzed transformations, correspond to positions of the light streaks that appear in micrographs of the uranium-invaded zone. Examinations of the material in the streaks suggest only the presence of regions of altered pyrocarbons; the presence of actinide carbides in identifiable forms in such regions has not been detected.

number based on specimen dimensions. The true C_0 values for pyrocarbon regions, wherein the actinide actually resides, are two to four times higher than those given in Table 10.2.

Table 10.2. Summary of Diffusion Results for the ⟨+c⟩ Direction of Uranium Migration Under Constant-Potential Conditions

Temperature (°C)	Effective U Content,[a] $\Delta M/A$ (μg/cm^2)	Diffusion Coefficient,[b] $D_\perp$ (cm^2/sec)	Expansion Ratio[c] ($V_T/V_{20°}$)	Uranium Solubility, C_0 (mg/cm^3)
2260	29.5	79.0×10^{-10}	1.065	1.33
2020	23.7	37.0	1.058	1.31
2020	35.7	13.0	1.058	1.39
1820	23.2	2.7	1.052	1.44
1640	14.8	0.57	1.047	1.20
1500	6.8	0.049	1.043	1.26

[a]Averages of Table 10.1 corrected for supersaturated regions near source-specimen interface.

[b]Based on curves of Fig. 10.7 and Eq. (2).

[c]For pyrocarbons, as estimated using data supplied by High-Temperature Materials, Inc., Boston, Mass., for columnar structures.

11. Reactions of Graphite with Oxidizing Gases

L. G. Overholser

Interest in gas-cooled reactor concepts using all-ceramic cores and helium coolant is increasing mainly because higher helium outlet temperatures are possible with such systems than with those employing metal-clad fuel elements. The AVR, for example, is to use spherical fuel elements consisting of graphite with pyrolytic-carbon-coated fuel particles. Graphite components present in the reactor core would be slowly attacked by low concentrations of oxidants (O_2, H_2O, CO_2) in the circulating helium, and a more rapid and extensive attack would occur if high partial pressures of steam were present in the helium following a tube failure in a steam generator. Mechanical failure of the fuel bodies and rupture of the coatings of the fuel particles might be produced by such severe attack. Hydrogen produced by the steam-graphite reaction could lead to explosive conditions in the event that the main coolant circuit also failed.

Experimental studies have been performed to establish reaction rates of ATJ graphite (the graphite used as the outer shell of AVR fuel spheres) with low concentrations of CO_2 and H_2O in helium. Unfueled spheres of ATJ graphite and fueled spheres having shells of ATJ graphite have also been studied in steam at temperatures of interest to the AVR and similar reactors. Brief presentations of the results of some of these experimental studies are given in the following sections.

OXIDATION OF ATJ GRAPHITE BY LOW CONCENTRATIONS OF OXIDANTS IN HELIUM

J. P. Blakely

Experimental results obtained from studies of the oxidation of Speer Mod-2 graphite by low concentrations of water vapor and carbon dioxide in helium were presented previously.[1–4] Similar studies of the oxidation of ATJ graphite were made more recently using the same experimental equipment and techniques.[1] Reaction rates were determined from weight changes caused by flowing contaminated helium at a total pressure of 1 atm by the spherical specimen and from analyses of the effluent gases with a Burrell K-7 gas chromatograph. The latter instrument was modified recently with a resultant increase in sensitivity and improved stability of detector output. A single 1-in.-diam sphere (same geometry as Speer Mod-2 specimen) of ATJ graphite was used in all the experiments. ATJ graphite contains ~1000 ppm of ash (largely calcium) compared to <30 ppm for Speer Mod-2 graphite. Grain-size and pore-size distribution of the two graphites also differ.

The effect of burnoff on the H_2O-graphite reaction during early stages of oxidation at 975°C using a water vapor concentration of 460 vpm (parts per million by volume) is shown in Fig. 11.1. The rapid increase in reaction rate at the onset of oxidation is noteworthy. Data obtained at larger burnoffs showed that the reaction rate continued to increase but more slowly for burnoffs up to 7 wt %, the maximum measured. Data were not obtained for Speer Mod-2 graphite at the very low burnoffs, but data obtained for burnoffs above

[1] J. P. Blakely and N. V. Smith, *Reactor Chem. Div. Ann. Progr. Rept. Jan. 31, 1963*, ORNL-3417, pp. 157–58.

[2] L. G. Overholser and J. P. Blakely, *GCR Program Semiann. Progr. Rept. Sept. 30, 1963*, ORNL-3523, pp. 254–59; *March 31, 1964*, ORNL-3619, pp. 180–86.

[3] J. P. Blakely, J. L. Rutherford, and L. G. Overholser, *The Reactivity of Graphite and Fueled Graphite Spheres with Oxidizing Gases*, ORNL-TM-751 (February 1964).

[4] L. G. Overholser and J. P. Blakely, *Oxidation of Graphite by Low Concentrations of Water Vapor and Carbon Dioxide in Helium* (in press).

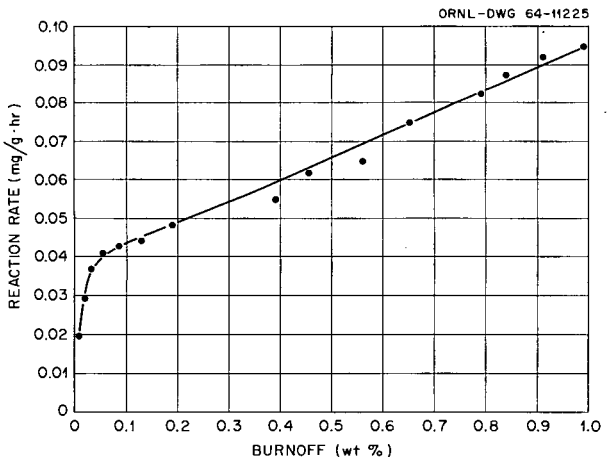

Fig. 11.1. Effect of Burnoff on the H_2O-Graphite Reaction at 975°C (Flow Rate of 150 cm^3/min, Inlet Concentration of 460 vpm of H_2O).

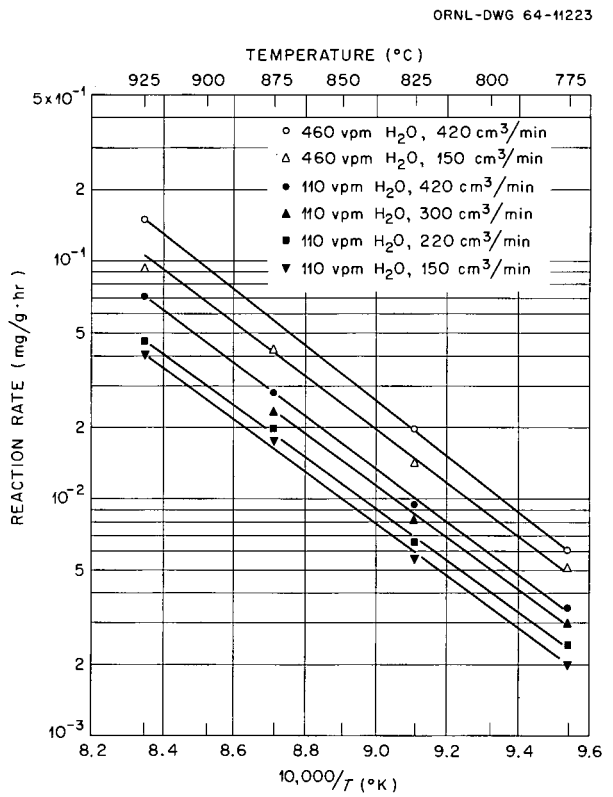

Fig. 11.2. Effect of Temperature and Flow Rate on the H_2O-Graphite Reaction at Inlet H_2O Concentrations of 110 and 460 vpm (~4 wt % Burnoff).

1 wt % indicate that the reactivity increased more slowly with increasing burnoff than did that of ATJ graphite. This behavior results from differences in the rate of surface development for the two graphites. A qualitative confirmation of this premise is shown (see Fig. 11.6) by similar rate changes on oxidation by a high partial pressure of steam.

The effect of temperature and of flow rate on the reaction rates of the H_2O-graphite system at two concentrations of water vapor are shown in Fig. 11.2. The increases in reaction rates with increasing flow rates at all temperatures examined suggest that the rates are controlled by diffusion through a gas film. This type of mass transport, however, should be characterized by a much smaller activation energy than the ~50 kcal/mole found from the plots in Fig. 11.2. Although the activation energy of ~50 kcal/mole suggests in-pore diffusion control, no apparent decrease in activation energy with increasing temperature occurs over the temperature range studied. Results reported earlier[3] for Speer Mod-2 graphite show the reaction to be affected only very slightly by changes in flow rate and also show a significant decrease in activation energy with increasing temperature (~60 kcal/mole at 850 to ~40 kcal/mole at 1000°C). A catalytic reaction involving the impurities present in the ATJ graphite might conceivably be responsible for the observed flow effect. Rate of reaction of ATJ graphite with CO_2 responds to changes in flow rate in a similar way over the same temperature and oxidant concentration interval. Activation energies of ~60 kcal/mole were found for the reaction of CO_2 with ATJ graphite; this is reasonably near to the ~55 kcal/mole reported earlier for CO_2 with Speer Mod-2 graphite.[3]

It is seen from Fig. 11.3 that the apparent order of both the H_2O and CO_2 reactions with ATJ graphite is between 0.6 and 0.7 at the designated temperature and flow rate. Data given in Fig. 11.2 suggest that the apparent order of the H_2O reaction is not markedly affected by temperature or flow rate. Although the apparent order of the H_2O and CO_2 reactions with ATJ graphite are in fair agreement with those found previously for Speer Mod-2 graphite,[3] the relative reactivity of the two grades of graphite with the oxidants is markedly different. Data in Fig. 11.3 show that the reaction rate of H_2O is less than twice that of CO_2 under comparable conditions. This is in marked contrast to a ratio of ~8 for the reactivity of H_2O to

CO_2 found for Speer Mod-2 graphite.[3] A possible explanation for the difference is that the impurities present in the ATJ graphite catalyze the CO_2-graphite reaction more strongly than the H_2O-graphite reaction.

Values of ~20 were found for the CO to CO_2 ratio in the effluent gases obtained by reacting H_2O with Speer Mod-2 graphite.[4] In the current studies using ATJ graphite, values for this ratio are near unity. This indicates that ATJ graphite is a more efficient agent for promoting the reaction, $CO + H_2O \rightleftharpoons CO_2 + H_2$, than is Speer Mod-2 graphite. The most plausible explanation is that the impurities present in ATJ graphite strongly catalyze the conversion of CO to CO_2. There is a possibility, however, that this conversion is also connected with the residence time of the CO in the pore structure of the respective graphites.

The retarding effect of various concentrations of H_2 or CO on the H_2O reaction with ATJ graphite is demonstrated in Fig. 11.4. It is evident that the reaction is strongly (and about equally) retarded by CO and H_2. The retardation by CO is more marked than found previously in the studies with Speer Mod-2 graphite.[4] Gadsby *et al.*[5] attributed the retarding effect of CO to the H_2 formed by the reaction $CO + H_2O \rightleftharpoons H_2 + CO_2$. The data in Fig. 11.4, however, show that CO *per se* retards the H_2O-graphite reaction, since the retardation was much greater than that due to the maximum concentration (110 vpm) of H_2 which could have been present.

[5]J. Gadsby, C. N. Hinshelwood, and K. W. Sykes, *Proc. Roy. Soc. (London), Ser. A* 187, 129 (1946).

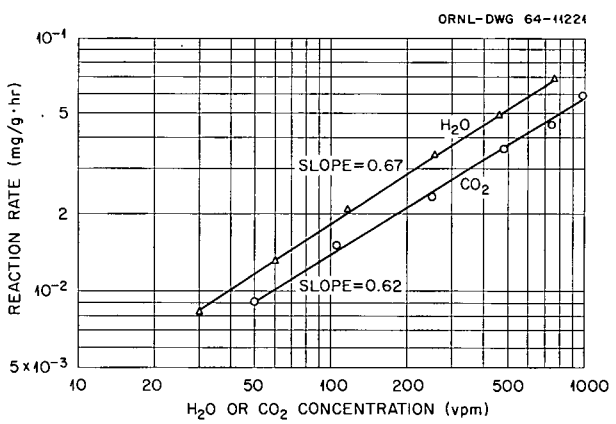

Fig. 11.3. Apparent Order of the H_2O- and CO_2-Graphite Reactions at 875°C and Flow Rate of 300 cm^3/min (~5 wt % Burnoff, Inlet Concentrations Given).

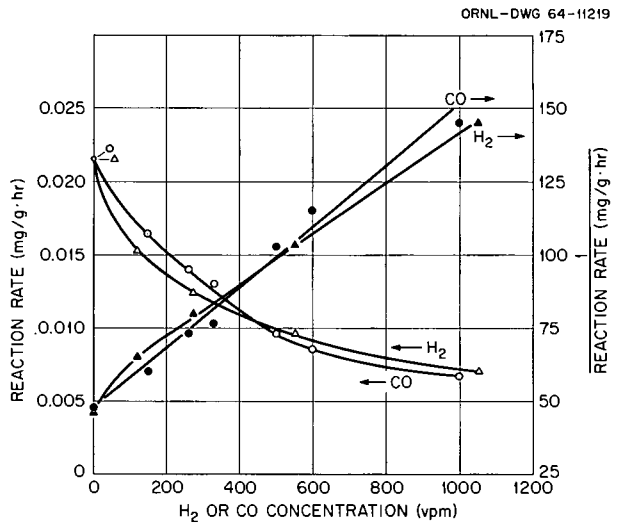

Fig. 11.4. Effect of Various Inlet Concentrations of H_2 and CO on the H_2O-Graphite Reaction at 875°C (~5 wt % Burnoff, Inlet Concentration of 110 vpm of H_2O).

The reaction of ATJ graphite with CO_2 was retarded to the same degree by H_2 and by CO. Plots of the reciprocal of the reaction rate against the concentration of either CO or H_2 gave curves bending downward rather than essentially linear relationships as found in Fig. 11.4. The lack of linearity for retardation by CO and the strong retarding effect of H_2 were unexpected; the causes are not understood.

REACTIVITY OF FUELED AND UNFUELED GRAPHITE SPHERES WITH STEAM

J. P. Blakely J. L. Rutherford

Results obtained by oxidizing 1.5-in.-diam fueled graphite spheres supplied by several vendors and 1.5-in.-diam unfueled graphite spheres machined from Speer Mod-2 and ATJ grades of graphite with steam at 800, 900, and 1000°C were reported previously.[3,6–8] More recently, the effect of burnoff

[6]L. G. Overholser, J. P. Blakely, and J. L. Rutherford, *GCR Program Semiann. Progr. Rept. March 31, 1963*, ORNL-3445, pp. 180–86.

[7]J. P. Blakely, J. L. Rutherford, and L. G. Overholser, *Nucl. Sci. Eng.* 20, 196–98 (1964).

[8]J. P. Blakely, J. L. Rutherford, and L. G. Overholser, *GCR Program Semiann. Progr. Rept. Sept. 30, 1964*, ORNL-3731, pp. 161–67.

on the reactivity of 1.5-in.-diam unfueled graphite spheres was examined in more detail, and the studies were extended to include 2.36-in.-diam spheres of ATJ graphite, simulated AVR fuel spheres, and fueled mold-injected AVR spheres. Reaction rates were determined from weight changes of the spheres as well as from analyses of the effluent gases. Steam flow rates of 600 and 1200 cm^3 STP/min were used for the 1.5- and 2.36-in.-diam spheres, respectively, at a partial pressure of steam of ~730 torrs.

The effect of burnoff and temperature on the reactivity of the unfueled 1.5-in.-diam graphite spheres is shown in Fig. 11.5. Activation energies determined from these plots (~60 kcal/mole) agree well with values obtained previously[3] for 1.5-in.-diam fueled and unfueled spheres. The activation energy appears to be essentially independent of burnoff; the slight increase with burnoff in the case of Speer Mod-2 graphite may or may not be significant.

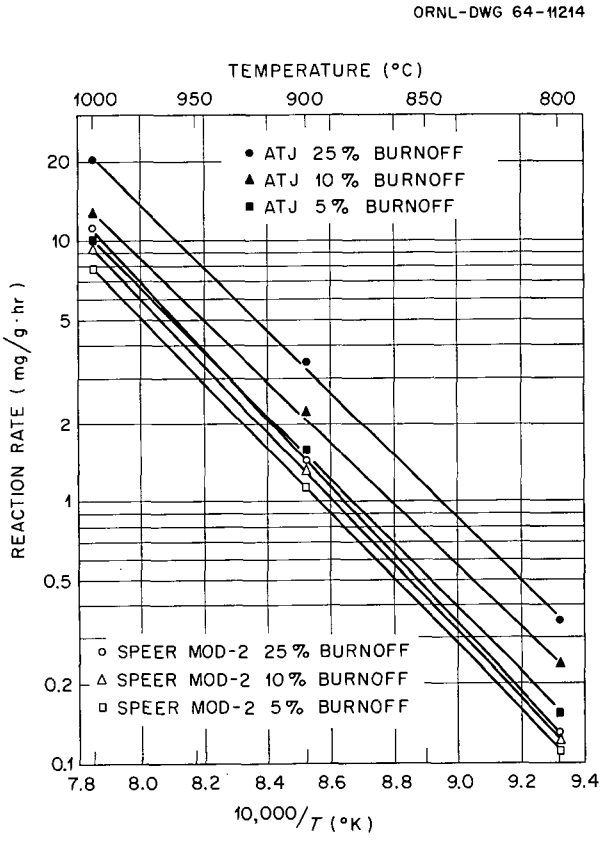

Fig. 11.5. Effect of Temperature and Burnoff on the Reactivity of 1.5-in.-diam Unfueled Spheres with Steam.

Data obtained at 1000°C are further detailed in Fig. 11.6. ATJ graphite showed a much larger increase in both reactivity and surface area at burnoffs above 5 wt % than did Speer Mod-2 graphite. Plots of reaction rate vs surface area (Fig. 11.7) showed the reaction rates to be proportional to the BET surface area of the remaining specimen. Increased reaction rates with increasing burnoff appeared to result from corresponding increases in surface area as determined by nitrogen adsorption. Surprisingly, the specific reaction rates (weight loss per unit BET surface area) obtained for the two graphites at 1000°C are essentially equal. Surface area measurements of sections cut from oxidized spheres showed that the increase in surface area was fairly uniformly distributed through Speer Mod-2 spheres, whereas the increase in surface area of the oxidized ATJ spheres was much greater in the outer than in the central region. Mercury porosimetry also showed that the oxidation of ATJ spheres was heavily concentrated in the outer region. This technique also disclosed some differences in the pore-size distribution of the unoxidized graphites; large pore volumes are contained in pores having radii of ~2.5 and ~10 μ in the case of ATJ and Speer Mod-2 graphite respectively.

The effect of burnoff on the CO to CO_2 ratio in the effluent gases was more pronounced at 900°C than that shown for 1000°C in Fig. 11.6. In the case of Speer Mod-2 graphite, this ratio increased rapidly at low burnoffs, attained a maximum of ~6.5 at 20 wt % burnoff, and then decreased at larger burnoffs. This ratio increased slowly with increasing burnoff and attained a value of ~2 at 30 wt % burnoff when ATJ graphite was oxidized. The fact that ATJ graphite yielded smaller CO to CO_2 ratios than did Speer Mod-2 graphite suggests that the former catalyzes the reaction $CO + H_2O \rightleftharpoons CO_2 + H_2$ more strongly than does the latter graphite. Equilibrium quotients calculated from the composition of the effluent gases from the steam reaction with Speer Mod-2 graphite were, in all cases, at least an order of magnitude less than the equilibrium constants for the water gas shift reaction at the temperatures of interest. Although closer agreement was found for ATJ graphite, the equilibrium quotients also were smaller than the theoretical values. The only conditions at which equilibrium prevailed was at 1000°C using 2.36-in.-diam spheres of ATJ graphite. The larger spheres gave significantly smaller CO to CO_2 ratios than

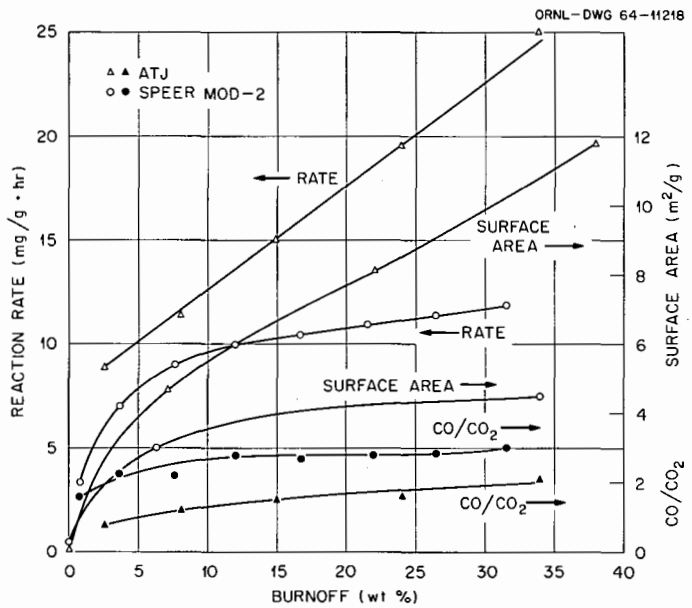

Fig. 11.6. Effect of Burnoff on Reaction Rates, Surface Areas, and CO to CO_2 Ratios of 1.5-in.-diam Unfueled Spheres at 1000°C.

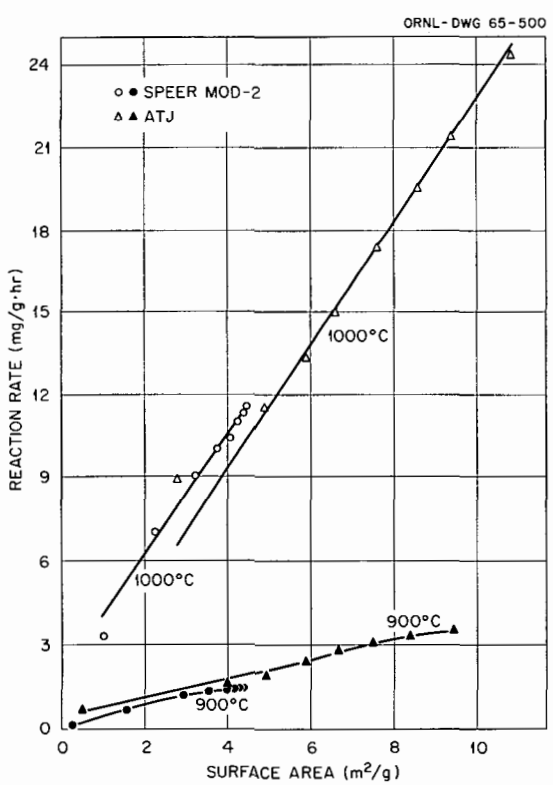

Fig. 11.7. Reaction Rates vs BET Surface Area.

did the 1.5-in.-diam spheres. This behavior indicates that the sphere diameter has an effect which may be associated with the longer residence times of CO in the pore structure of the larger spheres.

Some results obtained from steam exposures of fueled 2.36-in.-diam spheres prepared by Carbon Products Division, Union Carbide Corporation, using a mold-injection method are given in Fig. 11.8. The spheres had 1.0-cm ATJ graphite shells surrounding a graphite matrix containing pyrolytic-carbon-coated uranium dicarbide fuel particles. The effect of burnoff as seen in Fig. 11.8 appears to be similar to that found for the unfueled ATJ graphite spheres (Fig. 11.5). The activation energy is essentially independent of burnoff; it has the value ~50 kcal/mole for three levels of burnoff plotted. This value agrees satisfactorily with activation energies found for 2.36-in.-diam ATJ graphite spheres as well as for simulated AVR spheres having an ATJ graphite shell and a CS-312 graphite insert.[8] The fact that all 1.5-in.-diam spheres (fueled and unfueled) gave activation energies of ~60 kcal/mole indicates that the activation energy is affected by sphere diameter.[3] No serious attack of the fuel particles was observed despite extensive oxidation of the fueled spheres.

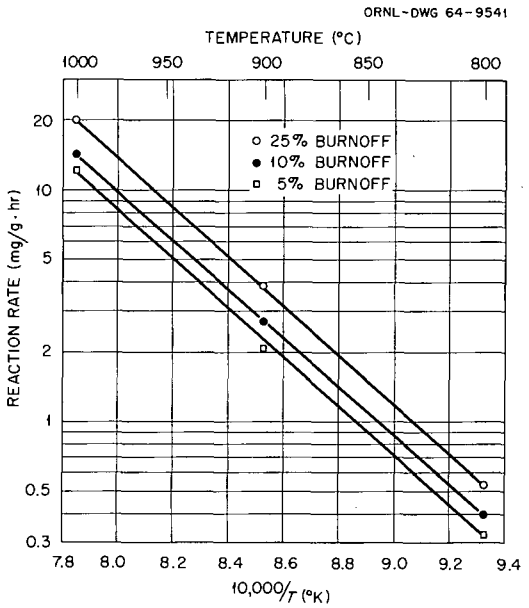

Fig. 11.8. Effect of Temperature and Burnoff on the Reactivity of 2.36-in.-diam Fueled Spheres with Steam.

12. Irradiation Behavior of High-Temperature Fuel Materials

Oscar Sisman J. G. Morgan

INTRODUCTION

The evaluation of the behavior of fuel material and fuel elements under irradiation is a cooperative effort of three divisions of the Laboratory. Preirradiation testing is performed by the Metals and Ceramics Division. Fuel-element design studies and the irradiation experiments are conducted by the Reactor Division. Postirradiation examination and radiation damage evaluation, summarized here, are the responsibility of the Reactor Chemistry Division. These studies are reported in detail in the semiannual progress reports of the GCR Project, and in topical reports.

RADIATION EFFECTS IN PYROLYTIC-CARBON-COATED FUEL PARTICLES[1]

P. E. Reagan J. G. Morgan
C. D. Baumann E. L. Long, Jr.[2]
T. W. Fulton J. W. Gooch

Previously described facilities and techniques[1,3] have been used in a continuing study of rates of release of fission gas from fuel particles. Recent studies have used temperatures of 1200 to 1400°C, and particles of uranium carbide or thorium-uranium oxide (see Table 12.1) with duplex or triplex[4] pyrocarbon coatings. Irradiations[1] were performed in the B-9 facility of the ORR.

The three batches of uranium carbide particles were irradiated at temperatures and to burnups shown along with the average fractional fission-gas release rates in Table 12.2. Release rates increased with temperature for each of the batches, but no bursts of fission gas occurred upon thermal cycling, and no dependence of release rate on flux at constant temperature (tried only on the triplex particles) was found. Release rates increased steadily with burnup (see Fig. 12.1) for all three batches of particles.

Metallographic examination of the coated uranium carbide particles after irradiation showed no failed

[1]P. E. Reagan and J. G. Morgan, *Fission Gas Release from Pyrolytic Carbon Coated Fuel Particles During Irradiation at 2000 to 2500°F*, submitted for publication to *Nuclear Science and Engineering*.

[2]Metals and Ceramics Division.

[3]R. M. Carroll and P. E. Reagan, *Nucl. Sci. Eng.* 21, 141 (1965).

[4]P. E. Reagan *et al.*, *Reactor Chem. Div. Ann. Progr. Rept. Jan. 31, 1964*, ORNL-3591, pp. 128–33.

Table 12.1. Characteristics of Coated Particles Tested Under Irradiation

Coating Type	Batch No.	Core Material	Average Particle Size (μ)	Coating Thickness (μ)
Triplex	GA-309	Uranium carbide	377	98
Duplex	NCC-216	Uranium carbide	390	93
Duplex	OR-138	Uranium carbide	430	115
Duplex	OR-206	Thorium-uranium oxide (Th:U = 13:1)	466	110

Table 12.2. Release of Fission Gases from Coated Uranium Carbide Particles Under Irradiation

Coating Type	Batch No.[a]	Temperature (°C)	Heavy-Metal Burnup (at. %)	Fractional Fission-Gas Release Rates, R/B				
				^{85m}Kr	^{87}Kr	^{88}Kr	^{133}Xe	^{135}Xe
				$\times 10^{-5}$	$\times 10^{-5}$	$\times 10^{-5}$	$\times 10^{-5}$	$\times 10^{-5}$
Triplex	GA-309	1375[b]	19.7	2.2	1.5	1.9	2.2	0.7
Duplex	NCC-216	1375[c]	15.8	1.2	0.9	1.0	0.7	0.3
Duplex	OR-138	1375[c]	13.1	1.2	0.9	1.1	0.9	0.3

[a]NCC – Carbon Products Division, UCC; GA – General Atomics; OR – Oak Ridge National Laboratory.

[b]Temperature was increased from 1100°C to 1375 during irradiation; near end of irradiation the flux was cycled with temperature constant at 1230°C.

[c]Near end of irradiation temperature was cycled over interval 1200 to 1375°C.

coatings in any batch. Both batches of duplex coated particles showed wedge-shaped fractures, extending from the core-coating interface to the outer columnar coating, and one (NCC-216, Fig. 12.2) showed a reaction product adjacent to the fuel. The triplex material (Fig. 12.3) showed no reaction zone, no migration of fuel into the coating, and no delamination of the coating; the triplex particles appeared unchanged by irradiation except for loss in crystalline detail and the presence of fine porosity within the carbide fuel. However, fracturing of the inner coating did not seem to enhance the loss of fission gases from the duplex coatings. It may be concluded that pyrolytic-carbon coatings of either the duplex or triplex type will operate at 1400°C to 16 at. % burnup with sufficient integrity to meet present gas-cooled reactor design criteria. These particles can withstand thermal cycles from 200 to 1400°C during power production.

The single batch of duplex-coated thorium-uranium oxide particles was irradiated at 1200°C to 0.53 at. % heavy-metal burnup. The fuel in these particles was made by the sol-gel process.[5] The average fractional fission-gas release rates were lower by about fivefold than those shown in Table 12.2. Metallographic examination of particles from this experiment revealed no failures, but straight-line fractures originating at the core-coating interface were found in the inner coating. A few of the fractures had penetrated the entire thickness of the inner laminar coating, but none extended into the outer columnar layer. In about 10% of the particles examined, a shiny particulate material was noted in these fractures that was not present before irradiation.

When the fractional fission-gas release rates for the various isotopes are plotted against their half-life on a log scale, the points follow one of two characteristic lines. If the experiment contains particles with broken coatings, the release rates will plot a nearly straight line, like the one shown in Fig. 12.4 for uncoated particles. However, if

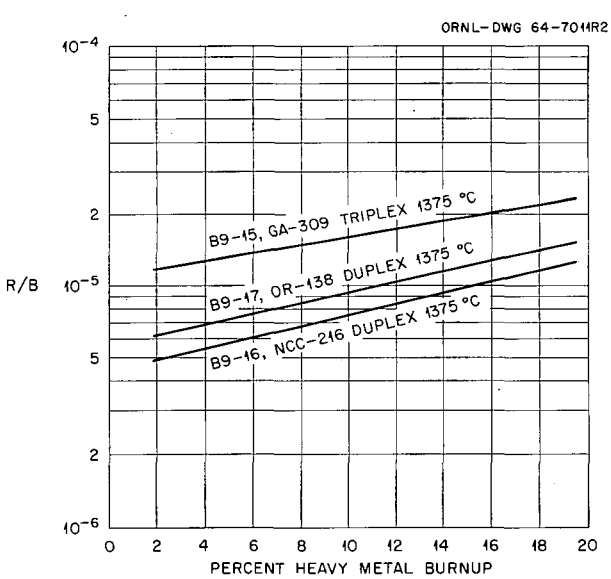

Fig. 12.1. Increase in ^{88}Kr Release with Burnup.

[5]D. E. Ferguson, *Status and Progress Report for Thorium Fuel Cycle Development*, ORNL-3385.

PHOTO 68704

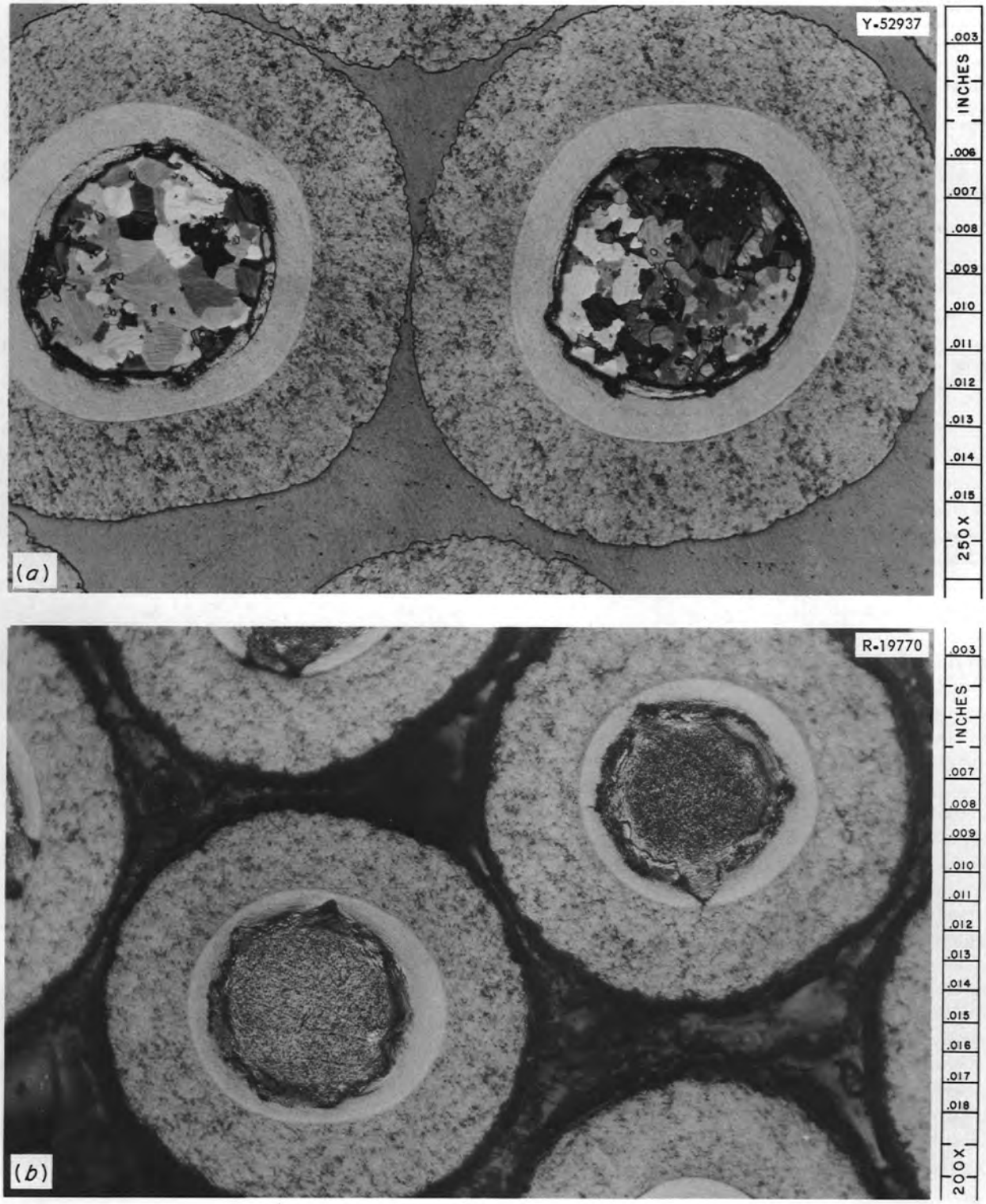

Fig. 12.2. Pyrolytic-Carbon-Coated Uranium Carbide Particles from Batch NCC-216. (a) Unirradiated. (b) From experiment B9-16, irradiated to 16.8 at. % uranium burnup at 1375°C.

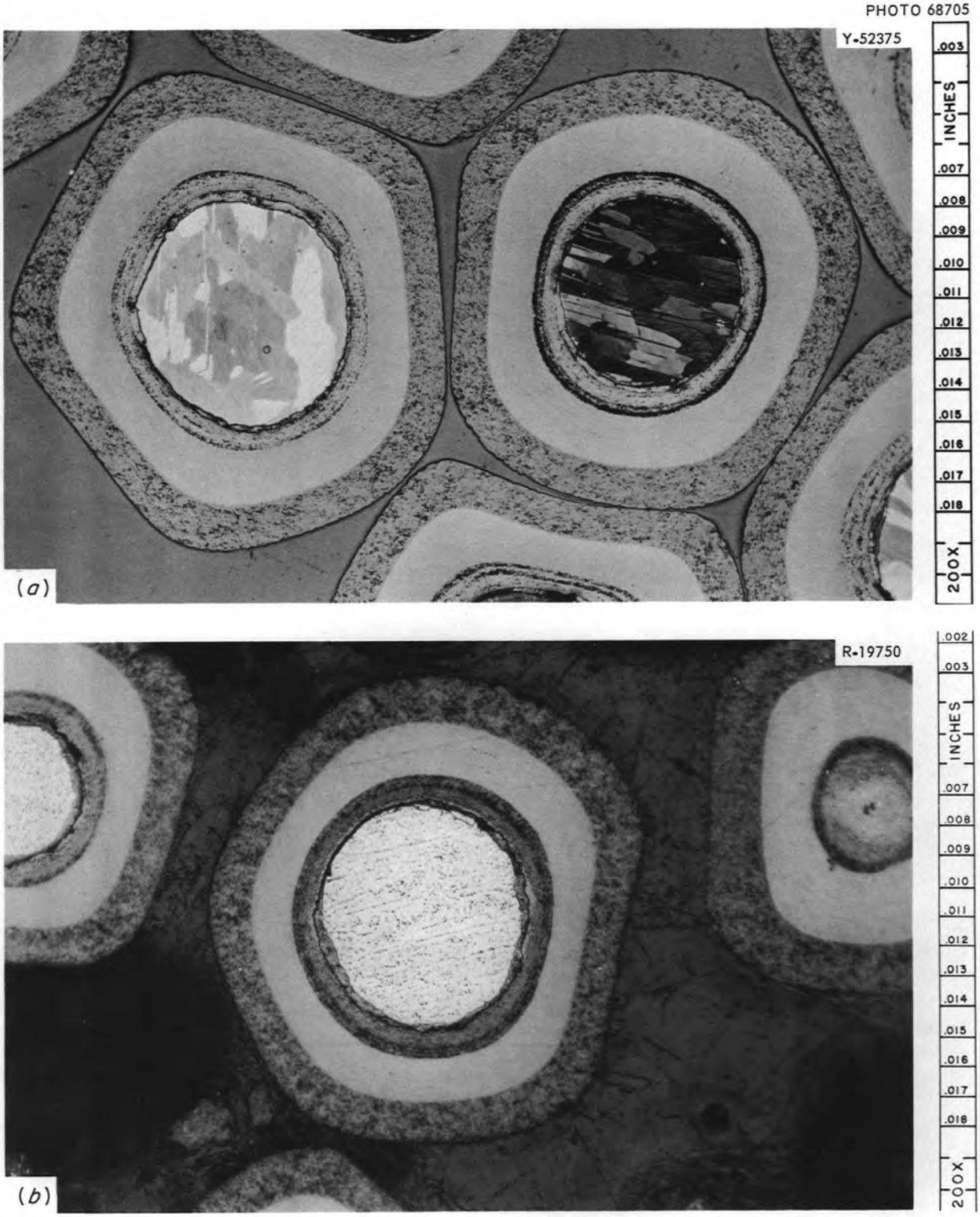

Fig. 12.3. Pyrolytic-Carbon-Coated Uranium Carbide Particles from Batch GA-309. (a) Unirradiated. (b) From experiment B9-15, irradiated to 19.7 at. % uranium burnup at 1375°C.

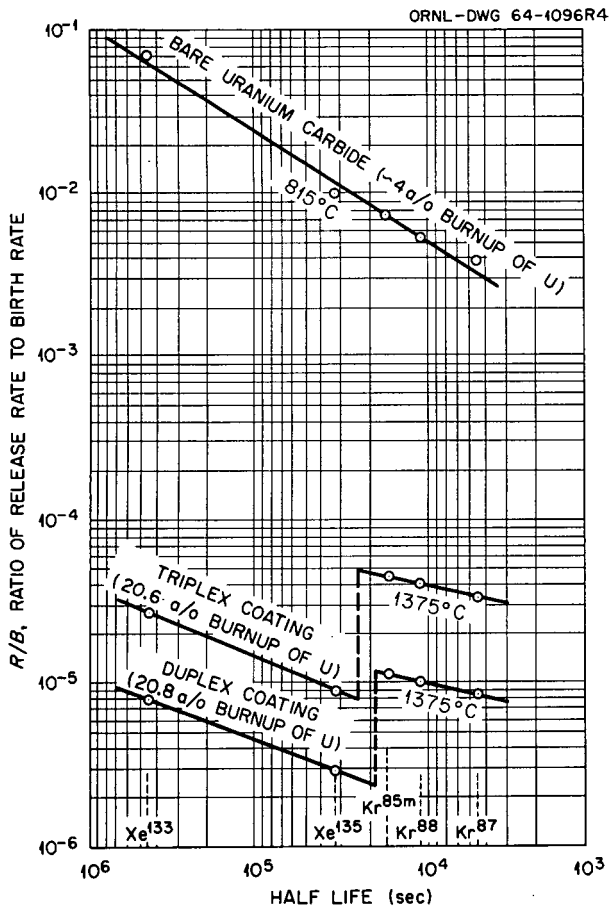

Fig. 12.4. Relationship Between R/B and Half-Life for Release of Inert Gases from Pyrolytic-Carbon-Coated Uranium Carbide Particles.

there are no broken coatings, the line (Fig. 12.4) will show an offset between the kryptons and the xenons. This discrimination between the kryptons and xenons may be a useful index to determine whether or not the gas is coming through cracked coatings.

POSTIRRADIATION TESTING OF COATED FUEL PARTICLES

M. T. Morgan R. L. Towns

Coated particles are irradiated in the B-9 facility, as described immediately above, to determine their ability to retain fission gases during irradiation. Portions of these batches are subsequently tested by annealing at high temperatures to determine (1) resistance of coatings to cracking, and (2) rate and extent of release of fission products at temperatures higher than those readily available in-pile. In addition, a few tests, in which the coating layers were sequentially removed, have been performed to determine the extent to which fission product migration has progressed within the coatings.

Fission Product Release on Annealing

Samples (generally 20 to 200 particles) from eight previously irradiated batches have each been annealed at progressively increasing temperatures in the range 1375 to 2000°C; release of ^{85}Kr was monitored continuously during heating and while the specimens were maintained (generally for 2 to 18 hr) at the annealing temperature. Release of "nonvolatile" fission products from three of these batches was evaluated by analysis of the graphite crucibles and quartz furnace tube liners, which were changed at each annealing step. Equipment and techniques used in this study are similar to those previously described.[6]

The eight batches of particles included one batch of UO_2 with duplex coatings and seven batches of UC_2, four with duplex and three with triplex coatings. The UO_2 particles had been irradiated to 4.6% burnup, and one batch of the triplex-coated UC_2 showed 8% burnup; all others showed burnups of 16 to 26%. Two of the batches had been irradiated at 950°C and below; all others had spent at least part of their irradiation time at 1310 to 1370°C.

Release of ^{85}Kr from these samples on annealing produced few surprises. Gas release rates during the first hour after temperature changes were generally slightly higher than the average rate after this period. The initial rate seldom exceeded the average by more than threefold, but one set of particles (UC_2 with duplex coatings irradiated to 16% burnup at 1370°C) showed initial rates 16- to 100-fold the subsequent average. Cracking or bursting of coatings (not involved in the phenomena described above) were easy to detect, since each such event released large gas bursts corresponding to about 50% of that contained by the particle.

[6] *GCR Program Semiann. Progr. Rept. Sept. 30, 1963*, ORNL-3523.

It is interesting to observe that of some 560 individual particles, heated at several temperatures through 2000°C for an average of approximately 8 hr at each temperature, only 19 coating bursts occurred. Of these, 14 of the 19 were in the batch of particles that yielded the large initial bursts.

The graphite crucibles and quartz furnace liners were examined for ^{140}Ba, ^{144}Ce, ^{137}Cs, ^{103}Ru, ^{106}Ru, ^{89}Sr, and ^{95}Zr. More than 95% of the barium, cerium, and strontium collected remained in the crucible at 1370°C. At 1700°C about 30% of the strontium collected was transferred to the furnace tube liner. Release of cesium, ruthenium, and zirconium was at, or below, limits of detection at these temperatures. At 2000°C, approximately 80% of the barium, 95% of the cerium, 10% of the cesium, 60% of the ruthenium, 10% of the strontium, and most of the zirconium collected remained on the crucible. The rest of the fission products released were transferred to the furnace tube liner. Fission products, except for ^{95}Zr, collected from other parts of the assembly totaled 1% or less of those collected on crucibles and liners. Approximately 12% of the ^{95}Zr collected was found on the nonremovable parts of the furnace system after an extended anneal at 2000°C.

The three batches of particles examined included one of UO_2 with duplex coating, one of UC_2 with duplex coating, and one UC_2 with triplex coating. Burnups ranged from 4 to 24%. These variables seem, however, to have had relatively little effect on the fission product release rates. Table 12.3 shows data typical of that obtained in the study. Barium, strontium, and, to a slightly lesser extent, cerium appear to be released from the particles at appreciable rates.

Fission Product Release into Outer Coating

Attempts were made to fracture, by mechanical means, the coatings of individual particles within a closed system at room temperature. Uranium dicarbide particles with triplex coatings (GA-309) irradiated at 1375°C to 19.7% burnup were used. Mechanical cracking of the coatings without crushing the cores was possible. When cracking of both outer coating layers occurred, the ^{85}Kr released corresponded to 15 to 35% of the total contained in the particle. When the outer coating was fractured alone (three cases), less than 0.01% of the contained ^{85}Kr was released. It is clear that no effective penetration by krypton of the inner coating layer had occurred.

Fragments of the outer coatings removed as above were analyzed for "nonvolatile" fission products. These analyses, combined with visual estimates of size of the coating fragment, suggest that the outer coating contained 6.3% of the total ^{140}Ba, 17% of the ^{144}Cr, 14% of the ^{137}Cs, 0.5% of the ^{103}Ru and ^{106}Ru, 2.3% of ^{89}Sr, and 0.9% of the ^{95}Zr produced in an average particle.

POSTIRRADIATION EXAMINATION OF FUELED GRAPHITE SPHERES

D. R. Cuneo M. F. Osborne
H. E. Robertson J. G. Morgan
C. D. Baumann

Fuel elements for the German AVR, a pebble bed reactor, are to be 2.36-in. (6 cm) diam spheres of graphite, containing fuel particles individually

Table 12.3. Fraction of Fission Product Isotope Released per Hour During Annealing of Duplex-Coated UC_2 After Irradiation at 1370°C to 16% Burnup

Experiment	Temperature (°C)	^{140}Ba	^{144}Ce	^{137}Cs	^{103}Ru	^{106}Ru	^{89}Sr	^{95}Zr
B9-17	1370	8.1×10^{-3}	1.3×10^{-3}	1.2×10^{-5}– 2.6×10^{-5}	$<1.4 \times 10^{-5}$	5.3×10^{-7}– 3.6×10^{-6}	4.6×10^{-3}	1.7×10^{-7}– 3.1×10^{-6}
	1700	1.2×10^{-1}	8.3×10^{-2}	4.5×10^{-4}	5.8×10^{-5}– 8.7×10^{-5}	3.3×10^{-5}– 5.0×10^{-5}	1.4×10^{-1}	$<1.6 \times 10^{-5}$
	2000	1.0×10^{-1}– 3.7×10^{-1}	6.4×10^{-2}– 1.0×10^{-1}	7.1×10^{-2}– 9.2×10^{-2}	1.5×10^{-4}	2.5×10^{-4}	1.1×10^{-1}– 5.2×10^{-1}	$<2.4 \times 10^{-5}$

coated with pyrolytic carbon. Effects of long-term irradiation on stability, mechanical properties, and fission-gas retentivity of these spheres remain an important problem. Each of the spheres tested (after irradiations and by methods which have been described in detail)[7] during this year has been of one of the following types.

1. Molded with no shell, fuel particles dispersed throughout.
2. Molded fuel cores contained in unfueled *molded* shells of various thicknesses.
3. Molded fuel cores contained in unfueled *machined* shells of various thicknesses.

The graphite spheres were either $1\frac{1}{2}$ in. or 2.36 in. (6 cm) in diameter; they contained pyrolytic-carbon-coated fuel particles, 300–500 μ in diameter, of either UC_2 or $(Th,U)C_2$. They were irradiated in an integrated flux ranging from 10^{19} to 10^{21} neutrons/cm^2; surface temperatures varied between 1000 and 1700°F; and the burnups (based on the enriched uranium particles) varied from 0.5 to 19%. The results of these studies have been reported in detail.[8–10]

Fuel Distribution and Burnup

Faulty fuel loading patterns or serious abnormalities in fuel distribution within the spheres can be detected by careful gamma-ray scanning of the irradiated spheres. Gamma scans of the three spheres of Fig. 12.5, for example, show a region of low fuel density in the interior of sphere No. 1, and indicate, by width of the gamma-emitting region, the thickness of the unfueled shell on each sphere.

Areas under such gamma scans are related to fuel burnup; they afford an easy check upon burnup values calculated from flux monitor analysis. Table 12.4 shows a comparison of values from these sources for a single experiment.

[7]J. G. Morgan *et al., Reactor Chem. Div. Ann. Progr. Rept. Jan. 31, 1964,* ORNL-3591, pp. 133–36.

[8]D. R. Cuneo, E. L. Long, Jr., and H. E. Robertson, *Hot Cell Techniques for the Evaluation of Fueled Graphite Spheres,* 12th Annual Conference on Remote Systems Technology, ANS Winter Meeting, Nov. 29–Dec. 3, 1964, San Francisco.

[9]J. G. Morgan *et al., GCR Program Semiann. Progr. Rept. March 31, 1964,* ORNL-3619, pp. 246–68.

[10]J. G. Morgan *et al., GCR Program Semiann. Progr. Rept. Sept. 31, 1964* (in press).

Mechanical Properties

Weight and Dimensional Changes. – All spheres were baked, prior to irradiation, at temperatures comparable to those expected during irradiation. Temperature distributions within the spheres cannot, however, be duplicated in preirradiation heating. During irradiation some of the spheres experienced more severe temperature excursions than those for which they were designed. Whether irradiation or these high temperatures are responsible for the observed changes cannot be ascertained.

Spheres irradiated at surface temperatures of 1000 to 1900°F have generally decreased in diameter by 0.2% to nearly 1%. The manufacturing method of the sphere seems more important than irradiation temperature in determining the extent of the decrease. Weight losses of up to 0.67% have been observed. The limited observations suggest that spheres with unfueled shells show larger weight losses, while those without shells show larger diameter changes.

Weight losses can lead to difficulty if the loss represents volatilization of the cementing layer between fueled core and unfueled shell. If this layer fails, the shell is unsupported against compression, and, with heat transfer impaired, the fuel core runs hotter than its design condition. Some examples of such failure have been observed (see next section).

Compression and Impact Testing. – Postirradiation test results have been reported[7] for $1\frac{1}{2}$-in.-diam fueled spheres. The compression test results on 6-cm spheres are inconclusive because of the lack of statistical data. However, use of the compression test allowed us to observe lack of sphere shell-core bonding. Figure 12.6 shows two spheres

Table 12.4. Comparison of Areas Under Gamma Scan Curves and Calculated Burnups for Spheres from Loop 2-2[a]

Sphere No.	Normalized	
	Burnup	Area Under Gamma Scan
A	100	100
B	59	57
C	40	37

[a]Normalized to sphere A.

after the compression test. The sphere on the left failed at 1450 lb, and the lack of a bond between the core and the shell is evident. The sphere on the right failed at 2500 lb. It had a negligible weight loss and a good shell-to-core bond.

Metallographic Examinations. – Representative specimens from the spheres are selected for metallographic examinations. Generally, a specimen is cut from the center portion of the sphere, and another specimen is taken from the fuel-core–unfueled-shell interface.

Figure 12.7 is a photomicrograph of a polished and etched section of a sphere containing a laminar-coated particle. This section is a sphere which experienced a 12% burnup at 1000–1150°F. A light-colored reaction product had formed around the perimeter of the fuel core. Fractures and tears had begun to form at the interface of the fuel core and the pyrolytic-carbon coating. No crystalline details are evident in the fuel core, and plastic flow is apparent. The uranium in this $(Th,U)C_2$ particle was 93% enriched. Examination

ORNL-DWG 65-2588

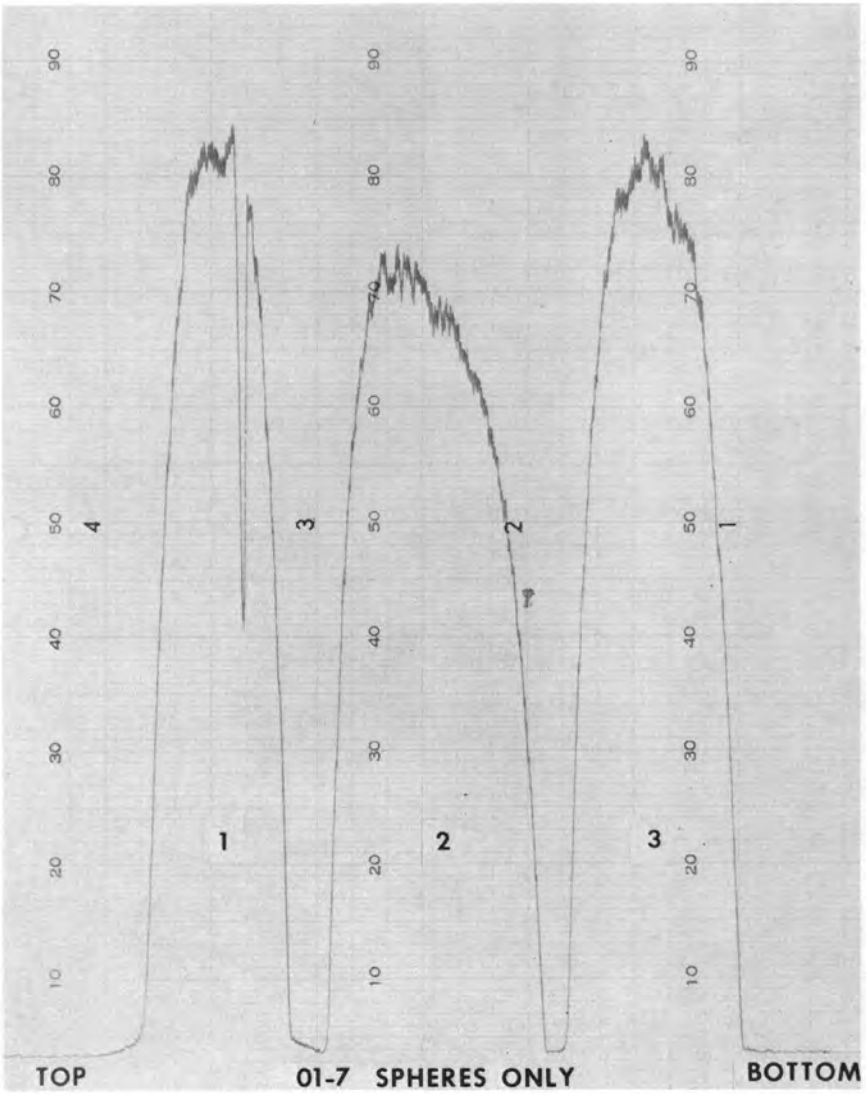

Fig. 12.5. Gamma Scans of Three 2.36-in.-diam spheres. Relative unfueled shell thickness (0.33, 0, and 0.25 in., respectively, for spheres 1, 2, and 3) is shown by width of curve bases. Low-density fuel region in sphere No. 1 is evident.

PHOTO 68706

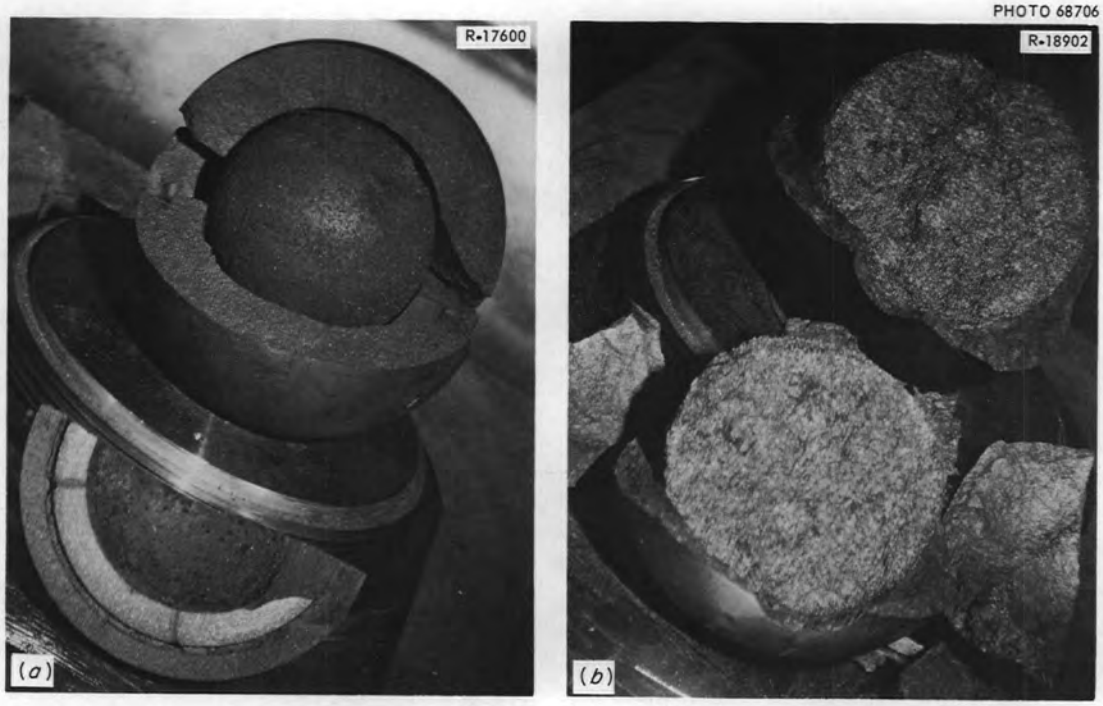

Fig. 12.6. Fuel Spheres After Compression Testing. (a) Failure at 1450 lb; lack of bonding of fuel core to unfueled shell evident. (b) Failure at 2500 lb; good bonding of fuel core to unfueled shell evident.

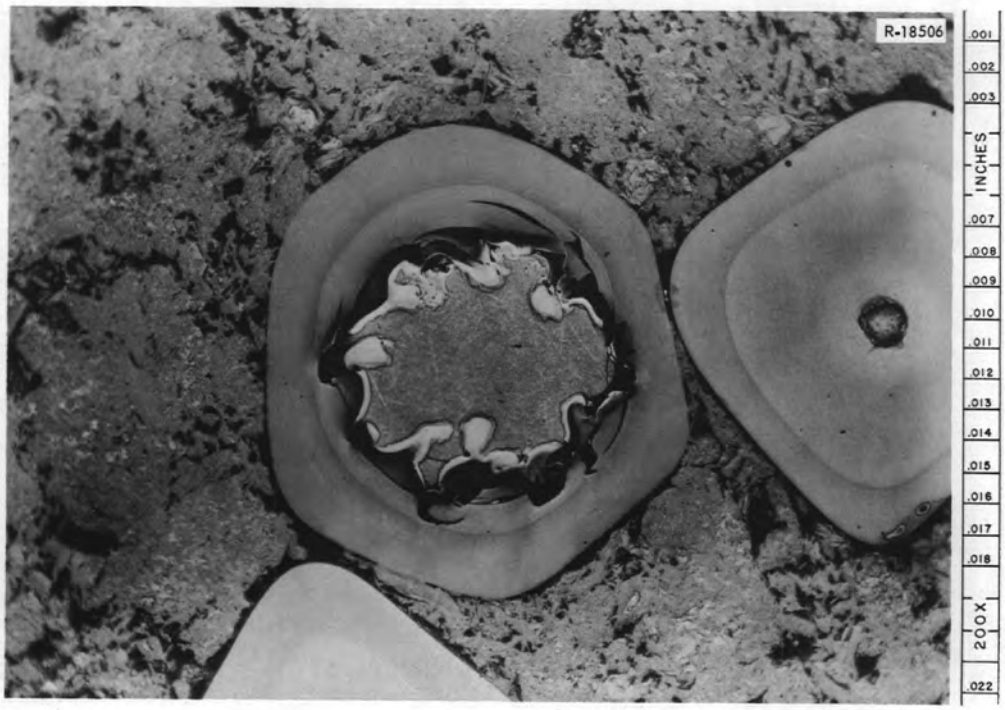

Fig. 12.7. Laminar Coated $(Th,U)C_2$ Particle from Experiment 8B-3, Sphere No. 1, 12% Burnup, 1000–1150°F. Uranium is 93% enriched. Reduced 20%.

of a laminar-coated $(Th,U)C_2$ particle containing normal uranium (irradiated in another sphere at ~1400°F and 14% burnup) showed none of these changes. Crystalline detail was quite sharp, and the fuel-core–coating interface was identical to unirradiated, unheated $(Th,U)C_2$ particles.

Figure 12.8 shows two duplex-coated particles of enriched UC_2 after polishing and etching. These particles are from a sphere which was irradiated to a burnup of 20 at. % at ~2500°F. As in the case of the laminar-coated $(Th,U)C_2$ particle (Fig. 12.7), no crystalline details are evident. Fracturing of the inner layer of coating is apparent, as well as a reaction product zone at the core-coating interface. Voids in the core are particularly noticeable in the right-hand particle. These features were typical also for the duplex-coated particles in the spheres.

Figure 12.9 is a photomicrograph of a triplex-coated $(Th,U)C_2$ particle which was irradiated at a maximum temperature of 1300°F to a burnup of 12%. The photomicrograph shows no crystalline detail in the fuel, but one possible reaction zone exists between the core and the shell.

Triplex coatings appear to show less damage than do duplex under the conditions of temperature and burnup for these experiments. In the triplex-coated particles the integrity of the outer two coatings was maintained completely, with only minor damage to the innermost coatings. The laminar coating on particles in Fig. 12.7 shows severe attack at about the same level of burnup and temperature. The duplex-coated particles operated at higher temperature and burnup; damage was more severe than in the triplex coating but was limited to the inner coating.

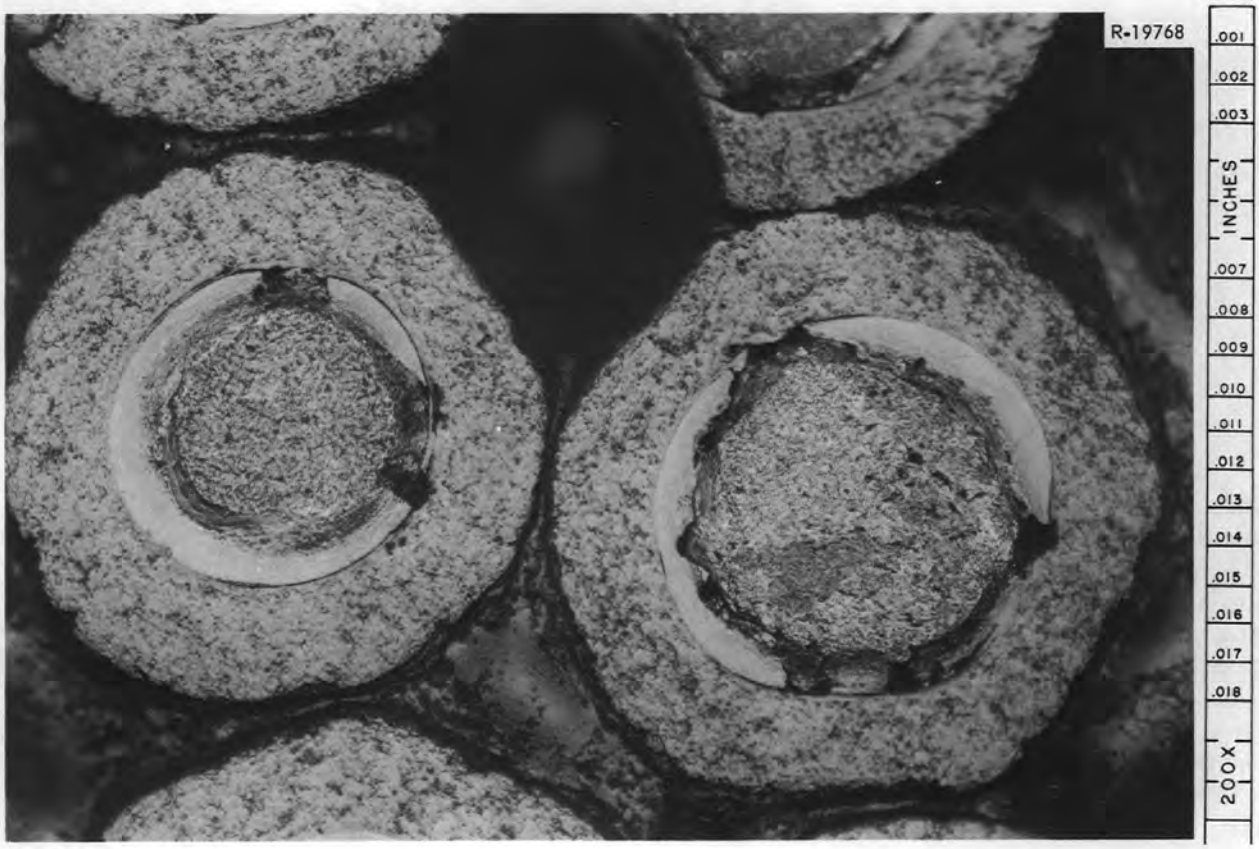

Fig. 12.8. Duplex Coated Particles from Experiment B9-16, 20% Burnup, 2500°F.

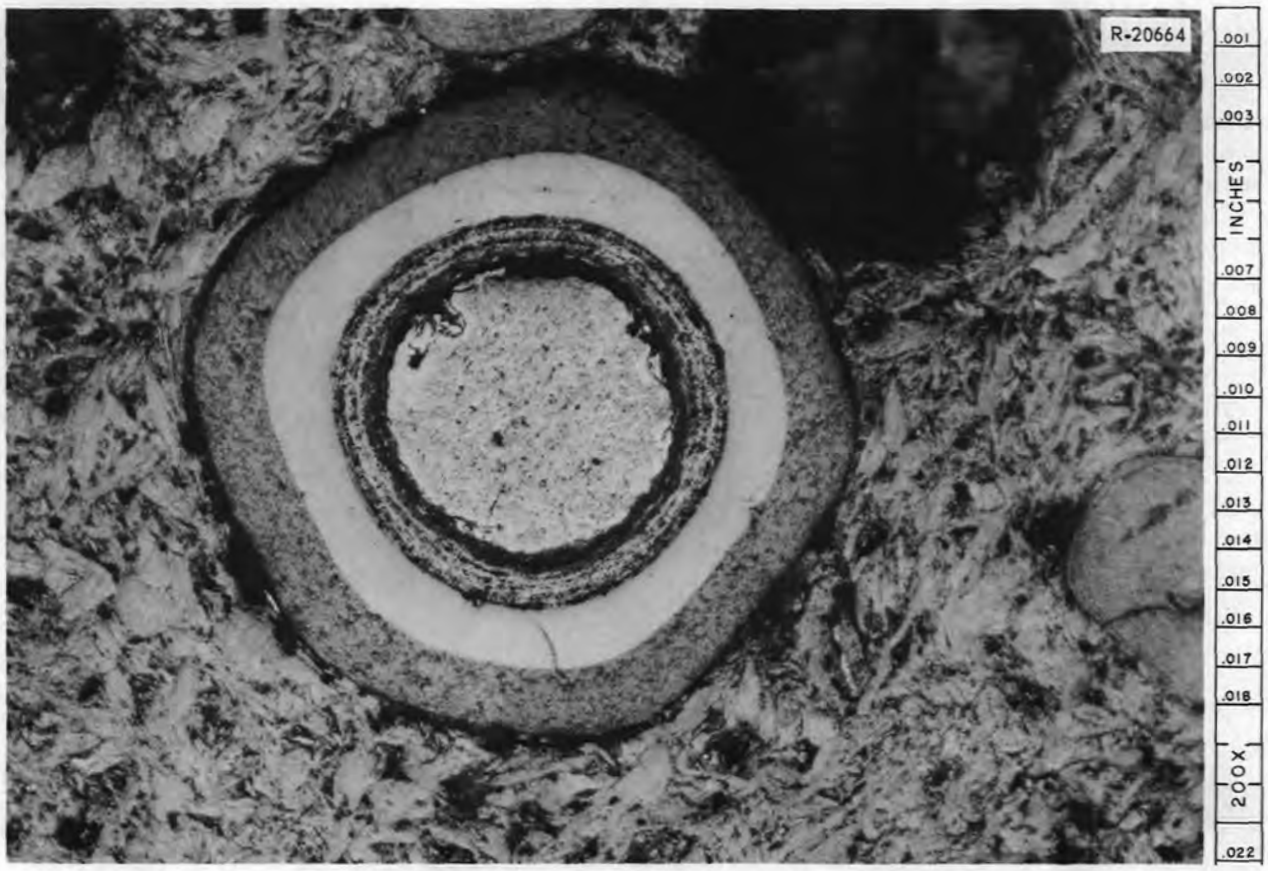

Fig. 12.9. Triplex Coated Particle from Experiment 8B-4, Sphere No. 1, 12% Burnup, 1300°F.

POSTIRRADIATION EXAMINATION OF EGCR FUEL ELEMENT PROTOTYPE CAPSULES

M. F. Osborne
E. L. Long, Jr.[2]
D. R. Cuneo
H. E. Robertson

The program for the evaluation of EGCR prototype fuel is nearly complete. The last ten capsules of the ETR irradiation series have been removed from the reactor; one capsule was examined in detail, and three other capsules were examined nondestructively. The other six capsules were removed from the NaK coolant, inspected visually, photographed, and stored for possible future examination. Two high-burnup irradiations are still in progress in the ORR.

Descriptions and results of earlier experiments in this series have been reported previously.[11–14] Data for these ETR-irradiated capsules are summarized in Table 12.5.

Analysis of the NaK coolant from each capsule indicated that capsules E-3 and E-7 had suffered cladding failures, but that the other capsules were intact. Visual inspection revealed severe distortions and two fractures in the cladding of capsule E-7. One of the fractures is shown in Fig. 12.10. Capsule E-3 was tightly stuck inside its NaK vessel and could not be inspected without further disassembly. No unusual irradiation effects on the cladding of the other eight capsules were apparent. With the exception of the badly damaged capsule

[11] J. G. Morgan, M. F. Osborne, and Oscar Sisman, *Nucl. Sci. Eng.* 14, 83–100 (1962).

[12] M. F. Osborne *et al.*, *Reactor Chem. Div. Ann. Progr. Rept. Jan. 31, 1964*, ORNL-3591, pp. 136–40.

[13] M. F. Osborne, E. L. Long, Jr., and J. G. Morgan, *Performance of Prototype EGCR Fuel at Extreme Operating Conditions*, ORNL-TM-832.

[14] J. G. Morgan *et al.*, *GCR Program Semiann. Progr. Rept. Sept. 30, 1964*, ORNL-3731, pp. 280–82.

Table 12.5. Data for EGCR Prototype Capsules Irradiated in EGCR

Capsule No.	Type of Fuel Pellet	Average Cladding Temperature (°F)	Maximum Power[a] (% of design)	Burnup[b] (Mwd/metric ton UO_2)
E-1R	Solid	1550	112	6500
E-2	Solid	1300	61	4500
E-3	Solid	1500	111	
E-4R	Solid	1250	97	7500
E-5	Hollow	1250	111	9500
E-5R	Hollow	1500	117	
E-7	Hollow	1250	170[c]	14,900
E-10	Hollow – BeO[d]	1500	110	7400
E-11	Hollow – BeO[d]	1300	87	
E-12R	Hollow	1450	98	

[a]Determined from operating data. Design power rating was 35,000 Btu hr^{-1} lin ft^{-1}.
[b]Calculated from neutron-flux data.
[c]Capsule ruptured.
[d]Beryllium oxide rod was inserted in center of UO_2 pellet column.

Fig. 12.10. Area of Cladding Fracture in Capsule E-7. 3.1×.

E-7, no significant changes in the capsule dimensions were found. Metallographic examination of the fuel and cladding from capsule E-7 indicated that the causes of failure were the same as those for three previous capsules;[13] that is, nitride impurity in the UO_2 caused cladding embrittlement, and accidental overheating of the UO_2 caused the fractures in the embrittled cladding. The results of these examinations have been reported in greater detail elsewhere.[14]

POSTIRRADIATION EXAMINATION OF METAL-CLAD FUEL ELEMENTS OF ADVANCED GAS-COOLED REACTOR DESIGNS

M. F. Osborne H. E. Robertson
D. R. Cuneo E. L. Long, Jr.[2]

The examination of five elements which had been irradiated in the ORR loop No. 1 facility has been

completed. The detailed results of these and earlier experiments in this series have been reported previously.[15–17]

General fabrication and irradiation data for these experiments are summarized in Table 12.6. The construction of the fuel elements is shown in Fig. 12.11; all elements were similar except for minor variations. Two of the elements had a spiral wire wrapping brazed to the exterior of the cladding, and a third element had fins machined in the cladding. This cladding roughening was designed to increase heat transfer from the element to the helium coolant. Very high heat ratings were achieved in two elements (see Table 12.6), but the third element failed during reactor startup. Examination showed that both wire-wrapped elements had bowed to the extent that poor heat transfer had caused local hot spots. The copper braze had melted, and the cladding had suffered intergranular fractures (Fig. 12.12). The element with machined fins, however, performed well throughout the irradiation and showed no significant change.

Two elements, 7D and 13, had $\frac{1}{16}$-in.-diam holes drilled in the cladding prior to irradiation. The purpose of this vent was to permit study of fission product evolution from the element and deposition of fission products within the loop. Very little fission product radioactivity was found in the coolant for element 13, and postirradiation examination revealed that the vent hole had not penetrated the inside surface of the cladding. A detailed study of these two elements was made, but no unusual effects were found.[16,18]

We examined one fuel capsule of advanced gas-cooled reactor design which had been irradiated in the ORR Poolside facility.[19] The stainless steel cladding was 0.85 in. OD and had machined grooves for improved heat transfer. The capsule was irradiated to a burnup of 4100 Mwd per metric ton of UO_2 at a maximum cladding temperature of 1600°F. The average linear power was about 50,000 Btu hr^{-1} ft^{-1}. No unusual irradiation effects were seen during the examination. Circumferential cladding ridges were faintly visible at fuel pellet interfaces. The cladding had collapsed against the fuel pellets, and about 5% of the fission gas had been released from the fuel.

[15] D. F. Toner *et al.*, *Reactor Chem. Div. Ann. Progr. Rept. Jan. 31, 1963*, ORNL-3417, pp. 190–92.

[16] J. G. Morgan, D. F. Toner, and E. L. Long, Jr., *Postirradiation Examination of EGCR Prototype Fuel Elements*, ORNL-TM-64-4-31.

[17] M. F. Osborne, E. L. Long, Jr., and J. G. Morgan, *Postirradiation Examination of ORR Loop 1 Advanced Fuel Elements*, ORNL-TM-862.

[18] J. G. Morgan *et al.*, *GCR Program Semiann. Progr. Rept. Sept. 30, 1964*, ORNL-3731, pp. 278–79.

[19] J. G. Morgan *et al.*, *GCR Program Semiann. Progr. Rept. March 31, 1964*, ORNL-3619, pp. 44–47.

Table 12.6. Fabrication and Irradiation Data for ORR Loop No. 1 Fuel Elements

Element	Cladding Surface	Cladding Failure	Fuel Manufacturer	Maximum Heat Generation Rate (Btu hr^{-1} ft^{-1})	Irradiation Time (weeks)	Burnup (Mwd/metric ton UO_2)
10P-1	Wire wrapped	Yes	ORNL and Westinghouse	69,000	3	~500
10P-2	Wire wrapped	Yes	ORNL and Westinghouse	*a*	*a*	*a*
7D	Smooth	No[b]	ORNL	23,000	4	345
11M	Machined fins	No	ORNL	74,000	8	~1400
13	Smooth	No[b]	Westinghouse	32,000	14	~1200

[a] Failed during startup.

[b] Deliberately vented element.

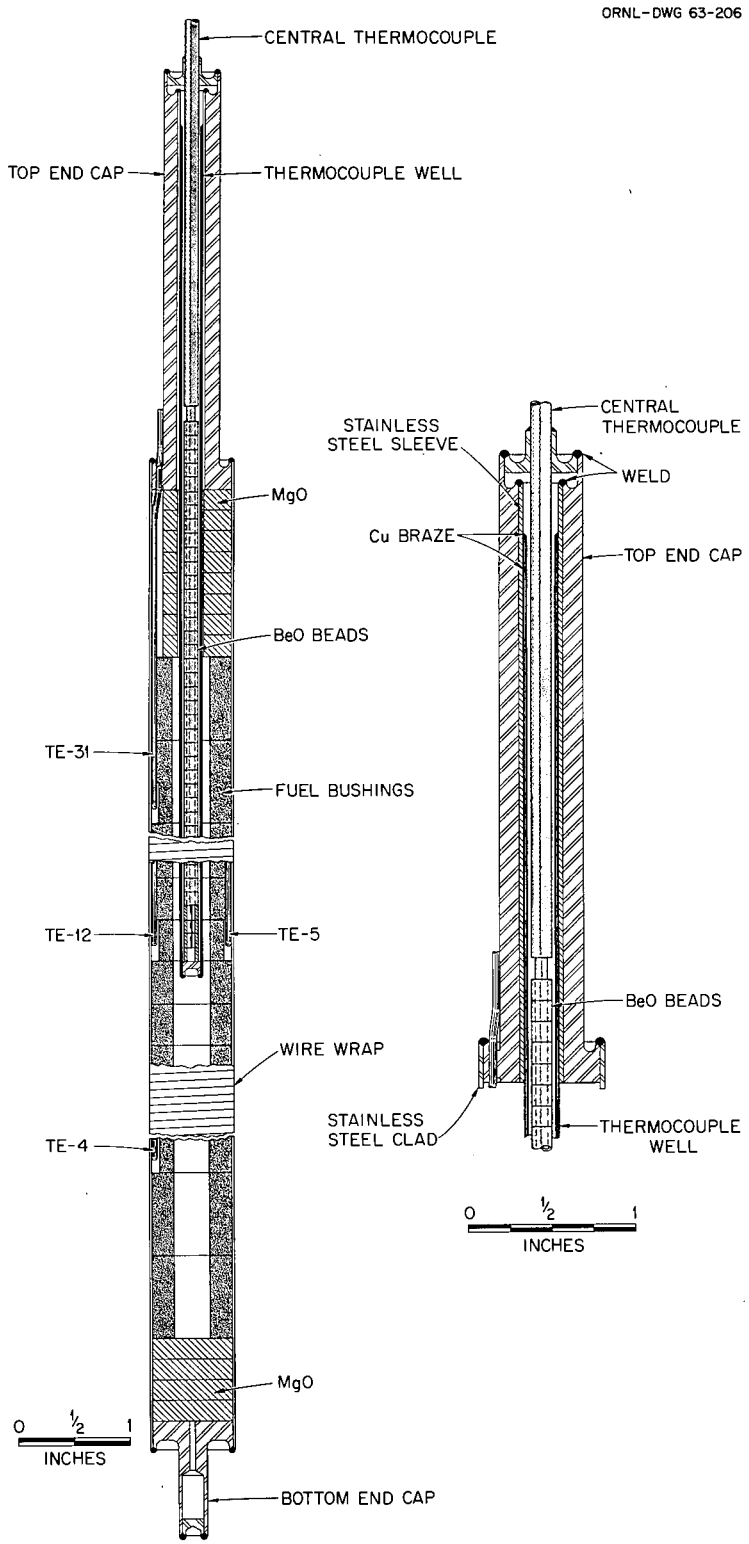

Fig. 12.11. Construction of ORR Loop 1 Fuel Elements with Spiral Wire Wrapping.

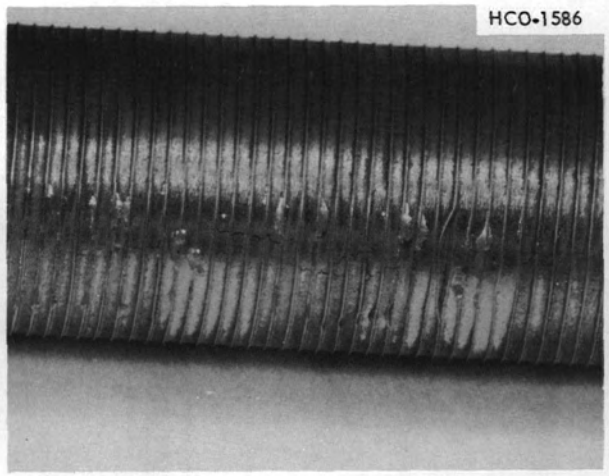

Fig. 12.12. Region of Cladding Fracture in Element 10P-1. Note the wire wrapping and the fractures in the cladding. 2.2X.

13. Fission-Gas Release During Fissioning of UO_2

R. M. Carroll Oscar Sisman T. W. Fulton
R. B. Perez[1] Kiyoshi Inoue[2]

INTRODUCTION

The safe operation of a fuel element may depend on the amount of fission gas that is released from the fuel during irradiation. Therefore, considerable effort has been devoted to obtaining a method to calculate the fission-gas release. Above a threshold temperature, the fission-gas release increases exponentially with temperature in UO_2, and in the past this effect has caused most experimenters to believe that the high-temperature release of fission gas was by a diffusion process.[3]

More recently the results of work by several experimenters have led to the conclusion that the temperature-dependent release of fission gas is not controlled by diffusion, but is controlled by a trapping process.[4] We have used an in-pile experiment to confirm and extend this theory.[5,6] The in-pile experiment (located on the C-1 lattice position of the ORR) eliminates many of the variables of other experimental methods by measuring the steady-state fission-gas release while the UO_2 specimen is producing nuclear power.[7] The specimen is heated by its own fission power, which is adjusted by moving the specimen into or out of the neutron flux. The UO_2 temperature is controlled by air cooling the specimen capsule. Fission gas is entrained in a stream of sweep gas, and the amount of each fission-gas isotope in the sweep gas is determined by gamma-ray spectrometry. The neutron flux is determined by adding argon to the sweep gas and measuring the subsequent activation of the argon.[8]

In order to simplify the problem as much as possible, we have been studying the fission-gas release from purified single crystals of UO_2. The results of these experiments showed that both burnup and fissioning rate had a large effect upon the steady-state fractional release rate of fission gas during irradiation. These and other observations could not be explained by a diffusion-controlled mechanism, and a defect-trap model was postulated.[9] This model appears to satisfy all the requirements for the experimental observations.

Very simply, the defect-trap model assumes that the rate-controlling process for fission-gas release in the temperature-dependent region is the probability of being trapped and the probability of being released from traps. The traps (see Fig. 13.1) are of three kinds: (1) intrinsic traps, which are voids, grain boundaries, or other flaws in the material, (2) point defects which are formed in the wake of a fission fragment, and (3) clustered point defects. The point defects are mobile, are created and destroyed by fission, and are annealed by heat; they reach an equilibrium number at a given temperature and fission rate. The intrinsic traps are not mobile at the temperatures considered here and act as permanent traps for any gas which diffuses into them.

[1]Consultant from the University of Florida.

[2]On loan from Hitachi Co., Tokyo, Japan.

[3]J. Belle (ed.), *Uranium Dioxide: Properties and Nuclear Application*, U.S. Govt. Printing Office, Washington, D.C., 1961.

[4]R. M. Carroll, *Nucl. Safety* 5(4), 356–60 (1964).

[5]R. M. Carroll, *Reactor Chem. Div. Ann. Progr. Rept. Jan. 31, 1963*, ORNL-3417, pp. 207–10.

[6]R. M. Carroll, *Reactor Chem. Div. Ann. Progr. Rept. Jan. 31, 1964*, ORNL-3591, pp. 141–46.

[7]R. M. Carroll and P. E. Reagan, *Nucl. Sci. Eng.* 21, 141–46 (1965).

[8]R. M. Carroll, *Nucleonics* 20(2), 42 (1962).

[9]R. M. Carroll and Oscar Sisman, *Nucl. Sci. Eng.* 21, 147–58 (1965).

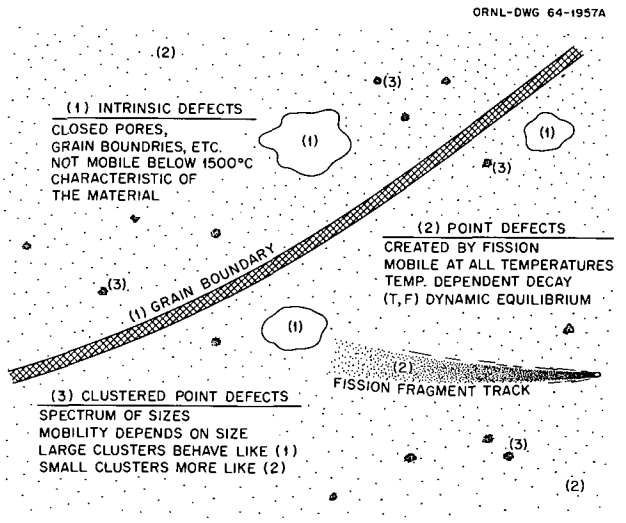

Fig. 13.1. Defect-Trap Characteristics.

RELEASE FROM FINE-GRAIN SPECIMENS

Single crystals have very few intrinsic traps. A good test of one aspect of the defect-trap theory would be to study the characteristics of fission-gas release from material with a large number of intrinsic traps. For this purpose we used specimens of very small grain size, but which in all other respects very closely resembled the single-crystal specimens of earlier experiments. In the discussion that follows we will compare the results from the fine-grain material with those from the single-crystal material.

The fine-grain specimens were prepared by the Ceramic Research Group at the Hanford Laboratories in the following manner. Micronized UO_2 powder was placed in a stainless steel can and evacuated. The canned UO_2 was then heated to 1200°C and pneumatically impacted at 380,000 psi. The compacted UO_2 was removed from the remains of the can and annealed in hydrogen at 1000°C for 12 hr. The density of the impacted specimens was nearly that of the single-crystal specimens. The essential difference between the single-crystal specimens and the high-energy compacted specimens was the small grain structure ($\approx 3\ \mu$) of the compacted specimens.

The temperature dependence of fission-gas release was determined by measuring the equilibrium release rate of ^{133}Xe, ^{135}Xe, ^{85m}Kr, ^{87}Kr, and ^{88}Kr over a range of temperatures at constant neutron flux. We then changed the position of the specimens in the reactor to change the fission rate and again measured the temperature dependence of the fission-gas release. More than 500 measurements of the release rates were made in this manner. The neutron flux levels ranged from 1.1×10^{13} to 8.4×10^{13} neutrons cm^{-2} sec^{-1}, and the temperature ranged from 420 to 1450°C. The overlapping temperature ranges allow the comparison of fission-gas release rates at the same temperatures but at different fission rates.

The temperature-dependent behavior of the fission-gas release was essentially the same for the fine-grain as for the single-crystal specimens. That is, below about 700°C a temperature-independent process dominates the gas release; above 700°C the release is primarily by a temperature-activated process. Figure 13.2 shows the release of ^{88}Kr as a function of temperature. The shape of the curves for the other isotopes of krypton is exactly the same. The slight temperature dependence of the curve below 700°C is likely caused by the contribution from the temperature-activated component. At lower temperatures there is no detectable temperature dependence in the gas release.

As was observed for the single-crystal specimens, the temperature-independent process was directly proportional to the fission rate (and therefore to the neutron flux). However, the recoil-activated release rate from the fine-grain specimens was higher than from the single-crystal

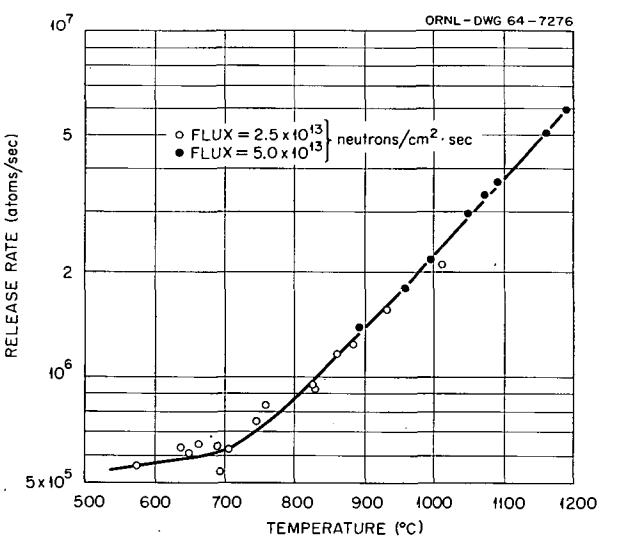

Fig. 13.2. Release Rate of ^{88}Kr from Fine Grain Specimen of UO_2.

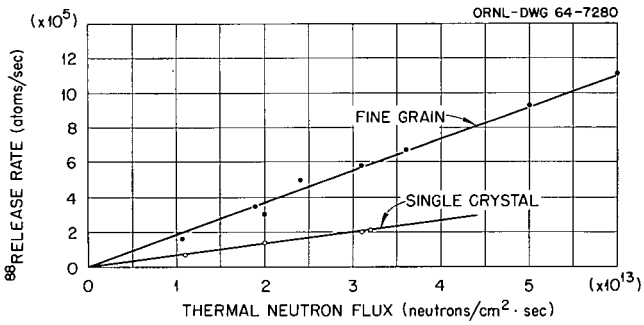

Fig. 13.3. Comparison of ^{88}Kr Recoil Release Between Single Crystal and Fine Grain UO_2 Specimens of the Same Size and Density.

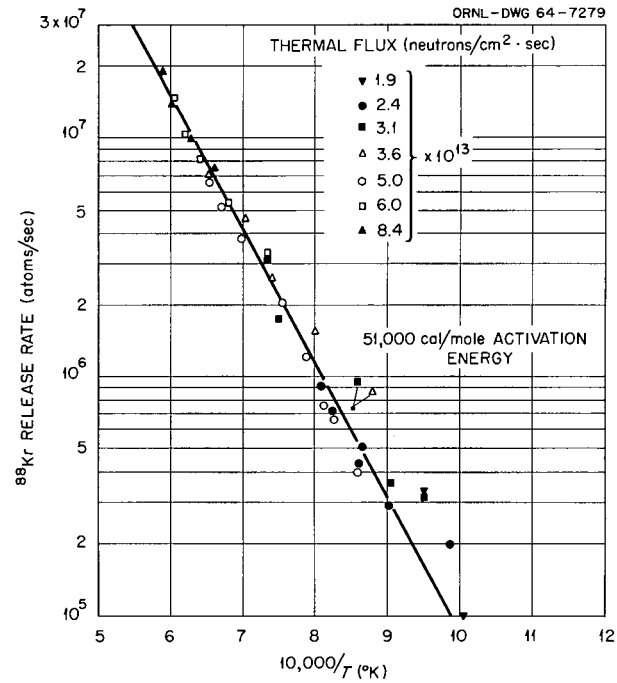

Fig. 13.4. Temperature Dependent Release Rate of ^{88}Kr from Fine Grain UO_2.

specimens (Fig. 13.3). The recoil-activated gas release is of gas which is trapped near the surface of the specimen and released when a fission fragment, passing through the surface, carries with it atoms of surrounding material.[9] The recoil process, therefore, depends on the total surface area of the specimen as well as on the fission rate. The data of Fig. 13.3 indicate that the surface area (total, not geometric) of the fine-grain specimens was 2.8 times that of the single-crystal specimens.

Effect of Fission Rate

The temperature-dependent component of the fission-gas release is found by subtracting the recoil contribution from the total measured gas released. The amount of ^{88}Kr released by the temperature-dependent process is plotted vs reciprocal absolute temperature in Fig. 13.4. Only a few of the data points obtained in this experiment are shown, but the data in Fig. 13.4 are typical of the other krypton isotopes and of duplicate measurements.

One of the very strongest arguments against the diffusion theory for fission-gas release from UO_2 is that in the in-pile experiments a change of neutron flux at constant temperature does not produce a change in the temperature-activated fission-gas release rate. This means, for example, that doubling the fission rate at 1000°C (which results in doubling the amount of radioactive fission gas at equilibrium) does not result in doubling the release rate. For the single-crystal experiments, changing the flux by a factor of 4 resulted in no change in the fission-gas release rate within the accuracy of the measurements (±20%).

The data plotted in Fig. 13.4 confirm these observations for the fine-grain specimens. Here the equilibrium release rate of ^{88}Kr is shown for the temperature-activated process for neutron fluxes between 1.9×10^{13} and 8.4×10^{13}. As with the single-crystal experiments, no difference was observed for the data taken over this range of flux and temperature.

Magnitude of Release Rate

Our theory proposes that grain boundaries will act as permanent traps for the fission gas and thus should lower the release rate for the temperature-activated process (over the temperature range studied here). A comparison of the release rates from the fine-grain material to that of the single-crystal material is shown in Fig. 13.5. Since the low-temperature (recoil-activated) release depends only on the surface area and fission rate, the data of Fig. 13.5 were normalized by adjusting the low-temperature part of the curve (as shown in Figs. 13.2 and 13.3) to that of the single crystals for the same neutron flux. The activation energies for these two sets of specimens are nearly the

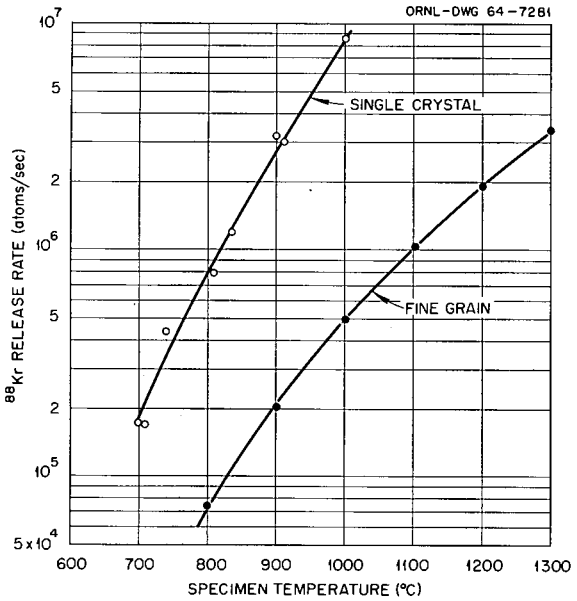

Fig. 13.5. Temperature Dependent ^{88}Kr Release Rate Normalized to Single Crystal Surface Area.

same (57 kcal/mole single crystal, 51 kcal/mole fine grain), but the release rate for the fine-grain material is lower by a factor of 17 at 1000°C. This is direct evidence that the grain boundaries are retarding the escape of fission gas.

This experiment has demonstrated that grain boundaries do not act as paths of rapid escape, as once believed, but rather as traps which anchor the migrating fission gas. Also, the effect of fission rate on the fission-gas release was predicted by our model,[9] which proposes that a defect-trap mechanism controls the escape rate of fission gas, so that the escape rate does not change much with change in fission rate. This relation was valid for temperatures up to 1450°C (the highest temperature of the experiment) and within the limits of the fission density of the experiment (from 2 to 9×10^{12} fissions cm^{-3} sec^{-1}).

MATHEMATICAL MODEL[10,11]

The mathematical model developed below describes a mechanism for the steady-state release of fission gas which fits the observations and conclusions presented above. This is a rather oversimplified starting point from which further refinements may be made. For the present we will consider that the clusters of defects (third type trap) are quite permanent. That is, we assume that a fission product can escape from a point defect (the second type trap) but has small probability of escaping from either the first or the third type trap, both of which we will treat as permanent traps. Note that an atom of gas born deep in the specimen has a high probability of falling into a permanent trap, and that only the gas which is born near the specimen surface has a high probability of escape.

We will, then, restrict ourselves to the consideration of the temperature-dependent gas-release processes, where large (permanent) and small (temporary) traps retard the escape of the fission gas. The small (type 2) traps reach a quick production-anneal equilibrium for a given fission rate and temperature. The fission products in a small trap have a probability of escaping the trap, but those in a large trap have vanishingly small escape probability. Fission-fragment tracks will create point defects in their wake and at the same time destroy any point defect traps in their path.

The mechanisms of trapping and release from traps are introduced by defining two parameters:

g = probability of trapping (sec^{-1}),
b = probability of escape from trap (sec^{-1}).

The other symbols to be used are:

M, H = density of mother, daughter isobars, respectively (atoms/cm^3),
r_0 = the fractional probability that a trapped mother atom will escape the trap because of recoil energy when the mother decays into the daughter isobar,
M_{tr}, H_{tr} = concentration (atoms/cm^3) of mother, daughter isobars in traps,
D = diffusion coefficient (cm^2/sec) = $D_0 \exp\{-E_D/RT\}$,
F = fission rate (fissions cm^{-3} sec^{-1}),
E_X = activation energy for process X,
R = gas constant,
T = absolute temperature, °K,
R_H = release rate per unit area of daughter isobars from the specimen,
β_x = fission yield of isotope x,
ϕ = neutron flux (cm^{-2} sec^{-1}),
λ_x = decay constant of isotope x (sec^{-1}),
Σ_f = macroscopic fission cross section (cm^{-1}).

[10] R. M. Carroll, R. B. Perez, and Oscar Sisman, *J. Am. Ceram, Soc.* 48(2), 55–59 (1965).

[11] R. B. Perez, R. M. Carroll, and Oscar Sisman, *A Mathematical Model for the High Temperature In-Pile Release of Fission Gases*, ORNL-TM-743.

The hypothesis is made that the trapping probability is proportional to the fission density. In the expression

$$g = g_0 + g_T(F,T) , \qquad (1)$$

the term g_0 will account for both the presence of the intrinsic trap population and the traps produced by condensation of the point defects. The $g_T(F,T)$ term of Eq. (1) states that the population of point defects is a function of fission density and specimen temperature.

The gas trapped in the point defects can also escape by tunneling through the potential barrier created by the defect. This tunneling process is governed by an Arrhenius factor, and can be expressed as

$$b = b_0 \exp - \frac{\Delta E_b}{RT} , \qquad (2)$$

where ΔE_b is the activation energy of the tunneling process. Under the hypothesis of a diffusion mechanism coupled with radioactive decay and a trapping-release mechanism, the equations for the transport of the parent-daughter isobars can be easily written by making use of the principle of the conservation of particles.[10]

The equation giving the release rate of an inert-gas isotope is shown in Fig. 13.6, along with the simplifying assumptions for this first model. The constant R_H^0 is the recoil yield (atoms-cm/fission).

OSCILLATING EXPERIMENTS

In order to more fully exploit the defect-trap theory and to evaluate the various factors in the equations, we have modified the experiment so that it can now be operated in a dynamic mode. These changes make it possible to oscillate either the neutron flux or the temperature in a controlled fashion. The frequency, amplitude, waveform, and base-line position of the temperature or flux oscillations can be controlled manually or in a programmed manner.

The fission gas released from the specimen during irradiation is monitored continuously by a gamma-ray spectrometer. By appropriate settings of the spectrometer controls, the variation in the

ORNL DWG. 64-7441

Release Rate of Gaseous Daughter, $R_H = R'_H(T,F)\, e^{-\Delta E/2RT} + R_H^0 F$

$$R'_H(T,F) = F\sqrt{\frac{D_0}{\lambda'_H}}\left\{\beta_H + \left(\frac{\lambda_M}{\lambda'_M}\right)\left(\frac{W\beta_M}{1+(\lambda'_H/\lambda'_M)^{1/2}}\right)\right\}$$

$$\lambda' = \lambda\left[1 + \left(\frac{g_0 + g_T F e^{\Delta E_g/RT}}{\lambda + b_0 e^{-\Delta E_b/RT}}\right)\right], \quad W = 1 + \left[\frac{g_0 + g_T F e^{\Delta E_g/RT}}{\lambda_M + b} r_0 + (1 - r_0)\frac{b}{\lambda_H + b}\right]$$

SIMPLIFYING ASSUMPTIONS

(1) No change of microstructure

(2) Release by recoil is not temperature dependent

(3) Trapping probability of intrinsic and cluster traps is constant with time

(4) Mother-daughter are affected the same by the traps.

(5) Diffusion of point defects are neglected.

(6) Homogenous distribution of traps.

Fig. 13.6. A Mathematical Model for Mother-Daughter Release.

emission rate of a single isotope can be recorded over a period of time. A record of the flux or temperature variations, during this same period of time, is kept by a digital recording voltmeter. By studying the amplitude and phase shift of the fission-gas release under various input conditions, we hope to develop our defect-trap model for fission-gas release and to experimentally establish the parameters (D_0, g_0, g_T, b_0, r_0, ΔE_g, ΔE_b) in the mathematical model.

Following the installation of the oscillating equipment, single-crystal specimens were irradiated. The specimens were sliced from the same crystal as some of the previous specimens but were polished to a metallographic finish before irradiation (the previous specimens had a ground finish). Specimens with the ground finish had become smoother during irradiation, and we believe this smoothing may have caused the observed reduction in fission-gas release rate as burnup progressed. We wished, therefore, to see if a specimen that was metallographically polished prior to irradiation would show this change. Preliminary analysis of the data indicates that the gas release from the polished specimen did not decrease with time. Also, the recoil release, which is associated with total surface area, was about the same as for the ground specimens after irradiation smoothing had occurred.

The emitted fission gas must travel some distance before an activity measurement can be made. The travel time is inversely proportional to the sweep flow rate (we normally use a 0.60-cm^3/sec flow rate, which gives 40 min travel time between the specimen and the detector probe). The delay time is measured by using a sweep gas containing 1% argon while oscillating the specimen into and out of the reactor. The flowing argon emerges from the reactor with an activity that varies according to the neutron flux at the specimen capsule. In this manner we find the neutron flux variation for a given oscillation program and also the exact delay time for a given flow of sweep gas.

The fission gas must escape from the specimen as well as travel outside the reactor; therefore the difference of time between the argon wave train and the fission-gas wave train is an indication of the time required for the fission gas to escape from the specimen. All the data given below have been corrected for the measured delay time of the sweep gas.

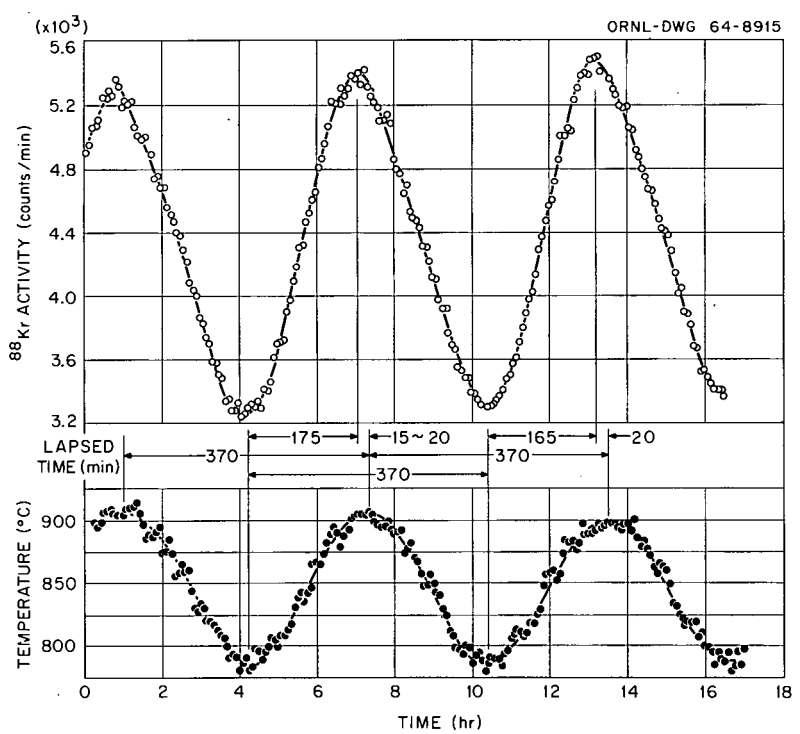

Fig. 13.7. Release of ^{88}Kr from UO_2 Single Crystal at Constant Flux and 6-hr Temperature Cycle.

A large mass of data has been obtained while the specimen temperature or fission rate was being oscillated through various amplitudes and frequencies. The data are still being analyzed, but the general behavior of the fission-gas release is given below.

1. Oscillating the specimen temperature, at temperatures above 700°C and at constant fission rate, produces a single smooth oscillation of temperature. However, the maximum in the fission-gas release rate occurs before the maximum temperature of the specimen (Fig. 13.7). This result implies that the gas being released as a function of temperature is gas which had been trapped, rather than a change in diffusion rate.
2. Oscillating the fission rate of the specimen at constant temperatures below 700°C produces a single smooth waveform of fission-gas release. The wave is symmetrical, but the fission-gas waveform attains its maximum and minimum about 20 min after the corresponding flux variation. The magnitude of the wave is proportional to the variation in fission rate. We think this fission-gas release is by knockout resulting from fission fragments penetrating the surface of the specimen. Note that the concentration of fission gas at the specimen surface will also vary with fission rate.
3. Oscillating the fission rate at constant temperatures above 700°C produces a double waveform of fission gas (Fig. 13.8). One activity peak follows the flux peak by about 20 min and is presumably caused by the knockout mechanism. The second activity peak follows the flux peak with a delay time depending upon the frequency of oscillation. This peak has a maximum value when the fission rate is approaching (or at) its minimum, and is thought to be a result of a changing concentration of fission-induced traps.

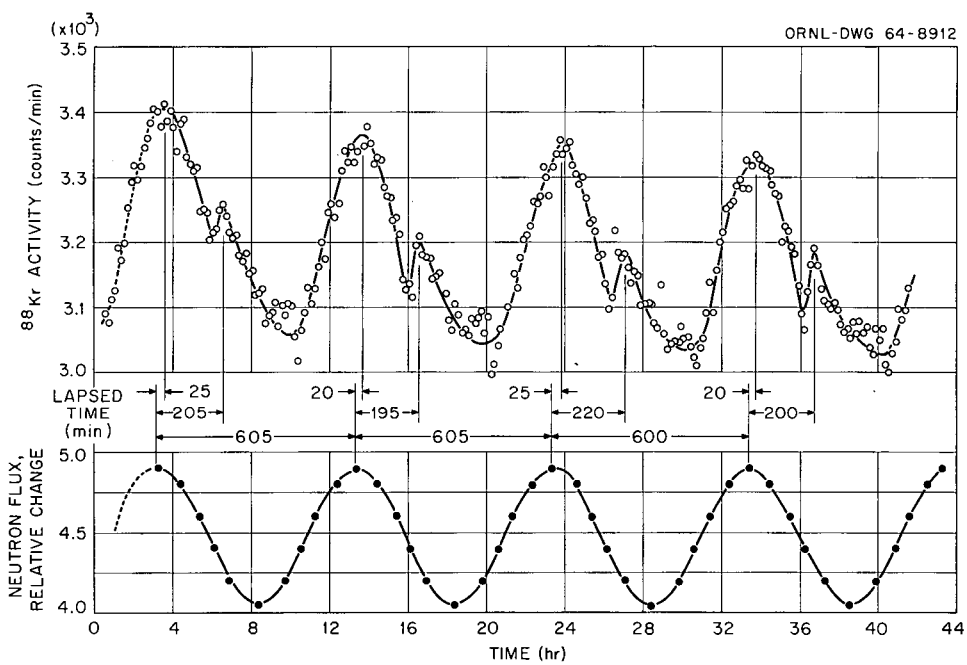

Fig. 13.8. Release of ^{88}Kr from UO_2 Single Crystal at 840°C and 10-hr Flux Cycle.

14. Behavior of Ceramic Materials Under Irradiation

RADIATION STABILITY OF SILICATE CERAMICS[1]

C. D. Bopp T. N. McVay[2]
O. Sisman R. L. Towns

X-ray diffraction was used to supplement a previous study by thermal analysis[3,4] of the annealing of radiation changes in silicate ceramics. The neutron doses for the five different radiation exposures used are listed in Table 14.1. The specimens were sintered compacts and consisted of small crystals (Table 14.2) which were embedded in a glassy matrix. Samples were irradiated in the form of disks ($\frac{3}{4}$ in. in diameter by 0.02 in. thick), which were powdered for diffractometer measurements after other studies had been made.[5] Diffractometer patterns were also obtained for unpowdered compacts in the instances noted. Although a higher integrated fast neutron flux is required to disorder silicates than to disorder quartz,[6] the qualitative similarity of the density-dosage relations suggests similarity of the disordering mechanism.[7] Recently, it was shown that disordering results in quartz from the strain produced by silicon interstitial clusters.[8] Disordering does not necessarily decrease strength, however. For example, a zircon compact (which was extensively disordered as discussed below) remained intact throughout irradiation and annealing treatments.

A comparison is made in Table 14.2 of the threshold temperature for stored-energy release[3,4] and the temperature at which restoration of the x-ray diffraction lines is initiated. A heating period of 15 min initiated restoration of the diffraction lines at the temperatures listed. The two temperatures coincide for cordierite and zircon. This indicates that dislocations are sufficiently mobile for recrystallization at the temperature of interstitial-vacancy recombination. For steatite, the lines are restored at a much higher temperature. In forsterite, which was not as much disordered as the other materials, partial recovery occurs at the temperature of stored-energy release, but a much higher temperature is required for complete recovery.

Cordierite

New lines in the x-ray diffraction pattern of the powdered compact indicate a partial breakdown to protoenstatite and mullite after exposures I and III. Exposure IV destroyed all the lines after heating at 900°C; the strongest x-ray diffraction line corresponds to that of a metastable, quartz-type solid solution such as that obtained with crystallizing glass of cordierite composition. This phase transforms to cordierite after 58 days at 900°C,[9] or in a shorter time at higher temperatures. Pyroceram 9606,[10] which is a partially crystalline glass containing very small cordierite crystals, shows similar behavior.

---

[1]Presented to the San Francisco meeting of the Basic Science Division of the American Ceramic Society, October 28–30, 1964.

[2]Consultant from Bureau of Mines, Tuscaloosa, Ala.

[3]O. Sisman, *Reactor Chem. Div. Ann. Progr. Rept. Jan. 31, 1964*, ORNL-3591, p. 152.

[4]C. D. Bopp, O. Sisman, and R. L. Towns, *Reactor Chem. Div. Ann. Progr. Rept. Aug. 31, 1962*, ORNL-3364, p. 194.

[5]Diffractometer patterns were obtained by R. E. Thoma.

[6]J. H. Crawford, Jr., and M. C. Wittels, *Proc. U.N. Intern. Conf. Peaceful Uses of At. Energy, 1st, Geneva, 1954*, **7**, 654 (1955).

[7]William Primak, *Phys. Rev.* **110**, 1240 (1958).

[8]Sigmund Weissman and Koicha Nakajima, *J. Appl. Phys.* **34**, 611 (1963).

[9]W. Schreyer and J. F. Schairer, *Z. Krist.* **116**, 60 (1961).

[10]A Corning Glass Company product.

Table 14.1. Definition of Irradiation Dosage

Exposure Code	Reactor	Integrated Flux, 10^{19} neutrons/cm^2			
		Thermal	Epithermal	>0.2 Mev	>1 Mev
I	MTR	9	6	6	2
II	Graphite	12	10	3	0.6
III	Graphite	20	18	6	1.1
IV	MTR	50	30	30	10
V	ORR	100	30	30	10

Table 14.2. Annealing Temperatures

Material	Radiation Exposure	Average Crystal Size (μ)	Threshold Temperature of Stored Energy (°C)	Temperature Which Initiates Appearance of Diffraction Lines (°C)
Cordierite (98% $2MgO \cdot 2Al_2O_3 \cdot 5SiO_2$)	IV	~1	900 ± 5	850–900
Zircon (95% $ZrSiO_4$, 5% SiO_2)	I	~30	880 ± 10	880–920
	IV	~30	880 ± 10	960–1050
Steatite (98% $MgO \cdot SiO_2$)	IV	2–10	860 ± 5	1100–1150
Forsterite (98% $2MgO \cdot SiO_2$)	IV	4–16	835 ± 10	800–980

Zircon

The x-ray diffraction lines are destroyed in zircon (Fig. 14.1*b*) at much lower exposures than for cordierite; this results from thermal-neutron-induced fission of a small amount of uranium impurity (0.022 wt % by activation analysis). Zircon crystals selected for low radioactive impurity content were not disordered until exposed to a much higher integrated fast neutron flux.[6] Comparison of the x-ray diffraction patterns for powdered and unpowdered material showed that there was a small effect of grinding on unirradiated material, but that extensive line broadening was produced by grinding after exposure I. This indicates an instability of the irradiated crystalline phase as suggested by Holland.[11] Restoration of the lines is initiated by heating to 920°C after exposure I (Fig. 14.1*d*), but higher temperatures or longer times are required after higher exposures (Figs. 14.1*f* and *g*). Both zircon and zirconia are formed by heating the irradiated material in the range 920 to 1150°C. The zircon content decreases and the zirconia content increases with increasing exposure until only zirconia is formed at exposure IV (Fig. 14.1*j*). Heating in the range 1150 to 1250°C converts zirconia to zircon. The temperature or time for the conversion increases with exposure (Fig. 14.1).

The formation of zirconia at high exposure results from an increase in the thermal stability of

[11] H. D. Holland and David Gottfried, *Acta Cryst.* **8**, 291 (1955).

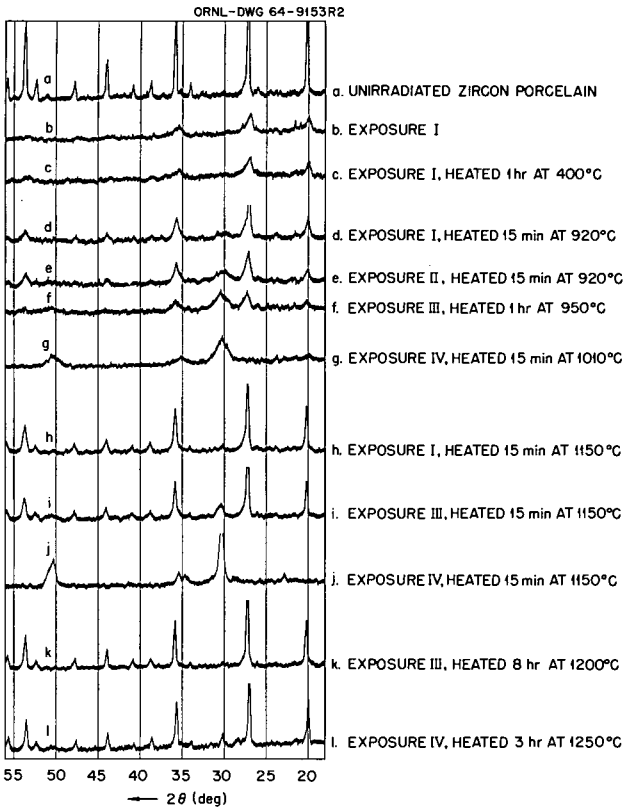

Fig. 14.1. X-Ray Diffraction Patterns for Zircon (Cu $K\alpha$ Radiation Was Used).

silicon interstitial clusters, due to interaction of the clusters with dislocations, such as was observed with quartz.[8] Zirconia is formed after a radiation dose sufficient to stabilize clusters at the recrystallization temperature.

Steatite

Clinoenstatite is the stable polymorph of $MgSiO_3$ at low temperature; however, protoenstatite is stable above about 700°C. Ordinary cooling rates produce only partial transformation of protoenstatite to clinoenstatite; sometimes grinding increases the amount of clinoenstatite.[12] In the present study, the same relative intensities for protoenstatite and clinoenstatite lines were obtained both with the unpowdered steatite compact and with material powdered at room temperature subsequent to irradiation. The principal phase was protoenstatite, which gives the strongest line at a *d* spacing of 3.18 A, although the presence of clinoenstatite is shown by weaker lines at 2.86 and 2.96 A.

Exposures I and III did not produce much change in the diffractometer pattern of unpowdered compacts. However, with material powdered after exposure I, the clinoenstatite phase was expanded as was evidenced by the appearance of a moderately strong line at 3.21 A. Before irradiation, this line was obscured by the 3.18-A protoenstatite line. With material powdered after exposure III, clinoenstatite was destroyed. These observations may be explained if the combined effects of irradiation and grinding produce expansion and eventual destruction of the clinoenstatite phase.

Exposure IV destroyed all of the diffraction lines. Heating for 3 hr at 1250°C after exposure IV did not restore clinoenstatite, although protoenstatite was restored by this treatment. The same treatment, however, did restore clinoenstatite after exposure III. Since clinoenstatite forms from protoenstatite on cooling, it appears that the protoenstatite-clinoenstatite transformation is impeded after heavy irradiation.

Forsterite

Changes in the x-ray diffraction pattern were not as pronounced in forsterite as in the other materials, because the crystalline lines were not as strong. After exposure IV, the lines were only about one-fourth of the initial intensity, and they were very broad. Heating to 980°C restored the lines to about one-half of the initial intensity; however, the lines were still broad. Heating to 1100°C did not produce further restoration. Further work is planned to determine the temperature of recrystallization.

IRRADIATION-INDUCED THERMAL CONDUCTIVITY CHANGES OF CERAMICS

C. D. Bopp O. Sisman

We have begun to study the annealing of the irradiation-induced defects in several ceramic materials by measuring thermal conductivity

[12] J. F. Sarver and F. A. Hummel, *J. Am. Ceram. Soc.* **45**(4), 152 (1962).

changes. Thin specimens are used to permit dissipation of the heat generated during irradiation, and a fluxmeter method was developed, which is accurate to about 5% with thin specimens (0.05 cm thick and 1 cm square) of conductivity 10^{-2} to 10 cal $(°C)^{-1}$ sec^{-1} cm^{-1}. Another method[13] is used for specimens with conductivity less than 10^{-2}.

With the fluxmeter method (Fig. 14.2), the temperature drop across a section of the specimen is compared with that across a fluxmeter, a standard conductor in series with the specimen.[14] A provision is made for easy removal of the specimen. The upper end of the specimen is clamped to a heater by an electrical-type spring clip, while the lower end is submerged in mercury. The temperature gradient is measured by the temperature difference between two bars held against the specimen by spring clips. The distance between the bars is fixed by a spacer attached to one of them. Cotton is packed loosely around the specimen, and the temperature of the lower bar is kept within about 0.2°C of the ambient temperature by adjusting the temperature of the water bath, which serves as a heat sink.

Experimentally, it was found that convection losses become less important at low heat flux. The losses are acceptably small (<5% of the total flux) at a flux equivalent to a 1°C/cm gradient in the specimen, with the specimen size mentioned above and the conductivity greater than 10^{-2}. This method may also be used with sufficiently thick specimens of lower conductivity, since the losses become less important with increasing thickness. An accuracy of about 10% was obtained with a cylinder about 0.5 cm in diameter and a conductivity of 2×10^{-3}. In this case the contact bars were machined to match the curvature of the specimen.

[13]C. D. Bopp, *J. Am. Ceram. Soc.* **47**, 151 (1964).

[14]C. N. Hooker *et al.*, *Proc. Roy. Soc. (London), Ser. A*, **276**, 83 (1963).

BEHAVIOR OF HIGH-TEMPERATURE MATERIALS UNDER IRRADIATION

G. W. Keilholtz J. E. Lee, Jr.
R. E. Moore

The behavior of ceramic oxides and refractory metal carbides toward large fast-neutron doses at high temperatures is being investigated in a program now of several years' duration. The

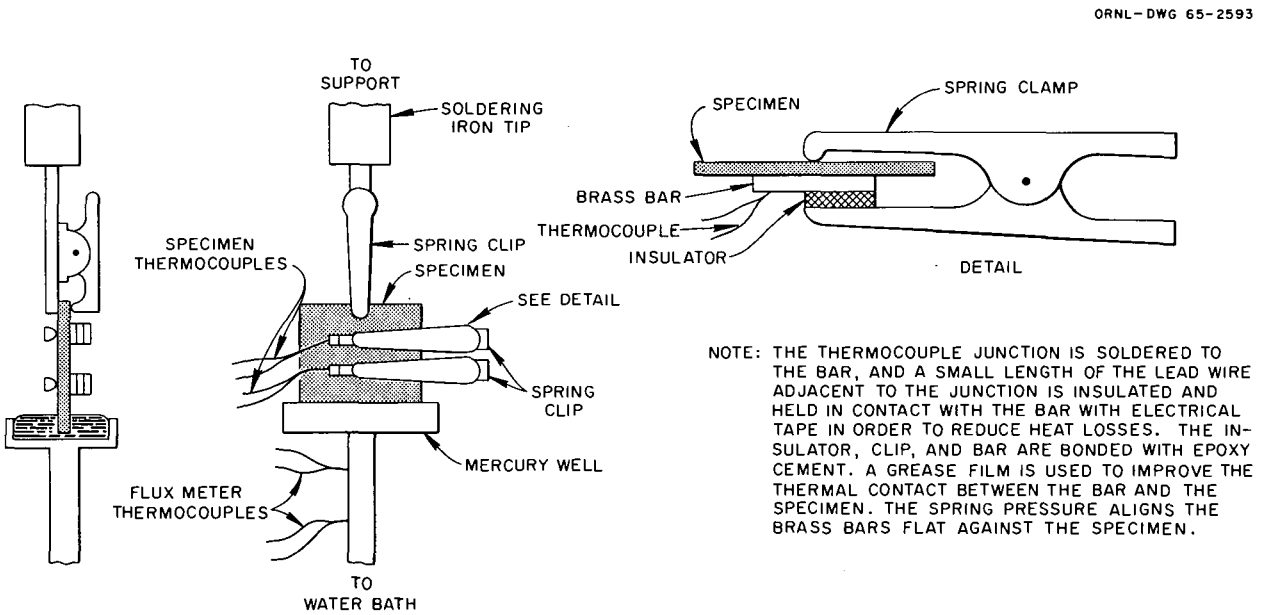

Fig. 14.2. Thermal Conductivity Apparatus.

objectives are to determine the limits of fast-neutron dose, fast-neutron flux, and temperature for the use of these materials in nuclear devices, and to establish, if possible, the mechanisms of damage. The radiation stability of sintered BeO compacts has been defined at temperatures from 110 to 1100°C over the fast-neutron dose range 0.3 to 8.0 × 10^{21} neutrons/cm^2 (>1 Mev) in a series of experiments designed to separate the effects of grain size, density, specimen size, flux, dose, and temperature.

A similar, though smaller, study of sintered MgO compacts is in progress; initial data are presented in this report. In addition, a series of experiments have been initiated to determine the changes in physical properties of the carbides of Ti, Zr, Nb, Ta, and W when exposed to fast-neutron doses as high as 10^{22} neutrons/cm^2 at temperatures from 130 to 1400°C. The behavior of high-purity Y_2O_3 and Al_2O_3 compacts over the same dose and temperature range is also under investigation.

Effect of Fast Neutrons on Beryllium Oxide

The BeO irradiation studies have accumulated a large amount of useful data for the engineering design of BeO-moderated reactors and for evaluating damage mechanisms.[15–17] In a series of ten assemblies, more than 500 cylindrical BeO specimens and 40 single crystals have been irradiated to fast-neutron doses as high as 8 × 10^{21} neutrons/cm^2 at temperatures from 110 to 1100°C in the Engineering Test Reactor (ETR). The experiments were designed to define the effect of grain size, density, specimen size, dose, flux, and temperature on pure BeO compacts under controlled conditions. Four types of specimens, consisting of combinations of two densities (2.7 and 2.9 g/cm^3) and two grain sizes (22 and 34–72 μ) were employed.

The results from the experiments are consistent with the hypothesis that point defects produced by fast neutrons cause anisotropic expansion of the BeO crystal lattice (predominantly in the direction of the c axis), which in turn causes grain-boundary separation in randomly oriented compacts. This grain-boundary separation can account for most of the changes in physical properties of irradiated BeO compacts. These include fracturing and powdering, large reductions in the crushing strength and thermal conductivity, and volume expansion. Photomicrographs of specimens irradiated at low temperatures or to high doses at high temperatures show, in addition to extensive grain-boundary separation, some transgranular fracture, particularly in specimens of large grain sizes.

In irradiations at 110°C, a temperature at which in-pile annealing of point defects is probably insignificant, severe fracturing of many specimens occurs during exposure to fast-neutron doses exceeding 10^{21} neutrons/cm^2. Most samples disintegrate to powder after irradiation to doses greater than 2 × 10^{21} neutrons/cm^2. Volume expansion, a reliable criterion of neutron damage to BeO compacts, increases from 2.5 to 6% over the dose range 0.7 to 2.2 × 10^{21} neutrons/cm^2. In comparison, crystal volume expansion calculated from lattice parameters increased only from 1.25 to 3.5% over the same dose range.

In-pile annealing of fast-neutron damage to BeO occurs to some extent at 650°C and is quite effective at 1100°C. Less gross damage, crystal expansion, and compact volume expansion occurs at 650 than at 110°C. In irradiations at a very high temperature (1100°C), the gross damage is much less severe than at 650°C. Beryllium oxide of low density and small grain size generally withstood irradiation better than BeO of high density or large grain size. The volume expansion at 1100°C was much less than that at 650°C. Specimens of low density and small grain size expanded least, and specimens of high density and large grain size expanded most.

Comparison of data for samples irradiated at 650°C in long- and short-term tests to equivalent dose values provides no indications of a flux intensity effect on gross damage, volume expansion, or lattice parameter expansion. In irradiations at 1100°C, there is no apparent effect of flux intensity on gross damage. Surprisingly, however, volume expansion was greater in low fluxes than in high fluxes for equivalent doses, as can be seen in Table 14.3. This unexpected result is difficult to explain as a radiation effect.

---

[15] G. W. Keilholtz, J. E. Lee, Jr., and R. E. Moore, *J. Nucl. Mater.* 11(3), 253–64 (1964).

[16] G. W. Keilholtz, J. E. Lee, Jr., and R. E. Moore, *Properties of BeO Compacts Irradiated to Fast-Neutron Doses Greater than 10^{21} neutrons/cm^2 at 110, 650, and 1100°C*, ORNL-TM-1011 (Dec. 1, 1964).

[17] G. W. Keilholtz, J. E. Lee, Jr., and R. E. Moore, *Reactor Chem. Div. Ann. Progr. Rept. Jan. 31, 1964*, ORNL-3591, pp. 147–52.

Table 14.3. Volume Expansion of Half-Inch BeO Specimens Irradiated in Experiments 41-8 and 41-9 at 1100°C[a]

BeO Type	Experiment	Volume Increase at Fast-Neutron Dose (%)		
		2.0×10^{21} neutrons/cm^2	4.0×10^{21} neutrons/cm^2	7.2×10^{21} neutrons/cm^2
I	41-8[b]	2.0	2.2	2.4
I	41-9[c]	0.7	1.4	
III	41-8[b]	2.8	3.1	3.5
III	41-9[c]	1.3	2.6	
IV	41-8[b]	4.0	4.3	4.7
IV	41-9[c]	1.8	3.6	

[a]The values of volume increase at the three neutron doses were interpolated from linear data plots. Type II was omitted because there were too little data available, but the expansion appears to lie between types I and IV.

[b]Irradiation time 1.4×10^7 sec.

[c]Irradiation time 7.33×10^6 sec.

A proposed explanation is that thermal cycling of the reactor can produce grain-boundary separation in compacts with anisotropically strained grain boundaries. Accordingly, more grain-boundary separation and consequently greater volume expansion could occur in long-term, low-flux irradiations.

For the use of BeO as a moderator in nuclear reactors designed for long-term performance, the temperature in all locations exposed to high fast-neutron fluxes should be 1100°C or above. Because of in-pile annealing at high temperatures, a low flux would probably minimize damage. A more important factor in minimizing damage, however, is the maintenance of reactor operation without shutdowns or significant temperature drops. The irradiation data at 1100°C indicate that grain-boundary separation in BeO, with the consequent deterioration of its physical and mechanical properties, may be promoted by thermal cycling.

Fast-Neutron Damage to Magnesium Oxide

The design of the MgO irradiation assemblies is very similar to those used for BeO. In addition to 440 MgO specimens, the assemblies also contained 123 Al_2O_3 samples and 112 BeO samples for comparison. Four types of cylindrical MgO specimens consisting of two densities (3.15 to 3.29 and 3.35 to 3.41 g/cm^3) and two grain sizes (10 and 45 to 55 μ) were irradiated at 150, 800, and 1100°C.

The effects of fast-neutron dose and flux were separated at each temperature by irradiating specimens for different periods of time in the same flux profile. Experimental conditions in the MgO irradiations are given in Fig. 14.3. Each wide bar represents a capsule containing 15 cylindrical specimens 0.5 in. long by 0.5 in. in diameter, and each narrow bar represents a capsule containing 30 specimens 0.25 in. long by 0.25 in. in diameter. Results from postirradiation examinations of samples from experiments 41-15, 41-17, and 41-21 are presented below.

Irradiation of Magnesium Oxide at ~150°C. – The four types of MgO compacts were irradiated at ~150°C in two experiments of different time periods over the same flux profile. The specimens, which were white before irradiation, were found to be gray or black at the conclusion of the experiments. About 40% of the samples were severely fractured, but no powdering occurred. The fracturing did not increase with increasing fast-neutron dose as it did in BeO, but instead appeared to be randomly distributed over the dose range of both experiments. No definite differences among the types of MgO were noted.

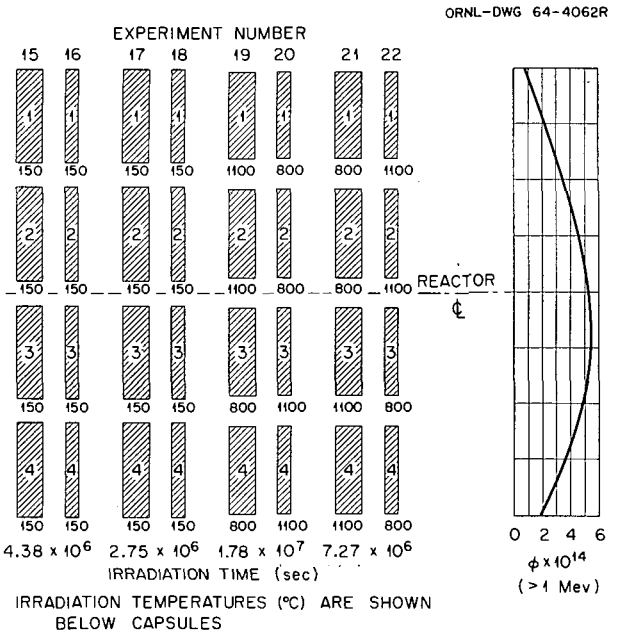

Fig. 14.3. Irradiation Conditions for Experimental Assemblies Containing MgO with BeO and Al_2O_3.

The volume expansion of samples that survived without severe fracturing is plotted against fast-neutron dose in Fig. 14.4. The MgO samples expanded in volume approximately 1% after receiving a dose of 1.1×10^{21} neutrons/cm^2, but irradiation to doses as high as 2.4×10^{21} neutrons/cm^2 did not produce greater expansion. There were no significant differences among the types of MgO, and, as expected in low-temperature irradiations, there was no definite flux intensity effect. As can be seen in Fig. 14.4, the BeO samples in the assemblies expanded much more than did the MgO samples.

Micrographic examination of MgO irradiated at 150°C revealed no grain-boundary separation whatsoever. Fractures present in some of the samples were transgranular.

Irradiation of MgO at 800 and 1100°C. – Approximately 30% of the MgO samples irradiated at 800°C and nearly all the samples irradiated at 1100°C over the dose range 0.75 to 4.9×10^{21} neutrons/cm^2 (>1 Mev) were severely fractured. No powdering was observed. As in the low-temperature irradiation, fracturing was randomly distributed over the dose range, and there were no significant differences among the four types of MgO. Unlike the irradiations at 150°C, the specimens did not darken during the experiments. The volume increase of MgO samples irradiated at 1100°C, which survived without severe fracturing, was less than 0.5%, even after exposure to doses exceeding 4.5×10^{21} neutrons/cm^2. Micrographic examinations showed no grain-boundary separation at either 800 or 1100°C. However, transgranular fractures were seen in photomicrographs of some of the specimens. Out-of-pile control tests were conducted to duplicate the thermal history of the irradiation experiment. No fracturing or significant dimensional changes occurred in the MgO samples heated at either temperature in these tests.

Mechanisms of Fast-Neutron Damage to MgO. – Damage to sintered compacts of MgO and BeO exposed to high fast-neutron doses apparently occurs through different mechanisms. It is generally agreed that anisotropic expansion of the BeO crystal lattice causes grain-boundary separation in irradiated BeO compacts. Since the MgO lattice is isotropic, lattice expansion resulting from point defects should not cause grain-boundary separation in MgO compacts. Micrographic examinations confirm this conclusion. Fractures seen in the photomicrographs (Fig. 14.5) were definitely transgranular, which means that the

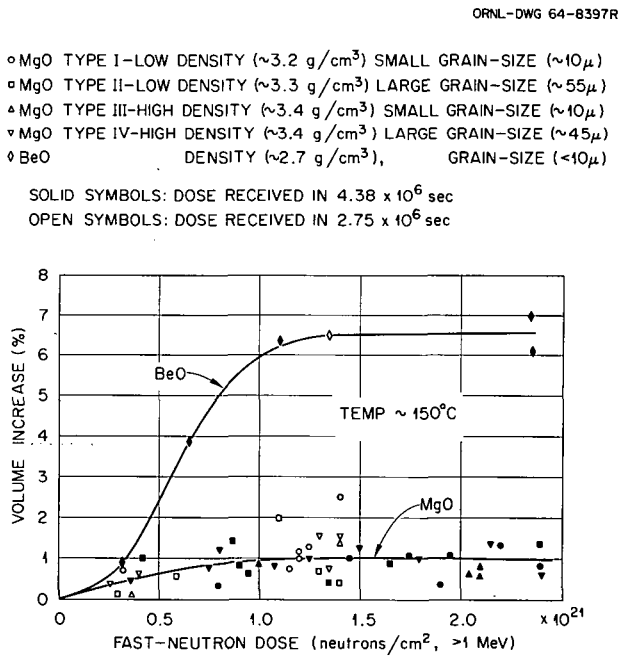

Fig. 14.4. Volume Increase of $^1/_2$-in. Sintered Cylindrical Compacts of MgO and BeO.

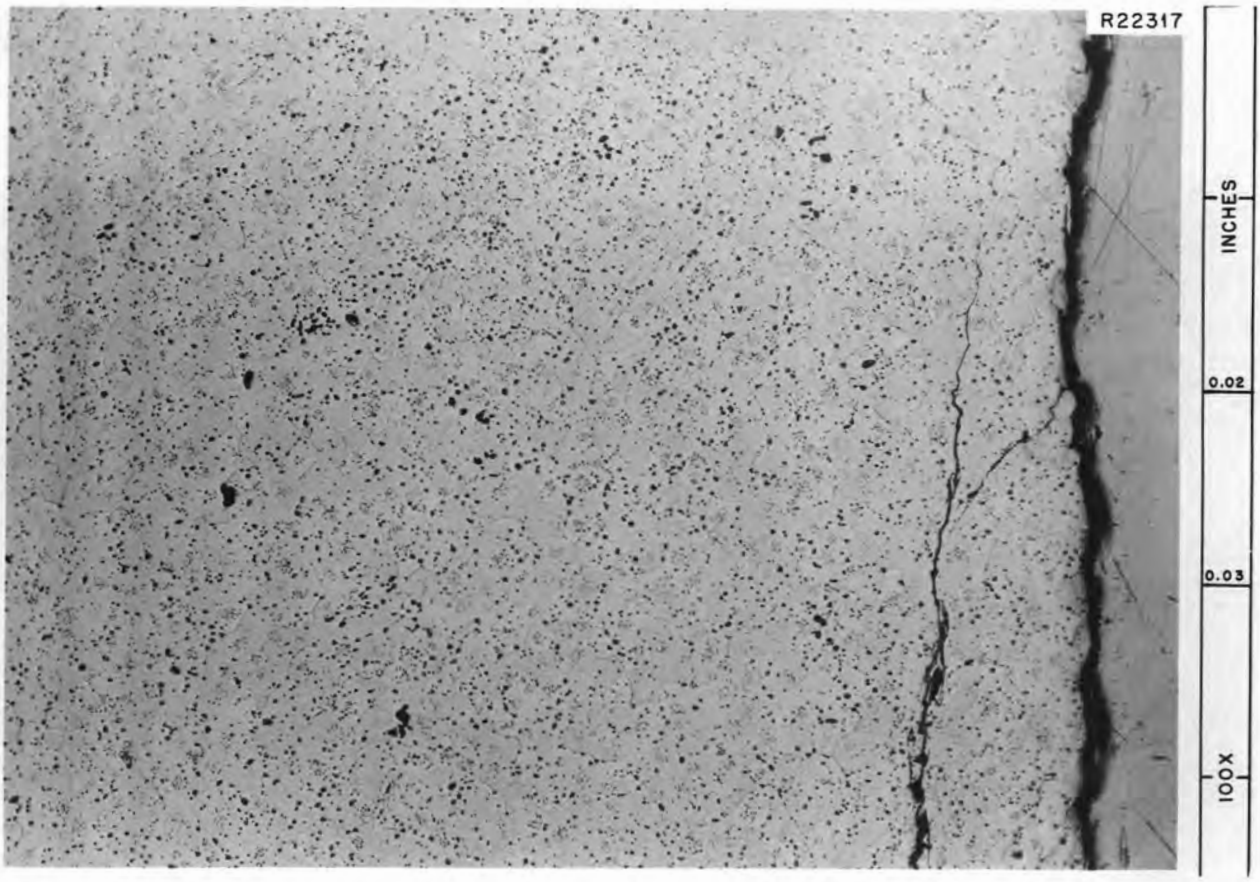

Fig. 14.5. Photomicrograph of MgO Specimen 4-27. Density, $\sim$3.4 g/cm^3; grain size, $\sim$45 μ; irradiated to a fast-neutron dose of 4.5×10^{21} neutrons/cm^2 (> 1 Mev) at 800°C; as polished, 100×.

fracturing of MgO compacts is a result of an intrinsic weakness of the irradiated MgO crystals themselves. Fracturing of compacts at low temperatures, then, is caused by random crack propagation through the relatively fragile MgO crystals which have been weakened by irradiation.

As judged from the very small volume expansion at 800°C, radiation damage is largely annealed at high temperatures. The fact that there is greater damage at 1100°C than at 800°C may mean, therefore, that thermal effects are responsible for fracturing at these temperatures. Results of out-of-pile tests show that neither thermal cycling nor long-term heating produces fracturing. Consequently, thermal stress, possibly in conjunction with thermal cycling, must initiate the fractures in high-temperature irradiations.

Effects of Fast-Neutron Irradiation on Al_2O_3

Samples of two types of sintered Al_2O_3 specimens (densities, 3.6 and 3.8 g/cm^3), both with grain size less than 10 μ, were irradiated in the experimental assemblies of the MgO series. The gross damage was similar to that of MgO samples in irradiations at 150°C. Of 12 samples receiving doses from 0.46 to 2.35×10^{21} neutrons/cm^2 (>1 Mev), seven were severely fractured, while five sustained little damage. No correlation of dose and gross damage was established, and no difference between the two types was apparent. Dimensional data from the samples that could be reliably measured indicate that the volume expansion of Al_2O_3 at 150°C is no greater than about 1.4% after irradiation to 2.35×10^{21} neutrons/cm^2.

These preliminary results show that even though the crystal structure of Al_2O_3 is anisotropic like that of BeO, the behavior of Al_2O_3 on exposure to fast neutrons is more like that of MgO.

Behavior of Refractory-Metal Carbides and High-Purity Oxides of Yttrium and Aluminum

Refractory-metal carbides have potential applications in high-performance power plants and in reactors for special applications requiring extremely high power densities.[18] For this reason, a carbide irradiation program has been initiated to study the stability of these high-melting materials toward fast neutrons. Both hot-pressed and slip-cast sintered samples of the monocarbides of Ti, Zr, Nb, Ta, and W will be irradiated over three temperature ranges: 130–420, 900–1000, and 1100–1400°C. Single crystals will also be included. It is planned to irradiate the carbides to doses as high as 10^{22} neutrons/cm^2 (>1 Mev) and to separate the flux and dose parameters at each temperature by varying the irradiation times.

Low-temperature experimental assemblies (130–420°C) are now being irradiated in the ETR and the ORR, and high-temperature assemblies are being prepared for insertion in the ETR early in 1965. The carbide experimental series also includes studies of the radiation stability of high-purity Y_2O_3 and translucent Al_2O_3 (Lucalox), which may have value for thermal conversion applications in reactor systems. In addition, it is planned to irradiate some BeO compacts in these experiments at temperatures as high as 1400°C to obtain information for special applications of this material.

[18] G. W. Keilholtz, J. E. Lee, Jr., and R. E. Moore, *Behavior of High-Temperature Materials Under Irradiation*, ORNL-TM-980, pp. 95–105 (Oct. 31, 1964).

15. Miscellaneous Studies for Solid-Fueled Reactors

EQUILIBRIUM STUDIES IN THE SYSTEM ThO_2-UO_2-UO_3

L. O. Gilpatrick C. H. Secoy

Study of the phases which compose the equilibrium system ThO_2-UO_2-UO_3 has been continued at temperatures ranging from 700 to 1550°C. Oxygen partial pressure has been limited to that contained in the normal atmosphere. Previously reported results[1-3] have established the general form of the phase diagram for this system. Additional insight has been possible due to improved techniques which have been used during this period. A new high-temperature tube furnace has been put into service. The element windings of heavy 50% platinum–50% rhodium wire are designed to operate at 1700°C in air. Temperature gradients are adjustable in detail to achieve an experimental value which can be held constant to ±1°C throughout. Better temperature control has helped to improve the quality of the data.

Some variations in the methods of quenching the high-temperature state were examined. Quenching under an argon cover in place of air, for example, was found to have no pronounced effect on the results at 1550°C in the high-urania region. Reducing the quench time to 15 sec did help the regularity of the data.

Compositions ranging from 100 to 40 mole % urania were examined at various temperatures of equilibration. After 174 days at 712°C the lowest-temperature set was analyzed and revealed no significant change as compared with prior data obtained at much shorter periods of time. Results are shown in Figs. 15.1, 15.2, and 15.3 for three additional temperatures, 1400, 1425, and 1550°C.

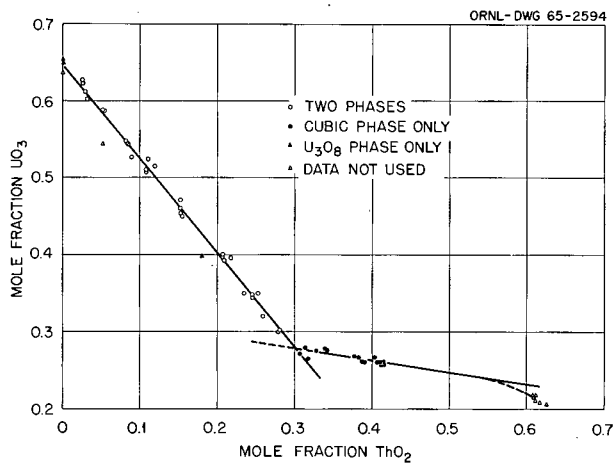

Fig. 15.1. 1400°C Isotherm for the System ThO_2-UO_2-UO_3 at P_{O_2} = 0.2 atm.

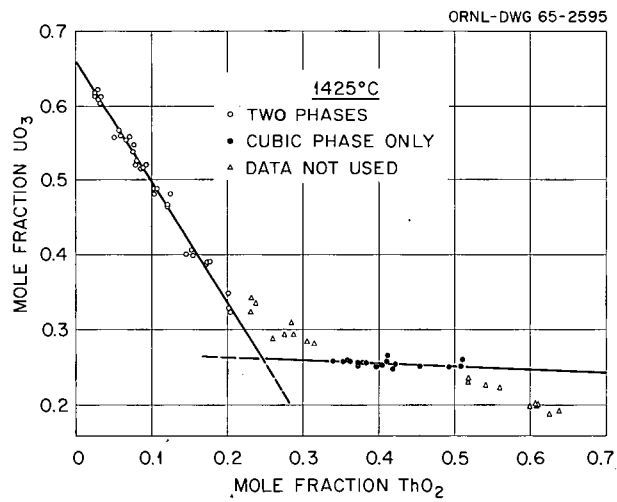

Fig. 15.2. 1425°C Isotherm for the System ThO_2-UO_2-UO_3 at P_{O_2} = 0.2 atm.

[1] H. A. Friedman and R. E. Thoma, *Reactor Chem. Div. Ann. Progr. Rept. Jan. 31, 1963*, ORNL-3417, pp. 130–34.

[2] L. O. Gilpatrick, H. H. Stone, and C. H. Secoy, *Reactor Chem. Div. Ann. Progr. Rept. Jan. 31, 1963*, ORNL-3417, pp. 134–39.

[3] L. O. Gilpatrick, H. H. Stone, and C. H. Secoy, *Reactor Chem. Div. Ann. Progr. Rept. Jan. 31, 1964*, ORNL-3591, pp. 160–64.

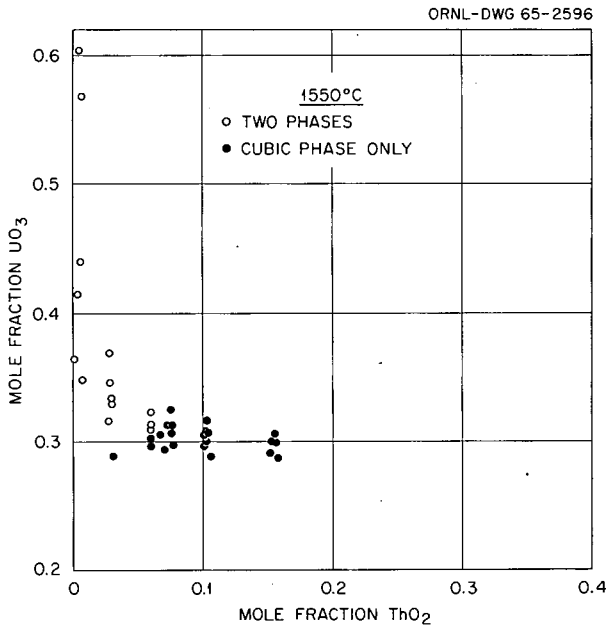

Fig. 15.3. 1550°C Isotherm for the System ThO_2-UO_2-UO_3 at P_{O_2} = 0.2 atm.

Table 15.1. Least-Squares Parameters for the Two-Phase Tie Lines $X_{UO_3} = a_0 - a_1 X_{ThO_2}$

Temperature (°C)	Number of Data Points	a_0	a_1
1400	32	0.6469	1.2274
1425	33	0.6592	1.6163

Table 15.2. Least-Squares Parameters for the One-Phase Isobars $X_{UO_3} = b_0 - b_1 X_{ThO_2}$

Linearity assumed

Temperature (°C)	Number of Data Points	b_0	b_1
1400	16	0.3265	0.1593
1425	19	0.2711	0.0419

Coefficients for the best straight lines representing the two-phase and the single-phase region were determined by the least-squares method of fitting and are listed in the separate Tables 15.1 and 15.2. In all cases the results of the first heats of a particular composition were excluded from consideration. In nearly all cases there is evidence that at least the first heats have not yet attained equilibrium. The values presented in Tables 15.1 and 15.2 are not in very good agreement with results reported earlier. Nor is it clear which present a more nearly correct picture. X-ray diffraction data discussed below suggest that both may err in indicating that the mole fraction UO_3 in the cubic phase rises well above the value 0.25.

The 1550°C heat is of particular interest because it demonstrates that after seven heat-grinds totaling 15 hr there is still evidence that the transition from U_3O_8-orthorhombic to the fluorite cubic structure for pure urania is still not complete. This temperature was purposely chosen to be above the transition temperature of 1525°C reported in the literature[4] for pure urania. Those heats containing ThO_2 more rapidly approached a composition containing about 0.30 mole fraction UO_3 and finally exhibited no detectable U_3O_8 phase. This lower value compares with 0.40 mole % UO_3 reported last year as a preliminary value of the limiting case for the composition of the system as the ThO_2 component approached zero. The situation is still unsatisfactory in that better techniques seem to yield lower values for the excess oxygen, although not as low as $UO_{2.25}$. There is still an unresolved question as to the role surface oxidation plays during the quenching and handling after firing. Currently steps are being taken to resolve this question experimentally.

Additional evidence also supporting this thesis is gained from x-ray diffraction studies. Previously this tool was used only to identify phases which were present. During this period, unit cell parameters (a_0) were determined, in addition, using a bench diffractometer for those cases where sufficiently well-crystallized face-centered cubic crystal patterns could be observed. This included all the single-phase region, most of the two-phase region, and excludes only that part of the two-phase region composed of greater than 95% urania at the higher temperatures.

[4]C. A. Alexander and T. S. Shevlin, *Uranium Oxide Pressure-Temperature-Composition Relationships from 1000 to 2000°K*, TID-7622, pp. 139–48 (October 1961).

The reduced system of $UO_{2.00}$ and ThO_2 has been reported to be monophasic solid solution exhibiting the cubic structure throughout.[5,6] The lattice parameter obeys Vegard's law to a first approximation and can be expressed analytically by the linear equation

$$a_0 = 5.473 + 0.123X_{ThO_2} . \quad (1)$$

Also well established[7,8] is the fact that when stoichiometric UO_2 adsorbs oxygen, the effect is to reduce the unit cell size at least up to the value of ½ atom oxygen per mole of UO_2. Schaner's data indicate that the dependence is not linear. His data can be described by a quadratic, the parameters of which were calculated by the least-squares method to yield

$$a_0 = 5.473 - 0.096X_{UO_3} - 0.150X^2_{UO_3} . \quad (2)$$

If one assumes no interaction between the two effects these expressions can be combined to give

$$a_0 = 5.473 + 0.123X_{ThO_2} - 0.096X_{UO_3} - 0.150X^2_{UO_3} . \quad (3)$$

This empirical relation, based on data obtained by chemical analysis, permits the calculation of the lattice parameter of all our observed values, 60 determinations, within ±0.003 A and nearly 50 of these within ±0.001 A.

The relation is obviously restricted to the condition that no other phase, such as U_3O_8, is present. If this limitation were not observed, the analytical results would represent the sum for the mixture and would bear no unique relation to the cubic component.

Anomalous behavior was disclosed by some of the data when applied to calculate a_0 by the above relation. Compositions containing less than 0.20 mole fraction ThO_2 consistently gave UO_3 mole fractions greater than 0.25 after equilibration in air at temperatures from 1400 to 1600°C. In no case could the presence of a second phase, such as U_3O_8, be detected in the diffraction patterns. In these cases the correct lattice constant for the cubic phase was obtained from Eq. (3) by using the value $X_{UO_3} = 0.25$ regardless of the higher analytical value. Several hypothetical explanations for this apparent discrepancy can be advanced. The most reasonable seems to be that the cubic phase is truly limited to $X_{UO_3} = 0.25$ and that the excess oxygen found by chemical analysis is actually present in a surface film of another phase, whose presence cannot be detected by x-ray diffraction. Table 15.3 presents the experimental data.

Progress toward equilibrium during successive heats at a given temperature can be followed by observing the unit cell constant for the cubic phase. Data for a_0 at 1550°C are displayed in Fig. 15.4. Plotting a_0 vs successive heating times demonstrates a typical minimum in a_0 for each composition. The heats up to a total of 7 hr reflect a contracting lattice as solid-solution formation approaches completion and the solution of excess oxygen reaches a maximum value. As the firing period grows longer, some urania is lost by volatilization, so that the composition of each material shifts toward a larger proportion of ThO_2. Since ThO_2 has the largest unit cell of any component of the system, the equilibrium solid solution reflects this fact in a progressively larger unit cell as urania is lost.

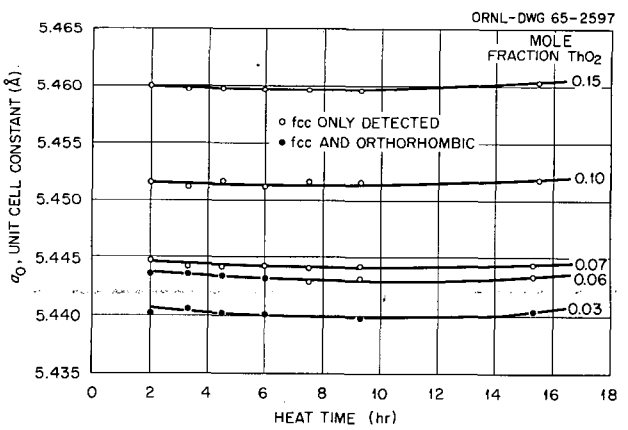

Fig. 15.4. Time Dependence of Face-Centered Cubic Lattice Constant at 1550°C.

[5]W. A. Lambertson, M. H. Mueller, and F. H. Gunzel, Jr., *J. Am. Ceram. Soc.* **36**, 397–99 (1953).

[6]E. Sidwinski and N. Elliott, *J. Am. Chem. Soc.* **72**, 4504–6 (1950).

[7]B. E. Schaner, *J. Nucl. Mater.* **2**, 110–20 (1960).

[8]P. Perio, *Contribution to the Crystallography of the Uranium-Oxygen System*, Doctoral Dissertation, University of Paris, 1955, CEAD-363.

Table 15.3. Compositions and Lattice Parameters for the Cubic Phase

Temperature (°C)	X_{ThO_2}	X_{UO_3}	a_0 (A) Observed	a_0 (A) Calculated	Δa_0
900	0	0	5.473	5.4730	0
900	0	0.008	5.472	5.4722	−0.0002
900	0	0.018	5.474	5.4712	+0.0028
900	0	0.020	5.472	5.4710	+0.0010
900	0	0.030	5.470	5.4700	0
900	0	0.040	5.470	5.4689	+0.0011
900	0	0.078	5.466	5.4646	+0.0014
900	0	0.146	5.456	5.4558	+0.0002
900	0	0.176	5.450	5.4515	−0.0015
1200	0	0.208	5.447	5.4465	+0.0005
1200	0	0.208	5.454	5.4465	−0.0011
1200	0	0.229	5.443	5.4431	−0.0001
1200	0	0.248	5.437	5.4400	−0.0030
1200	0	0.248	5.441	5.4400	+0.0010
1200	0	0.248	5.441	5.4400	+0.0010
1550	0.0007	0.3486	5.4371	5.4397	−0.0026
1550	0.0267	0.3163	5.4396	5.4429	−0.0033
1550	0.0279	0.3691	5.4412	5.4430	−0.0018
1550	0.0283	0.3465	5.4405	5.4431	−0.0026
1550	0.0286	0.3456	5.4402	5.4431	−0.0029
1550	0.0300	0.2888	5.4407	5.4433	−0.0026
1550	0.0301	0.3335	5.4403	5.4433	−0.0030
1550	0.0559	0.2975	5.4468	5.4470	−0.0002
1550	0.0580	0.2936	5.4480	5.4467	+0.0013
1550	0.0597	0.3233	5.4472	5.4469	+0.0003
1550	0.0599	0.3128	5.4468	5.4470	−0.0002
1550	0.0599	0.3097	5.4464	5.4470	−0.0006
1550	0.0604	0.3026	5.4458	5.4470	−0.0012
1550	0.0669	0.3062	5.4464	5.4478	−0.0014
1550	0.0695	0.2936	5.4485	5.4481	+0.0004
1550	0.0722	0.3166	5.4495	5.4485	+0.0010
1550	0.0740	0.3134	5.4481	5.4487	−0.0006
1550	0.0745	0.3256	5.4483	5.4488	−0.0005
1550	0.0754	0.3123	5.4483	5.4489	−0.0006
1550	0.0764	0.3063	5.4480	5.4490	−0.0010
1550	0.0766	0.2976	5.4483	5.4490	−0.0007
1550	0.1015	0.3607	5.4487	5.4521	−0.0034
1550	0.1019	0.2894	5.4532	5.4521	+0.0011
1550	0.1019	0.2982	5.4534	5.4521	+0.0013
1550	0.1028	0.3075	5.4532	5.4522	+0.0011
1550	0.1032	0.3079	5.4523	5.4523	0
1550	0.1036	0.3167	5.4523	5.4523	0
1500	0.1036	0.2995	5.4530	5.4523	+0.0007
1550	0.1059	0.2882	5.4530	5.4526	+0.0004
1475	0.1422	0.3542	5.4567	5.4571	−0.0004
1550	0.1518	0.3069	5.4590	5.4583	+0.0007

Table 15.3 (continued)

Temperature (°C)	X_{ThO_2}	X_{UO_3}	a_0 (A) Observed	a_0 (A) Calculated	Δa_0
1475	0.1532	0.3469	5.4574	5.4584	−0.0010
1550	0.1532	0.2668	5.4600	5.4584	+0.0016
1550	0.1540	0.3004	5.4590	5.4585	+0.0005
1500	0.1541	0.3477	5.4588	5.4586	+0.0002
1550	0.1542	0.3007	5.4593	5.4586	+0.0007
1550	0.1549	0.3063	5.4594	5.4587	+0.0007
1550	0.1558	0.3081	5.4605	5.4588	+0.0017
1550	0.1580	0.2873	5.4590	5.4590	0
1475	0.1598	0.3444	5.4595	5.4593	+0.0002
1450	0.2362	0.3192	5.4658	5.4687	−0.0029
700	0.3458	0.3051	5.4825	5.4821	+0.0004
1200	0.3542	0.2738	5.4834	5.4832	+0.0002
1200	0.5058	0.3012	5.5002	5.5018	−0.0016
1425	0.5596	0.2220	5.516	5.5131	+0.0029

The chemical analysis upon which this work is based was performed by Analytical Chemistry Division personnel with W. R. Laing as supervisor.

PHASE EQUILIBRIUM STUDIES IN THE UO_2-ZrO_2 SYSTEM

K. A. Romberger D. R. Sears H. H. Stone
R. E. Thoma C. F. Baes

In a previous report[9] it was stated that precipitates of UO_2 and ZrO_2, formed in a fluoride melt at 600°C, showed no measurable solution either of UO_2 in ZrO_2 or of ZrO_2 in UO_2. This observation was in sharp disagreement with published phase diagrams[10–15] for the UO_2-ZrO_2 system, which indicated appreciable solubility of both UO_2 in ZrO_2 and ZrO_2 in UO_2. Because it is necessary to avoid precipitating uranium in any form in the MSRE, and also because of the importance of UO_2-ZrO_2 compacts for solid fuel elements, an investigation of the phase equilibrium relationships in this system was initiated.[16]

This study is being pursued by two different techniques. In the first, various mixtures of powdered UO_2, ZrO_2, their solid solutions, and a molten flux composed of lithium, beryllium, uranium, and zirconium fluorides are equilibrated, with agitation, under an inert, nonoxidizing atmosphere. After equilibration, the solids are freed from most of the fluoride melt by filtration at temperature, cooled to room temperature, freed from any residual fluorides by an aqueous wash, and finally investigated by x-ray and petrographic techniques. In the second technique being used for study of the system, mixtures of appropriate solid compositions are examined with an x-ray

[9] J. E. Eorgan *et al.*, *Reactor Chem. Div. Ann. Progr. Rept. Jan. 31, 1964*, ORNL-3591, p. 45.

[10] I. Cohen and B. E. Schaner, *J. Nucl. Mater.* **9**, 18 (1963).

[11] W. A. Lambertson and M. H. Mueller, *J. Am. Ceram. Soc.* **36**, 365 (1953).

[12] G. M. Wolten, *J. Am. Chem. Soc.* **80**, 472 (1958).

[13] N. M. Voronov, E. A. Voitekhova, and A. S. Damlin, *Proc. U.N. Intern. Conf. Peaceful Uses At. Energy, 2nd, Geneva, 1958*, **6**, 221 (1958).

[14] P. E. Evans, *J. Am. Ceram. Soc.* **43**, 443 (1960).

[15] T. R. Wright, D. E. Kizer, and D. L. Keller, *Studies in the UO_2-ZrO_2 System*, BMI-1680 (Apr. 27, 1964).

[16] The contributions of Prof. J. E. Ricci, consultant to the Reactor Chemistry Division from the Department of Chemistry, New York University, are gratefully acknowledged.

diffractometer equipped with attachments permitting the use of controlled or variable high temperatures and simultaneous protection of the sample in a vacuum.

Equilibration with Molten Fluoride Fluxes

The results obtained from 12 samples equilibrated at 915 and 1020°C showed no measurable evidence of solution of UO_2 in the monoclinic ZrO_2 at either temperature. Also, at 915°C, there was no evidence of any solution of ZrO_2 in cubic UO_2. With the 1020°C samples, a slight change in UO_2 lattice constant was observed indicating a small (several mole %) zirconium solubility. Eight of these twelve samples contained tetragonal UO_2-ZrO_2 solid solutions in the starting mixtures. The disappearance of these solid solutions during the equilibration is evidence not only that reaction has occurred, but also that these solid solutions are not stable with respect to the pure cubic UO_2 and monoclinic ZrO_2 phases at temperatures below 1020°C.

Analysis of the liquid phase obtained from the high-temperature filtration provides a complementary means for following any changes occurring with the solid phases, since the relative amounts of ZrF_4 and UF_4 in the melt are fixed by the equilibrium:

$$ZrF_4(d) + UO_2(s) \rightleftharpoons UF_4(d) + ZrO_2(s) . \qquad (4)$$

Thus, any changes in the relative activities of the solid phases, that is, solid-solution formation or the disappearance of one of these solids, will affect the relative ZrF_4 and UF_4 concentrations.

For the melts equilibrated at 915°C, the mole ratio of ZrF_4 to UF_4 was $1.51_3 \pm 0.26_5$ to 1 for ZrF_4 concentrations varying from 0.38_7 to 0.51_7 mole per kilogram of melt. For the 1020°C samples, this ratio was $1.41_2 \pm 0.07_7$ to 1 for a concentration range of 0.55_0 to 0.89_3 mole per kilogram of melt. The deviations from the mean followed no pattern except that ascribable to the variation of this ratio with ZrF_4 concentration. These results are consistent both with the x-ray and petrographic results given above and with previous investigations of the ZrF_4-UF_4 equilibrium at 500, 600, and 700°C.[9,17]

[17] C. F. Baes, Jr., J. H. Schaffer, and H. F. McDuffie, *Trans. Am. Nucl. Soc.* **6**, 393 (1963).

X-Ray Diffractometric Observation of Transformations

In one series of experiments, a starting material of preformed pure tetragonal solid solution of 19% UO_2 + 81% ZrO_2 composition was examined at temperatures from 25 to 1483°C. Partial transformation of the tetragonal solid solution to monoclinic ZrO_2 and cubic UO_2 was observed at 1045°C after one day at this temperature. No attempt was made to determine whether the transformation would occur at lower temperatures. Reversion to the tetragonal phase was observed after 2.5 hr at 1264°C.

In other experiments, intimate mixtures of 40% cubic UO_2 and 60% monoclinic ZrO_2 were observed in the temperature range 25 to 1441°C. Crystallite growth of monoclinic phase was observed at 997°C; this implies that monoclinic ZrO_2 is a stable phase in the presence of cubic UO_2 at this temperature. No evidence for dissolution of UO_2 in the monoclinic phase was seen in this, or in any other, high-temperature experiment. The precision with which lattice constants could be measured in the high-temperature diffractometer would not, however, permit such an observation unless the limits of solid solubility were quite high. With this same composition, rapid reaction to form a tetragonal phase was observed at 1144°C but not at 1095°C. Because both the cubic and monoclinic diffraction patterns were markedly diminished in intensity at 1144°C, it is believed that the observed transition represented, at least in part, the formation of tetragonal solid solution, rather than pure tetragonal ZrO_2. The reverse transformation, that is, the decomposition of the solid solution, which has been stated to be sluggish, was not effected by heating a sample for several hours at 1009°C; nevertheless, after cooling the sample quickly to room temperature and examining it within 6 min, the transformation was found to have proceeded essentially to completion.

Tentative Phase Diagram

Although it would be clearly premature to publish a corrected phase diagram for the UO_2-ZrO_2 system, the information available does appear to support inferences which lead to a tentative proposal, shown in Fig. 15.5, which we are using as a guide

to further study of the system. The following points should be noted:

1. At temperatures significantly below 1100°C (the temperature of the monoclinic-tetragonal inversion of ZrO_2) equilibrium phases consist only of the components. Between 800 and 1100°C there is some, but not conclusive, evidence of a slight solubility of ZrO_2 in UO_2. The magnitude of the solubility we find is of the order of one-tenth that reported by the most recent report[15] of a study of this region; the discrepancy is not resolved, but it could conceivably be due to the large effect on the UO_2 lattice parameter of very small quantities of extra oxygen included in the encapsulated material used in the solid-state equilibration study. The tetragonal ZrO_2-UO_2 solid solution at low temperatures, whose presence has been reported or accepted by all previous investigators, is rejected on the basis of our ability to achieve equilibrium conditions in the presence of molten fluoride fluxes. Previous work involved only solid-state equilibration attempts.
2. At temperatures of 1100 to 1450°C, face-centered UO_2 and tetragonal ZrO_2 solid solutions comprise the equilibrium solids. The solubility of UO_2 in ZrO_2 in this temperature range is believed to be less than 10 mole %.
3. The high-temperature data reported by Cohen and Schaner[10] are provisionally accepted.
4. A high-temperature intermediate phase of composition near $UO_2 \cdot 3ZrO_2$ is postulated, although it has not been found, in order to rationalize the discontinuity in the solubility of UO_2 in the tetragonal ZrO_2 solid phase. The alternatives of either a eutectoidal relationship of the high-temperature intermediate phase or a continuous retrograde solubility of UO_2 in ZrO_2 seem less consistent with the curvature of the phase boundaries at 60 to 100 mole % ZrO_2 and 1700 to 2300°C.

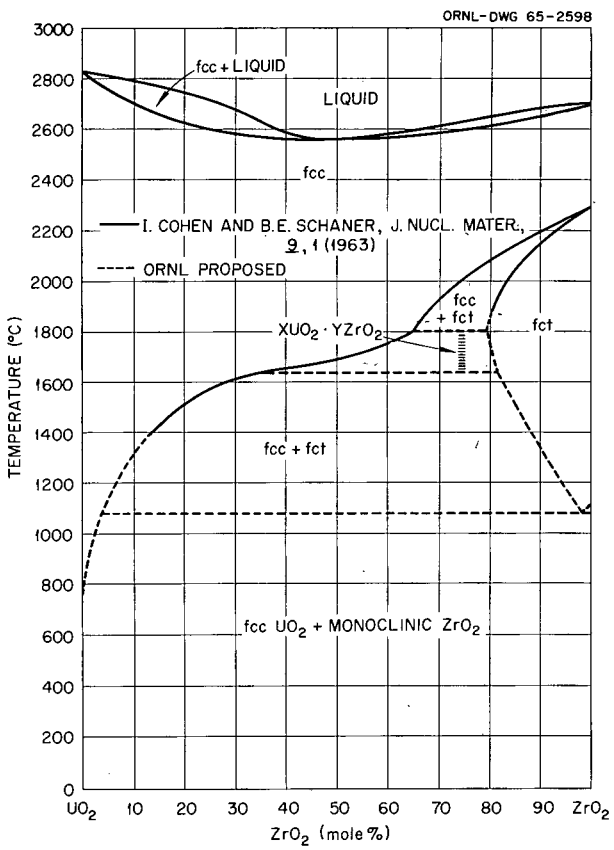

Fig. 15.5. Equilibrium Phase Diagram for the System UO_2-ZrO_2.

IRRADIATION OF SULFUR DIOXIDE WITH ALPHA PARTICLES

P. S. Rudolph[18] R. L. Bennett

Recent examinations[19] of the performance characteristics of gas-cooled fast reactor designs show that the use of high-density, supercritical SO_2 allows a core structure sufficiently compact to compare favorably with sodium-cooled systems. In reactors using oxide fuel, SO_2 as a coolant in the range 1000 to 1500 psia would give a slightly higher breeding potential (due to less neutron energy degrading effect) than would sodium. Although SO_2 has a high thermal stability, knowledge of its radiation stability is limited.

According to Rothschild,[20] who recently made a study of the gamma irradiation of liquid SO_2 at −17°C, disproportionation occurred essentially according to the overall equation: $3SO_2 \rightarrow 2SO_3 + S$. Small amounts of oxygen were also found. Values of G (molecules per 100 ev absorbed) found were 1.31, 0.65, and 0.02 for the production of SO_3, S,

[18] Chemistry Division.

[19] Gas-Cooled Reactor Project staff, *Gas-Cooled Fast Reactor Concepts*, ORNL-3642 (September 1964).

[20] W. G. Rothschild, *J. Am. Chem. Soc.* **86**, 1306–9 (1964).

and O_2; the value for decomposition of SO_2 was 1.35.

The current investigation of the alpha-particle irradiation of SO_2 with radon and its decay products at room temperature is the first reported[21] in the gaseous state. A 3-liter Pyrex reaction sphere containing SO_2 at 755 torrs was charged with a 150-mc sample of radon. A very strong Tyndall effect was observed when, several hours after addition of the radon, a collimated beam of light was focused through the reaction sphere; it was apparent that reaction was occurring in the gas phase. After about 24 hr very small droplets of brown viscous liquid were observed on the bottom of the reactor flask. These droplets, however, began to slowly diminish and had almost completely disappeared after two weeks. After one week the Tyndall beam, while still observable, was greatly diminished. Measurement of the final pressure after essentially complete decay of the radon showed no change within experimental error.

Preliminary mass spectrometry analyses of the initial gas (commercial anhydrous grade) and the irradiated gas indicate little net change had occurred. Gas chromatographic analyses show the irradiated gas contained no detectable oxygen (less than 0.004%) and only a few hundredths of a percent of SO_3.

This evidence, combined with the disappearance of the visual evidence of change, suggests that under the conditions of the experiment, back reaction of the initially formed products occurred.

NEUTRON FLUX SPECTRA IN THE EXPERIMENTAL FACILITIES OF THE OAK RIDGE RESEARCH REACTOR

C. D. Baumann

A compilation of the neutron flux spectra in the various experimental facilities (including the horizontal beam hole, poolside, and capsule irradiation facilities) has been made.[22] The compilation includes both the energy and the spatial variations of the neutron flux, whenever data were available. The results are presented in both tabular and graphical form.

The data were obtained mainly by personal communication with the current users of the facilities in order to obtain up-to-date values of the neutron flux. The values presented are to be considered nominal values, for the actual flux depends strongly upon (1) the current fuel loading of the reactor, (2) the position of the nearest shim and control rods, (3) the amount and nature of heavy neutron absorbers in the pertinent and nearby facilities, and (4) the presence of large water gaps (which cause thermal flux peaking).

The neutron flux varies across a facility as well as axially. Usually the axial flux peaks slightly (2 to 4 in.) below the midplane of the reactor at the start of a reactor cycle, with the peak moving upwards during the course of a cycle as the shim and control rods are withdrawn. One would also expect a slight change in the flux distribution during the course of a reactor cycle due to the uneven burnout of the fuel elements.

If the flux at a particular facility is not monitored continuously, some idea of the change in flux from cycle to cycle may be obtained from the occasional flux measurements made by the Operations Division for purposes of burnup calculations. Prior to the start of some fuel cycles, the Operations Division obtains a flux map of the core by irradiating, at low power (N_L), flux monitor wires which have been positioned in each fuel element. Caution must be exercised in using these results because the wires cannot be positioned in a consistent location within an element, and there may be a large radial flux gradient across the element or facility.

The neutron flux energy spectrum as a function of position was measured for capsule irradiation position P-05 during the last year.[22] It is shown in Fig. 15.6 as a typical example of the data in the compilation.

[21] P. S. Rudolph and R. L. Bennett, *Alpha Particle Irradiation of Gaseous Sulfur Dioxide*, to be published as an ORNL-TM report (March 1965).

[22] C. D. Baumann, *Neutron Flux Spectra in the Experimental Facilities of the Oak Ridge Research Reactor*, ORNL-3756 (1964).

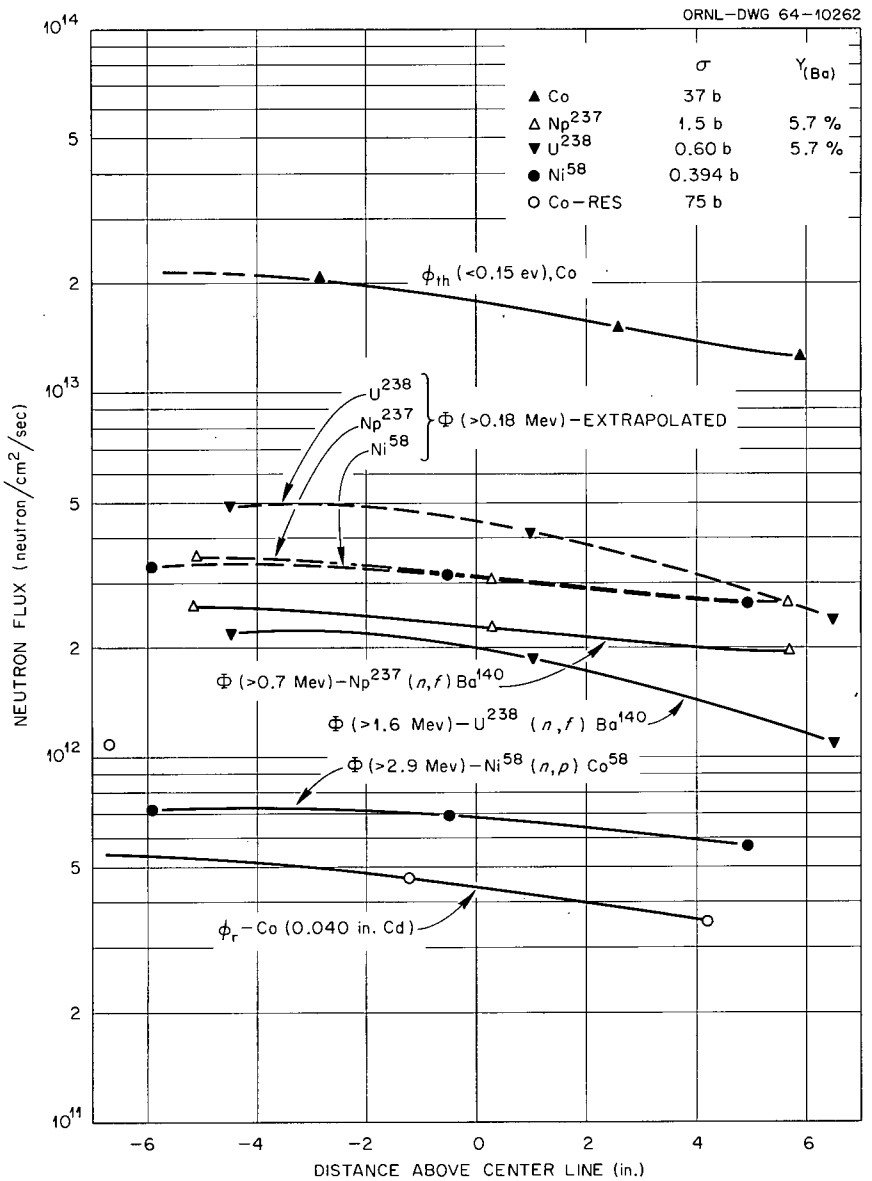

Fig. 15.6. The Neutron Flux in ORR Capsule Irradiation Facility P-05 at 30 Mw.

Part IV

Nuclear Safety

16. Experiments with the Containment Mockup Facility

G. W. Parker

C. J. Barton
G. E. Creek
J. G. Wilhelm[1]
W. J. Martin

The Containment Mockup Facility (CMF), described in previous reports,[2-4] consists, in brief, of a 180-liter stainless steel tank to which gases bearing fission products released from fuel elements can be added and from which samples of the gas can be drawn (through special filter and absorber assemblies, if desired) for analysis. Location of the CMF in a hot cell permits operation with relatively high levels of activity, and the complex manifold system permits study of the effect of various atmospheres upon fission product behavior over a limited temperature range.

The CMF has been modified during the past year to permit operation with air or steam pressures up to 30 psig. When the facility is operated with appreciable steam pressure, however, the procedure is simplified by deferring sampling until the temperature of the tank and its contents has dropped and most of the steam has condensed. Additions to the facility have included (1) a more elaborate filter pack (May pack), (2) a condensation nuclei counter, (3) a heated catalytic converter to free iodine from organic iodides, and (4) a commercial (Andersen) aerodynamic particle separator.

[1]Visiting scientist from Karlsruhe Center for Nuclear Research and Development, Karlsruhe, Germany.

[2]G. W. Parker *et al.*, *Nucl. Safety Program Semiann. Progr. Rept. June 30, 1963*, ORNL-3483, p. 33; *Nucl. Safety Program Semiann. Progr. Rept. Dec. 31, 1963*, ORNL-3547, p. 3.

[3]W. B. Cottrell *et al.*, "U.S. Experience on the Release and Transport of Fission Products Within Containment System Under Simulated and Actual Reactor Accident Conditions," paper presented at the Third International Conference on Peaceful Uses of Atomic Energy, Geneva, Switzerland, 1964.

[4]G. W. Parker *et al.*, *Nucl. Safety Program Semiann. Progr. Rept. June 30, 1964*, ORNL-3691, p. 3.

FISSION PRODUCT RELEASE FROM MELTING TRACE-LEVEL-IRRADIATED UO_2

Two experiments on melting trace-level-irradiated stainless-steel-clad UO_2 in the CMF have been completed. The UO_2 was melted over a period of several minutes while a stream of air flowing at 3 liters/min was passed over the crucible to transport the smoke and volatile fission products into the stainless steel confinement tank. The two experiments differed only in that one had a portion of unfiltered cell air, approximately 25% of the tank volume, accidentally added to the tank after melting of the fuel was completed. This difference in the conditions of the two experiments had a significant effect on the chemical form of the released radioiodine. The proportion of penetrating forms (possibly organic iodine compounds) was increased by a factor of approximately 10. This was the ratio between the amounts of iodine found to penetrate a $1\frac{1}{2}$-in. charcoal bed (ORR specifications) in these tests. Data on iodine behavior, total fission product release from the UO_2, and the amount of each fission product deposited during a 3-hr aging period in the confinement tank are summarized in Table 16.1.

It is interesting that the rate of removal of radioactivity from the aerosol was low in these experiments, which suggests that the particles remained too small to deposit rapidly. Analyses of the diffusion tube, of the absolute filter, and of the charcoal bed showed that approximately equal parts of particulate and molecular iodine were present in the confinement tank at the end of the 3-hr period. The amount of iodine in a penetrating (organic) form was only a fraction of either form and varied between the runs.

Table 16.1. Distribution of UO_2 Aerosol and Fission Products from UO_2[a] Melted in Air[b]

	Distribution (% of inventory)									
	Iodine			Tellurium			Cesium			Plutonium
	A	B	C	A	B	C	A	B	C	C
Total release	84	64	91	12	12	55	29	37	37	0.005
Hot-zone deposition[c]	6.3	11	0.4	3.3	1.9	2.5	3.2	16	6.2	0.0005
Total in aerosol tank	47	24	25	3.1	3.4	46	20	9.3	14	0.004
Activity remaining airborne after 3 hr	31	30	62	3.3	6.5	6.2	5.7	13	16	0.0001
Amount of iodine in penetrating form	3.7	0.4	0.3							
Iodine loss through 1.5 in. of charcoal	1.3	0.1	0.01							

[a]Runs A and B were made with tracer-level-irradiated UO_2. Run C was made with 20 g of stainless-steel-clad UO_2 irradiated to 7000 Mwd/ton.

[b]Run A was performed with filtered air diluted by ~25% with unfiltered air. Runs B and C were performed with air entirely filtered by absolute filters and a charcoal bed.

[c]Temperature in the "hot zone" varied from an undetermined value close to that of the fuel to approximately room temperature.

FISSION PRODUCT RELEASE FROM HIGHLY IRRADIATED UO_2

Comparison of Release Behavior from Trace-Level-Irradiated UO_2 with That from High-Burnup-Level Fuel

The initial meltdown of highly irradiated (7000 Mwd/ton) UO_2 was performed in ambient air in the CMF. This experiment was of special interest, since it provided the first opportunity to compare fission product release values from fuel irradiated to a realistic level with the results of trace-level experiments. Total release values, as expected, were not markedly different except in the case of tellurium, which increased from about 12 to 55%. The total release data are summarized for this experiment in Table 16.1, and more detailed data are given in Table 16.2.

The release of plutonium was in good agreement with previous estimates that its volatility would correspond to that of UO_2. Under the conditions of melting (20 g of stainless-steel-clad UO_2 in a zirconia crucible with air flowing at 18 fpm), only 5×10^{-3}% of both plutonium and UO_2 vaporized; most of this vaporized fraction deposited rapidly in the confinement tank.

Data obtained by sampling the confined aerosol at intervals showed a rapid reduction from the calculated initial concentration of fission products in the tank to that in the first sample, which was drawn 10 min after melting. Iodine concentration dropped from 91 to 10%; cesium dropped from 35 to 19%; and tellurium dropped from 53 to 7%. Evidence of probable deposition of all three fission products in the sampling tubes was observed. In addition, it was found that about 75% of the iodine that deposited on the walls of the confinement tank was desorbed by passing 1.5 tank volumes of argon (270 liters) through the tank.

Table 16.2. Distribution of Fission Products Released from High-Burnup (7000 Mwd/ton) UO_2 (Run C)

Location	Release as Percent of Total in Sample						
	Iodine	Cesium	Tellurium	Ruthenium	Plutonium	Strontium	Gross Gamma
Furnace tube	0.4	6.2	2.5	0.0006	0.0006	0.001	0.03
Aerosol tank	25.2	13.9	46.3	0.001	0.004	0.007	0.5
Filter pack:							
Roughing filter	3.4	16.5	6.2	0.0008	0.0001	0.002	0.004
Absolute filter	0.5	0.04	0.008	0.00003			
Copper screens	52.7	10^{-6}					
Charcoal paper	4.1						
1st charcoal	4.4						
2d charcoal	0.07						
3d charcoal	0.01						
4th charcoal	0.002						
5th charcoal	0.0005						
2d absolute	0.00003						
2d copper screens	0.000005						
Misc backup	0.002						

Total Nuclei Count in the Aerosol

A condensation nuclei counter (supplied by Gardner Instrument Co.), which is a light-scattering ion-chamber device with a maximum scale reading of 10^7 nuclei/cm^3, was employed to follow the rapid change in the total nuclei concentration released in the preceding test. Agglomeration of small particles is one of the processes expected to influence the deposition of activity from the tank aerosol. In Fig. 16.1, a comparison of the number of particles is given, as well as the relative quantity of filterable activity in the aerosol. The rapid agglomeration rate (which can be extrapolated to approximately 10^{10} nuclei/cm^3 at release time) dropped from about 10^7 to 10^5 in 15 min and then decreased slowly to 10^4 nuclei/cm^3. The total amount of filterable activity in the gas samples removed during this period (with the fan operating 1 min before each sample) did not change appreciably over the first 3-hr period. This suggests that while the nuclei did increase in size, growth was terminated by a reduction in concentration of particles, so that deposition was not appreciably enhanced.

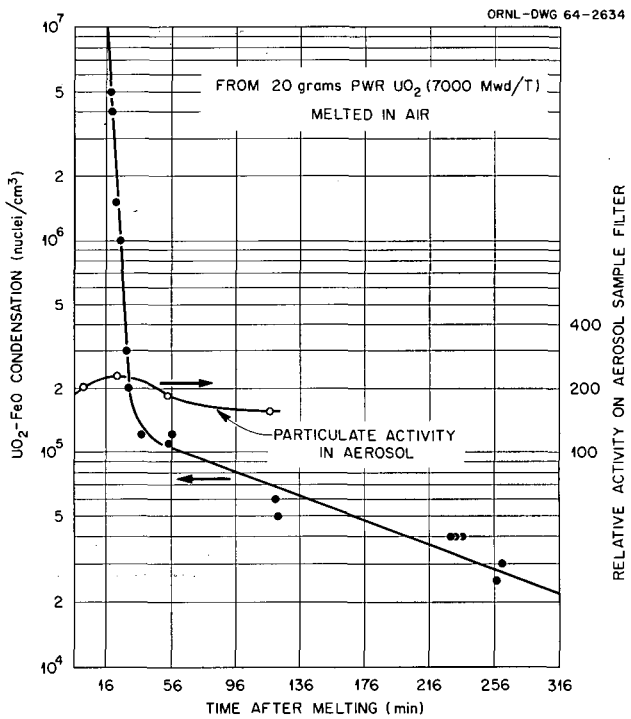

Fig. 16.1. Comparison of Nuclei Concentration and Particulate Aerosol Activity from High-Burnup UO_2.

Fission Products Remaining Airborne as a Function of Time

Radiochemical data obtained from samples of the aerosol in the confinement tank during the preceding test with the 7000-Mwd/ton UO_2 were supplemented by data at two additional calculated points: activity at the initial (zero) time and activity at final (300 min) time. The initial value is based on knowledge of the total amount released (all of which was initially airborne), and the final value is based on knowledge of the amount displaced by the argon gas sweep. Some unexplained variations are noted in the data shown in Fig. 16.2, such as a peak in the iodine curve at the third point and an apparent increase in the concentration of cesium and tellurium at the calculated end point. This latter condition is very likely due to deposition of the aerosol activities (cesium and tellurium) in the sample lines. The most pleasing aspect of the data in Fig. 16.2 is the very low release (10^{-3}%) of strontium, plutonium, and ruthenium.

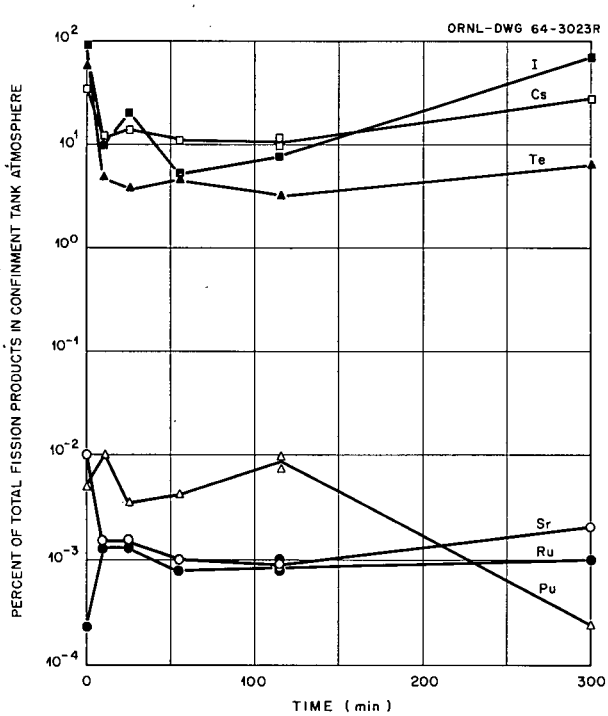

Fig. 16.2. Concentration of Airborne Fission Products as a Function of Time After Melting.

FACTORS AFFECTING THE BEHAVIOR OF IODINE IN A CONTAINMENT SYSTEM

Gas-Phase Reactions

Occurrence of organic iodine compounds in the aerosol formed during simulated reactor experiments and experiments with other types of iodine sources is mentioned below and elsewhere in this report. The mechanism by which these compounds are formed in these experiments is not clear. It is important to establish the factors controlling the conversion of molecular iodine or hydriodic acid, which are reactive and easily trapped by charcoal beds, to the more difficultly trapped organic compounds. Several attempts to produce methyl iodide by the direct gas-phase reaction of elemental iodine and methane at temperatures from 200 to 800°C and pressures up to 150 psig, in the absence of radiation, failed to produce more than trace amounts of methyl iodide. Exposure of an autoclave containing methane and iodine at 200°C for 12 hr to a 10,000-curie cobalt gamma source likewise resulted in production of trace amounts of methyl iodide, indicating that the gamma energy of fission products present in reactor accidents would not significantly increase the rate of the reaction of these materials in the gas phase. It appears probable, therefore, that gas-phase reactions do not contribute significantly to the production of methyl iodide and other organic compounds.

Iodine History

Two processes, thermal decomposition of PdI_2 in air and deposition and desorption of iodine from metal surfaces, have been observed to lead to partial conversion of I_2 to organic iodides, and the second process (desorption from a mild-steel surface) has produced a substantial yield of the penetrating forms.

In a recent series of iodine release tests in the CMF, part of the iodine which was introduced into the containment tank entirely in the form of I_2 was converted to a mixture of other forms of which from 0.2 to 20% was definitely a "penetrating" variety. "Penetrating iodine" is defined as any gaseous form which is poorly adsorbed by charcoal, in contrast to the reactive forms, which are readily adsorbed. An illustration of the adsorption rates of iodine in the different forms is given in Fig. 16.3. The exponential type of adsorption which is

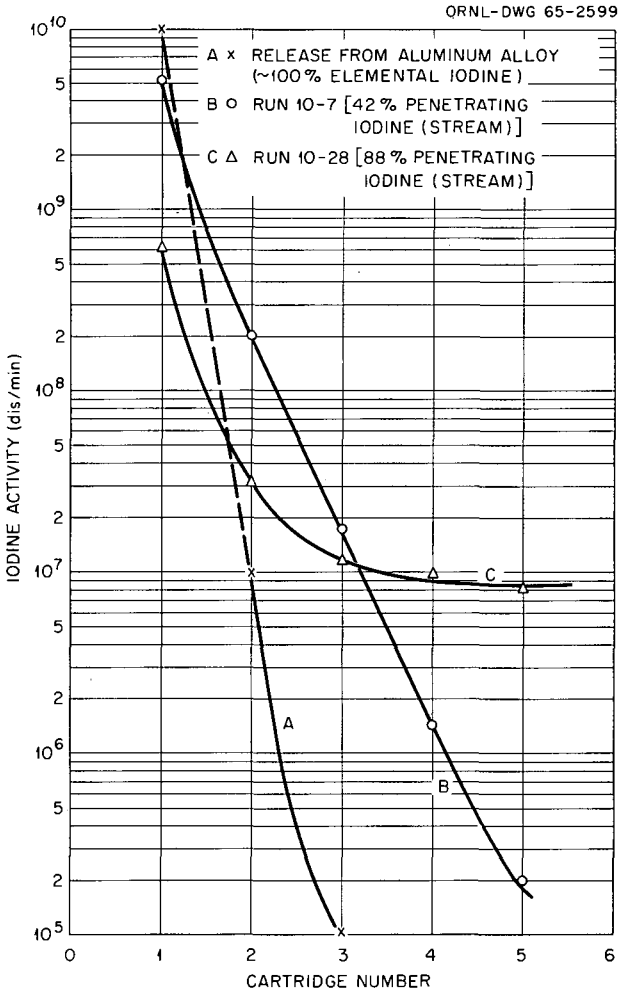

Fig. 16.3. Comparison of the Effect of Chemical State on the Distribution of Iodine in Charcoal Cartridges.

characteristic of reactive iodine is shown by curve A, while that of iodine which was almost completely of the penetrating variety is represented by curve C. Curve B represents a mixture of nearly equal portions.

The curves shown in Fig. 16.3 represent data obtained in runs 10-28 and 10-7 (Table 16.3), in which penetrating iodine (inventory) was 21 and 7% respectively. The nearly pure iodine (curve A) was released from molten uranium-aluminum alloy. The difference in amount of penetrating iodine in the two tests (10-28 and 10-7), both of which had gaseous hydrocarbons added to the containment atmosphere, may be attributed either to the different aging times in the containment shell or to variations in the method of release of the iodine. The major difference between the two tests was that a fuel capsule containing UO_2 was melted and partially vaporized along with the iodine tracer in run 10-28. The extra heating time or the presence of vaporized UO_2 or metallic oxide particles may possibly be responsible for the higher yields of penetrating iodine.

Effect of Atmosphere and Concentration of Iodine

Other factors affecting the behavior of iodine in release tests are illustrated by the data in Table 16.4. Trace-level-irradiated UO_2 was melted in runs A and B, and the retention of iodine in the containment shell, as well as the amount airborne after an aging period of 3 hr, was determined. In both these runs a rather large fraction of the iodine inventory (~30%) remained airborne at the end of the aging period. A higher iodine concentration (2 mg/m^3) was used in runs C and D. Highly irradiated UO_2 was used in run C and simulated high-level irradiated fuel in run D. The lower fraction of iodine deposition obtained in runs C and D suggests that some surface activity interference was provided by the presence of the dry UO_2 aerosol. In contrast to these experiments, run E, in which no UO_2 aerosol was present, showed a rapid rate of uptake by the stainless steel containment shell wall. Run 10-28 (Table 16.3), in which the released aerosol was aged in steam and air, illustrates two opposing effects. The wet metallic surface did not retain iodine as well as a dry surface, but "washout" of iodine from the tank atmosphere by steam condensation more than compensated for the reduced surface adsorption. Another, and possibly more important, conclusion concerns the prevalence of the "penetrating" form of iodine in the run where the tank contained steam as well as UO_2 aerosol. Since the total time in containment (9 hr) was only slightly longer than in several other runs lasting 5 hr, the contribution due to the longer aging time was considered to be small. It is necessary, on the basis of presently available information, to conclude that the UO_2 aerosol in the presence of steam leads to a higher conversion of iodine to the penetrating varieties. The presence of organic gases appears also to be a contributing factor, but neither the extent nor the mechanism can be cited at present.

Table 16.3. Iodine Deposition and Desorption in the Containment Mockup Facility

Percent of total iodine released

	Air	Steam-Air		Steam-Air and Organics			
	Run 6-11[a]	Run 6-25[b]	Run 8-4[c]	Run 7-16[d]	Run 9-10[e]	Run 10-7[e]	Run 10-28[f]
Iodine held in containment tank							
Retained on tank walls	79.6	60.8	38.2	19.3	20.9	24.4	18.3
Collected in steam condensate		34.9	54.0	52.9	47.3	58.2	43.5
Total retention	79.6	95.7	92.2	72.2	68.2	82.6	61.8
Iodine removed from tank							
By pressure release	3.0	1.1	2.4	12.9	8.5	6.2	14.6
By argon displacement	7.4	1.2	2.4	13.3	15.9	7.2	15.7
By air sweep	2.9	0.3	1.7	0.5	2.6	1.2	1.8
Total removed, airborne	13.3	2.6	6.5	26.7	27.0	14.6	32.1
Iodine removed on test samples	6.1	1.7	1.4	0.8	2.2	1.9	0.9
Distribution of airborne iodine from tank							
Retained on filters	4.1[g]	0.5	1.5	0.1	0.3	0.03	0.01
Retained on silver/copper screens	5.3	0.8	2.3	6.4	8.5	2.6	9.1
Retained on charcoal papers	3.0	0.4	0.4	2.0	15.8	1.7	16.3
Retained in charcoal cartridges	0.3	0.6	2.0	16.4	2.3	9.1	6.6
Penetration loss through $\frac{3}{4}$ in. charcoal	0.01	0.08	0.3	3.8	0.17	0.8	0.5
Penetrating iodine (% of inventory)	0.3	0.5	1.2	1.6	2.5	7	21

[a]Iodine was released to the containment shell filled with filtered air only at 30 psia (containment time at full pressure, 4 hr).

[b]Iodine released in steam (20 psia) and air (20 psia) under conditions providing a larger amount of condensate (containment time at full pressure, 4 hr).

[c]Iodine released in steam (~21 psia) and air (~21 psia) and held in containment 18 hr.

[d]An undetermined amount of organic material, acetone, and solid CO_2 was inadvertently included in the iodine tracer preparations. Release was with steam (~20 psia) and air (~20 psia); held in containment 5 hr.

[e]In 9-10 (steam, ~22 psia; air, ~22 psia; containment time, 5 hr) and 10-7 (steam, ~22 psia; air, ~22 psia; containment time, 16 hr) 500 cm^3 of mixed hydrocarbons prepared by hydrolysis of UC-UC_2 were added.

[f]In 10-28, UO_2 was melted above the iodine tracer which in turn was released when the molten UO_2 mixture heated a quartz ampul to its melting or softening point. Released with steam (~22 psia) and air (~22 psia); 9 hr containment time. The same amount of mixed hydrocarbons was present in the tank atmosphere as in runs 9-10 and 10-7.

[g]One organic membrane filter which probably reacted with and retained some molecular iodine in addition to particulate iodine.

Table 16.4. Comparison of the Behavior of Iodine from UO_2 Fuel Meltdown Tests[a] with That of Tracer Iodine in the Absence of Vaporized UO_2

Iodine Disposition	Percentage of Iodine Inventory				
	Low Iodine Concentration		High Iodine Concentration		
	A	B	C	D	E
Total release from fuel	83.8	63.8	90.9	91.6	100
Amount deposited in furnace chimney	6.3	10.6	0.4	0.4	0
Total on aerosol tank wall after 2-hr aging and 2.5-hr gas sweep period	46.5	23.8	25.2	34.2	86
Amount airborne and desorbed from tank wall during 2.5-hr gas sweep period	31.0	29.6	60.4	57.0	13
Amount in penetrating form[b]	3.7	0.4	0.3	0.5	0.3
Loss through 1.5-in. charcoal bed[c]	1.3	0.14	0.03	0.03	0.003

[a]Run A – trace-irradiated UO_2 (approx 1 μg I) with 20% unfiltered air (~5 μg I per m^3).
Run B – trace-irradiated UO_2 (approx 1 μg I) with 100% filtered air (~5 μg I per m^3).
Run C – 7000-Mwd/ton UO_2 (20 g UO_2, approx 400 μg I) with filtered air (~3 mg I per m^3).
Run D – tracer ^{131}I simulation with approx 200 μg I and with filtered air (~1.5 mg I per m^3).
Run E – tracer ^{131}I in filtered air without vaporized UO_2.

[b]Determined from distribution of iodine activity in charcoal beds after removal of elemental iodine.

[c]This is a part of the penetrating iodine activity.

DIFFERENTIATION OF IODINE FORMS BY USE OF COMPLEX FILTER PACKS

An illustration of the technique used in determining the presence of the two major gaseous forms of iodine, "reactive" and "penetrating," is given by data obtained in run 10-28 and shown in Table 16.5. The complex filter pack used to obtain these data is shown in Fig. 16.4.

The effectiveness of some of the components of the filter pack has been found to be substantially reduced by steam, and it has been found necessary to determine the operational efficiency of each stage by means of devices such as a tandem filter pack, as shown in Fig. 16.4, utilizing only a small side stream and a low gas flow rate for maximum performance.

The gas mixture in the containment tank and the iodine desorbed from the tank walls were analyzed in three steps: pressure letdown to atmospheric pressure, displacement of gas in the tank by two or more volumes of argon, and prolonged sweeping of the tank with air. Most of the iodine was transported in the first two fractions, and only a small

Table 16.5. Characterization of Airborne Iodine in Run 10-28[a] as Determined by a Complex Filter Pack

Distribution	Percent of Released Iodine
Retained on absolute filter	0.01
Retained on silver screens	9.1
Retained on charcoal papers	16.3
Retained in charcoal cartridges	6.6
Iodine in penetrating form (% of gaseous iodine in stream which is not reactive to silver)	21.0

[a]Atmosphere contained approximately equal parts of steam and air at 45 psia and 0.15% by volume of mixed hydrocarbon gases. Iodine was released by melting a quartz ampul by exposure to melted stainless-steel-clad UO_2. The initial concentration of iodine was about 2 mg/m^3. The distribution shown here was determined at the end of the 9½-hr aging period in the stainless steel CMF tank.

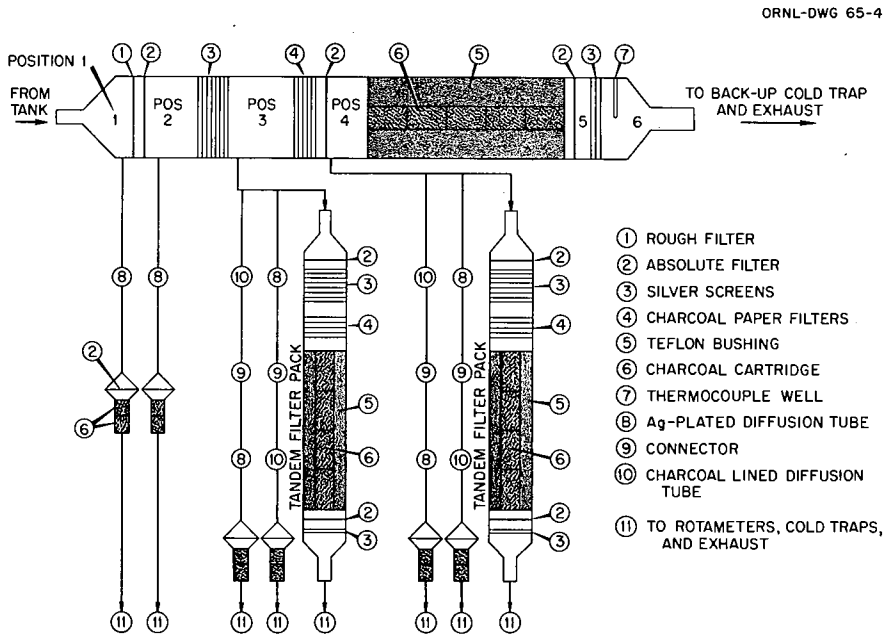

Fig. 16.4. Complex Filter Pack.

amount, with a decidedly higher proportion of free "reactive" iodine, was in the air-sweep fraction.

A side stream was diverted into a tandem filter pack from a small cavity ahead of the charcoal paper (position 3 in Fig. 16.4) to measure the distribution of iodine forms not sorbed by the silver screens. Comparison of the iodine fractions on the silver with that on the charcoal paper and on the charcoal cartridges in the tandem filter pack indicated that only about 13% of the total iodine not sorbed by the silver screens of the main filter pack was in a "reactive" form. The efficiency of the eight silver screens thus appeared to be about 87% for the removal of "reactive" iodine under the conditions of this experiment.

The results outlined above show that in order to obtain reliable characterization results from a filter pack under steam conditions, the efficiencies of the components must be determined by additional means such as tandem filter packs or composite diffusion tubes which accommodate only a small fraction of the gas stream to avoid surface saturation effects.

SIMULATION OF HIGH-BURNUP FUEL

There are strong incentives for using simulated fission products in nuclear safety experimentation instead of obtaining them from high-burnup fuel. Simulation of fission product iodine, which is considered to be the principal hazard in nuclear accidents, has been accomplished in several ways. Methods of simulating other fission products have received very little experimental testing to date. One of the most promising methods, which was used in the test described here, is to incorporate in the fuel material the amount of inactive fission product element corresponding to the desired burnup, together with just enough radioactive tracer to facilitate analysis.

Two 10-g fuel pellets were fabricated containing the following concentration of fission product elements (in milligrams of element per 100 g of UO_2, corresponding to equivalent concentrations for 10,000-Mwd/ton burnup): Te, 14; Ru, 49; I, 7.2; Cs, 27.5; Sr, 11.5; Mo, 60. A slurry of Cs_2CO_3 and $SrCO_3$ was prepared, and iodine was added as

HI, which was neutralized by the carbonate. Millicurie amounts of $^{137}CsCl$, $^{90}SrCl_2$, and $Na^{131}I$ solutions were added to the slurry, which was mixed with 100 g of fine-grain, depleted UO_2. The quantities listed above of ruthenium, tellurium, and molybdenum were added to the UO_2 mixture as the powdered metal after irradiating them for about three days at a flux of 3×10^{14} and allowing a week or more for decay of the shorter-lived activities. After tumbling this mixture in a ball mill, 1-cm-diam pellets were formed by use of a hydraulic press and a maximum total pressure of 15,000 lb. Two 10-g pellets were placed in a stainless steel can and sealed with a press-fit lid to make the fuel specimen. This specimen was melted in the CMF fuel melting furnace, and the resulting aerosol was transferred by an air stream into the stainless steel containment tank filled with a steam-air mixture at a total pressure of 27 psig.

An experiment on release and transport of fission products from high-burnup UO_2 fuel under the conditions used in the present simulation run has not yet been performed, and it is necessary to compare the results of this experiment (run 12-9) with those obtained in run 3-5, in which UO_2 irradiated to 7000 Mwd/ton was melted in air at atmospheric pressure, even if the conditions were not identical. In addition, there were differences in density and in the O/U ratio of the UO_2 specimens as well as in the uniformity of dispersion of fission products in the fuel, and in their chemical form; but in both experiments the fuel melted in air, making release conditions fairly comparable. It was found that release values for four of the most important fission products (iodine, cesium, strontium, and ruthenium) obtained in these two experiments were in reasonable agreement, as shown in Table 16.6. Tellurium release was apparently lower in the simulation experiment by a factor of about 10. The higher O/U ratio in the UO_2 fuel used in the simulation experiment might be expected to favor volatilization of ruthenium, but there seems to be no obvious explanation for the low tellurium release. Molybdenum release results are omitted from this tabulation because of questionable analytical results. The distribution of released iodine in the experimental assemblies in the two experiments was not drastically different, except for the retention of iodine by the condensate in the simulation experiment. Meaningful comparisons of transport behavior of real and simulated fission products must be deferred until other experiments are performed.

Table 16.6. Comparison of Fission Product Release from Highly Irradiated UO_2 with Release from Simulated High-Burnup Fuel

Fission Product Element	Release (%)	
	Run 3-5[a]	Run 12-9[b]
Iodine	91	100
Cesium	37	63
Tellurium	55	8
Ruthenium	<0.1	0.5
Strontium	0.01	0.05

[a]7000 Mwd/ton.
[b]Simulated fuel.

The Containment Research Installation (CRI)

A recent series of unpublished discussions defined the application of small-scale nuclear safety research data on fission product release to the analysis of the proposed meltdown of a 50-Mw test reactor in the Loss-of-Fluid Test (LOFT) being conducted by Phillips Petroleum Company[5] and indicated that serious deficiencies existed in our knowledge of the probable behavior of fission products in an overheated core vessel as well as in a pressurized containment shell.

Demonstration of the extent that fission products, and especially iodine, are retained on the structural material of the stainless steel pressure vessel and in the broken coolant line is of particular importance. There appear to be several factors of particular importance to the LOFT which are not readily studied in existing facilities such as the Nuclear Safety Pilot Plant or the CMF. The needed provisions which are not available in these facilities are:

1. a primary vessel that can be heated to 800°C;
2. a large pressurized containment shell that can be supplied with different interior surfaces including various paints;

[5]T. R. Wilson, O. M. Hauge, and G. B. Matheny, *Feasibility and Conceptual Design for the Step Loss-of-Coolant Facility*, IDO-16833 (Dec. 4, 1962).

3. a fission product aerosol generator capable of melting, oxidizing, or controlling high-temperature heating of 100 g of UO_2 irradiated to the 20,000 Mwd/ton burnup level;
4. a recycle filter test facility with demisting or water-removal equipment for handling steam-air mixtures;
5. provision for alternate simulation of top or bottom breaks in the primary vessel.

In the illustration given in Fig. 16.5, a schematic diagram of the CRI indicates the relative size of the meltdown furnace, the primary simulator, and the containment vessel and also shows the location of some of the proposed instrumentation. In addition to the induction-type heating equipment shown in Fig. 16.5, a high-temperature resistance furnace will be provided for use during long heating cycles.

The Primary Simulator. – The primary heat source will be inside the 30-gal stainless steel tank, and it will be shaped like the cylindrical thermal shields provided in the core vessels of pressurized-water reactors. Auxiliary heating and thermal in-

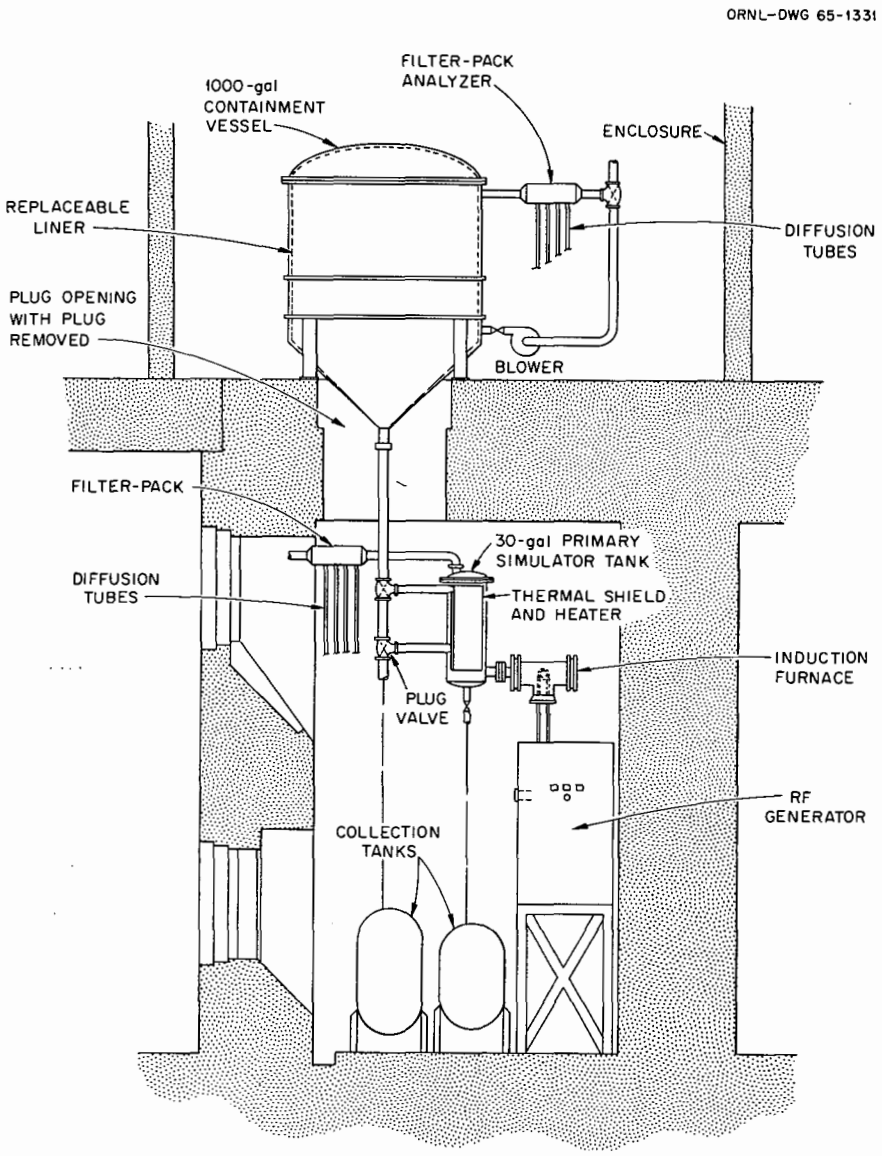

Fig. 16.5. Schematic Diagram of Containment Research Installation.

sulation will be provided externally. The material of construction will be type 304 stainless steel, and the tank dimensions are roughly 12 by 36 in. A flanged head will permit inspection of the interior of the tank, and sample removal ports will also be provided.

Transfer of the fuel aerosol will be mainly by diffusion, convection, and steam expansion resulting from the water heel in the bottom head. A small sample of the vessel aerosol will be withdrawn for assay and for determination of the chemical state of fission products. Material balance will be determined by complete decontamination of the vessel and radiochemical analysis.

The Containment Vessel. – This vessel is to be constructed of heavy-gage stainless steel with a polished interior surface. Provision will be made to insert complete liners through a flanged head. These may be painted or unpainted, as desired, or a single liner may be of several different materials. In this way some special surfaces such as porcelain-enameled steel or Teflon-plated steel may be tested after factor fabrication. Steam and air mixtures will comprise the major part of the atmospheres used in these tests.

Interior sprays will be used for decontamination and material recovery. Because of the size of the tank, most of the aerosol will be displaced through a large disposable filter, and only a small side stream will be passed through a filter pack for sampling. The test filter will be used to measure such effects as organic iodine penetration of the charcoal beds and the decontamination of air by absolute filters.

MELTING POINTS OF MIXTURES OF OXIDIZED FUEL CLADDING WITH UO_2

The presence of oxidized cladding in residues from fuel melting experiments and the probable lowering of the UO_2 melting temperature have been observed in many instances.[6] The presence of a single-phase residue following the melting of zirconium-clad UO_2 in a zirconium oxide crucible has been reported,[7] although the melting point of the product has not been previously measured.

Low melting points resulting from the interaction of oxidized cladding material with UO_2 can affect the release of fission products from the fuel and also drastically affect the distribution of fissionable material in the reactor core in a loss-of-coolant accident. It is conceivable that the fuel could flow into a puddle in the bottom of the core at much lower temperatures than have generally been assumed in hazards analyses.

In a recent experiment to observe the rate of oxidation and the nature of the resulting oxide, a single stainless-steel-clad UO_2 fuel pin was heated slowly in a steam atmosphere to a surface temperature of approximately 1500°C (just above the stainless steel melting temperature). The technique involved was the center-resistor method with a rhodium or graphite resistor element in the center of the cored fuel pin. The rate of reaction of stainless steel with steam was qualitatively observed to increase rapidly as the 1500°C temperature was approached. In fact, it is probable that the limiting factor was the rate of addition of steam to the system.

Closer observation of the fuel surface showed that some of the UO_2 was missing, especially from small, round, spalled-out areas on the surface of each pellet. It was speculated that a low-melting eutectic was being formed occasionally at a point of contact of UO_2 with the oxides of stainless steel. This low-melting material then flowed away with the major part of the cladding. These observations and speculations stimulated interest in preparing some definite mixtures of UO_2 powder and oxidized stainless steel and determining their melting points. In Tables 16.7 and 16.8, some values are given that were obtained both in the presence and in the absence of air. The melting points observed in air (on iridium foil) were always significantly lower than those observed in vacuum (on tungsten foil). The most obvious explanation involves the presence of U_3O_8 instead of UO_2 as the melting phase.

A single specimen of the three-component ZrO_2-Zr-UO_2 system was also melted in air and in vacuum. The melting points are given in Table 16.8.

[6] W. E. Browning *et al.*, *Nucl. Safety Program Semiann. Progr. Rept. June 30, 1964*, ORNL-3691, p. 30.

[7] G. W. Parker *et al.*, *Nucl. Safety Program Semiann. Progr. Rept. June 30, 1962*, ORNL-3319, p. 27.

Two types of stainless steel oxide were tested. One sample was prepared by oxidation in air at 1350 to 1400°C, while the other was made by reacting stainless steel with steam at the same temperature and cooling to 200°C in steam. Results of observations with these materials are also given in Table 16.8. Small differences were observed in the apparent melting point of the oxide, which presumably resulted from the different atmospheres in which oxidation occurred.

A more extensive study of the nature of these low-melting forms and of their significance as a reactor hazard will be pursued as time permits.

Table 16.7. Observed Melting Points of UO_2–Oxidized Stainless Steel Mixtures

Mixture No.	UO_2 (wt %)	Melting Point (°C)	
		In Air	In Vacuum
1	76[a]	1435	1750
2	86[b]	1475	2250
3	93[c]	1650	2600

[a]Approximate composition if all the stainless steel cladding in a given reactor core is oxidized and mixed homogeneously with all the UO_2.

[b]Mixture contains one-half the normal amount of oxidized stainless steel that would be present in oxidized fuel elements.

[c]Mixture contains one-fourth the normal amount of oxidized stainless steel that would be present in oxidized fuel elements.

Table 16.8. Observed Melting Points of Oxidized Stainless Steel and Zirconium Oxide Solid Solution

Product	Melting Point (°C)	
	In Air	In Vacuum
Oxidized SS preparations	~1650[a]	1500–1600[b]
ZrO_2-Zr-UO_2[c]	2150	2450

[a]Exact melting point uncertain; softening occurred 100–150° lower than the temperature of complete melting.

[b]Differences in observed melting points of the two SS oxide preparations indicated that the air-oxidized form melted somewhat lower than the steam-oxidized form.

[c]Sample prepared by melting Zircaloy-clad UO_2 fuel specimen in air by induction heating.

17. Behavior of Fission Products Released During In-Pile Simulated Loss-of-Coolant Accidents

W. E. Browning, Jr.
C. E. Miller, Jr.
R. P. Shields
B. F. Roberts
J. G. Wilhelm[1]
W. H. Montgomery
O. W. Thomas[2]

The characteristics and behavior of fission products released during simulated reactor accidents are being studied in a continuing series of experiments in which fission products are released by melting miniature UO_2 fuel elements in the ORR. The effects of variation of the maximum temperature of the UO_2 and of the effects of rate of sweep-gas flow were studied in earlier experiments.[3] The latest experiments have been performed to study the effects of atmosphere and the effects of sustained heating below the melting point of UO_2. In one experiment fuel having a burnup of 21,000 Mwd/ton was used in the first of a series to investigate the effects of fuel burnup. The use of high-burnup fuel has necessitated the development of equipment for irradiating miniature fuel elements and for hot-cell assembly of the fuel melting apparatus. Detailed results and conclusions of these experiments, together with a discussion of the retention of fission products by cool metal surfaces, filters, and steam condensers, and a discussion of the behavior of iodine released during simulated reactor accident conditions have been reported elsewhere[4] and are summarized here.

[1]Visiting scientist from the Karlsruhe Center for Nuclear Research and Development, Karlsruhe, West Germany.

[2]General Engineering and Construction Division.

[3]W. E. Browning, Jr., *et al.*, *Reactor Chem. Div. Ann. Progr. Repts. Jan. 31, 1961*, ORNL-3127, pp. 149–52; *Jan. 31, 1962*, ORNL-3262, pp. 172–76; *Jan. 31, 1963*, ORNL-3417, pp. 235–43; and *Jan. 31, 1964*, ORNL-3591, pp. 175–81.

[4]W. E. Browning, Jr., *et al.*, *Nucl. Safety Program Semiann. Progr. Repts. June 30, 1964*, ORNL-3691, pp. 29–46; and *Dec. 31, 1964*, ORNL-3776.

EFFECTS OF ATMOSPHERE ON BEHAVIOR OF RELEASED FISSION PRODUCTS

The behavior of released fission products has been studied in atmospheres consisting of moist helium (experiment 12), moist air (experiments 13, 14, 18, and 20), dry air (experiment 15), 87% steam–13% air (experiment 16), and 87% steam–12% helium–1% hydrogen (experiments 17 and 19). Each of these atmospheres simulates a possible atmosphere in a reactor at the time of an accident. Generally, experiments have been performed with trace levels of preirradiation. However, the fuel in experiment 19 had a burnup of 21,000 Mwd/ton. Experiment 20 was performed in order to characterize the released aerosol by means of a fibrous filter analyzer[5] and a composite diffusion tube.[6]

Physical Condition After Melting of Fuels

Visual examination of experiments 12 to 20 in the hot cell showed that the fuel had melted completely in all experiments except experiment 12. The fuel residues were black and glassy in appearance and, in most cases, could not be removed from the ThO_2 container. A significant variation in the environment of the fuel results from the effects of the atmosphere on the stainless steel cladding. Similar changes in the chemical state

[5]M. D. Silverman and W. E. Browning, Jr., *Science* 143, 572 (1964).

[6]W. E. Browning, Jr., R. D. Ackley, and R. E. Adams, *Reactor Chem. Div. Ann. Progr. Rept. Jan. 31, 1964*, ORNL-3591, pp. 185–86.

of the released fission products may result from chemical reaction with the components of the atmosphere. In experiments in which a helium atmosphere was used, the stainless steel remained in the metallic form. In experiments in which moist helium was used, there was partial oxidation of the steel, and in the first experiment using a steam-helium-hydrogen atmosphere there was nearly complete oxidation of the steel. Complete oxidation of the steel occurred in all experiments in which air was a component of the atmosphere.

Distribution of Fission Products and Uranium

Radiochemical analyses of the components of experiments 12 to 18 have been completed. The results from these analyses have been expressed as material released from the fuel zone and as material released from the high-temperature zone. Releases from the fuel zone are somewhat arbitrary in the later experiments because of difficulties in defining the boundary of this zone. In the early experiments, for example, experiment 9, the fuel zone was defined to include the fuel holder and the fuel residue in the holder. In later experiments the fuel holder has been held tight in the ThO_2 cylinder and could be removed only by breaking the ThO_2 cylinder and holder. Graphical techniques are being developed to interpret the distribution of fission products throughout the experimental assembly as a function of the distribution of the fuel rather than with reference to an arbitrary boundary.

The interpretation of the release from a high-temperature zone having a minimum temperature of 1000°C is not complicated by sampling since the zone is well defined and remains the same for all experiments. Table 17.1 gives the quantity of fission products found outside the high-temperature zone expressed as the percent of the total amount found.

The release of iodine, tellurium, and cesium was high in experiment 12 since the fuel was only 20% melted. The data from experiments 13 and 18, which were performed in a moist air atmosphere, show that iodine was released from the high-temperature zone in greater than usual amounts.

Table 17.1. Material Released from the High-Temperature Zone of the Furnace in UO_2 Melting Experiments

Experiment No.	UO_2 Melted (%)	Atmosphere	Gas Velocity at 2850°C (fpm)	Material Released[a]						
				I	Te	Cs	Ru	Sr-Ba	Zr-Ce	UO_2
4, 5, 9[b]	100	Dry helium	60	86	86	71	4	1.4	0.4	0.09
12	0–20	Moist helium	60	86	63	71	0.21	0.79	0.24	0.18
13	100	Moist air	40	95	95	92	22	1.4	0.75	1.1
14[c]	100	Moist air	60	49	42	49	45	21	3.8	5.0
15	100	Dry air	6	68	60	53	0.21	1.6	0.11	0.006
16	100	87% steam, 13% air	60	67	92	42	0.79	0.83	0.13	0.17
17	100	87% steam, 12% helium, 1% hydrogen	60	73	87	30	1.2	3.6	0.47	1.3
18	100	Moist air	60	94	82	74	11	1.4	0.46	0.80

[a]Expressed as percent of total found for each material.

[b]Previously reported data included for comparison.

[c]No preirradiation; irradiated for 105 min. Effects are those of precursors.

The distribution of iodine was unusual in these experiments in that a large amount penetrated all filters and appeared in the first layer of charcoal. The release of zirconium-cerium activity and UO_2 was also greater than usual in both experiments; no explanation for these high releases has been found. These same experiments also show a substantial increase in the release of ruthenium. This is probably due to the formation of the volatile RuO_4, but it is not clear why this volatile oxide was not formed in experiments 15 and 16, which also contained air in the sweep gas. Compared with experiments performed in dry helium, the data for experiment 15, which was performed in a very low flow of dry air, show a reduction in the amount of volatile fission products; this reduction probably results from the reduced sweep-gas flow rate. For all experiments, the iodine behavior is complex; it is discussed in more detail in a later section. The release of tellurium generally does not appear to be affected by the composition of the atmosphere. The release of cesium appears to be affected more by the presence of steam than by the air or hydrogen in the sweep gas, since the release is significantly less in both experiments (16 and 17) which used steam than in experiments performed in dry helium. The releases of the nonvolatile fission products Sr, Ba, Zr, and Ce are much lower than for the volatile fission products and do not appear to be greatly affected by the composition of the sweep gas.

EFFECTS OF SUSTAINED OVERHEATING OF REACTOR FUELS

Experiment 14 was performed to study the effect of long irradiation at high temperature on the behavior and release of fission products. The fuel in this experiment was not preirradiated; it was held at a temperature above the melting point of the stainless steel cladding but below the melting point of UO_2 for 105 min. The sweep gas was moist air. Visual examination showed that the fuel appeared to have melted, contrary to all indications that the fuel temperature was below the melting point of UO_2. A possible explanation can be developed by considering the liquidus curves for mixtures of UO_2 and oxides of the metal components of stainless steel. These curves are not available directly from the literature, but their general nature may be inferred by reference to available data for mixtures with ZrO_2, which is similar to UO_2 in many respects. Figure 17.1 illustrates this similarity for Al_2O_3, for which data are available[7] on both the UO_2 and the ZrO_2 systems. Aluminum oxide is also similar to Fe_2O_3, which is of principal interest here. Figure 17.2 shows the liquidus curves for mixtures of ZrO_2 with the oxides of iron, chromium, and nickel, the constituents of stainless steel.[8] Figure 17.2

[7] E. M. Levin, F. H. McMurdie, and F. P. Hall, *Phase Diagrams for Ceramists*, Part I (1956), Figs. 121 and 149, American Ceramic Society, Columbus, Ohio, 1956.

[8] *Ibid.*, Part I (1956), Figs. 148 and 149, and pt. II (1959), Fig. 1035.

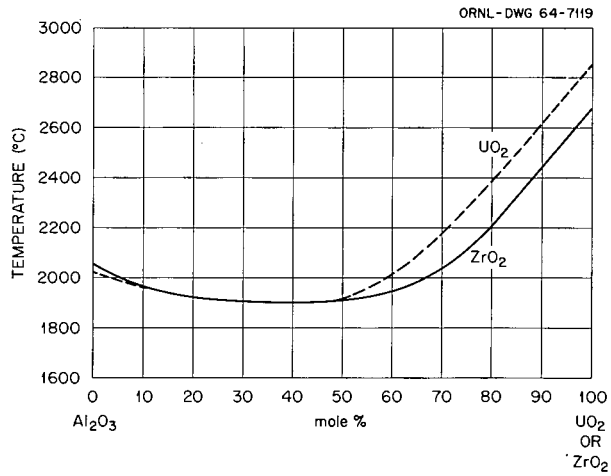

Fig. 17.1. Comparison of Liquidus Curves of the Systems Al_2O_3-UO_2 and Al_2O_3-ZrO_2 to Justify the Use of ZrO_2 as a Stand-In for UO_2 in Phase Diagrams.

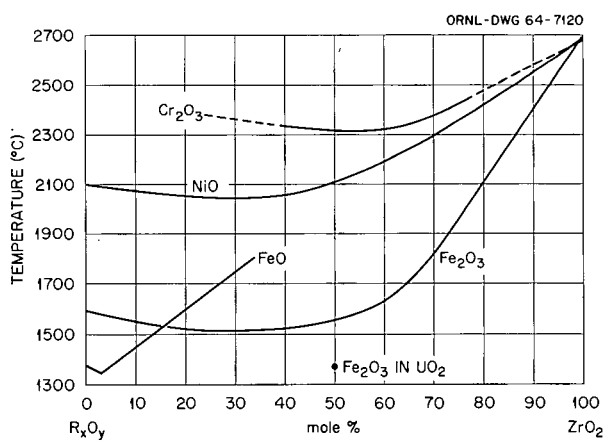

Fig. 17.2. Depression of Melting Point of ZrO_2, a Stand-In for UO_2, by Oxides of Stainless Steel.

also shows a single point which has been reported for the system UO_2-Fe_2O_3.[9] The fuel residue may consist of a relatively low-melting flux of UO_2-Fe_2O_3 with the undissolved excess of UO_2 dispersed as fine grains. This material would be expected to have a slushy consistency and may not flow rapidly from the overheated part of a reactor core; however, it could release fission products readily. Since there were no aged fission products present in the fuel of experiment 14, the release results depend upon the precursor form of the fission product rather than the analyzed form. The release of iodine and tellurium from the fuel itself was reduced. These elements have nonvolatile precursors (tin and antimony). The release of cesium, strontium, and barium occurred as volatile precursors (xenon and krypton). Other fission products, such as zirconium and cerium, and the transported fuel were released to the small degree expected.

The release of fission products from the high-temperature zone (Table 17.1) again indicates the effects of precursors and the long time period. The high release of zirconium, cerium, and UO_2 is believed to be due to the long time period of sweeping. The apparent melting of the fuel (experiment 14) in moist air at a temperature well below the melting point of UO_2 is of potential significance in predicting the movement of fuel in reactor accidents.

FISSION PRODUCTS RETAINED BY COOL METAL SURFACES, BY FILTERS, AND BY STEAM CONDENSERS

To estimate effectiveness of selected components of a simulated reactor safeguards system, retention of fission products and uranium by selected components of the off-gas system of the in-pile fuel meltdown assembly have been determined for the several experiments. Important components for such a study are a "high-efficiency" filter and the relatively cool metal surfaces of the furnace chamber (250 to 400°C), the diffusion tube, and steam condenser, which simulate the reactor vessel and the pipes leading to the containment vessel of an actual reactor.

[9] S. G. Tresvyatskii and V. I. Kushakovskii, *At. Energ.* (USSR) 8, 56 (1960).

The results of this study emphasize the fact that much iodine deposits on the cool metal surface of the reactor furnace, and considerable iodine, tellurium, and cesium deposit in the diffusion tube. However, in experiments 13 and 18 iodine was not deposited on the metal surfaces. Although there is wide variation, generally less than half of the material released from the high-temperature zone of the furnace is found downstream of the diffusion tube. Only very small fractions of the total inventory of nonvolatile elements (ruthenium, strontium, barium, zirconium, and cerium) and only slightly larger amounts of volatile elements (iodine, tellurium, and cesium) are found downstream of a high-efficiency filter. The large amounts of iodine shown for experiments 13 and 18 are probably due to its oxidation to the elemental form by the moist air atmosphere. In this form the iodine was deposited to a lesser extent prior to the charcoal, but only 0.7% penetrated the first 2 in. of charcoal.

In the in-pile melting experiments, it has been generally observed that the efficiency of a "high-efficiency filter" is much lower than the expected value. These low efficiencies could possibly be due to leakage around the filter; a redesigned filter unit, which permits in-place testing after assembly, has been used for the most recent experiments. The efficiency of the high-efficiency filter of experiment 18 (the first experiment for which reliable test data were obtained) is still low for most isotopes; filter efficiency is similar to the efficiency of the old-style filter of the duplicate experiment 13. The low efficiencies may possibly be due to penetration by short-lived gaseous precursors. Another possibility is contamination of certain components of the experimental assembly by material from other components, despite the considerable precautions which are taken to prevent such contamination. This contamination effect is being investigated, and findings will be reported at a later date.

One purpose of adding steam as a component of the sweep gas in certain experiments was to investigate the removal of fission products from the gas stream by condensing steam. The modifications of the experimental assembly to permit the use of steam are described in a later section of this report.

The steam condenser may affect the behavior of fission products in the gas stream in three ways: (1) it condenses steam and may thereby remove

fission products, (2) it provides additional metallic surface area for fission product deposition, and (3) it reduces the sweep-gas velocity by providing additional volume to the system and increasing the time available for deposition. The latter two effects are both due to the physical presence of the condenser and are not distinguished separately here. The conclusions reached from this study are:

1. Generally less than half of the material released from the high-temperature zone of the furnace is found downstream of the diffusion tube.
2. Although the efficiency of high-efficiency filters is generally lower than expected, only a very small fraction of the nonvolatile fission products (ruthenium, strontium, barium, and cerium) and slightly larger amounts of the volatile elements (iodine, tellurium, and cesium) are found downstream of the filter.
3. Fission products investigated (except ruthenium) appear to be removed significantly from the gas stream by condensing steam.
4. Retention of the fission products studied (except ruthenium) due to the physical effects of the condenser (surface area, deposition time) are small compared to that due to condensing steam.
5. The retention of fission products by condensed water can be expected to be a significant factor in reactor accidents where steam is formed.

IODINE BEHAVIOR IN IN-PILE UO_2 MELTING EXPERIMENTS

A large bulk of data on the distribution and behavior of fission product iodine has been obtained from UO_2 fuel melting experiments described in this report. In this section, the methods of obtaining iodine data, assumptions concerning the data, supplemental iodine adsorption experiments performed out-of-pile, and conclusions based on interpretations of iodine data are discussed.

Iodine Analyses

Samples obtained from the experimental assembly are analyzed for eight isotopes: iodine, tellurium, cesium, ruthenium, strontium, barium, zirconium, and cerium. While the usual practice in fission product release experiments is to measure the amounts of isotopes in the system and report the data as percent of the total found, it has been the practice in this in-pile work to calculate the number of fissions occurring by measuring neutron flux, position, time, and ^{235}U content. The recovered isotopes are converted to numbers of equivalent fissions and checked against the calculated number of fissions to ensure a fission product balance. In all cases except iodine, such a balance is usually obtained. In the case of iodine, a balance is seldom obtained, and, in general, less than 50% of the iodine produced is found. Desorption of iodine from the apparatus during disassembly in the hot cells has been observed in one experiment, but such desorption accounted for only about 1% of the total iodine. Iodine loss from standing solutions has also been observed. Future investigations are planned both to measure and control these losses and to detect other losses.

Comparison of iodine data expressed as percent found with data of other volatile isotopes, in which a balance is generally obtained, indicates that the data are consistent and leads to the assumption that the iodine loss from each sample is proportional to the amount of iodine in the sample. Thus, the iodine data are accepted as a valid expression of iodine distribution, but continual efforts are being made to obtain a complete inventory balance.

As much as 30% of the iodine is sometimes found in the hot zone, where the temperature during fuel melting is greater than 1000°C. Since iodine has been observed to desorb from the experimental apparatus during disassembly in the hot cell, this iodine may have deposited in the hot zone after desorbing from some other area during the cooling period. To better understand the adsorption and desorption of iodine in the hot zone, supplemental out-of-pile experiments are being performed. In the first two of these, the effects of stainless steel oxide on the adsorption of iodine from air and steam-helium atmosphere, respectively, have been investigated. The stainless steel oxides were prepared by oxidizing stainless steel in the test atmosphere.

From these experiments, it is concluded that: (1) none of the materials will trap significant quantities of iodine in a temperature region between 1300 and 1400°C; (2) the stainless steel oxide showed a much greater volatility in steam than in air; (3) a considerable amount of iodine plated out together with oxides of stainless steel or on metallic oxides from the stainless steel below 1300°C;

and (4) the plate-out of iodine on ceramic materials at temperatures above 500°C will increase when metallic oxides from stainless steel are present. Thus, it appears possible that the iodine found in the high-temperature zone of the in-pile UO_2 melting experiments results from desorption and readsorption as the zone cools. The possibility of iodine redistribution is to be studied in future in-pile experiments.

Behavior of Iodine Released from the High-Temperature Zone

The distribution of iodine released from the high-temperature zone has been studied. Some important characteristics of iodine behavior which can be observed from this study are: (1) A major fraction of the iodine stops on metal surfaces, but this deposition is inhibited by moisture in the atmosphere. (2) In most experiments iodine which reaches the filters stops on the filters. (3) Less than 0.5% of the total iodine found penetrates the first layer of charcoal. (4) In experiments in which a refrigerated charcoal trap outside the reactor was available, the maximum amount of iodine which penetrated the filter system, in-pile charcoal trap, and outlet tubing was only 0.0001% in three experiments and 0.11% in one experiment. (5) In experiments in which steam atmosphere was used and a steam condenser was present, as much as 50% of the iodine which entered the condenser was stopped in the condenser. (6) Moist air atmospheres are the most likely to produce forms of iodine which penetrate particulate filters; these forms are readily retained by charcoal.

MAJOR MODIFICATIONS AND ADDITIONS TO EXPERIMENTAL EQUIPMENT

Miniature fuel elements with high burnup are required for the study of effects of higher burnups on the characteristics and behavior of fission products released during simulated accidents. A separate facility in the ORR was prepared and is being used to irradiate these UO_2 specimens. Seven capsules can be irradiated simultaneously to provide an adequate supply of high-burnup specimens for future experiments. Most of the irradiated specimens are clad with 347 stainless steel, but some are clad with Zircaloy-2. Power densities attained in the facility will provide irradiated specimens with approximately 21,000 Mwd/ton burnup in a 10.24% enriched UO_2 specimen in approximately six months.

Radioactivity from a capsule whose fuel has been so irradiated requires that the final construction of an experimental assembly be done in a hot cell. The furnace end of the experimental assembly is fastened in a welding machine which is used in the hot cell over the ORR pool (Fig. 17.3). The top of the assembly extends through the top of the hot cell and rests on a framework designed to hold the weight of the experiment and give it rotational freedom. In this position the high-burnup fuel is inserted, and final construction of the assembly, including remote welding, is performed. After the final weld, the experiment is removed from the welding machine and lowered through a hole in the bottom of the cell into the pool water. From here it can be moved, with the radioactive part always under water, to the facility, where the meltdown experiment is performed in the usual way.

In order to perform UO_2 melting experiments in a steam atmosphere, major modifications of the experimental assembly were necessary. These modifications were designed to provide controlled steam injection, to prevent premature condensation, and finally to condense the steam. The problem of supplying the steam at a controlled rate was solved by designing an injector which will supply water at a controlled rate. The water is changed to steam upon entering the hot furnace chamber. If a mixed gas atmosphere is desired, the second gas enters the chamber through a separate line and mixes with the steam inside the chamber. To prevent the condensation of steam before it reaches the condenser, the gas exit tube leading from the furnace to the filter and condenser section of the assembly is surrounded by a steam jacket. At the top of the steam jacket, the gas exit tube turns downward, leaves the steam jacket, and empties into a steam condenser in the shape of an annular can. Any uncondensable gas flows from the condenser to the filters and charcoal adsorber.

Changes in the construction of the filter and charcoal adsorbers have also been made. The

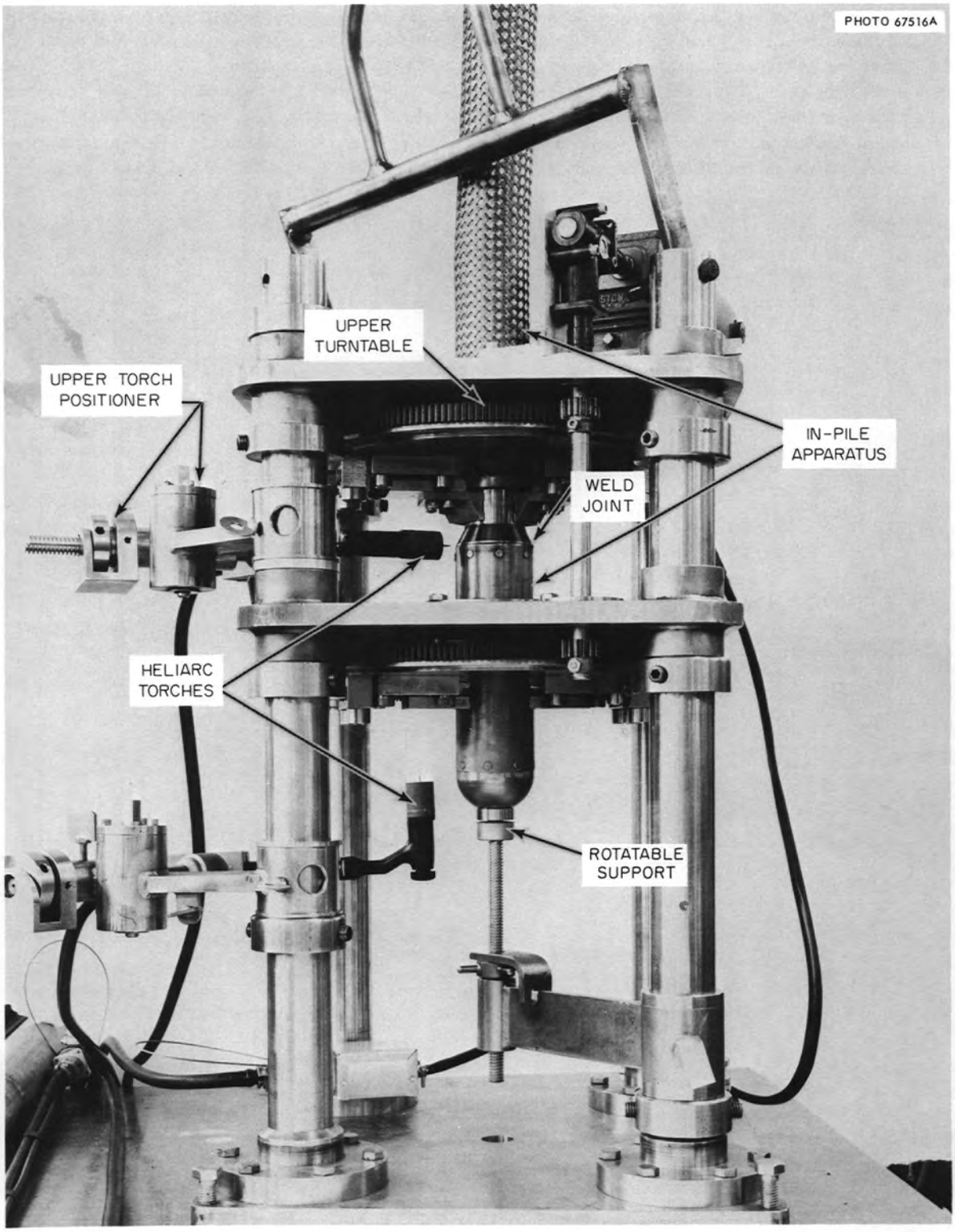

Fig. 17.3. Remote Welder for Assembling Apparatus for In-Pile Melting of High-Burnup Fuels.

new design provides an increased filter area and easier handling in the hot cell. Most importantly, however, it permits in-place testing with a test aerosol of each filter; so the integrity and leak-tightness of each filter is assured after the filter unit is assembled. Finally, greater usefulness and flexibility of the off-gas analysis equipment have been obtained by recent modifications to permit (1) monitoring of the radioactivity of the gas during operation, (2) collection of rare gases in a refrigerated charcoal trap, (3) transfer of the collected gases into an evacuated tank by heating the charcoal trap, and (4) collection of gaseous samples in biological serum bottles.

18. Release of Fission Products During Melting of Fuels Under Reactor Transient Conditions

G. W. Parker R. A. Lorenz J. G. Wilhelm[1]

Miniature fuel elements are melted in a special assembly in the TREAT reactor facility to study the release of radioactive material when the fuel cladding and the fuel are melted or vaporized rapidly, as in a nuclear accident resulting from a reactor transient. The program attempts to measure and interpret the effect upon fission product release of fuel type, cladding, atmosphere during the transient, inventory of fission products, and characteristics of the transient. The extent of reaction of the cladding and of the UO_2 fuel with the covering atmosphere is also determined. Table 18.1 gives a brief summary of progress toward the objectives.

[1]Visiting scientist from Karlsruhe Center for Nuclear Research and Development, Karlsruhe, West Germany.

BEHAVIOR ON MELTING IN MOIST AIR

The initial experiments, designated 1 and 2 and described in some detail along with the experimental assembly and procedures in previous publications,[2] employed unirradiated UO_2; the only fission products available for release were those formed during the reactor transient. Nearly 25% of the gaseous and highly volatile fission product isotopes (which later decayed to and were detected as ^{89}Sr and ^{137}Cs) were released in

[2]G. W. Parker *et al.*, *Nucl. Safety Program Semiann. Progr. Rept. Dec. 31, 1963*, ORNL-3547, p. 25; G. W. Parker *et al.*, *Reactor Chem. Div. Ann. Progr. Rept. Jan. 31, 1964*, ORNL-3591, p. 182; G. W. Parker *et al.*, *Nucl. Safety Program Semiann. Progr. Rept. June 30, 1964*, ORNL-3691, pp. 16–28.

Table 18.1. Summary of TREAT Experiments

Experiment No.	Experiment Status	Cladding	Burnup (Mwd/ton)	Atmosphere Around Fuel During Transient	Initial Fuel Temperature (°C)	Fuel Conditions During Transient
1	Completed	347 SS	0	Ar	800	~2700°C maximum temperature
2	Completed	347 SS	0	Ar	800	65% melted
3	Completed	347 SS	0.3	Air + 3 mole % H_2O, 40 psia	800	75% melted
4	Completed	347 SS	0.3	Air + 30 mole % H_2O, 45 psia	800	75% melted
5	Completed	347 SS	50	1000 psia steam	400	UO_2 heated to approximately melting point
6	Completed	Zircaloy-2	50	1000 psia steam	400	UO_2 and cladding fragmented
7	Under construction	347 SS	50	Under water; low-pressure steam	~100	Complete melting, ~50% vaporization
8	Under construction	347 SS	50	Under water; high-pressure steam	~285	Complete melting, ~50% vaporization

experiment 1 even though little, if any, of the UO_2 melted; from experiment 2, in which about 65% of the UO_2 melted, about 50% of these volatile materials were released.

Two of the experiments (designated 3 and 4) conducted during the past year employed previously irradiated UO_2 clad in stainless steel. The conditions under which the meltings were performed in TREAT are shown in Table 18.2. Reactor transients sufficed to melt the cladding in both cases; the stainless steel flowed to form, in each case, a clean puddle in the bottom of the heater. The fuel appears to have been hotter in experiment 3 than in experiment 4. About 50% of the UO_2 flowed, leaving an outer fuel shell, in experiment 3; only about 30% of the UO_2 flowed in experiment 4. The bulk density of the flowed and frozen material was about one-half that of the original pellet. Neither experiment yielded evidence of fracturing or shattering of the fuel or cladding during the transient. Figure 18.1 shows the appearance of fuel specimen and heater after disassembly of experiment 4.

The steam-air atmosphere produced no drastic oxidation of the fuel or cladding, but subsequent analysis revealed that about 75% of the oxygen had been consumed. Mass spectrometric determinations showed that 38 cm^3 of oxygen (STP) was consumed in each experiment and that 11 cm^3 of CO_2 and 0.4 cm^3 of hydrogen were produced. The CO_2 may have been formed by oxidation of organic material introduced when the irradiated fuel specimen was installed. The amount of hydrogen formed in the system cannot be used as a measure of metal-water reaction, since the reaction of H_2 with O_2 to form H_2O can occur at the high-temperature conditions in these experiments. The size distribution of particles on the first filters of each experiment was identical.

The amounts of eight fission products and uranium in all parts of the apparatus exposed to released aerosol were determined, and a complete fission product balance was obtained. The pretransient irradiation for fission product buildup was only 0.3 Mwd/ton; transient-formed fission products, therefore, contributed significantly to the

Table 18.2. Summary of Operating Conditions for Melting of Preirradiated UO_2 in Moist Air

	Experiment 3	Experiment 4
Reactor integrated power, Mwsec	378	363
Reactor period, msec	74	77
Estimated UO_2 temperature range, °C	800 to mp	800 to mp
Stainless steel cladding temperature, °C	800 to mp	800 to mp
Alumina heater temperature, °C	710 to 1020	780 to 1140
Autoclave wall temperature, °C	108 to 138	162 to 195
Fission energy input, cal per g of UO_2[a]	291	280
Initial fuel autoclave fill:		
Air at 25°C, psia	25	25
Water, g	0.05	0.21
Volume percent steam (assuming complete vaporization)	3	50
Fuel autoclave pressure at start of transient:		
Total pressure, psia	43	53–58
Air partial pressure, psi	42	48
Water partial pressure, psia	1.2	5–10

[a]Calculated using a value of 0.77 cal per gram of UO_2 per megawatt-second determined from experiments 1 and 2.

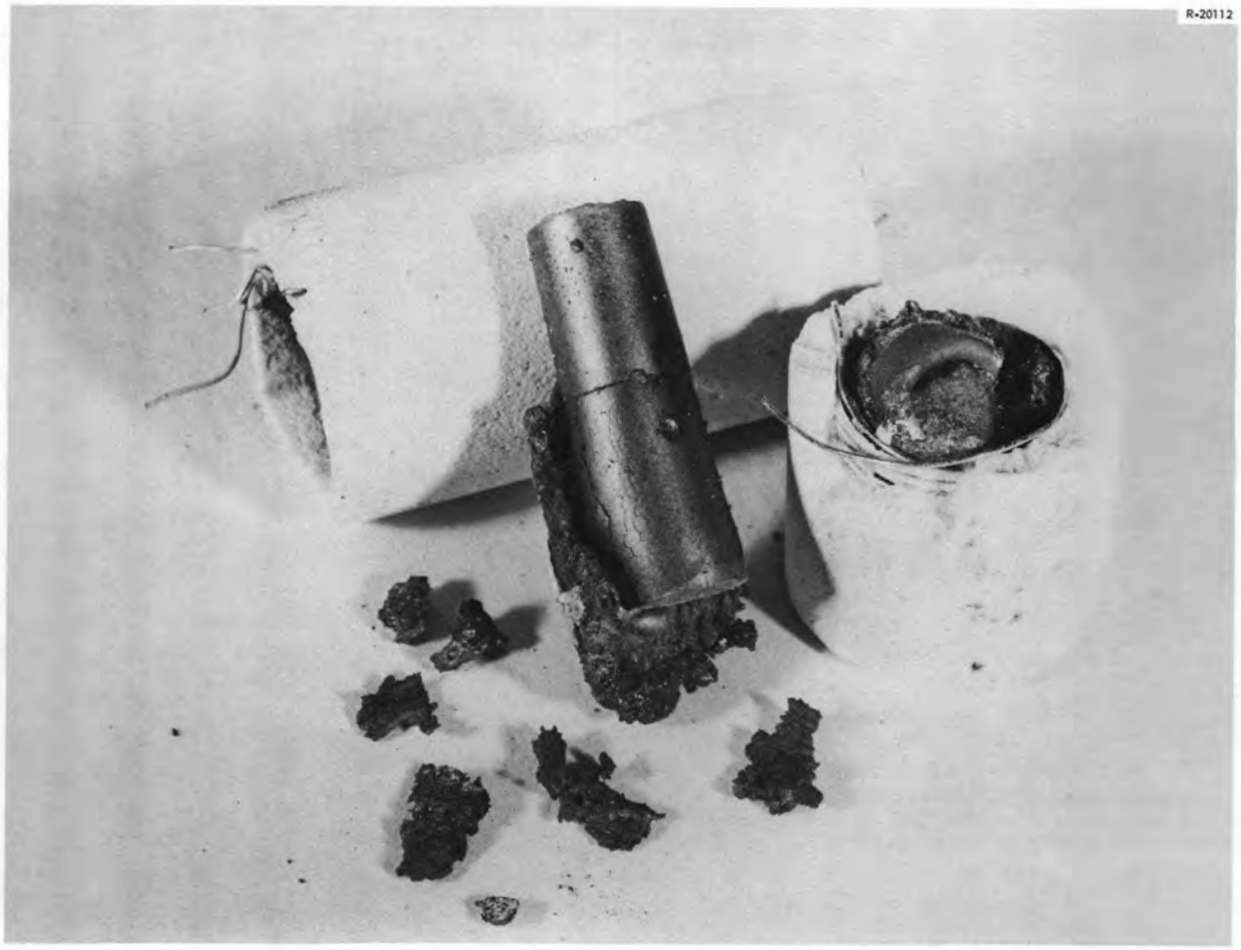

Fig. 18.1. Melted Fuel Assembly and Heater After In-Pile Melting in a Steam-Air Atmosphere Under Transient Reactor Conditions (Experiment 4).

total inventory. As fissioning occurred, the transient-formed fission products existed as short-half-life precursors of the particular isotopes selected for radiochemical analysis. A correction was made for the transient-formed fission products based on release and distribution data obtained in experiment 2. Table 18.3 shows the distribution of fission products in experiments 3 and 4 after this correction was made. The correction was greatest (and individual data points must be considered less reliable) for ^{89}Sr and ^{140}Ba, because their precursors are gases and other volatile isotopes, whose release behavior is greatly different from the daughter isotope of interest. Cross comparisons between similar experiments and isotopes with similar volatilities (I, Te, Cs, for example) are necessary in order to determine the reproducibility and reliability of the data.

In these experiments, the release of aged fission products from UO_2 was less than the release of fission products formed during the transient (experiments 1 and 2); this difference is due primarily to the fact that the "young" transient-born fission products are more volatile than their daughters. Aged fission products did not escape so readily in these transient meltings as did aged fission products in UO_2 melted by slower methods. Release of the "nonvolatile" fission products Sr, Ba, Zr, and Ce were of the same magnitude, in general, as release of uranium in both types of

Table 18.3. Distribution of Material Released from Transient-Heated UO_2 with Transient-Formed Precursors Removed (%)

Release Zone	^{131}I	^{129}Te	^{137}Cs	^{106}Ru	^{89}Sr	^{140}Ba	^{95}Zr	^{144}Ce	UO_2
Experiment 3									
Total release from UO_2 fuel	45	32	38	8	2[a]	3[a]	4	3	3
Release from high-temperature zone[b]	7.0	0.88	1.2[a]	1.5	0[a]	0.7[a]	1.0	0.92	0.86
Transported release[c]	1.2	0.10	0.22[a]	0.0007[a]	0[a]	0.7	0.0006	0.0003[a]	0.0008
Experiment 4									
Total release from UO_2 fuel	41	28	31	1.2	1.6[a]	3[a]	0.6	0.2[a]	0.7
Release from high-temperature zone[b]	8.2	0.70	1.6[a]	0.031	0.56[a]	1.2[a]	0.003[a]	0.002[a]	0.006
Transported release[c]	1.4	0.25	1.2[a]	0.026	0.56[a]	1.2	0.002	0.002	0.001

[a]These numbers required more than a factor of 2 adjustment for transient-formed fission products.

[b]The high-temperature zone includes the fuel, cladding, heater, and autoclave liner.

[c]Transported release includes all material swept out of the fuel autoclave by a 47-cm^3/min flow of gas. No correction was made for the fact that only approximately 60% of the transient-generated aerosol left the fuel autoclave and entered the gas transport zone.

Table 18.4. Summary of Operating Conditions in Experiments 5 and 6

	Experiment 5	Experiment 6
Reactor integrated power, Mwsec	372	366
Reactor period, msec	77	78
Estimated UO_2 temperature range, °C	310–2800	350–2800
Estimated cladding temperature range, °C	310 to mp	350 to mp
Alumina heater temperature, °C	310–630	350–420
Autoclave wall temperature, °C	270+	270–316
Pressure range, psia	1000–50	1000–1360
Fuel autoclave system fill:		
Water, g	30.0	30.0
Argon purge system fill:		
Ar, liters (STP)	9.0	9.0

experiments. Approximately one-third of the volatile fission products I, Te, and Cs were released from the fuel in the transient release experiments; only about 1% of these were released from the fuel autoclave.

BEHAVIOR ON MELTING IN STEAM

Two experiments, designated 5 and 6, were performed using atmospheres of high-pressure steam (1000 psia at the calculated fuel autoclave temperature). The operating conditions for these experiments were chosen to resemble those expected to prevail during an actual reactor transient accident in a water-cooled or water-moderated reactor. Such an accident is most likely to begin while the reactor is shut down and the temperature and pressure are below those of normal operating conditions. The fuel temperature during such an accident should rise quickly, and the environment near the fuel should attain temperature and pressure conditions similar to the starting conditions (see Table 18.4) used in experiments 5 and 6.

A schematic diagram of the apparatus used in experiments 5 and 6 is shown in Fig. 18.2. The specimen and autoclave were electrically heated to the desired operating conditions before the transient was initiated. Immediately after the reactor transient, explosive valve No. 1 was opened; the resulting aerosol rapidly transferred from the fuel autoclave to the condenser, and excess water in the fuel autoclave vaporized to flush out the autoclave. The condensate, collected in two water traps, should contain particles and dissolved gases similar to those which would be trapped by condensing steam in an actual reactor accident. Hydrogen formed as a result of metal-water reaction would pass through the condenser, water traps, filters, and charcoal beds into the gas-collection autoclave. After the steam release was completed, the second explosive valve was opened, and argon gas was passed slowly through the fuel autoclave to sweep gases and vapors through the condenser, water traps, filters, and charcoal bed.

Experiment 5 attempted to melt a stainless-steel-clad UO_2 fuel specimen in steam at 1000 psia. Both valves functioned properly to permit flushing of released materials to sampling devices.

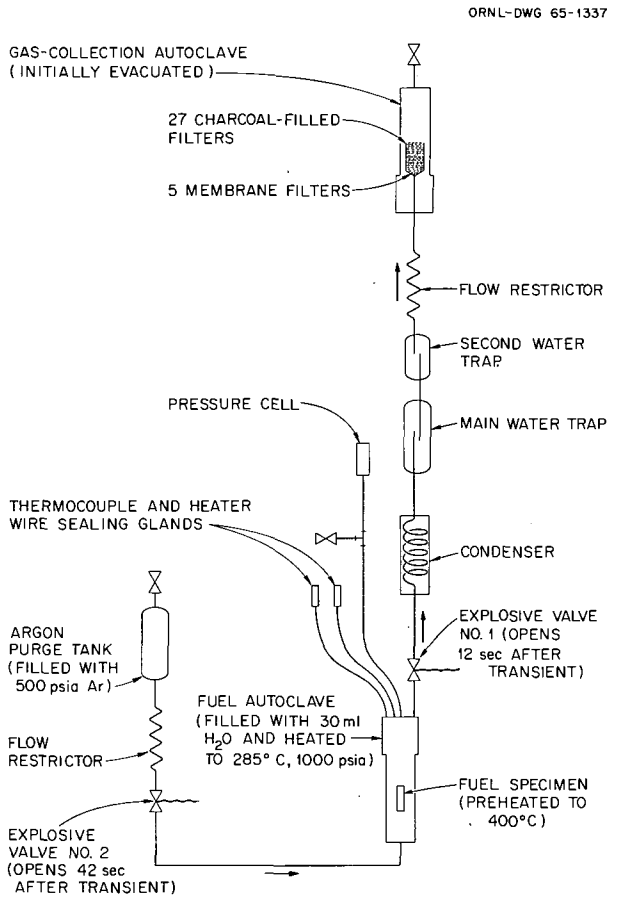

Fig. 18.2. Flow Diagram for Melting Fuel Under Transient Melting Conditions in 1000 psia Steam (Experiments 5 and 6).

The stainless steel cladding melted and oxidized heavily, but it adhered strongly to the UO_2 pellets. The UO_2 did not melt; it appeared to be very nearly in its original condition.

A Zircaloy-2-clad UO_2 fuel specimen was used in experiment 6 with initial conditions and reactor transient very similar to those of experiment 5. The explosive valve failed to function in this experiment. The steam and aerosol remained in the fuel autoclave, and no external steam sampling or argon purge was possible. The fuel and cladding were, therefore, exposed to a total steam and hydrogen pressure above 1000 psia for 23 min following the reactor transient. Figure 18.3 shows the fragmented cladding and fuel which resulted.

The difference in degree of fuel and cladding dispersion between experiments 5 and 6 could have an important effect on fission product release and on possible metal-water reactions. Further studies are in progress to determine the cause or causes of the different fuel behavior observed in these experiments.

Analysis of samples obtained from these experiments is progressing, but no conclusions are yet available.

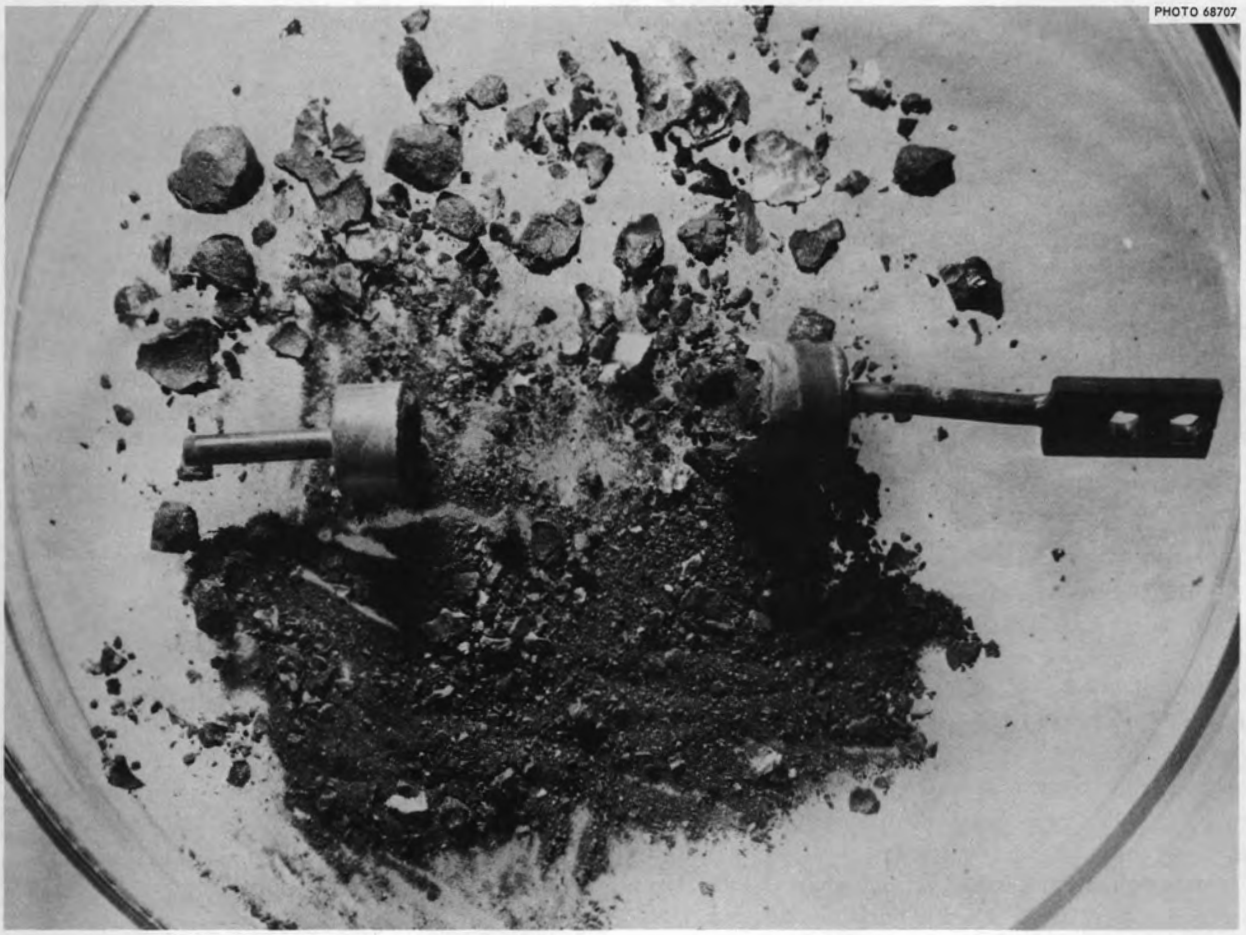

Fig. 18.3. Zircaloy-2-Clad UO_2 Fuel Specimen Heated Under Transient Reactor Conditions in 1000 psia Steam, Showing Fragmented Cladding and UO_2 (Experiment 6).

19. Behavior of Radioiodine

IDENTIFICATION AND BEHAVIOR OF RADIOIODINE VAPORS

Elemental iodine, iodine compounds, and iodine adsorbed on, or combined with, particulate matter will all be present in the gases resulting from a nuclear accident. The behavior of iodine (its retention by charcoal adsorbers, for example) depends markedly upon the form in which it is present. It is necessary, therefore, if adequate decontamination and gas-cleanup systems are to be provided, to ascertain the identity, occurrence, and behavior of these possible forms of radioiodine.

By Solubility Behavior

W. E. Browning, Jr. R. E. Adams
J. G. Wilhelm[1]

Radioiodine, when produced as I_2 by decomposition of palladium iodide or by action of dichromate on alkali iodides, frequently contains chemically combined iodine in small quantities.[2] This chemically combined fraction is of interest because of its similarity to forms of iodine which occur in simulated reactor accidents and is more difficult to trap in "standard" absorber systems. At least one of these forms can be considerably concentrated by volatilization at −78°C. In this study the fraction volatile at −78°C from radioiodine prepared from palladium iodide was equilibrated with the two-phase system: water and nonradioactive methyl iodide. The radioactive compound concentrated (partition coefficient about 55) in the methyl iodide phase. Similar equilibration of a standard (methyl iodide tagged with radioiodine) yielded 46 for the partition coefficient. These results[3] suggest that the volatile fraction includes methyl iodide or an iodine compound of quite similar solubility.

By Knudsen Effusion Cell

W. E. Browning, Jr. R. E. Adams
D. I. Ford[4]

The classical Knudsen effusion method was adapted to study the radioiodine species volatile at −78°C from an elemental iodine source. The apparatus was standardized with ^{85}Kr and ^{131}Xe to determine the effective ratio of orifice area to chamber volume before application of the method to the radioiodine species.[5] The molecular weight of the volatile fraction was shown to be 145; methyl iodide has a molecular weight of 142 to 146, depending upon which isotope of iodine is involved. Results indicate that the volatile fraction consists almost exclusively of methyl iodide.

Work is under way to apply this technique to other forms of radioiodine and to iodine vapors from simulated accidents. Limitations of the method in this application include the requirement that the total pressure of the gas sample be low or that the gas of interest be the major component of the gas mixture.

---

[1]Visiting scientist from Karlsruhe Center for Nuclear Research and Development, Karlsruhe, Germany.

[2]W. E. Browning, Jr., R. D. Ackley, and R. E. Adams, *Reactor Chem. Div. Ann. Progr. Rept. Jan. 31, 1964*, ORNL-3591, pp. 185–86.

[3]W. E. Browning, Jr., R. E. Adams, and J. G. Wilhelm, *Nucl. Safety Program Semiann. Progr. Rept. June 30, 1964*, ORNL-3691, pp. 66–69.

[4]ORINS temporary student employee, 1964.

[5]W. E. Browning, Jr., R. E. Adams, and D. I. Ford, *Nucl. Safety Program Semiann. Progr. Rept. Dec. 31, 1964*, ORNL-3776.

By Gas Chromatographic Identification

W. E. Browning, Jr. R. E. Adams
J. E. Attrill[6]

Gas chromatography has been used to identify some of the volatile (−78°C) iodine compounds which are formed when elemental iodine is produced. This technique has also been used to trace the behavior of known vapors in composite diffusion tubes and to calibrate these characterization devices. Initial work is being conducted with nonradioactive iodine sources. Equipment is being assembled which will permit a parallel study using radioactive iodine sources.

Samples of nonradioactive elemental iodine, produced by both the palladium iodide and the dichromate method, were processed through the chromatograph. Two to six chromatographic peaks appeared; the number depended upon the history of the iodine source being studied.[7] The volatile fraction (at −78°C) from the various iodine sources has been shown to include methyl iodide, propyl iodide, and hydrogen iodide in addition to the noniodine materials, water, air, and methyl chloride.

The response of composite diffusion tubes was studied with known vapors of elemental iodine and methyl iodide. Several samples of elemental iodine were passed through either glass tubing or silver-lined copper tubing maintained at room temperature. The iodine vapor passed through the glass tubing without change, but all the iodine was retained by the silver surface. No compounds of iodine were observed in the effluent from either tube. The effluent gas obtained by passing small samples of methyl iodide (0.1 μl of liquid) through glass or silver-lined tubes was shown by gas chromatography to be methyl iodide, unchanged and unadsorbed by the tubes. When a charcoal-lined tube was used, both iodine and methyl iodide were completely adsorbed. This behavior is consistent with interpretations previously reported of results obtained with radioactive iodine sources.

[6]Analytical Chemistry Division.

[7]W. E. Browning, Jr., R. E. Adams, and J. E. Attrill, *Nucl. Safety Program Semiann. Progr. Rept. Dec. 31, 1964*, ORNL-3776.

By Fractional Sublimation and Mass Spectrometry

W. E. Browning, Jr. M. E. Davis

Samples of ^{127}I labeled with ^{131}I were prepared from palladium iodide and were fractionally sublimed at temperatures of −78, −66, −58, −7, and +10°C. The relative intensities of the mass peaks observed in the various fractions were compared with those in methyl iodide and hydrogen iodide standards.[8] In all samples the prominent peaks could be accounted for by iodine, methyl iodide, and hydrogen iodide. The higher relative intensities of peaks corresponding to methyl iodide were found in the sample sublimed at −78°C.

By Composite Diffusion Tubes

W. E. Browning, Jr. R. D. Ackley
A. F. Roemer, Jr.[6]

Investigation of the nature and behavior of volatile radioiodine by diffusional deposition has been continued using the previously described composite diffusion tubes.[2] These tubes, developed to distinguish and measure various vapor species of iodine, have consecutive inner walls of silver, rubber, and finely divided activated carbon. Silver is employed for the deposition of elemental iodine; rubber, for a species as yet unidentified but which yields a fairly characteristic deposition profile; and activated carbon lining, for methyl iodide and for other species penetrating the silver and rubber sections. This work on vapor forms of iodine is described in detail elsewhere.[9,10]

An experiment was performed to examine in greater detail certain previously observed aspects of iodine behavior in composite diffusion tubes. Iodine was volatilized from a melt of $Na^{131}I$, $K^{127}I$, and $K_2Cr_2O_7$, collected in a cooled U-tube, and introduced into the experimental apparatus by a small air stream flowing into a diluent air stream.

[8]W. E. Browning, Jr., and M. E. Davis, *Nucl. Safety Program Semiann. Progr. Rept. Dec. 31, 1964*, ORNL-3776, and ORNL-TM-1009 (Nov. 30, 1964).

[9]W. E. Browning, Jr., and R. D. Ackley, *Nucl. Safety Program Semiann. Progr. Rept. June 30, 1964*, ORNL-3691, pp. 58–65.

[10]W. E. Browning, Jr., R. D. Ackley, and A. F. Roemer, Jr., *Nucl. Safety Program Semiann. Progr. Rept. Dec. 31, 1964*, ORNL-3776.

The air employed was filtered and was relatively dry. After mixing, the combined air streams flowed into a Teflon header to which was attached a number of diffusion tubes of various configurations.

Data derived from two separately located, but simultaneously exposed, composite diffusion tubes are illustrated in Fig. 19.1. Of the indicated diffusion coefficients, those regarded as real, that is, based upon predominantly diffusion-controlled deposition, are denoted by D, while those regarded as apparent are denoted by D'. The data show that the only significant change as the gases flowed through the Teflon header between the sampling stations was in the concentration of that iodine species which deposits on a rubber surface.

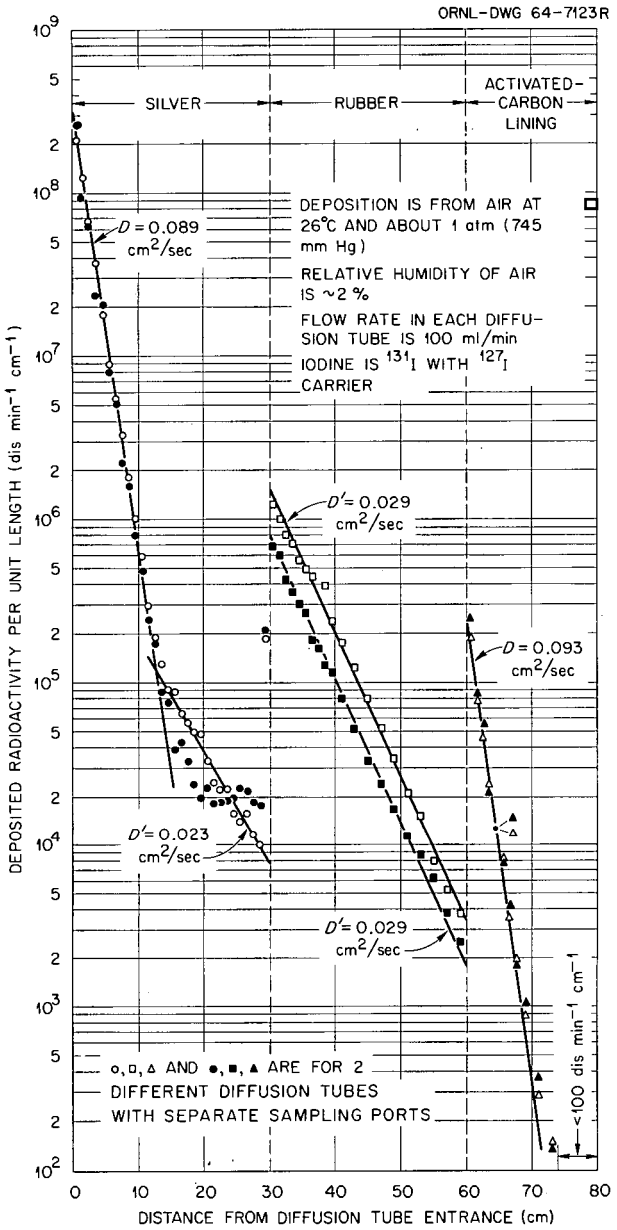

Fig. 19.1. Deposition of Airborne Radioiodine Species in Composite Diffusion Tubes.

Information from these and from modified diffusion tubes and from related experiments in which the temperature of the iodine source and the diameter of the diffusion tube were varied lead to the following observations concerning airborne iodine prepared by the dichromate method: The vapor contains at least two distinct species besides I_2; one of these is probably methyl iodide. The other species, which appears somewhat unstable, has not as yet been identified; it or its decomposition product(s) tends to deposit on a rubber surface. It exhibits a complex deposition behavior which is not solely diffusion controlled, and it may consist of more than one compound. At 0°C, the bulk of this species has an indicated vapor pressure ~1% that of I_2. This or a similarly behaving species has recently been observed in iodine vapor experiments performed in the Nuclear Safety Pilot Plant. Efforts to determine its nature and identity more explicity will receive emphasis in future work.

Identification and Determination of Radioiodine Species in Steam

W. E. Browning, Jr. R. E. Adams

Since steam would probably be released in a reactor accident, it is necessary to be able to measure the amounts of the various forms of radioiodine occurring in steam atmospheres. In the planned Loss of Fluid Test (LOFT), it will be necessary to make such measurements in the containment vessel.

Composite diffusion tubes have been demonstrated to serve these purposes at room temperature and under dry conditions, but relative humidity levels ranging from 30 to 80% produced some interference with the deposition of the organic iodide (Ch_3I) on the activated-charcoal-lined portion of the diffusion tube assembly.[2] This effect probably results from water interfering with retention of the iodine compound on the charcoal surface rather than its reacting to form a new, less-reactive compound of iodine. The moisture has less effect on the silver-lined portion of the

diffusion tube assembly. Composite diffusion tubes at 100°C yield reliable information (though the deposition profile was altered slightly) when dry air is the test medium.[9] Development of conditions under which composite diffusion tubes could serve in a steam-air environment seemed possible.

Experiments were conducted in which a diffusion tube assembly was heated to temperatures above 100°C to minimize condensation of steam on the surfaces and, hopefully, to keep the interference of water on the adsorption of organic iodides to a negligible level. A modified diffusion tube assembly containing only a silver-lined tube followed by a charcoal-lined tube was studied initially. The tubes were heated by a steam jacket to temperatures ranging from about 110 to 130°C, and air-steam mixtures, 60 to 80% saturated, containing iodine vapors were used. Iodine sources were fractionated into the organic iodides, volatile at −78°C, and less volatile, primarily elemental I_2; the behavior of both fractions was studied in steam environments. Deposition profiles from the volatile fractions were affected in much the same manner as those profiles obtained at room temperature with moist air. Deposition of iodine vapor from the less-volatile fraction was not as badly affected. The diffusion tube response was not as helpful as was hoped; however, with temperature control of steam condensation and adsorption, it was sufficiently discriminative to indicate the presence or absence of compounds of iodine in a steam environment.

Preliminary attempts to adsorb the water vapor selectively have been unsuccessful. Type 3A molecular sieves trapped both H_2O and the organic iodide(s). Further tests with selective adsorbents will be made.

CHEMICAL BEHAVIOR OF RADIOIODINE VAPORS

Iodine Sorption by Filter Materials in a Particulate-Free Atmosphere

G. W. Parker Alberto Ferreli[11]

Filters have been used in May packs to separate particles carrying iodine from other forms of iodine and from other fission products. There have been indications that molecular iodine reacted with, and was thus retained by, some filter materials, giving erroneous indications of the amount of particle-borne iodine present in the sample gas stream. Apparently, there has been no systematic investigation of iodine retention by filter materials.

The iodine adsorption behavior of six different filters in a particulate-free atmosphere was investigated. The filters tested were:

1. Whatman No 40 (cellulose);
2. AEC high-efficiency filter (asbestos and fiber glass);
3. Millipore Microfiber glass, type AP-20, high-efficiency filter (glass fibers with acrylic binder);
4. Millipore Microweb membrane, type WH, 0.45-μ pore size (cellulose ester, nylon reinforced);
5. Gelman Polypore membrane, type GM-3, 1.2-μ pore size (cellulose acetate);
6. Gelman Acropore, type VNW 450, 0.45-μ pore size (polyvinyl chloride, nylon reinforced).

The test equipment (see Fig. 19.2) consisted of an iodine injection system, a sample section, a bypass line, and a vacuum source (building vacuum). Stable iodine tagged with ^{131}I released by heating sodium iodide with potassium dichromate in a U-tube was introduced into the system by passing room air through the heated U-tube. Filter containers, each with two AEC filters, were located upstream and downstream of the U-tube to provide a particulate-free atmosphere in the sample section.

The sample section consisted of six filter containers, connected in parallel, each followed by a ¾-in.-deep activated-charcoal cartridge. The flow rate through each 1-in.-diam filter was measured by a rotameter, and kept at a constant value of about 200 cm^3/min in all tests. The corresponding linear velocity was about 88 cm/min.

The percent of the iodine adsorbed on each filter, referred to all the iodine that passed through it, was measured. The results, with the averages and the probable errors, shown in Table 19.1, indicate that the cellulose filter (Whatman No. 40) adsorbed the smallest amount of iodine and that polyvinyl chloride and cellulose acetate filters had the highest adsorption capacity under the test conditions employed. The Millipore microweb filter adsorbed the least iodine among the membrane-type filters tested.

[11] Visiting scientist from Euratom, Ispra, Italy.

ORNL-DWG 65-1309

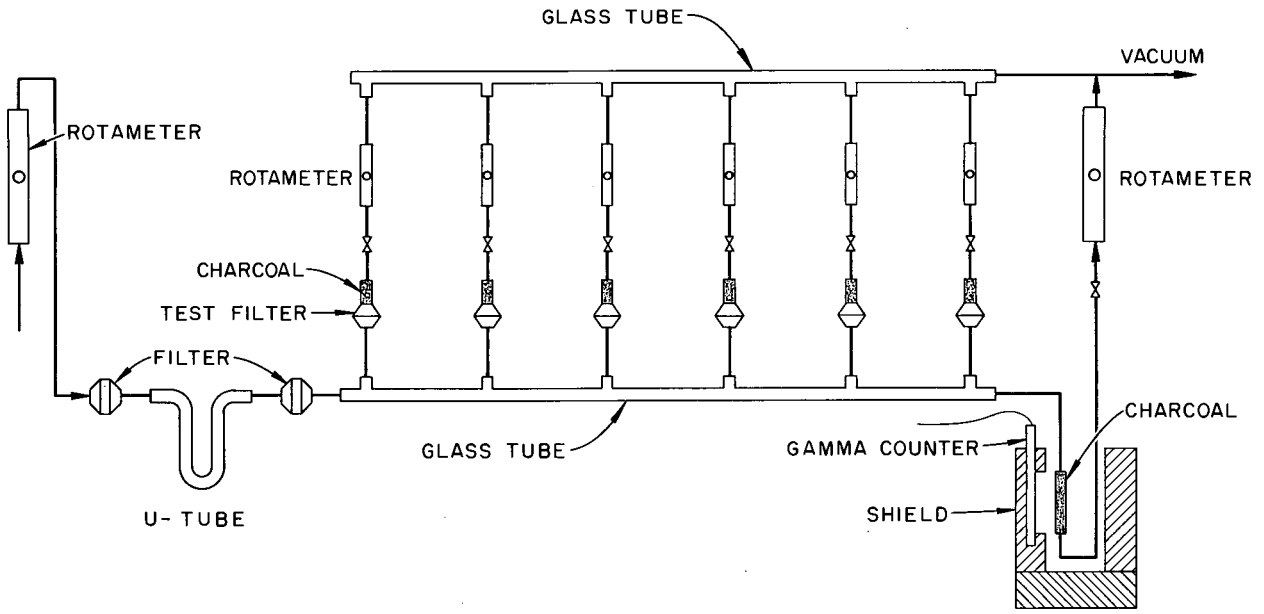

Fig. 19.2. Filter Test Assembly.

Table 19.1. Percent of the Iodine Adsorbed on Various Filter Materials Referred to All the Iodine Passed

Run No.	Filter Position[a]	Whatman No. 40	AEC	Millipore Microfiber Glass, Type AP-20	Millipore Microweb Membrane, Type WH	Gelman Polypore Membrane, Type GM-3	Gelman Acropore Membrane, Type VNW-450
1	a		2.5	2.2	6.0	31	
2	a	0.55	1.6	3.5	4.0	27	49
2	b	0.70	2.0	2.7	4.5	29	42
3	a	2.1			7.1	27	33
3	b	2.0			7.1	37	25
3	c	0.97		2.3	7.0	30	23
3	d	0.74	3.3		6.9	22	33
Average ($\bar{\mu}$)		1.2	2.3	2.7	6.1	29	36
Probable error (ϵ)		0.5	0.5	0.4	0.9	3	
$\bar{\mu} \pm \epsilon$		1.2 ± 0.5	2.3 ± 0.5	2.7 ± 0.4	6.1 ± 0.9	29 ± 3	36 ± 6

[a]Positions expressed sequentially, starting upstream.

The iodine concentration did not seem to have an important effect on the retention of iodine by filters in the range explored (1 to 10 mg/m^3). Other aspects of the filter absorption phenomenon, such as linear velocity dependence and desorption, will be explored in future experiments.

Reaction of Radioiodine Vapors with Organic Vapors

W. E. Browning, Jr. R. E. Adams

Reaction between elemental iodine and organic vapors in a reactor containment vessel following an accident could produce radioiodine compounds which are more difficult to trap than the original iodine. To assess this possibility, composite diffusion tubes have been used to measure radioiodine in various vapor forms in an air stream upstream and downstream from the point of introduction of air contaminated with organic vapors. The initial experiments have been made in a dry air atmosphere at 24°C, with contact time between the organic vapors and vapors of iodine or iodine compounds ranging from 12 to 15 sec. Two heated sources of organic vapors have been used; one was a mixture of items commonly found in reactor containment zones (lubricating oil, plastic and rubber insulation material, and paint scrapings) and the other was dioctyl phthalate (DOP), an organic used for in-place testing of particulate filters in off-gas systems. Very little or no effects by organic vapors from either organic source were noted on the volatile constituent (mainly CH_3I) separated from an iodine source. It appears from these initial experiments, however, that some of the I_2 vapor did react with the organic vapors and was changed into iodine forms which presented a different deposition profile in the downstream diffusion tube.

In the first experiments it was not apparent whether the altered deposition profile was produced by an organic iodine compound or by interference by adsorbed organic vapors with deposition of iodine on the inner surface of the diffusion tube. A third diffusion tube, pretreated with the appropriate organic vapor(s), was installed adjacent to and in parallel with the tube upstream of the point where the organic vapor(s) was added. Diffusion tube deposition profiles for the three tubes in an experiment with DOP vapors are shown in Fig. 19.3. It appears that there is no significant difference in the deposition profiles in the two upstream diffusion tubes, while there is a significant difference produced in the profile of the downstream tube. The deposits on both silver and rubber have changed, while the deposit on charcoal remains the same. These data suggest that 10% of the I_2 reacted with the organic vapor to produce an iodine compound which deposits on silver and on rubber surfaces.

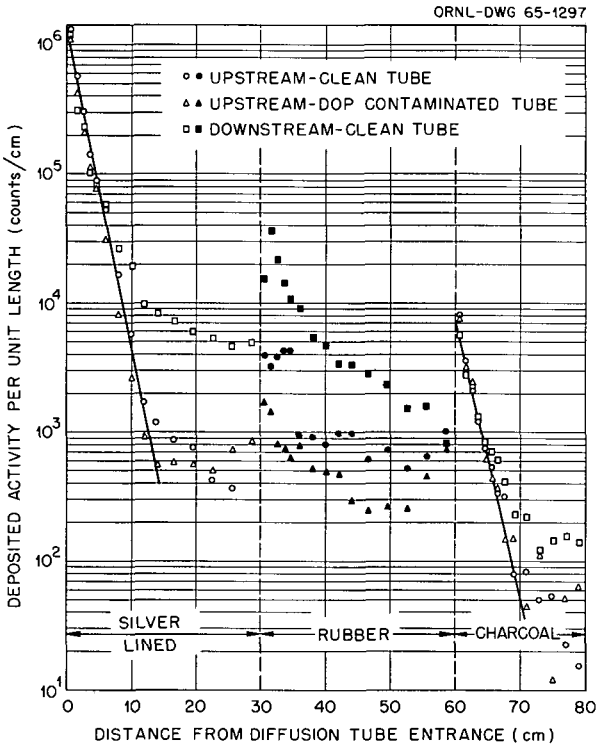

Fig. 19.3. Effect of Dioctyl Phthalate (DOP) Vapor on Forms of Radioiodine.

This study of the influence by organic vapors on the behavior of elemental iodine is being continued under varying conditions of temperature and contact time between the vapors.

Deposition of Radioiodine on Heated Steels

G. W. Parker G. E. Creek

A study was made of the deposition of iodine from flowing gas streams on heated mild steel and stainless steel surfaces. Two-foot-long tubes of

Table 19.2. Deposition of Iodine on Heated Metal Surfaces Exposed to Flowing Gas Streams

Trial No.	Temperature at Peak of Distribution Curve (°C)	Atmosphere, 600 cm^3/min of carrier gas	Condensate (ml)	Tubing Tested	Percent of I_2 Deposited in Tube	Percent of I_2 in Condensate	Percent of I_2 in Charcoal	Total Not Deposited
1	400	He-steam	2	Stainless	95.8	1.9	2.4	4.3
2	550	He-steam	2	Mild steel	99.7	0.08	0.3	0.4
3	150	Air-steam	12	Stainless	14.6	76.1	9.3	85.4
4	400	Air-steam	8	Mild steel	74.0	15.1	10.9	26.0
5	300	H_2-steam	5	Stainless	94.1	3.9	2.0	5.9
6	550	H_2-steam	5	Mild steel	96.5	2.4	1.1	3.5
7	250	He-steam	8	Stainless	69.2	17.4	13.4	30.8
8	460	He-steam	4	Mild steel	94.5	4.5	1.0	5.5

these metals were placed in a furnace with a temperature gradient of about 30°/in., and the distribution of iodine in the tubes was determined as a function of wall temperature after exposure to an iodine concentration of approximately 30 mg/m^3 in streams of different carrier gases including helium-steam, hydrogen-steam, and air-steam mixtures. Data obtained in eight experiments are given in Table 19.2. Mild steel tubes retained 95 to 98% of the gas-borne iodine when air was absent as compared with 70 to 95% for stainless steel tubes. In the presence of air, the retention on mild steel was 75%, while stainless steel retained only 15%. A wide variation in the temperature at the peak of the iodine distribution curves was noted. The data confirm observations by other investigators that heated mild steel retains iodine rather efficiently in reducing, neutral, or oxidizing atmospheres, while very little iodine stays on stainless steel in oxidizing atmospheres at temperatures above 250 or 300°C.

Sorption of Radioiodine and Radiocesium by Metals

W. E. Browning, Jr. M. E. Davis

Studies of the sorption of gas-borne fission products by stainless steel are being continued to provide information on surface contamination that may be expected in gas-cooled-reactor coolant systems and to ascertain, in the event of nuclear accidents, the extent that structural surfaces may act as traps for released fission products. The sorption of iodine, tagged with ^{131}I, and of cesium, tagged with ^{134}Cs, formed by neutron irradiations, is studied on metal surfaces (generally stainless steel tubing) under vacuum.[12] Previous information[12] showed that sorption of I_2 by stainless steel apparently changes the surface, and reproducible sorption isotherms cannot be obtained. Reaction of I_2 with stainless steel surfaces seems to follow a logarithmic rate law; this surface reaction is slower the more highly oxidized the steel surface.[13] Sorption of cesium by stainless steel, under investigation using similar techniques, occurs much more slowly, but surface coverages are much higher than those observed with iodine.[13] Analysis of data from experiments with cesium on stainless steel with differing surface oxidation is in progress.

The number of curies of fission product tellurium, iodine, and cesium that would be deposited in the ducts of gas-cooled reactors has been estimated, assuming that a monolayer of each element could be sorbed by the duct surface.[13] After

[12] W. E. Browning, Jr., and M. E. Davis, *Reactor Chem. Div. Ann. Progr. Rept. Jan. 31, 1964*, ORNL-3591, pp. 186–88.

[13] W. E. Browning, Jr., and M. E. Davis, *GCR Program Semiann. Progr. Rept. Oct. 31, 1964*, ORNL-3731, p. 145.

three years' operation the largest deposits are 22 mc/cm^2 for ^{133}I, 5.2 mc/cm^2 for ^{129m}Te, and 0.94 mc/cm^2 for ^{131}I.[8]

Fission products deposited on structural surfaces may subsequently desorb as a different chemical species with altered behavior toward adsorption systems. Estimation of the predominating desorbed species for certain fission-product–metal interactions has been undertaken using thermochemical information. Preliminary calculations indicate that over the range 100 to 1000°C, iodine would desorb from silver and iron surfaces as AgI and FeI_2 respectively. Experimental work is being extended to include surface and transport conditions that simulate reactor accident situations, to obtain fundamental kinetic and thermodynamic information on sorption in such systems. Theoretical calculations will be extended to include various fission product compounds that would be important in fission product transport and deposition.

Iodine Behavior in May Packs

W. E. Browning, Jr. R. D. Ackley

The iodine samplers referred to as May packs[14] have been extensively employed by British and, more recently, by American workers in studying the nature and behavior of the various forms of gas-borne radioiodine. They are currently employed in the Nuclear Safety Pilot Plant (NSPP), and are being considered for use in the Containment Systems Experiment (CSE) and in the Loss-of-Fluid Test (LOFT) at Arco, Idaho. In view of this widespread application of May packs, investigation of their capability for discriminating between the different forms of iodine encountered in gases became desirable. Composite diffusion tubes have been used in this study.

Two experiments, described in considerable detail elsewhere,[15,16] have been performed. In both, iodine, prepared by the dichromate method, was introduced into an air stream which flowed through a May pack equipped with diffusion tubes between the various parts. In the first experiment, the relative humidity of the air was about 2%, while in the second, it was approximately 60%. The apparatus used for the high-relative-humidity test is shown in Fig. 19.4. The component parts of the May pack and their functions are as follows: (1) copper gauze to remove I_2, (2) a membrane filter to remove iodine associated with particulates, (3) carbon-loaded filter papers to remove readily adsorbed iodine compounds, and (4) granular activated carbon to remove less readily adsorbed iodine compounds. The diffusion tube heated to 100°C was included to augment the data corresponding to diffusion tube application at higher temperatures. The May pack and the other five diffusion tubes were at 25°C.

The depositions for the diffusion tubes of the 60% relative humidity test were resolved by statistical analysis into various components, as illustrated for one of the tubes in Fig. 19.5. There, the depositions on silver, rubber, and activated-carbon lining are regarded as the manifestations of two, three, and one iodine species respectively. Processing of the diffusion tube data was facilitated by use of a digital computer and a machine curve plotter.

The behavior of volatile iodine in the two May packs, one operated with fairly dry air and one operated with moderately moist air, was observed to be generally consistent with the designed functions of the May pack components. However, for the case of fairly dry air, the May pack did appear to identify about 1% of the elemental iodine as being in a nonelemental form. Such a discrepancy, even though small, could be of considerable significance in the design of iodine-removal systems of high efficiency. On the other hand, this apparent mislabeling of elemental iodine (not observed when moist air was used) may have been the result of the presence of an unstable iodine compound which produced I_2, or a similarly behaving substance, as it traversed the May pack. This aspect is to be investigated further.

---

[14] W. J. Megaw and F. G. May, *J. Nucl. Energy: Pt. A & B* [Reactor Sci. Technol.] **16**, 427–36 (1962).

[15] W. E. Browning, Jr., and R. D. Ackley, *Nucl. Safety Program Semiann. Progr. Rept. June 30, 1964*, ORNL-3691, pp. 52–58.

[16] W. E. Browning, Jr., and R. D. Ackley, *Nucl. Safety Program Semiann. Progr. Rept. Dec. 31, 1964*, ORNL-3776.

ORNL-DWG 65-1299

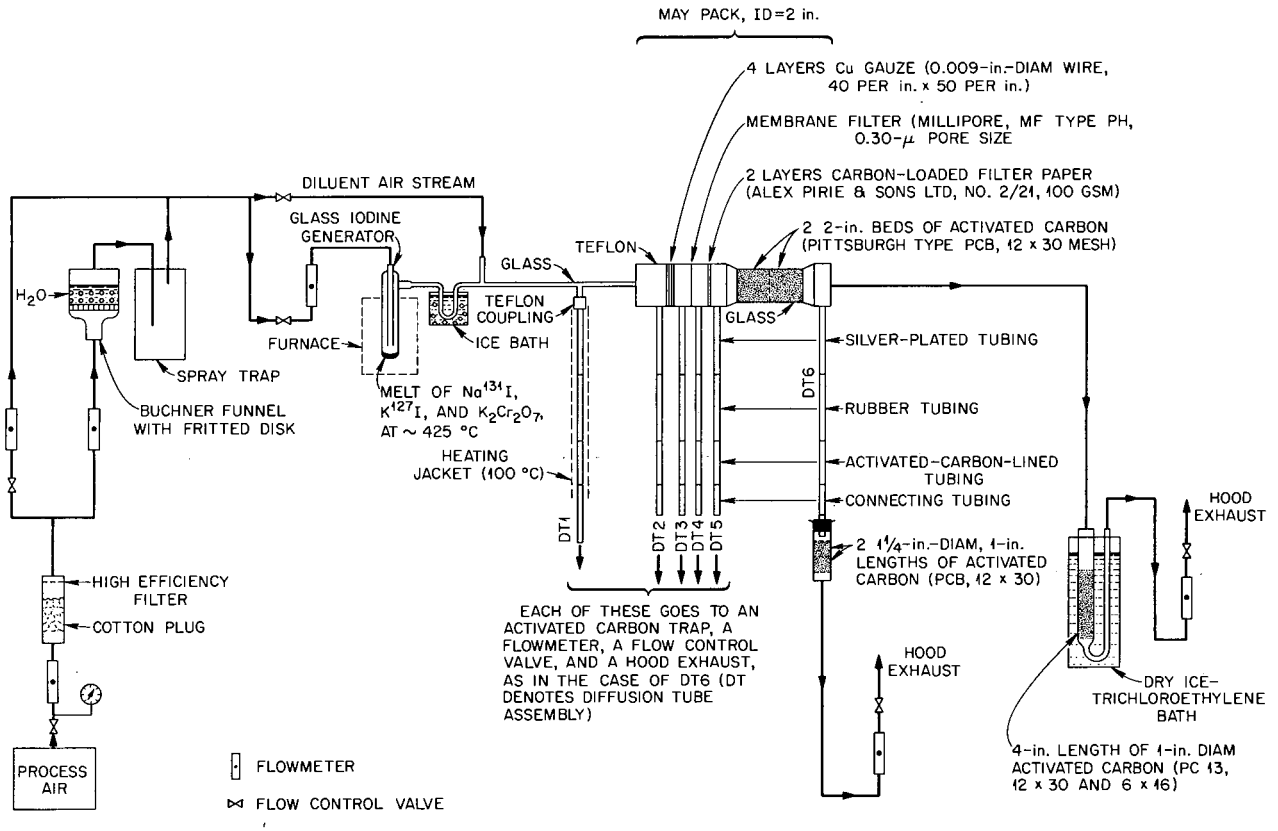

Fig. 19.4. Experimental Setup for Investigation of Iodine Behavior in a May Pack, Under Moderately Moist Conditions, by Means of Diffusion Tubes.

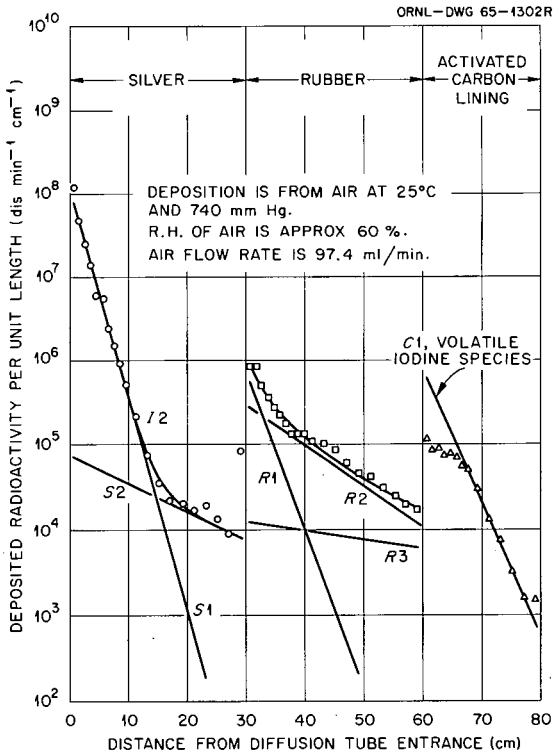

Fig. 19.5. Composite Diffusion Tube Data Resolved into Various Radioiodine Species (Tube corresponds to DTA-2 of Fig. 19.4).

REMOVAL OF IODINE AND VOLATILE IODINE COMPOUNDS FROM AIR SYSTEMS BY ACTIVATED CHARCOAL

W. E. Browning, Jr. R. E. Adams

From Dry and Moist Air

The effectiveness of activated-charcoal adsorbers against the various forms of iodine must be determined so that their reliability as an engineered safeguard can be evaluated for containing radioiodine released in a reactor accident.

It has been noted that an iodine vapor source can be divided into two parts which have different volatilities and which behave differently in a charcoal adsorber. It has been shown that the fraction volatile at $-78°C$ is composed of organic iodides, mainly methyl iodide, and the less volatile material is almost entirely elemental I_2. The behavior of these fractions of an iodine source toward four types of activated charcoal under varying degrees of temperature and humidity has been investigated. The activated charcoals studied were selected to represent four types of this material: bituminous coke (Pittsburgh BPL), petroleum base (Columbia GC), coconut shell (Pittsburgh PCB), and a charcoal containing metallic impregnants (Whetlerite, BPL charcoal impregnated with silver, copper, and chromium). (Equivalent activated charcoals produced by other manufacturers will probably produce comparable results.) The volatile fraction (primarily methyl iodide) is the more difficult to remove from gases under humid conditions at room temperature; under humid conditions, the coconut type (PCB) seems to be the most effective for removing this fraction. Under dry conditions (relative humidity less than 3%) and at room temperature, all the charcoal types seem to be effective against the volatile fraction. The less-volatile fraction (primarily elemental iodine) is removed effectively by any of the four charcoal types, but again the coconut type seems to be somewhat more efficient. In similar experiments at 100 and 150°C, both iodine fractions under various degrees of humidity are removed efficiently by all four charcoal types.

Two experiments were performed using an activated charcoal (207B) obtained from Sutcliffe, Speakman, and Company, Ltd., England. British workers have reported this particular type of charcoal to be superior to other charcoals available in England for adsorption or removal of methyl iodide at room temperature from CO_2-CO mixtures.[17] The moisture content of the CO_2-CO mixture is not known. Our experiments indicate that this charcoal (207B) is equivalent to the other charcoals of the same type tested for removing the methyl iodide fraction from air at room temperature; and like them it is seriously reduced in efficiency under humid conditions.

From Steam-Air Mixtures

The study was also extended to cover conditions where the iodine vapor and iodine compounds are contained in steam-air mixtures at elevated temperatures. As before, the iodine sources were fractionated into the volatile and nonvolatile parts, and charcoal efficiencies were determined for each fraction. None of the charcoals tested had a sufficient efficiency for the adsorption of the volatile fraction from mixtures containing considerable steam. This is not surprising in the light of the influence of moisture noted in the studies reported above. The less-volatile fraction is removed with a somewhat lower efficiency than was noted at 100° with smaller quantities of water present. This somewhat reduced efficiency for elemental iodine under steam conditions has been noted previously.[15] Related studies are continuing, with emphasis on this influence of moisture on the adsorption of methyl iodide.

---

[17] R. D. Collins and A. E. J. Eggleton, "Control of Gas-Borne Activity Arising from Reactor Faults," paper presented at the Third United Nations International Conference on Peaceful Uses of Atomic Energy, Geneva, Paper A/Conf. 28/P/186.

20. Behavior of Radioactive Aerosols

SIMULATION OF DISPERSIONS

Properly engineered safeguards, including massive containment vessels and gas cleaning systems with suitable filters and adsorbent beds, should, by ensuring confinement and positive control of fission products released from the fuel in (unlikely) reactor accidents, permit large nuclear reactors to be built near centers of population. Ideally, these safeguards should be tested, after installation, with radioactive fission products similar to those expected in an accident. Such tests would themselves prove dangerous to perform. Accordingly, attempts are being made to develop less hazardous preparations whose behavior toward gas cleaning systems is similar to that of released fission products. Such "simulants" should include molecular dispersions of appropriate elements and their compounds, and particles of sizes which are expected to carry radioactive species following a nuclear accident.

Tests of Iodine Removal Systems

W. E. Browning, Jr. R. E. Adams

Since radioiodine is generally considered to be the most significant of the volatile fission products from a hazards standpoint, the behavior of radioiodine in gas cleaning systems has been given first consideration. A procedure has been developed and applied for testing the efficiency for iodine removal of full-scale operating charcoal adsorber systems in the NS "Savannah"[1] and in the ORR. This procedure uses elemental iodine vapor. When laboratory studies of the behavior of the organic iodides found in iodine sources are sufficiently complete, the more significant of the iodides will be applied in full-scale tests simulating iodine behavior. The application of gas chromatography for detecting nonradioactive organic iodides in very small concentrations is being studied.

Simulation of Particulate Dispersions

W. E. Browning, Jr. R. E. Adams

In addition to charcoal adsorbers for iodine control, off-gas systems also contain high-efficiency particle filters for control of radioactive particles of very small size. A quality control technique has been scaled up by other workers and widely applied at many locations in the in-place testing of full-scale filters. An organic liquid (dioctyl phthalate) is vaporized, condensed (producing a fog with particle sizes ranging from 0.2 to 0.8 μ), and passed into the filter bank. Excessive penetration by the organic droplets indicates damage to the filter medium or improper installation of the units. While this testing technique has been invaluable in the examination of high-quality filter units, it cannot be considered an adequate simulant for fission product particles. Such a simulant should be produced from materials closely resembling the fuel materials, and its particle-size distribution and behavior should correspond to those observed in fuel meltdown experiments. The aerosol generation techniques being developed for the filter evaluation program show promise of fulfilling this need. This method uses an electric arc to heat fuel and cladding materials to melting temperatures. The portability of the equipment for arc production and the close correspondence of the aerosols with those produced in the Nuclear Safety Pilot Plant

[1] R. E. Adams and W. E. Browning, Jr., *Iodine Vapor Studies for the Nuclear Ship SAVANNAH Project*, ORNL-3726 (February 1965).

and in the in-pile fuel meltdown tests are encouraging. Aerosol sampling in the filter system ducts can be accomplished by using the fibrous filter techniques to observe different size groups independently, as reported elsewhere in this section. Thus, in-place tests could be conducted with aerosols which realistically simulate those expected in reactor accidents.

FILTRATION OF DISPERSIONS OF REACTOR MATERIALS

W. E. Browning, Jr. R. E. Adams
G. L. Kochanny, Jr.[2]

Filtration of particulate dispersions is being studied by using simulant aerosols produced by high-intensity arcs powered by a commercial welding machine and struck between electrodes consisting of reactor fuel materials (Fig. 20.1). The aerosol produced by this arc has been examined by electron microscopy, electron diffraction, and by a technique which measures depth of penetration in a deep Dacron filter pack,[3] and has been found to simulate closely the aerosol produced by the in-pile melting of reactor fuels. The filtration efficiency of one commercial filter (Flanders 700 absolute filter), which was exposed to an arc-generated U_3O_8 aerosol at a flow rate of air of 1400 cc/min, was found to be >99.9916% and >99.914% for the two particle size ranges which comprise the aerosol.

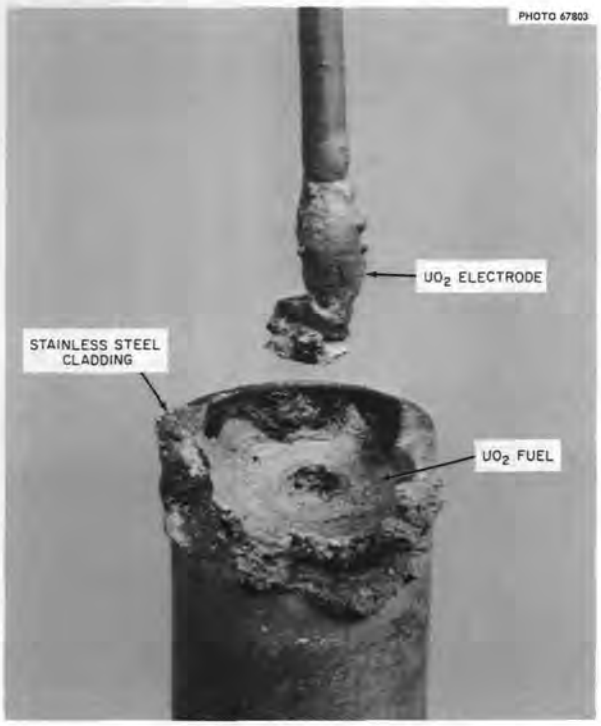

Fig. 20.1. Aerosol Generator Which Simulates a Reactor Accident by Arc-Heating Electrodes of Uranium Oxide and Stainless Steel Packed with UO_2.

Work is continuing on the evaluation of commercial filters in removing these aerosols from the gas streams, as well as on the development of a technique for generation of U_3O_8 and UO_2 aerosols with and without stainless steel from the cladding, and on the characterization of aerosols produced under various conditions (flow rate, atmosphere, etc.). The techniques for generation and characterization of the simulated aerosols, and for the interpretation of the filter evaluation studies, have been reported in detail elsewhere.[4]

MEASUREMENTS OF THE CHARACTERISTICS OF RADIOACTIVE AEROSOLS BY USE OF FIBROUS FILTERS

W. E. Browning, Jr. M. D. Silverman
L. F. Franzen[5]

Development of the method for characterization of radioactive aerosols by the use of fibrous filters has been reported elsewhere.[3,6,7] The distribution of radioactive particles in a series of uniform fiber filters is interpreted in terms of three main filtration mechanisms, denoted as diffusion, interception, and inertial impaction. Several experiments were performed in order to compare filters of 72 and 94% porosity. Streams of air flowing at linear velocities from 0.4 to 88 fpm,

[2]Analytical Chemistry Division.

[3]M. D. Silverman and W. E. Browning, Jr., *Science* **143**, 572 (1964).

[4]W. E. Browning, Jr., R. E. Adams, and G. L. Kochanny, Jr., *Nucl. Safety Program Semiann. Progr. Rept. Dec. 31, 1964*, ORNL-3776.

[5]Visiting scientist, Technischer Uberwachungs-Verein Essen e.V.

[6]W. E. Browning, Jr., M. D. Silverman, and L. F. Franzen, *Nucl. Safety Program Semiann. Progr. Rept. June 30, 1964*, ORNL-3691, pp. 72–74.

[7]W. E. Browning, Jr., M. D. Silverman, and L. F. Franzen, *Nucl. Safety Program Semiann. Progr. Rept. Dec. 31, 1964*, ORNL-3776.

and carrying particles (labeled with ^{65}Zn) ranging in diameter from 20 to 300 A, were passed through successive layers of identical filters. The filtration curves obtained were resolved into three straight lines indicating three different particle size groups. The results showed that decreasing the filter porosity reduced the amount of penetration. Decreasing the porosity improves filter efficiency, particularly at intermediate flow rates (40 fpm), less so at lower (10 fpm) and higher (80 fpm) velocities, and negligibly so at very low flow rates (2.5 fpm). The results obtained are now being used to test the latest theories of filtration. When the tests are completed they should provide a useful basis for the interpretation of high-velocity filter deposition distributions in terms of the characteristics of aerosols.

The experimental assembly has undergone a number of improvements: (1) photoetched stainless steel screens with very uniform and smooth surfaces have been introduced to better define the filter boundaries, and (2) the aerosols are now generated under gas flow conditions that are constant and independent of parametric flow changes through the filters. Pressure-drop experiments were conducted with the improved arrangement, and reproducible data have been obtained to determine the effects of α (solids fraction) on pressure drop across the filters. A computer program is presently under development in order to handle larger outputs of data, to improve the basis for comparison, and to save considerable time and effort in evaluating the various filtration theories.

Part V

Other ORNL Programs

21. Chemical Support for Saline Water Program[1]

SOLUBILITY OF $CaSO_4$ IN AQUEOUS SOLUTIONS OF $NaNO_3$ AT TEMPERATURES OF 125 TO 350°C

W. L. Marshall Ruth Slusher

In previous solubility studies of $CaSO_4$ in aqueous NaCl solutions,[2] the logarithm of the solubility quotient (K_{sp}) of $CaSO_4$ at temperatures to 200°C was shown to vary linearly with a function $\sqrt{I}/(1 + 1.5\sqrt{I})$, where I = ionic strength; from extrapolation to zero ionic strength, the (thermodynamic) solubility product, K^0_{sp}, was obtained. Similar data for another electrolyte ($NaNO_3$) both at temperatures below and above 200°C (above 200°C some corrosion difficulty with NaCl solutions was experienced) were obtained to permit (1) the comparison of the solubility behavior of $CaSO_4$ in different electrolytes, (2) a test of whether the data continued to adhere to a modified Debye-Hückel relationship, (3) hopefully, a precise extrapolation of the solubilities of $CaSO_4$ to zero ionic strength, and (4) a test of the reliability of presently available values for the solubility of $CaSO_4$ in H_2O at temperatures above 200°C.[3]

The experimentally determined solubilities of anhydrous $CaSO_4$ at temperatures of 125, 150, 200, 250, 300, and 350°C in $NaNO_3$-H_2O solutions, in good agreement with the analogous solubilities in NaCl-H_2O at 125, 150, and 200°C, are plotted in Fig. 21.1 as the logarithm of the molal solubility vs $\sqrt{I}/(1 + 1.5\sqrt{I})$, where I = ionic strength = 4 m $CaSO_4$ + m $NaNO_3$. The parameter 1.5 was selected since this value gave the best linear fit to the solubilities in NaCl-H_2O solutions. For comparison, the theoretical Debye-Hückel limiting slopes at the various temperatures are also shown. There appears to be a general significance in the divergency between the limiting (theoretical) and the experimental slopes at temperatures above 250°C. This divergency, to nearly the same extent at each temperature, has been observed above 250°C in plots of the solubilities of $CaSO_4$ both in NaCl-H_2O and H_2SO_4-H_2O solutions, and also in exploratory solubilities with some other electrolytes.

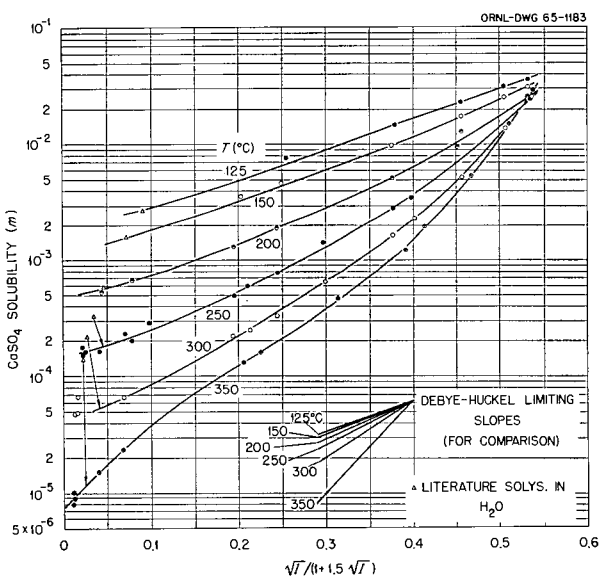

Fig. 21.1. The Solubility of $CaSO_4$ in $NaNO_3$-H_2O Solutions, 125–350°C, vs a Function of the Ionic Strength I.

[1]Research sponsored by the Office of Saline Water, U.S. Department of Interior, under Union Carbide Corporation's contract with the U.S. Atomic Energy Commission.

[2]W. L. Marshall, E. V. Jones, and Ruth Slusher, *J. Chem. Eng. Data* **9**, 187 (1964).

[3]H. S. Booth and R. W. Bidwell, *J. Am. Chem. Soc.* **72**, 2567 (1950); F. G. Straub, *Ind. Eng. Chem.* **24**, 914 (1932).

At temperatures above 200°C, it is evident that the literature values (included in Fig. 21.1) for the solubility of $CaSO_4$ in H_2O are considerably higher than the values from this study, which are consistent with the overall variation in solubility with ionic strength. Accordingly, we believe the literature values at temperatures above 200°C to be substantially in error.

CALCULATION OF ALLOWABLE CONCENTRATION LIMITS OF SALINE WATERS BEFORE PRECIPITATION OF $CaSO_4$

W. L. Marshall

Solubilities of $CaSO_4$ and its hydrates have been determined previously at temperatures from 40 to 200°C in NaCl-H_2O solutions from 0 to 4 *m*.[2] These solubilities were shown to fit an extended Debye-Hückel equation,

$$\log K_{sp} = \log K^0_{sp} + 8S\sqrt{I}(1 + 1.5\sqrt{I})$$

[where I is the ionic strength, S is the Debye-Hückel limiting slope for a 1-1 electrolyte, K_{sp} is the solubility quotient, and K^0_{sp} is the (thermodynamic) solubility product at $I = 0$], to about 2 *m* NaCl and at least to 4 *m* NaCl at temperatures near and above 100°C. Values for K^0_{sp} were determined.

In distillation technology, the concentration of brine at which $CaSO_4$ or one of its hydrates precipitates needs to be known as a function of temperature. By making use of previously determined and additional data to 350°C and the above relationships, with the assumption that any saline water containing predominantly a 1-1 electrolyte salt would behave similarly to NaCl-$CaSO_4$-H_2O solutions, a computer program was written to evaluate saline waters with respect to concentration limits before precipitation of calcium sulfate. The ionic strength I_0 of the normal (unconcentrated) saline water, the molal concentration of calcium, in this water, the molal ratio $R = (SO_4^{2-})/(Ca^{2+})$, the limiting Debye-Hückel slopes, and the (thermodynamic) solubility products were used to iterate the following two equations until successive values of the concentration factor, I/I_0 (initially approximated to be unity), differed by less than 0.001:

$$K_{sp} = K^0_{sp} \exp\,[2.303(8 \cdot S\sqrt{I}/(1 + 1.5\sqrt{I}) - BI^2)]\,, \quad (1)$$

$$I = I_0\sqrt{K_{sp}/Rm^2_{Ca^{2+}}}\,. \quad (2)$$

The term BI^2, where B is an adjustable parameter with temperature, was included in Eq. (1) to account for deviations at concentrations of NaCl over 2 *m*. The values of K^0_{sp} for anhydrous $CaSO_4$ were interpolated from the previous study.[2] Those used for the hemihydrate were read from an extended curve of log K^0_{sp} vs $1/T$°K through the two values at 100 and 125°C given previously. The curve nearly parallels an analogous plot for anhydrous $CaSO_4$. The values of K^0_{sp} for the dihydrate, given previously to 60°C, were extrapolated to 110° in an analogous manner. In Fig. 21.2 the calculated concentration limits for normal seawater as a function of temperature are shown. Thus at 100°C seawater can be concentrated by a factor of 1.5 before precipitation of stable anhydrous $CaSO_4$ occurs. In practice, however, at this temperature there seems to be a moderately long induction period for precipitation of this stable phase, and a concentration factor

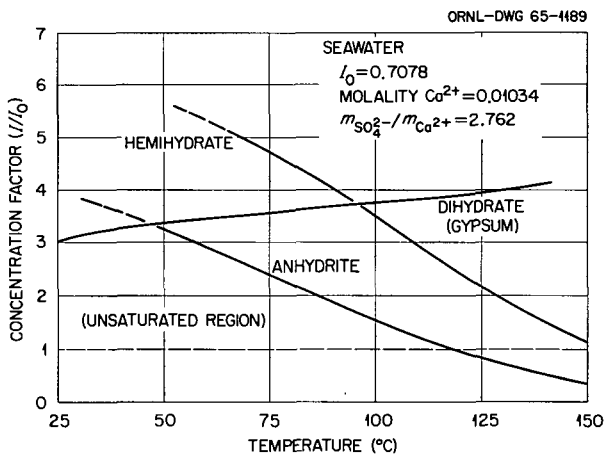

Fig. 21.2. Concentration Limits of Seawater Before Precipitation of $CaSO_4$. Derived from data in *J. Chem. Eng. Data* **9**, 187 (1964).

of 3.8 (Fig. 21.2) for the metastable $CaSO_4 \cdot \frac{1}{2}H_2O$ may be the more important. However, at temperatures somewhat above 100°C the induction period decreases markedly, and therefore the curve for anhydrous $CaSO_4$ becomes more important; precipitation in normal (unconcentrated) seawater occurs at 116°C.

In Tables 21.1 and 21.2 some calculated limits for other saline waters are given, with initial ionic strengths, molalities of calcium, and R

Table 21.1. Representative Saline Waters: Temperature Limits for Precipitation of $CaSO_4$ and Its Hydrates

Location	I_0 [a]	$m_{Ca^{2+}}$	R [b]	Temperature (°C)		
				$CaSO_4$	$CaSO_4 \cdot \frac{1}{2}H_2O$	$CaSO_4 \cdot 2H_2O$
Seawater	0.7078	0.01034	2.762	116	153	>160
Caspian Sea	0.341	0.0134	3.78	57	101	120
Miller, S.D.	0.0500	0.00511	2.461	92	125	160
Webster, S.D. (A)	0.0358	0.00513	1.411	105	131	170
Webster, S.D. (B)	0.0426	0.00550	1.622	95	129	160
Buckeye, Ariz.	0.0971	0.01150	0.959	85	119	155
Grandfalls, Tex.	0.2195	0.01856	1.649	50	95	80
Roswell, N.M.	0.4295	0.02335	1.426	62	105	140

[a] I_0 = initial ionic strength = $\frac{1}{2}\Sigma(mz^2)$, molal units.
[b] R = molality SO_4^{2-}/molality Ca^{2+}.

Table 21.2. Representative Saline Waters: Concentration Limits (at 50 and 90°C) for Precipitation of Gypsum

Location	I_0 [a]	$m_{Ca^{2+}}$	R [b]	Concentration Factor for Gypsum ($CaSO_4 \cdot 2H_2O$)	
				T = 50°C	T = 90°C
Seawater	0.7078	0.01034	2.762	3.3	3.6
Caspian Sea	0.341	0.0134	3.78	1.2	1.1
Miller, S.D.	0.0500	0.00511	2.461	2.3	2.2
Webster, S.D. (A)	0.0358	0.00513	1.411	2.9	2.7
Webster S.D. (B)	0.0426	0.00550	1.622	2.7	2.4
Buckeye, Ariz.	0.0971	0.01150	0.959	2.1	1.9
Grandfalls, Tex.	0.2195	0.01856	1.649	1.3	1.2
Roswell, N.M.	0.4234	0.02335	1.426	1.1	1.2

[a] I_0 = initial ionic strength = $\frac{1}{2}\Sigma(mz^2)$, molal units.
[b] R = molality SO_4^{2-}/molality Ca^{2+}.

values specified.[4] The Caspian Sea water is included since Russia presently is constructing a desalination plant on this Sea. It is of interest to note that, although the Caspián Sea's initial ionic strength is about half that of ocean water, the concentration of Ca^{2+} and the molal ratio SO_4^{2+}/Ca^{2+} are higher. As a consequence, $CaSO_4$ and its hemihydrate and dihydrate precipitate at lower temperatures and lower concentration factors. Of more general interest is the observation from the calculations that several representative saline waters [locations: (1) Caspian Sea, (2) deep well – Roswell, New Mexico, (3) Pecos River – Grandfalls, Texas] appear to be saturated or just saturated with gypsum at low temperatures, although the ionic strengths vary from 0.07 to 0.42 *m* and the molal ratios, $(SO_4^{2-})/(Ca^{2+})$, from 1.4 to 3.8. In contrast to these waters, seawater is considerably undersaturated with respect to gypsum, the solid phase that usually precipitates upon concentrating saline waters at temperatures below 100°C.

CORROSION OF ALUMINUM ALLOYS IN SALT SOLUTIONS

E. G. Bohlmann F. A. Posey[5]
J. F. Winesette

As described in the previous annual report,[6] the so-called "replacement or area effect" observed in studies of aluminum corrosion in high-purity water is also a significant characteristic of its behavior in sodium chloride solutions. This is the designation given to the observation that the initial and continuing corrosion of aluminum in dynamic systems is substantially affected by the area, location, and corroded state of the exposed aluminum as well as the loop volume, refreshment rate, and other variables. The dynamic loop studies have shown that this effect is most pronounced during the initial film formation period (<100 hr) and profoundly affects the continuing corrosion of aluminum alloys in salt solutions. In order to be able to study film growth and characteristics as a function of various parameters during this period, a small titanium loop has been adapted for electrochemical corrosion studies under flowing conditions. The loop is shown diagrammatically in Fig. 21.3. Three electrically isolated tubular electrodes, through which the loop flow passes, are provided for electrochemical measurements; the reference electrode is a saturated calomel electrode connected to the loop by an asbestos wick bridge similar to that described by Bacarella.[7] The loop itself has been used as the polarizing electrode. The loop can be operated to temperatures of 200°C and flow rates to ~30 fps; pulse pumps for pH control and continuous refreshment are also provided. Equipment is available for measuring and recording electrode potentials and polarizing currents for both potentiostatic and galvanostatic modes of operation. Corrosion rates are calculated from measurements of the polarization resistance as described by Stern.[8]

Initial experiments showed that measurements of polarization resistance with this experimental configuration are feasible and that the variation of corrosion rate with time calculated from these measurements is consistent with the data obtained from weight-loss measurements in the dynamic loops. Polarization data have also been obtained using the conventional galvanostatic method; however, analysis of the experimental curves was complicated considerably by the presence of *IR* drops in the solution phase. The electrode assembly has been modified to minimize such *IR* drops.

[4]Values calculated from representative analyses included in (1) K. S. Spiegler, *Salt Water Purification*, Wiley, New York, 1962; (2) OSW Report PB-181680, R and D Report 101 (March 1964); (3) W. L. Badger and Associates, Report No. 438 (Dec. 27, 1957); (4) OSW Report PB-161375, *A Standardized Procedure for Estimating Costs of Saline Water Conversion* (March 1956).

[5]ORNL Chemistry Division.

[6]E. G. Bohlmann, *Reactor Chem. Div. Ann. Progr. Rept. Jan. 31, 1964*, ORNL-3591, pp. 208–12.

[7]A. L. Bacarella, *Reactor Chem. Div. Ann. Progr. Rept. Jan. 31, 1963*, ORNL-3417, p. 75.

[8]M. Stern, *Corrosion* 14, 440t (1958).

ORNL-DWG 65-2600

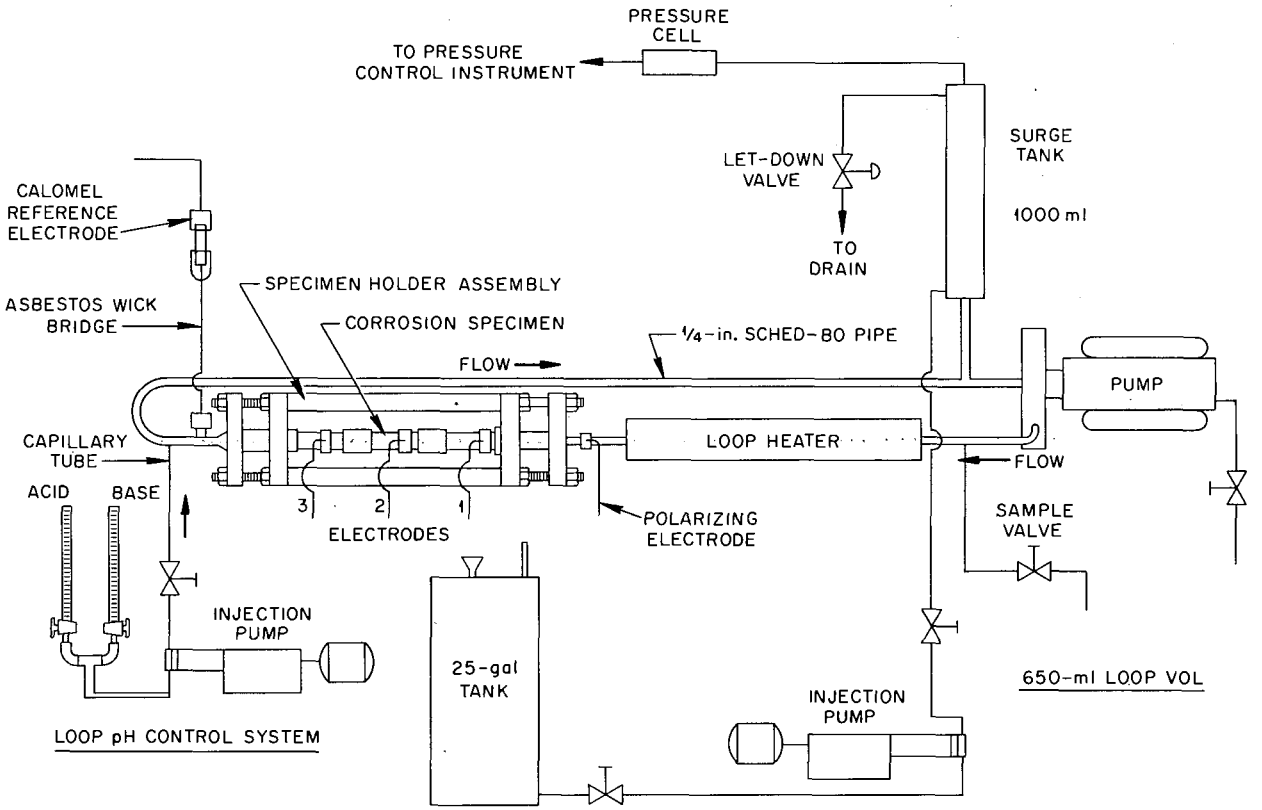

Fig. 21.3. Titanium Loop Dynamic Electrochemical Corrosion Facility.

TITANIUM CORROSION IN SALINE WATER

E. G. Bohlmann J. C. Griess

Observations In Loop Tests

Titanium is usually reported to be immune to attack in brine environments;[9–11] consequently observations of severe corrosion attack in connection with the studies of aluminum corrosion in salt water were significant. The attack was initially observed on the titanium bands used in the assembly of loop specimen holders. Open and assembled holders are shown in Fig. 21.4; note the three bands holding the halves of the holder together and the Teflon sleeves used to insulate the pin specimens from the titanium holder. The assembled specimen holders are slipped into $1\frac{1}{2}$-in. titanium pipe sections flanged into the loops and equipped with fittings which direct the fluid flow through the channel in the holder. Thus the bands are in a semistagnant annulus ($\sim\frac{1}{32}$ in. thick) between the holder and pipe wall. Strips of Teflon are also often used to cover the ends of the pins to eliminate the possibility of inadvertent contact between the bands and pins. In the early observations, a strong correlation between the area of attack and contact with Teflon suggested that the attack might be initiated by fluoride ions released by the Teflon. Investigations of this possibility demonstrated that very small amounts of fluoride are leached from the Teflon used, but further observations and autoclave tests showed the attack

[9] N. D. Greene and G. Judd, *Corrosion* 21, 15–18 (1965).

[10] F. R. LaQue and H. R. Copson, *Corrosion Resistance of Metals and Alloys*, 2d ed., pp. 654–56, Reinhold, New York, 1963.

[11] L. L. Shreir, ed., *Corrosion, Vol. I, Corrosion of Metals and Alloys*, p. 5.35, Wiley, New York, 1963.

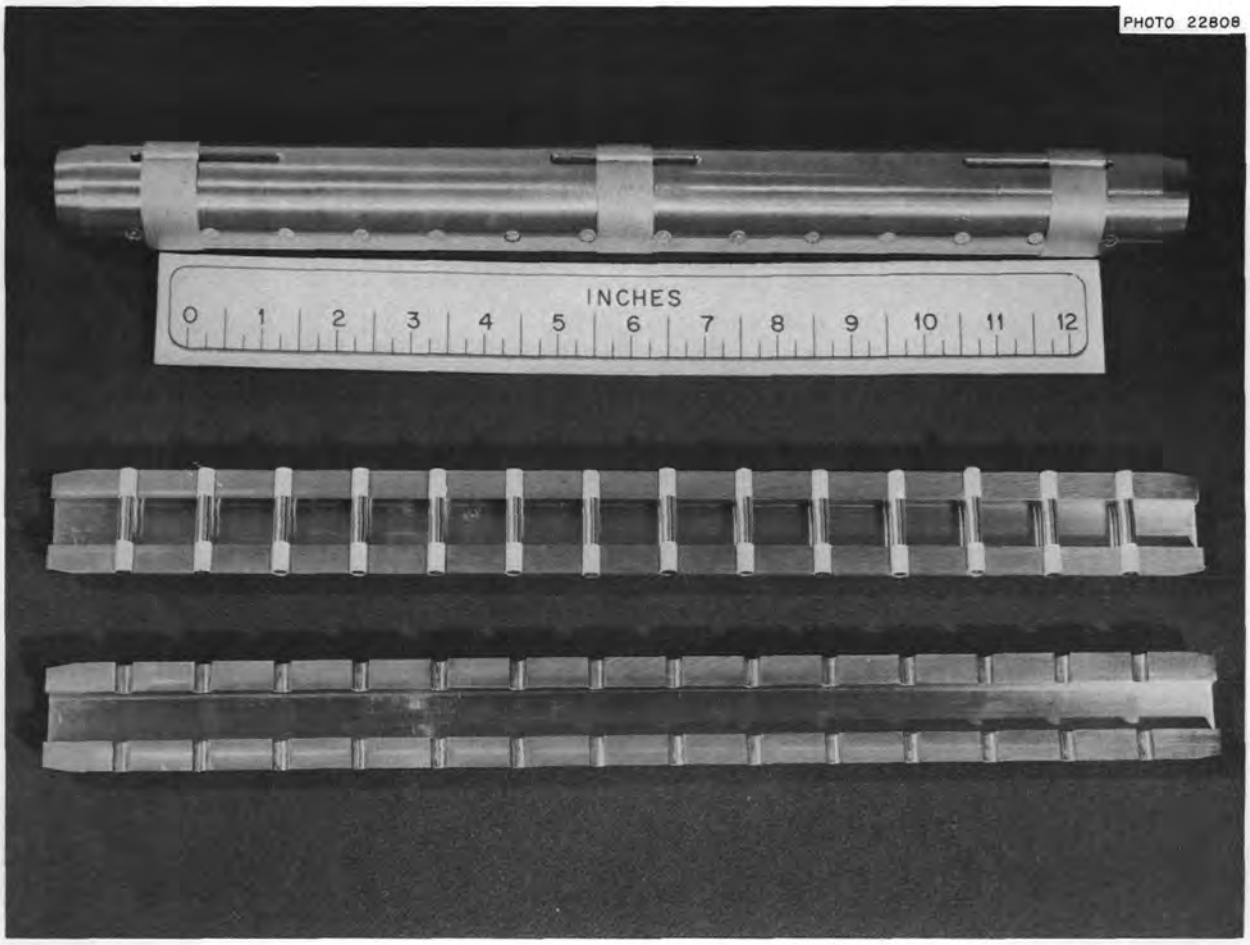

Fig. 21.4. Titanium Specimen Holder.

occurred in the absence of Teflon. However, contact with Teflon clearly promotes the attack; this has also been observed in wet chlorine service.[12] The attack has also been observed in our studies in areas of contact with a silicone rubber containing no fluoride and has been reported for the contact area in the hole of a rubber stopper.[12]

Figure 21.5 shows a number of clamping bands (made from 0.008-in. A55 titanium sheet) after exposure to pH 6.4 2 *M* sodium chloride at 150°C for 192 hr. Seven of the twenty bands show gross attack, but the remaining thirteen show none (the small holes in and near the welds were produced in fabrication). Similar attack has been observed under the Teflon insulation on pin specimens and on bolted plate crevice specimens (see "Observations in Autoclave Tests," below). The attack, however, is quite inconsistent as shown in Fig. 21.5 and in Tables 21.3 and 21.4. This inconsistency has made quantitative evaluation of the effects of various parameters difficult, but some trends have been indicated by the accumulated observations.

Existence of a Crevice. – Crevices seem to promote initiation of the attack; however, it is clear that crevice conditions are not required for it to continue. As shown in Fig. 21.5, the attack continues in the semistagnant annulus between the specimen holder and the pipe after the crevice is eliminated by perforation of the band. Also, studies at 200°C have shown that the attack was initiated on the outside of the bands as well

[12] L. W. Gleekman, *Chem. Eng.* 70(23), 223–24 (1963).

as on the inside. No instance of attack on the pin area in the flow channel has been observed, nor has attack which had been initiated under a Teflon sleeve penetrated into that area.

Temperature. – The effect of temperature on the frequency of attack is shown in Table 21.3. The attack has been observed only once at 100°C, but increases in frequency with rising temperature. At 150°C it begins at a point and spreads like a grass fire, consuming the entire band thickness along a sharply defined front. At 200°C, however, the attack is more general, spreading over the surface on which it initiates rather than penetrating the band thickness. Also, the attack often

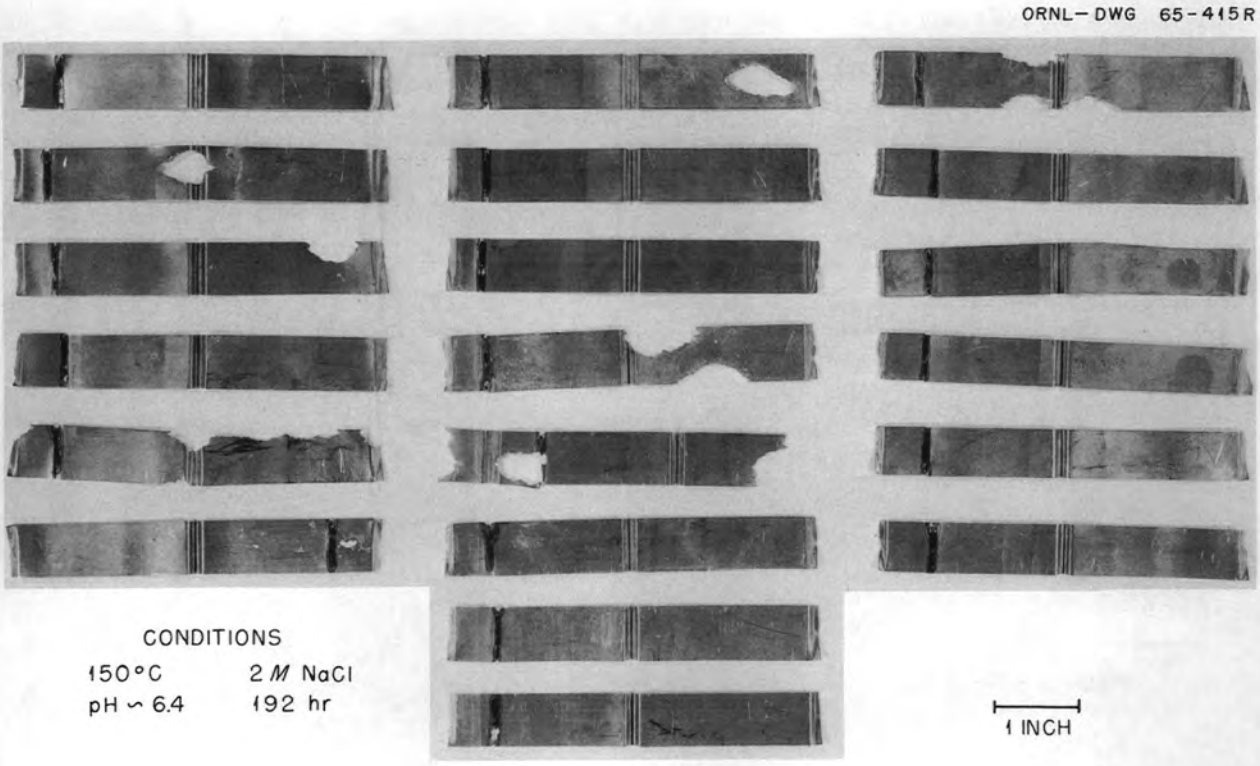

Fig. 21.5. Corrosion of Specimen Holder Assembly Bands.

Table 21.3. Effect of Temperature on Titanium Attack

Conditions: 1 *M* NaCl, pH 6–7

Temperature (°C)	Bands		Pins	
	Number Exposed	Percent Attacked	Number Exposed	Percent Attacked
100	202 (14)[a]	0	24 (4)	0–13
150	120 (6)	11–50	8 (1)	100
200	98 (3)	48–83	106 (4)	62–95

[a]Number in parentheses = number of runs.

initiates in the absence of macro crevices (on outside of band), presumably at surface imperfections or inclusions.

pH. – The effect of pH is shown in Table 21.4. The attack is inversely dependent on pH and was only observed at the higher pH's (>7) in contact with Teflon. Similar results were obtained in autoclave experiments (see section on "Observations in Autoclave Tests").

Time and Concentration. – The inconsistent results make an evaluation difficult, but indications are that the frequency of attack increases with time and concentration (1–5 *M*).

Alloy Composition. – Table 21.5 shows the composition of a number of alloys which have been tested. Only the titanium-palladium alloy has resisted the attack, 26 pins having shown no attack in a series of studies in which 87% of 48 pins of the other compositions were attacked. A total of 134 pins of the compositions other than the titanium-palladium alloy have been tested under various conditions with no distinguishable difference in behavior.

In spite of the severity of the attack on the bands and pins, little difficulty has been experienced with the titanium loops and equipment in

Table 21.4. Effect of pH on Titanium Attack

Conditions: 150°C, 1 *M* NaCl

pH Range	Bands		Pins	
	Number Exposed	Percent Attacked	Number Exposed	Percent Attacked
4^+			8 (1)	100
5^+	49 (3)[a]	18–47	3 (1)	0
6^+	120 (6)	11–50	8 (1)	100
7^+	82 (4)	0–32	3 (2)	50–100
8^+	62 (3)	0–14	2 (1)	0
9^+			8 (1)	0

[a]Number in parentheses = number of runs.

Table 21.5. Titanium Alloy Compositions Tested

Alloy	Composition (%)								
	Al	Cr	Mn	V	Zr	Cb	Ta	Fe	Pd
A-45	(Commercial purity – >99.2% Ti)								
A-55	(Commercial purity – >90.0% Ti)								
Al-Cr	3.5	4.9						0.2	
Al-Mn	4.2		4.6					0.3	
Al-V	6.4			4.2				0.2	
821	7.4					2.0	1.1	0.2	
881	8.2				8.5	0.7	0.5		
Ti-Pd[a]									0.2

[a]The Ti-Pd alloy was the only composition not attacked.

thousands of hours of operation. Several factors may account for this:

1. Prior to use in this program, the loops were used in studies with strongly oxidizing solutions to temperatures as high as 300°C. Consequently the surfaces are generally coated with heavy oxide films; studies with anodized pins indicate oxide films inhibit the attack.
2. Crevices were minimized by design and welded construction.
3. Most surfaces are exposed to rapidly flowing solution.

Observations in Autoclave Tests

In view of the observations made in the loop tests, a series of autoclave tests was conducted in sodium chloride solution using titanium crevice specimens. The specimens were prepared from two rectangular flat pieces of titanium bolted together near one end with titanium nuts and bolts. Before tightening the nut, a small piece of 8-mil-thick titanium was placed near the opposite end of the specimen to form a crevice of variable thickness (see Fig. 21.6). Thus on the end nearer the bolt, the titanium pieces were in direct contact, and the crevice at the opposite end was somewhat greater than 8 mils. One or more such specimens and a single control coupon were exposed to 600 ml of solution in a 1-liter titanium autoclave. All tests were conducted in 1 *M* NaCl at 150°C. In some cases the pH of the solution was adjusted to 3.0 with HCl, and in the other tests the solution was used directly as prepared from reagent-grade sodium chloride. In those tests conducted in the absence of oxygen, the solution was placed in the autoclave, sparged with helium, frozen, evacuated, thawed, refrozen, and evacuated again before use.

In addition to the test conducted with commercially pure titanium, three separate tests were conducted with a titanium–0.2% palladium alloy, and three tests were made with commercially pure titanium crevice specimens to which a small piece of titanium was electrically connected to the outside of the specimen. Also, in two other tests all parts of the crevice specimen were anodized at 30 v in 5% H_2SO_4 solution before assembly.

The conditions and results of the tests are shown in Table 21.6. In all cases, essentially no attack was found on the control coupons except occasionally there was slight attack at the point where the coupon was in contact with the titanium hook from which it was suspended. The description of the crevice attack used in the table is as follows: none – no evidence of attack under 30× magnification; very slight – attack not visible to the naked eye, but observable at 30× (or less) magnification; slight – visible to the naked eye, but both areas affected and depth of penetration small; moderate – area affected fairly large, but depth of attack and corrosion product accumulation small; heavy – area and depth relatively large, with large accumulation of corrosion products in crevice region.

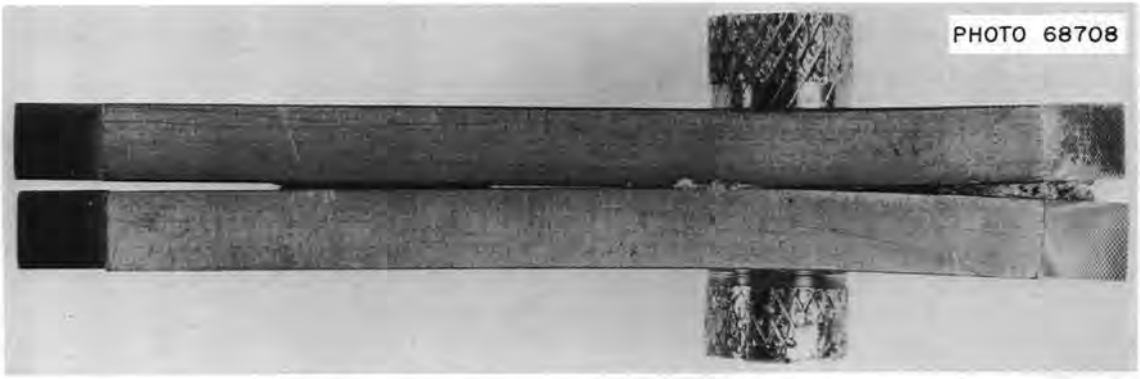

Fig. 21.6. The Appearance of a Titanium Crevice–Corrosion Specimen After Exposure to Air-Saturated 1 *M* NaCl Solution with a pH of 3.0 at 150°C.

Table 21.6. The Results of Tests with Titanium Crevice Specimens in 1 *M* NaCl at 150°C

Solution pH	Time (hr)	Air	Crevice Attack
6.5	233	No	Very slight
6.6	209	Yes	Moderate
6.8	308	Yes	None
3.0	234	Yes	Heavy
3.0	190	Yes	Heavy
3.0	215	No	Slight
3.0	215	No	Very slight
3.0	185	Yes	Heavy
3.0	163	Yes	None
3.0	234	Yes	Heavy
3.0	262	Yes	Heavy
3.0	262	Yes	Very slight
3.0[a]	262	Yes	None
3.0[a]	262	Yes	Heavy
3.0[b]	262	Yes	None
3.0[b]	257	Yes	None
3.0[b]	231	Yes	None
3.0[c]	262	Yes	None
3.0[c]	185	Yes	None
3.0[c]	234	Yes	None

[a]Specimen parts anodized prior to test.

[b]Titanium–0.2% palladium alloy.

[c]Platinum electrically connected to outside of specimen.

Although only three tests were conducted in the essentially neutral sodium chloride solution, the attack was either nonexistent or slight in all cases. Of the seven tests conducted with the pH adjusted to 3.0 and in the presence of air, five specimens showed heavy attack, one showed very slight attack, and one showed no evidence of attack. The one showing no attack was disassembled and repolished. In a subsequent test under the same conditions, it underwent heavy attack. Only two tests were conducted at a pH of 3.0 in the absence of air, and in both cases the attack was either slight or very slight. With the two anodized specimens, one was unattacked and the other was heavily damaged. None of the specimens prepared from the titanium-palladium alloy and none of the specimens to which platinum was coupled were attacked in the tests. In summary, the tests generally indicated that titanium crevice attack was more severe in 1 *M* NaCl at a pH of 3 than in neutral solution and in solutions containing air than in degassed solutions. Either palladium alloyed with the titanium or platinum electrically connected to it appeared to prevent attack.

In aerated pH 3 solutions, the extent of corrosion was usually so great that the corrosion products formed in the tight crevice were sufficient to deform the specimen and in two cases to actually break the bolt holding the specimen together. Figure 21.6 is a photograph of a specimen showing how the corrosion products have forced the end of the specimen closest to the bolt apart. These metal surfaces were in contact at the start of the test. It is interesting to note that at the other end, where the crevice was wider, corrosion is absent. All tests have indicated that the crevice must be very small before attack is observed. Figure 21.7 is a photomicrograph of a cross section through a heavily corroded area, showing the nature of the attack and of the corrosion product (TiO_2).

Electrochemical Studies

To gain some insight into the electrochemical reactions occurring during the corrosion process, the cathodic polarization of commercially pure titanium was studied. These tests were carried out in an electrically heated titanium autoclave, through the head of which was introduced an electrically insulated titanium wire and a salt bridge to a saturated calomel electrode located outside of the autoclave. Figure 21.8 shows how temperature influences the polarization of titanium in 1 *M* NaCl when the autoclave contained air at the time of closing. Since both the volume of gas and its solubility change with temperature, the concentration of oxygen in the solution was different at the different temperatures. The calculated concentrations are shown on the graph. Figure 21.9 shows the effect of oxygen on cathodic polarization at 150°C, and Fig. 21.10 shows how

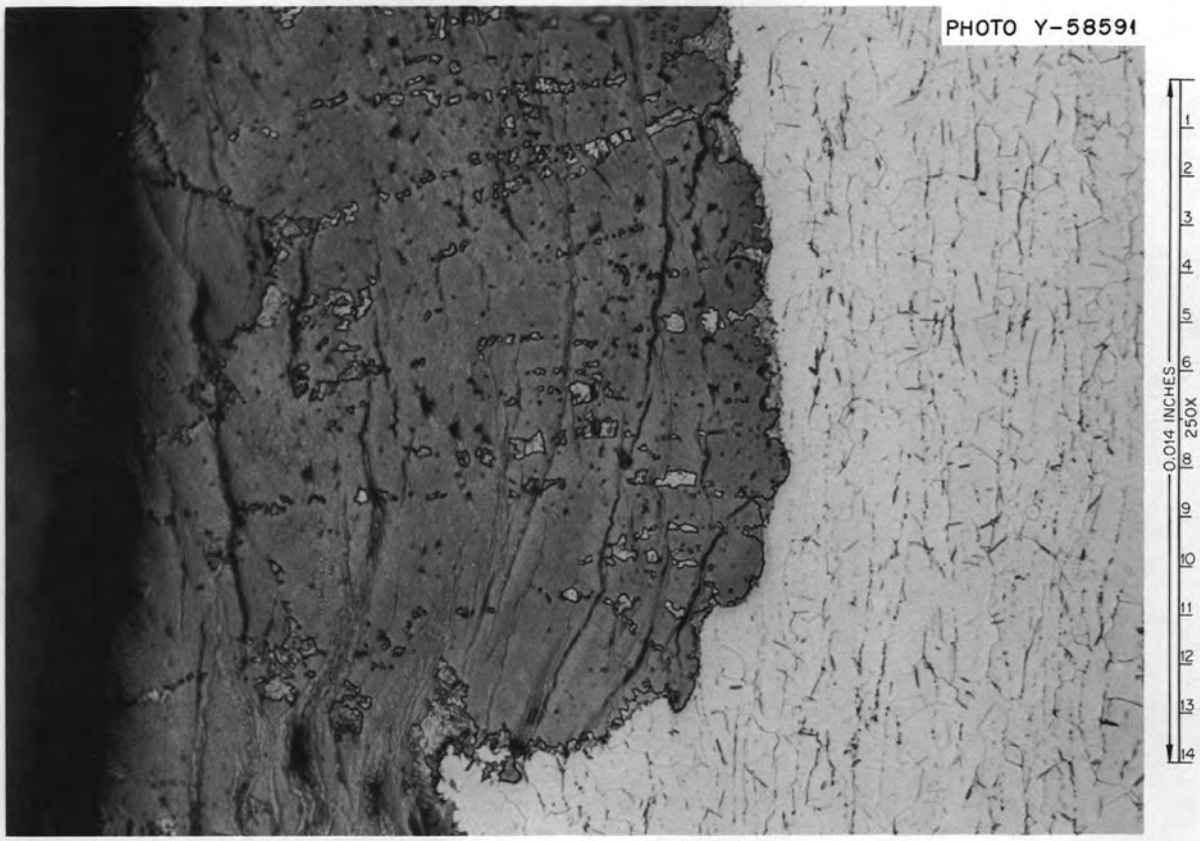

Fig. 21.7. A Photomicrograph Through a Corroded Area Showing Nature of Attack and Corrosion Product in Place.

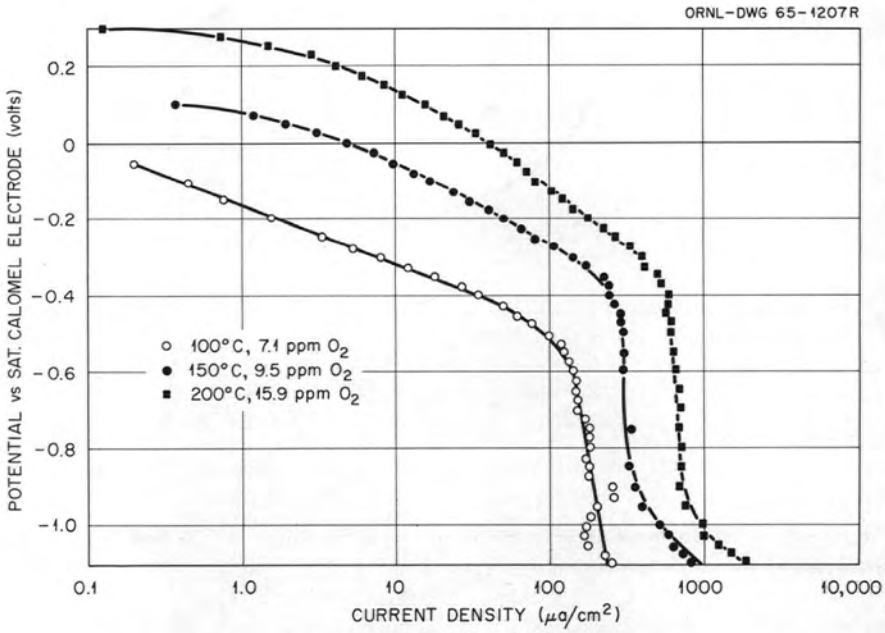

Fig. 21.8. Cathodic Polarization Curves for Titanium in 1 *M* NaCl.

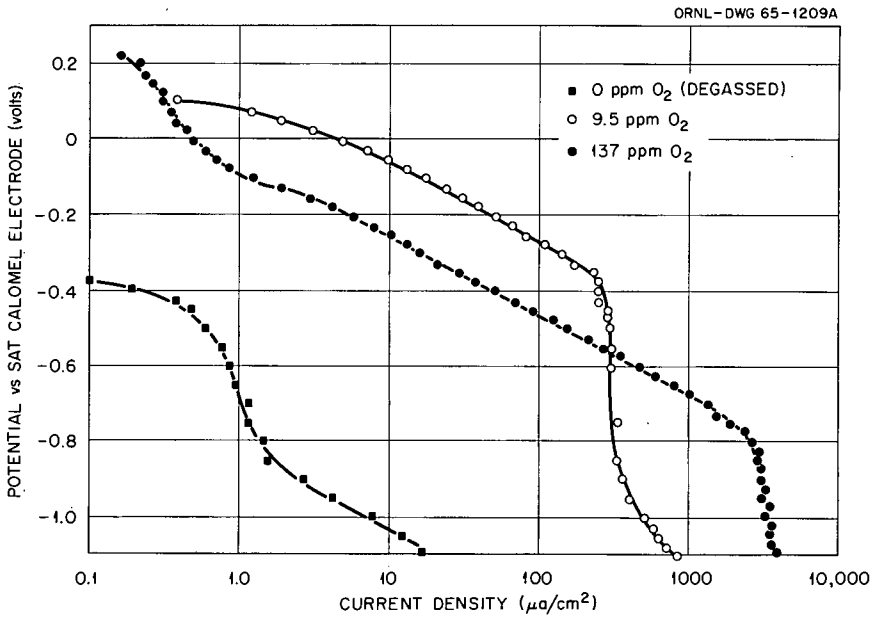

Fig. 21.9. The Effect of Oxygen Concentration on the Cathodic Polarization of Titanium in 1 *M* NaCl at 150°C.

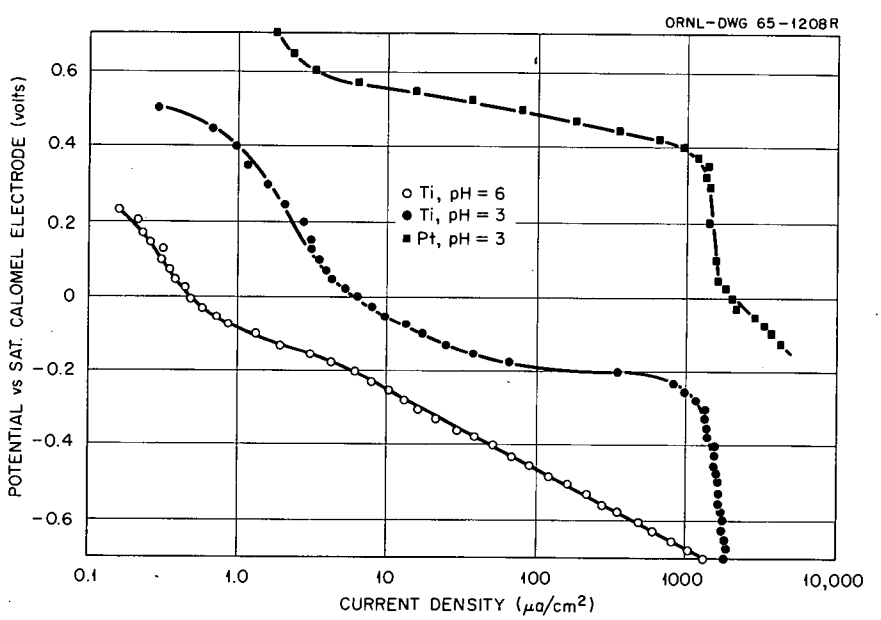

Fig. 21.10. The Effect of pH on the Cathodic Polarization of Titanium in 1 *M* NaCl Containing 137 ppm O_2 at 150°C and the Polarization of Platinum in the Same Solution at a pH of 3.

pH influenced the cathodic process. Also shown on Fig. 21.10 is the cathodic polarization curve for platinum obtained in the solution with the pH of 3.

Anodic polarization of titanium has not been examined in as much detail as has the cathodic polarization, but in all cases titanium polarized easily, with anodic currents in the range of a microampere per square centimeter being sufficient to raise the potential to that of oxygen evolution. For titanium to corrode at the rates observed in crevices, it appears that the pH of the solution in those regions must become substantially lower than that in the bulk of the solution.

Although the mechanism of the titanium crevice corrosion is not fully understood, the data presented above may qualitatively explain some of the observed results. As shown in Fig. 21.9, the potential difference between titanium exposed to solutions containing oxygen and titanium exposed to solutions without oxygen is greater than 0.5 v. Thus the loss of oxygen from the very small volume of solution in the crevice could create a differential aeration cell of appreciable driving force. If such a cell existed, the cathodic current density would be greater (or a given cathode area could support more corrosion current) the greater the oxygen concentration or the lower the pH of the electrolyte. The data presented in Fig. 21.8 also show that the overvoltage for the reduction of oxygen on titanium is less the higher the temperature. Thus in the presence of oxygen, greater crevice corrosion is observed at a pH of 3 than in neutral solutions, and corrosion has only rarely been observed at less than 150°C.

The fact that no crevice attack has been observed on the titanium-palladium alloy or with titanium electrically coupled to platinum is probably related to the fact that the overvoltage for the reduction of oxygen (or hydrogen discharge) on the platinum metals is so low that the cathodic reaction polarizes the crevice into the passive region. As shown by Stern,[13] titanium possesses an active-passive behavior similar to that of the austenitic stainless steels in sulfuric acid, and if the titanium potential is raised above some critical value (undetermined for this system), it becomes passive.

---

[13] M. Stern and H. Wissenberg, *J. Electrochem. Soc.* 106, 755 (1959).

22. Solvents for the Fluorine Volatility Process

R. E. Thoma B. J. Sturm

In the ORNL version of the Fluoride Volatility Process, uranium is recovered as volatile UF_6 by fluorination from molten fluoride mixtures in which solid fuel elements from nuclear reactors have been dissolved by hydrofluorination. The process has been notably successful with zirconium-uranium alloy fuels[1] and in preliminary tests with fuels of aluminum-uranium alloy.[2–5] The fluoride solvent for this process must dissolve high concentrations of the major fuel constituent at temperatures (generally 600°C or below) at which corrosion by the melt is not a problem. Favorable phase behavior of the system is, therefore, a necessary qualification of an acceptable solvent.

THE SYSTEM $KF\text{-}ZrF_4\text{-}AlF_3$

The $KF\text{-}ZrF_4\text{-}AlF_3$ system appeared from preliminary studies[2] to be the best available medium for processing aluminum-uranium alloy fuels. This system has been examined in some detail to establish precisely the 600 and 550°C isotherms, the initial and final temperatures for the dissolution process.

Most of the data were taken by a visual procedure,[2,3] that is, by location of the liquidus by visual detection of a precipitate which generally clouded the melt. Sublimation of the ZrF_4 and AlF_3 under inert atmospheres and distillation of KF from a melt containing 2.3 mole % UF_4 (ref. 4) were used to prepare material of purity sufficient for these studies. Such treatment virtually eliminated oxide, which when present, substantially raises the liquidus temperatures in the $KF\text{-}ZrF_4\text{-}AlF_3$ system. The effect of oxide is most marked in compositions near that of $KF{\cdot}ZrF_4$, where the liquidus is raised about 5°C for every 0.01 mole % oxygen. The 550 and 600°C isotherms of the phase diagram are now well defined and show that the ideal process path is that shown by line *AB* on the diagram (Fig. 22.1). The precise location of point *A* was

ORNL-DWG 65-2601

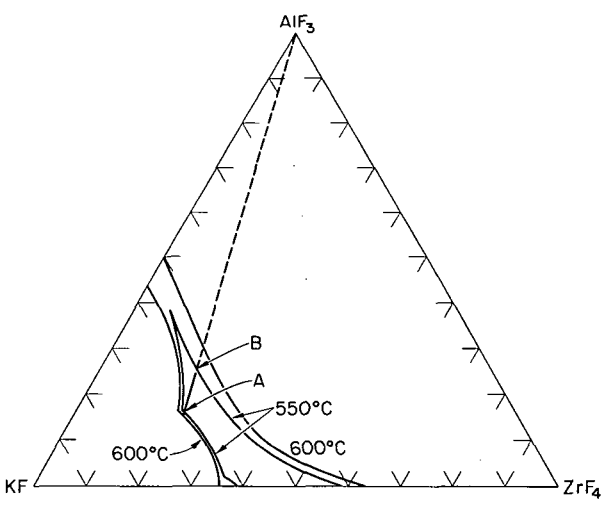

Fig. 22.1. Diagram of the System $KF\text{-}ZrF_4\text{-}AlF_3$ Showing 550 and 600°C Isotherms and a Proposed Process Composition Path AB.

[1] *Chem. Technol. Div. Ann. Progr. Rept. May 31, 1963*, ORNL-3452, p. 26.

[2] B. J. Sturm *et al.*, *Reactor Chem. Div. Ann. Progr. Rept. Jan. 31, 1964*, ORNL-3591, pp. 214–17.

[3] R. L. Boles and R. E. Thoma, *Volatility Process Phase Studies — A Survey of Molten Fluoride Solvent Mixtures Suitable for Dissolution of AlF_3*, ORNL-TM-400 (Oct. 22, 1962).

[4] R. E. Thoma, B. J. Sturm, and E. H. Guinn, *Molten-Salt Solvents for Fluoride Volatility Processing of Aluminum-Matrix Nuclear Fuel Elements*, ORNL-3594 (1964).

[5] *Chem. Technol. Div. Ann. Progr. Rept. May 31, 1964*, ORNL-3627, p. 40.

important, because with increasing KF concentration the liquidus temperature rises very steeply to the K_3ZrF_7-K_3AlF_6 join. Because of the resemblance of structures of cubic K_3AlF_6 [isostructural with $(NH_4)_3AlF_6$] and K_3ZrF_7 [isostructural with $(NH_4)_3ZrF_7$],[6] there is considerable solid solution along this join.

ZIRCONIUM-MATRIX FUELS OF HIGH URANIUM CONTENT

Application of the Fluoride Volatility Process has heretofore been restricted to high-enrichment fuels in which the concentration of dissolved uranium is so low that it has little or no effect on phase behavior of the mixture. Recently, investigations of the feasibility of adapting the process to low-enrichment fuels were begun. Adaptability to fuels of the Dresden type, in which UO_2 is clad in Zircaloy-2, will require solvents capable of handling approximately equimolar mixtures of ZrF_4 and UF_4 produced in the dissolution step. Initial solubility measurements were obtained with KF-ZrF_4 and LiF-NaF-ZrF_4 mixtures. Equimolar increments of UF_4 and ZrF_4 were added to a KF-ZrF_4 (64-36 mole %) melt and an LiF-NaF-ZrF_4 (37.5-37.5-25.0 mole %) melt to simulate approximately the progressive change in solvent composition during dissolution of such a fuel element of high uranium content. Liquidus curves suggest that the maximum UF_4 concentrations in these systems at 600°C are 11 and 15 mole % respectively. For the LiF-NaF-ZrF_4-UF_4 system, liquidus curves indicate that even higher UF_4 solubility may be obtainable if the processing solvents contain somewhat less than 25 mole % ZrF_4.

SOLVENTS APPLICABLE TO STAINLESS STEEL MATRIX FUELS

Preliminary consideration was given to solvents for reprocessing stainless steel fuel elements. All three of the major constituents of the stainless steel, iron, chromium, and niobium, would form fluorides during the process. Furthermore, the iron and chromium are expected to have different valence states during dissolution by HF than they have after fluorination. The presence of all these components produces complex phase relationships in the solvent. Much study would be required to provide sufficient information to permit the processing of stainless steel elements.

Potassium fluoride–zirconium tetrafluoride and KF-LiF mixtures were considered as possible reprocessing solvents. The LiF-FeF_2 system was found to have a eutectic at 38 mole % FeF_2 melting at 620°C. In the LiF-NiF_2-FeF_2 system, FeF_2 and NiF_2 were found to be approximately equivalent in effect on the liquidus. It is possible that the KF-LiF eutectic melting at 492°C could dissolve sufficient FeF_2, NiF_2, and CrF_3 to permit its use as a processing solvent.

Because of the extensive study required for such a complex system to permit its use in processing stainless steel materials, and the indication that fluidized-bed fluorination[7] can avoid this problem, further study of these solvents has been postponed until the alternative process has been tested.

---

[6] R. W. G. Wyckoff, *Crystal Structures*, p. 31, vol. II, Interscience, New York, 1951.

[7] R. L. Jarry *et. al.*, *Laboratory Investigations in Support of Fluid-Bed Fluoride Volatility Processes*, ANL-6742 (September 1963).

23. Support for Space Programs

SNAP-8 CHEMISTRY STUDIES: THE CHEMISTRY OF HYDROGEN IN LIQUID ALKALI METAL MIXTURES

E. L. Compere H. C. Savage
J. E. Savolainen T. H. Mauney

The fate of the hydrogen entering the circulating liquid-metal primary coolant (NaK-78) of the SNAP-8 and similar reactors from zirconium-uranium hydride fuel elements is believed[1,2] to depend on diffusion of the hydrogen through the system walls and on factors governing the solubility of the hydrogen in the liquid alkali metal mixture.

The loss of hydrogen by diffusion from the primary system should lead to a steady state at a comparatively low partial pressure of hydrogen. This partial pressure was estimated[1e] to be approximately 2×10^{-5} atm, if the walls of the system are oxide free, and the presence of NaK does not affect the permeation of hydrogen through system walls. The hydrogen is expected to diffuse through the walls of the primary coolant circuit into space, or more importantly into the mercury boiler system, where it may accumulate and affect system operation. Practical means of lowering the hydrogen activity in the liquid alkali metal system are thereby of interest.

Two types of studies are reported. In the hydrogen permeation studies given below, the permeation of hydrogen through metals relevant to the SNAP-8 program was studied in the absence, and in one case, in the presence of NaK.

In a second type of study, the solubility of hydrogen in NaK-78 was studied as a function of hydrogen pressure, including concentrations and temperatures which involved the precipitation of a solid hydride phase.

The possibility of reducing the partial pressure of hydrogen in NaK solution by adding substances of greater hydrogen affinity was recognized. Initial phases of a study examining the characteristics of the use of added metallic lithium for this purpose are described.

Hydrogen Permeation Studies

The permeation of hydrogen through metals in which hydrogen atoms are the diffusing species depends on the difference in the square root of upstream and downstream pressures.[3] This relationship may be expressed by the equation

$$\frac{d(H_2)}{dT} = \frac{kA}{d}\left(\sqrt{P_1} - \sqrt{P_2}\right) ,$$

where $d(H_2)/dT$ is hydrogen permeation rate (std cm^3/hr), A is area (cm^2), d is thickness (mm) of metal through which diffusion occurs, P_1 and P_2 are upstream and downstream hydrogen pressures (atm), and k is the hydrogen permeability coefficient for the metal at the given temperature, expressed in std cm^3 (H_2) mm cm^{-2} hr^{-1} $atm^{-1/2}$. Thus the permeation characteristics of a metal at a given temperature may be expressed in terms of its permeation coefficient, as is done in the studies reported below.

[1] H. W. Savage, E. L. Compere, W. R. Huntley, and A. Taboada, *SNAP-8 Corrosion Program Quart. Progr. Repts.* (a) *Aug. 31, 1963*, ORNL-3538, pp. 28–40; (b) *Nov. 30, 1963*, ORNL-3604, pp. 29–45; (c) *Feb. 29, 1964*, ORNL-3618, pp. 28–33; (d) *May 31, 1964*, ORNL-3671, pp. 26–33; (e) *Aug. 31, 1964*, ORNL-3730, pp. 32–64; (f) *Nov. 30, 1964*, ORNL-3784, pp. 35–59.

[2] E. L. Compere, J. E. Savolainen, H. C. Savage, and T. H. Mauney, "SNAP-8 Chemistry Studies: The Chemistry of Hydrogen-NaK Systems," *Reactor Chem. Div. Ann. Progr. Rept. Jan. 31, 1964*, ORNL-3591, pp. 217–22.

[3] R. M. Barrer, *Diffusion In and Through Solids*, Cambridge University Press, Cambridge, Mass., 1951.

The permeation apparatus is described in detail elsewhere.[1b] However, a modified permeation cell was developed[1e] to relieve difficulties due to high NaK vapor pressure encountered when operating at elevated temperatures with NaK in the upstream region of the cell.

The improved model of the permeation cell is shown in Fig. 23.1 in component form. The cell has an Armco iron barrier in the form of a thimble of large area-to-thickness ratio, providing for ready diffusion of hydrogen into the high-pressure side of the cell, while preventing the transport of NaK vapor into the hydrogen feed line. Thus, use of the measured upstream hydrogen pressure, rather than the interior pressure, does not cause errors in the calculated permeability of more than 4%, in the most extreme case (1300°F, unoxidized cell outer walls) based on permeability data of Flint.[4]

Permeability of Type 316 Stainless Steel to Hydrogen in the Absence and Presence of NaK. – Hydrogen permeation studies using a type 316 stainless steel cell of the above design have been made at temperatures of 1300, 1100, and 1000°F, in the absence and in the presence of NaK on the high-pressure side of the diaphragm. Upstream hydrogen pressures from a few millimeters to 1 atm were used. The downstream side was evacuated, and the gases were collected by a Toepler pump.

Results obtained in the absence of NaK in the cell are plotted in Fig. 23.2, in which the logarithm of permeation rate is plotted against the logarithm of upstream pressure. The data exhibit the theoretical slope of $\frac{1}{2}$ except at low pressures. The permeability coefficient appears to drop off

[4]P. S. Flint, *The Diffusion of Hydrogen Through Materials of Construction*, KAPL-659 (Dec. 14, 1951).

Fig. 23.1. Components of Permeation Cell with Internal Iron Thimble.

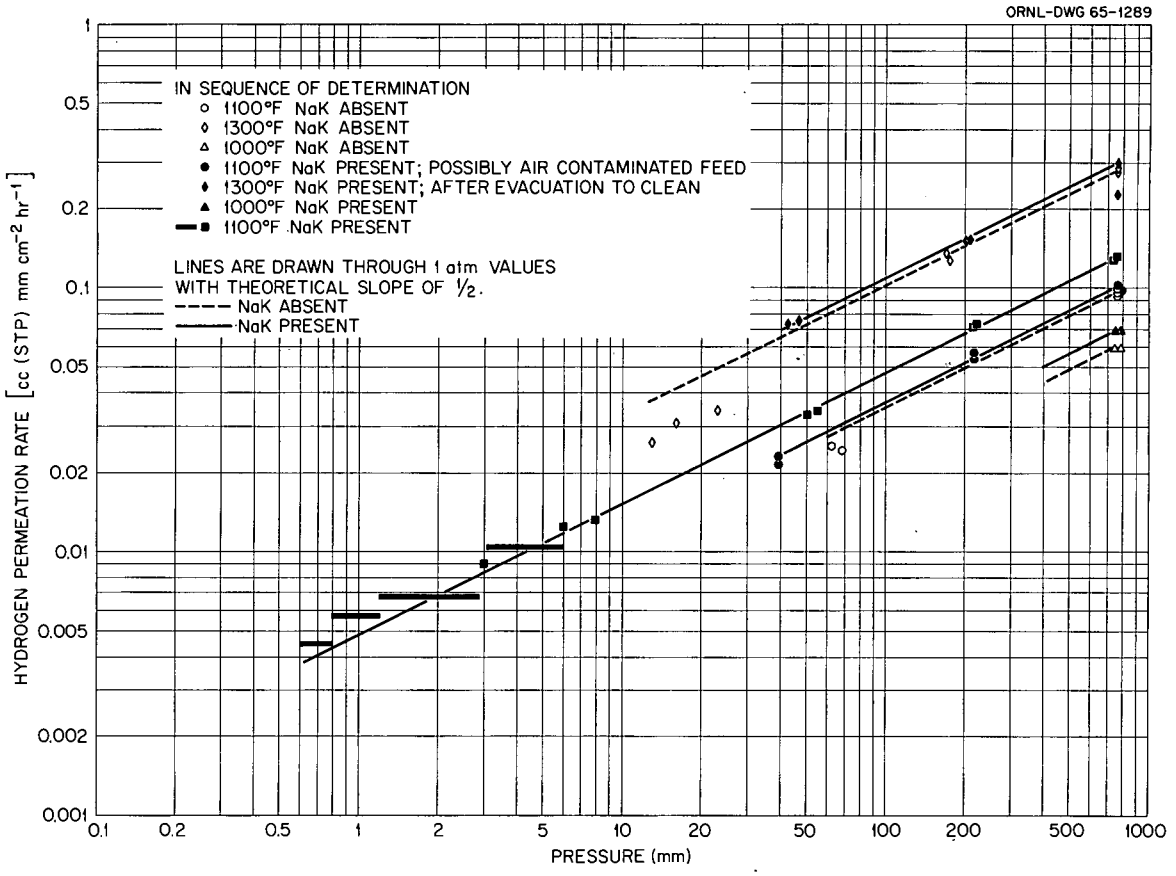

Fig. 23.2. Permeability of Type 316 Stainless Steel to Hydrogen in the Absence and Presence of NaK at Various Pressures and Temperatures.

with decreasing pressure at the lower temperatures. The data agree almost exactly with the values for type 316 stainless steel reported by Flint[4] and are higher than those for type 304 stainless steel reported by Flint and by Steigerwald.[5]

After concluding the determinations in the absence of NaK, a charge of 2.6 cm^3 of NaK was loaded into the chamber between the thimble and the upstream side of the diaphragm. Subsequent hydrogen permeability measurements were made at pressures from 1 atm to 42 mm at 1300°F and to below 1 mm at 1100°F in two series, described below, and at 1 atm at 1000°F. The results are also plotted in Fig. 23.2.

In the first series of determinations after NaK was present at 1100°F, the permeation rate was slightly higher than in the absence of NaK. This was attributed to the possible removal of slight oxide films from the surfaces contacted by the NaK. Feed-gas analyses indicated slight air contamination. Consequently, the system was charged with hydrogen at 1300°F and the feed-gas region evacuated, thereby reversing the hydrogen flow for a time, with the intent of reducing any surface oxides and removing the associated moisture. When measurements were again made at 1100°F, following those at 1300 and 1000°F, the rate appeared to be about one-third higher than the original measurements.

There was no particular effect of time (aging) on the permeability coefficient indicated by the data, although it is not easy to separate such effects from others acting concurrently. Certainly any such effect is not great.

These results indicate that the presence of NaK has no adverse effect on the permeation of

[5]E. A. Steigerwald, *The Permeability of Hydrogen Through Materials for the Sunflower System*, NASA CR-54005 (May 1964).

hydrogen through type 316 stainless steel at SNAP-8 temperatures. Indeed permeation rates may be moderately increased in the presence of NaK, as a result of the reduction of resistance to hydrogen passage at the NaK-metal interface. This may be largely due to dissolution of slight oxide films. It could also be affected by easier entry into the structural metal of hydrogen atoms from the liquid metal as compared with hydrogen from molecules of the gas phase.

Croloy 9M Cells Without NaK. – A permeation cell with an Armco iron entrance thimble similar to the stainless steel cell but with a Croloy 9M diaphragm was operated in the absence of NaK to determine the characteristics of the cell. The data were obtained after extended hydrogen permeation to obtain a steady state across the cell for each temperature and pressure condition. Table 23.1 presents the results in the sequence in which they were obtained, along with comparative data from determination[1d] on another cell of the same material without the internal iron thimble.

The paired values obtained agree fairly well with each other. Replicate determinations at 1300°F at the end of the series gave higher values at 1 atm and 196 mm than were obtained at the start of the series, indicating that the continued permeation of hydrogen over the period of three weeks may have resulted in a moderate increase in permeability. The permeabilities at 1 atm obtained at 1100 and

Table 23.1. Permeability to Hydrogen of Croloy 9M in the Absence of NaK

Values given in the sequence obtained

Pressure (mm Hg)	Permeation Coefficient (std cm^3 mm hr^{-1} cm^{-2} $atm^{-1/2}$)		
	1000°F	1100°F	1300°F
Cell with Internal Thimble			
760			0.590
760			0.588
199			0.359
196			0.342
28.5			0.374
23			0.374
760		0.263	
760		0.263	
137		0.225	
112		0.226	
39		0.170	
36.5		0.166	
760	0.178		
760	0.180		
760			0.656
760			0.664
196			0.612
Results for Croloy 9M Cell Without Internal Thimble			
760		0.29	0.53
760		0.27	0.57

1300°F agree fairly well with data from the previous Croloy 9M cell.

At lower pressures the permeation coefficients were lower, both at 1100 and 1300°F. Surface resistances such as oxide films, which affect permeation in proportion to the first power of the pressure, are believed to be the cause of this behavior.

Solution Chemistry of Hydrogen in Liquid Alkali Metal Mixtures

As discussed in the prior report,[2] very little information is available on the solution chemistry of hydrogen in mixtures of liquid alkali metals, and only a limited amount for the hydrogen–single-alkali-metal system.

At low concentrations of hydrogen, hydrogen dissolves in the liquid metal to form unsaturated solutions obeying Sieverts' law, wherein the concentration of dissolved hydrogen is proportional to the square root of the hydrogen pressure. As the concentration of dissolved hydrogen is increased, it may become great enough to exceed the solubility of solid metal hydride in the system, and this salt will begin to precipitate. In accord with the phase rule, in the presence of two condensed phases at a given temperature the pressure is invariant, except as the composition of the metal mixture changes. Thus the pressure does not alter appreciably with the addition of more hydrogen, which only results in more hydride precipitation.

Three characteristic parameters, two of which are independent, may be extracted from pressure–hydrogen-uptake data. These parameters are the Sieverts solubility coefficient for unsaturated solutions, the decomposition-precipitation plateau pressure when solution and solid hydride phases are present (in particular when precipitation has just begun, and only a very small amount of solid phase exists), and the terminal hydrogen (or hydride) solubility value, at which precipitation just begins. Each coefficient is expected to vary exponentially with inverse absolute temperature. These coefficients are adequate to describe the behavior of systems involving hydrogen and a single metal, or a metal mixture of fixed composition. This is the case treated in the hydrogen solubility studies with NaK-78. In the case of the hydrogen solubility studies with dilute solutions of lithium in NaK-78, the proportions of lithium were varied in different experiments. Also, in some cases, it was possible to add enough hydrogen to exceed the stoichiometric equivalent of all the lithium. Thus it became possible to extract from the data an equilibrium constant, similar to a solubility product, which characterized the relative affinity of lithium for hydrogen dissolved in the liquid-metal solution. Although these measurements are available at only one temperature, they provide the basis for a concept of the chemistry of hydrogen in liquid-metal mixtures.

Techniques. – Careful observations of the pressure and amount of hydrogen taken up by the liquid metal as increments of hydrogen are added or removed permit the evaluation of the above parameters. Such measurements have been made for the NaK-78 system at pressures from about 5 mm to 1 atm, and at temperatures ranging approximately between 300 and 700°C. A number of experiments were also conducted at 593°C (1100°F) in which the NaK contained 1 to 4 at. % lithium, in order to determine the effect of this substance on hydrogen solubility.

The NaK was contained[2] in thin-walled Armco iron capsules, which were loaded and sealed by electric-arc welding in a helium-filled glove box. The capsule was placed into a quartz envelope which was inserted into a furnace. The envelope was connected to a gas-feed system which consisted of a manometer, two gas burets, and a vacuum system.

Previous preparatory measurements enabled the hydrogen lost by permeation through the quartz walls of the envelope to be estimated and a correct inventory to be maintained. The distribution of the hydrogen inventory in the envelope was calculated from the pressure and temperature information for each point. The distribution accounted for the hydrogen in the envelope dead space at the furnace temperature and the portion at room temperature, the hydrogen dissolved in the iron of the capsule, and that in the vapor space of the capsule. The residual hydrogen was assumed to be dissolved in the NaK.

In the temperature range at 400°C and above, the rate at which hydrogen permeated the capsule wall was sufficiently rapid for the system to approach a steady or equilibrium pressure in a few hours or less. At 330 and 300°C, several days were required for each equilibrium point. The equilibrium pressures were verified by increasing the amount

of hydrogen in the system and then decreasing the amount and obtaining the equilibrium value at each step. The uptake data were further verified by direct hydrogen determination. When the equilibrations were complete, the envelope was closed off and quenched to room temperature by removing it from the furnace. The gas from the envelope dead space and the capsule vapor space was recovered, measured, and analyzed, and the NaK was recovered for analysis. The total hydrogen recovered in the analyses and its distribution in the NaK were calculated for the terminal condition of the experiment, and compared with the addition-removal inventory data.

Phase Equilibria in the H-Na-K System. – The solubility of hydrogen in NaK-78 was measured over a temperature range from 300 to 704°C and from 5 mm Hg to atmospheric pressure. The saturation concentration of hydrogen in NaK and the hydrogen pressure at which precipitation was indicated to have begun were determined at 300, 330, and 400°C.

Pressure–hydrogen-uptake data for the several experiments are shown in Fig. 23.3, in which the logarithm of hydrogen uptake of the NaK is plotted vs the logarithm of pressure. The sloping lines, which have been given the arbitrary Sieverts slope of $\frac{1}{2}$, fit the data of the respective experiments well. Points for which the gas was entering the capsule are in most cases consistent with those in which gas was removed, indicating that an adequate approach to equilibrium had been achieved. The final uptake based on chemical analysis is also indicated for four of the experiments in which such data were available.

In the experiments at 400, 330, and 300°C, precipitation occurred below 1 atm, and hydrogen uptake continued without appreciable pressure changes. Vertical lines for these experiments characterize the precipitation-decomposition pressure, and the intersection with the Sieverts line fixes the value of the terminal solubility.

In the experiments at 300°C, and to a lesser extent at 330°C, the rate of equilibration was very slow, because of the lower hydrogen pressures and the lower capsule permeabilities. Equilibration times of more than a week were required. In some points shown in Fig. 23.3 it appears certain that

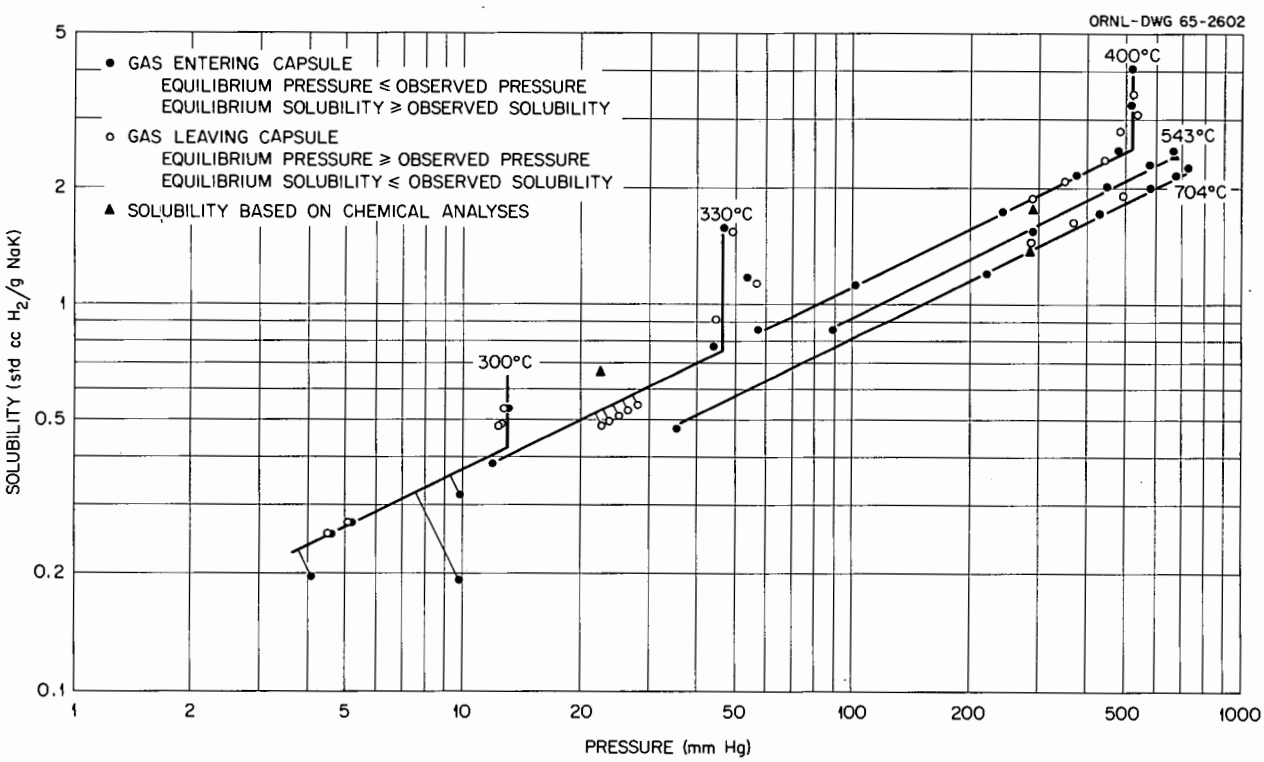

Fig. 23.3. Solubility of Hydrogen in NaK-78 as a Function of Pressure at Various Temperatures.

equilibrium was not attained, and the points are useful only in showing that the equilibrium lies on a given side of the point.

Values of Sieverts' coefficient, terminal solubility, and precipitation-decomposition pressure are given for temperatures of 300, 330, and 400°C in Table 23.2. Values of Sieverts' coefficient for temperatures of 543, 593, and 704°C are also given. It will be seen that only slight changes occurred in Sieverts' coefficient over the entire range.

The precipitation-decomposition pressure was compared with values for the KH system and the NaH system reported by Herold.[6] The variation with temperature exhibited on the usual plot of the logarithm of pressure vs the inverse of absolute temperature is entirely parallel. Values for NaK-78 were higher than those for potassium or sodium respectively. For example, at 400°C, we observed a value of 517 mm for hydride precipitation from NaK, while for KH, a value of 327 mm and for NaH a value of 395 mm is obtained from Herold's data. Since each of the constituent metals in NaK-78 is necessarily at a mole fraction less than 1, the principle of mass action requires that a higher hydride precipitation pressure should be anticipated.

Values for the terminal solubility of hydrogen in NaK-78 have been compared[1e] with data[7,8] for NaK-30, reported in connection with the British Dounreay Reactor Project, and are reasonably consistent with it. Data for the single-metal system H-Na, reported by Williams *et al.*,[9] however, are in disagreement, particularly with regard to the temperature coefficient, which they find to be much higher. For example, they report a terminal solubility of approximately 0.2 std cm^3 of H_2 per gram of Na at 300°C and 7 std cm^3 of H_2 per gram of Na at 400°C. Thus in the range 300 to 400°C they report a thirty-five-fold variation in solubility, whereas we find (Table 23.2) about a sixfold variation. It is doubtful that the NaK system is actually so different from the pure sodium system. It is desirable that the indicated differences be resolved. Practical aspects of this discrepancy are important, with respect to estimating the possibility of hydrogen precipitation at lower temperatures, either in undesired locations or as desired in cold traps.

Phase Equilibria in the H-Na-K-Li System. – Consideration of the relatively low decomposition pressures reported[10] for lithium hydride suggested that addition of moderate quantities of this substance to NaK systems might be capable of appreciably lowering the activity of dissolved hydrogen by preferentially combining with it and possibly precipitating it.

In examining this possibility, it is desirable to study the hydrogen uptake as a function of pressure, lithium concentration, and temperature. Experiments at constant temperature described below

[6] A. Herold, "Contribution a L'Etude des Hydrures Alkalins," *Ann. Chim. (Paris)* **6**, 536–81 (1951).

[7] V. M. Sinclair, R. A. H. Pool, and A. E. Ross, "Impurities in a Liquid Metal Coolant and Their Effect on the Fuel Element Canning Materials Niobium and Vanadium," *Nucl. Reactor Chem., 2d Conf., Gatlinburg, Tenn., Oct. 10–12, 1961*, TID-7622, pp. 35–56.

[8] A. Thorley and C. Tyzack, "The Embrittlement of Niobium by Hydrogen-Contaminated NaK," *Thermodyn. Nucl. Mater., Proc. Symp., Vienna, 1962*, pp. 365–97.

[9] D. D. Williams, J. A. Grand, and R. R. Miller, "The Solubility of Sodium Hydride in Sodium," *J. Phys. Chem.* **61**, 379–81 (1957).

[10] F. K. Heumann and O. N. Salmon, *The Lithium Hydride, Deuteride, and Tritide Systems*. KAPL-1667 (Dec. 1, 1956).

Table 23.2. Hydrogen Solubility Characteristics of NaK-78

Temperature, °C	300	330	400	543	593	704
Precipitation-decomposition pressure, mm Hg	13	46	520			
Terminal solubility, std cm^3 H_2/g NaK	0.42	0.76	2.6			
Sieverts' coefficient, $\frac{\text{std cm}^3\ H_2/\text{g NaK}}{(P_{atm})^{1/2}}$	3.2	3.1	3.1	2.6	2.3	2.3

permit consideration of the way in which lithium affects the activity of hydrogen in NaK solution, and suggest some generalizations regarding the chemistry of hydrogen in liquid alkali metal mixtures.

Experiments were conducted at 1100°F, determining the hydrogen solubility relationships for NaK containing different quantities of lithium (approximately 4.4, 2.2, and 1.2 at. % Li in NaK respectively). These experiments were conducted in the fashion similar to those used in determining the phase equilibria in the H-Na-K system.

Data from these experiments have been brought to a self-consistent basis by a simple mass-action model. According to this model, hydrogen dissolving in the NaK solution combined to some extent with the lithium, forming an undissociated lithium hydride molecule. The concentration of hydrogen and lithium bound in this way, and the free or unbound concentrations of each, could be determined by simple stoichiometry for each gas addition by using the Sieverts solubility coefficient for NaK, obtained from the data reported above. The total undissociated LiH included both dissolved and precipitated material.

It was thus possible to calculate a free-atom product (similar to a solubility product) which should be independent of the total undissociated LiH as long as precipitated LiH was present. When no precipitate was present, however, the free-atom product should be proportional to the total undissociated LiH.

The data from the three lithium experiments are shown in Fig. 23.4, in which the logarithm of the free-atom product is plotted against the logarithm of the total LiH. The behavior anticipated on the basis of the above model is indeed exhibited.

Furthermore, the stoichiometric calculations indicate that in the solution containing 1 at. % lithium, 20% of the dissolved hydrogen existed as undissociated LiH molecules.

These findings indicate that lithium does indeed act to limit the hydrogen activity, partially by competing with the other alkali metals of the mixture for the hydrogen, but largely by means of the precipitation of lithium hydride as its solubility limits are exceeded.

Experiments to determine the effect of temperature on these phenomena are in progress.

Discussion. – The form in which the hydrogen dissolved in liquid alkali metals exists is not identified in the available literature. Ultimate precipitation as the alkali metal hydride suggests that hydride ions or undissociated molecules could

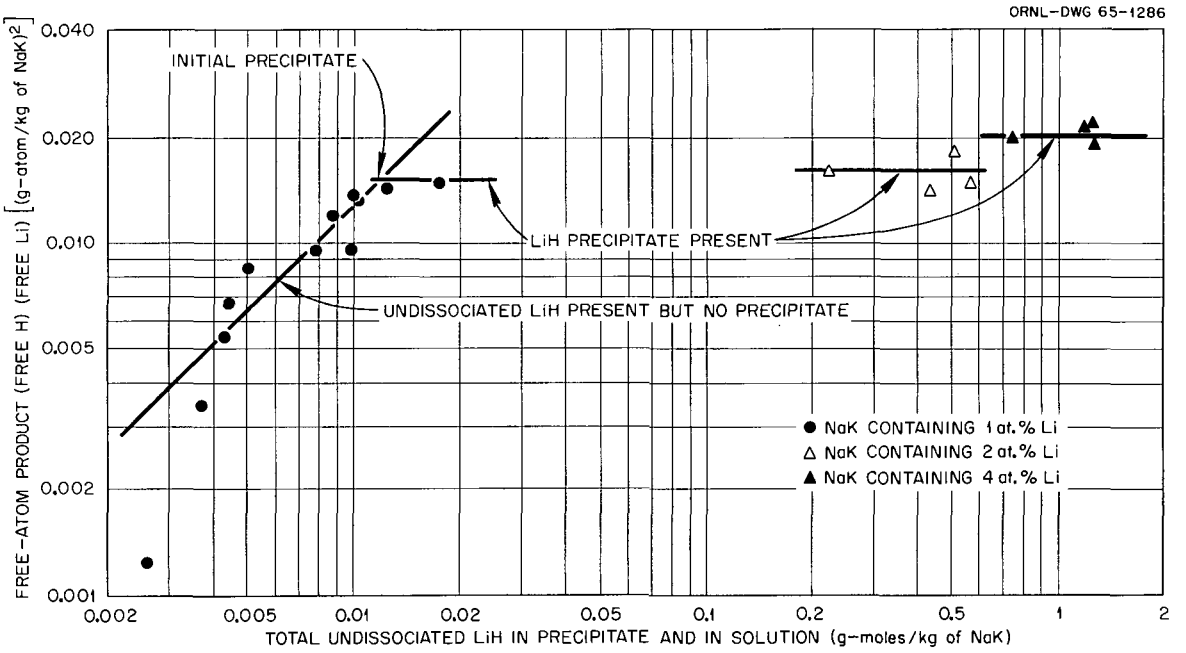

Fig. 23.4. Solubility Relationships at 1100°F in the H-Li-Na-K System.

be involved. The fact that the solubility is proportional to the square root of the pressure implies that the hydrogen could exist as free atoms, as dissolved undissociated metal hydride, or perhaps other monohydrogen forms. However, the existence of a negatively charged hydride ion in significant quantities would require equal quantities of positive metal ions, and would appear to require that the solubility be proportional to the fourth root of hydrogen pressure, in contradiction of the evidence of Fig. 23.3.

In the 1 mole % lithium solution discussed above, in the absence of precipitation a relatively constant proportion of about 20% of the dissolved hydrogen was indicated as being in the form of undissociated lithium hydride. It seems strongly implied that the remaining hydrogen similarly exists substantially in the form of undissociated hydrides of sodium and potassium. The proportions of these would be constant for a fixed metal ratio at a given temperature. Sieverts' coefficients reported in Table 23.2 for the NaK-78 are thus characteristics of that particular mixture. Resolution of the solubility phenomena in terms of the properties of the component elements will require data from liquid-metal mixtures of suitably altered compositions.

It is suggested that, in liquid alkali metal mixtures, dissolved hydrogen exists in the form of largely undissociated metal hydride molecules, with the different metals combining with different proportions of hydrogen dependent on their proportions and their affinity for hydrogen.

SPACE MATERIALS PROPERTIES INFORMATION CENTER

R. L. Bennett C. H. Secoy

ORNL has agreed to provide personnel and services to establish data for the Sandia Corporation on the physical and chemical properties pertinent to the operational safety of aerospace nuclear systems. The Sandia Corporation, which is responsible for the development of safety design and analyses for the SNAP Program, has selected properties and materials which are to be described in handbook form. The properties being investigated by personnel from Reactor Chemistry, Reactor, Metals and Ceramics, and Isotopes Divisions are listed in Table 23.3. Reactor Chemistry Division is primarily responsible for the chemical and thermodynamic (equilibrium) properties. Certain aspects of the project are classified.

The objective of the ORNL project is to (1) collect available information and data on the thermophysical, electrical, mechanical, and chemical properties of power source and capsule container materials; (2) critically evaluate and estimate limits of confidence of the data; (3) evaluate the capabilities of ORNL and other organizations to obtain any particular data; and (4) forecast data which may be forthcoming for current or projected programs of other organizations.

The work is being done by literature search, contact with other organizations, and other appropriate means.

Preliminary data sheets have been prepared and are being sent to Sandia as the data are collected. These preliminary collections will be evaluated and are subject to correction. Emphasis is placed on the experimenter and experimental procedure in trying to evaluate the results and probable errors. Theoretical considerations are used, when possible, to establish trends and magnitudes in the experimental data. When adequate theoretical grounds are available, these will be used to predict property values where no experimental data exist.

In order to avoid duplication and encourage cooperation with other data-collecting groups, this program has been registered with the ORNL Coordinator of Information Centers and has been assigned the title "Space Materials Properties Information Center." Access to the information of the Center is restricted to persons or organizations approved by the Sandia Corporation.

Table 23.3. Space Materials Properties for Sandia Program

A. Composition

1. Isotopic content
2. Chemical composition and phase diagram
3. Decay scheme
4. Impurities and effects

B. Thermophysical properties

1. Density
2. Thermal expansion; volumetric changes due to changes of phase
3. Specific heat and enthalpy
4. Temperatures of phase change (see also A.2)
5. Latent heats of phase change
6. Vapor pressure
7. Thermal conductivity
8. Thermal diffusivity
9. Viscosity
10. Surface tension
11. Total hemispherical emittance
12. Spectral emissivity

C. Electrical properties

1. Electrical resistivity, temperature coefficient of resistivity
2. Thermoelectric properties

D. Mechanical properties

1. Crystallography (see also A.2 and B.3)
2. Hardness
3. Ultimate strength, tensile yield strength, tensile compressive strength
4. Poisson's ratio, Young's modulus, shear modulus, bulk modulus
5. Creep behavior
6. Elongation, brittle-to-ductile transition temperature

E. Chemical properties

1. Solubilities (water, seawater, liquid metals, other)
2. Standard free energies, entropies, enthalpies
3. Chemical reactions and reaction rates (oxygen, nitrogen, water, steam, hydrogen, liquid metals, other)
4. Diffusion rates
5. Compatibility

24. Effect of Radiation on Organic Materials

W. W. Parkinson O. Sisman

EFFECT OF RADIATION ON POLYSTYRENE

R. M. Keyser R. A. Weeks[1]

Earlier work demonstrated that fast neutrons, which have a linear energy transfer (LET) rate of ~3 ev/A, were more efficient in producing cross links in polystyrene than gamma radiation (LET ~0.02 ev/A).[2,3] For neutrons the yield is G(cl) = 0.096 cross link per 100 ev, and for ^{60}Co gamma radiation, G(cl) = 0.034. The ratio of molecular scission to formation of cross links is 0.28 in both cases. The yields of volatile decomposition products (H_2, C_6H_6, and CH_4) show an even greater dependence on LET. This dependence of yield on LET can show the relative importance of first-order and higher-order reactions.

In the present study we have attempted to determine whether the LET effects in final products result from a radical process or from reactions of precursors of the radicals. The concentrations of long-lived free radicals were measured approximately by electron spin resonance (ESR). The techniques for exposure of evacuated polystyrene samples to the mixed neutron-gamma field of the ORNL Graphite Reactor and to ^{60}Co gamma radiation have been previously described.[2]. Sample temperatures during irradiation were about 25°C in both cases, so that only free radicals stable at these temperatures were observed. After removal from the radiation source, the samples were maintained at −196°C to prevent radical decay, and the ESR measurements were also made at this temperature.

The spectrum shown in Fig. 24.1, in which the first derivative of the resonance curve is plotted against magnetic field strength, was characteristic of all the gamma-irradiated specimens. The spectrum consists of two sets of peaks, labeled *A* and *B*, in the central portion of the curve with separations of 19 and 40 gauss respectively. Both sets of peaks are about equal in intensity. A third set of peaks, labeled *C* and of much lower intensity, is evident in the outer regions of the curve. The separation of this set is 113 gauss. The spectra of the reactor-irradiated samples consisted of a similar distribution of peaks, but the intensity of the *A* peaks was slightly greater than that of the *B* peaks.

It was not possible to assign the observed spectrum to a definite radical species because of the unresolved nature of the peaks. However, Florin *et al.*[4,5] have concluded from an ESR study of free radicals in irradiated normal and deuterated polystyrenes that the spectrum results from a cyclohexadienyl-type radical. Florin's spectra consist of two sets of peaks having relative intensities and separations similar to those of *A* and *C* in Fig. 24.1. The main difference between Florin's spectra and ours is the occurrence of the *B* peaks, indicating that our spectra may arise from two radical species, one possibly being the cyclohexadienyl-type radical.

The concentration of free radicals was determined by a comparison technique in which the area under the resonance curve of the sample is compared with the area of a standard containing a known number of unpaired spins. The standard

[1]Solid State Division.

[2]W. W. Parkinson *et al.*, *J. Phys. Chem.* **69**, 828 (1965).

[3]R. M. Keyser *et al.*, *Reactor Chem. Div. Ann. Progr. Rept. Jan. 31, 1963*, ORNL-3591, p. 224.

[4]R. E. Florin, L. A. Wall, and D. W. Brown, *Trans. Faraday Soc.* **56**, 1305 (1960).

[5]R. E. Florin, L. A. Wall, and D. W. Brown, *J. Polymer Sci.* **A1**, 1521 (1963).

Fig. 24.1. Typical Electron Spin Resonance Spectrum of Gamma-Irradiated Polystyrene.

consisted of Cr^{3+} ions in a single crystal of MgO.[6] The number of Cr^{3+} ions in the crystal, measured by neutron activation techniques,[7] was $(4 \pm 2) \times 10^{15}$. Areas were determined by double integration of sample and standard spectra, using numerical methods.[8]

Free-radical concentration as a function of dose is plotted in Fig. 24.2 for three series of irradiations. Curve *A* shows radical yields from fast-neutron bombardment (solid triangles) and from ^{60}Co gamma irradiation (open triangles). The fast-neutron yields were determined from the observed reactor yields by subtracting the contribution from the gamma component of the reactor field. It is apparent that the yields of radicals for both gamma and fast-neutron irradiation are the same within ±10%, at least in the dose range $(1–3) \times 10^{20}$ ev/g.

Curves C and *D* are radical yields from specimens subjected to ^{60}Co radiation. In the low-dose region the slope of curve *C* is similar to that of *A*, whereas that of *D* is somewhat greater. Curve *C* also shows that free-radical concentration is not a linear function of dose above 8×10^{20} ev/g and that it eventually reaches a limiting concentration where further increase in radiation dose results in no increase in radical concentration.

The values of *G* (radicals), calculated from the slopes of the lines in the dose range $(1–7) \times 10^{20}$

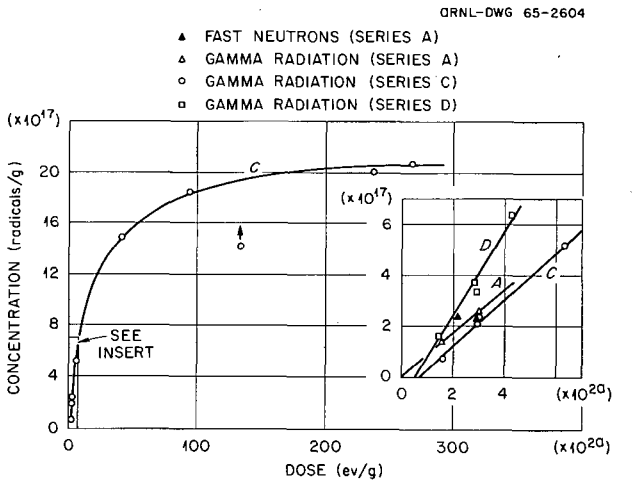

Fig. 24.2. Free Radical Concentration in Irradiated Polystyrene.

[6]R. A. Weeks and T. Purcell, to be published in the *Journal of Chemical Physics*.

[7]Analysis performed by the Neutron Activation Analysis Group.

[8]A double integration is required, since it is the first derivative of the resonance curve that is recorded.

ev/g are 0.086, 0.10, and 0.16 radicals per 100 ev for series *A*, *C*, and *D* respectively. The differences in the *G* values are ascribed to different positions of the standard in the cavity of the spectrometer such that the standard is in a microwave field of slightly different intensity for each of the three series of experiments. Differences in the intensity of the microwave field seen by the standard will appear as differences in area under the resonance peak and ultimately in the radical concentrations. These difficulties do not, however, vitiate the conclusion that *G* (radicals) is the same for both fast-neutron and gamma irradiation, because the standard is not moved during any given series. A further difficulty in obtaining an absolute measure of *G* (radicals) is the fact that the number of spins in the standard is known only to about 50%. The best estimate then for *G* (radicals) is 0.12 ± 0.08.

The equivalence of the radical yield for both fast-neutron and gamma radiation is surprising in view of the considerable differences found earlier for cross-linking, scission, and low-molecular-weight decomposition products. If these LET effects were the result of second-order radical recombination reactions, more radicals would be expected to recombine in the overlapping spurs produced by fast neutrons than in the isolated spurs from gamma photons. Thus, the constancy of the radical yields at different LET values indicates that the radicals observed are not the major intermediates involved in the production of cross links and volatile products. Since the concentration of radicals reaches a steady state at a relatively moderate dose of gamma radiation (Fig. 24.2, curve *C*), a comparison of the limiting value for gamma radiation with that for neutron bombardment would be another way of comparing LET effects. This has not yet been done.

CHEMONUCLEAR STUDIES

Radiation-Induced Reactions of Hydrocarbons

W. W. Parkinson R. M. Keyser
W. K. Kirkland

A basic program has been initiated to study the radiation-induced reactions of hydrocarbons simulating two processes: the hydrogenation of coal and the introduction of nitrogen into hydrocarbons. These studies will be started using gamma radiation from a ^{60}Co source. Linear energy transfer effects, using heavy-particle radiation and fission fragments, will follow.

For the hydrogenation studies we will start with an investigation of the radiolysis of solutions of naphthalene in hexane. Apparatus is being assembled for handling samples and for vapor chromatographic analysis of hydrogen and light hydrocarbon products. The extent of alkylation of the naphthalene will be measured by infrared spectra of CCl_4 and CS_2 solutions of the nonvolatile fraction of the irradiated mixtures. Chromatographic methods will be required for identification of individual products. The reactions to be expected are numerous, but the predominant reactions should be those shown in Fig. 24.3.

The ammonia-hydrocarbon system is another one in which radiation-induced reactions have been little studied. Since irradiation of aqueous hydrocarbon mixtures has resulted in the formation of alcohols and other oxygenated products,[9] one might expect, in view of the similarity between many of the properties of ammonia and water, that amines may be formed when hydrocarbons are irradiated in the presence of ammonia.

The hydrocarbons chosen for the initial experiments are hexane, 1-hexene, and benzene. Apparatus has been constructed for ammonia purification and sample preparation. Amine radiolysis products will be separated from the irradiated mixture by extraction with dilute acid followed by neutralization and a second extraction, using an organic phase. Product identification and determination of yield will be accomplished by using infrared spectrometry and vapor phase chromatography of the extracted material. Chromatography will also be employed to study the effect of ammonia on the yields of hydrogen and light hydrocarbons from the parent hydrocarbon.

Radiation Flux Measurements in the Gamma-Irradiation Facility

R. M. Keyser W. K. Kirkland

An irradiation facility has been constructed with adequate space for the irradiation of specimens undergoing mechanical testing over a range

[9] W. T. Spinks and R. J. Woods, *An Introduction to Radiation Chemistry*, pp. 299–300, Wiley, New York, 1964.

ORNL-DWG 65-2605

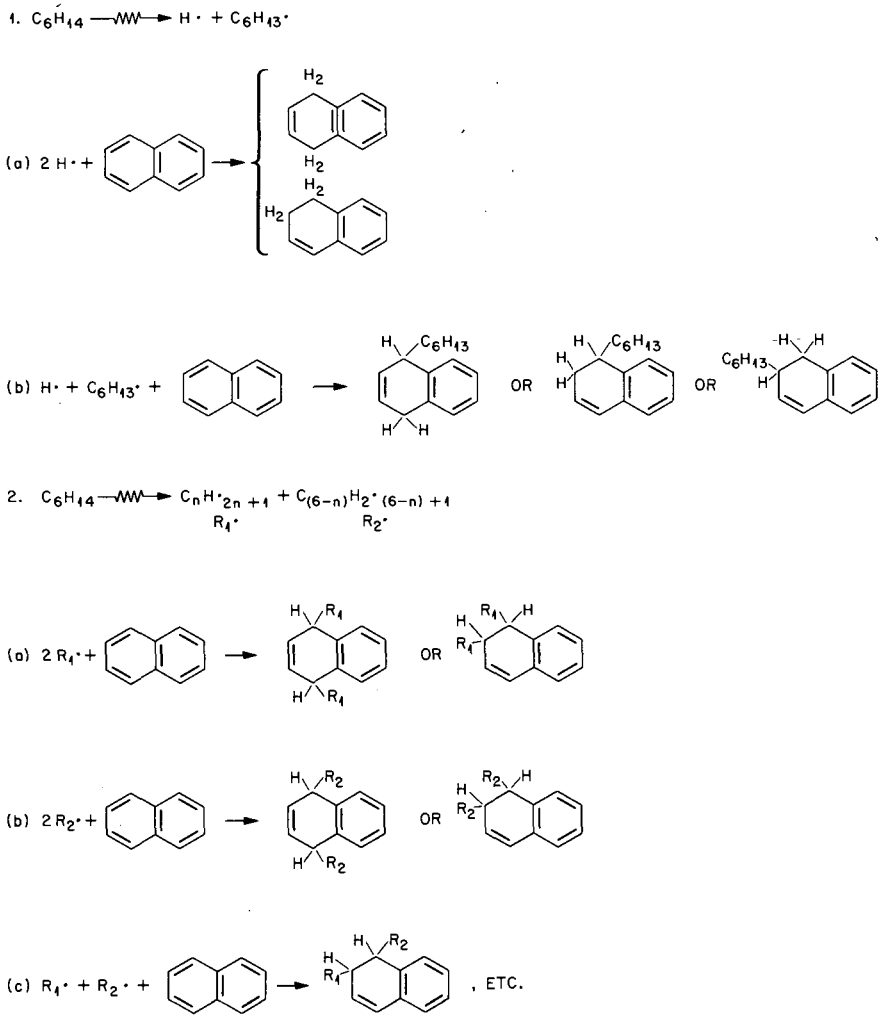

Fig. 24.3. Radiolysis Reactions of Hexane and Naphthalene.

of temperatures. The facility comprises a shielded compartment 7 × 10 × 7 ft high with a ^{60}Co source which can be retracted into the floor for storage or for manipulation of specimens. The source assembly is a vertical cylinder $11\frac{1}{2}$ in. high with an inside diameter of $1\frac{7}{8}$ in. when contracted and $3\frac{3}{4}$ in. when expanded. The upper $7\frac{1}{2}$ in. of the source assembly contains cobalt pellets (18,900 curies were loaded) in double-walled capsules.

The gamma-radiation intensity in and around the source was measured so that doses to specimens may be calculated. We used the conventional ceric sulfate procedure, in which the reduction of Ce^{4+} is followed spectrometrically.[10] Three solutions, 4×10^{-4}, 4×10^{-3}, and 4×10^{-2} *M* in Ce^{4+} ion and 0.4 *M* in H_2SO_4, were prepared to cover the dose range 10^{16} to 10^{19} ev/g. The cerous ion yield for the three solutions was determined by measuring the decrease of Ce^{4+} concentration in a ^{60}Co gamma source in which the dose rate had been accurately established by means of the Fricke dosimeter. Irradiations were made in Pyrex weighing bottles; exposure times

[10] S. I. Taimuty, L. H. Towle, and D. L. Peterson, *Nucleonics* 17(8), 103 (1959).

were chosen such that 20 to 80% of the Ce^{4+} was reduced. Even though air cooling was employed during the irradiations in the calibrating source, the temperature rose gradually to a steady state of 34°C over a period of 45 min. The exposure times of the more concentrated solutions were long enough for the yield to be reduced by the elevated temperature, and the variation of $G(Ce^{3+})$ with temperature reported by Taimuty *et al.*[10] was applied to convert all results to yields at 27°C. The observed yield was $G(Ce^{3+}) = 2.45 \pm 0.03$.

Radiation intensity profiles were measured both inside and outside the source assembly and with the source in the contracted and the expanded condition. The profile along the vertical line through the center of the source assembly (contracted) is shown in Fig. 24.4. Within this cylinder, very high and uniform (±2.5%) doses are available over a distance of 8+ cm. Radiation intensities available outside the source are typified by Fig. 24.5, which shows those available in the horizontal center plane of the source along a line due north from the center; intensities calculated from the reciprocal-square law and a point source are also shown in this figure. The intensity distribution along the south bearing was found to duplicate the north distribution within experimental error, but the distribution in the east and west directions was slightly lower and followed the reciprocal-square law more closely.

With the source in the expanded configuration the intensity distribution was found to be less uniform, and the distribution outside the source deviated more from the inverse-square law for a point source. In the center of the source the dose rate was found to be uniform within ±2.5% over a vertical distance of only 5.3 cm, compared with a uniform region of 8.2 cm in the contracted configuration.

These measurements of the radiation intensity in and around the source assembly are now considered sufficient to enable the doses to irradiated specimens to be calculated and to permit planning of exposure periods for various types of specimens.

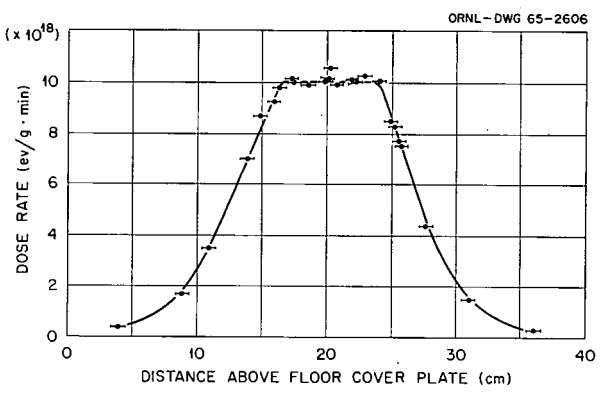

Fig. 24.4. Radiation Dose Rate Along Vertical Center Line of Source (Contracted Configuration).

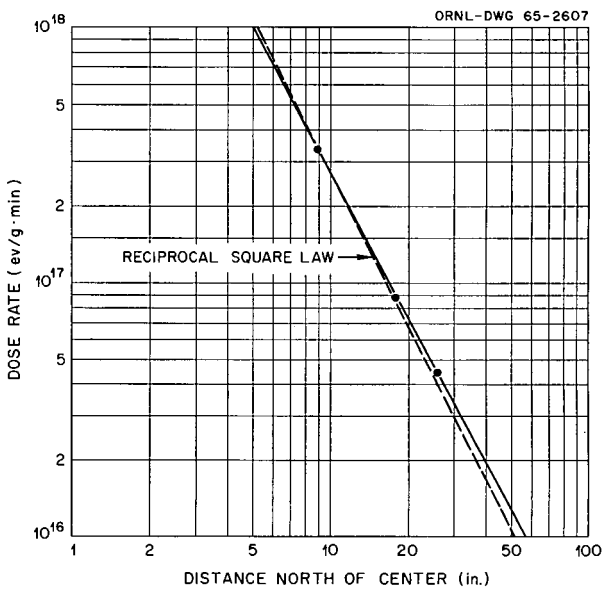

Fig. 24.5. Radiation Dose Rate Along North Bearing Outside Source (Contracted Configuration).

25. Preparation of Pure Materials

PREPARATION OF SINGLE-CRYSTAL LITHIUM FLUORIDE

R. E. Thoma

G. D. Brunton R. G. Ross
H. L. Hemphill A. J. Singh[1]

Standardized techniques for preparing lithium fluoride single crystals by a modified Stockbarger method developed at ORNL[2] were employed for growing three large (approximately 350 g each) single crystals of LiF. The isotopic compositions of these crystals were 50.77, 79.24, and 87.60 at. % ^{7}LiF. The ORNL-produced crystals were all made available for use at the Materials Science Center of Cornell University as part of an AEC Pure Materials Program. At Cornell, the crystals were first cleaved to obtain fresh specimens of the desired dimensions. Then low-temperature thermal conductivity was measured for each specimen, and the effect of isotopic composition upon phonon scattering was inferred from the results of these measurements.

By refinement of the details of our previously published procedures[2] and improvements in handling techniques, crystals were produced this year for which activation analysis indicated that the metallic impurity concentration did not exceed 30 ppb. The last crystal (87.60 ^{7}LiF) was vacuum annealed throughout the usual 10-day cooling and annealing period to minimize the possibility that minor contaminants in the helium cover blanket atmosphere, usually used to protect the crystal during this step, would diffuse into the crystal. All subsequent handling steps were performed in vacuum or inert atmosphere so that thermal conductivity measurements at Cornell could be made with the assurance that atmospheric contamination had not previously occurred.

Several theories concerning phonon scattering in LiF crystals are currently being developed. All are tentative and subject to modification as increasing numbers of experimental thermal conductivity data are obtained. The maximum values of thermal conductivity of LiF of various isotopic

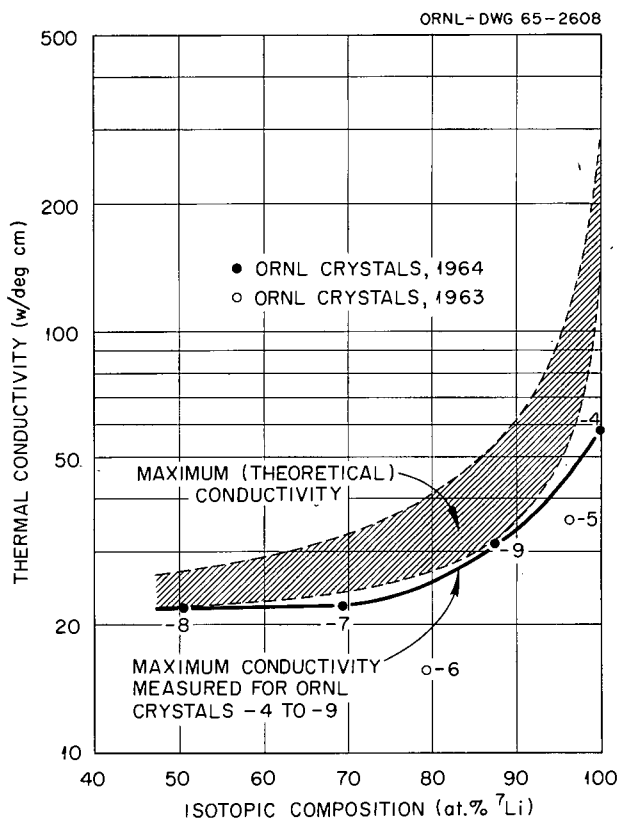

Fig. 25.1. Thermal Conductivity of LiF Crystals ORNL-4 to ORNL-9.

[1]International Atomic Energy Agency Fellow from Atomic Energy Establishment, Trombay, Bombay, India.

[2]C. F. Weaver *et al.*, *The Production of LiF Single Crystals with Selected Isotopic Ratios of Lithium*, ORNL-3341 (March 1964).

contents expected by a current theory being developed by J. A. Krumhansl of Cornell University are shown in the banded region of Fig. 25.1. The maximum values of the thermal conductivity of LiF crystals ORNL-4 to ORNL-9, measured[3] at the Cornell Materials Science Center, are also shown in Fig. 25.1. It is strikingly evident from these data that the thermal conductivity is extremely sensitive to minor variations in isotopic composition and purity at high ^{7}LiF concentrations. The high thermal conductivities of the ORNL crystals produced this year also reflect the utility of continual refinement of experimental methods for producing high-purity crystals.

PURIFICATION OF LiF BY VACUUM SUBLIMATION

A. J. Singh R. G. Ross R. E. Thoma

In their attempts to grow LiF single crystals at 10^{-3} and 10^{-4} torr, Weaver and co-workers[2] found that the melt distilled and condensed as a polycrystalline mass at the top of the capsule. Even at much higher pressures, LiF tended to vaporize in thermal gradients to deposit as crystals of LiF at surfaces where the temperature was slightly below the melting point of LiF (848°C). To examine fractional distillation as a means of obtaining extremely pure LiF, we studied the high-temperature distillation of LiF doped with NaF, CaF_2, MgF_2, and MnF_2. Under the experimental conditions used,[4] more than 95% of the LiF charge was transferred to the cold region of the apparatus (Fig. 25.2). Distribution of impurity ions in the LiF condensate is shown by the analyses listed in Table 25.1. These results show, as expected, that the contaminants in the deposited LiF decrease with decreasing vapor pressure. Practically all of the CaF_2 and most of the MgF_2 were found in the residue.

Table 25.1. Spectrographic Analysis of LiF Deposits[a]

Sample Position[b]	Concentration of Impurity (ppm)			
	Na	Ca	Mg	Mn
Experiment 1[c]				
1		*d*	*d*	580
2		*d*	*d*	100
4		*d*	*d*	300
5		*d*	*d*	100
6		*d*	*d*	*d*
7		*d*	*d*	*d*
9		*d*	*d*	*d*
10		*d*	530	*d*
11[e]		~200,000	~90,000	200
12[f]		920	460	960
Experiment 2				
1	540	*d*	*d*	1700
2	200	*d*	*d*	710
3	*d*	*d*	*d*	*d*
4	*d*	*d*	*d*	350
5	*d*	*d*	*d*	*d*
6	*d*	*d*	*d*	*d*
7	*d*	*d*	*d*	*d*
8	*d*	*d*	*d*	*d*
9	*d*	*d*	*d*	*d*
10	*d*	*d*	210	*d*
11[e]	Sample insufficient for analysis			
12[f]	450	420	220	420

[a]A rapid photoelectric analysis technique was employed. Detection limits (in ppm) were: Na, 20; Ca, 50; Mg, 50; and Mn, 50.

[b]As marked in Fig. 25.1.

[c]Starting material not doped with NaF.

[d]Not detected.

[e]Residue.

[f]Starting material.

[3]R. O. Pohl and P. D. Thacher, unpublished work, 1964.

[4]Experimental details of these experiments are included in the paper "Vacuum Distillation of LiF," by A. J. Singh, R. G. Ross, and R. E. Thoma, *J. Appl. Phys.* (in press).

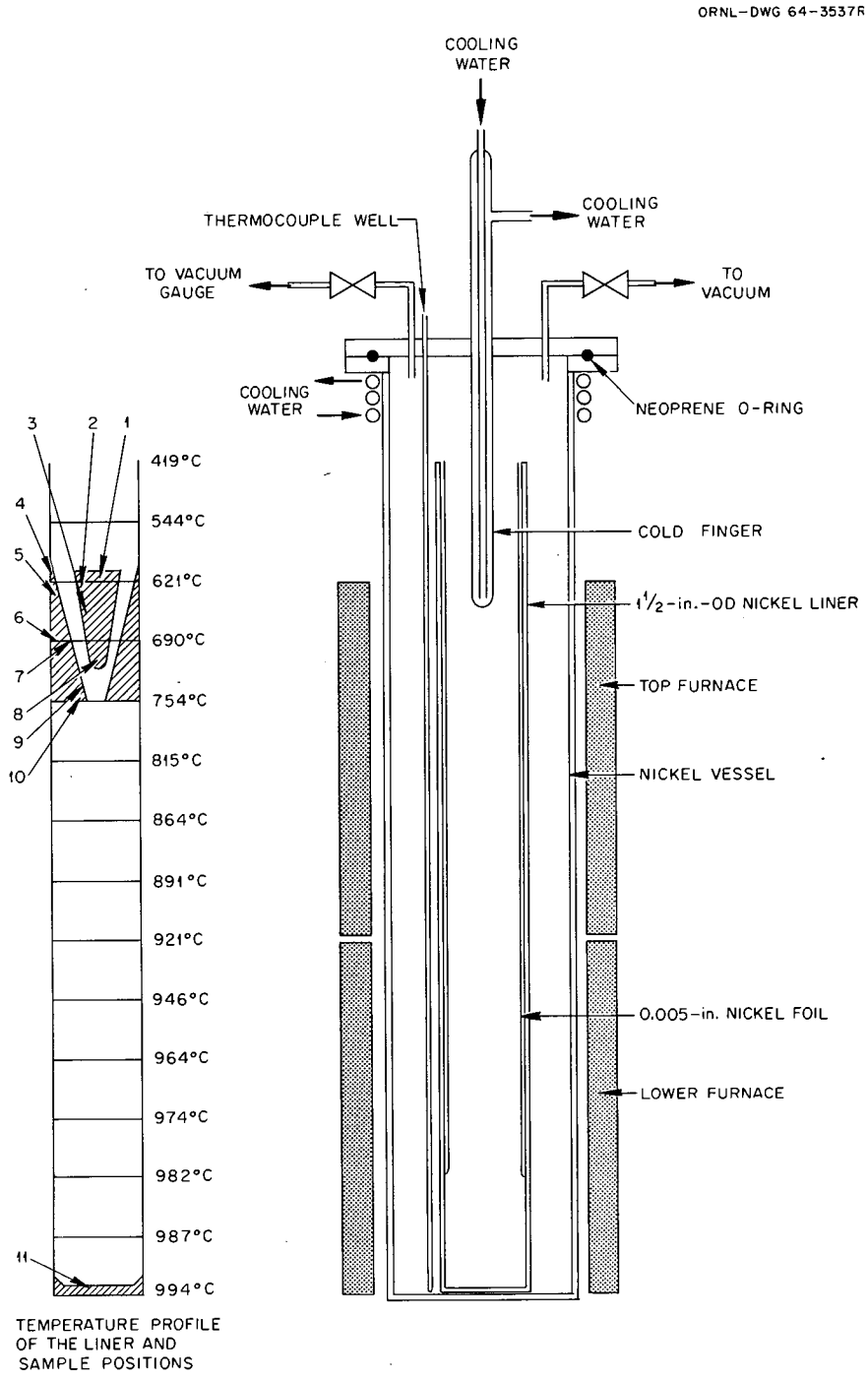

Fig. 25.2. Schematic Drawing of Apparatus for Vacuum Distillation of LiF and Temperature Profile.

PURIFICATION OF LiF BY ZONE REFINING

A. J. Singh R. G. Ross R. E. Thoma

The extreme sensitivity of thermal conductivity of pure LiF single crystals to isotopic composition and impurity level is described in a previous section of this report. The inequalities between measured and theoretically expected values for the low-temperature thermal conductivity of pure (less than 1 ppm metallic impurities) LiF are indicative of the need for even higher purity material. New methods of purification must, therefore, be developed if significant improvement in the purity of the material is to be attained.

Spectroscopic analyses of LiF single crystals reveal that as LiF is grown by the Stockbarger method, cationic impurities such as Na^+, Ca^{2+}, Mg^{2+}, and Mn^{2+} accumulate in that region of the crystal which freezes last.[2] In an effort to investigate the utility of such methods, we conducted zone-melting experiments with commercial LiF doped with NaF, CaF_2, MgF_2, and MnF_2. Procedures and experimental details are given else-

Table 25.2. Spectrographic Analysis of Horizontal Zone-Refined LiF[a]

Number of Zone Passes	Traverse Rate (cm/hr)	Charge Material	Sample Distance from Zone Entry (in.)						
			0	1	4	7	10	11	12
			Na^+ Concentration (ppm)						
1	1	540	30	60	480	640	880	4700	8,800
3	1	510	*b*	*b*	20	*b*	320	1600	1,800
3	2	450	*b*	*b*	*b*	*b*	100	550	23,000
3	4	680	*b*	*b*	*b*	*b*	420	3000	25,000
12	1	800	*b*	*b*	*b*	*b*	110	510	39,000
			Ca^{2+} Concentration (ppm)						
1	1	700	*b*	*b*	*b*	450	360	3100	4,500
3	1	840	*b*	*b*	*b*	*b*	*b*	800	10,000
3	2	450	300	320	328	390	380	440	630
3	4	820	*b*	*b*	*b*	*b*	70	1600	11,000
12	1	1100	*b*	*b*	*b*	*b*	*b*	70	32,000
			Mg^{2+} Concentration (ppm)						
1	1	460	310	310	360	370	360	4400	3,300
3	1	500	280	330	350	340	420	440	740
3	2	450	300	320	328	390	380	440	630
3	4	550	330	350	400	400	520	550	920
12	1	1000	200	250	260	350	480	640	1,600
			Mn^{2+} Concentration (ppm)						
1	1	1000	90	160	500	850	490	1600	4,000
3	1	1100	*b*	65	60	110	240	740	7,800
3	2	1070	240	*b*	*b*	160	130	680	13,000
3	4	910	*b*	100	60	100	540	1000	6,900
12	1	1000	*b*	*b*	*b*	*b*	150	270	11,000

[a]Zone length, 3 cm; ingot length, 30.5 cm.

[b]Not detected. Detection limits for Na, Ca, and Mn are estimated to be 20, 50, and 50 ppm respectively.

where.[5] Results of five experiments in which the molten zones were passed horizontally along the charge are given in Table 25.2. Figure 25.3 shows the distribution curves after 12 passes. Results of the horizontal zone purification experiments are in good agreement with the values of the distribution coefficients computed by Pfann[6] using Hamming's method. The following values of k, the distribution coefficient (the ratio of the concentration of the impurity in the freezing solid to that in the liquid at equilibrium), were obtained: Ca^{2+}, 0.1; Na^{+}, 0.1; Mg^{2+}, 0.7 to 0.8; Mn^{2+}, 0.2 to 0.3. The lower k values for Na^{+} and Ca^{2+} suggest that efficient removal of these impurities from LiF by zone-melting techniques is possible (see Fig. 25.4).

An interesting correlation between k and the size of ions of impurities can be made from the following data:

[5]A. J. Singh, R. G. Ross, and R. E. Thoma, *Zone Melting of Inorganic Fluorides*, ORNL-3658 (in preparation).

[6]W. G. Pfann, *Zone Melting*, Wiley, New York, 1958.

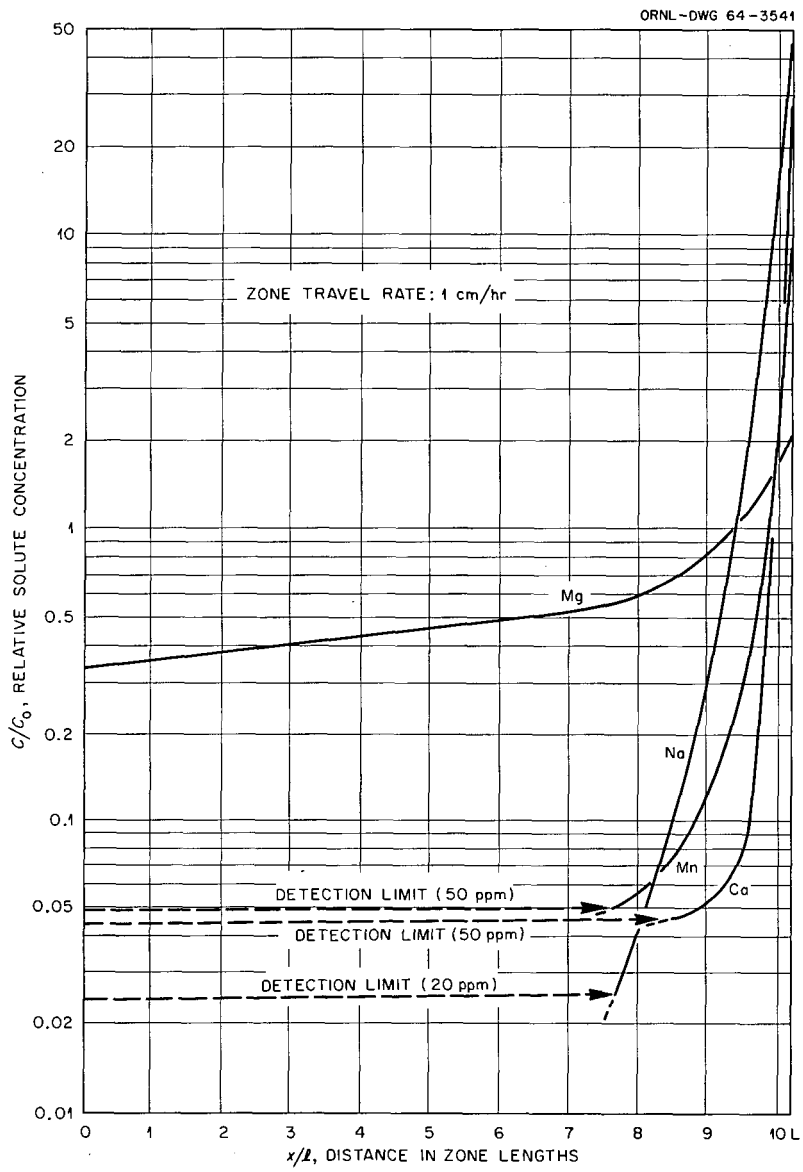

Fig. 25.3. Relative Solute Concentration (C/C_0) vs Distance in Zone Lengths (x/l) from Beginning of Charge After 12 Passes.

Cation	Size (A)	Difference (A)	Experimental k
Ca^{2+}	0.99	0.31	<0.1
Na^{+}	0.94	0.26	<0.1
Mn^{2+}	0.80	0.12	0.2–0.3
Li^{+}	0.68		
Mg^{2+}	0.67	0.01	0.7–0.8

These data suggest that the greater the disparity between the size of an impurity cation and Li^{+}, the smaller will be the distribution coefficient.

An interesting feature in vertical zone melting of LiF may be the significant role played by gravity and convectional factors in bringing about the segregation of Na^{+}, Ca^{2+}, Mg^{2+}, and Mn^{2+} in LiF. The results in Table 25.3 show that whenever a

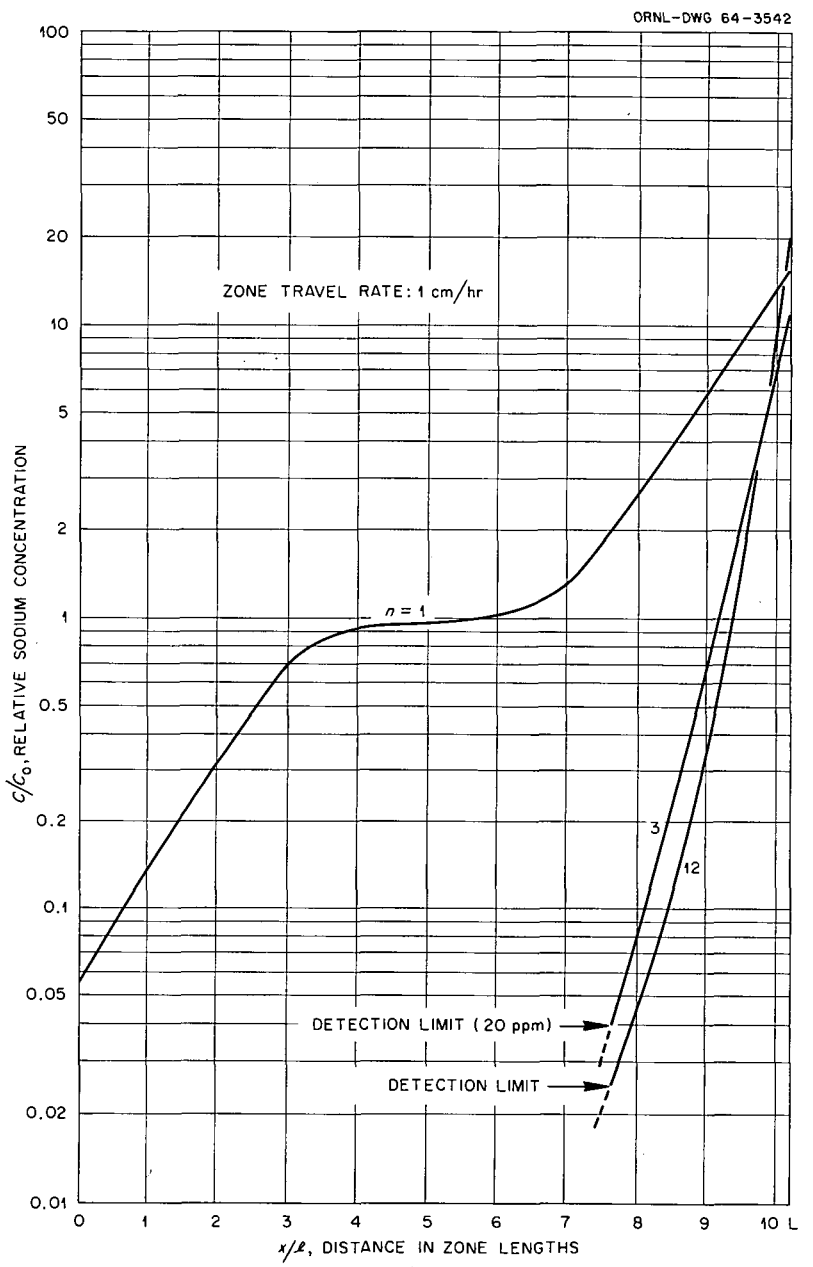

Fig. 25.4. Relative Sodium Concentration (C/C_0) vs Distance in Zone Lengths (x/l) from Beginning of Charge for Various Numbers of Passes, n.

Table 25.3. Spectrographic Analysis of Vertical Zone-Melted LiF[a]

No. of Zone Passes	Zone Movement Direction	Ingot Length (in.)	Sample Distance from Bottom of Ingot (in.)	Impurity Concentration (ppm)			
				Na	Ca	Mg	Mn
1	Upward	19	*b*	540	700	460	1000
			0	5	<100	1000	50
			2	10	<100	970	50
			4	30	100	1200	3300
			8	50	1000	1000	2200
2	Upward	16	*b*	c	700	460	1000
1	Downward		0	c	1400	1100	5000
			1	c	1300	930	2600
			2	c	1250	930	640
			10	c	1650	920	<100
			12	c	760	810	360
			14	c	60	690	<100
1	Upward	11	*b*	5	100	c	c
1	Downward		0	50	500	c	c
			5	5	20	c	c
			11	<5	10	c	c
2	Upward	10	*b*	5	100	c	c
			0	<5	20	c	c
			1	<5	10	c	c
			2	<5	10	c	c
			3	<5	10	c	c
			7	5	40	c	c
			8.5	5	60	c	c
			10	<5	100	c	c

[a]Zone length, 3.5 cm; traverse rate, 1 cm/hr.

[b]Starting material.

[c]Not detected.

downward pass was made, accumulation of impurities at the bottom of the capsule took place to such an extent that even two subsequent upward passes did not restore the original concentration distribution of impurities. For example, in the first experiment with a single upward pass, as expected, Na^+, Ca^{2+}, Mg^{2+}, and Mn^{2+} are swept along with the molten zone, but in the next experiment, where one downward pass was followed by two upward passes, these impurities remained at the bottom. This behavior is explained on the basis that higher density of impurities and convectional stirring of the melt (which is present only when the molten zone travels downward) enhance the segregation to an appreciable extent. Differences in the densities of the fluorides also become evident in vertical zone purification. Densities of the salts LiF, NaF, MgF_2, CaF_2, and MnF_2 are 2.64, 2.78, 3.15, 3.18, and 3.98 g/cm^3 respectively. The effect of density differences is so marked that the most dense fluoride, MnF_2, was routinely accumulated to the greatest extent when the molten zone was passed downward through LiF.

PREPARATION OF PURE TERBIUM METAL CRYSTALS

R. E. Thoma R. G. Ross

In a research program of the ORNL Solid State Division, measurements of crystal dynamics require large (~5 cm × 1 cm^2) single crystals of

pure terbium. The inaccessibility of such crystals and the adaptability of our techniques for their production led us to attempt to produce single crystals of pure terbium. A 175-g ingot (~8.0 cm × 1.83 cm OD) of terbium was produced from chips of high-purity metal.[7] The ingot was subsequently frozen at a rate of 1 cm/hr in a Stockbarger furnace in an attempt to produce single crystals. The capsule container was formed from recrystallized alumina within which was placed a conical-tipped tantalum liner. An atmosphere of pressurized helium was maintained in contact with the metal during the freezing process. Although the frozen ingot was not wholly single crystal, it did contain one grain (3.8 × 1.3 × 0.6 cm) that was somewhat larger than previously available. The concentrations of tantalum and oxygen impurities in the final product (0.2% each) were not significantly lower than those of the starting material. Innovations in growth methods are currently being made as part of our continuing efforts to improve purity as well as crystal size.

[7]Obtained from the Research Chemicals, Phoenix, Ariz.

PURIFICATION OF ZIRCONIUM TETRAFLUORIDE

L. B. Yeatts, Jr. W. T. Rainey, Jr.

Relatively small quantities of pure zirconium tetrafluoride were desired to determine stability of this material to bombarding x rays. Commercial preparations of this salt contained carbon, water, and iron and zirconium oxides as the major impurities. All of these react with fluorine liberated by the x irradiation of zirconium tetrafluoride and obscure the radiation stability of the salt itself.

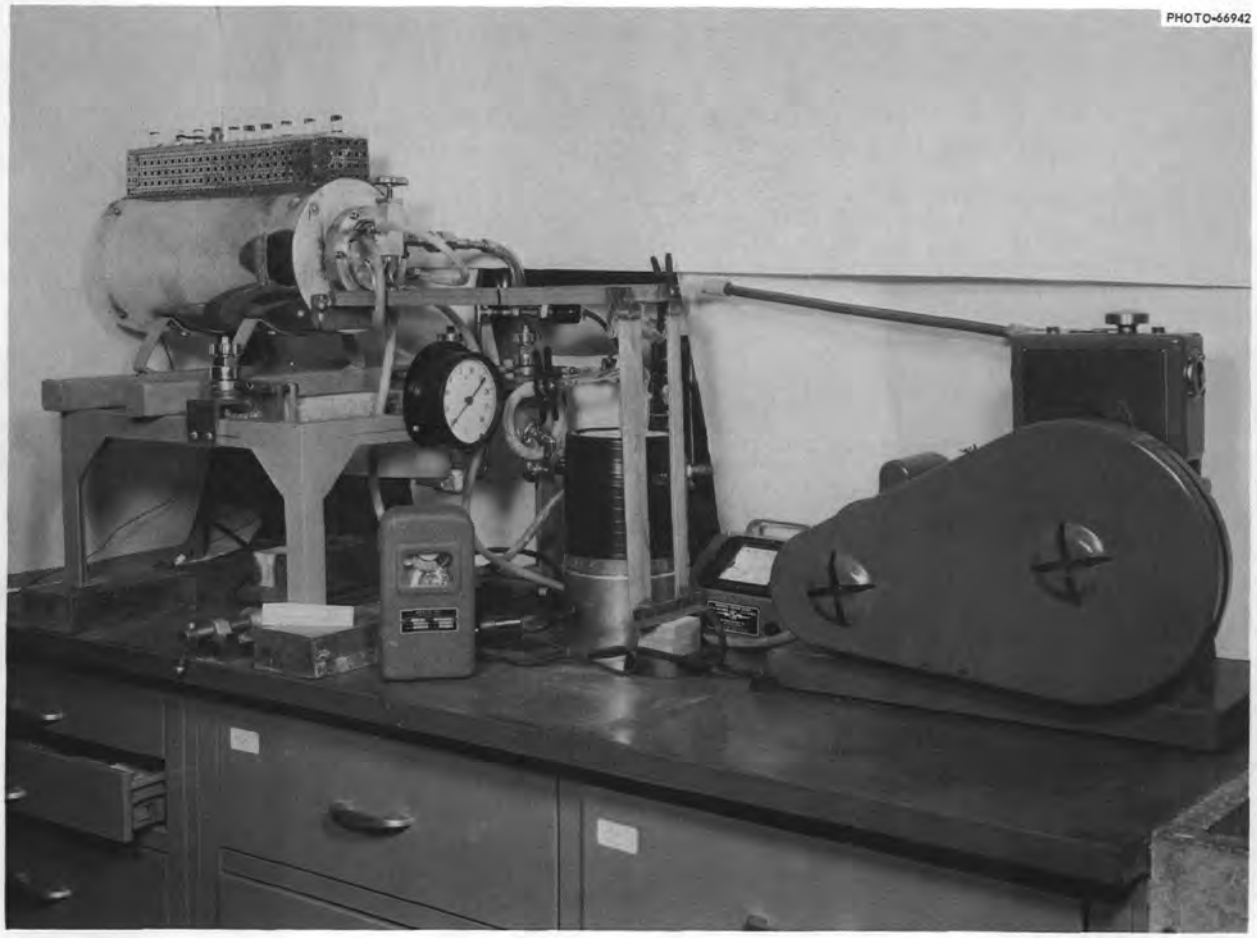

Fig. 25.5. Evacuating and Heating System for the Sublimation of ZrF_4.

Vacuum sublimation techniques were tried in an effort to markedly improve the sample purity.

Apparatus for single-stage sublimation studies consisted essentially of nickel baffles, a nickel boat to contain the charge, and a nickel vessel 11.5 in. long made from 3-in. IPS pipe. The equipment, containing about 50 g of commercial-grade ZrF_4, was evacuated at room temperature to 100 μ. A Marshall furnace was used to provide heat for the sublimation process (see Fig. 25.5). Product ZrF_4 was obtained by dismantling the sublimation equipment in a dry helium atmosphere within a glove box.

The temperature of sublimation was varied by changing the controls on the Marshall furnace from one experiment to the next. Analyses indicated no significant difference in the impurity level of the products produced over the temperature range of 700 to 800°C. A similar lack of significant effects was obtained upon varying the rate of condensation of sublimate by using (1) a water-cooled condensing surface, (2) a forced-air cooling condensing surface, and (3) a condensing surface with an appreciable temperature gradient. In each of these experiments, the concentration of iron was reduced from 550 ppm in the starting material to 80 ppm in the product; oxygen was reduced from 7000 to 1400 ppm. Resublimation had little effect upon the iron content, but it did reduce the oxygen level to 750 ppm; a third sublimation failed to improve the quality of the product. The use of six baffles, with $^3/_4$-in. spacing between successive baffles, was, however, sufficiently efficient to reduce the oxygen level in a single sublimation from 7000 ppm in the starting material to 480 ppm in the product. This baffle system was used in the subsequent experiments (see Fig. 25.6).

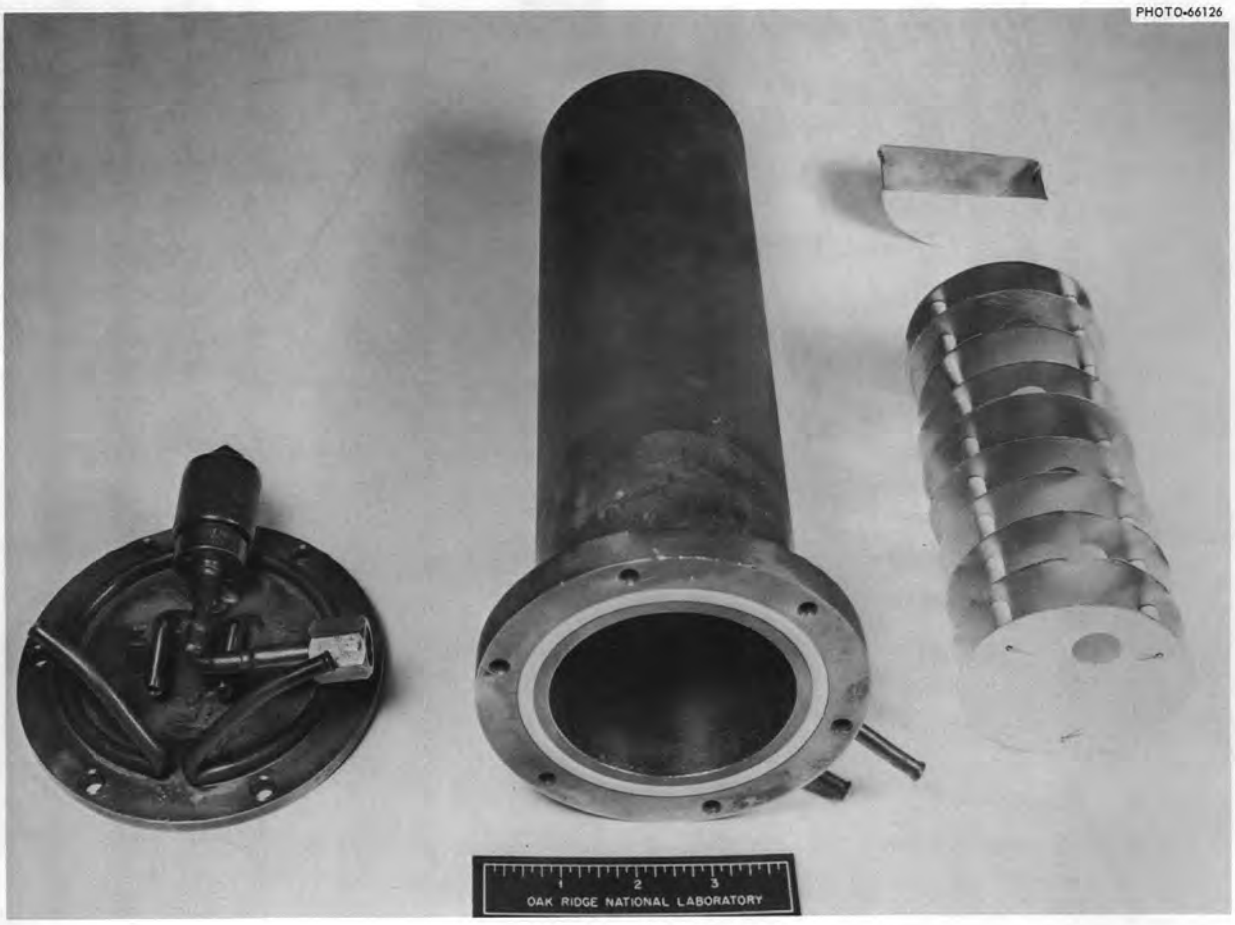

Fig. 25.6. Container and Baffle System for the Sublimation of ZrF_4.

PHOTO 67166

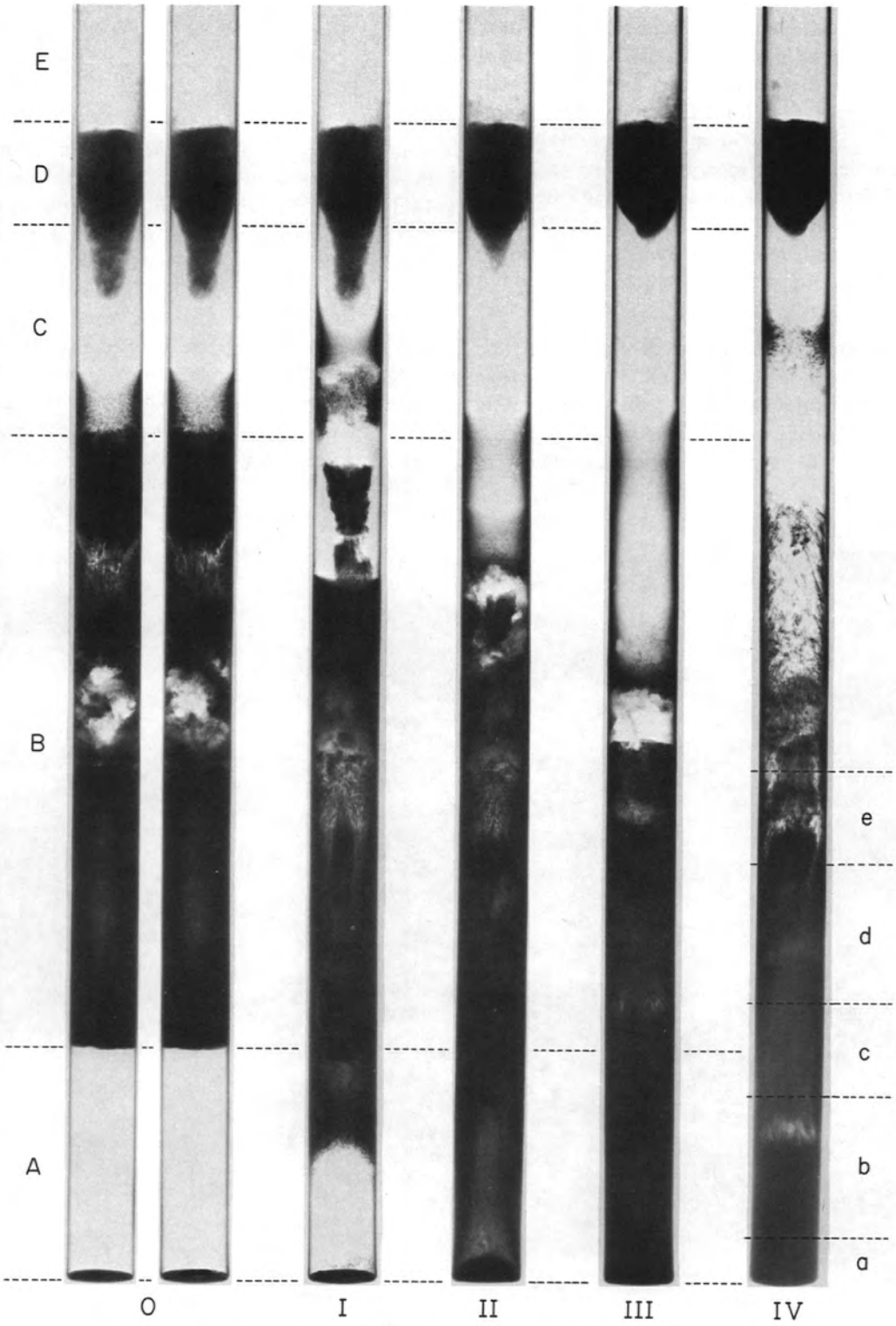

Fig. 25.7. Vapor-Zone Sublimation of ZrF_4.

Pretreatment of commercial ZrF_4 with fluorine, hydrogen fluoride, or ammonium bifluoride was tested in an effort to convert metallic oxides in the starting material to fluorides. Sublimation of the material pretreated with ammonium bifluoride produced by far the purest ZrF_4; the product had 260 ppm oxygen. A single experiment was done in which commercial-grade ZrF_4 was vapor-zone refined.[8] A nearly solid plug of ZrF_4 was formed inside an evacuated nickel tube by passing the tube at a slow, steady rate through a 1-in.-long furnace. The location of this solid plug in the tube is shown in the x-ray photograph, Fig. 25.7, as section B of the first two photographs in the left; the tube was rotated 90° to obtain these two views, which show the symmetrical form of the starting ingot. Sections A, C, and E represent voids in the tube initially, while section D is unsublimed starting material. The roman numerals under the photographs represent the number of passes through the furnace experienced by the tube. The tube was moved downward through the hot zone at a rate of 1.2 in./hr. The progression of the ingot toward the bottom of the tube after each pass can be seen in Fig. 25.7. Following the fourth pass, the tube was cut into the sections shown, and samples of ZrF_4 were taken for analysis of oxygen, iron, nickel, and chromium. Oxygen, as ZrO_2, was found to have concentrated in sample section e, while the iron, nickel, and chromium impurities appeared to concentrate about equally in sections *a* and *e*. The impurity level was lowest in the ZrF_4 from section c, where the iron, nickel, and chromium content were each less than 100 ppm and the oxygen content was 700 ppm. These results indicate the desirability of investigating more fully this multistage procedure for the purification of volatile materials.

[8]E. F. G. Herrington, *Zone Melting of Organic Compounds*, p. 130, Blackwell Scientific Publications, Oxford, 1963.

26. Chemical Support for the Controlled Thermonuclear Program

R. A. Strehlow D. M. Richardson

The program of chemical research in support of the ORNL controlled thermonuclear effort includes short-range studies related to improvements in vacuum technology and longer-range consideration of the chemical aspects of the design of thermonuclear reactors. The vacuum studies conducted during the past year have been described in Thermonuclear Division reports[1] and are summarized here. A study of the anticipated tritium cycle chemistry for a tritium-burning device was made and is discussed in greater detail.

[1] *Thermonuclear Div. Semiann. Progr. Rept. April 30, 1964,* ORNL-3652, and *Thermonuclear Div. Semiann. Progr. Rept. Oct. 31, 1964,* ORNL-3760.

VACUUM STUDIES

Oil Behavior in Vacuum Systems

Since the ORNL plasma research involves the use of vacuum techniques which introduce oil into the experimental chambers, studies of oil behavior were continued. A bakeable apparatus was constructed in which oil was allowed to flow from a source through two parallel branches of a tubing assembly as shown in Fig. 26.1. Between a pair of nude gages in one branch there was a $^1/_{16}$-in. circumferential gap and an envelope of larger tubing, while in the other branch there was no gap. This resulted in creep paths between gages of 140 cm for one branch and 60 cm for the other (a ratio of 2.3). The variables observed

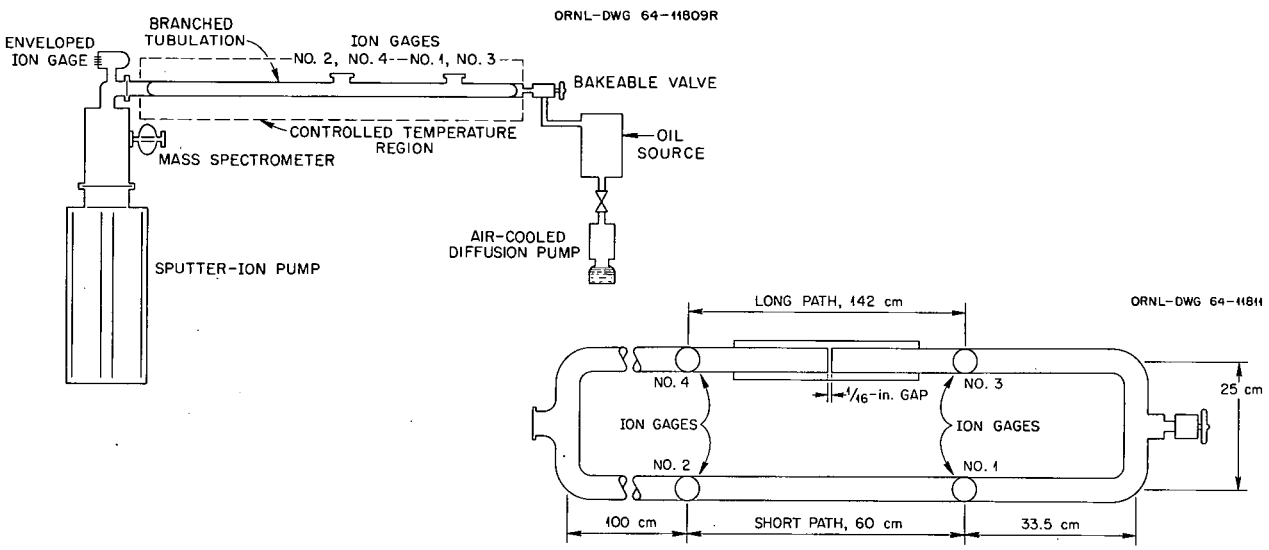

Fig. 26.1. Surface Creep Study Apparatus and Tubulation Detail.

experimentally were the time delay for response of gage No. 2 after gage No. 1 responded and the time delay for response of gage No. 4 after gage No. 3 responded. The experiment was conducted at 50 ± 1°C. The ratio of delay time for gage No. 4 to that for gage No. 2 was found to be 2.3 ± 0.7. This experiment did not distinguish between various possible mechanisms for surface diffusion of oil, but verified the assumption that hydrocarbon diffusion pump oil contamination (detectable with nude gages) occurred by surface transport and not by vapor transport.

An additional diagnostic technique for the presence of oil in very small amounts was developed using electron bombardment of a surface to produce neutral molecules, which were then analyzed in a mass spectrometer after they had left the test surface. A block diagram for this technique is shown in Fig. 26.2. Electron bombardment of oil adsorbed on the test surface resulted in the formation of numerous gaseous species and caused a pressure increase during bombardment. This increase of partial pressures of the various neutral gas species was analyzed by the mass spectrometer. The oil used for these electron bombardment studies was bis-2-ethylhexyl phthalate, which has a well-characterized mass spectrum. Hydrogen was observed to be the dominant species. Other gases observed to be produced by the bombardment were methane, ethane, ethylene, butanal, butenes, and some carbon dioxide. Methane was identified on the basis of the 16:15 ratio (CH_4^+:CH_3^+) and appeared to be the second most abundant product of the bombardment. Ethane and butanal were identified on the basis of distinctive mass peaks at 30 and 72 u respectively. The other species were identified on the basis of the various peak height ratios.

Electron bombardment of a mixed saturated hydrocarbon oil on the grid of a contaminated ionization gage produced methane, ethane, and, of course, hydrogen. The amount of hydrogen produced was found to vary linearly with electron flow to the grid, although some hydrogen was produced even at very low electron emissions (presumably by filament pyrolysis).

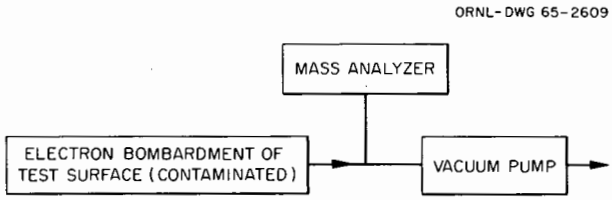

Fig. 26.2. Method for Diagnosis of Surface Contamination Showing Flow of Product Gas.

Synthesis and Decomposition of Methane in Vacuum Systems

The origin of methane in vacuum systems at ORNL has been of concern since it was recognized that methane and carbon dioxide were desorbed in significant amounts in the DCX-1 experiment and appeared to affect adversely the pumping speed of vapor-deposited titanium. In addition to the electron bombardment synthesis of methane, discussed above, some studies were made of gas evolution from freshly sputtered titanium plate in a commercial ion pump. The dominant gases found to evolve when the pump was turned off were hydrogen, methane, carbon monoxide, and ethane. The first three of these were evolved at comparable rates when the water partial pressure was about 2×10^{-7}. Hydrogen and carbon monoxide evolution rates were found to be a direct function of water partial pressure. At water pressures of about 3×10^{-9} torr, the evolution rates of hydrogen and carbon monoxide were about two orders of magnitude lower than the methane evolution rate, which was approximately constant at both water pressures. The conclusion based on these data was that water probably reacts with the clean carbon-containing titanium surface to form hydrogen and carbon monoxide. Ionically pumped and occluded hydrogen in the titanium presumably can react with carbon atoms on the titanium surface yielding the hydrocarbons, which desorb as they are formed. When the pump is turned off, the hydrocarbons are not ionically pumped and contribute to a pressure rise. Since methane was found to be pumped at a speed of 0.29 liter/sec by a tubulated ionization gage, gage reactions yielding CO, CO_2, and H_2 were avoided by not using ionization gages during the experiments.

Analysis of mass spectral data from the DCX-2 experiment has recently verified that, during injection of the molecular hydrogen ion beam, methane, ethane, and higher hydrocarbons are indeed produced. The region of the machine in which this synthesis occurred has not been

established, but hydrogen atom reactions with oil-contaminated surfaces in the plasma region or electron reactions at the ends of the machine seem to be likely. Although methane and ethane were produced only in small amounts, their appearance indicated a degree of surface contamination that was not beneficial to the experiment.

THE CHEMISTRY OF TRITIUM IN CONTROLLED-FUSION DEVICES

R. A. Strehlow

If tritium is used in controlled-fusion devices, efficient recovery will be essential. The chemistry of tritium must be carefully examined to determine if such recovery will be possible. An initial survey of factors affecting chemical behavior of tritium in a conceptual power reactor was made. A breeder reactor was chosen for consideration because this concept appeared to present the most promising route to the control of fusion energy.[2,3] Expected chemical aspects of the fuel cycle were developed using published information for hydrogen. Problems in estimating tritium inventories were found and are discussed.

A generalized tritium flow path includes tritium flow to and from three functional regions (source, plasma, and blanket) as shown in Fig. 26.1. In the assumed reactor, tritium is injected into a plasma, where a portion burns. Part of the unburned portion may flow to the vacuum processing region, the balance into the blanket. Tritium in the blanket will be lost by decay (which is not serious if helium is recoverable and burnable), permeation, and processing inefficiencies. Since the atom density (cm^{-3}) of tritium will probably be about 10^{15} in the source, 10^{10} in the vacuum system, and possibly 10^{19} in the blanket region, separate processing methods for these regions appear to be desirable. To provide a basis of cost estimation, one of the reactor concepts of Homeyer[4] has been examined. Table 26.1 shows some of the operational parameters which he derived. Table 26.2 shows the estimated approximate volumes of various blanket-assembly materials required for such a reactor.

Source Processing

Un-ionized tritium effuses from the ionizing region of an ion source to the vacuum volume of the source accelerating region, where it must be removed rapidly to maintain low pressure. This gas could be immediately recycled by recompression to a higher partial pressure. This may be accomplished by mechanical molecular pumping or diffusion pumping with mercury as the pump fluid (to avoid exchange of tritium with diffusion pump oil).

The inventory of tritium in a source structure may be estimated for an assumed 50-lb mass of steel per source. Inasmuch as atomic or ionic hydrogen fluxes on metals result in the formation

Table 26.1. Assumed Parameters for a Mirror-Field Reactor with Ion-Injection Feed

Thermal power	1000 Mw
Fuel burnup rate	8×10^5 atm cm^3/day
Fractional burnup	0.1 of the injected tritium
Injected current per source	5 amp
Number of sources	~200
Length of reactor	130 m
Diameter (wall to wall)	2 m
Capital cost	\$600 per kwhr (electrical) (\$$1.5 \times 10^8$)

Table 26.2. Volume of Materials in Blanket

Material	Volume (cm^3)
Mo (first wall)	2×10^7
Coolant (Li_2BeF_4)	10^9
Graphite	2×10^8
Pb	3×10^8
INOR-8 (Hastelloy-N)	6×10^7

[2]D. J. Rose and M. Clark, *Plasma and Controlled Fusion*, p. 294, MIT Press, Cambridge, and Wiley, New York, 1961.

[3]W. R. Allis (ed.), *Nuclear Fusion*, p. 20, Van Nostrand, Princeton, 1960.

[4]W. G. Homeyer, Ph.D. thesis, MIT, December 1962.

of "surcharged" hydrogen alloys containing many times the equilibrium amounts of hydrogen,[5] precise estimation of the hydrogen content is difficult. Literature data for nickel exposed to high-pressure gaseous hydrogen indicate that Sieverts' relation (solubility is proportional to the square root of the pressure) begins to fail at about 120 atm; the solubility approaches a value at 200 atm which is not a function of pressure.[6] This corresponds to a solubility of about 10 cm^3-atm/cm^3 for nickel at room temperature (atom ratio of 2×10^{-3}). With electrochemically discharged fluxes of hydrogen ions on iron up to 2.4×10^{17} sec^{-1} cm^{-2}, no solubility limit has been observed to concentrations of 0.5 cm^3-atm/cm^3 (ref. 7) (much higher than the equilibrium value at 1 atm and room temperature of 0.05 atm cm^3/cm^3). Estimates 10^5 times the equilibrium solubility have been made for the extent of occlusion of electrochemically discharged hydrogen in copper, based on the relation derived by Tafel[8] [$\log P_{atm} = 34\ (0.8 + 0.1 \log I_c$ amp/cm)]. Since electrochemically derived estimates include electrophoretic effects and involve a liquid-solid interface, the appropriateness of the direct application of the Tafel relation to the plasma-wall hydrogen flux is questionable. However, the data for nickel[6] suggest that a factor of 10 to 15 in excess of the equilibrium value at 1 atm (1 atom per 10^3 metal atoms) may be used to give a minimum hydrogen content. Consequently, a single 50-lb source assembly might contain 10^5 atm cm^3; for the assumed reactor design with 200 such sources, between 10^7 and 10^8 atm cm^3 seems a reasonable lower boundary to the inventory. If the permeation loss rate is as much as 1% per day, processing of the gas surrounding the exterior surfaces of the sources will be needed. If subsurface voids exist or form in the source housing, the hydrogen pressure in them might exceed the 100-atm level. This would increase the tritium inventory and lead to structural problems.

[5]See, for example, D. P. Smith, *Hydrogen on Metals*, pp. 145–55, 276–79, Univ. of Chicago Press, Chicago, 1948.

[6]See A. Sieverts, *Z. Metallk.* **21**, 37–44 (1929) for a review.

[7]G. Borelius and S. Lindblom, *Ann. Physik.* **82**, 201 (1927).

[8]J. Tafel, *Z. Physik. Chem.* **50**, 641 (1905); **34**, 187 (1900).

Vacuum System Processing

The nature of the vacuum system processing will be dictated primarily by the fuel-element characteristics: volume, fractional burnup, feed rate, and the fraction of tritium which enters the blanket assembly. A minimum tritium atom flux to the wall of 10^{12} cm^{-2} sec^{-1} (0.1% of the injected tritium) is expected. For any of the injected tritium which strikes the walls as ions or atoms, the fraction released from the surface will depend on the kinetics of transport through the wall (and ultimate removal) relative to that of desorption. In this section we will arbitrarily assume that equal amounts are desorbed and otherwise removed and that any desorbed tritium reaching the plasma region does not yield an additional atom or ion impact with the wall (e.g., desorbed tritium which is ionized by electrons can escape the plasma region in a flow along a magnetic line of force). In this case, half of the unburned fraction must be reprocessed. For a fractional burnup of 0.1 and using the standard source of Homeyer for comparison (Table 26.1), the vacuum system processing rate would have to be 3×10^6 atm cm^3/day. At a lower fractional burnup of 0.02, perhaps 1.5×10^7 atm cm^3/day would have to be processed. The processing rates given for tritium must be multiplied by the atomic ratio (D + T + H)/T, a factor equal here to at least 2. The inefficiency of the source processing should increase this load by no more than a factor of 2 (estimating effusive flow at 200 liters/sec from each source at a pressure of 10^{-5} torr). Mercury diffusion pumps or turbomolecular mechanical compressors (with appropriate lubricants) might be used in possible recovery processes for the vacuum system; palladium membranes might serve to separate the tritium from helium.

Thermal cycling of exothermic absorbers would require the dissociation energy plus a specific heat energy for the absorber and could be accomplished with the expenditure of about 10^6 cal/g-mole. At 10^3 moles per day, about 2 Mwhr per day would be the resulting power cost for this process.

Cryogenic trapping offers one possibility of separating the various hydrogen isotopes from each other as well as from helium. An estimate[9] for the helium cost of 3 kwhr/liter, with a hydrogen adsorption energy of 3 kcal/mole and ΔH_v of

[9]R. B. Scott, *Cryogenic Engineering*, p. 68, McGraw-Hill, New York, 1959.

helium = 5×10^3 joules/liter, leads to the need for 10 kwhr per mole of T_2. This [multiplied by the atom ratio (D + T + H)/T] is about 10 Mwhr/day for the hypothetical reactor. The power required for temperature cycles to 8°K would require perhaps an equal amount of energy for the specific heat of the adsorber material. The total cryogenic trapping process would use some 1 to 2% of the total electrical power output. A liquid-helium plant of about 200 to 400 liters/hr (0.5 Mw installed power for liquefaction) would be needed for this process.

A more serious consideration in the vacuum process design, however, is the possibility that intermittent dumping of the entire fuel volume might be required in order to purge the plasma of accumulated helium. If we follow Rose and Clark[2] and assume that introduction of nonadiabatic regions will allow continuous purging, we, of course, have assumed nonexistence of the problem. We will, nonetheless, consider this possible process requirement, and, if it is necessary to dump after 0.05 of the tritium is burned, then our fractional burnup is decreased by a factor of 20; if we assume that dumping is required on an hourly schedule, an additional 10^5 atm cm^3/hr would have to be processed, presumably at a much higher than steady-state rate, in order to reprepare the plasma region for another startup. The mercury pump compression process mentioned above appears to offer the simplest means for accomplishing the needed task. Some ten or so 50,000-liter/sec pumps and a foreline surge volume of probably less than 10^2 m^3 should be adequate for this method. Restarting in a system having an elevated wall temperature might present several more serious problems because of the high neutral flux from the wall as compared with that at first startup. Coupled with the power cost, problems such as these would add heavily to process costs.

Since unburned fuel leaving the plasma will be ionized, the surcharging effect might be utilized to allow isotope separation and recovery of the hydrogen isotopes. Processes similar to those described below for blanket processing may be applied to vacuum processing.

Blanket Assembly Processing

To this point no serious impediments have appeared regarding fuel cycle costs or feasibility based upon existing technology. However, with the expected flux of tritium atoms to the blanket wall of 10^{12} cm^{-2} sec^{-1} (0.1% of the fuel feed), crude application of the Tafel relation mentioned above leads to a possible equivalent pressure of some 10^5 atm. Therefore, in the absence of effective sinks for the tritium contained in the metal wall and blanket assembly, the blanket inventory may fall in the range of 1 to 10 atmospheric cm^3 per cm^3. This corresponds to a steady-state inventory of from 5×10^7 to 5×10^8 atm cm^3 total (10^2 to 10^3 days supply) in the wall. Moreover, this inventory would be located in close proximity to the plasma and consequently would be important in stability considerations for any tritium-burning fusion device.

A different method of estimating the inventory may be described which, nevertheless, leads to a similar result. For the endothermic hydrides (Mo, W, Fe, Ni, etc.), collision statistics on the surface facing the vacuum will determine the emission rate. A tritium-metal atom ratio of perhaps 5×10^{-5} (0.2 atm cm^3/cm^3) with a tritium jump frequency of 10^{-7} sec (based on a 20,000 cal/mole activation energy and a 10^{-13} sec frequency factor) yields an expected emitted molecular flux of about 10^{12} sec^{-1} cm^{-2} (equal to the loading flux). With this estimate one would expect the total inventory for the blanket assembly to be more than 10^7 atm cm^3.

To the extent that these estimates are valid, a process is needed in which tritium is removed efficiently from a wall containing only low concentrations at the surface. Three possible methods for accomplishing this removal are:

1. those which increase the frequence of T-T collisions at the solid-vacuum interface leading to T_2 desorption;
2. those which form a sink for tritium in the blanket by solid-state reactions; and
3. those which permit removal of individual atoms of tritium rather than molecules.

Thermal cycling of the blanket assembly or inclusion of a palladium region in the blanket assembly, for example, would be of the first type, but because of thermal stress, nuclear, and design problems, they do not seem presently attractive.

Inclusion of masses of zirconium, an example of the second type listed above, would pose numerous problems because of the need for periodic

disassembly. Mechanical separation and thermal processing might be advantageous to the neutron economy of the reactor and might not prove too costly if the accumulation periods were of the order of six months or more. Vapor deposition of titanium, cerium, zirconium, or yttrium in a region of the vacuum system on a surface contiguous with the blanket assembly volume would allow the recovery of the tritium by a vacuum system process. All of these approaches require extensive study to establish their technological feasibility.

The greatest decrease of the inventory, however, appears to be afforded by processes of the third class listed above. This type includes oxidation and reduction of contained tritium atoms, removal as individual atoms or ions to a vacuum, isotopic dilution with hydrogen or deuterium, or removal as a covalent compound (e.g., as tritomethane or tritoethane, from carbon-containing titanium which has been freshly sputtered in the absence of water).[10] Inasmuch as the molybdenum will probably have a large carbon content, either due to the presence of graphite or as initial impurity, it is possible that similar processes will occur at the plasma wall interface. We have not yet observed this reaction except with titanium.

A chemical reduction of occluded tritium to tritide ion presumably would be accomplished if liquid lithium were used as coolant. Work by members of the ORNL Reactor Chemistry Division[11] on permeation of nickel by hydrogen has shown that the permeation rate and (therefore presumably) the charging kinetics are independent of the presence of a layer of liquid sodium-potassium alloy between the gaseous hydrogen and the metal surface. The use of lithium therefore as a breeder-coolant fluid offers a process possibility for the plasma exhaust to the vacuum system (where magnetohydrodynamic problems of lithium pumping need not be severe).

Oxidative processes for the removal of tritium atoms from the surcharged metal appear to be possible for $LiF\text{-}BeF_2$, previously discussed as a breeder coolant.[12] Since the breeding process is oxidizing,[13] if $LiF\text{-}BeF_2$ is used, with or without an added chemical oxidant, it seems likely that the surcharged tritium will be efficiently removed as HF without danger that deposition of metal may occur. (This may even eliminate the need for addition of reducing agents to the coolant for the purpose of minimizing corrosion.)

Removal of individual tritium ions by field emission, for example, or some controlled sputtering process seems to offer a remote possibility. Preliminary experiments with molybdenum have been conducted yielding a hydrogen ion to neutral ratio of about 10^{-5} at red heat with an impressed gradient of 200 v/cm. Detailed studies have not been conducted, since the need for this type of process is presently undemonstrated.

One of the additional complications regarding the blanket inventory and other losses is that, if removal of tritium atoms is not possible, permeation of hydrogen to voids in the blanket assembly will result in hydrogen pressures of perhaps hundreds of atmospheres or more. The structural integrity of the blanket assembly under surcharging conditions must be examined. The flux of tritium through the entire assembly can also result in a total leak of perhaps several percent per day to the gaseous region surrounding the reactor. Even in the best case, with an efficient sink for tritium in the blanket assembly, a total leakage to the ambient gas of perhaps 10^4 atm cm^3/day may exist.

To summarize the blanket processing outlook, intolerable steady-state inventories may occur. Fuel cycle studies regarding hydrogen transport in and removal from blanket materials are required; surcharging processes must specifically be investigated.

Coolant Processing

The simplest assumption regarding the coolant is that the tritium is contained as lithium tritide or as tritium fluoride (for the two coolants considered here). In this case the estimates of Homeyer will hold approximately, and no particular problem should be expected. If there is an appreciable quantity of tritium gas in the coolant salt, however, from whatever source, tritium leakage to the heat exchangers, piping,

[10] *Thermonuclear Div. Semiann. Progr. Rept. Oct. 31, 1964*, ORNL-3760.

[11] *Reactor Chem. Div. Ann. Progr. Rept. Jan. 31, 1964*, ORNL-3591, pp. 217–22.

[12] C. J. Barton and R. A. Strehlow, *Blankets for Thermonuclear Reactors*, ORNL-3258 (June 27, 1962).

[13] Mark Robinson, *On the Chemistry of Thermonuclear Reactor Breeder Blankets*, ORNL-CF-57-12-39 (rev. Feb. 8, 1958).

etc., could require processing of the gas surrounding this allied equipment. This possibility would presumably not increase the total inventory by more than perhaps 10^4 or so atm cm^3.

Tritium Inventory

The estimated amounts of tritium in the various parts of the proposed reactor are listed in Table 26.3.

Table 26.3. Estimated Inventory of Tritium (atm cm^3)

Sources	10^6 to 10^7
Blanket, structure	10^7 to 10^9 without processing 10^5 to 10^8 with processing
Blanket and coolant	10^7
Total	2×10^7 to 1.1×10^9

Startup Processing

An additional problem regarding the nature of reactor startup should be considered here. If we assume an initial protium content in the blanket components equal to an atom ratio of 10^{-4}, there will be in the reactor perhaps 10^{10} atmospheric cm^3. Isotope separation would ultimately be required to remove this protium. Cyrogenic separation techniques, considered above, might be used. The isotope effect (especially pronounced for temperatures less than 400°C, where ^1H tunneling dominates) during a surcharging process to load the metal could lead to a promising recovery and isotope separation scheme. Gas chromatographic separation offers a third processing possibility. At this point it should be noted that the diffusion rates of protium and of tritium will differ but that since the doubling time of this reactor concept is quite a complex problem, only the estimates of steady-state tritium inventory have been considered.

Publications

JOURNAL ARTICLES

AUTHOR(s)	TITLE	PUBLICATION
Adams, R. E.	Eighth AEC Air-Cleaning Conference	*Nucl. Safety* 5(3), 250 (1964)
Attrill, J. E., L. B. Yeatts, Jr., and W. T. Rainey	Retention Data for Polyphenyl Compounds	*J. Gas Chromatog.* 2(1), 46 (1964)
Barton, C. J., and G. W. Parker	Behavior of Released Fission Products in Actual Reactor Incidents	*Nucl. Safety* 5(4), 389 (1964)
Blakely, J. P., J. L. Rutherford, and L. G. Overholser	Compatibility of Fueled Graphite Spheres with Water Vapor	*Nucl. Sci. Eng.* 20, 196–97 (1964)
Bopp, C. D.	Measurement of Thermal Conductivity with Mercury Contacts	*J. Am. Ceram. Soc.* 47(3), 151 (1964)
	Vibrational Method for the Elastic Constants of Small Plates	*Rev. Sci. Instr.* 35, 703–7 (1964)
Browning, W. E., Jr., C. E. Miller, Jr., R. P. Shields, and B. F. Roberts	Release of Fission Products During In-Pile Melting of UO_2	*Nucl. Sci. Eng.* 18, 151–62 (1964)
Burns, J. H., R. D. Ellison, and H. A. Levy	The Crystal Structure of the Molecular Addition Compound Xenon Difluoride–Xenon Tetrafluoride	*Acta Cryst.* 18, 11 (1965)
Cantor, Stanley, and W. T. Ward	Freezing Point Depressions in Sodium Fluoride. IV. Effects of Trivalent Fluorides	*J. Phys. Chem.* 67, 2766 (1963)
Carroll, R. M.	Fission-Product Release from UO_2	*Nucl. Safety* 5(4), 356 (1964)
Cuneo, D. R., E. L. Long, Jr., and H. E. Robertson	Hot Cell Techniques for the Evaluation of Fueled Graphite Spheres	*Trans. Am. Nucl. Soc.* 7(2), 477 (1964)
de Bruin, H. J., and R. L. Clark	Precision Lapping Device for the Determination of Diffusion Coefficients in Ceramic Materials	*Rev. Sci. Instr.* 35(2), 227 (1964)
Evans, R. B., III, and Jack Truitt	Diffusion of Actinides in Pyrolytic and Porous Carbon	*Nucl. Sci. Eng.* 20, 197 (1964)

AUTHOR(s)	TITLE	PUBLICATION
Fletcher, W. H., C. S. Shoup, Jr., and W. T. Thompson	Mixing of Symmetry Coordinates in Methyl Cyanide and Methyl Isocyanide	*Spectrochim. Acta* **20**, 1065 (1964)
Griess, J. C., and J. L. English	Stress Corrosion Cracking of Austenitic Stainless in Uranyl Sulfate Solutions	*Corrosion* **20**, 138–44 (1964)
Grimes, W. R.	Molten Salts as Reactor Materials	*Nucl. News* **7**(5), 3–8 (1964)
Hebert, G. M., and T. N. McVay	New Fluoride Compounds Predicted from Cation Size Considerations – Synthesis and Properties	*J. Tenn. Acad. Sci.* **39**(2), 63 (1964)
Holmes, H. F., and C. H. Secoy	Heats of Immersion in the Thorium Oxide–Water System	*J. Phys. Chem.* **69**, 151 (1965)
Jenks, G. H.	Zircaloy-2 Corrosion In-Pile in Aqueous Homogeneous Reactor Solutions	*Am. Soc. Testing Mater., Spec. Tech. Publ.* **368**, 41 (1964)
Jones, E. V., and W. L. Marshall	Aqueous Systems at High Temperature. XIII. Investigations on the System UO_3-Li_2O-SO_3-D_2O; Liquid-Liquid Immiscibility and Critical Phenomena, 300–410°C	*J. Inorg. Nucl. Chem.* **26**(2), 281 (1964)
Keilholtz, G. W., J. E. Lee, Jr., and R. E. Moore	The Effect of Fast Neutron Irradiation on BeO Compacts at High Temperature	*J. Nucl. Mater.* **11**(3), 253 (1964)
Keilholtz, G. W.	Fission-Product Iodine Release, Transport, and Removal Within Reactor Containment Systems	*Nucl. Safety* **6**(3), in press
McDuffie, H. F., J. H. Shaffer, C. F. Baes, Jr., R. E. Thoma, Stanley Cantor, and F. F. Blankenship	Preparation and Properties of Fuel and Coolant for MSRE	*Trans. Am. Nucl. Soc.* **7**(2), 400 (1964)
Malinauskas, A. P.	Gaseous Diffusion. The Systems Helium-Argon, and Helium-Xenon	*J. Chem. Phys.* **42**, 156 (1965)
Marshall, W. L., and J. S. Gill	Aqueous Systems at High Temperature. XII. The Compound $NiO \cdot 3UO_3$	*J. Inorg. Nucl. Chem.* **26**(2), 277 (1964)
Marshall, W. L., Ruth Slusher, and E. V. Jones	Aqueous Systems at High Temperature. XIV. Solubility of $CaSO_4$ in NaCl-H_2O Solutions from 40 to 200°C, 0 to 4 Molal NaCl; Thermodynamic Values	*J. Chem. Eng. Data* **9**(2), 187 (1964)
Mason, E. A., and A. P. Malinauskas	Gaseous Diffusion in Porous Media. IV. Thermal Diffusion	*J. Chem. Phys.* **41**, 3815 (1964)
Manning, D. L., and Gleb Mamantov	Rapid Scan Voltammetry and Chronopotentiometric Studies of Iron in Molten Fluorides. Fabrication and Use of a Pyrolytic Graphite Indicator Electrode	*J. Electroanal. Chem.* **7**, 102 (1964)
Mamantov, Gleb, J. H. Burns, J. R. Hall, and D. B. Lake	Potassium Dihydrogen Peroxyphosphate: Preparation and Characterization	*Inorg. Chem.* **3**, 1043 (1964)

AUTHOR(s)	TITLE	PUBLICATION
Miller, C. E., Jr., W. E. Browning, Jr., B. F. Roberts, and R. P. Shields	Fission Product Fractionation During In-Pile Destruction of Reactor Fuels	*Trans. Am. Nucl. Soc.* 7(1), 96 (1964)
Osborne, M. F., J. G. Morgan, and E. L. Long, Jr.	Effects of Extreme Operating Conditions on Prototype EGCR Fuel	*Trans. Am. Nucl. Soc.* 7(2), 449 (1964)
Parker, G. W., R. A. Lorenz, and C. E. Miller, Jr.	Release of Fission Products on In-Pile Melting of Reactor Fuels Under Transient Reactor Conditions	*Trans. Am. Nucl. Soc.* 7(1), 92 (1964)
Rainey, W. T., Jr., T. H. Mauney, D. N. Hess, and H. F. McDuffie	Chemical Effects of X-Rays on Inorganic Fluorides. I. Apparatus, Techniques, and Preliminary Results	*Trans. Am. Nucl. Soc.* 7(2), 440 (1964)
Rainey, W. T., Jr., and L. B. Yeatts, Jr.	Purification and Quantitative Recovery of Volatile Materials	*J. Chem. Educ.* 41, 451 (1964)
Reagan, P. E., F. L. Carlsen, and R. M. Carroll	Fission-Gas Released from Pyrolytic-Carbon Coated Fuel Particles During Irradiation	*Nucl. Sci. Eng.* 18(3), 301 (1964)
Reagan, P. E., R. M. Carroll, and E. L. Long	Irradiation Tests	*Nucl. Sci. Eng.* 20, 189 (1964)
Sears, D. R., and J. H. Burns	Crystal Structure of $Li_6BeF_4ZrF_8$	*J. Chem. Phys.* 41, 3478 (1965)
Shaffer, J. H., W. R. Grimes, G. M. Watson, D. R. Cuneo, J. E. Strain, and M. J. Kelly	The Recovery of Protactinium and Uranium from Molten Fluoride Systems by Precipitation as Oxides	*Nucl. Sci. Eng.* 18, 177 (1964)
Silverman, M. D., and W. E. Browning, Jr.	Fibrous Filters as Particle-Size Analyzers	*Science* 143, 572 (1964)
Sweeton, F. H., and C. F. Baes, Jr.	Magnetite as a High-Temperature Adsorbent in Pressurized Water Systems	*Trans. Am. Nucl. Soc.* 7(1), 158 (1964)
Steinfink, H., and J. H. Burns	The Crystal Structure of Cr_2F_5	*Acta Cryst.* 17, 823 (1964)
Thoma, R. E., C. F. Weaver, H. Insley, and H. A. Friedman	Phase Equilibria in the System $NaF-BeF_2-ThF_4$	*Nucl. Sci. Eng.* 19(4), 406 (1964)

BOOKS AND PROCEEDINGS

Barton, C. J., D. R. Cuneo, M. J. Kelly, and J. E. Strain	Protactinium Stability in Thorium Nitrate—Nitric Acid Solutions	*Proc. Protactinium Chemistry Symp., Gatlinburg, Tenn., April 1963*, TID-7675, pp. 35–45 (February 1964)

AUTHOR(s)	TITLE	PUBLICATION
Bopp, C. D., and W. W. Parkinson	Nuclear Reactors as Sources of Radiation	Chap. 1 in *Radiation Sources*, ed. by A. Charlesby, Pergamon, London, 1964
Browning, W. E., Jr., R. D. Ackley, and M. D. Silverman	Characterization of Gas-Borne Fission Products	*Proc. 8th AEC Air Cleaning Conference, Oak Ridge, Tenn., October 1963*, TID-7677, p. 155, RID-7677 (1964)
Fuller, E. L., H. F. Holmes, and C. H. Secoy	Gravimetric Adsorption Studies of Thorium Dioxide Surfaces with a Vacuum Microbalance	*Proc. 4th Conf. Vacuum Microbalance Techniques, Pittsburgh, Pa.*, ed. by P. M. Waters, vol. 4, p. 109, Plenum, New York, 1965
Grimes, W. R.	Materials Problems in Molten Salt Reactors	Chap. 7 in *Materials and Fuels for High Temperature Nuclear Applications*, ed. by M. T. Simnad and L. R. Zumwalt, MIT Press, Cambridge, Mass., 1964
McDuffie, H. F., M. J. Kelly, G. L. Johnson, and D. R. Cuneo	Removal of Protactinium and Uranium from Thorium Nitrate–Nitric Acid Solutions	*Proc. Protactinium Chemistry Symp., Gatlinburg, Tenn., April 1963*, TID-7675, p. 46 (February 1964)
Shaffer, J. H., G. M. Watson, D. R. Cuneo, J. E. Strain, and M. J. Kelly	Recovery of Uranium and Protactinium from Molten Fluoride Systems by Precipitation as Oxides	*Proc. Protactinium Chemistry Symp., Gatlinburg, Tenn., April 1963*, TID-7675, p. 86 (February 1964)
Shields, R. P., W. E. Browning, Jr., C. E. Miller, Jr., and B. F. Roberts	Release of Fission Products on the In-Pile Melting or Burning of Reactor Fuels	*Proc. 8th AEC Air Cleaning Conference, Oak Ridge, Tenn., October 22–25, 1963*, TID-7677, pp. 7–15 (1964)
Thoma, R. E., G. M. Hebert, H. Insley, and C. F. Weaver	Order-Disorder Effects and Solid Solutions in the System $NaF-YF_3$	*Proc. 3d Conference on Rare Earth Research, Clearwater, Fla., April 21–24, 1963*, ed. by K. S. Vorres, Gordon and Beach Science Pub., New York, pp. 297–302 (1965)
Watson, C. D., and W. W. Parkinson	Irradiation of Bituminous Materials	Chap. 6 in *Bituminous Materials: Asphalts, Tars, and Pitches*, vol. I., ed. by A. J. Hoiberg, Interscience, New York, 1964

THESIS

Shor, A. J.	*A Study of the Phase Behavior of the Aluminum Trichloride–Zirconium Tetrachloride System*	Thesis submitted in partial fulfillment of the requirements for M.S. degree, University of Tennessee, December 1964

REPORTS ISSUED

AUTHOR(s)	TITLE	PUBLICATION
Bamberger, C. E. L., H. F. McDuffie, and C. F. Baes, Jr.	*The Preparation of Pure Beryllium Oxide by Solvent Extraction with Acetylacetone in the Presence of Ethylenediamine Tetraacetic Acid; Procedure and Chemistry*	ORNL-3733 (November 1964)
Baumann, C. D.	*Neutron Flux Spectra in the Experimental Facilities of the Oak Ridge Research Reactor*	ORNL-3756 (January 1965)
Blakely, J. P., and L. G. Overholser	*Outgassing Behavior of EGCR Moderator Graphite*	ORNL-3560 (February 1964)
Blakely, J. P., N. V. Smith, and L. G. Overholser	*Compatibility of Unsupported Pyrolytic-Carbon Coated Uranium Dicarbide Particles with Water Vapor*	ORNL-3598 (April 1964)
Davis, M. E., and W. E. Browning, Jr.	*Separation and Identification of Volatile Iodine Compounds by Fractional Sublimation and Mass Spectrometric Analysis*	ORNL-TM-1009 (November 1964)
Evans, R. B., and G. M. Watson	*Calculations for Ventilated Fuel Element Configurations*	ORNL-TM-893 (September 1964)
Evans, R. B., III, J. O. Stiegler, and Jack Truitt	*Actinide Diffusion in Pyrocarbons and Graphite*	ORNL-3711 (December 1964)
Griess, J. C., H. C. Savage, and J. L. English	*Effect of Heat Flux on the Corrosion of Aluminum by Water. Part IV. Tests Relative to the Advanced Test Reactor and Correlation with Previous Results*	ORNL-3541 (February 1964)
Griess, J. C., H. C. Savage, and J. M. Baker	*The Effect of Gamma Radiation on the Thermal Conductivity of Aluminum Corrosion Product Films*	ORNL-TM-849 (April 1964)
Griess, J. C., G. H. Jenks, D. M. Eissenberg, and E. G. Bohlmann	*An Evaluation of the Chemical Problems Associated with the Aqueous Systems in the Tungsten Water Moderated Reactor*	ORNL-TM-913 (August 1964)
Grimes, W. R.	*Reactor Chemistry Division Annual Progress Report for Period Ending Jan. 31, 1964*	ORNL-3591 (May 1964)
Keilholtz, G. W., J. E. Lee, Jr., and R. E. Moore	*Properties of BeO Compacts Irradiated to Fast-Neutron Doses Greater than 10^{21} Neutrons/cm^2 at 110, 650, and 1100°C*	ORNL-TM-1011 (December 1964)
Malinauskas, A. P.	*Results of Preliminary Experiments on Thermal Transpiration*	ORNL-TM-801 (April 1964)
	Gaseous Diffusion. The Systems He-Ar, Ar-Xe, and He-Xe	ORNL-TM-941 (September 1964)
Mason, E. A., and A. P. Malinauskas	*Gaseous Diffusion in Porous Media. IV. Thermal Diffusion*	ORNL-TM-912 (August 1964)
	The Effect of Accommodation on Thermal Transpiration	ORNL-TM-754 (January 1964)

AUTHOR(s)	TITLE	PUBLICATION
Morgan, J. G., M. F. Osborne, and E. L. Long, Jr.	*Examination of UO_2 Irradiated at High Temperatures*	ORNL-TM-763 (March 1964)
Osborne, M. F., E. L. Long, Jr., and J. G. Morgan	*Performance of Prototype EGCR Fuel at Extreme Operating Conditions*	ORNL-TM-832 (May 1964)
	Postirradiation Examination of ORR Loop 1 Advanced Fuel Elements	ORNL-TM-862 (July 1964)
	Postirradiation Examination of EGCR Prototype Capsule O2A-6	ORNL-TM-877 (September 1964)
Osborne, M. F., and E. L. Long, Jr.	*Postirradiation Examination of Maritime-ORR Loop Experiments 5, 7, and 8*	ORNL-TM-921 (October 1964)
Redman, J. D.	*High Vacuum Flange Test of a Bakeable Aluminum Wire Seal*	ORNL-3509 (March 1964)
Reed, S. A., and J. C. Moyers	*Estimation of Interim Replacement Costs of Dual-Purpose Nuclear-Electric Sea Water Conversion Stations*	ORNL-TM-994 (December 1964)
Savage, H. W., E. L. Compere, W. R. Huntley, R. E. McPherson, and A. Taboada	*SNAP-8 Corrosion Program Quarterly Progress Report for Period Ending November 30, 1963*	ORNL-3604 (March 1964)
	SNAP-8 Corrosion Program Quarterly Progress Report for Period Ending February 29, 1964	ORNL-3618 (April 1964)
	SNAP-8 Corrosion Program Quarterly Progress Report for Period Ending May 31, 1964	ORNL-3671 (July 1964)
	SNAP-8 Corrosion Program Quarterly Progress Report for Period Ending August 31, 1964	ORNL-3730 (November 1964)
Sweeton, F. H., V. O. Haynes, and D. E. Tidwell	*Irradiation Data for the Army PM Fuel Experiment in the ORR Pressurized-Water Loop for ORR Cycle 49*	ORNL-TM-841 (June 1964)
	Irradiation Data for the Army PM Fuel Experiment in the ORR Pressurized-Water Loop for ORR Cycle 50	ORNL-TM-903 (September 1964)
	Irradiation Data for the Army PM Fuel Experiment in the ORR Pressurized-Water Loop for ORR Cycle 51	ORNL-TM-939 (October 1964)
Thoma, R. E., B. J. Sturm, and E. H. Guinn	*Molten Salt Solvents for Fluoride Volatility Processing of Aluminum-Matrix Nuclear Fuel Elements*	ORNL-3594 (August 1964)
Thurber, W. C., F. R. McQuilkin, E. L. Long, Jr., and M. F. Osborne	*Irradiation Testing of Fuel for Core B of the Enrico Fermi Fast Breeder Reactor*	ORNL-3709 (November 1964)
Weaver, C. F., R. G. Ross, B. J. Sturm, J. E. Eorgan, and R. E. Thoma	*The Production of LiF Single Crystals with Selected Isotopic Ratios of Lithium*	ORNL-3341 (March 1964)
Yeatts, L. B., Jr., D. N. Hess, H. F. McDuffie, and W. T. Rainey, Jr.	*Kinetics of the Thermal Decomposition of Biphenyl*	ORNL-3602 (May 1964)

PATENTS

AUTHOR(s)	TITLE	NUMBER
Gill, J. S., and W. L. Marshall	Double Oxide of Uranium and Copper	U.S. Patent 3,157,461, Nov. 17, 1964

Papers Presented at Scientific and Technical Meetings

AUTHOR(s)	TITLE	PLACE PRESENTED
Bien, P. B., and B. A. Soldano	High Temperature Isopiestic Technique as a Research Tool	Tennessee Academy of Science, Annual Meeting, Memphis, Tenn., Nov. 27–28, 1964
Blakely, J. P., J. L. Rutherford, and L. G. Overholser	Reactivity of Fueled and Unfueled Graphite Spheres with Water Vapor	US/UK Libby-Cockcroft Exchange Meeting, Richland, Wash., May 11–13, 1964
Blakely, J. P., N. V. Smith, and L. G. Overholser	Compatibility of Unsupported Pyrolytic-Carbon Coated Uranium Dicarbide Particles with Water Vapor	US/UK Libby-Cockcroft Exchange Meeting, Richland, Wash., May 11–13, 1964
Bopp, C. D., and T. N. McVay	Postirradiation Annealing of Silicates	American Ceramic Society, San Francisco, Calif., Oct. 28–31, 1964
Browning, W. E., Jr.	Behavior of Fission Products Released from Nuclear Reactors	Conference of Biomedical Contractors, University of Chicago, Chicago, Ill., Jan. 30, 1964
Burns, J. H.	The Crystal Structure of Sodium Fluoro-neodymiate(III)	American Crystallographic Association Meeting, Bozeman, Mont., July 26–31, 1964
	Recent Developments in the Chemistry of Noble Gases	American Chemical Society, SW Regional Meeting, Shreveport, La., Dec. 3–5, 1964
Cantor, Stanley	Some Structural Features of Molten Fluorides Inferred from Freezing Point Depressions of Sodium Fluoride	Norwegian Technical Institute, Trondheim, Norway, June 16, 1964 Euratom, Ispra, Italy, June 23, 1964 Meeting of Molten Salt Discussion Group at Avonmouth, England, July 17, 1964
Carroll, R. M., R. B. Perez, and Oscar Sisman	Release of Fission Gas During Fissioning of UO_2	American Ceramic Society, 66th Annual Meeting, Chicago, Ill., Apr. 18–23, 1964
Carroll, R. M.	Release of Fission Gas During Fissioning of UO_2	Chemistry Seminar, Argonne National Laboratory, April 1964

AUTHOR(s)	TITLE	PLACE PRESENTED
Cottrell, W. B., W. E. Browning, Jr., G. W. Parker, A. W. Castleman, and R. L. Junkins	U.S. Experience on the Release and Transport of Fission Products Within Containment Systems Under Simulated and Actual Reactor Accident Conditions	3rd United Nations Conference on Peaceful Uses of Atomic Energy, Geneva, Switzerland, Aug. 31–Sept. 9, 1964
Cuneo, D. R., E. L. Long, Jr., and H. E. Robertson	Hot Cell Techniques for the Evaluation of Fueled Graphite Spheres	American Nuclear Society, San Francisco, Calif., Nov. 30–Dec. 4, 1964
DeBruin, H. J., C. M. Blood, J. L. Rutherford, W. W. Johnson, Jr., and G. M. Watson	Self-Diffusion in Beryllium Oxide Matrices	American Ceramic Society, San Francisco, Calif., Oct. 28–31, 1964
Fuller, E. L., H. F. Holmes, and C. H. Secoy	Gravimetric Adsorption Studies of Thorium Dioxide Surfaces with a Vacuum Microbalance	4th Conference on Vacuum Microbalance Techniques, Pittsburgh, Pa., May 7–8, 1964
Grimes, W. R., E. G. Bohlmann, and L. O. Kirkbride	Irradiation Behavior of Fluid Fuels	3rd United Nations Conference on Peaceful Uses of Atomic Energy, Geneva, Switzerland, Aug. 31–Sept. 9, 1964
Grimes, W. R.	Molten Salts as Reactor Fuels	CENS, Saclay, France, Aug. 25, 1964
		C.C.R., Ispra, Italy, Aug. 28, 1964
		Institute of Silicate Science, Trondheim, Norway, Sept. 15, 1964
		AERE, Harwell, England, Sept. 21, 1964
Holmes, H. F., E. L. Fuller, Jr., and C. H. Secoy	Calorimetric Investigation of the Thorium Oxide–Water Interface	19th Annual Calorimetry Conference, Washington, D.C., Oct. 13–16, 1964
Karraker, R. H., and R. E. Thoma	The Sodium Fluoride–Scandium Fluoride System	Tennessee Academy of Science, Annual Meeting, Memphis, Tenn., Nov. 27–28, 1964
Kreyger, P. J., and S. S. Kirslis	Sessile Drops of Molten Halides on Graphite and Metals	American Chemical Society, Winter Meeting, Denver, Colo., Jan. 19–24, 1964
Malinauskas, A. P., and F. L. Carlsen, Jr.	Gas Transport Characteristics of Uranium Fueled Graphites	American Ceramic Society Meeting, 66th Annual, Chicago, Ill., Apr. 18–23, 1964
Manning, D. L., J. M. Dale, and Gleb Mamantov	Polarography in Molten Fluorides	3rd International Congress on Polarography, Southampton, England, July 19–23, 1964
	Voltammetric Measurements in Molten Fluoride Salt Systems	Comité International de Thermodynamique et de Cinétique Electrochimiques, London, England, Sept. 21–26, 1964

AUTHOR(s)	TITLE	PLACE PRESENTED
McDuffie, H. F., J. H. Shaffer, C. F. Baes, Jr., R. E. Thoma, Stanley Cantor, and F. F. Blankenship	Preparation and Properties of Fuel and Coolant for MSRE	American Nuclear Society, San Francisco, Calif., Nov. 30–Dec. 3, 1964
Miller, C. E., Jr., W. E. Browning, Jr., B. F. Roberts, and R. P. Shields	Fission Products Fractionation During In-Pile Destruction of Reactor Fuels	American Nuclear Society Meeting, Philadelphia, Pa., June 15–17, 1964
	Theory of Fission Product Fractionation in Reactor Fuel Experiments, Reactor Accidents, and Weapons Fallout	American Chemical Society, Chicago, Ill., Aug. 30–Sept. 4, 1964
Neumann, P. D.	Measurement and Control of Corrosion in the Oak Ridge Research Reactor Cooling Water Systems	International Water Conference, 25th Annual, Pittsburgh, Pa., Sept. 28–30, 1964
Osborne, M. F., J. G. Morgan, and E. L. Long, Jr.	Effects of Extreme Operating Conditions on Prototype EGCR Fuel	American Nuclear Society, San Francisco, Calif., Nov. 30–Dec. 3, 1964
Overholser, L. G., and J. P. Blakely	Oxidation of Graphite by Low Concentrations of Water Vapor and Carbon Dioxide in Helium	US/UK Libby-Cockcroft Exchange Meeting, Richland, Washington, May 11–13, 1964
Parker, G. W., R. A. Lorenz, and C. E. Miller, Jr.	Release of Fission Products on In-Pile Melting of Reactor Fuels Under Transient Reactor Conditions	American Nuclear Society, Philadelphia, Pa., June 15–17, 1964
Rainey, W. R., Jr., T. H. Mauney, D. N. Hess, and H. F. McDuffie	Chemical Effects of X-Rays on Inorganic Fluorides. I. Apparatus, Techniques, and Preliminary Results	American Nuclear Society, San Francisco, Calif., Nov. 30–Dec. 3, 1964
Sears, D. R., and J. H. Burns	Crystal Structure of $Li_6BeF_4ZrF_8$	American Crystallographic Association Meeting, Bozeman, Mont., July 26–31, 1964
Secoy, C. H.	Adsorption of Water on Polar Solids	ORNL Chemistry Colloquium, Oak Ridge, Tenn., Aug. 10, 1964
Strehlow, R. A.	Experimental Studies of Gaseous Desorption at Low Pressures and Liquid Nitrogen Temperatures	AEC Surface Physics Meeting, Germantown, Md., Jan. 30–31, 1964
Sweeton, F. H.	Decontamination Work in the Reactor Chemistry Division of the Oak Ridge National Laboratory – Apr. 1963 to Feb. 1964	Reactor Decontamination Information Exchange Group, Pittsburgh, Pa., Feb. 26–28, 1964
Sweeton, F. H., and C. F. Baes, Jr.	Magnetite as a High-Temperature Adsorbent in Pressurized-Water Systems	American Nuclear Society, Philadelphia, Pa., June 15–17, 1964
Thoma, R. E.	Complex Compounds in the Sodium Fluoride–Rare-Earth Trifluoride Systems	4th Rare Earth Research Conference, Phoenix, Ariz., Apr. 22–25, 1964
Thoma, R. E., and B. J. Sturm	Molten Salt Solvents for Fluoride Volatility Processing of Aluminum-Matrix Nuclear Fuel Elements	American Chemical Society Meeting, Chicago, Ill., Aug. 30–Sept. 4, 1964

AUTHOR(s)	TITLE	PLACE PRESENTED
Watson, G. M.	Gas Transport in Porous Media as Applied to Gas-Cooled Reactors	ORINS Traveling Lecture Program, Loyola University, New Orleans, La., Apr. 16, 1964
	Self Diffusion of Beryllium in Beryllium Oxide	ORINS Traveling Lecture Program, Loyola University, New Orleans, La., Apr. 16, 1964
		ORINS Traveling Lecture Program, Louisiana State University, Baton Rouge, Apr. 14, 1964
		ORINS Traveling Lecture Program, Louisiana State University, New Orleans, Apr. 17, 1964
	Physico-Chemical Problems of Nuclear Reactors	ORINS Traveling Lecture Program, University of Florida, Gainesville, May 4, 1964
	Gas Transport in Porous Media as Applied to Gas-Cooled Reactors	Union Carbide Research Institute, Tarrytown, N.Y., Aug. 12, 1964
	Self Diffusion of Beryllium in Beryllium Oxide	Union Carbide Research Institute, Tarrytown, N.Y., Aug. 13, 1964
	Chemical Aspects of Nuclear Safety	ORINS Traveling Lecture Program, Tarleton State College, Stephenville, Tex., Oct. 6, 1964

ORNL-3789
UC-4 – Chemistry
TID-4500 (39th ed.)

INTERNAL DISTRIBUTION

1. Biology Library
2–4. Central Research Library
5. Reactor Division Library
6. Laboratory Shift Supervisor
7–8. ORNL Y-12 Technical Library
Document Reference Section
9–58. Laboratory Records Department
59. Laboratory Records, ORNL R.C.
60. C. E. Larson
61. A. M. Weinberg
62. H. G. MacPherson
63–77. G. E. Boyd
78. F. R. Bruce
79. F. L. Culler
80. W. H. Jordan
81. A. H. Snell
82. G. Young
83. A. F. Rupp
84. M. Bender
85. A. L. Boch
86. R. B. Briggs
87. W. B. Cottrell
88. A. P. Fraas
89. K. A. Kraus
90. J. A. Lane
91. A. J. Miller
92. D. B. Trauger
93. G. D. Whitman
94. S. E. Beall
95. D. S. Billington
96. D. E. Ferguson
97. J. H. Frye, Jr.
98. M. T. Kelley
99. E. H. Taylor
100. M. A. Bredig
101. L. T. Corbin
102. J. E. Cunningham
103. J. H. Crawford
104. E. M. King
105. R. N. Lyon
106. R. B. Parker
107. M. J. Skinner
108. J. C. White
109. G. C. Williams
110. W. R. Grimes
111. E. G. Bohlmann
112. H. F. McDuffie
113. G. M. Watson
114. F. F. Blankenship
115. C. H. Secoy
116. C. F. Baes
117. A. L. Bacarella
118. C. J. Barton
119. C. D. Bopp
120. W. E. Browning
121. G. D. Brunton
122. J. H. Burns
123. S. Cantor
124. R. M. Carroll
125. E. L. Compere
126. M. E. Davis
127. R. J. Davis
128. J. L. English
129. R. B. Evans III
130. E. L. Fuller, Jr.
131. J. C. Griess
132. H. F. Holmes
133. G. H. Jenks
134. G. W. Keilholtz
135. M. J. Kelly
136. S. S. Kirslis
137. R. A. Lorenz
138. A. P. Malinauskas
139. W. L. Marshall
140. C. E. Miller
141. R. E. Moore
142. J. G. Morgan
143. L. G. Overholser
144. G. W. Parker
145. W. W. Parkinson
146. A. S. Quist
147. W. T. Rainey
148. S. A. Reed
149. D. M. Richardson
150. K. A. Romberger
151. H. C. Savage
152. D. R. Sears
153. J. H. Shaffer
154. A. J. Shor
155. M. D. Silverman
156. O. Sisman
157. B. A. Soldano
158. R. A. Strehlow

159. F. H. Sweeton
160. R. E. Thoma
161–168. G. C. Warlick
169. C. F. Weaver
170. L. B. Yeatts
171. L. Brewer (consultant)
172. F. Daniels (consultant)
173. R. W. Dayton (consultant)
174. J. W. Cobble (consultant)
175. J. F. Eastham (consultant)
176. P. H. Emmett (consultant)
177. D. G. Hill (consultant)
178. H. Insley (consultant)
179. H. R. Jolley (consultant)
180. E. V. Jones (consultant)
181. T. N. McVay (consultant)
182. G. Mamantov (consultant)
183. E. A. Mason (consultant)
184. R. F. Newton (consultant)
185. R. B. Perez (consultant)
186. J. E. Ricci (consultant)
187. G. Scatchard (consultant)
188. D. A. Shirley (consultant)
189. H. Steinfink (consultant)
190. T. F. Young (consultant)

EXTERNAL DISTRIBUTION

191. L. R. Zumwalt, General Atomic Division, General Dynamics Corp., San Diego, Calif.
192. R. W. McNamee, Union Carbide Corporation, New York
193. Research and Development Division, AEC, Washington
194. Research and Development Division, AEC, ORO
195. Reactor Development Division, AEC, Washington
196. Reactor Development Division, AEC, ORO
197. Union Carbide Corporation, Chemicals Division, South Charleston
198–755. Given distribution as shown in TID-4500 (39th ed.) under Chemistry category (75 copies – CFSTI)